Study of surrogate reactions at heavy-ion storage rings

Michele Sguazzin

Université de Bordeaux

École Doctorale des
Sciences Physiques et de l'Ingénieur

Étude des reactions de substitution auprès des anneaux de stockage d'ions lourds

Study of surrogate reactions at heavy-ion storage rings

Thèse présentée pour obtenir le titre de
DOCTEUR
Spécialité: Astrophysique, Plasmas et Nucléaire

Par **Michele Sguazzin**

Soutenue publiquement le 28/03/2023 devant un jury composé de:

Rapporteurs:	Francois De Oliveira	Directeur de recherche GANIL, Caen
	Jonathan Wilson	Directeur de recherche IJCLab, Orsay
Examinateurs:	Marlène Assié	Chargée de recherche IJCLab, Orsay
	Manfred Grieser	Chercheur senior Max-Planck Institute, Heidelberg
Président:	Sara Naimi	Directrice de recherche IJCLab, Orsay
Directrice de thèse:	Beatriz Jurado	Directrice de recherche LP2I, Bordeuax

---

This work was supported by the European Research Council (ERC) under the European Union's Horizon 2020 research and innovation programme (ERC-Advanced grant NECTAR, grant agreement No 884715) and the Prime 80 program from the CNRS.

Acknowledgements

In the meanwhile I'm writing these words, I realise the speed with which the years of my Ph.D. have passed and the multitude of tough but also extremely pleasant moments that I have experienced. It only seems like yesterday that among the various Ph.D. offers, luckily for me, I decided to apply for the one proposed by Beatriz. When I left Italy and embarked me on the adventure of this Ph.D. abroad, I can not hide that I was a little bit scared from what was waiting for me. Anyway, shortly after my arrival at the laboratory I felt right at home thanks to the kind welcome and support of the fantastic people that I found. In this respect I know, even if I will try to do my best, that I cannot describe in the few sentences of these acknowledgements the gratitude and admiration I feel for them.

First of all I would like to thank my closest colleagues, Beatriz Jurado and Jerome Pibernat, the "permanent NECTARians", for the amazing years we spent together at the laboratory. Working with you on the NECTAR project was not only a pleasure but also a great honour. From each of you I learnt several things and you helped me to grow from both a cultural and a personal point of view. Particular thanks go to Beatriz! You have always believed in me and my abilities even when (very often!) I doubted it myself. You have driven me as a lighthouse from the beginning up to the end of my Ph.D. and pushed me in particular during the difficult last year. Thank you for the long discussions we had together, from which I learnt several things and for having transmitted to me all your passion and made me enjoy even more physics... To Jerome I want to give special thanks for all the work done on the solar cells and not only, for his sympathy and for having taught me the real meaning of "Sopa de Caracol"!

If I now know several things about vacuum and pumps, it was only possible thanks to Bertrand Thomas and the time spent together on our big boy "TREVO". In the next months and years I will really miss working together! I would like also to express my gratitude to the "Nectarians postdocs" Ana Henriques, Paola Marini and Jacobus Swartz with whom I had the great pleasure to work intensively, even if for a short period, during the years of my Ph.D. I also dedicate a small thought to Camille Berthelot the new Ph.D. of NECTAR, whom I had the pleasure of meeting in the last year of my Ph.D. and to whom I wish the best of luck.

I must necessarily stress the very welcome contribution given to this thesis but also to the

whole project by Manfred Grieser from the MPIK in Heidelberg. You are an honorary member of the NECTAR team and it is only thanks to your expert guide that we were able to do such amazing things with storage rings. I will bring forever the memory of our weekly Friday meetings from which I learnt so many things about rings. I wish we will have the opportunity to work together in the future.

Between all other collaborators who made it possible to carry out the experiments and without whom this thesis would not have been possible, I must deeply thank Jan Glorious from the GSI and Jean-Charles Thomas from GANIL for their fundamental contributions. I would also like to express my gratitude to the collegues of CEA, Marc Dupuis and Vincent Meot for their availability and crucial help in the theoretical interpretation of the experimental data.

Thank you so much to the members of the jury for their time and for having read my thesis. It was a great honour to meet you and being able to present you my Ph.D. work! Merci beaucoup infinitement aux services du LP2iB (ex-CENBG), au groupe ACEN et en particulier aux membres du groupe NEX pour m'avoir accueilli pendant mes années de doctorat. Je tiens également à remercier Sylvie Perreve et Nadine Carmona pour leur gentillesse et leur aide avec les tâches administratives.

In the end, I would like to leave a special dedication to my parents, my brothers and my life partner Giulia. You are my wonderful family! You were my real strength during all these years, and all the accomplishment I was able to achieve would not have been possible without you. In both the most difficult and the happiest moments of my life you have always been there to support me and I want to show my eternal gratitude dedicating to you this thesis.

Abstract

Neutron-induced reaction cross sections of unstable nuclei are essential for understanding the synthesis of heavy elements in stars and for applications in nuclear technology. However, their direct measurement is very complicated due to the radioactivity of the targets involved. We propose to circumvent this problem by using the surrogate reaction method in inverse kinematics, where the compound nucleus formed in the neutron-induced reaction of interest is produced by an alternative or surrogate reaction involving a radioactive heavy-ion beam and a stable, light target nucleus. The probabilities as a function of the compound-nucleus excitation energy for gamma-ray emission, neutron emission and fission, which can be measured with the surrogate reaction, are particularly useful to constrain fundamental model parameters that describe the de-excitation of the compound nucleus and significantly improve the predictions of the neutron-induced reaction cross sections of interest.

In the first part of this thesis work, the first proof of principle experiment conducted within the frame of the NECTAR (Nuclear rEaCTions At storage Rings) project is described. In this experiment, a surrogate reaction in inverse kinematics was combined for the first time with the unique possibilities at heavy-ion storage rings. This measurement took place at the Experimental storage ring (ESR) of the GSI/FAIR facility (Germany), where the inelastic scattering $^{208}Pb(p,p')$ reaction was used as a surrogate reaction for the neutron-capture reaction of ^{207}Pb. With our new experimental set-up we were able to simultaneously measure for the first time both the gamma- and neutron-emission decay probabilities of the compound nucleus $^{208}Pb^{\star}$. The obtained results allowed us to validate our new methodology and demonstrate the significant advantages of storage rings, which enable the measurement of the excitation energy with high precision and a dramatic increase of the detection efficiencies for gamma-ray and neutron emission. In addition, the comparison of the measured probabilities with the statistical model implemented in the Talys code has allowed us to gain insight into the de-excitation process of $^{208}Pb^{\star}$.

Storage rings are operated in ultra-high vacuum (UHV) conditions (10^{-10}-10^{-11} $mbar$), a pressure level four to five orders of magnitude lower than in standard experiments. This sets severe constrains for in-ring detection systems. In this work, we propose a completely new solution based on the use of solar cells, which represent an interesting option for the use in storage rings thanks to their radiation hardness. The second part of this thesis describes the studies we have performed to study the feasibility of using solar cells for the in-ring detection of heavy

ions. We performed an experiment at GANIL facility (Caen, France) with a ^{84}Kr beam of energies ranging from 5 to 15 MeV/u to investigate the response of solar cells and their radiation resistance. Our results reflect the good performances of solar cells in terms of energy resolution, time resolution and their larger radiation resistance compared to silicon detectors. The comparison with simulations carried out with the ATLAS Silvaco software allowed us to significantly improve our understanding of the mechanism responsible for the signal generation in solar cells. In parallel, we have studied the UHV compatibility at our test bench, which has shown a very low outgassing rate of solar cells well below the limits established by GSI/FAIR for integration into the ring.

Synthèse (en français)

Les réactions induites par neutron sur des noyaux radioactifs sont très importantes en astrophysique nucléaire, notamment pour comprendre la nucléosynthèse stellaire des éléments au-delà du fer, mais aussi pour certaines applications, comme pour la production d'énergie et de radio-isotopes médicaux. Généralment les mesures des sections efficaces de réaction induite par neutron se réalisent en cinématique directe où un faisceau de neutrons interagit avec une cible.

Cependant, lorsque les noyaux cibles ont des courtes durées de vie, ce type de mesures devient très difficile, voire impossible, en raison de la très forte radioactivité des cibles nécessaires. Ces sections efficaces sont aussi difficiles à calculer, car en absence de données expérimentales nous ne savons pas décrire de manière précise le processus de désexcitation du noyau suite à la capture d'un neutron. L'approche la plus prometteuse pour surmonter ces difficultés consiste à utiliser des réactions de substitution en cinématique inverse. La figure 1 montre schématiquement le principe de la méthode de substitution. Un même noyau composé que celui produit par la réaction induite par neutron d'intérêt est produit dans une réaction alternative ou de substitution qui est, elle, expérimentalement réalisable. La réaction de substitution est une réaction à deux corps, typiquement une réaction de diffusion inélastique ou de transfert. Les probabilités de désexcitation par émission de rayon gamma, émission d'un neutron ou par fission sont mesurées en fonction de l'énergie d'excitation du noyau composé. L'énergie d'excitation $E^\star$ est obtenue et en appliquant la conservation de l'énergie et de l'impulsion avec la mesures de l'énergie du faisceau, de l'énergie de l'éjectile w et de l'angle entre le deux. Les probabilités de désexcitation sont des observables précieuses pour contraindre différentes propriétés nucléaires fondamentales (coefficients de transmission, les densités de niveaux, les barrières de fission, etc). Ces quantités sont essentielles pour décrire la désexcitation des noyaux et obtenir des prédictions beaucoup plus précises des sections efficaces induites par neutron d'intérêt.

La cinématique inverse permet l'étude de noyaux à très courte durée de vie car il est possible de les produire en forme de faisceaux radioactifs et de les faire interagir avec un noyau cible léger. En outre, la cinématique inverse permet aussi la détection de résidus lourds produits après l'émission gamma et l'émission neutron, augmentant ainsi significativement l'efficacité de détection par rapport aux experiences en cinématique directe, dans lequelles il est nécessaire de détecter les rayonnements gamma et les neutrons pour obtenir les probabilités d'émission gamma et neutron. Cependant, les probabilités de désexcitation changent très rapidement avec

l'énergie d'excitation aux seuils d'émission de neutrons et de fission. La résolution en énergie d'excitation nécessaire pour étudier cette évolution rapide est de quelques 100 keV, ce qui est assez difficile à réaliser avec des faisceaux d'ions lourds en cinématique inverse, en raison de problèmes de longue date liés à la cible. En effet, la densité et l'épaisseur importantes de la cible entraînent une perte d'énergie significative et des effets de "straggling" qui se traduisent par une grande incertitude sur l'énergie du projectile au point d'interaction, ainsi que sur l'angle d'émission et l'énergie du résidu de la cible. En outre, la présence de fenêtres et d'impuretés dans la cible induit un bruit de fond.

L'objectif principal de la première partie de cette thèse, réalisée dans le cadre du projet NEC-

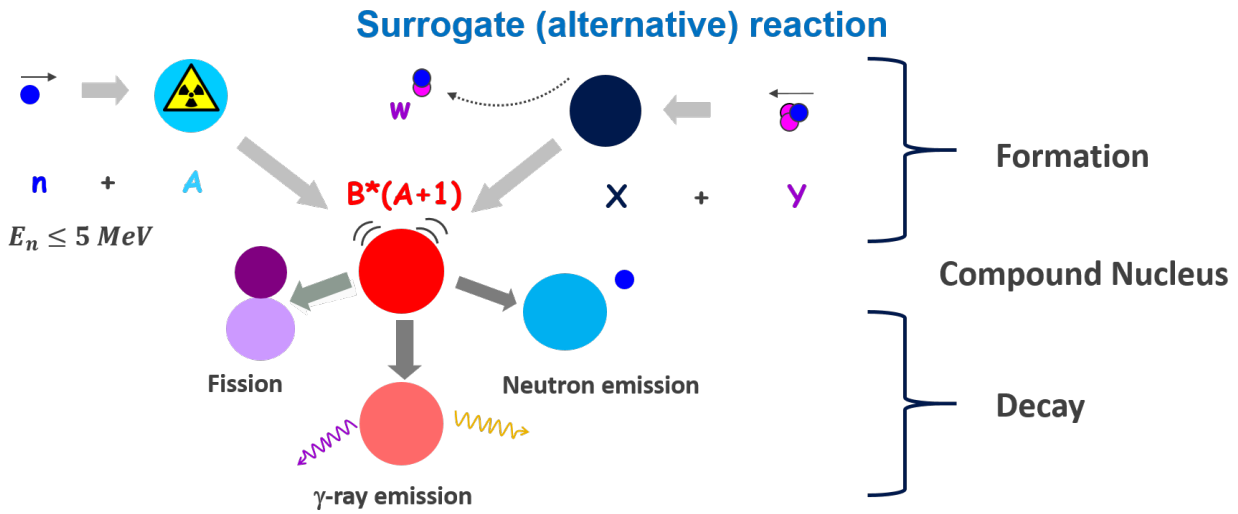

Figure 1: Représentation schématique d'une réaction de capture neutronique, $n + A \rightarrow B^{\star}$, et d'une des réaction de substitution en cinématique directe, $X(y, w)B^{\star}$. Lorsque le noyau composé $B^{\star}$ est formé il se désexcite avec une certaine probabilité par l'émission de rayonnements gamma (P_{γ}), d'un neutron (P_n) ou par fission (P_f). Le noyau cible utilisé dans la réaction de substitution est moins radioactif que le noyau cible associé à la réaction neutronique.

TAR (Nuclear rEaCTions At storage Rings), est d'utiliser pour la première fois la méthode de substitution en cinématique inverse auprès d'un anneau de stockage. Cette combinaison offre des conditions expérimentales uniques en termes de précision et d'efficacité de détection pour la mesure des probabilités de désexcitation.

Dans les anneaux de stockage d'ions lourds la grande qualité des faisceaux radioactifs stockés, combinée avec l'utilisation de cibles ultra-minces et sans fenêtre, permet de déterminer l'énergie d'excitation avec une résolution de quelques centaines de keV. En outre, les dipôles magnétiques de l'anneau permettent de séparer les résidus lourds de réaction produits après l'émission de rayons γ et de neutrons, rendant alors possible leur détection avec une très grande efficacité. Il est ainsi possible de déterminer les probabilités de désexcitation de nombreux noyaux à courte durée de vie avec une haute précision. Cependant, les anneaux de stockage sont opérés en ultravide (10^{-10}-10^{-11} $mbar$), ce qui pose de sérieuses contraintes, sur les systèmes de détection qui peuvent être insérés.

En Juin 2022 nous avons mené avec succès une première expérience de preuve de principe dans l'anneau de stockage ESR de l'installation GSI/FAIR en Allemagne. Dans cette expérience nous avons étudié la diffusion inélastique d'un faisceau de $^{208}Pb^{82+}$ à 30.77 MeV/u sur une cible à jet de gaz d'hydrogène (H_2). L'objectif était de mesurer, pour la première fois, simultanément les probabilités d'émission gamma ($^{208}Pb^{\star} \rightarrow \gamma + {}^{208}Pb$) et neutron ($^{208}Pb^{\star} \rightarrow n + {}^{207}Pb$) du ^{208}Pb. Le ^{208}Pb excité a été produit au moyen d'une réaction de substitution était donc du $^{208}Pb(p,p')^{208}Pb^{\star}$ qui est associée à la réaction neutronique $n + {}^{207}Pb \rightarrow {}^{208}Pb^{\star}$. Pour mesurer les probabilités d'émission gamma et neutron en fonction de l'énergie d'excitation du ^{208}Pb, nous avons mis au point deux systèmes de détection, l'un pour les protons diffusés et l'autre pour les noyaux de $^{208}Pb^{82+}$ et de $^{207}Pb^{82+}$ produits respectivement après la désexcitation par émission de rayon gamma et par l'émission d'un neutron. Dans la figure 2, une vue d'ensemble

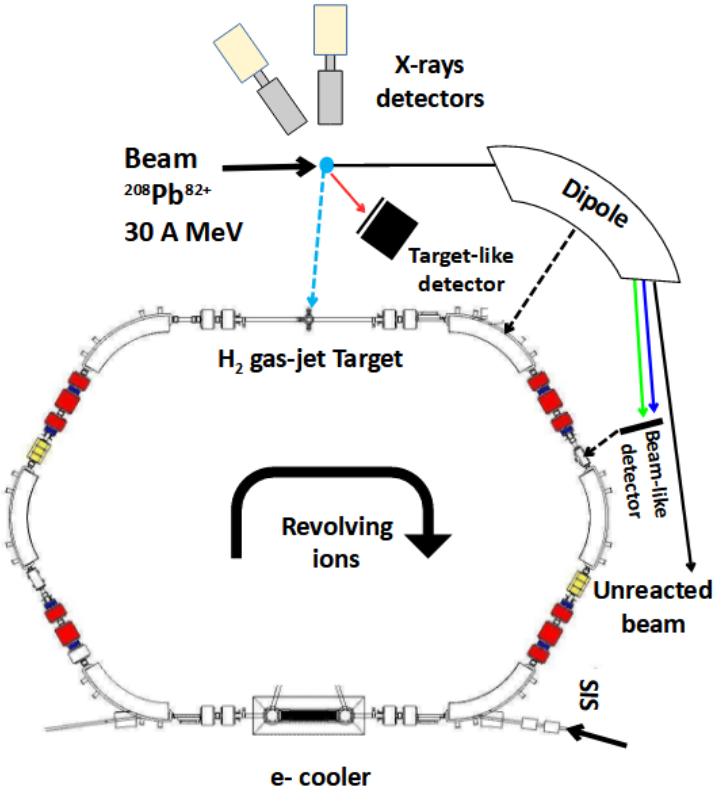

Figure 2: Représentation schématique de l'anneau de stockage ESR au GSI. La section zoomée en haut illustre la partie de l'anneau où nous avons installé nos détecteurs. Le télescope pour la détection des protons (flèche rouge) est représenté. Le détecteur des résidus lourds est représenté après le premier dipôle magnétique. La flèche noire indique le faisceau qui n'a pas interagi avec la cible. Les résidus lourds produits après l'émission γ et neutron sont indiqués par les flèches bleue et verte, respectivement.

de l'installation utilisée pour l'expérience à l'ESR est présentée. Le détecteur de protons était situé à proximité de la cible et consistait en un télescope de silicium (ΔE-E) segmenté. Le détecteur de résidus lourds était un détecteur de silicium segmenté, placé après le premier dipôle situé en aval de la cible. Pour préserver les conditions d'ultravide de l'ESR, les détecteurs ont

été placés dans des enceintes (dites pockets) avec des fenêtres minces en acier inoxydable de 25 μm, par lesquelles les protons et les résidus de plomb atteignaient les détecteurs. En outre, deux détecteurs au germanium ont également été placés autour de la cible pour mesurer les rayons X émis après la capture d'électrons par le faisceau dans la cible. Ceci nous a permis de monitorer la luminosité lors de l'expérience.
Le télescope nous a permis de mesurer l'énergie cinétique et l'angle d'émission des protons diffusés pour déterminer l'énergie d'excitation du ^{208}Pb. Les résidus lourds (ou résidus du faisceau) ont été détectés en coïncidence avec les protons diffusés. Comme on peut le voir sur la figure 2, le dipôle agit comme un spectromètre de recul séparant le faisceau qui n'a pas interagi (flèche noire), les résidus $^{208}Pb^{82+}$ produits après émission gamma (flèche bleue) et les résidus $^{207}Pb^{82+}$ produits après l'émission d'un neutron (flèche verte).
Les probabilités de désexcitation associées à la réaction de substitution $P_{\chi}^{surr.}(E^{\star})$, sont déterminées à partir de l'équation suivante:

$$P_{\chi}^{surr.}(E^{\star}) = \frac{N_{\chi}(E^{\star})}{N_s(E^{\star}) \cdot \epsilon_{\chi}(E^{\star})} \tag{1}$$

Où $N_{\chi}(E^{\star})$ est le nombre de résidus lourds détectés pour la voie de désexcitation χ en coïncidence avec des protons, $N_s(E^{\star})$ est le nombre total de protons détectés et $\epsilon_{\chi}(E^{\star})$ est l'efficacité de détection des residus lourds pour les réactions dans lesquelles le proton diffusé a été détecté. Dans le cadre de cette expérience, nous avons développé un programme de simulation qui inclut une description très détaillée du dispositif expérimental. Ce programme a été utilisée pour concevoir nos systèmes de détection et a été validé avec nos données expérimentales. Cela montre que nous avons un bon contrôle de notre expérience et que nous pouvons valider notre dispositif expérimental et notre méthodologie pour déduire simultanément les probabilités d'émission de gamma et de neutron. Au moyen de cette simulation il a été possible de déterminer l'efficacité de détection en fonction de l'énergie d'excitation $\epsilon_{\chi}(E^{\star})$.

Lors de cette première expérience, nous avons pu confirmer la séparation complète, comme le montre la figure 3, et la détection très efficace des résidus de $^{208}Pb^{\star}$ et de $^{207}Pb^{\star}$ produits après l'émission de rayons γ et d'un neutron, respectivement. Nous avons obtenu une efficacité de détection pour l'émission γ allant de 55 à 100% et une efficacité de détection pour l'émission neutron de 100%. Cela représente une avancée majeure par rapport aux expériences en cinématique directe où il faut détecter les rayons γ et les neutrons, ce qui se traduit par des efficacités de détection de quelques pourcents seulement. C'est grâce à des efficacités si élevées qu'il a été possible d'atteindre des incertitudes inférieures à 5% pour les probabilités, notamment pour la probabilité d'émission neutron, malgré les statistiques limitées de l'expérience. Nous soulignons que c'est la première fois que la probabilité d'émission de neutron a été mesurée.
La résolution en énergie d'excitation varie entre 600 et 750 keV à $E^{\star}$=0 pour cette première expérience. Cette résolution est dominée par l'incertitude sur l'angle d'émission des protons due au grand rayon de la cible d'hydrogène d'environ 2.5 mm. Nos simulations prévoient qu'avec

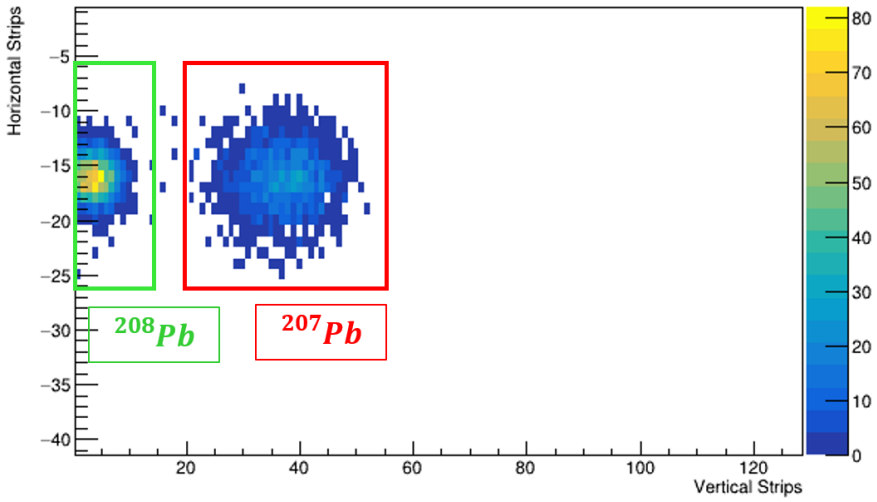

Figure 3: Nombre d'événements en fonction du nombre de pistes verticales et horizontales mesurées pour le détecteur HR. Nous pouvons clairement identifier deux distributions bien séparées, l'une à gauche et l'autre à droite, appartenant respectivement aux ions $^{208}Pb^{82+}$ provenant des réactions de diffusion inélastique où le HR se désexcite par émission de rayons gamma et aux ions $^{207}Pb^{82+}$ provenant des réactions de diffusion inélastique où le HR se désexcite par émission de neutrons.

un rayon de 0.5 mm nous pourrions atteindre une résolution de 250 keV, voire meilleure. Une cible de telle dimension sera disponible pour notre prochaine expérience.

Les probabilités de désexcitation mesurées expérimentalement en fonction de l'énergie d'excitation sont présentées dans la figure 4. On voit que pour des énergies d'excitation inferieures à l'énergie de séparation neutron ($S_n = 7.37\ MeV$), la probabilité d'émission neutron P_n est nulle et P_γ est égale à 1, car à ces énergies d'excitation, l'émission gamma est la seule voie ouverte pour la désexcitation du noyau composé. A partir de 7.37 MeV, l'émission d'un neutron devient possible et cette voie de désexcitation rentre en compétition avec la voie d'émission gamma. Lorsque P_n augmente P_γ diminue, mais puisqu'il s'agit des seules voies de désexcitation possibles leur somme doit être égale a 1, ce qui est correspond bien à nos données. Les probabilités de désexcitation mesurées en fonction de l'énergie d'excitation ont été comparées aux calculs basés sur le modèle statistique de Talys, où les distributions de spin/parité peuplées dans la réaction $^{208}Pb(p,p')$ ont été calculées avec un modèle développé par Marc Dupuis basé sur la quasiparticle random phase approximation (QRPA) et la distorted wave Born approximation (DWBA). Comme on peut le voir dans la figure 4, l'accord entre nos données et les calculs est en général très bon.

Ce travail de thèse sera complété à court terme par une étude de sensibilité afin d'identifier les paramètres les plus pertinents des calculs du modèle statistique et d'utiliser nos probabilités de désexcitation pour les fixer. Les paramètres ajustés seront ensuite implémentés dans Talys pour déduire la capture radiative induite par neutron et les sections efficaces inélastiques du ^{207}Pb. En 2024, nous prévoyons de réaliser une deuxième expérience de preuve de principe avec

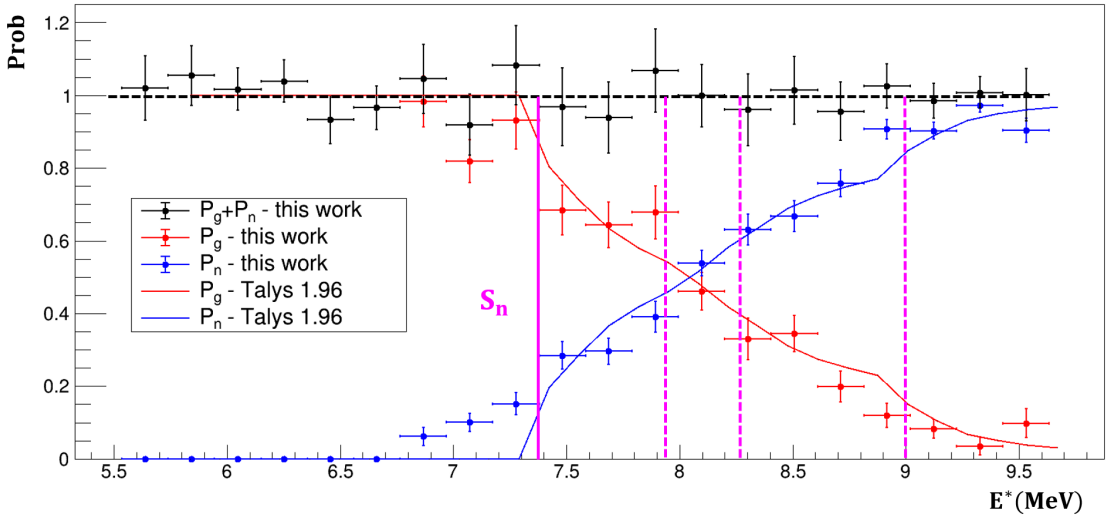

Figure 4: Comparaison des probabilités expérimentales en fonction de l'énergie d'excitation du ^{208}Pb avec celles calculées avec Talys. La probabilité de désexcitation γ est représentée en rouge et la probabilité d'émission neutron en bleu. Les symboles représentent les données expérimentales et les lignes pleines les calculs de Talys. Dans la figure, la somme expérimentale des deux probabilités est représentée en noir. Les lignes pleines verticales représentent l'énergie de séparation du neutron et les lignes verticales en pointillés la position des premiers états excités du ^{207}Pb. La ligne horizontale à $P = 1$ sert à guider le regard.

un faisceau de $^{238}U^{92+}$ et une cible de deutérium. Nous étudierons les réactions de substitution $^{238}U(d,d')^{238}U^{\star}$ et $^{238}U(d,p)^{239}U^{\star}$ en mesurant, en plus des probabilités d'émission gamma et neutrons, la probabilité de fission. À cette fin, nous complèterons le dispositif utilisé dans la première expérience avec trois détecteurs de fission, dont l'un sera constitué de cellules photovoltaïques. Ce sera la première fois qu'une réaction de fission sera étudiée dans un anneau de stockage.

À plus long terme, nos expériences auprès de l'ESR bénéficieront de la disponibilité d'une cible à jet de gaz d'un rayon de 0.5 mm. En outre, dans le cadre de NECTAR, nous développerons une chambre de réaction dédiée pour l'ESR, qui nous permettra d'augmenter de manière significative l'angle solide des détecteurs de résidus de la cible et de fission et de mesurer non seulement les probabilités d'émission γ, d'émission neutron et de fission, mais aussi les probabilités d'émission de deux neutrons. Une fois la méthodologie et le dispositif expérimental validés et optimisés, nous serons en mesure d'atteindre l'objectif ultime de NECTAR, qui est de déduire indirectement les sections efficaces de réaction induites par neutron de nombreux noyaux à durée de vie courte dans différentes régions en utilisant des faisceaux radioactifs.

Dans un premier temps, nous utiliserons des faisceaux primaires de ^{238}U et ^{208}Pb, par exemple, et des faisceaux secondaires proches produits par fragmentation.

À plus long terme, nous visons à explorer la région des actinides et pré-actinides déficients en neutrons vers la fermeture en couche $N = 126$. Ce sera la première fois que les probabilités de

fission seront mesurées près d'une fermeture en couche. Ceci est particulièrement intéressant car la faible densité d'états typique des noyaux magiques peut avoir un impact significatif sur leurs probabilités de désexcitation. Ces études permettront de fournir de bien meilleures prévisions théoriques pour les barrières de fission et les sections efficaces des noyaux riches en neutrons vers la fermeture en couche $N = 184$, qui sont essentielles pour la compréhension du processus de capture rapide (processus r) et qui ne sont pas encore accessibles aux expériences.
Dans la première partie du manuscrit, nous avons vu que nos détecteurs étaient placés dans des poches derrière des fenêtres très fines en acier inoxydable. Cependant, cette solution ne sera pas possible pour nos futures études de fission, car les fragments de fission peuvent avoir des énergies aussi basses que quelques MeV/u et peuvent être arrêtés dans la fenêtre en acier inoxydable. C'est pourquoi les détecteurs de fission doivent être placés directement dans l'anneau.

La deuxième partie de cette thèse est dédiée à l'étude d'une technologie innovante, basée sur l'utilisation des cellules solaires pour la détection d'ions lourds dans les anneaux de stockage. Les cellules solaires apparaissent comme une alternative très prometteuse aux détecteurs au silicium standard pour la détection d'ions lourds. En effet, les cellules solaires se sont révélées plus résistantes à l'irradiation que les détecteurs silicium. En outre, elles sont très robustes et fournissent une bonne réponse en énergie et temps. Toutes ces propriétés ont été observées lors d'études précédentes sur ions lourds jusqu'à 1 MeV/u.
L'utilisation des cellules solaires est particulièrement intéressante pour les expériences menées à l'intérieur des anneaux de stockage. C'est pourquoi le projet NECTAR vise à développer un détecteur de fission composé de cellules photovoltaïques. Pour ce faire, il faut d'évaluer tout d'abord la réponse des cellules photovoltaïques aux fragments de fission dont l'énergie est supérieure à 1 MeV/u et leur compatibilité avec l'ultravide. Ces deux aspects constituent l'objectif de la deuxième partie de cette thèse.
Nous avons réalisé une expérience au GANIL (Grand Accélérateur National d'Ions Lourds) avec un faisceau de ^{84}Kr à 5, 10, 15 MeV/u où nous avons caractérisé la réponse de différentes cellules solaires de 10x10 mm^2 et 20x20 mm^2. Une partie des cellules sert à la production d'électricité sur Terre et une autre partie à la production dans l'espace. Nous avons observé une saturation du signal d'amplitude des cellules solaires avec l'augmentation de l'énergie du faisceau et nous avons mesuré une résolution en énergie ($RMS(E)/ < E >$) allant de 1% à 3%, la résolution en temps variant entre 2.5 et 4.5 ns (FWHM). C'est la première fois que nous observons d'aussi bonnes performances pour des cellules aussi grandes que 20x20 mm^2.
La réponse des cellules est restée stable lors de l'irradiation pendant 1 heure à un taux de quelques milliers de pps. Au-delà d'une heure d'irradiation, l'amplitude a commencé à diminuer progressivement et la résolution en énergie à se détériorer, jusqu'à ce qu'une stabilisation soit atteinte. Un comportement similaire a été observé à des taux d'irradiation plus élevés de 50k pps. Il est intéressant de noter que la réponse temporelle est restée stable pour tous les taux. Les cellules solaires destinées aux applications spatiales se sont révélées plus résistantes

aux rayonnements.
Nous avons fait des efforts considérables pour comprendre la réponse observée des cellules photovoltaïques et le mécanisme impliqué dans la génération du signal de la cellule, appelé "field funnelling effect". Dans ce cadre, nous avons utilisé le logiciel ATLAS Silvaco pour simuler l'impulsion de courant générée par interaction avec un ion ^{84}Kr de différentes énergies. Cela nous a permis de reproduire la saturation observée, qui a lieu autour de 7 MeV/u et qui est due à une perte d'efficacité de collection des charges qui se produit lorsque les ions énergétiques pénètrent plus profondément dans le substrat. À notre connaissance, c'est la première fois qu'une telle étude a été réalisée.
Nous avons étudié la compatibilité avec l'ultravide des cellules spatiales de 20x20 mm^2. Les études ont été réalisées pour une cellule standard et une cellule encapsulée dans une enveloppe de polymide. Dans les deux cas, le dégazage mesuré était bien en dessous des limites imposées par le GSI, en outre, la réponse n'a pas été affectée par les processus d'étuvage à 200 $°C$.
Tous ces travaux ont démontré les bonnes performances de cellules photovoltaïques lorsqu'elles sont utilisées pour la détection d'ions lourds avec des énergies $E > 1$ MeV/u. En particulire, il faut insister sur le bon comportement des cellules solaire 20x20 mm^2 provenant des applications spatiales qui seront utilisées pour construire un détecteur des fragments de fission pour notre prochaine expérience en 2024. Dans cette expérience, nous utiliserons de nouveaux préamplificateurs qui sont en cours de développement au LP2iB. Il serait intéressant d'étendre l'étude de la réponse des cellules solaires pour d'autres ions et énergies. Un autre axe de recherche à explorer est la lecture des contacts sur la surface des cellules afin d'extraire des informations sur la position des ions. Les applications futures des cellules photovoltaïques dépendront également de la possibilité de produire des détecteurs personnalisés en termes d'épaisseur, tout en garantissant un faible coût de production.

Contents

Introduction

The accurate knowledge of neutron induced reaction cross sections of short-lived nuclei is an essential point for the understanding of several processes occurring in nature. These neutron induced reaction cross sections play a key role in multiple fields such as applications in nuclear technologies, medical physics and nuclear astrophysics. In this latter frame, they represent a crucial information for modelling stellar element nucleosynthesis via the slow(s) and rapid(r) neutron capture processes [Rei14].
Nowadays the existing data on many unstable nuclei are missing. If available, they are often of very limited quality, with large uncertainties and important discrepancies between the different sets of data. The reason for this is that the high radioactive nature of the required target samples complicates significantly the direct measurement, due to radiation protection requirements and the huge background arising from the target radioactivity. Alternative approaches must then be used to obtain the neutron induced cross sections of interest.

While the elements from carbon to iron are found to be produced by fusion reactions during the evolutionary phases from stellar He to Si burning, most of the elements heavier than iron are essentially built up by neutron capture reactions in the slow (s) and rapid (r) processes. The s-process occurs in asymptotic giant branch (AGB) stars and massive stars ($M > 8M_{\odot}$), where there are relatively small neutron densities ($10^6 - 10^{11} cm^{-3}$) and intermediate temperatures (0.1-0.3 GK). Under these conditions, the radioactive nuclei will undergo β-decay more likely than capture a neutron, yielding a nucleosynthesis path that deviates only one or two neutrons from the stability valley (see fig. 5).
In the case of the r-process, on the contrary, the neutron density is very high, seed nuclei will capture many neutrons in a row and form very neutron-rich nuclei before they decay. This drives the r-process path very far away from the stable isotopes. As can be seen in figure 5, the r-process is terminated at extremely neutron-rich nuclei in the actinide region, which are very likely for undergo fission (pink arrow). Fission recycling can then occur where the fission fragments continue to undergo neutron captures and β-decays running up over the r-process path until fission again terminates the r-process path. After a few cycles, the abundances in the mass region $120 \lesssim A \lesssim 200$ can become dominated by the fission-fragment distributions [Gor15]. The r-process takes place in explosive scenarios, e.g., neutron star mergers (NS-NS) or the extremely neutron rich zones in supernovae, where very high neutron densities (10^{20} cm^{-3})

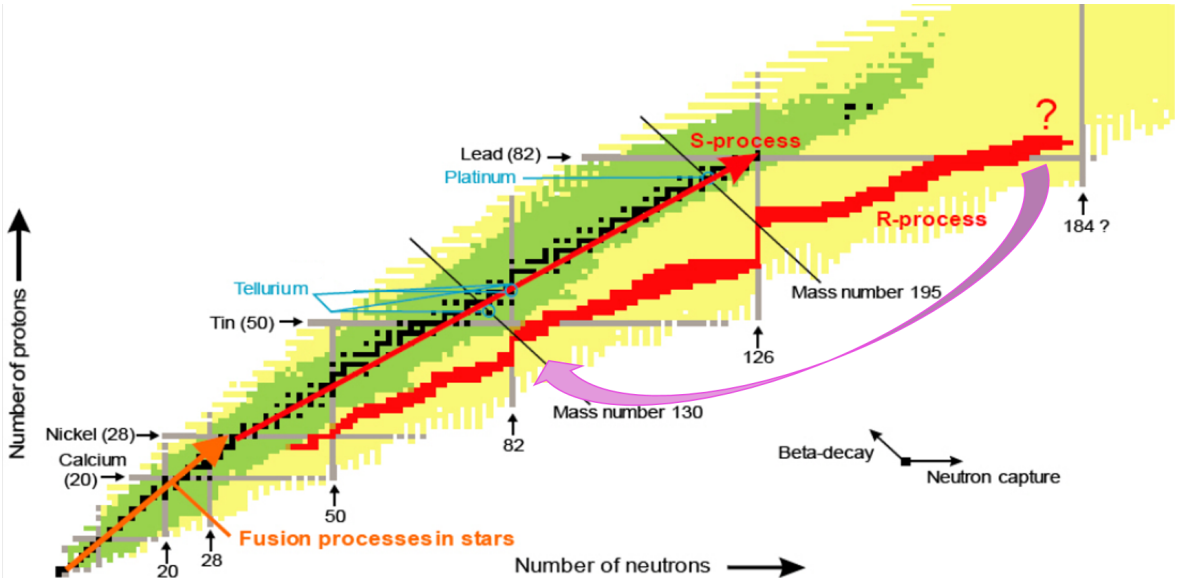

Figure 5: Nuclear chart showing the nucleosynthesis processes occurring during stellar burning (in orange), the s-process (red arrow, close to the stability valley) and the r-process (in red). The pink arrow going from Z=184 to Z=82 indicates the effect of fission.

and high temperatures (3 GK) are possible. The recent observation of the gravitational waves associated with a neutron-star merger [Abb17], and the subsequent kilonova understood to be powered by the decay of lanthanides [Sie19, Wat19], demonstrated that neutron-star mergers are an important r-process site.

Despite the present knowledge of the r-process, many uncertainties and open questions remain. For instance, it is not yet clear whether the r-process abundance distribution in the solar system is the result of one or multiple scenarios. The measurement of neutron-induced cross sections of key nuclei is essential to answer this question [Kaj19]. Sensitivity studies on neutron radiative capture cross sections described in [Mum19] show that the key nuclei are concentrated near closed shells and in the rare-earth region, where they impact the formation of the rare-earth peak of the r-process abundance pattern.

Furthermore, the role of nuclear fission is still unclear, since we do not know whether fission recycling occurs and how fission influences r-process observables such as abundance patterns and light curves [Wan20]. The most important physical quantities for understanding the impact of fission are neutron-induced fission cross sections, fission barriers and fission-fragment yields [Gor15, Vas19, Eic15, Zhu21]. It is difficult to predict the range of fissioning nuclei of interest since this significantly depends on the fission barriers, for which models give very different predictions. According to [Vas19], the nuclei that play a major role are located near the N=184 shell closure with Z∼90-98. However, in [Eic15] the key fissioning nuclei are not only located near N=184 but also at N<184, because, according to their models, fission is still very active during the decay back to stability. Fission barriers have also a dramatic impact on spontaneous fission half-lives, because a modification of the fission barrier of typically 1 MeV can affect the

half-life up to 9 orders of magnitude. These half-lives determine if spontaneous fission powers the late-time-kilonovae light curves, for example in [Zhu21] the potential importance of spontaneous fission heating was pointed out.
Neutron induced reaction cross sections of short-lived nuclei are key-input information also for technological applications. In the last years a large effort has been done towards the development of advanced nuclear systems that will use more efficiently the uranium resources, and produce a minimal amount of long-lived nuclear waste. The main activity concerns Generation IV reactors, with full or partial waste recycling capability, innovative fuel cycles like the thorium cycle and the transmutation of nuclear waste. The present knowledge of the neutron cross-sections is largely inadequate for new applications in the field of emerging nuclear technologies. In order to reduce uncertainties in the design and operation of new generation reactors, high precision data on the cross-section for neutron-induced reactions on a variety of nuclei are required, from thermal energy to several tens of MeV. The nuclei of interest are Np and Am isotopes for transmutation, $^{238,240,241}Pu$ for fast reactors, as well as $^{230,231,232}Th$ and $^{232,233,234,235}U$ isotopes for the thorium cycle. Pb and Bi isotopes are also interested in Bi/Pb-cooled reactors [Can21]. For many of these nuclei the existing data are of very limited quality [Zer18]. Even the fission cross sections are often measured with uncertainties larger than 20% and important discrepancies between different sets of data are observed [Tal15].

As said above, direct measurements of neutron-induced cross sections are very challenging for short-lived nuclei due to the radioactivity of the required targets. For most of these nuclei, the neutron-induced cross sections rely on theoretical model predictions, which often yield huge uncertainties due to the difficulties in describing the de-excitation process. The de-excitation process is ruled by fundamental properties (level densities, fission barriers, transmission coefficients, etc.) for which the existing nuclear models give very different values. This leads to discrepancies between the calculated cross sections as large as two orders of magnitude or more when no experimental data are available [Arn03, Arn07].
The problem of the target radioactivity can be solved by reversing the reaction kinematics. This implies to use, instead of a heavy radioactive target and a light beam, a heavy radioactive ion beam and a light target. However, in neutron-induced reactions inverting the kinematics would imply to use a free neutron target, which is currently not available. We propose an elegant solution to the problem of measuring neutron induced reaction cross sections of short-lived nuclei based on the use of surrogate reactions.
The surrogate-reaction method, proposed for the first time by J.C. Cramer and H.C. Britt [Cra70a], allows one to solve the challenge of producing a radioactive target by forming the excited nucleus of the desired neutron-induced reaction with an alternative or surrogate reaction that is experimentally accessible. The de-excitation (or decay) probabilities of the excited nucleus formed in the surrogate reaction are then measured as a function of the excitation energy and used to constrain the models for the fundamental nuclear properties described above,

enabling much more accurate predictions of the desired neutron induced cross sections.
Up to now, the surrogate reaction method has been used in experiments in direct kinematics. This type of experiments has many limitations. Again, reaching nuclei far from the stability valley requires to use radioactive targets which are unavailable or difficult to produce and handle. Competitive reactions in target contaminants and target backings can induce a high background very complicated or even impossible to remove. Moreover, the measurement of γ and neutron emission probabilities requires the detection of γ-rays and neutrons, which is very difficult due to the very low detection efficiencies.
Using the surrogate-reaction method in inverse kinematics enables for the formation of very short-lived nuclei and for the detection of the heavy, beam-like residues produced after the emission of γ-rays and neutrons. However, the decay probabilities of the excited nucleus change very rapidly with excitation energy at the neutron separation energy and at the fission threshold and they may show strong structures. The required excitation energy resolution to scan this evolution of the probabilities is about a few 100 keV, which is quite difficult to achieve for heavy nuclei in inverse kinematics due to multiple target issues.
Indeed, the required large target density and thickness lead to significant energy loss and straggling effects that translate into a large uncertainty in the energy of the projectile and in the emission angle and energy of the target residue at the reaction vertex. These target issues can be addressed by performing the surrogate reaction experiments in inverse kinematics at storage rings, which have many advantages with respect to the conventional single pass experiments in inverse kinematics, where the heavy ion beams pass the target only once. The most interesting capability of storage rings is beam cooling, possible thanks too the electron cooler technology [Steck04], which allows for a significant reduction of the size and energy spread of the stored ions. Furthermore, if a gas target is used in the ring, the electron cooler can compensate for the energy loss as well as the energy and angular straggling caused by the beam interaction with the target. This ensures the same beam conditions (in terms of energy and outstanding quality) at each passage through the target. In addition the frequent passing of the target zone (about 1 million of times per second at 10 MeV/u) allows gas-jet targets with ultra-low density (10^{13} $atoms/cm^2$) to be used and no windows are necessary.
The aim of this work is to contribute to the development of the NECTAR (Nuclear rEaCTion At storage Rings) project, whose objective is to combine for the first time surrogate reactions in inverse kinematics with the unique and largely unexplored possibilities at heavy-ion storage rings. This investigation was performed at the storage-ring complex of the GSI/FAIR facility (Germany) [Fra87, Les17] where we performed our proof of principle experiment. In this experiment the proton inelastic scattering $^{208}Pb(p,p')$ was used as surrogate for the $^{207}Pb + n$ reaction. This will be described in the first part of the thesis.
However, developing and performing experiments at storage rings requires facing important difficulties. One of the greatest challenges lies in the fact that the storage of heavy ions requires to reduce as much as possible the atomic interactions between the stored beam and the

residual gas inside the ring. For this reason, heavy-ion storage rings are operated in ultra-high vacuum (UHV) conditions (10^{-10}-10^{-11} $mbar$), a pressure level five to six orders of magnitude lower than in standard experiments [Lit13]. Reaching this vacuum quality is a complicated operation, which requires the use of very sophisticated pumping systems and special materials with very low outgassing rates. For this reason, UHV-compatible silicon detectors have started to be used only recently for pioneering in-ring nuclear reaction experiments [Zam17, Glo19]. Here, we propose a completely new idea based on the use of solar cells.

Solar cells have been used since several years for the detection of heavy ions. They represent an interesting option for the use in storage rings thanks to their radiation hardness [Sie79, Aji91]. The reason is that replacing damaged detectors implies venting the ring (or part of the ring) and re-establishing the UHV. This operation can take several weeks. Therefore, robust detectors are needed that show good performances until the end of the experimental campaign. However, in order to use solar cells in NECTAR, it is necessary to evaluate their response and radiation resistance with heavy ions of energies above 1 MeV/u and to study their UHV compatibility. These studies are described in the second part of this thesis.

Part I

Chapter 1

Compound-nuclear reactions and the surrogate-reaction method

The surrogate reaction method is based on the assumption that both the neutron induced and surrogate reaction proceed through the formation of a compound nucleus, which is the decaying nucleus. In this chapter we describe first the compound nucleus concept and the theoretical formalism to describe the compound nucleus reactions. At the end of the chapter, the principle of the surrogate reaction method is presented.

1.1 Reaction mechanism

A nuclear reaction can occur via different stages (direct, pre-equilibrium and compound) which can be classified depending on the reaction time. A simple conceptual model to describe a nuclear reaction was presented by E. Weisskopf [Wei57] and it can be seen in figure 1.1.
When a nucleus is bombarded with a particle, different scenarios can be described. If the projectile and target are within the range of nuclear forces for a very short time (typically 10^{-22} s), allowing for the interaction with a few individual nucleons only, a direct reaction takes place [Aus70]. This reaction mechanism accounts for processes in which the projectile causes individual particle excitations, like a particle-hole (p-h) pair.
As shown in figure 1.2, successive two-body single-particle interactions can happen after the entrance channel 1p-0h state (one-particle-zero-hole) is created. In this case, the energy of the incident particle can be equally distributed among all the nucleons, resulting in multiple p-h interactions, leading to the formation of a compound nucleus with a characteristic reaction time of about 10^{-17} s. The exit channel of a direct and a compound nuclear reaction can be the same. For example, in both cases the incident particle can be re-emitted with an energy equal to the incident energy leaving the target nucleus in the ground state. In the case of a direct reaction we call this process "shape-elastic" and in the case of a compound nuclear reaction it is called "compound elastic".

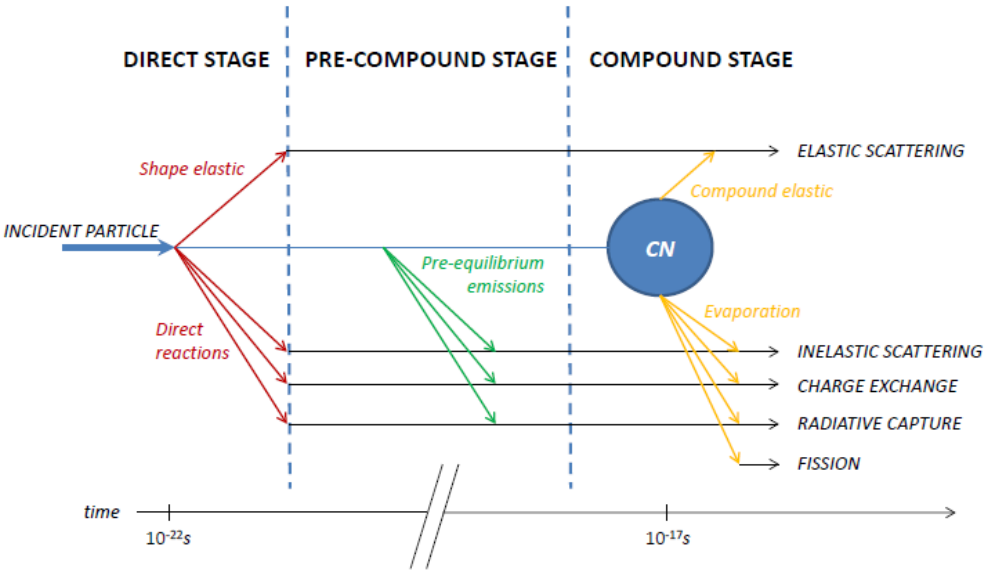

Figure 1.1: Schematic illustration of the different mechanisms of nuclear reactions, [Wei57].

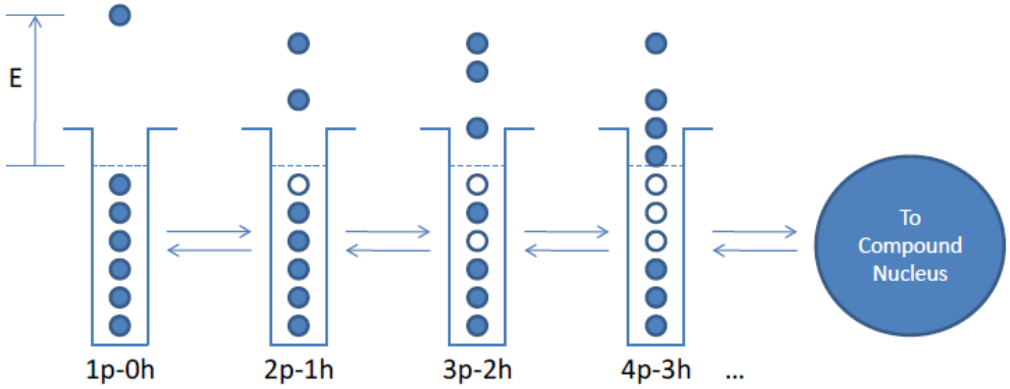

Figure 1.2: Intermediate stages on the way to the formation of a compound-nucleus.

During the successive formation of intermediate states (2p-1h,3p-2h, 5p-4h,...) particle emission may be possible before the compound nucleus is formed. In this case, we are speaking about pre-equilibrium (or pre-compound) emissions.

1.2 The compound nucleus concept and neutron-induced reactions

The process of formation of a compound nucleus is dominant for neutron-induced reactions on heavy nuclei at neutron incident energies below few MeV. In the formation of the compound nucleus the neutron is absorbed and its energy is shared between all the nucleons in a "thermalization" process. It takes time for the compound nucleus to accidentally concentrate all the energy back again to a single nucleon, which can be remitted. In the end, this inter-

mediate state is found to have a lifetime with timescales between $10^{-14} - 10^{-18}$ s, much longer than the time it takes to a nucleon with the Fermi velocity to cross the nucleus, about 10^{-22} s. Therefore, the compound nucleus lives long enough for statistical equilibrium to be established. Statistical equilibrium means that all the possible configurations or states of the excited nucleus at a given excitation energy $E^\star$, spin J and parity π are equiprobable. This implies that the compound-nucleus decay can be described statistically by counting the available states after decay and that the compound-nucleus forgets the memory of the entrance channel. This latter point leads to an uncoupling between the process of formation and decay of the compound nucleus, which can be considered completely independent of each other (see figure 1.3). This is known as Bohr's independence hypothesis.
Based on Bohr's independence hypothesis the neutron-induced cross section for a given decay channel χ can be written in the Hauser-Feshbach formalism, [Hau52], as:

$$\sigma_{n,\chi}(E_n) = \sum_{J,\pi} \sigma_n^{CN}(E^\star, J^\pi) \cdot G_\chi(E^\star, J^\pi) \tag{1.1}$$

where $\sigma_{n,\chi}(E_n)$ is the neutron-induced cross section for the reaction ${}^{A}X(n,\chi)$ at an incident neutron energy E_n. $\sigma_n^{CN}(E^\star, J^\pi)$ is the cross section for the formation of compound nucleus ${}^{A+1}X^\star$ at an excitation energy $E^\star$ with spin J and parity π after the capture of a neutron. $G_\chi(E^\star, J^\pi)$ is the probability that the compound nucleus with excitation energy $E^\star$, spin J and parity π decays via the exit channel χ. In the following we will call these probabilities G_χ branching ratios. Equation (1.1) can be factorized as:

$$\sigma_{n,\chi}(E_n) = \sigma_n^{CN}(E^\star) \sum_{J,\pi} \frac{\sigma_n^{CN}(E^\star, J^\pi)}{\sigma_n^{CN}(E^\star)} \cdot G_\chi(E^\star, J^\pi) \tag{1.2}$$

with $\sigma_n^{CN}(E^\star) = \sum_{J,\pi} \sigma_n^{CN}(E^\star, J^\pi)$. In this way we can define the probability $P_\chi^n(E^\star)$ that the compound-nucleus decays through the channel χ as:

$$P_\chi^n(E^\star) = \sum_{J,\pi} F_n^{CN}(E^\star, J^\pi) \cdot G_\chi(E^\star, J^\pi) \tag{1.3}$$

where $F_n^{CN}(E^\star, J^\pi) = \frac{\sigma_n^{CN}(E^\star, J^\pi)}{\sigma_n^{CN}(E^\star)}$ is the probability for forming the compound nucleus ${}^{A+1}X^\star$ with given values for $(E^\star, J^\pi)$ after neutron capture. This is nothing but the spin-parity distribution of the compound-nucleus at $E^\star$. The excitation energy $E^\star$ of the compound-nucleus is related to E_n via the neutron separation energy S_n of the compound-nucleus:

$$E^\star = S_n + \frac{A}{A+1} \cdot E_n \tag{1.4}$$

Finally, equation (1.1) can be rewritten as the product of the cross section for the formation of the compound nucleus σ_n^{CN} and the probability P_χ^n that the compound nucleus decays through

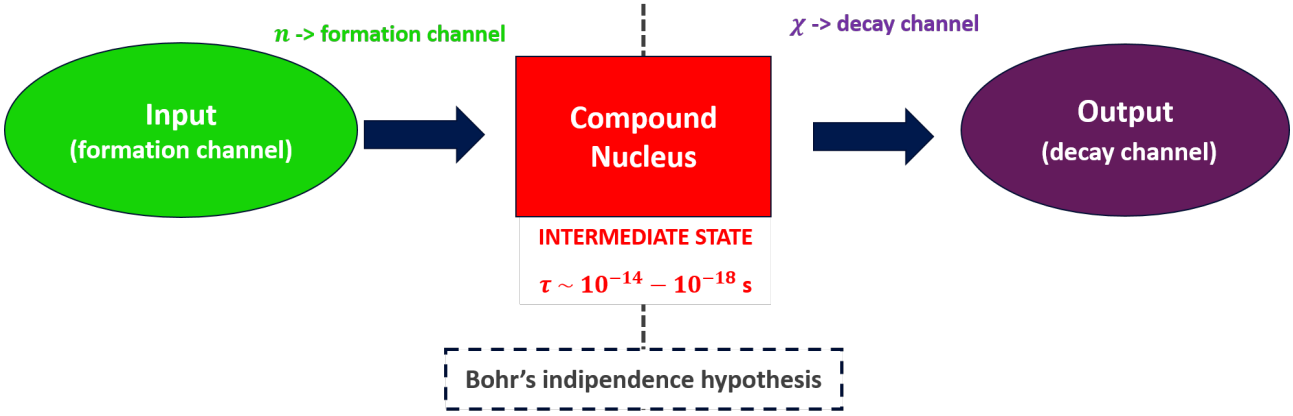

Figure 1.3: Schematic representation of the independence of formation and decay in the frame of Bohr's independence hypothesis.

the de-excitation channel χ after neutron capture:

$$\sigma_{n,\chi}(E_n) = \sigma_n^{CN}(E_n) \cdot P_\chi^n(E^\star) \tag{1.5}$$

The compound nucleus concept is a reasonable hypothesis for heavy nuclei with excitation energies near or above the neutron separation energy S_n, where a high level density is present. In this case, the large degree of configuration mixing that appears thanks to the large number of states allows the nucleus to reach statistical equilibrium by the time it decays.

1.3 The Weisskopf-Ewing (WE) hypothesis

Neutron induced reactions and surrogate reactions produce a compound nucleus with the same (Z,A) at an excitation energy $E^\star$. The decay probabilities are given by the expressions:

$$P_\chi^n(E^\star) = \sum_{J^\pi} F_n^{CN}(E^\star, J^\pi) \cdot G_\chi(E^\star, J^\pi) \tag{1.6}$$

$$P_\chi^{surr.}(E^\star) = \sum_{J^\pi} F_{surr.}^{CN}(E^\star, J^\pi) \cdot G_\chi(E^\star, J^\pi) \tag{1.7}$$

where the indexes n and $surr.$ stand for neutron-induced and surrogate reactions, respectively. As proven in the previous works of the collaboration [Sán20], the angular momentum and the parity distributions $F_{surr.}$ populated by the surrogate reactions are in general different from the ones populated by the neutron induced reactions F_n. This can be intuitively understood by the fact that for neutron induced reactions, when the neutron energy is low, the angular momentum transfer is low. However, surrogate reactions involve charged projectiles and require larger incident energies to overcome to Coulomb barrier, and induce an excitation energy close to S_n, thus leading to large angular momentum transfer.

As can be seen in equations (1.6) and (1.7) the decay probabilities G_χ depend on J^π. For

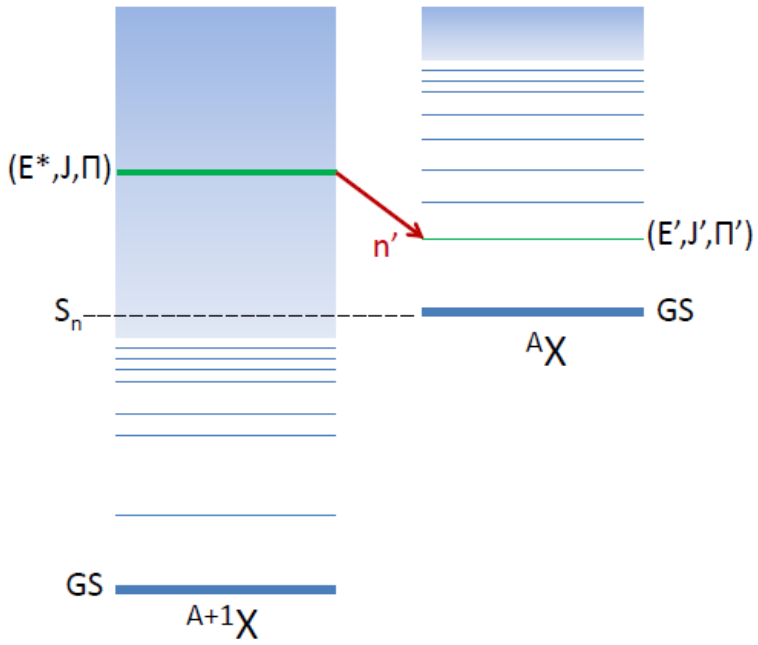

Figure 1.4: Decay scheme via neutron emission for a compound-nucleus $^{A+1}X(E^\star, J^\pi)$ to a $(E'^\star, J', \pi')$ state of the residual nucleus ^{A}X.

neutron emission it is at $E^\star$ just above the neutron separation energy S_n that this dependence is the strongest. This can be understood by looking at figure 1.4, where the decay via neutron emission of a compound-nucleus ^{A+1}X to a state of the residual nucleus ^{A}X is shown. The low-lying discrete states of the residual nucleus A have generally low spins. On the other hand, the change of the angular momentum of ^{A+1}X caused by neutron emission is in general quite low (0 or $1\hbar$). Therefore, if the angular momentum of ^{A+1}X induced in the surrogate reaction is much larger than the angular momentum of the first states of nucleus ^{A}X, neutron emission to the low-lying states of the residual nucleus will be strongly suppressed and the de-excitation will essentially proceed by gamma emission.

The probabilities P_χ^n and $P_\chi^{surr.}$ are equal only in two cases:

1. If the J^π distributions populated in both reactions are the same. This means that:

$$F_n^{CN}(E^\star, J^\pi) = F_{surr.}^{CN}(E^\star, J^\pi) \tag{1.8}$$

   Unfortunately, as explained before, this equivalence is seldom satisfied.

2. If the branching ratios are independent of J^π:

$$G_\chi(E^\star, J^\pi) = G_\chi(E^\star) \tag{1.9}$$

   then the branching ratios can be taken out from the summations in equation (1.6) and

(1.7). And since:

$$\sum_{J^\pi} F_n^{CN}(E^\star, J^\pi) = 1, \quad \sum_{J^\pi} F_{surr.}^{CN}(E^\star, J^\pi) = 1 \tag{1.10}$$

we obtain:

$$P_\chi^n(E^\star) \approx P_\chi^{surr.}(E^\star) = G_\chi(E^\star) \tag{1.11}$$

This second limit is known as the Weisskopf-Ewing (WE) approximation and is justified for sufficiently high excitation energies where the level densities are extremely high. Under the Weisskopf-Ewing hypothesis, the selected surrogate reaction is used to measure the decay probabilities $P_\chi^{surr.}(E^\star)$, which are used instead of the decay probabilities $P_\chi^n(E^\star)$ to obtain the desired neutron induced cross section:

$$\sigma_{n,\chi}(E_n) = \sigma_n^{CN}(E_n) \cdot P_\chi^{surr.}(E^\star) \tag{1.12}$$

1.4 Theoretical description of the formation and de-excitation of a compound nucleus

1.4.1 Formation of the compound nucleus

For neutron-induced reactions the compound-nucleus formation cross section σ_n^{CN} is usually deduced from optical model calculations [Fes54]. The elastic scattering matrix elements S_l are obtained from the solution of the Schrödinger equation of the system formed by the projectile and the target nucleus using a complex optical potential. The imaginary part of the potential takes into account the absorption of the reaction flux from the shape elastic channel to the reaction channels. A S_l value gives the probability for the scattering of an incoming neutron with a given orbital angular momentum l. Note that S_l is the identity matrix if the particles do not interact with each other. Once the S-matrix is known, the total, shape elastic and reaction cross sections are given by:

$$\sigma_{tot} = \frac{2\pi}{k^2} \sum_{l=0}^{\infty} (2l+1) \cdot (1 - Re[S_l]) \tag{1.13}$$

$$\sigma_{SE} = \frac{\pi}{k^2} \sum_{l=0}^{\infty} (2l+1) \cdot |S_l - 1|^2 \tag{1.14}$$

$$\sigma_{reaction} = \frac{\pi}{k^2} \sum_{l=0}^{\infty} (2l+1) \cdot (1 - |S_l|^2) \tag{1.15}$$

where $k = \frac{\sqrt{2\mu E}}{\hbar}$ is the wave number, μ is the reduced mass ($\mu = \frac{1}{\frac{1}{m_1}+\frac{1}{m_2}} = \frac{m_1 m_2}{m_1+m_2}$) of the projectile-target system and E is the system energy in the center of mass. The total cross section σ_{total} is the sum of σ_{SE} (optical model scattering) and $\sigma_{reaction}$ (optical model absorption). The transmission coefficients T_l, which give the probability for the absorption of the incoming neutron projectile with orbital angular momentum l, are determined from the elastic scattering matrix elements S_l as:

$$T_l = 1 - |S_l|^2 \tag{1.16}$$

In general, the reaction cross section $\sigma_{reaction}$, which corresponds to the loss of flux from the elastic channel, is calculated with the transmission coefficients T_l as:

$$\sigma_{reaction} = \frac{\pi}{k^2} \sum_{l=0}^{\infty} (2l+1) \cdot T_l \tag{1.17}$$

The term "reaction" includes the absorption of the flux by the long-lived compound-nucleus states. The compound-nucleus reaction cross section σ_{CN} is obtained by subtracting the pre-equilibrium component σ_{PE} (which can be obtained via the exciton-model, [Obl87], or the Feshbach-Koonin-Kermin-model, [Fes80]), and the direct inelastic contributions σ_{Direct} from the reaction cross section:

$$\sigma_{CN} = \sigma_{reaction} - \sigma_{Direct} - \sigma_{PE} \tag{1.18}$$

As mentioned before, for neutron induced reactions at low energies we assume that direct and pre-equilibrium contributions are negligible. Consequently, the compound-nucleus formation cross section is equal to the reaction cross section. Note that it is usual to distinguish between the compound elastic σ_{CE} and the compound inelastic σ_{NE} components. The latter includes the radiative capture cross section σ_γ, the fission cross section σ_f, the neutron inelastic cross section $\sigma_{n'}$, etc. To summarize, figure 1.5 gives all components of the total cross section. The optical model thus provides the transmission coefficients, direct cross sections, and the total and shape elastic cross sections. From the compound nucleus cross section $\sigma_n^{CN}(E_n, J^\pi)$ it is possible to obtain the angular momentum and parity distribution populated in the neutron induced data $F_n^{CN}(E^\star, J^\pi) = \sigma_n^{CN}(E_n, J^\pi)/\sigma_n^{CN}(E_n)$. This defines the initial conditions $(A, Z, E^\star, J^\pi)$ of the statistical model which governs the decay of the compound-nucleus, via fission, γ emission, neutron emission, etc. Figure 1.6 shows how the statistical model is linked to the optical model. In the calculation performed with Talys 1.96, the default spherical optical models with local parametrisations of Koning and Delaroche was used [Kon03]. In the local parametrization Talys retrieves all the parameters of the local OMPs automatically from the nuclear structure and model parameter database.

The surrogate reaction we consider in this work are typically inelastic scattering or transfer reactions involving light charged projectiles such as protons, deuterons or alpha particles

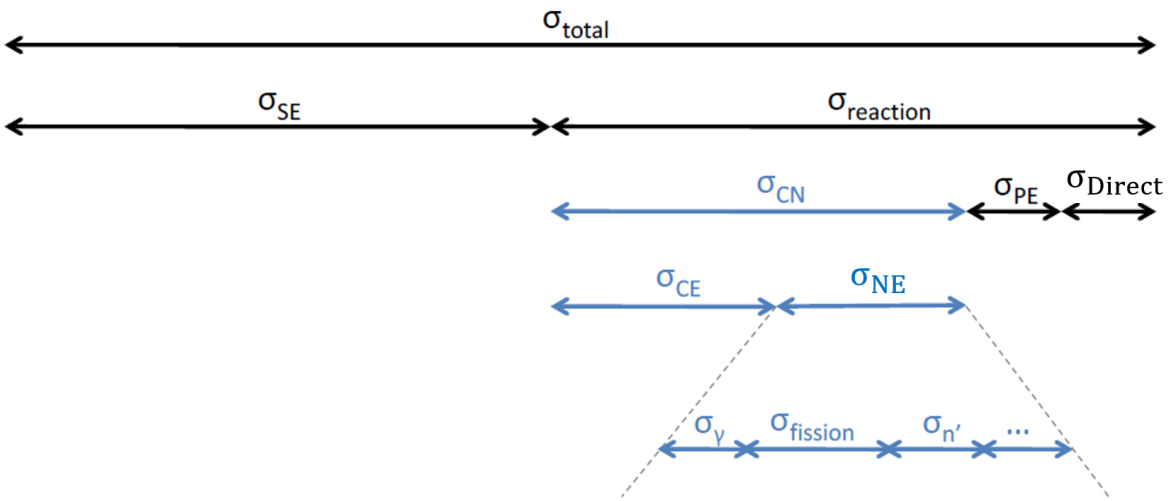

Figure 1.5: Components of the total cross section.

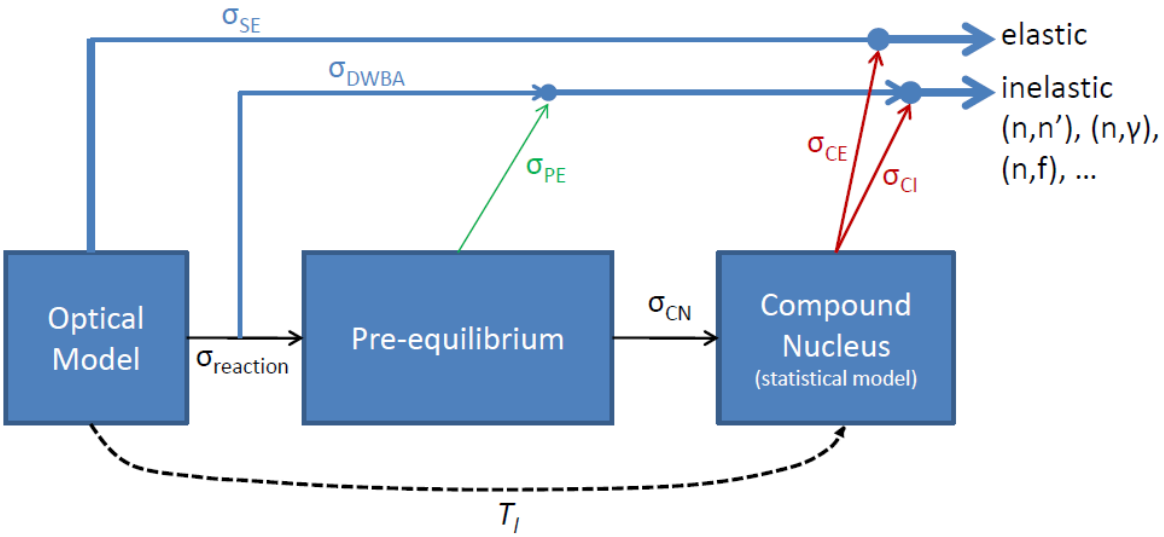

Figure 1.6: Coupling of nuclear models for the complete description of a neutron-induced reaction.

and heavy target nuclei. As described in [Esc12] the surrogate reactions can be viewed as a two-step process where the single particle state initially populated by the inelastic scattering or transfer reaction readily mixes with the continuum of the compound levels that have the same quantum number (J^π) leading eventually to the formation of a compound nucleus. [Esc12] describes how several works have estimated how the initial single particle states are fragmented into the complex many-body states in the continuum. In this work, the spin-parity distributions $F^{CN}_{surr.}$ populated by the $^{208}Pb(p,p')$ reaction is calculated following the microscopic description developed in [Dup06, Dup19]. In this approach, the excited states of ^{208}Pb in the continuum are determined with the Quasi Particle Random Phase approximation (QRPA). The distorted-wave Born Approximation (DWBA) is then used to determine the cross section to populate the excited states with the $^{208}Pb(p,p')$ reaction. For the population of natural parity states the Jeukenne, Lejeune, and Mahaux (JLM) microscopic optical model potential is employed [Dup19], whereas the Melbourne microscopic optical model is used for non-natural parity states [Dup06]. The above theoretical description is very well adapted to described the initial part of the surrogate reaction process, the direct interaction, which is essential for determing the probabilities with which the states of ^{208}Pb are populated by the $^{208}Pb(p,p')$ reaction. This is why we have chosen this description to infer the spin-parity distribution rather than other models available in Talys. We will further discuss the pertinence of the compound nucleus assumption in chapter 6.

1.4.2 Decay of the compound-nucleus

1.4.2.1 Branching ratios G_χ

It is interesting to note that the branching ratios G_χ are the same in equation (1.6) and (1.7) reflecting that the decay of the compound nucleus is independent of the reaction used to produce it. In the description of the de-excitation process and the calculation of G_χ we used the statistical model implemented in Talys code.

As said before, statistical equilibrium implies that all the available states of nucleus after decay are equiprobable. Therefore, the branching ratios or de-excitation probabilities G_χ are given by the number of states, or open channels, available after the decay. If a centrifugal, Coulomb or other type of potential barrier is present, the probability of population of that channel is reduced by the transmission coefficient. For the nuclei and $E^\star$ range considered in this work, the de-excitation of a compound nucleus can take place following three different decay paths, namely the emission of gamma rays, the emission of neutrons and fission, as shown by the diagram in figure 1.7. The branching ratio for the decay channel χ is defined according to the expression:

$$G_\chi(E^\star, J^\pi) = \frac{< N_\chi(E^\star, J^\pi) >}{\sum_i < N_i(E^\star, J^\pi) >} \tag{1.19}$$

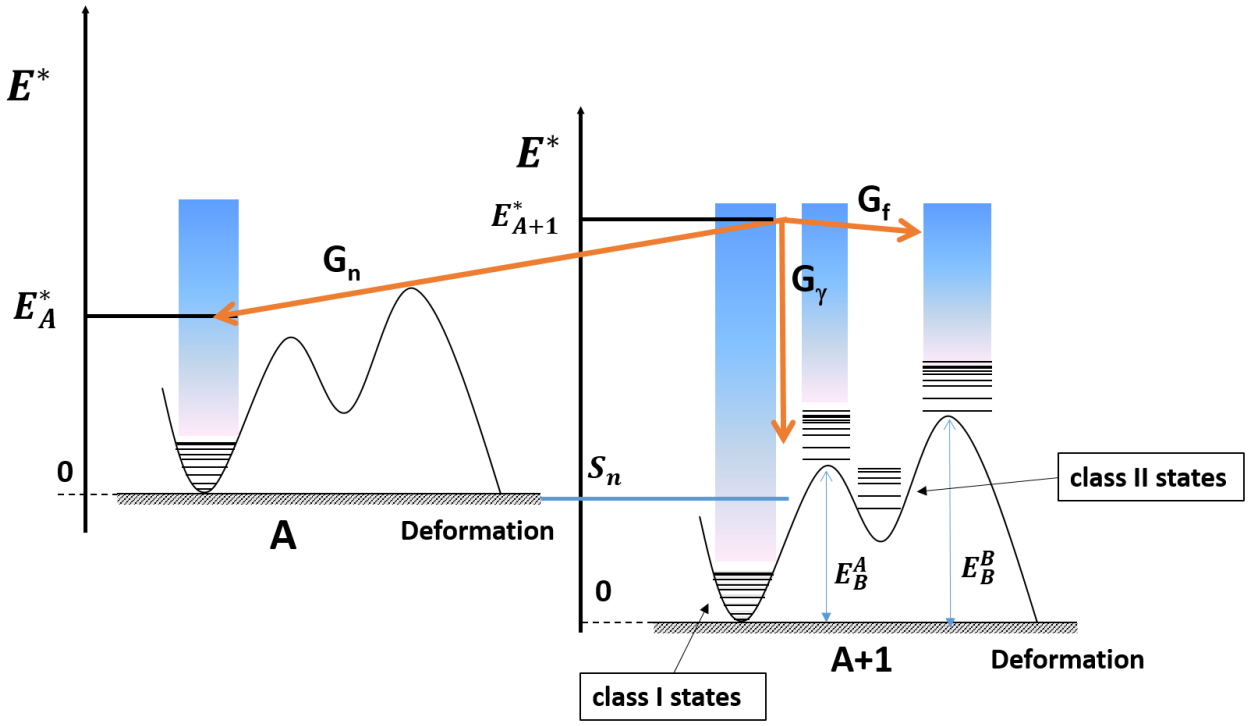

Figure 1.7: Illustration of decay pathways accessible for a compound nucleus that can de-excite by gamma emission, neutron emission n or fission f. The potential energy as a function of the CN deformation is represented by a double-humped fission barrier. Discrete levels are shown at low $E^\star$ and the continuum, described by level densities, is shown at higher $E^\star$.

where $< N_\chi >$ is the average number of open channels and the sum $\sum_i$ runs over all the possible decay channels. Determing $< N_\chi >$ requires the knowledge of fundamental ingredients described by models, such as the level densities, gamma-ray strength functions and the transmission coefficients. These quantities will be described in detail in the following sections.

1.4.2.2 Gamma emission and gamma-ray strength functions

In the gamma-emission decay channel, the compound nucleus in an initially excited state, emits a cascade of γ-rays with a number x of γ-rays until it reaches the ground state according to:

$$(A+1)^\star \rightarrow (A+1) + x\gamma \tag{1.20}$$

The γ-ray carries an angular momentum L, which depends on the spin values of the initial J and final states J':

$$|J - J'| \leq L \leq J + J' \tag{1.21}$$

The average number of open channels for gamma emission of the compound nucleus is given by:

$$\begin{aligned} < N_\gamma(E^\star, J^\pi) > = 2\pi C \cdot [\sum_{discret} \sum_{J',\pi'} \sum_{XL} f_{XL}(\epsilon_{\gamma i}) \cdot \epsilon_{\gamma i}^{2L+1} \cdot \delta_i \\ + \int_{E_{cont}}^{E^\star_{A+1}} \sum_{J',\pi'} \sum_{XL} f_{XL}(\epsilon_\gamma) \cdot \epsilon_\gamma^{2L+1} \rho(E^\star - \epsilon_\gamma, J', \pi') \cdot d\epsilon_\gamma] \end{aligned} \tag{1.22}$$

The first sum $\sum_{XL}$ runs over all the accessible multipole transitions XL. The transition type from one level towards another is of electric nature if $X = E$ or of magnetic nature if $X = M$. The values L=1,2,3,.. correspond to the multipole nature of the transition. The second sum $\sum_{J',\pi'}$ runs over all the final levels of angular momentum J', π' that respect the selection rules:

$$\pi' = \pi(-1)^{L+1} \; for \; electric \; transitions \; E_L \tag{1.23}$$

$$\pi' = \pi(-1)^{L} \; for \; magnetic \; transitions \; M_L \tag{1.24}$$

The third sum term runs over the energy of the gammas emitted between the initial level of energy $E^\star_{A+1}$ and the final energy level. A distinction is made between the discrete part δ_i and the continuous part described by $\rho_\gamma(E^\star - \epsilon_\gamma, J', \pi')$, the level density of the compound nucleus. The transmission coefficient f_{XL} is called the gamma ray strength function and it directly depends on the transition energy between the initial and final level ϵ_γ. The description of the level density and the γ-ray strength function is given by different models that will be discussed below. The quantity C is a constant that serves to normalise $< N_\gamma >$ to the experimental radiative decay width Γ_γ in the resonance region. This normalization is essential to avoid a significant bias of the values of $< N_\gamma >$. In general, only electric dipole transitions are considered ($X = E$ and $L = 1$) because they are predominant compared to the other types of transitions.

Gamma emission and absorption phenomena can both be described through the gamma strength functions [Lon86, Bar73]. There are two types of strength functions: one is related to the radiative width for gamma emission Γ_γ. For Transitions E1, this is expressed as:

$$f_{E_1}(\epsilon_\gamma) = \frac{< \Gamma_\gamma(\epsilon_\gamma) > \cdot \rho(E^\star, J^\pi)}{\epsilon_\gamma^3} \tag{1.25}$$

The other type of strength function depends on the absorption cross section of a gamma ray of energy E_γ:

$$f_{E_1}(\epsilon_\gamma) = \frac{1}{3(\pi\hbar c)^2} \cdot \frac{\sigma_{abs_{E_1}}(\epsilon_\gamma)}{\epsilon_\gamma} \tag{1.26}$$

where $\sigma_{abs_{E1}}(\epsilon_\gamma)$ is the photo-absorption cross-section of a photon E1 from the ground state of the considered nucleus. The absorption and emission of gammas of energy up to about 20 MeV

is mainly governed by the excitation or de-excitation of the giant dipole resonance (GDR). The two types of strength functions are assumed to be equal and of Lorentzian shape. Two different models developed for $E1$ transitions are commonly used for statistical model calculations, the Standard Lorentzian Model (SLO) and the Enhanced Generalized Lorentzian Model (EGLO) model. In this work for the statistical description of the gamma decay we chose the default option of Talys code. For the photons $E1$ transitions, the SLO model was used, while for the $M1$ transition, the IAEA photon strength function database [RIPL-3] was used.

1.4.2.3 Neutron emission and transmission coefficients

The statistical de-excitation by emission of a neutron from the compound nucleus can be illustrated by the following mechanism:

$$(A+1)^{\star} \rightarrow A + n \tag{1.27}$$

The residual nucleus A can be in its ground state if the kinetic energy of the emitted neutron is equal to the total excitation energy of the compound nucleus minus the neutron separation energy. This is the compound elastic scattering process. If the residual nucleus A is in an excited state below the neutron separation energy S_n of A, it will release the remaining $E^{\star}$ by gamma emission (for non-fissile nucleus). This is the neutron inelastic scattering process. The emitted neutron has a kinetic energy E_n, a total angular momentum j_n and an orbital angular momentum l_n which can be deduced from the conservation laws:

$$\vec{J}_{(A+1)^{\star}} = \vec{I_A} + \vec{j_n} \;\; with \;\; \vec{j_n} = \vec{l_n} + \vec{s_n} \;\; , \;\; s_n = \frac{1}{2} \tag{1.28}$$

$$\pi_{(A+1)^{\star}} = \pi_A \cdot (-1)^{l_n} \tag{1.29}$$

$$E^{\star}_{(A+1)} = E^{\star}_A + S_n + E_n \tag{1.30}$$

The average number of open channels available after neutron emission is given by:

$$\begin{aligned} < N_n(E^{\star}, J^{\pi}) > = & \sum_{discret} \sum_{j=|j_i - I|}^{j_i+I} \sum_{l=|j-\frac{1}{2}|}^{|j+\frac{1}{2}|} T_{lj}(E^{\star} - S_n - \epsilon_i)\delta_{\pi_i, \pi(-1)^l} \\ & + \int_{E_{cont}}^{E^{\star}_{A+1}-S_n} \sum_{J'} \sum_{j=|J'-J|}^{J'+J} \sum_{l=|j-\frac{1}{2}|}^{|j+\frac{1}{2}|} T_{lj}(E^{\star} - S_n - \epsilon) \cdot \rho(\epsilon, J', \pi(-1)^l) \cdot d\epsilon \end{aligned} \tag{1.31}$$

where ϵ is the excitation energy of the residual nucleus formed after neutron emission. The calculation of $< N_n >$ includes all the accessible discrete (ϵ_i, J_i, π_i) and continuous (ϵ, J', π) levels that fulfil the selection and conservation rules and whose energies are less than $E^{\star}_{A+1} - S_n$. The level density in the continuum of the residual nucleus formed after neutron emission is

described by ρ. The T_{lj} represent the transmission coefficients, they are also used to infer the reaction cross section (see equation 1.17) and strongly depend on the chosen optical model and the associated parameters.

1.4.2.4 Fission and fission barrier parameters

The fission process may compete with the two previously described decay channels. The statistical de-excitation by fission of the compound nucleus can be illustrated as follows:

$$(A+1)^{\star} \rightarrow Fragment_1 + Fragment_2 \tag{1.32}$$

In the frame of the liquid drop model, the potential energy as a function of the deformation of the CN is given by the interplay between the Coulomb repulsion and the surface energy (whose origin is the short-range nuclear force). The potential energy is characterised by a fission barrier. Shell effects modify the shape of the potential energy leading to double or even triple-humped fission barriers. Generally, the fission process is modelled by a double-humped barrier. The fission barrier of ^{208}Pb is larger than the $E^{\star}$ populated by the $^{208}Pb(p,p')$ in our proof of principle experiment. Therefore, the excited nucleus ^{208}Pb cannot decay by fission. However, fission was an important decay channel in many surrogate reaction experiments, including many experiments of our collaboration which are discussed in chapter 2. For this reason, we briefly describe below the modelling of fission probabilities.
As stated by N. Bohr and J.A. Wheeler, [Boh39], the fission probability is defined by the number of states at the top of the fission barrier, the so-called "transition" states, and not by the states of the fission fragments. If the $E^{\star}$ is lower than the barrier height, tunnelling occurs. The states of the second potential well (qualified as class II, see figure 1.7) have a strong influence on the penetrability of the barriers and can lead to a significant increase of the fission probability at the energy where the states are located. The equation for the average number of open fission channels $< N_f >$ is given by the standard Hill-Wheeler expression:

$$< N_f(E^{\star}, J^{\pi}) >= \sum_{discret} \frac{\delta_{J,j_i}\delta_{\pi,\pi_i}}{1+e^{2\pi\frac{\epsilon+E_b-E^{\star}}{\hbar w_b}}} + \int_{E_{cont}}^{E^{\star}_{A+1}-S_n} \frac{\rho_b(\epsilon, J^{\pi})}{1+e^{2\pi\frac{\epsilon+E_b-E^{\star}}{\hbar w_b}}} d\epsilon \tag{1.33}$$

where ϵ is the energy above the considered barrier, $\hbar w_b$ and E_b represent respectively the curvature and the height of the fission barrier. The continuum E_{cont} starts here at the pairing energy of the nucleons, which represents the energy required to break a pair of nucleons:

$$E_{cont} = n \cdot \frac{14}{\sqrt{A}} \tag{1.34}$$

where n can be 0 (Z odd, N odd), 1 (Z odd, N even or Z even, N odd), 2 (Z even, N even). Therefore, one makes the assumption that odd-odd nuclei do not have discrete states above the

barriers, which may not always be the case. For excitation energies above E_{cont}, the breaking nucleons pairs induces more microscopic configurations accessible to the nucleus and therefore a strong increase of the level density at the barrier. For excitation energies below E_{cont}, the levels above the barriers are discrete states, which due to the large deformation are different from those of the first potential well.
If the coupling between the transmission coefficients through the two barriers A and B is neglected and class II states are not considered, the total number of open fission channels $< N_f >$ as a function of the number of open channels $< N_A >$ and $< N_B >$ of barriers A and B is expressed as follows:

$$< N_f(E^\star, J^\pi) >= \frac{< N_A(E^\star, J^\pi) > \cdot < N_B(E^\star, J^\pi) >}{< N_A(E^\star, J^\pi) > + < N_B(E^\star, J^\pi) >} \tag{1.35}$$

Thus the calculation of the fission probabilities requires knowledge of the barrier parameters (height and width), the level densities and transition states over the barriers and the class II states.

1.4.2.5 Level-density and spin distribution

The continuum is described by the nuclear level density $\rho(E, J^\pi)$ that corresponds to the number of nuclear levels at an excitation energy $E^\star$, for a certain J^π. From a physical point of view, it represents the total number of configurations or micro-states of the nucleus with a given J^π accessible at a given excitation energy $E^\star$.
Unfortunately, for a nucleus it is possible to give the values of $(E^\star, J^\pi)$ for only a limited number of levels at low energies. In fact, from a certain excitation energy on the number of levels becomes so large that it is more appropriate to speak about a level density. There are different level density models. The latter are characterized by their assumptions and their field of application, but they have to respect the constraints brought by the experimental levels densities. All level density models can be described by the product of three factors:

$$\rho(E^\star, J^\pi) = \rho(E^\star) \cdot \rho_J(E^\star, J) \cdot \rho_\pi(\pi) \tag{1.36}$$

where the $\rho(E^\star, J^\pi)$ is the level density at an energy $E^\star$ and a spin and parity J^π, $\rho(E^\star)$ is the total level density for all possible existing J^π at $E^\star$, $\rho_J(E^\star, J)$ is the fraction of levels with spin J around the energy $E^\star$ such that $\sum_J \rho_J(E^\star, J) = 1$, and $\rho_\pi(\pi)$ is the fraction of levels of parity π such that $\sum_\pi \rho_\pi(\pi) = 1$. The choice of a realistic total level density $\rho(E^\star)$ is of crucial importance. As can be seen in figure 1.8, different models for the total density can be adopted and each of them has a specific domain of application.
At high excitation energies the Fermi-Gas model (FGM) can be used, where the nucleus is considered like a gas of no interacting fermions. This model is only valid at high excitation energies where there is no longer any influence of pairing correlations on the number of accessible

microstates of the nucleus. The total density of levels is then expressed as follows:

$$\rho_{FGM}(E^\star) = \frac{1}{12\sqrt{2}\sigma} \cdot \frac{e^{2\sqrt{aU}}}{a^{1/4} \cdot U^{5/4}} \tag{1.37}$$

where U corresponds to the effective excitation energy taking into account pairing:

$$U = E^\star - n \cdot \Delta \tag{1.38}$$

where n is -1 (for Z and N even), 0 (for Z odd - N even or Z even - N odd) and 1 (for Z and N odd). Δ is a correction factor determined empirically over a large number of nuclei, which takes into account the differences observed for the level densities of even-odd nuclei caused by pairing correlations. The quantity a is the level density parameter which, as described by Ignatyuk's model [Igna75], takes into account nuclear shell effects:

$$a = \widetilde{a} \cdot [1 + \frac{\delta W}{U}(1 - \exp^{-\gamma U})] \tag{1.39}$$

where δW is the shell correction of the considered nucleus. The values of the parameters $\widetilde{a}$ and γ are given by systematic studies involving a large number of nuclei, see for example the RIPL-3 database [RIPL-3]. In equation (1.37), σ is the spin cut-off parameter which is related to the angular momentum distribution of the level density and is directly present in the formulation of $\rho_J(E^\star, J)$ as we will see later.

At low $E^\star$ the experimental level densities are rather well represented by the constant temperature formula,

$$\rho_{CTM}(E^\star) = \frac{1}{T} \cdot e^{(E-E_0)/T} \tag{1.40}$$

where the T and E_0 are empirical parameters. The inverse logarithmic slope of the level density corresponds to the temperature. In equation (1.40) the inverse logarithmic slope is equal to the parameter T, and this is the reason why it is call constant temperature formula. The constant temperature behaviour indicates that the increase of the $E^\star$ does not lead to an increase of temperature, because the additional energy is used to break pairs of nucleons, i.e. to increase the number of degrees od freedom of the nucleus. This behaviour resembles the behaviour of a phase transition, like when the ice melts into water.

A very reasonable assumption for the level density is to consider a composite description which combines the CT level density at low $E^\star$ and the FG description at high $E^\star$. This is called Gilbert-Cameron composite formula described in [Gil65], which is schematically represented in figure 1.8. The Gilbert-Cameron model is used in this work for the representation of the compound nucleus level density. Regarding the quantities ρ_J and ρ_π of equation 1.36, we make the reasonable assumption that for heavy nuclei the proportion of positive and negative parity

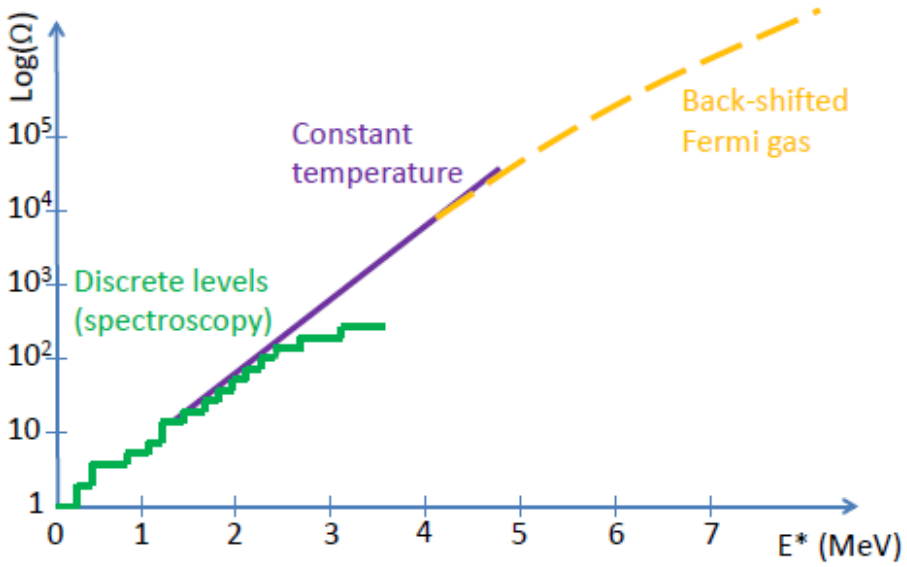

Figure 1.8: Schematic illustration of the construction of the Gilber-Cameron composite formula for the level density as function of the excitation energy [Gil65].

of the levels is equally distributed, that is:

$$\rho_\pi = \frac{1}{2} \tag{1.41}$$

The spin distribution ρ_J is given by:

$$\rho_J(J, E^\star) = \frac{2J+1}{2\sigma^2(E^\star)} \cdot \exp^{-\left(\frac{(J+1/2)^2}{2\sigma^2(E^\star)}\right)} \tag{1.42}$$

where σ is the spin cut-off parameter for the considered nucleus at energy $E^\star$.

1.5 Principle of the surrogate reaction method

As described in the previous sections, the de-excitation process of the compound nucleus is ruled by fundamental properties such as the level densities, fission barriers, transmission coefficients, etc., whose parameters are not known for nuclei where no experimental data are available. The objective of the surrogate method is to measure the de-excitation probabilities $P_\chi(E^\star)$, through the exit channel χ, by the use of an alternative reaction leading to the formation of the same compound nucleus as in the desired neutron induced reaction. As we will see in chapter 2, in same cases the WE hypothesis is satisfied and the neutron-induced cross sections can be obtained by using equation (1.5). However, the WE hypothesis is not applicable in many cases. Still, we will show in chapter 2 that the measured de-excitation probabilities are very useful to constrain the above-mentioned parameters.

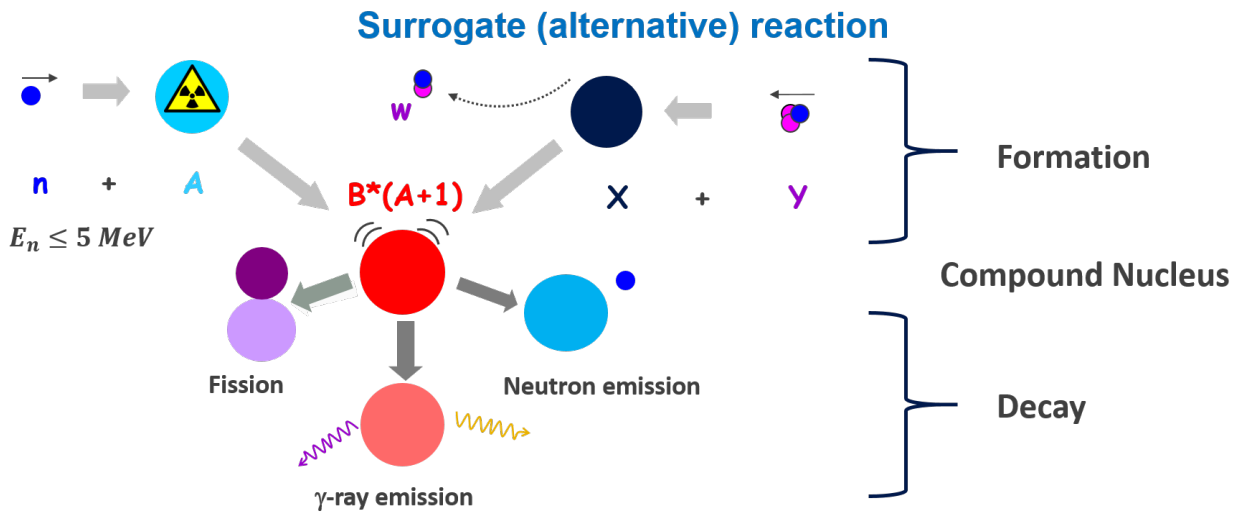

Figure 1.9: Principle of the surrogate-reaction method. On the left the neutron induced reaction is represented. A compound nucleus $A+1$ is formed. The de-excitation modes of the compound nucleus by fission, γ ray emission and neutron emission are represented. On the top right side the surrogate reaction involving a projectile y and a target nucleus X is shown. The surrogate reaction is a two body reaction leading to the ejectile w and the same nucleus $A+1$ as in the neutron-induced reaction.

The principle of the surrogate reaction method is illustrated in figure 1.9. The left side of figure 1.9 shows the neutron-induced reaction of interest, where neutron capture by the target A leads to the formation of compound nucleus $(A+1)^\star$. Subsequently, depending on the excitation energy $E^\star$, the compound nucleus can decay in different ways: (a) by emitting γ-rays, this is the radiative neutron capture reaction (n,γ), (b) by emitting a neutron leaving the nucleus mass A and proton Z numbers unchanged, this is called inelastic scattering (n,n') or (c) by fission (n,f) for heavy compound nuclei.
On the right side of the figure 1.9, the same compound nucleus is formed by the use of an alternative reaction or surrogate reaction involving a projectile y impinging on the target X. As said before, this reaction is a two body reaction typically an inelastic scattering or transfer reaction. Therefore in addition to the compound nucleus $A+1$, there is also an outgoing particle w, often called ejectile. The measurement of the ejectile's mass and charge, as well as its kinetic energy (E_k) and emission angle (θ), enables to determine the mass, charge and the excitation energy of the formed compound nucleus $(A+1)^\star$. The decay of the compound nucleus through the channel χ is identified by detecting the emitted particles, γ-rays $(\chi=\gamma)$, fission fragments $(\chi=f)$ and neutrons $(\chi=n)$ in coincidence with the ejectile w.

As expressed by equation 1.43, the decay probability $P_\chi^{surr.}(E^\star)$ obtained with a surrogate reaction is experimentally determined by measuring the ratio between the number of ejectiles detected in coincidence with the emitted particles from the decay channel χ, $N_\chi(E^\star)$, and the total number of ejectiles $N_s(E^\star)$, the so-called "single events". This ratio is corrected by the detection efficiency of the emitted particles from the decay channel χ for the reactions in which

the outgoing ejectile w is detected, $\epsilon_\chi(E^\star)$:

$$P_\chi^{surr.}(E^\star) = \frac{N_\chi(E^\star)}{N_s(E^\star) \cdot \epsilon_\chi(E^\star)} \tag{1.43}$$

As already mentioned, multiple advantages are coming from the surrogate reaction method. Firstly it allows to use a target X, which is less radioactive than the target A required by the neutron induced reaction. Moreover, the energy of the incident particle y is distributed in the exit channel between the ejectile w and the compound nucleus $(A+1)^\star$. Therefore, with only one incident beam energy it is possible to populate a broad excitation-energy distribution of the compound nucleus $(A+1)^\star$ (from 0 to about 15 MeV). In addition, several reactions can take place and be investigated simultaneously with a single projectile-target combination.

Chapter 2

State of the art of surrogate-reaction experiments

2.1 Results obtained with the surrogate reaction method within the WE hypothesis for fission

Transfer or inelastic scattering reactions have been used since many years to determine the fission barrier of actinide nuclei. They were first used by Northrop, Stokes, and Boyer [Nor59] to determine the fission barrier of the fissile nuclei ^{236}U, ^{234}U, and ^{240}Pu, whose fission barriers lie below their neutron binding energies. The surrogate reaction method was proposed and applied for the first time in Los Alamos National Laboratory by J.C. Cramer and H.C. Britt, [Cra70b], for the determination of neutron-induced fission cross sections.

The experimental set-up used in fission studies performed with the surrogate reaction method did not change significantly between the different experiments. It consisted of one or more $\Delta E - E$ charged-particle telescopes for the detection of the ejectiles and an array of detectors, which surrounded the target, to detect the fission fragments in coincidence with the ejectiles. The required target was often produced by evaporating a deposit of oxide material on thin carbon backings.

In their experiments Cramer and Britt investigated the (t,pf) and (t,df) reactions using a 15 and 18 MeV tritium beam impinging on targets of ^{230}Th, ^{232}Th, ^{234}U, ^{236}U, ^{238}U, ^{240}Pu and ^{242}Pu. Despite problems due to the presence of target contaminants, the neutron-induced fission cross sections were determined using equation 1.12 and the uncertainties were estimated to 10% for the fission probabilities and 5-20% for the optical model calculation of the CN formation cross section $\sigma_n^{CN}(E_n)$.

The work of Cramer and Britt was pursued subsequently by Back et al., who determined the fission cross sections of several odd-A, doubly-odd [Bac74b] and doubly-even [Bac74a] actinide nuclei, studied via other surrogate reactions such as (d, p) or (p, p').

Few years later, H. Britt and J. Wilhelmy used the $(^3He, d)$ and $(^3He, t)$ surrogate reactions with

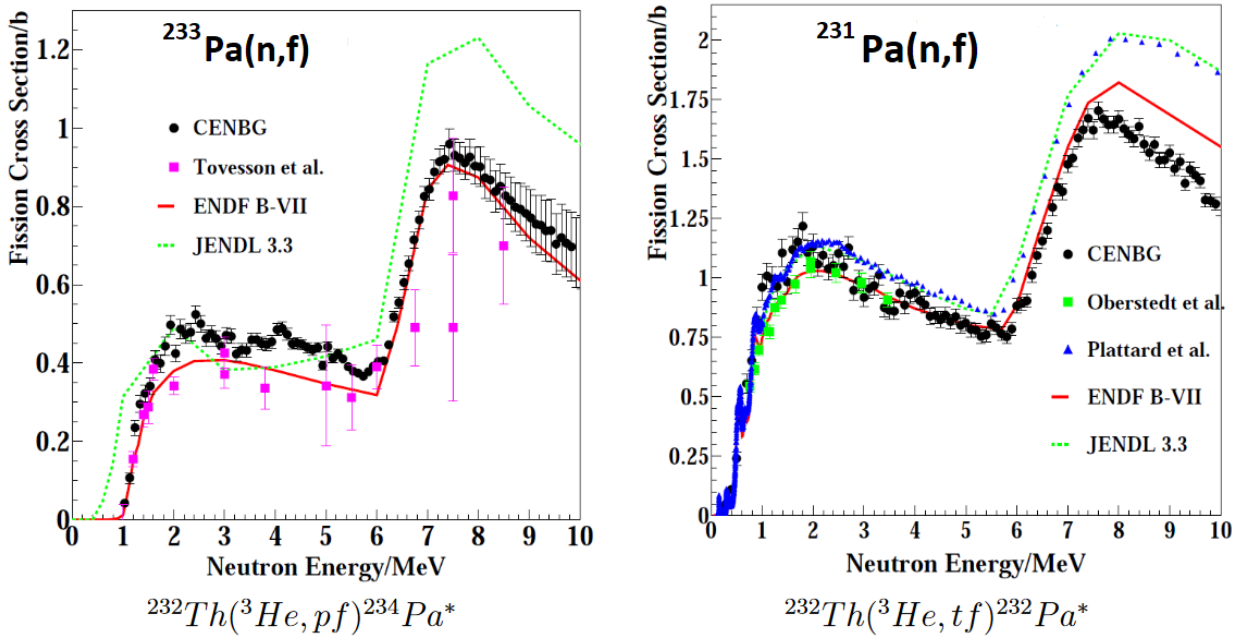

$^{232}Th(^{3}He, pf)^{234}Pa^{*}$ $^{232}Th(^{3}He, tf)^{232}Pa^{*}$

Figure 2.1: ^{233}Pa (left figure) and ^{231}Pa (right figure) fission cross sections as function of the incident neutron energy, [Pet04]. The results obtained by the CENBG collaboration (in black) are compared the with other experimental data and the evaluations of the nuclear data libraries ENDF-B/VII and JENDL-3.3.

various actinide targets to infer (n,f) cross sections for 34 nuclei for $E_n \sim 0.5 - 6\ MeV$ [Bri79]. Note that the compound-nucleus formation cross section was approximated to $\sigma_n^{CN}(E_n) = 3, 1b$ and assumed constant within a precision of 20%. A good agreement was observed with directly measured cross sections, where available, and uncertainties were similar to those of the previous work. However, below 1 MeV, in several cases there were serious discrepancies, and the reason for this mismatch was attributed to the failure of the Weisskopf-Ewing approximation.
Another test of the WE approximation was done by B. Lyles et al. in 2007. In their experiment, they measured the $^{236}U(n, f)$ cross section by using the $^{238}U(^{3}He, \alpha)^{237}U^{\star}$ reaction [Lyl07]. The experiment took place at the Lawrence Berkeley National Laboratory where the 88 Inch Cyclotron was used to produce the ^{3}He-beam at an energy of 42 MeV. The results measured in this experiment reflect the dependence of the cross section obtained with surrogate reactions on the transferred angular momentum. Indeed, the data showed an important sensibility to the detection angle of the ejectiles. In addition, large discrepancies were observed between the cross section data from the surrogate reaction and the desired neutron induced reaction at incident neutron energies $E_n < 1.5\ MeV$. The authors interpreted these results as a clear failure of the Weisskopf-Ewing approximation in this energy range.

In parallel to the experiments previously described, the CENBG collaboration performed different experiments to determine the fission cross sections of short-lived nuclei using the surrogate reaction method. In 2001, a first measurement on very short-lived nuclei of interest for the

Transfer channel	**Neutron-induced reaction**	**Equivalent neutron energies [MeV]**	**Half-life (neutron reaction target)**	**Half-life (^{243}Am)**
$^{243}\mathrm{Am}(^3He,d)^{244}Cm$	$^{243}\mathrm{Cm}(n,f)$	0-3	^{243}Cm(29.1 y)	7364 y
$^{243}Am(^3He,t)^{243}Cm$	$^{242}\mathrm{Cm}(n,f)$	0-10	^{242}Cm(162.8 d)	7364 y
$^{243}\mathrm{Am}(^3He,\alpha)^{242}Am$	$^{241}\mathrm{Am}(n,f)$	0-10	^{241}Am(432.2 y)	7364 y

Table 2.1: Transfer channels investigated in the reaction $^3He + ^{243}Am$ at 24 MeV and the corresponding neutron induced reactions, [Kes08].

development of reactors based on the Thorium fuel cycle was performed. Fission probabilities of $^{232,233,234}Pa^\star$ and $^{231}Th^\star$ were determined via the $^{232}Th(^3He,tf)^{232}Pa^\star$, $^{232}Th(^3He,pf)^{234}Pa^\star$, $^{232}Th(^3He,tf)^{232}Pa^\star$ and $^{232}Th(^3He,\alpha f)^{231}Th^\star$ surrogate reactions, respectively. As detailed in Ref. [Pet04], a 24 MeV ^3He beam was provided by the Tandem accelerator of the IJClab at Orsay. In this case, for the detection of the fission-fragments a system of 15 solar cells (20×40 mm^2) placed mainly at forward angles was designed to achieve a large efficiency and good granularity for fission-fragment angular-distribution measurements. The latter are used to measure the fission fragment angular anisotropy. The left part of figure 2.1 shows the fission cross section of $^{233}Pa(n,f)$ obtained from the Weisskopf-Ewing analysis of the $(^3He,p)$ transfer channel. The CENBG data are shown in comparison with the neutron-induced data. The lines represent the international evaluations. There is a reasonable agreement between the two sets of data at the fission threshold. On the right part of the same figure, the results for $^{231}Pa(n,f)$ obtained from the Weisskopf-Ewing analysis of the $(^3He,t)$ transfer channel are compared with the neutron-induced data and evaluations. Again, a good agreement was found between the surrogate results and the neutron-induced data at the fission threshold.

Later on, a surrogate experiment was conducted by the CENBG collaboration to determine the neutron-induced fission cross sections of $^{242,243}Cm$ and ^{241}Am via the transfer reactions $^{243}Am(^3He,tf)^{243}Cm^\star$, $^{243}Am(^3He,df)^{244}Cm^\star$ and $^{243}Am(^3He,\alpha f)^{242}Am^\star$, using a ^{3}He beam at 24 MeV impinging on a ^{243}Am target. This work is described in the Ph.D. thesis of G. Kessedjian [Kes08], followed by the article [Kes10]. Table 2.1 lists the transfer reaction channels, the equivalent neutron energy regions considered and the half-life of the targets associated to the different neutron-induced reactions. As can be seen, the target used in the surrogate reactions has a much longer half-life with respect to the ones required by the corresponding neutron-induced reactions. As shown in figure 2.2, the results are in very good agreement with those obtained in the neutron-induced measurements. Only in the case of the $^{243}Cm(n,f)$ reaction the situation is more complicated. For incident neutron energies larger than 1 MeV, a disagreement with the Fursov experimental data and the JENDL-3.3 evaluation can be observed. However, as explained in [Kes10], a detailed analysis shows that Fursov's data clearly over-predict this cross section.

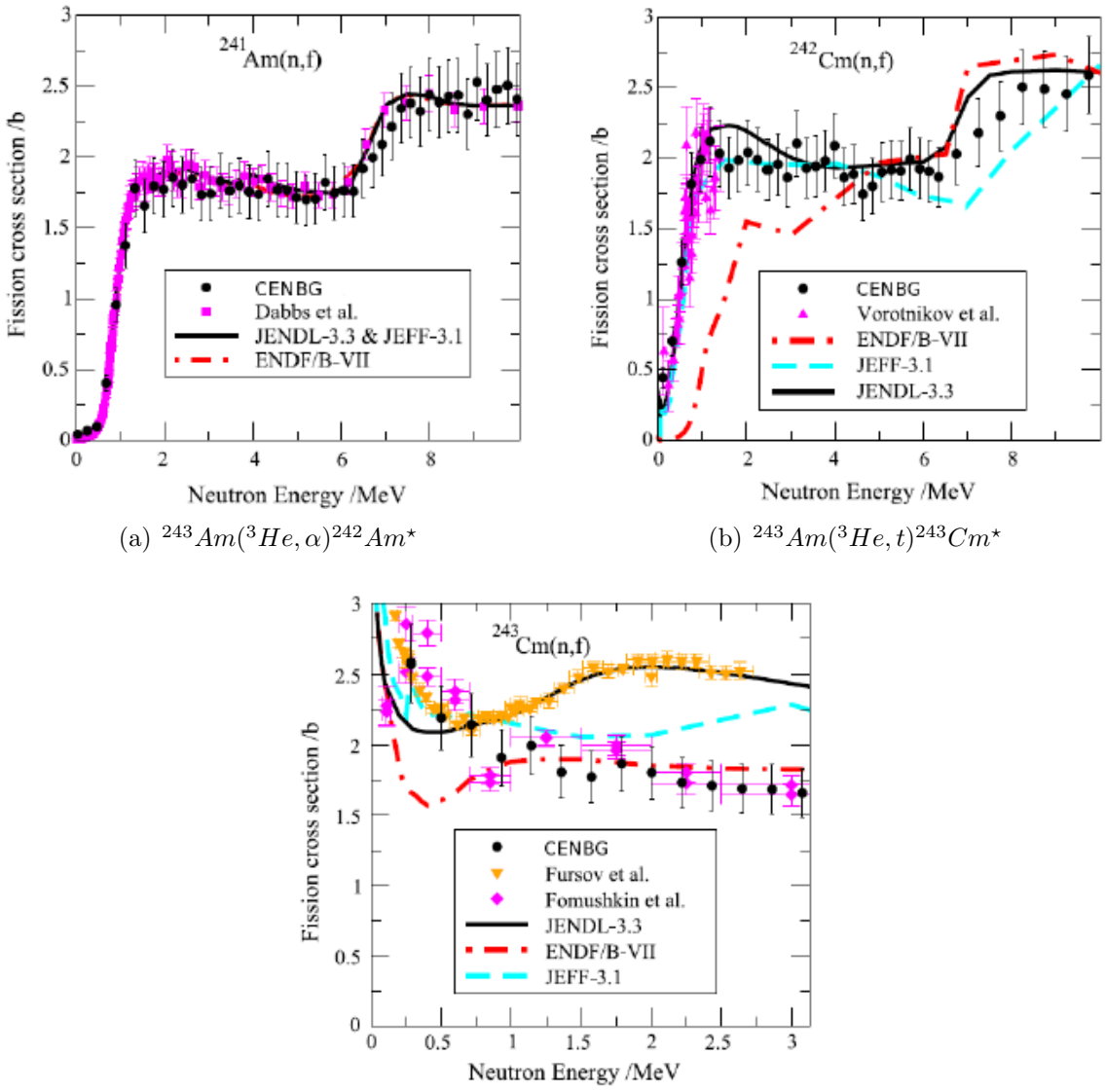

(a) $^{243}Am(^{3}He,\alpha)^{242}Am^{\star}$ (b) $^{243}Am(^{3}He,t)^{243}Cm^{\star}$

(c) $^{243}Am(^{3}He,d)^{244}Cm^{\star}$

Figure 2.2: Fission cross sections for ^{241}Am, ^{242}Cm and ^{243}Cm, [Kes08], as a function of neutron energy compared with neutron-induced data and the evaluations from several international libraries. The corresponding surrogate reaction is indicated below each panel.

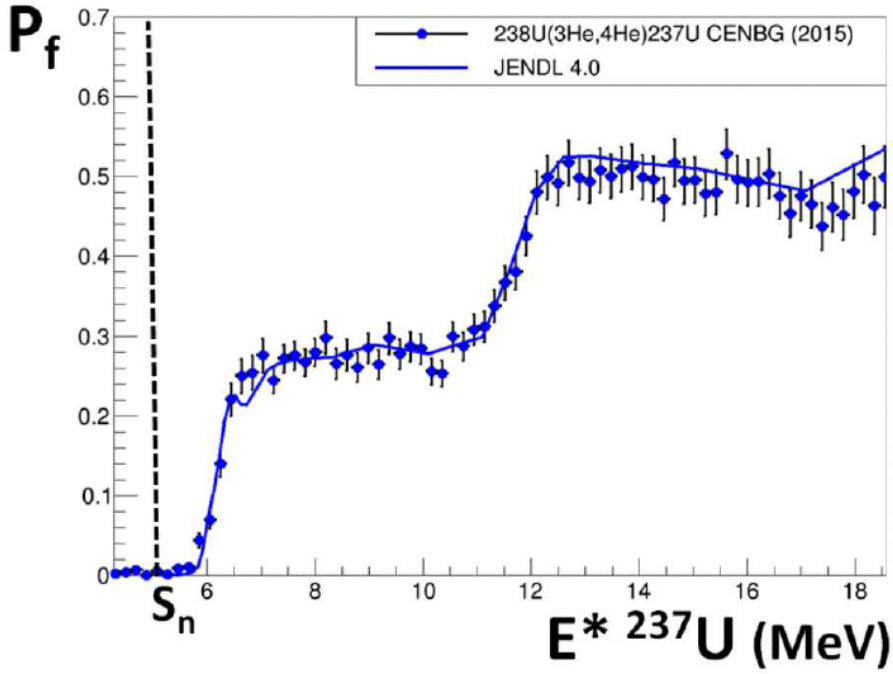

Figure 2.3: Fission probability of ^{237}U as function of excitation energy $E^{\star}$, [Duc15]. The experimental data represented by the dots were obtained with the surrogate reaction $^{238}U(^{3}He, ^{4}He)^{237}U^{\star}$. The full line represents the probability obtained with the JENDL evaluation while the vertical dashed line is the neutron separation energy S_n for ^{237}U.

In another experiment described in the Ph.D. thesis of Q. Ducasse [Duc15] and performed in 2016, the fission and γ-decay probabilities of several neptunium and uranium isotopes were measured simultaneously. The experiment, realized at the University of Oslo, was done using a ^{238}U target and two beams (^{2}H at 15 MeV and ^{3}He at 24 MeV). In figure 2.3, the fission probability of $^{237}U^{\star}$ as a function of excitation energy is compared with the JEFF 4.0 evaluation of the $^{236}U(n, f)$ reaction. In general, for the experiments previously described, a good agreement was found between the neutron-induced and the surrogate data within the frame of the WE approximation. This is particularly useful since the theoretical predictions for the fission probabilities are quite uncertain due to the lack of knowledge on the level structure in the vicinity of the fission barrier.

2.2 Results obtained with WE hypothesis for radiative capture

The determination of radiative capture cross sections is more difficult than of fission cross sections and the reasons for this complexity are many. In this case, the excitation energy range considered is smaller than for fission and the γ-emission probabilities are expected to decrease very rapidly with E*. When the γ-emission probability only represents few % of the decay, any

variation of few % due to the spin-parity mismatch represents in relative several factors. For fission, the measurement of the probabilities is simplified by the strong signature of the fission fragments, which can be easily detected. In the case of γ-emission, the heavy residues are stopped in the target and only the γ-rays can be detected. In surrogate reaction experiments the detection efficiency for γ-rays is generally very low ($\epsilon_\gamma \approx 5\%$). In addition, the γ-rays from the compound nucleus of interest have to be discriminated from those emitted after the emission of a neutron or by the fission fragments, if the compound nucleus can fission.

The two main experimental set-ups used for the measurement of γ-emission decay probabilities with a surrogate reaction were developed in 2006 by S. Boyer et al. [Boy06] and Bernstein et al. [Ber05]. These detection systems were then adopted and re-proposed with some variations in the later works. In Boyer's experiment the γ-ray emission probability of $^{234}Pa^\star$ was measured using the $^{232}Th(^3He, p\gamma)^{234}Pa^\star$ transfer reaction at a ^3He-beam incident energy of 24 MeV. A system of four C_6D_6 liquid scintillator detectors was implemented for the γ-ray detection. The total number of γ-ray cascades emitted by the compound-nucleus was obtained via the total-energy detection principle coupled to the pulse-height weighting function technique. In addition, four silicon telescopes were implemented and arranged to detect the ejectiles in coincidence with γ-rays. The experimental set-up is shown in figure 2.4(a). The obtained data were compared with the $^{233}Pa(n,\gamma)$ cross section from evaluations, see figure 2.4(b). The absence of directly measured data for the $^{233}Pa(n,\gamma)$ cross section does not allow a direct check of the validity of the surrogate method, the surrogate data are likely to be overestimated by about a factor 2.

In their experiment performed at the Lawrence Berkeley National Laboratory (LBNL), Bernstein et al. [Ber05] implemented a γ-ray detection array called Livermore-Berkeley Array for Collaborative Experiments (LiBerACE). LiBerACE consists of five clover-type high-purity germanium (HPGe) detectors with bismuth-germanate-oxide (BGO) Compton-suppression shields. The ejectiles were detected at forward angles using a telescope array called STARS. The experimental set-up is shown in figure 2.5(a). In this work, the $^{238}U(\alpha,\alpha'\gamma)$ inelastic scattering reaction was used as surrogate reaction to infer the $^{237}U(n,\gamma)$ cross section. The ^{238}U targets were bombarded with 55 MeV α-particles from the 88-Inch Cyclotron of the LBNL. The $^{237}U(n,\gamma)$ cross section deduced using the surrogate reaction method is presented in figure 2.5(b). The surrogate data appear to be about a factor of 2 to 4 higher than the neutron induced data. The observed discrepancies were attributed to a mismatch between the spin parity distributions associated to the surrogate and the neutron-induced reactions.

Another important contribution in the measurement of radiative capture cross sections was done by Scielzo et al. [Sci10] in 2010. They used the $(p,p'\gamma)$ inelastic scattering as surrogate reaction to infer the $^{153,155,157}Gd(n,\gamma)$ cross sections with the same experimental set-up as the one used by Bernstein et al. The obtained γ-decay probabilities yielded $^{155,157}Gd(n,\gamma)$ cross sections that were over-estimated by a factor of three with respect to the directly-measured cross sections. The results are given in figures 2.6(a) and 2.6(b) where they are compared

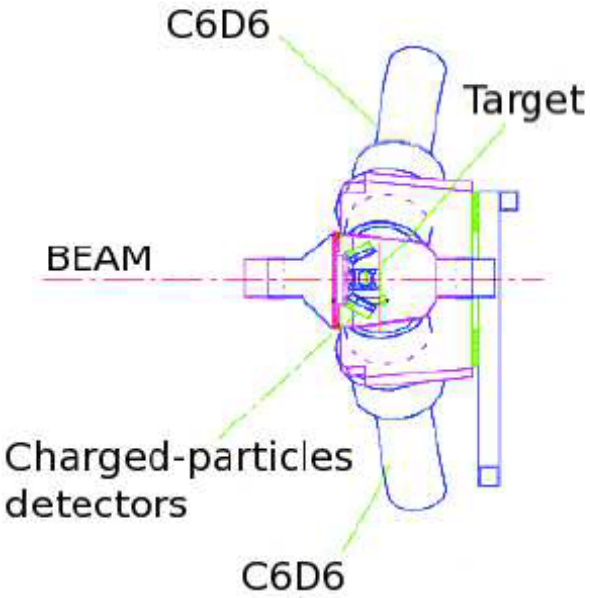

(a)

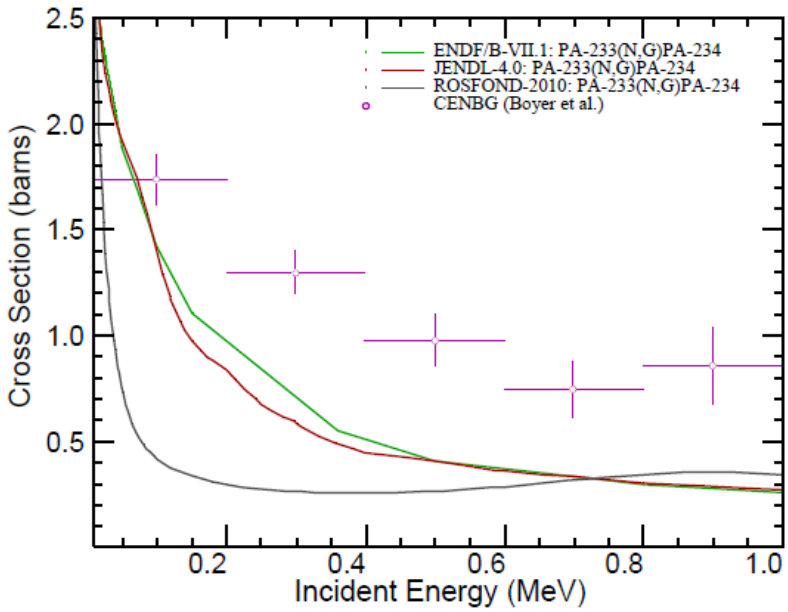

(b)

Figure 2.4: The set-up of Boyer's experiment performed at the IJClab is shown on the top. The neutron-induced radiative capture cross section of ^{233}Pa obtained from the surrogate method (pink symbols) is compared to the evaluations in figure (b) [Boy06].

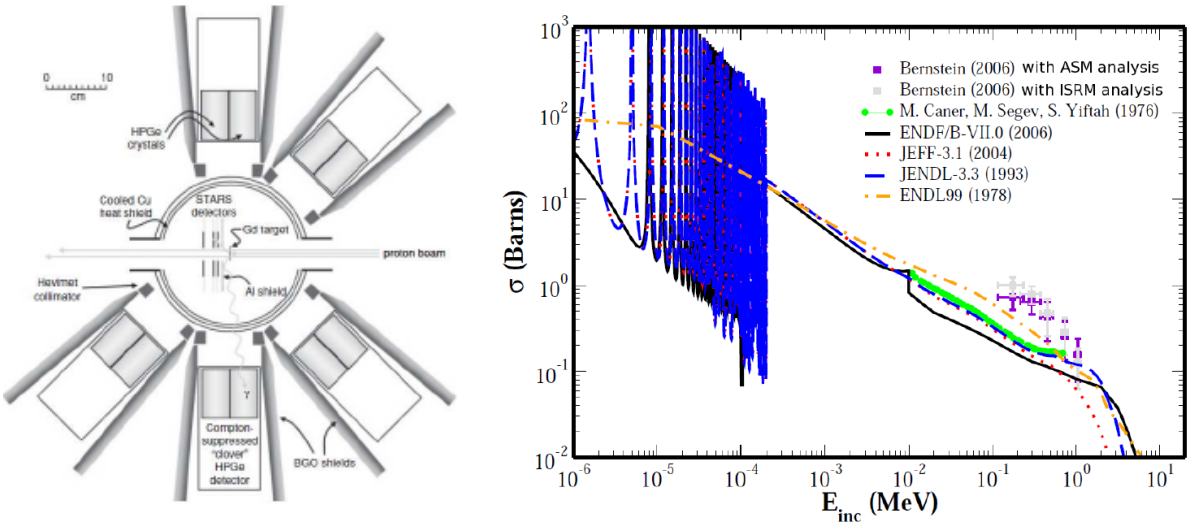

(a) (b)

Figure 2.5: Experimental STARS/LiBerACE set-up (on the left) and the determined radiative capture cross section for ^{237}U (on the right), [Ber05]. The surrogate data are compared with the evaluations and the existing neutron-induced reaction data (in green) by M. Caner et al. The data obtained with the surrogate method are represented by the pink squares and the ones obtained with the surrogate ratio method by the grey squares.

with the direct measurements. To investigate the origin of such discrepancies, the authors performed several Hauser-Feshbach calculations for schematic spin-parity distributions representing possible (p, p') population probabilities. The calculations done with the higher average spin, $J_{avg} = 5 - 8\hbar$, were in better agreement with the surrogate data, while the ones done for $J_{avg} = 2\hbar$ were in better agreement with the neutron induced data. This was a clear evidence that in surrogate reactions the transferred angular momentum is higher than in the case of neutron induced reactions.

The year after, Wilson et al. [Wil12] used the $^{232}Th(d, p\gamma)$ surrogate reaction to deduce the neutron capture cross section of ^{232}Th. The experimental methodology was similar to the one used by Boyer et al. In this case, the CACTUS array at the Oslo Cyclotron Laboratory, consisting of 28 NaI γ-ray detectors covering a solid angle of 15% of 4π was used for the γ-ray detection. This was the first time that the (n,γ) cross section of an actinide was measured using the surrogate method and compared to high quality neutron-induced data, as can be seen in the figure 2.7(a). Again the surrogate data were observed to be systematically higher than the neutron induced ones up to an equivalent neutron energy of 0.4 MeV. Above this energy a better agreement was found with a difference of $\sim$ 15%. This work does not consider the break-up effect, where the deuterium has a certain probability of breaking up in a proton and a neutron when approaching the Coulomb and nuclear field of the target. The final effect is the detection of protons, which are not related to the formation of a compound nucleus. This causes an overestimation of the singles spectrum $N_s(E^\star)$ for excitation energies larger than

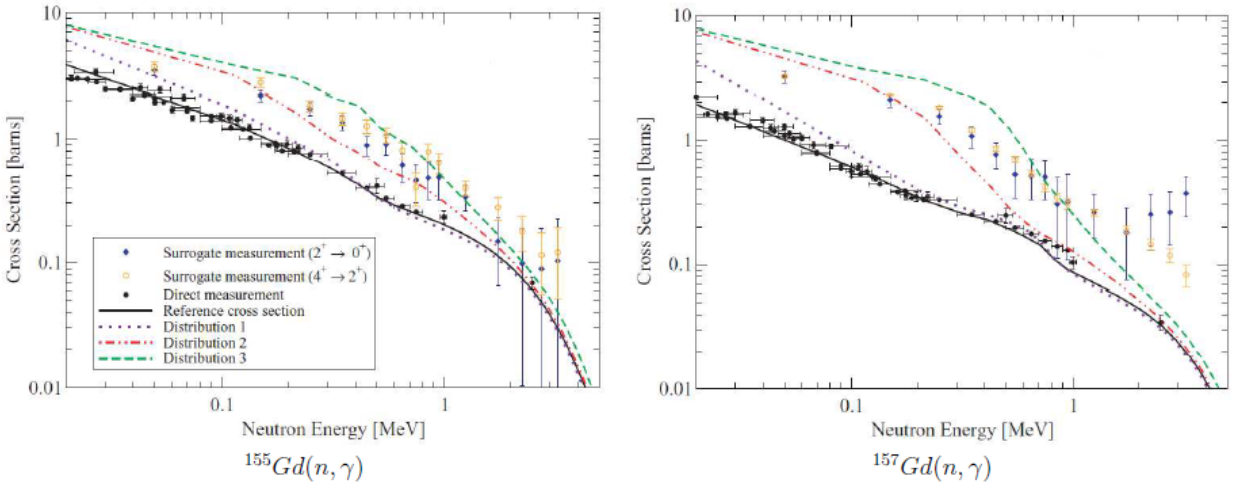

Figure 2.6: The radiative capture cross sections of ^{155}Gd (on the left) and of ^{157}Gd (on the right) obtained with a surrogate reaction are compared with the data from evaluations and neutron induced reaction experiments, (see ref. [Sci10]). In purple, red and green calculations obtained using different spin/parity distributions are reported.

S_n. Therefore, the cross section of $^{232}Th(n,\gamma)$ obtained with the surrogate reaction is expected to be larger than the one shown in figure 2.7(a). Note that deuteron breakup is not possible at excitation energies lower than S_n. If γ-decay is the only possible de-excitation mode, the γ-emission probability must be 1 below S_n. In figure 2.7(b), we can see that the γ-emission probability starts to decrease about 200 keV before S_n. This problem may be due to problems with the energy calibration of the ejectile detectors or to the excitation energy resolution.

To better understand the origin of the discrepancies between the results provided by the surrogate reaction method and the neutron induced-reactions in the case of radiative capture, the CENBG collaboration performed a detailed study of the surrogate reaction method in the frame of Boutoux's Ph.D. thesis [Bou11]. In this work realized in 2011, they investigated the $^{174}Yb(^3He,\alpha\gamma)^{173}Yb^\star$ reaction. The data showed the similar discrepancies between neutron induced and surrogate probabilities. In figure 2.8, the γ-emission probability obtained with the surrogate reaction as a function of the excitation energy of the compound nucleus $^{173}Yb^\star$ is compared to the ones obtained with the $^{172}Yb(n,\gamma)$ and $^{173}Yb(\gamma,\gamma)$ reactions. In this study, the theoretically calculated branching ratios G_χ were used to fit the gamma decay probabilities with a Gaussian spin distribution by varying its parameters. The authors found that the average spins populated in the transfer reaction are 2 $\hbar$ to 4 $\hbar$ larger than the ones populated in the neutron-induced reaction. Right above S_n, neutron emission to the ground state of the residual nucleus is the dominant way of de-excitation for a neutron-induced reaction. Due to the large difference in spin between the ground state of the residual nucleus and the compound nucleus produced in the used transfer reaction, neutron emission is highly suppressed and γ-decay is favoured.

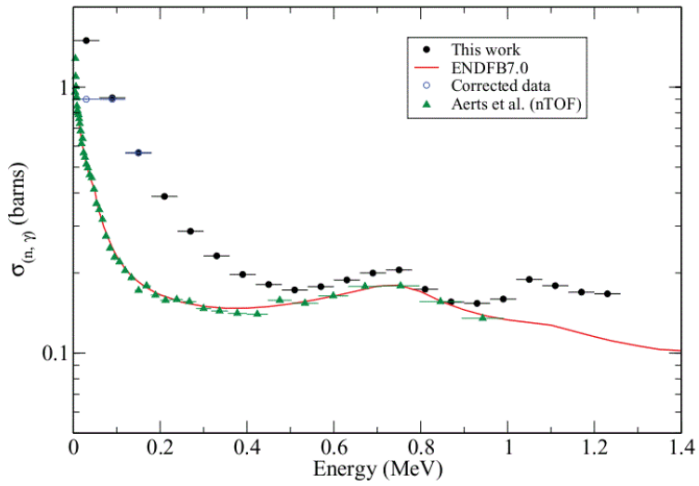

(a)

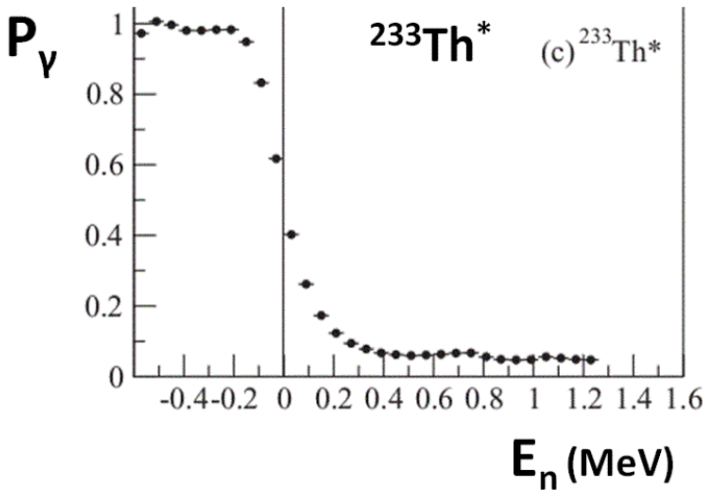

(b)

Figure 2.7: On the top the radiative capture cross section of ^{232}Th obtained with the transfer reaction $^{232}Th(d,p)$ by Wilson et al. [Wil12] is compared to the neutron induced data [Aer04] and an evaluation. On the bottom, the γ-emission probability of ^{233}Th measured in the transfer reaction $^{232}Th(d,p)$ is shown.

In order to further study the validity of the WE approximation, the CENBG proposed another study in 2016 to measure for the first time simultaneously fission and gamma-decay probabilities in a surrogate-reaction experiment. In this work, described in detail by Ducasse et al. [Duc15], the $^{238}U(d,p)$ reaction was used to simultaneously measure the fission and the γ-decay probabilities of $^{239}U^{\star}$. The results were corrected for the deuteron break-up. In figure 2.9(a), the corrected γ and fission probabilities are shown together with the evaluations and the fission data of Britt and Cramer. The larger angular momentum transferred in surrogate reactions at low equivalent neutron energy E_n was considered as being responsible for the disagreement

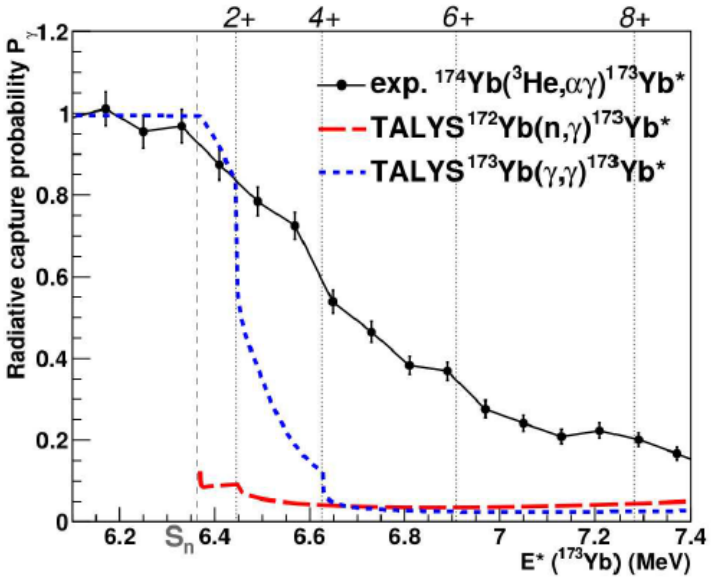

Figure 2.8: Experimental γ-emission probability for the compound nucleus $^{173}Yb^{\star}$ as a function of the excitation energy obtained with the $^{174}Yb(^{3}He,\alpha)$ surrogate reactions (symbols), [Bou11]. The red and blue lines represent the probabilities derived using TALYS for the neutron-induced reaction $^{172}Yb(n,\gamma)$ and the γ-induced reaction $^{173}Yb(\gamma,\gamma)$. The vertical lines indicate the position in $E^{\star}$ of the first excited states of ^{172}Yb.

with the neutron radiative capture data, while for fission the difference observed at $E^{\star} > 6.3$ MeV was attributed to the presence of oxygen in the target. In figure 2.9(b), both the γ-decay and fission probabilities are shown with a zoom in the 5 to 6.3 MeV energy region. In this region, fission is in good agreement with the neutron induced data, but $P_{\gamma}^{surr.} > P_{\gamma}^{n}$, which proves that P_{γ} is more sensitive than P_f to the J^{π} mismatch. No spin distribution could be found to fit both decay probabilities, most likely because it was assumed that negative and positive parities were equally populated, which is not true particularly at low E*, as it will be shown later.

2.3 The surrogate ratio method

In 2005, a variation of the standard surrogate method was developed by Plettner et al. to avoid the problem of contaminants in the singles spectrum [Ple05], which has been widely used since then by the Livermore collaboration [Esc12]. In this approach, also based on the WE hypothesis, two different surrogate reaction experiments are used for the calculation of a ratio factor $R(E^{\star})$. This factor is obtained by determining the ratio of two neutron induced reactions on target nuclei A and B:

$$R(E^{\star}) = \frac{\sigma_{n,\chi}^{A}(E^{\star})}{\sigma_{n,\chi}^{B}(E^{\star})} \tag{2.1}$$

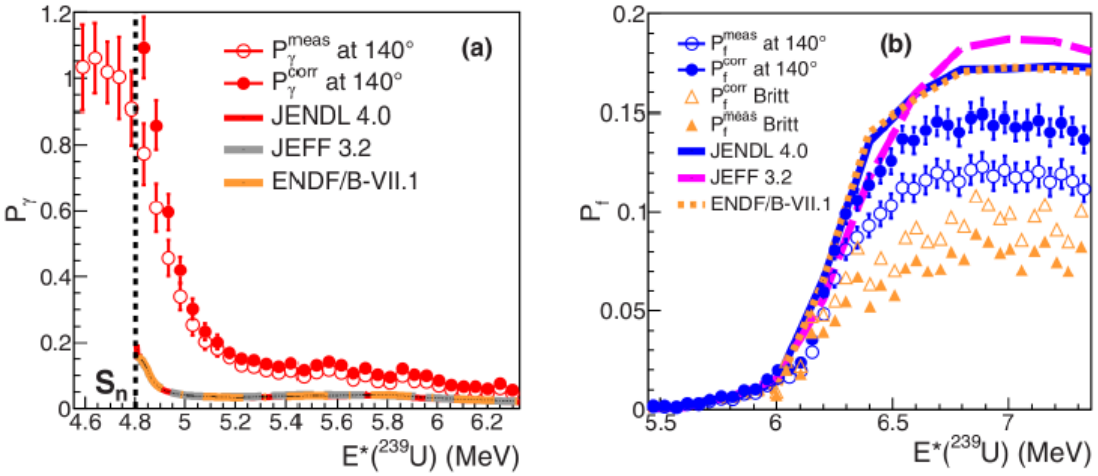

(a)

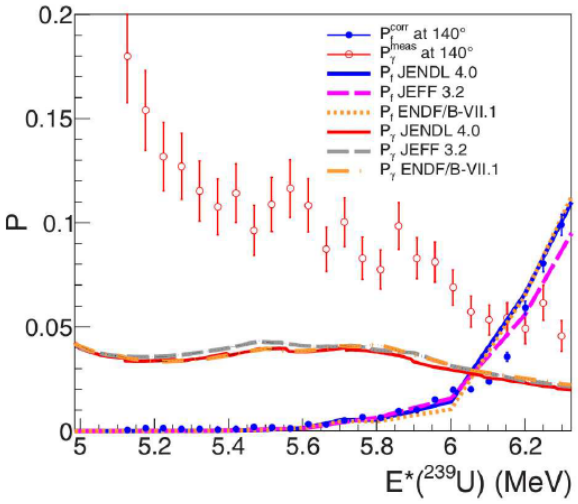

(b)

Figure 2.9: Probabilities for γ-emission and fission of ^{239}U as a function of excitation energy obtained with the $^{238}U(d,p)$ reaction, [Duc15]. The probabilities have been corrected for the deuteron break-up and are compared with different evaluations and available data. In the top figure the probabilities are shown over the full excitation energy range available, while in the bottom a zoom on the excitation energy range between 5 and 6.3 MeV is shown.

where $\sigma^A_{n,\chi}(E^\star)$ corresponds to the cross section for the $n + A \rightarrow c + C$ reaction and $\sigma^B_{n,\chi}(E)$ to the $n + B \rightarrow c' + C'$ reaction. Using equation (1.5) the ratio $R(E^\star)$ can be expressed as:

$$R(E) = \frac{\sigma_n^{CN,A}(E_n) P_\chi^{surr.,A}(E^\star)}{\sigma_n^{CN,B}(E_n) P_\chi^{surr.,B}(E^\star)} \tag{2.2}$$

where σ_n^{CN} is the compound nucleus formation cross section which, as we showed before, can be calculated within the optical model formalism, and $P_\chi^{surr.}$ is the probability for the decay

channel χ obtained with the surrogate reaction. The excitation energy of the compound nucleus and the kinetic energy of the incident neutron E_n are related by equation (1.4). Combining equation (2.2) with equation (1.43) we get:

$$R(E^\star) = \frac{\sigma_n^{CN,A}(E_n)}{\sigma_n^{CN,B}(E_n)} \cdot \frac{N_s^{surr.,B}(E^\star)}{N_s^{surr.,A}(E^\star)} \cdot \frac{N_\chi^{surr.,A}(E^\star)}{N_\chi^{surr.,B}(E^\star)} \cdot \frac{\epsilon_\chi^B(E^\star)}{\epsilon_\chi^A(E^\star)} \tag{2.3}$$

If the target nuclei A and B have similar physical properties one can consider $\sigma_n^{CN,A}(E_n) \approx \sigma_n^{CN,B}(E_n)$ and $\epsilon_\chi^A(E^\star) \approx \epsilon_\chi^B(E^\star)$. If the two surrogate reactions involve the same projectile and ejectile and the associated cross sections are similar, then we can write:

$$R(E^\star) = F \cdot \frac{N_\chi^{surr.,A}(E^\star)}{N_\chi^{surr.,B}(E^\star)} \tag{2.4}$$

where F is a constant that can be determined from the beam current, the target thickness and the experiment duration. The ratio $R(E^\star)$ can be measured experimentally and if $\sigma_{n,\chi}^B(E^\star)$ is known, the cross section of interest $\sigma_{n,\chi}^A(E^\star)$ can be derived using equation (2.1):

$$\sigma_{n,\chi}^A(E^\star) = \sigma_{n,\chi}^B(E^\star) \cdot R(E^\star) \tag{2.5}$$

The surrogate ratio method (SRM) involves the use of two surrogate reactions to form compound nuclei A+1 and B+1 with two targets and the same experimental set-up. In addition, the SRM requires one of the cross sections to be known in order to infer the desired one.
The main advantages of the ratio method over the standard one is that it eliminates the necessity to accurately measure the total number of single events $N_s(E^\star)$, which correspond to the number of detected ejectiles. In this way one can avoid the problem of target impurities that induce a background. This is true for fission reactions. However, for radiative capture reactions the light contaminants may also emit γ-rays and pollute also the number of coincidences. As explained in [Esc06], the comparison of the neutron-induced and the surrogate-ratio data has shown that the ratio method reduces somewhat the effect of the spin-parity mismatch at excitation energies where the WE hypothesis fails, but does not eliminate it. The surrogate ratio method has also some drawbacks. First of all, it requires the use of two target nuclei whose physical properties are close. This limits the study of nuclei far from the valley of stability where target fabrication becomes problematic due to the high radiotoxicity of the nuclei of interest. In addition, the approximations leading to equation (2.4) introduce additional sources of errors that are difficult to quantify.

As for the standard surrogate method, the surrogate ratio method has been used to determine fission and radiative capture cross sections. Even though the J^π mismatch effects can be reduced with the SRM, many experiments applied to fission were found to fail at the fission threshold (see Refs. [Lyl07], [Gol09] and [Res11]). It was not observed that when using dissim-

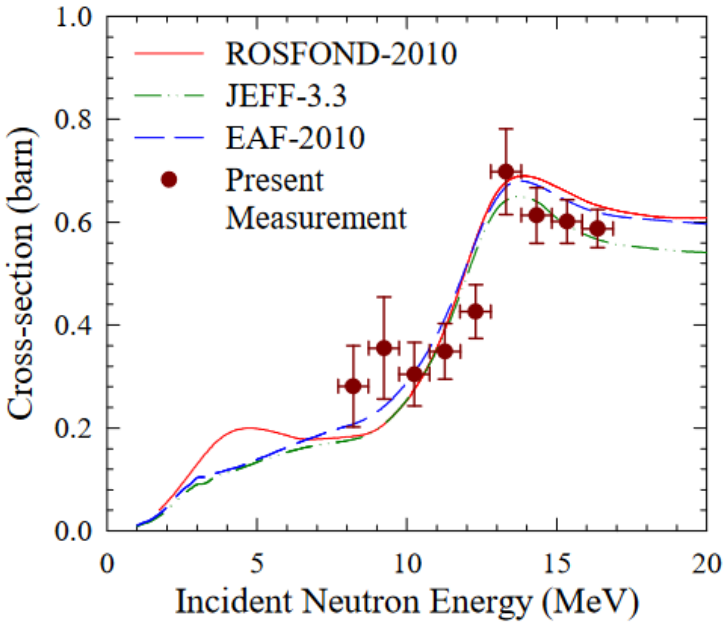

Figure 2.10: The experimental $^{53}Mn(n,xp)$ cross section obtained with the surrogate ratio method is shown as a function of equivalent neutron energy along with the results from various nuclear data libraries, [Gan19].

ilar compound nuclei, angular momentum effects were enhanced.

For radiative capture the results obtained with the surrogate ration method show significant discrepancies with respect to neutron induced data at the lowest equivalent neutron energies [Esc12]. No clear conclusion can be done on the utility of using similar targets. For example [Gol08] a good agreement with neutron induced data was found even though the target nuclei had very different masses and ground-state J^{π}.

In conclusion, we can say that the cross sections extracted by the ratio method can be in good agreement, or in disagreement with the neutron data for different reasons which are currently not always precisely defined and understood. This complicates significantly the interpretation of the results. Although many efforts have been done to understand how the SRM works, the conditions under which the SRM can be used with confidence are still unclear.

The latest application of the SRM was done by Gandhi et al. in 2019, [Gan19]. In this experiment, carried out at the BARC-TIFR Pelletron accelerator facility at Mumbai, they determined the $^{53}Mn(n,xp)$ cross section. A ^{6}Li beam was used to bombard a ^{52}Cr and a ^{59}Co target at an incident energy of 33 MeV and 40.5 MeV respectively. The surrogate reactions investigated were the $^{52}Cr(^{6}Li,\alpha)^{54}Mn^{\star}$ and the $^{59}Co(^{6}Li,\alpha)^{61}Ni^{\star}$. The compound systems $^{54}Mn^{\star}$ and $^{61}Ni^{\star}$ were formed at overlapping excitation energies in the range of ~17 - 25 MeV. The $^{53}Mn(n,xp)$ cross section was determined using equation (2.5) with the known cross section for the $^{60}Ni(n,xp)$ taken from [Pan19]. In figure 2.10, the experimental results are compared with the evaluation libraries EAF-2010, ROSFOND-2010, and JEFF-3.3.

2.4 Beyond the WE hypothesis

As demonstrated by the previously described experiments, discrepancies have been found between the cross sections obtained with surrogate reactions using the WE hypothesis and the desired neutron induced reactions. The reason is that the J^π distribution of the compound nucleus produced by the surrogate reaction can be very different from the one obtained with the desired reaction. The experiments performed up to now have revealed that the γ-decay probability obtained from surrogate reactions is higher than the one from neutron-induced reactions due to this J^π mismatch. As already explained, this effect is coming from the competition with neutron-emission, which is suppressed when the difference between the spin of the parent nucleus $A+1$ and the daughter nucleus A is large.
In order to go beyond the WE hypothesis, a different strategy must be used in the determination of neutron induced cross section by the surrogate reaction method. The new strategy consists in predicting the spin and parity distributions populated in the surrogate reaction. The calculated J^π distributions are then combined with the decay probabilities obtained with the surrogate reaction to fix the values of the parameters of some of the key ingredients of the statistical model. With the newly-tuned parameters the model gives an accurate prediction of the desired neutron cross section.

A first attempt to correct the data provided by the WE approximation was done by W. Younes and H. Britt in 2003. In their work, they investigated if nuclear models could be used to correct for the J^π population mismatch (see Ref. [You03a] for the methodology used and [You03b] for the detailed results). They did a theoretical work based on the data of J.Cramer [Cra70b, Cra70a] and B. Back [Bac74b, Cra70a]. More in detail, Younes and Britt used a Hauser-Feshbach description for the statistical competition between γ-decay, neutron emission and fission. They fitted their calculated P_f to the surrogate data. They only allowed the heights of the fission barriers to vary. Discrete levels, level densities, γ-ray strength functions and the neutron transmission coefficients were considered to be fixed. The resulting fission probabilities were in good agreement with the measured data below S_n but showed deviations as large as 35% above S_n. Therefore, a re-normalisation factor was introduced to account for the differences, which was also used to renormalise the calculated (n, f) cross sections. On the upper part of figure 2.11, the results for the $^{235}U(n, f)$ cross section are shown.

More recently, Escher et al. [Esc18] considered a short-lived nucleus in a well-studied but challenging area of the nuclear chart. For this reason they first provided an assessment of the approach by selecting a nearby nucleus for a benchmark study. They focussed on the determination of the neutron-capture reaction of the short-lived $^{87}Y(\tau = 79.8h)$ using the $^{89}Y(p, d)^{88}Y$ reaction as a surrogate. To benchmark the methodology they determined the known $^{90}Zr(n, \gamma)$ cross section with the $^{92}Zr(p, d)$ surrogate reaction. The data were measured at the K250 Cyclotron at Texas University, where natural ^{89}Y and enriched ^{92}Zr targets were bombarded with 28.5 MeV protons. The interesting innovation of this experiment was that the spin-parity

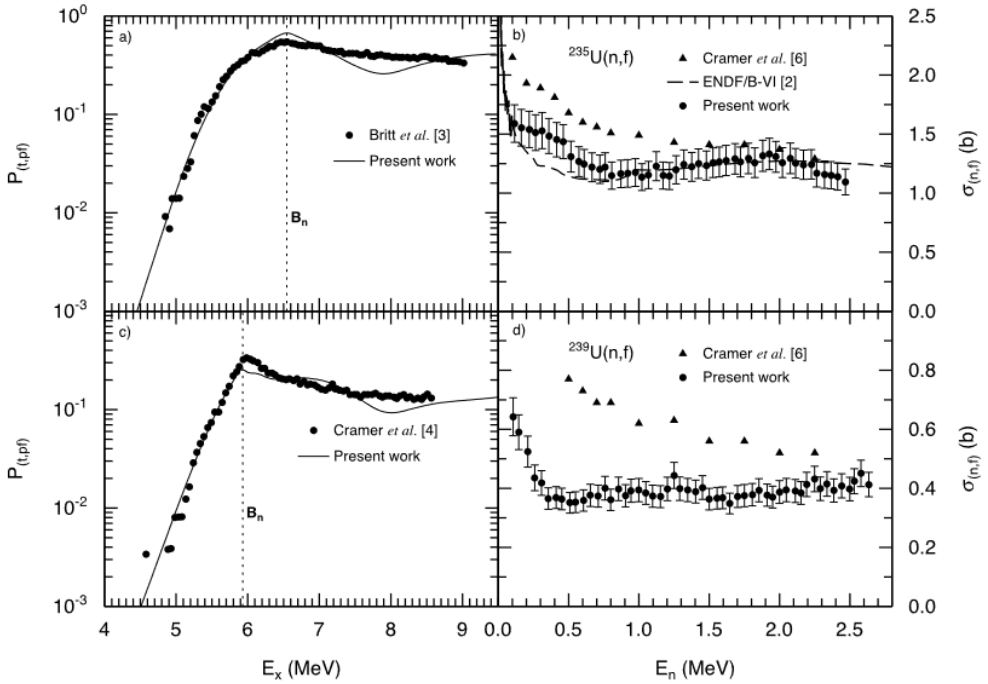

Figure 2.11: The left panels shows the comparison of the model of [You03b] to (t, pf) data (filled circles) for $^{234}U(t, pf)$ (a) and $^{238}U(t, pf)$ (c) measurements. The corresponding deduced $^{235}U(n, f)$ and $^{239}U(n, f)$ cross sections are shown in panels (b) and (d). In panels (a) and (c), the vertical dotted lines mark the position of the neutron binding energy of the compound system. Comparisons to estimated (n,f) cross sections using the WE hypothesis by Cramer and Britt [Cra70a] and to the ENDF/B-VI evaluation are also shown in panels (b) and (d).

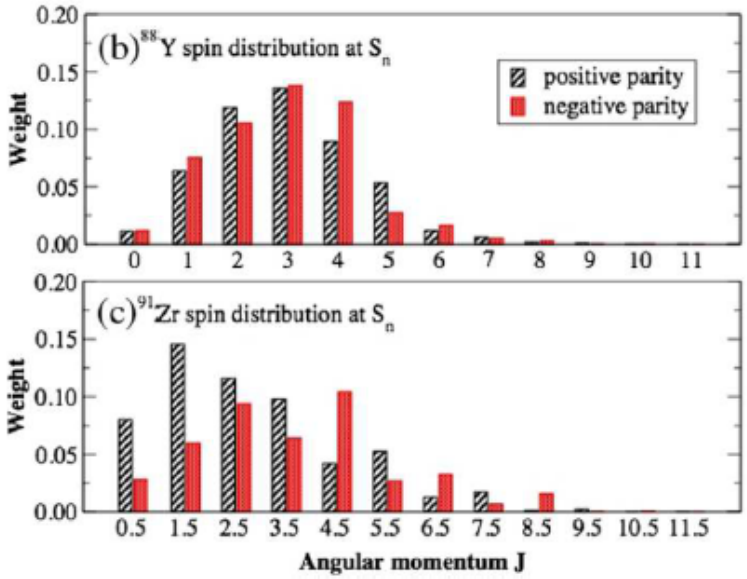

Figure 2.12: Calculated J^π distributions at the neutron separation energy populated in the surrogate reactions $^{89}Y(p, d)$ and $^{92}Zr(p, d)$, from [Esc18].

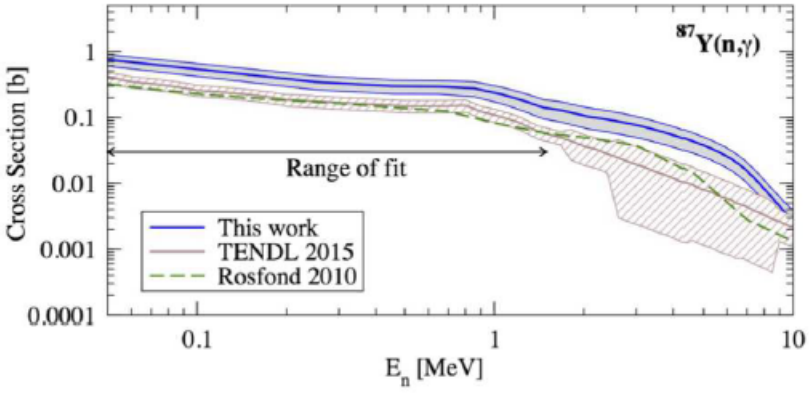

Figure 2.13: Capture cross section for ^{87}Y obtained from the surrogate reaction $^{89}Y(p,d)^{88}Y$. The results are compared with evaluations, unfortunately no neutron induced reaction data is available, from [Rat19].

distributions $F(J^{\pi}, E^{\star})$ of the compound nuclei were calculated using the two-step Distorted-Wave Born Approximation (DWBA) model. The spin-parity distributions are shown in fig. 2.12 for both reactions. The authors measured the probabilities for specific γ-ray transitions at $E^{\star}$ between 6 and 10 MeV from which they derived constraints for the decay model parameters (level densities and γ-ray strength functions). After validating the procedure for $^{90}Zr(n,\gamma)$, the authors deduced the $^{87}Y(n,\gamma)$ cross section. In figure 2.13, the results obtained by the authors are compared with the evaluations (TENDL 2015, Rosfond 2010). The results are found globally to be a factor two larger than the evaluations. However, this is already a significant improvement over previous attempts to determine capture cross sections from surrogate reaction data, especially because it was achieved for a nucleus that is very sensitive to spin-parity effects.

In 2019, Ratkiewcz et al. [Rat19] used the procedure proposed by Escher et al., to determine the $^{95}Mo(n,\gamma)$ cross section with the $^{95}Mo(d,p)$ surrogate reaction. The J^{π} distribution populated in the (d,p) reaction was corrected for deuteron breakup effects. An interesting aspect of this work is that the calculated spin distribution shows a strong dependence on the parity, see figure 2.14 (on the top). This is in clear contradiction with the assumption of equal population of positive and negative parities. The cross section obtained with a Hauser-Feshbach calculation with the fitted parameters is shown in figure 2.14 (on the bottom). As can be seen, the agreement with the neutron-induced data (see red and black points) and the evaluation ENDF/B-VIII.0 is very good. The improvement of the cross section determination reached with this new approach becomes clear when comparing with the results obtained with the WE approximation shown in gold.

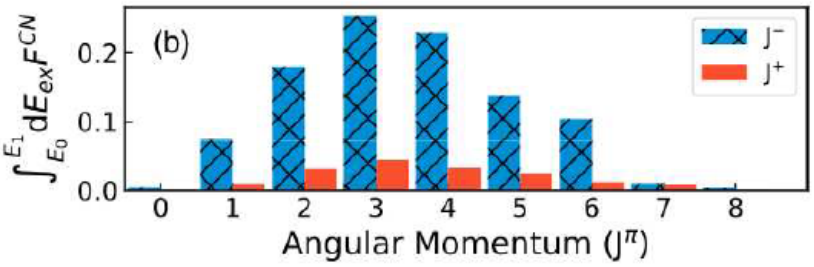

(a)

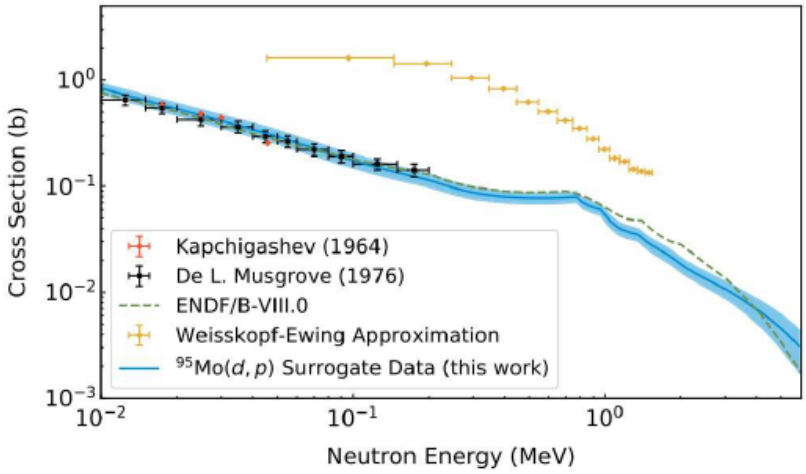

(b)

Figure 2.14: Figure (a) shows the calculated spin distribution populated in the $^{95}Mo(d,p)$ reaction for the excitation energy range 8.55 MeV and 10.65 MeV (see ref. [Rat19]). In the bottom figure the capture cross section for ^{95}Mo deduced from the surrogate reaction $^{95}Mo(d,p)^{96}Mo^{\star}$. With the new approach (solid blue line) is shown in comparison to the results obtained applying the WE approximation (gold points), (see ref. [Rat19]).

2.4.1 Simultaneous determination of neutron-induced fission and radiative capture cross sections

An important step forward in the application of the surrogate-reaction method was done in 2020 by our collaboration [Sán20]. In this work, the new approach was successfully used, for the first time, to simultaneously infer σ_f^n and σ_γ^n of an even-even actinide nucleus. More

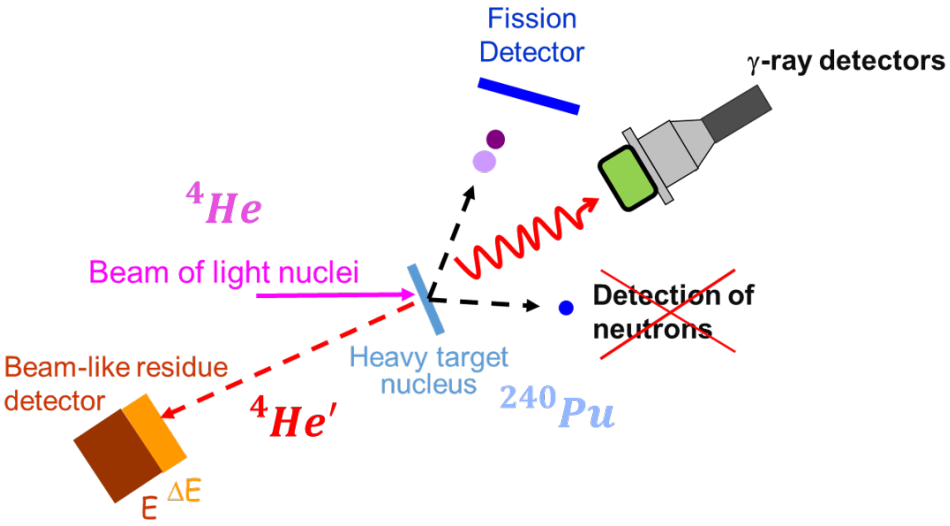

(a) Experimental set-up

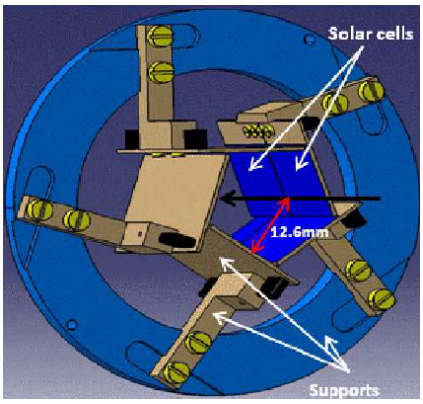

(b) Fission fragment detectors

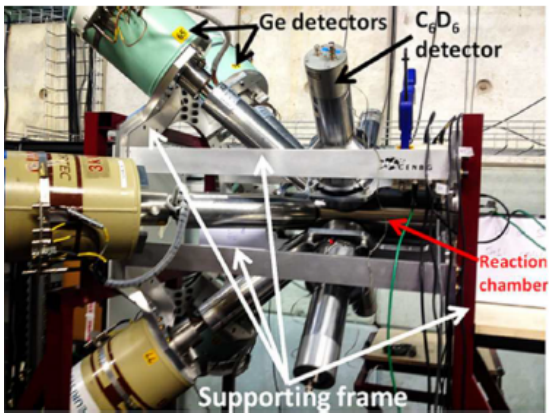

(c) Scintillators and germanium detectors for γ-ray detection

Figure 2.15: Schematic view of the experimental set-up used to simultaneously measure the fission and gamma-decay probabilities of $^{240}Pu^\star$ (ref. [San19]).

precisely, the inelastic scattering reaction $^{240}Pu(^4He, ^4He')^{240}Pu$ was used as a surrogate for the $n + ^{239}Pu$ reaction. In this experiment performed in direct kinematics, a 30 MeV beam of ^4He delivered by the Tandem accelerator of the ALTO facility in Orsay (France) impinged on a 100 $\mu g/cm^2$ PuO_2 target deposited on a carbon support of the same areal density. In figure 2.15(a), a schematic representation of the experimental set-up is shown. The probabili-

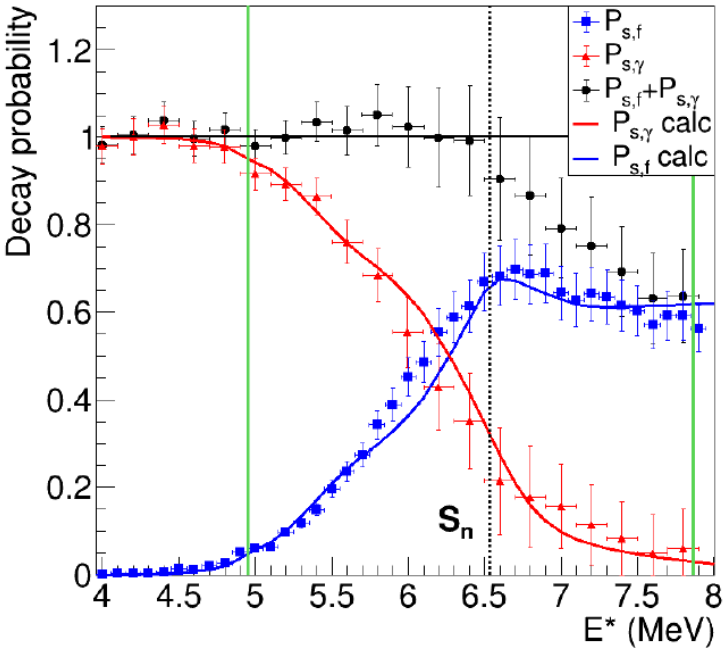

Figure 2.16: Decay probabilities from [Sán20] for fission (blue squares) and γ-emission (red triangles) measured for the $^{240}Pu(^4He, ^4He')^{240}Pu^\star$ reaction as a function of the excitation energy $E^\star$ of $^{240}Pu^\star$. The sum of the two probabilities is given by the black circles. The $E^\star$ range used for parameter adjustment is delimited by the vertical green lines. The vertical dotted line indicates the neutron separation energy S_n of ^{240}Pu. The horizontal black line at a constant value of 1 serves to guide the eye.

ties $P_f^{surr.}$ and $P_\gamma^{surr.}$ were obtained from the measured number of scattered $^4He'$ as well as of fission fragments and γ-ray cascades detected in coincidence with the $^4He'$. The $^4He'$ nuclei were detected with two position-sensitive silicon telescopes centred at a polar angle θ of 138.5° with respect to the beam axis. Fission fragments were detected with an array of solar cells and γ rays with four C_6D_6 liquid scintillators and five high-purity germanium detectors (see figs. 2.15(b) and 2.15(c)). The simultaneous measurement of $P_f^{surr.}$ and $P_\gamma^{surr.}$ provided a stringent test of the used experimental method because below the neutron separation energy $\approx$6.5 MeV the sum of the probabilities of the two open decay channels (γ and fission) must be equal to 1. As can be seen in figure 2.16 this condition is fully verified by the experimental data. When the excitation energy $E^\star$ overcomes the neutron separation energy S_n, the sum of the two probabilities is no longer 1 because neutron emission becomes possible and competes with fission and γ-emission. As it is visible in figure 2.17, there is a clear disagreement between the directly measured neutron-induced fission cross section and the cross section obtained following the WE approximation, especially at low energies. For σ_γ^n, the red squares obtained with the WE approximation are well above the evaluations and neutron-induced data. However, due to the large uncertainties no clear conclusion can be drawn.

As already shown by Escher and Ratkiewcz, in order to go beyond the WE approximation, the spin-parity distribution $F(E^\star, J^\pi)$ populated by the surrogate reaction $^{240}Pu(^4He, ^4He')$ must

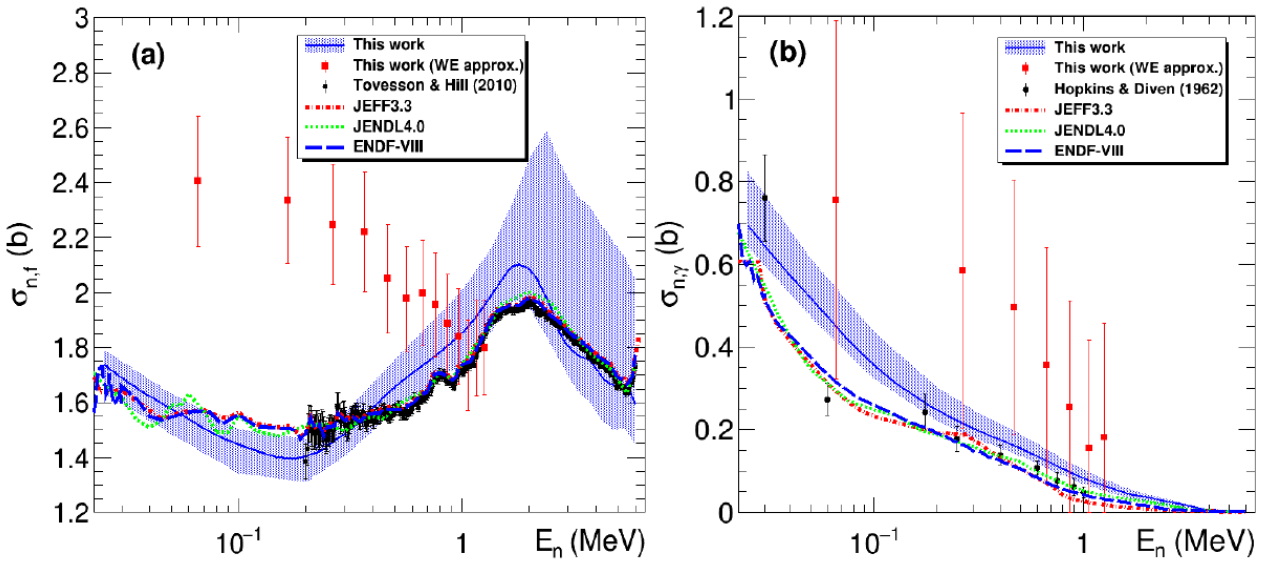

Figure 2.17: Neutron-induced fission (a) and radiative-capture (b) cross sections of ^{239}Pu as a function of neutron energy (ref. [Sán20]). The red squares are the cross sections obtained with the WE approximation. The cross sections calculated with the parameters deduced from the measured decay probabilities are shown as blue solid lines. The shaded blue areas indicate the associated uncertainties. The dash-dotted, dotted and dashed lines represent different evaluations. The black dots indicate the neutron-induced data of [Tov10] (a) and [Hop62] (b).

be calculated. An example of the calculated J^π distribution at $E^\star$ =7.5 MeV and $\theta_{^4He'}$=140° is shown in fig. 2.18. The probabilities $P_f^{surr.}$ and $P_\gamma^{surr.}$ were determined with the calculated $F(E^\star, J^\pi)$ and the probabilities $G(E^\star, J^\pi)$ calculated with the Hauser-Feshbach formalism of Talys 1.95 [Tal19]. The values and the uncertainties of several key parameters needed to model the decay of $^{240}Pu^\star$ were tuned to reproduce the experimental P_f^{surr} and P_γ^{surr} in the range $E^\star$ between 5 and 7.8. These parameters were the normalization factor of the γ-ray strength function, the heights and widths of the two fission barriers, the two temperature parameters of the Gilbert-Cameron formula at the barrier deformations and the energy of few class II states. After, being fixed the parameters were implemented in Talys to calculate the σ_f^n and σ_γ^n shown in figure 2.17.

The obtained σ_f^n agrees rather well with the evaluations and the directly-measured neutron-induced cross sections. Also a fairly good agreement can be seen for σ_γ^n. The CENBG collaboration data are slightly above the evaluations (with the largest discrepancy of about 50% at 60 keV) and most data points of [Hop62]. Such a good level of agreement demonstrates that the authors were able to account for the spin/parity differences between the considered surrogate and neutron-induced reactions and obtain, for the first time simultaneously, reliable results for both fission and radiative-capture cross sections.

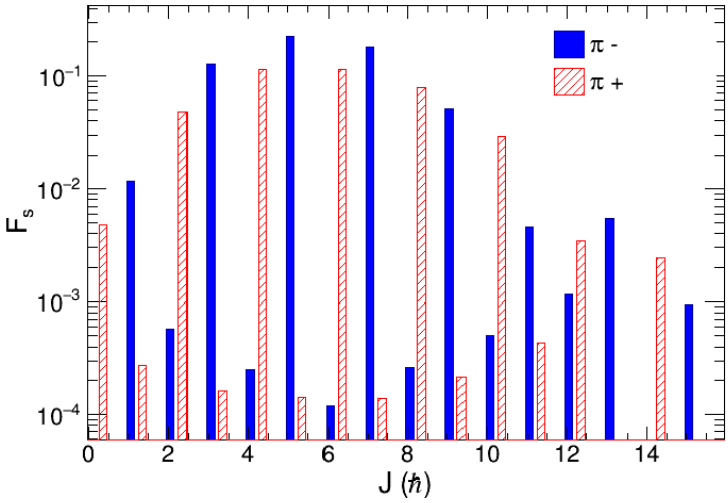

Figure 2.18: Calculated spin-parity distribution F_{surr} of $^{240}Pu^{\star}$ populated by the $^{240}Pu(^{4}He, ^{4}He')$ reaction at $E^{\star}$ =7.5 MeV and $\theta_{^4He'}$=140°, (ref. [Sán20]).

2.5 Limitations of direct kinematics

As demonstrated by the experimental results described in this chapter, the surrogate reaction method represents a powerful approach for the determination of neutron induced reaction cross section of short-lived nuclei. However, surrogate reaction experiments in direct kinematics have significant limitations: (a) when the nuclei of interest are short-lived the necessary targets are unavailable. (b) Competing reactions in target contaminants and backings produce a high background that is very complicated or even impossible to remove. (c) The heavy products of the decay of the compound nucleus are stopped in the target sample and cannot be detected. Therefore, the measurement of γ- and neutron-emission probabilities requires detecting the emitted γ-rays and neutrons, which is very difficult due to the very low detection efficiencies.
Some of these limitations can be addressed performing the required surrogate reaction in inverse kinematics, where the heavy nucleus is accelerated and impinges on a light target nucleus which is at rest (see figure 2.19). Indeed, the use of radioactive ion beams (RIB) can solve the problem of the target radioactivity and give access short-lived nuclei. In addition, thanks to the high energy of the ion beams, the heavy residues produced after γ and neutron emission are not stopped in the target and can be detected with high efficiency.
Still, radioactive ion beams have low intensities and experiments have to be designed such that the reaction probability in the target is high enough for the measurement to be performed in a few days. This requires a high areal density of target atoms. However, the different isotopes of H and He, as the most promising candidates for surrogates, are gases. High areal densities of these materials are very difficult to achieve and cause several problems: (a) Pressurized gas cells and cryogenic targets require entrance and exit windows. The beam can interact with the window material generating a strong background. (b) Chemical compounds like CH_2 have the same disadvantages as windows. (c) Windowless gas or cryogenic targets with high areal

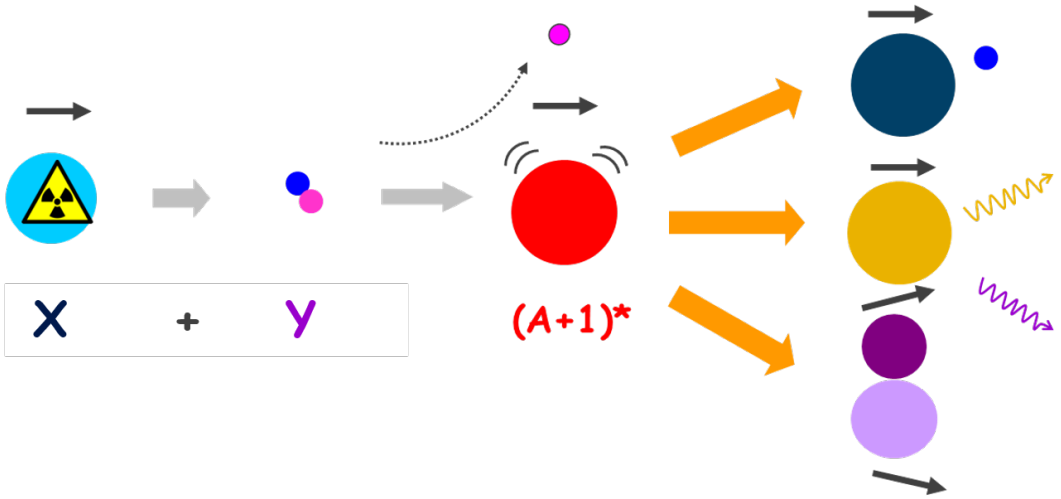

Figure 2.19: Schematic representation of a surrogate reaction in inverse kinematics. Contrary to direct kinematics experiments, a heavy radioactive ion beam (X) is produced and interacts with a light target (y). The black horizontal arrows indicate that the heavy residues produced after neutron and γ-emission have similar velocities as the beam.

densities are large. This results in a very limited resolution of the interaction point. (d) The resolution of the emission angle of the target-like residue relative to the direction of the incoming projectile is reduced if the nuclei straggle in the target material before and after the reaction. (e) The projectile ions and reaction products lose energy due to the interaction with the electrons of the thick target. The emission angle and the energy of the target-like residue as well as the projectile energy are therefore uncertain, which significantly limits the resolution in the excitation energy of the compound nucleus. However, the decay probabilities change very rapidly with excitation energy at S_n and at the fission threshold, and they often show structures. The excitation-energy resolution required to scan this rapid evolution is a few 100 keV, quite difficult to achieve in inverse kinematics [Cat14]. The experiments described so far are called single-pass experiments, because each ion passes the target only once. Afterwards the expensively produced ions are lost.

With the NECTAR project we propose to overcome the previously described limitations with a completely new solution. Our goal is to investigate for the first time surrogate reaction experiments in inverse kinematics at storage rings. This new approach together with the first proof of principle experiment will be described in the following chapters.

2.6 State of the art of inverse kinematics experiments

Before going into the detail of the surrogate reaction studies at storage rings, it is interesting to mention the present state of the art of experiments in inverse kinematics. Note that all these experiments are focussed on the determination of fission probabilities.

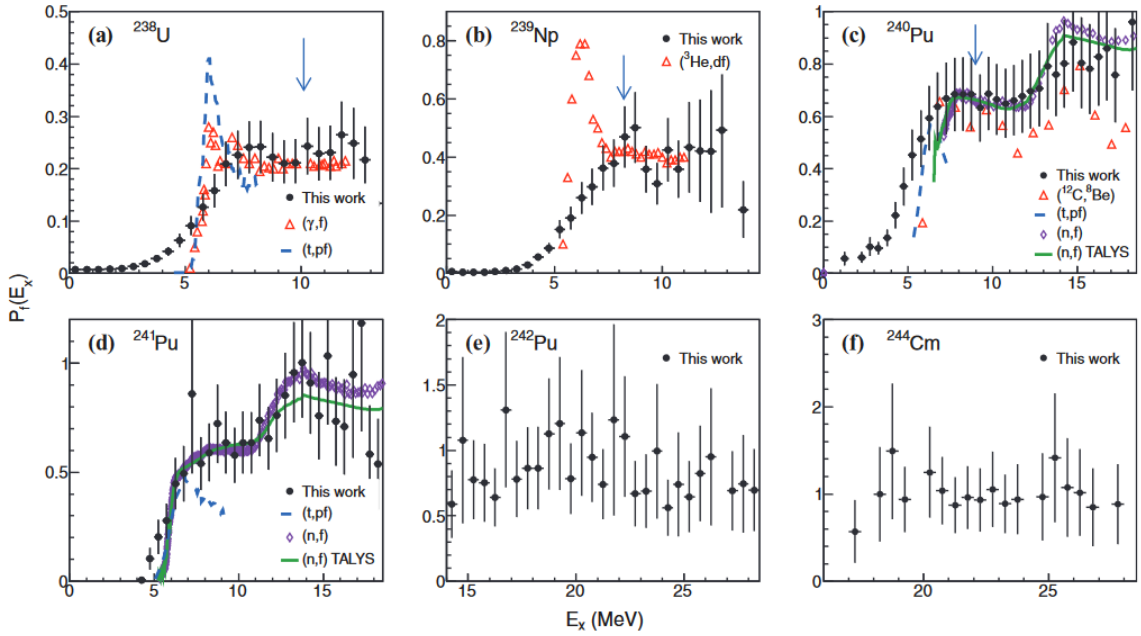

Figure 2.20: (Color online) Fission probabilities as a function of the excitation energy. Results are presented for $^{238}U + ^{12}C$ inelastic scattering (a) and transfer-induced fission reactions (b)–(f), [Rod14]. The fissioning nucleus is indicated in each figure. In some panels earlier γ-, transfer-, and neutron-induced fission data are included for comparison, as well as TALYS calculations of neutron-induced fission probabilities.

Fission experiments in inverse kinematics have been performed at GANIL with the VAMOS spectrometer. In these single-pass experiments, inelastic and multi-nucleon transfer reactions between a ^{238}U beam and a ^{12}C target were used for the production of the fissioning systems of interest. The use of a heavy beam and a light target defines an inverse-kinematics scenario in which the fission fragments are emitted in forward direction with relatively high kinetic energies. The detection of target-like residues was performed with a Si telescope named SPIDER, while the large acceptance VAMOS spectrometer was used to determine the mass and the charge of the fission fragments as well as their kinetic energy E_k.

Results regarding isotopic fission fragment yields can be found in [Caa13, Del16]. In [Rod14] the fission probabilities of ^{238}U, ^{239}Np and $^{240,241,242}Pu$ and ^{244}Cm were determined as a function of the excitation energy, see figure 2.20. Important differences can be observed with respect to other data at the fission threshold. The interpretation of these differences is complicated due to some experimental problems, which had a significant impact on the quality of the results. Indeed, there was a large background produced by the solid target and the related collimator, the excitation energy resolution was limited to about 2.7 MeV (FWHM), and there was a significant uncertainty in the determination of the acceptance of the VAMOS spectrometer.
In the last decade, fission experiments have also been carried out at the GSI/FAIR facility using the inverse-kinematics technique in combination with the state-of-the-art detectors of SOFIA [Mar14]. These experiments are done at much larger energy than the experiments performed in

GANIL. The incident energy typically ranges between 500 and 700 MeV/u. Fission is induced by Coulomb excitation with heavy targets such as lead or uranium. Thanks to the high energy of the fissioning projectile the fission fragments are emitted in a narrow cone in the forward direction with very high velocities, permitting to detect both fragments simultaneously and to measure the isotopic yields with the SOFIA set-up. The fission fragments isotopic distributions are measured with high precision. However, it is not possible to determine the $E^{\star}$ of the fissioning nucleus. For this reason, A. Grana et al. [Gra22] have recently performed an experiment to use the quasi free $(p, 2p)$ scattering reaction in combination with the SOFIA set-up to measure fission probabilities. In this reaction, the projectile nucleus is excited through particle-hole excitations that can lead to excitation energies with mean values around few tens of MeV. By measuring the energy and scattering angle of the two protons it is possible to infer the $E^{\star}$ of the fissioning nucleus. In this first experiment a primary beam of ^{238}U at 560 MeV/u delivered by the SIS18 synchrotron was guided to the experimental area to impinge on a liquid hydrogen target in order to produce the quasi-free reaction. The outgoing protons were detected with a silicon tracker consisting in array of DSSSDs and the CsI scintillator array CALIFA. When the $(p, 2p)$ reaction takes place the resulting nucleus is an excited $^{237}_{91}Pa$. At the moment, the analysis of the experimental results is still under progress and is strongly hampered by the huge background of δ-electrons that blinds the Si detectors. In the near future further $(p, 2p)$-fission experiments are planned to be carried out at GSI/FAIR with exotic neutron-rich projectiles close to the neutron shell N=152 to obtain their fission yields and fission barrier heights for constraining r-process calculations [Gra22]. In any case, the best excitation energy resolution achievable with this experimental methodology will be hardly lower than few MeV.

A very promising approach for the determination of fission probabilities using single-nucleon transfer in inverse kinematics is coming from the solenoidal-spectrometer technique [Wuo07]. In this type of experiments, a large-bore uniform-field magnetic solenoid, is used as a charged particle spectrometer, see figure 2.21. As can be seen, the heavy-ion beam is aligned with the magnetic axis of the solenoid and interacts with a target (consisting of either a foil or a windowed gas cell) located inside the field. The target residues follow helical trajectories in the magnetic field and after a single orbit return to the solenoid axis where they can be detected. The particles are detected using a hollow array of silicon detectors, which can be located downstream and upstream from the target.

The emission angle of the particle in the laboratory system can be calculated from the position along the axis and the energy of the detected particle.

This method eliminates a large class of potential background processes due to the fact that only particles with the appropriate magnetic rigidity are transported from the target to the detector. Electrons, beta particles, and scattered beam ions are eliminated. This technique allows to cover a wide solid angle for the detection of target-like residues increasing the geometrical efficiency. In addition, the surface area of Si detectors and their segmentation can be significantly lower in a solenoid than in a conventional detector array covering a comparable

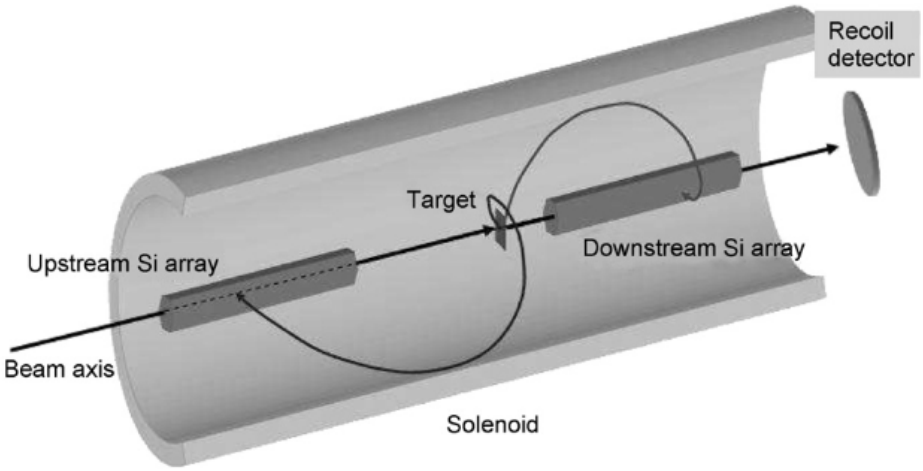

Figure 2.21: Scheme for a solenoidal charged-particle spectrometer.

solid angle in inverse kinematics. For this reason, the excitation energy resolution achievable using the solenoid method is improved with respect to conventional single pass experiments. However, the problems related to the use of a solid target, e.g. the energy-loss, straggling and contaminants or windows are still present.
Recently, this experimental methodology was applied by Bennet et al. [Ben22], to determine the fission probability of ^{239}U induced by the $^{238}U(d,p)$ reaction using a CD_2 target. The protons were detected at backward angles and the fission fragments at forward angles with a set of gas filled heavy-ion detectors. The data suffer from a very strong background due to the presence of C in the target.

2.7 Other indirect methods

2.7.1 The Oslo method

The Oslo method allows for extracting the level density ρ and the gamma-ray strength function simultaneously from a data set of charge particle and γ-ray coincidences using transfer reactions such as $(^3He, \alpha\gamma)$ and inelastic scattering reactions like e.g., $(^3He, ^3He'\gamma)$ and $(p, p'\gamma)$ to excite the desired nuclei to excitation energies close to S_n. Even if this method was not conceived to produce neutron induced cross sections as the surrogate method does, in some articles the authors use the measured level density and gamma-ray strength function to deduce the neutron radiative capture cross section, for instance Laplace et al. [Lap16]. Contrary to the surrogate reaction method it cannot be used to extract other cross sections like e.g. fission cross sections.
The starting point is a set of excitation-energy tagged γ-ray spectra containing γ rays from all possible cascades originating from a given initial excitation energy. This is achieved by doing charged-particle–γ-ray coincidence measurements. The Oslo method consist of four main steps:

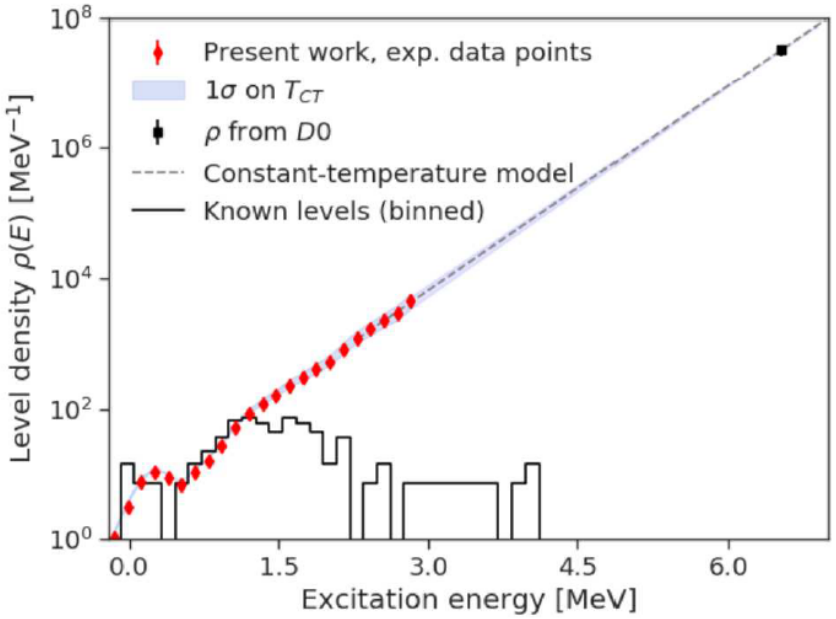

Figure 2.22: The level density of ^{240}Pu obtained with the Oslo method is compared to known discrete levels, the level density at S_n from the neutron induced data, calculated with D_0, and a curve representing the constant temperature model with T_{CT}=0.41, [Zei19]. The reference to "present work" is the work of Zeiser et al., [Zei19].

- First generation: extract primary γ-rays from the total gamma spectra [Gut87].
- Unfolding: correct the gamma spectra from the detector response [Gut96].
- Simultaneously extraction of the level density and gamma strength from the matrix of primary γ-rays [Gut13].
- Revision of the method and the uncertainties associated with the hypothesis done [Lar11].

However, there are other limitations to this method due to the need of normalising the obtained quantities with structure data at low energy and thermal neutron induced data at S_n. For example in 2019 Zeiser et al. [Zei19] applied the Oslo method to obtain the level density and the γSF of ^{240}Pu with the reaction $^{239}Pu(d,p)$. In the experiment, they bombarded the ^{239}Pu target with 12 MeV deuterons produced at the Oslo Cyclotron Laboratory. In figure 2.22, the level density of ^{240}Pu measured experimentally is shown together with known levels at low $E^{\star}$ and to the level density at S_n from neutron induced data. The measured data are in very good agreement with the constant temperature model (CTM) level density [Gil65].
Laplace et al. [Lap16] in 2016, bombarded a ^{242}Pu target with a 12 MeV deuterium beam produced at the Oslo Cyclotron Laboratory. The authors did a remarkable work to extract the level density and γSF of ^{243}Pu and used them to deduce the $^{242}Pu(n,\gamma)$ cross section. In figure 2.23, the obtained radiative capture cross section is shown. The agreement with the neutron-induced data and different evaluations is very good up to 200 keV. Above this energy there are no data and the differences between the calculation and the evaluations increase.

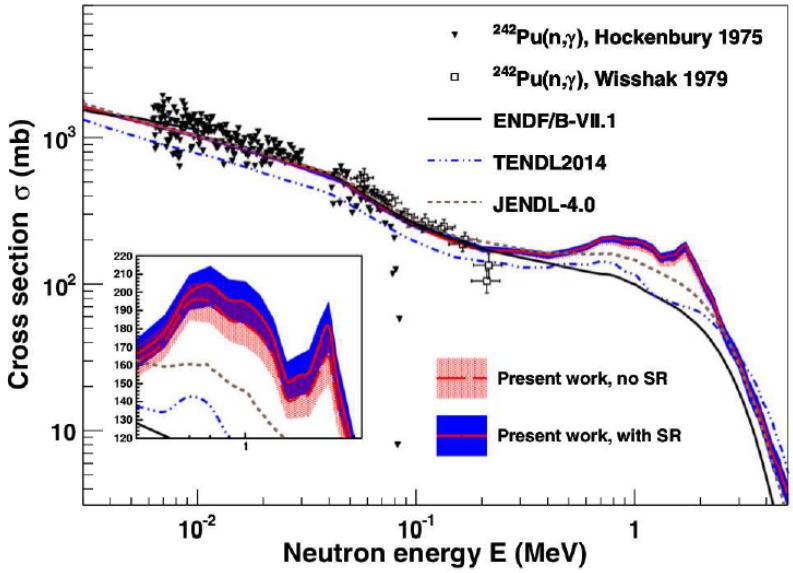

Figure 2.23: Calculated $^{242}Pu(n,\gamma)$ cross section using the measured level density and gamma-ray strength function including the M1 collective "scissors" mode (continuous red curve with blue error-band) and without it (dashed red curve with red dots error-hand). A zoom in the energy region 0.5 to 2 MeV, where the impact of the scissor mode is the most important, is shown in the inset. The predictions are compared at low energy with measured data from Hockenbury et al., [Hoc75]. Wisshak and Kappeler (empty squares), and the ENDF/B-VII.1, JENDL-4.0 (dashed grey curves), and TENDL2014 (blue dotted-dashed curve) evaluations. The reference to "present work" is the work of Laplace et al. [Lap16].

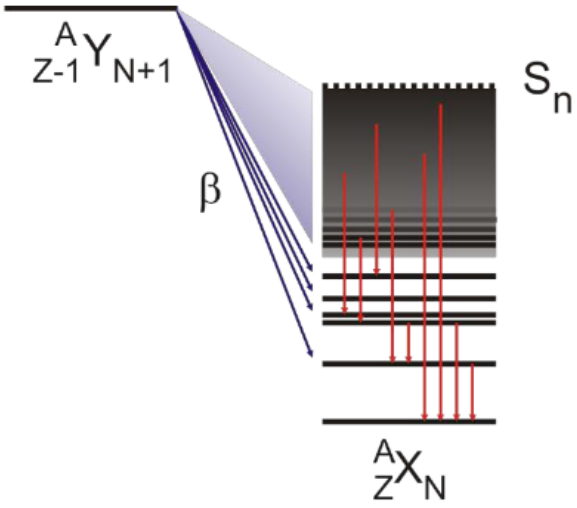

Figure 2.24: Scheme of the β-decay.

2.7.2 The β-Oslo method

While the Oslo method uses charged particle reactions to populate highly-excited states in the nucleus, the β-Oslo method populates the excited states by β-decay, see figure 2.24. The use of β decay gives the advantage to experimentally constrain the level density and γ-ray strength function of nuclei further away from stability than the Oslo method or other reaction-based techniques. However, this method has limitations due to β-decay selection rules and is restricted to nuclei that have large β-decay Q values and a high level density at the neutron separation energy (S_n), to ensure that the statistical region of the nucleus is populated.
The β-Oslo method was first applied on ^{76}Ga beta-decaying into ^{76}Ge [Spy14]. The experiment was performed at the National Superconducting Cyclotron Laboratory (NSCL) of the Michigan State University (MSU). A 130 MeV/u ^{76}Ge primary beam was used to produce ^{76}Ga by fragmentation on a thick beryllium target. The detection set-up consisted of the Summing NaI (SuN) detector, a γ-ray total absorption spectrometer, and a small silicon surface barrier detector. In figure 2.25(a), the normalized NLD of ^{76}Ge is shown. We observe an excellent agreement with the known, discrete levels. We also see that the ^{76}Ge data points resemble the ^{74}Ge data measured at the Oslo Cyclotron Laboratory [Ren14] as expected from previous studies of isotopic chains [Mor14]. These findings give confidence in the β-Oslo method. The measured level density and strength function enabled a significant reduction of the uncertainty of the prediction of the $^{75}Ge(n,\gamma)^{76}Ge$ reaction cross section, which has not been measured directly and relies on theoretical estimates. The calculated cross section is shown in fig. 2.25(b).
The β-Oslo method has recently been applied to the neutron-rich ^{70}Co isotope, beta-decaying into ^{70}Ni [Lid16]. The final goal of the authors was to study the $^{69}Ni(n,\gamma)^{70}Ni$ reaction and its impact on astrophysical abundance predictions. The isotope under investigation, ^{69}Ni, has five neutrons more than the heaviest stable Ni isotope and has a short half-life of 11.4 s, making it

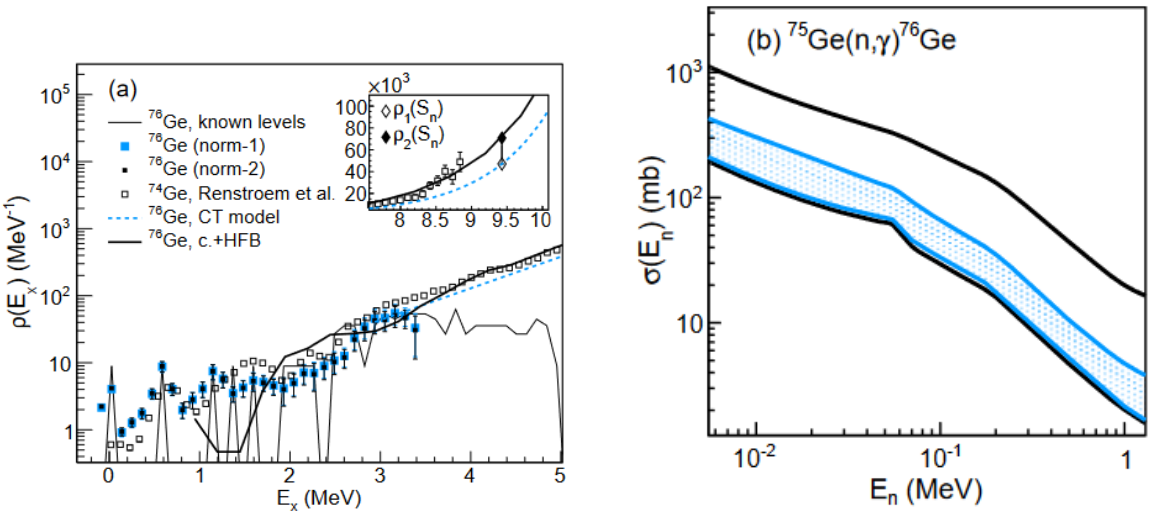

(a) (b)

Figure 2.25: On the left side the level density of ^{76}Ge is compared to known, discrete levels, ^{74}Ge data from Ref. [Ren14], the constant temperature model [Egi09], and the microscopic HFB model [Gor08]. The results show the estimated $\rho(S_n)$ for two normalizations norm-1 and norm-2, [Spy14]. On the right side, (color online) the blue, filled area indicates the constraints obtained with the present data, and the black lines indicate the lower and upper limits for the TALYS calculations prior to the present work for the ^{75}Ge radiative neutron-capture cross section.

unsuitable for direct measurements. The experiment was performed at NSCL, MSU, where a primary 140 MeV/u ^{86}Kr beam hit a beryllium target to produce ^{70}Co, which was delivered to the experimental set-up, which this time included a double-sided Si strip detector inside SuN. The latter was again used to detect the γ-ray cascades from the daughter nucleus, ^{70}Ni. The level density was normalized to the low-energy level density and the level density at S_n. The low-energy level density was taken from the experimentally known levels with less than a few MeV excitation energy [Ach15]. The authors accounted for the lack of knowledge on the discrete levels around 3 MeV. The gamma ray strength function was normalized to recent Coulomb excitation data on ^{68}Ni [Chi15]. The results are presented and compared with previous results in fig. 2.26(a) and 2.26(b). Using the experimentally normalized level density and γ-strength function as inputs, the neutron capture rate for ^{69}Ni was calculated using TALYS [Ber07]. The calculated neutron capture rate is shown in fig. 2.26(c). The obtained reaction rate is compared with the ones from the widely used reaction rate libraries BRUSLIB [BNL15] and JINA REACLIB [Cyb10]. As can be seen, the β-Oslo method also requires experimental data to normalize the results at low excitation energies and at S_n.

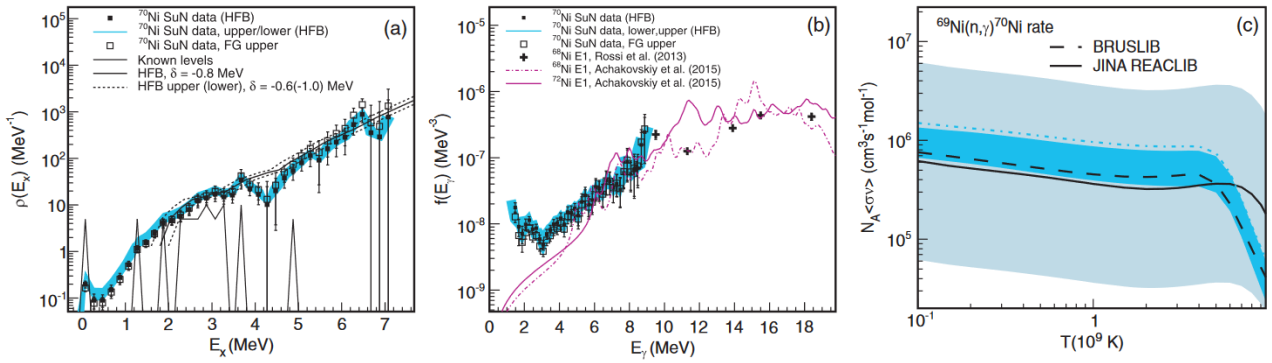

Figure 2.26: (a) Nuclear level density as a function of excitation energy compared to known levels given by the thin red line. High and low experimental bounds using the HFB microscopic normalizations are shown by the blue band. An upper limit from the phenomenological model [Egi09] is provided by the open squares. (b) γSF as a function of γ-ray energy. Experimental data are shown by the black squares with the upper and lower bounds from the microscopic normalization given by the blue band. The experimental data from Rossi et al. [Ros13] at higher energies from Coulomb excitation are also shown. (c) $^{69}Ni(n,\gamma)^{70}Ni$ reaction rate as a function of temperature. JINA REACLIB [Cyb10] and BRUSLIB [BNL15] reaction rate recommendations are shown by solid and dashed lines, respectively. The light-blue shaded band corresponds to a factor of 10 uncertainty in the $^{69}Ni(n,\gamma)^{70}Ni$ reaction rate.

Chapter 3

Storage rings

Many storage rings were designed in the middle of the 1980s and commissioned around 1990. The design of these storage rings was defined by the accelerator facilities, which were available in the different laboratories and were planned to serve as injectors to provide fast ion beams for storage.

Storage rings are a type of circular lattice consisting of bending and focussing magnetic multipole elements (dipoles, quadrupoles, etc.) whose purpose is the storage of ions. Storage rings can be categorized as light-ion storage rings if protons and light ions at energies in the range of a few hundred MeV to a few GeV are stored. The heavy-ion storage rings cover an energy range from few hundred keV/u to several hundred MeV/u and provide ion beams from protons up to fully-ionized uranium. Thanks to their operation in ultra-high vacuum (UHV) (in the order of 10^{-10}-10^{-12} $mbar$), highly charged ions can be stored for extended periods of time (up to several hours). This vacuum level is required to reduce the atomic interaction with the residual gas present in the ring. Depending on the ion charge and the energy, the stored ions can have a high probability to capture or lose an electrons. If the charge state of the ions changes, their magnetic rigidity will change and they will be lost. The storage rings depend on the nuclear half-lives, atomic charge states and kinetic energy of the ions to be stored [Lit11]. They consequently can be used for a broad range of studies in molecular, atomic and nuclear physics.

The most important capability of storage rings is beam cooling, which allows the reduction of the energy and momentum spread of the stored ions induced by the reaction used to produce them, the interaction with internal targets, or the recoil after decay [Nol09].

Several of the storage rings built during the first phase have been closed down. Furthermore, a fraction of the remaining rings are part of an accelerator chain and used for specific beam manipulations, particularly beam cooling and beam accumulation, but they are not hosting experiments. An example is the Low Energy Ion Ring (LEIR) [Cha02], which is part of the heavy ion chain at CERN and is used to deliver high-intensity heavy-ion bunches for collision experiments in the Large Hadron Collider (LHC).

In Table 3.1, the few heavy-ion storage rings that are in operation worldwide are listed. These are the unique storage rings where nuclear physics studies can be performed. The meager number of heavy-ion storage rings available for experiments is representative of the difficulties and challenge in the storage of heavy ions and the realization of the related experiments.
The Experimental Storage Ring (ESR) [Fra87] and the CRYRING, which will be described in detail later, are in operation since 1990 and 2017 respectively. The ESR is able to store almost all the ions (from carbon to bare uranium) and it is equipped with electron [Ste04] and stochastic [Nol04] cooling systems, an internal gas target [Pet11], laser setups [Nor15], spectrometers to detect recoil ions [Kle03], electrons [Hag07], and non-destructive Schottky diagnostic [San20, Nol11]. Furthermore, deceleration of the stored beams to an energy of about 3 MeV/u can be achieved [Ste00]. The CRYRING was moved from Sweden and re-built downstream the ESR. It is optimized for low energies down to few hundred keV/u. The ring is equipped with an electron cooler, an internal gas-jet target, Schottky detectors, an electron target, fast and slow extraction, etc.
The experimental cooler-storage ring CSRe is part of the high-energy facility in Lanzhou, which comprises the heavy-ion synchrotron CSRm and the fragment separator RIBLL2 [Xia02]. The CSRe can be operated in isochronous mode and it is equipped with electron [Yan09], stochastic [Zhu19] and laser cooling [Wen19], an internal target [Zha19] and non-destructive Schottky diagnostic [Zen17]. The deceleration option, although feasible in principle, is not yet available.
Another very special storage ring is the medium-energy Rare-Ion Ring (R3) at RIKEN/Japan [Yam13] which recently become operative. In this ring no beam cooling is applied, it is based on the principle of a weak focusing synchrotron and its main purpose is to measure the mass of very neutron-rich nuclei for which the production rate and the lifetimes are very small (hence "rare ion"). The ring is composed only of dipole magnets and is run solely in isochronous optics at a fixed rigidity of 5.5 Tm.
It is important to stress that new storage ring facilities are under construction. In this respect we can mention the new High Intensity Heavy-ion Accelerator Facility (HIAF) in China [Yan13] and the FAIR facility at the GSI site in Darmstadt, which will extend significantly the portfolio of storage rings [Spi06].

3.1 The GSI accelerator facility

The Experimental Storage Ring (ESR) [Fra87] and the CRYRING [Nov19], are located at the GSI Helmholtzzentrum für Schwerionenforschung GmbH in Darmstadt, Germany. A schematic drawing of the GSI facility is shown in figure 3.1. GSI is able to provide a multitude of light- and heavy-ion beams ranging from hydrogen up to uranium. It comprises the UNILAC (UNIversal Linear ACcelerator), the heavy ion synchrotron SIS18 and the experimental storage rings ESR and CRYRING. Stable-ion beams are produced in one of the three injector sites, i.e. Terminal South, Terminal North and High Charge State Injector (HLI), by the use of

Table 3.1: Heavy ion storage rings presently available for nuclear physics experiments.

Name	Facility	Particles	Energies	Internal gas Target	Cooling
ESR[1]	GSI	all ions	MeV/u to GeV/u	Yes	stochastic, electron
CSRe[2]	IMP	all ions	MeV/u to GeV/u	Yes	electron
R3[3]	RIKEN	all ions	MeV to GeV	No	No
CRYRING[4]	GSI/FAIR	ions	keV to MeV	Yes	electron

[1] Experimental Storage Ring [Fra87]
[2] Cooler-Storage Ring [Xia02]
[3] Rare-Ion Ring [Yam13]
[4] [Les16]

different ions sources as the Penning Ionization Gauges (PIG), the Chordis/Mevva ion sources and the ECR source [GSI]. These injectors can provide independently different ion species of all elements from hydrogen to uranium to the UNILAC, which consists of four Alvarez structures and 15 single gap cavity resonators. It delivers ion beams of energies between 2 and 15 MeV/u. The UNILAC is pulsed at a frequency of 50 Hz. The pulse widths are of typically 5 ms, which enables a time sharing between low energy experiments and the injection into the heavy-ion synchrotron SIS18 (SchwerIonen Synchrotron) [Bla85]. Before the injection into the SIS18 the ion beams are accelerated in the UNILAC up to 11.4 MeV/u. For achieving high energies in the SIS the ions are stripped at this energy (e.g. uranium charge states from 28+ to 73+). The synchrotron accelerates the ions with a maximum magnetic rigidity $B\rho$ of 18 Tm to energies ranging from 1 to 4500 MeV/u. The ion beam intensity can be increased by stacking, i.e. by successively injecting ions into the synchrotron.
Beams from the SIS18 synchrotron can be transferred to the ESR either via the FRagment Separator (FRS) or a separated beam line, which contains a stripper foil that enables the production of bare ions with Z>36 [Fra93]. Energies about 300 MeV/u are necessary to obtain high charge states after stripping (see Appendix B.1 for more details).
For the production of radioactive nuclei, the beam from the SIS is sent through a fragmentation target followed by the magnetic fragment separator for isotope selection, via the so called in-flight separation method [Gei92], before the injection into the ESR.
The GSI accelerator facility is the unique one in the world where two heavy-ion storage rings, the ESR and the CRYRING are linked. This provides significant advantages since the ESR can be used to slow down and cool the beams, while the CRYRING is used to perform the measurements.

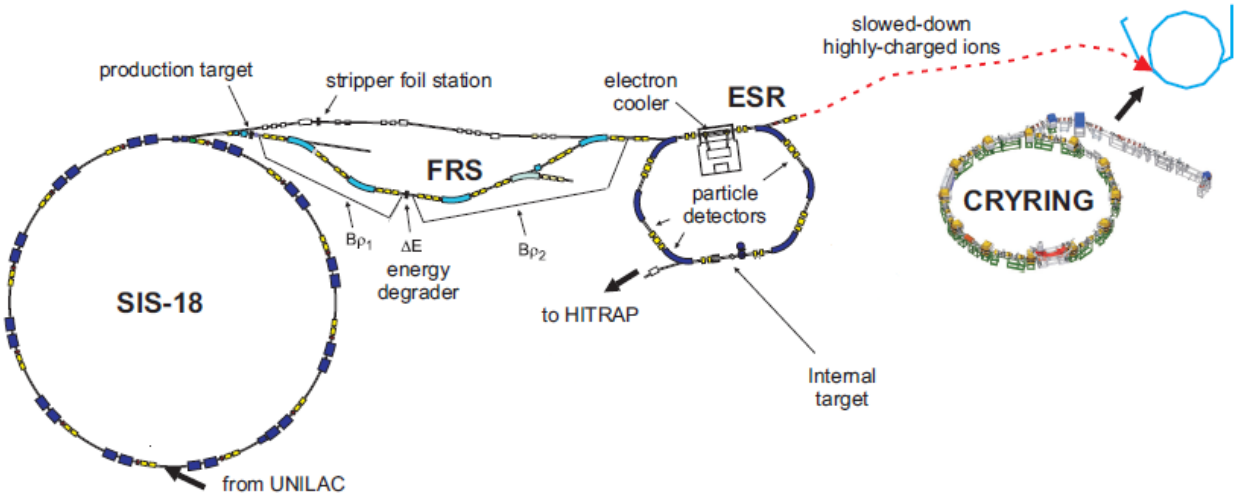

Figure 3.1: Schematic view of a part of the GSI ion accelerator facility.

3.2 The Experimental Storage Ring (ESR)

The Experimental Storage Ring (see figure 3.2) was constructed as a versatile storage ring for light and heavy ions from carbon to uranium. Six dipole magnets keep the ions on a track of 108.36 m in circumference. It has a maximum magnetic rigidity of 10 Tm and is capable of storing for example $^{238}U^{92+}$ ions with an energy from 3 MeV/u up to 560 MeV/u [Fra93]. The resulting revolution frequency is in the order of MHz, e.g. during our experiment ≈0.6 MHz for ^{208}Pb at 30 MeV/u.

As already said, UHV vacuum conditions are required inside storage ring facilities. This is needed to reduce the atomic interactions with the residual gas in the ring and ensure long storage times. To achieve UHV vacuum conditions the whole ring has to be baked at 300 $°C$. This operation allows for a drastic reduction of the outgassing of the ring walls, enabling a vacuum level of about 10^{-10} $mbar$. Under these conditions, the impact of atomic interactions with the residual gas in the ring is significantly reduced.

Primary fully stripped beams, injected at energies above 300 MeV/u are stored and can be decelerated to 3-80 MeV/u by synchronous ramping of the magnetic fields and the frequency of two Radio Frequency (RF) resonators. Beam cooling is done with the electron cooler [Steck04], which can be used for beam energies from 3 MeV/u to 420 MeV/u [Fra93] and a wide range of beam intensities.

By the multi-turn injection process in the SIS (see Appendix B.2), up to few times 10^9, $^{238}U^{73+}$ ions can be accelerated. After the transmission and stripping process the number of ions is reduced typically by a factor 10 at the injection in the ESR and, depending on the stored beam energy, beam currents of few mA can be achieved (see Appendix A.2). The global preparation time of the heavy ion beam at the ESR, which involves the deceleration and cooling processes,

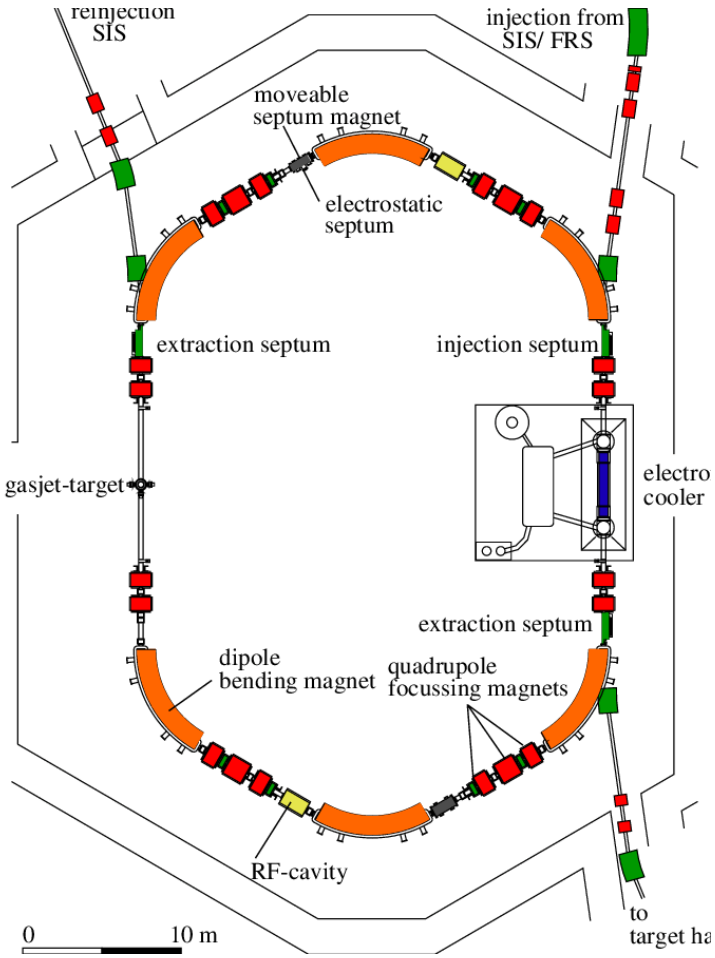

Figure 3.2: Schematic view of the Experimental Storage Ring (ESR) at GSI.

depends on the beam type and final energy required. For a stable SIS18 beam it can typically take a few tens of seconds. Secondary-fragment beams from the FRS, however, have larger emittance and momentum spread due to the interaction with the target in the production process. In this case, the cooling force of the electron cooler is reduced and a larger cooling time up to few minutes is required. Therefore, stochastic pre-cooling can be first applied to decrease emittance and momentum spread before electron cooling takes over. In this way the cooling times can be kept as low as a few tens of seconds also for secondary beams.
Once the beam has reached the desired energy and has been cooled, the internal gas jet target can be switched on to realize in-ring reaction experiments. Again, energy losses as well as energy and angular straggling of the beam due to the interaction with the target are compensated by the electron cooler, which allows for the maintenance of the outstanding beam quality during the full experiment.

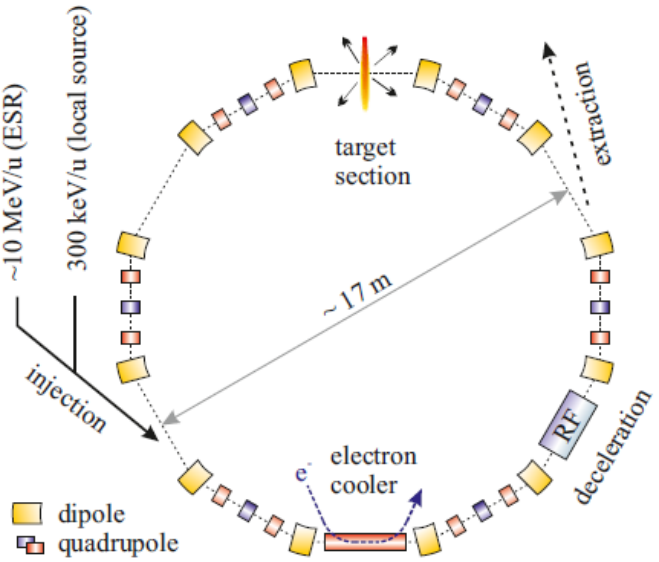

Figure 3.3: An overview of the CRYRING storage ring installed at GSI/FAIR downstream from the ESR storage ring.

3.3 The CRYRING storage ring

A schematic overview of the CRYRING storage ring is shown in Fig. 3.3. The CRYRING has a maximum magnetic rigidity of 1.44 Tm. It is capable to decelerate, cool and store for example $^{238}U^{92+}$ from about 14.5 MeV/u down to a few 100 keV/u. The total circumference of the ring is 54.17 m and it is equipped with a high performance electron cooler and an internal gas jet target.
For the low energy regime below 10 MeV/u, the CRYRING has several advantages compared to the ESR, such as its compactness and the excellent UHV conditions which enable respectively larger revolution frequencies and larger storage times.
Both rings, the ESR and the CRYRING operate in complementary ion energy ranges. Therefore, intense beams of highly charged ions and exotic nuclei covering the energy range from 500 MeV/u to few 100 keV/u are available for experiments at GSI/FAIR.

3.4 Beam properties

Heavy ion rings can store ions as a bunched or continuum (coasting) beam consisting of a collection of many particles whose longitudinal and transverse momentum are similar and remain more or less close to each other in space. Particle beams are characterized by a set of properties or parameters being either constants of motion or functions varying from point to point along a beam transport line. The parameters may be a single particle property like the betatron function, which is the same for all particles within a beam, or quantities that are defined only for a collection of particles like the beam size or the beam intensity. To help

the reader understanding experiments at storage rings, some properties such as the beam energy, beam structure and current, and beam space charge are introduced in appendix A. In this section, concepts such as the beam emittance and temperature, which are fundamental to understand the necessity of an efficient beam cooling system, will be presented.

3.4.1 Beam emittance

In the description of the beam properties, the emittance is generally used because, unlike the physical dimensions of the beam which vary with the location in the storage ring, the emittance is independent of the ring position. In simple terms, the emittance is a measure of the beam spread in position and momentum. In this respect, a low-emittance particle beam is a beam where the particles are confined in a small volume and have nearly the same momentum, which is a desirable property for ensuring that the entire beam is transported to its destination. In general, the state of a particle in a beam is described by three position and three momentum coordinates (x,p_x,y,p_y,s,Δp). The 6-dimensional space obtained is called "phase space". The coordinate s is the coordinate along the beam trajectory and Δp is the momentum deviation from the central momentum of the nominal trajectory. The transverse momenta can be expressed as the product between the particle momentum p_0 and the angle x' or y' with respect to the considered beam direction:

$$p_x \approx p_0 \cdot x' \qquad p_y \approx p_0 \cdot y' \tag{3.1}$$

The phase space is used to study the evolution of the beam through the accelerator. Usually, the longitudinal motion along the beam axis is decoupled from the motion in the plane transverse to the beam axis, which is also decomposed into two independent motions along two orthogonal directions. This means that the 6-dimensional phase space can be split into a longitudinal phase space (2-dimensional) and a two transverse (2-dimensional) phase spaces.
As can be seen in figure 3.4, each particle of a beam is a point in the phase space and the envelope of all these points represents the region occupied by the beam in phase space. The phase space area A occupied by the beam divided by π is called geometrical beam emittance. We can define three independent geometrical beam emittances associated to each specific two-dimensional space, e.g. (x,x'), (y,y'), (s,Δp) which are related to the momentum by the equation (3.1). When the emittance is calculated in the dimension parallel to the motion of the particle, we define it as longitudinal emittance, while for the other two dimensions we refer to the transverse emittance.
The horizontal and vertical beam widths (σ_x and σ_y) depends on the longitudinal position s and can be described by (see figure 3.4):

$$\sigma_{x,y}(s) = \sqrt{\epsilon_{x,y} \cdot \beta_{x,y}(s)} \tag{3.2}$$

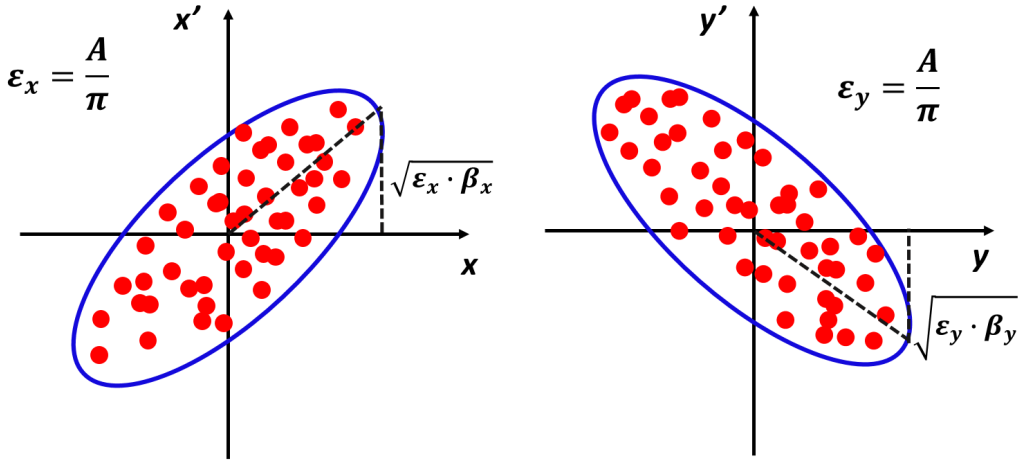

Figure 3.4: Beam particles position in the phase spaces (x,x') and (y,y') for a specific longitudinal position s.

where $\beta_{x,y}(s)$ are characteristic functions of the storage ring (beta-functions), which depend on the dipole and on the quadrupole settings of the storage ring. If $\sigma_{x,y}$ are the RMS values of the beam position distribution, then the emittances defined with equation 3.2 are the RMS emittances of the beam.

The definition of the beam emittance given assumes a constant beam energy. When the beam energy is increased, the transverse momentum remains constant but the longitudinal momentum increases. Therefore, the beam emittance is reduced with acceleration, see figure 3.5. In order to have a constant quantity for all the energies, the normalized emittance is defined like:

$$\epsilon_{norm} = \frac{v}{c} \cdot \gamma_{rel} \cdot \epsilon \tag{3.3}$$

where v/c and γ_{rel} are respectively the velocity of the particles divided by the speed of light and the Lorentz factor. The normalized emittance is the quantity of interest when considering emittance growth and conservation in an accelerator.

The beam emittance can be also defined by considering the distribution of particles in phase space. This is particularly useful in the case of particle simulations, where we have knowledge of the phase space coordinates of all the particles in the beam. In this case, the emittance of the x-x' distribution can be calculated via [Cha02]:

$$\epsilon = \sqrt{(< x^2 >< x'^2 > - < x \cdot x' >^2)} \tag{3.4}$$

where <> denotes the average over all the particles in the distribution, $< x^2 >$ is the variance of the particle position, $< x'^2 >$ is the variance of the angle, and $< x \cdot x' >$ represents the position-angle correlation of the particles in the beam.

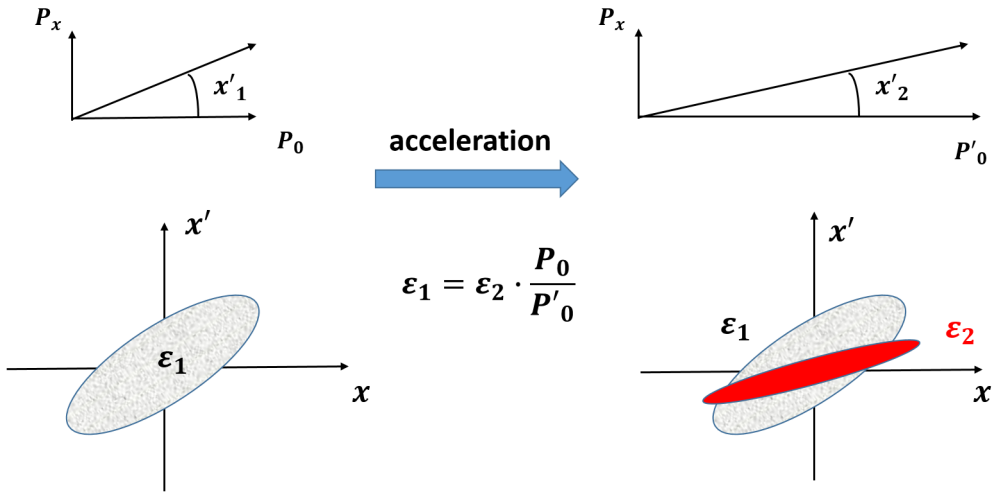

Figure 3.5: Emittance variation due to the beam acceleration. On the left side the angle x' and the space region occupied by the beam having a momentum P_1 is shown before the acceleration. When the beam momentum is changed from P_0 to P'_0, keeping the same transverse momentum, the angle x' decreases. As can be seen on the right side, this decrease of the angle reduces the region of phase space occupied by the beam particles.

The Liouville's theorem [Pet18] states that the area of a distribution in phase space, and hence the normalized emittance, is conserved in presence of external conservative forces. A variation of the emittance can occur in the presence of statistical effects in the form of collisions with other particles or emission of synchrotron radiation[1]. Intra-beam scattering, where the particles within the beam collide and exchange energy, can lead to an increase of the emittance, in particular when particles exchange longitudinal momentum into transverse momentum and gain back the loss of longitudinal momentum from the accelerating cavities. In that case, the beam "heats up" transversely leading to an increase of the beam emittance and size. As we will see later cooling techniques, which are non-Liouvillean processes, can be used to reduce the beam emittance.

[1] As mentioned in [Kun74] the synchrotron radiation intensity is inversely proportional to the fourth power of the particle mass. In the case of electrons and positrons, the radiation power is larger by thirteen orders of magnitude than it is for protons. Therefore, the effect is without any practical importance for protons and even less for heavy ion machines.

3.4.2 Beam temperature

In general it is possible to define the longitudinal temperature T, as a function of the velocity spread δv of the ions in the beam:

$$\frac{1}{2} \cdot k_B \cdot T = \frac{1}{2} \cdot m \cdot (\delta v)^2 \tag{3.5}$$

where m is the mass of the beam ions, k_B is the Boltzmann's constant. In more practical units, temperatures for ion beams can be expressed as,

$$T_{\parallel} = \frac{2}{k_B} \cdot (\frac{\delta p}{p_0})^2 \cdot E_0 \tag{3.6}$$

$$T_{\perp,u} = \frac{2}{k_B} \cdot (\frac{\epsilon_u}{< \beta >}) \cdot E_0 \tag{3.7}$$

where $T_{\parallel}$ is the longitudinal temperature, $T_{\perp,u}$ are the transverse temperatures along x or y, E_0 and p_0 are the average ion kinetic energy and initial momentum, $< \beta >$ are the average lattice beta functions, δp the momentum spread and ϵ_u the transverse emittance in the (x,x') or (y,y') phase space of the particles. Typically, beam dimensions are defined in terms of the rms value of a Gaussian distribution.
The beams, if not cooled, can have very high temperatures and can be treated as classical thermodynamical ensembles of particles confined to some volume. When stored, the ensemble is in a steady state, has a constant energy and behaves like an ideal gas. The particles of the beam are necessarily charged and can interact with each other through intra-beam collisions, as well as with the residual gas and, if present, with internal gas targets. These processes can cause beam heating, increasing the momentum spread and beam emittance. Particle beams can be anisotropic, i.e. $T_{\parallel} \neq T_{\perp}$. It is important to stress that the beam energy and beam temperature must not be confused (e.g. a beam of energy 100 GeV can have a temperature of 1 eV).

3.5 Electron Cooling

As already pointed out, the electron coolers are key elements of the CRYRING and ESR storage rings. They enable efficient compression of the phase-space region occupied by the beam particles by merging the ion beam in an intense cold electron beam of the same velocity. In the electron cooler, the thermal energy of the ions is transferred by Coulomb interaction to the electron beam, which is continuously renewed and therefore constitutes a reservoir of cold electrons. In figure 3.6(a), a schematic view of the electron cooler section of the ESR is shown, where we can see how the electron beam coming from the electron gun is merged and then separated from the ion beam. In the bottom, the interaction between an ion and the

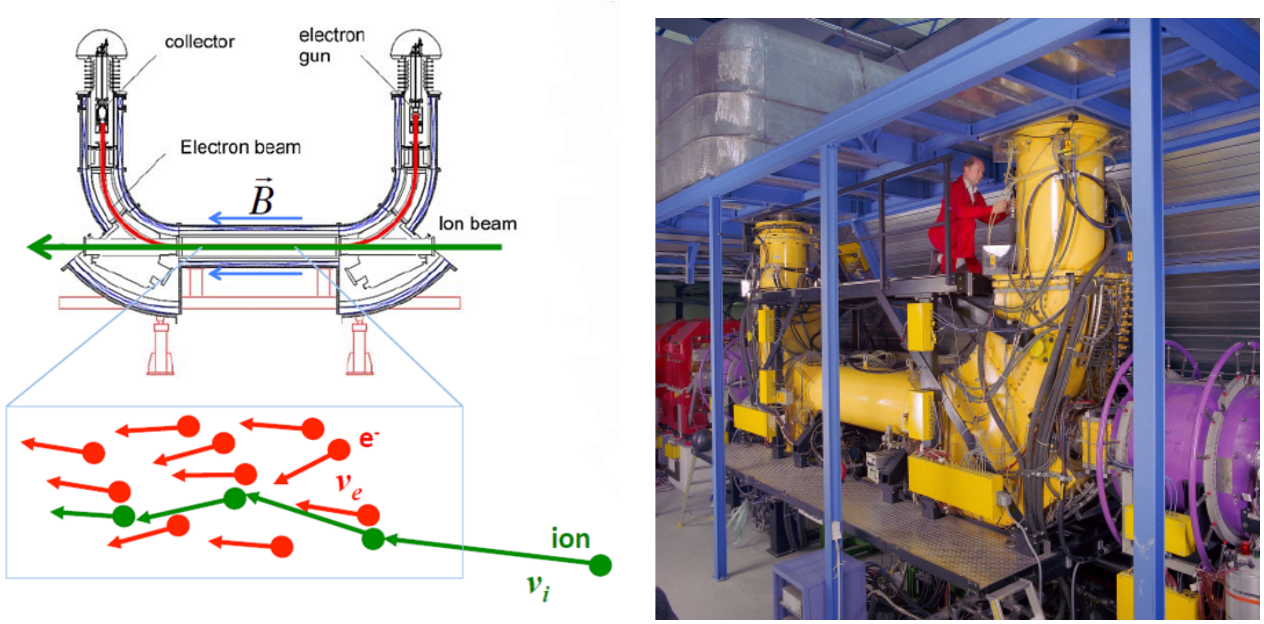

(a) (b)

Figure 3.6: Figure (a) shows a drawing of an electron cooler. A magnetic guiding system provides a longitudinal magnetic field in which the electrons move from the electron gun to the electron collector. The magnetic guiding field is provided by solenoid and toroid magnets. The electron and ion beams are merged in the horizontal 2.5 m long cooling section where the beam heat is transferred to the electron beam via collisions, as shown in the lower part. A picture of the ESR electron cooler is shown in figure (b) this electron cooler has an horizontal cooling section of 2.5 m. The beam comes from the right and the operator at work allows one to image the device dimensions.

electron beam is shown, illustrating how the heat is transferred from the ions to the electrons. An extensive introduction into electron cooling is given in [Pot90, Mas94].

The ESR electron cooler is a typical medium-energy electron cooling system since the electron energy used is about few tens of keV. As can be seen in figure 3.6(b), a magnetic guiding system provides a longitudinal magnetic field in which the electrons move from the electron gun to the electron collector. The magnetic guiding field is provided by solenoid and toroid magnets.

The cooling rate $(1/\tau)$ can be defined as the emittance or momentum spread $(\Delta p/p)$ change per unit time:

$$\frac{1}{\tau} = -\frac{d\epsilon}{\epsilon \cdot dt} \qquad \frac{1}{\tau} = -\frac{d(\Delta p/p)}{(\Delta p/p) \cdot dt} \tag{3.8}$$

It increases with the reduction of the ion beam emittance and energy spread. The cooling rate depends on many parameters such as the charge $q = Q \cdot e$ and the mass $M \approx A \cdot m_0$ of the ion (with A being the mass number and m_0 the average nucleon mass), the density n_e of the electron beam and the ratio $\eta_e = L/C$ of the length L of the cooling section to the ring circumference C. The cooling time strongly depends on the velocity deviation δv of the ion

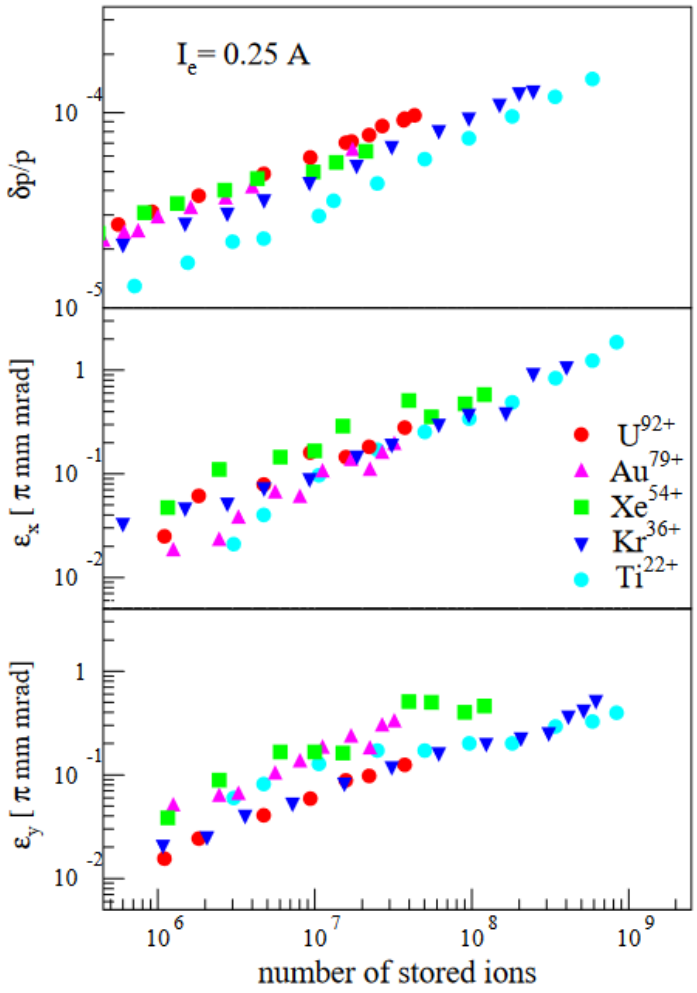

Figure 3.7: Equilibrium values of beam emittance and momentum spread for coasting beams of various bare ions cooled with an electron current of 0.25 A. Figure taken from [Ste03].

from the average electron velocity in all degrees of freedom. For the regime of tempered and only moderately pre-cooled beam the cooling rate $1/\tau$ scales as:

$$\tau^{-1} \propto \frac{Q^2}{A} n_e \eta_e \gamma^{-2} (\delta v)^{-3} \tag{3.9}$$

where γ is the ion beam Lorentz factor. The cooling rate increases strongly as the δv decreases. Consequently, electron cooling is most powerful for ion beams which are pre-cooled or already have small energy spread and emittance. Note that the cooling rate will also increase as the ion beam velocity decreases. For powerful cooling the electron beam should have low temperature, large electron density and a long interaction section with the ion beam.
However, cooling increases the beam density and forces the beam in a regime where intra-beam scattering counteracts the effects of the cooling forces with a heating rate, which is inversely proportional to the phase space volume occupied by the ion beam and increases linearly with

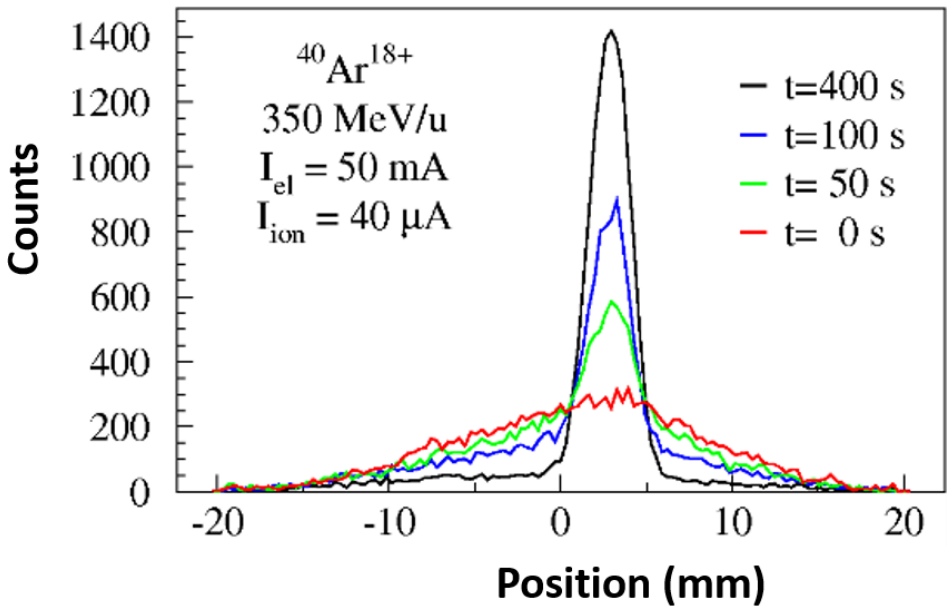

Figure 3.8: Demonstration of transverse electron cooling at the ESR storage ring with an $^{40}Ar^{18+}$ ion beam (350 MeV/u), an electron current of 50 mA and an ion current of 40 μA. The decrease of the transverse beam size as a function of time can be clearly seen. Figure taken from [Ste15].

the ion number. Therefore, the reduction of the emittance with cooling techniques is limited by intra-beam scattering. The two mechanism act in opposite directions until an equilibrium state is reached. The final cooling time can range between seconds down to some ten ms for cold ion beams close to the equilibrium with intra-beam scattering.
Figure 3.7 shows some examples of equilibrium beam properties achievable of the ESR using electron beam cooling for fully stripped heavy-ion beams at different intensities. At the injection from the SIS, before any cooling is applied at the ESR, primary beams can carry an emittance of few $mm \cdot mrad$ and a momentum spread around $3{\cdot}10^{-3}$. The electron cooling process can reduce, depending on the electron and ion beam conditions, the emittance and the momentum spread by few orders of magnitude. A momentum spread of $\delta p/p \sim 5 \cdot 10^{-5}$ is achievable for 10^7 fully-ionised $^{238}U^{92+}$ ions at 400 MeV/u. The momentum spread can be further reduced by an order of magnitude for a few 10^3 stored ions. In figure 3.8, the effect of the electron cooler applied to a $^{40}Ar^{18+}$ beam at 350 MeV/u can be seen. The decrease of the beam size as a function of time is clear. However, it is important to remark that the cooling time and the time evolution presented in this figure can change significantly depending on the ion beam parameters and the electron current.

The electron capture or recombination process increases with the electron beam density. Therefore, a stronger cooling results in faster particle losses. Normally, even for highly charged ions the storage lifetime in the ring is two to three orders of magnitude longer than the cooling

time and most of the experiments are not seriously hampered. In experiments aiming at long storage time, a compromise has to be found between storage time and cooling rate.

3.6 The ESR internal target

Most of the standard target technologies do not cope with the restrictions imposed by the storage rings environment. The most severe constraints are the high ion-beam current and the UHV conditions in the ring. The only concept which can fulfil the requirements is a very cold, molecular gas-jet crossing the ion beam perpendicularly coupled to a very efficient differential coupling system. For in-ring reaction experiments, internal targets can be used with gas-jet targets from a wide range of target species, like H_2, D_2, ^3He, ^4He, Ar, Xe, CH_4, etc [Ege03]. At the ESR and CRYRING the internal targets are installed in the long straight sections of the rings opposite to the electron cooler (see figure 3.2 and 3.3).
The targets have small diameter of less than few mm at the interaction zone and are very thin. If the target diameter is small enough, the reaction vertex can be accurately defined which combined with the compensation of the beam energy loss and straggling by the e^- cooler results in a very good resolution of the beam energy at the interaction point. Furthermore, such targets are pure and windowless, which is essential since no corrections are needed to subtract the background from the interactions with contaminants and windows. Although the targets are thin, relatively high luminosities are obtained owing to the high revolution frequencies of the ions in a ring, which are typically $10^5 - 10^6\ Hz$. Assuming a stored beam with a moderate intensity of 10^5 ions, a luminosity of $10^{25} - 10^{26}$ $(cm^{-2} \cdot s^{-1})$ can be achieved with a target thickness of $10^{15}\ atoms/cm^2$.
The very low target thickness reduces significantly the probability for having two subsequent reactions in the target. This means that the probability to have atomic reactions before and after a nuclear reaction is negligible. The upper limit for the target density is either defined by the storage lifetime of the ion beam or the capability of the e^- cooler to compensate for the energy loss and straggling of the beam particles in the target. Target densities exceeding the restoring capabilities of the e^- cooling system result in fast beam losses [Pet11].

A schematic view of the ESR gas jet target is shown in figure 3.9. The target consists of three parts: the jet injection system which produces the jet with the help of a Laval nozzle and several collimating orifices (top part), the interaction chamber where the ion beam hits the jet (center part), and the jet dump (bottom part) which has to ensure that the jet is pumped away without significant backstreaming. To meet the UHV requirements of the ESR, the actual set-up consists of an injection and dump part, four stage of differential pumping system are required for the jet injection and the jet dump to preserve the ESR vacuum level.

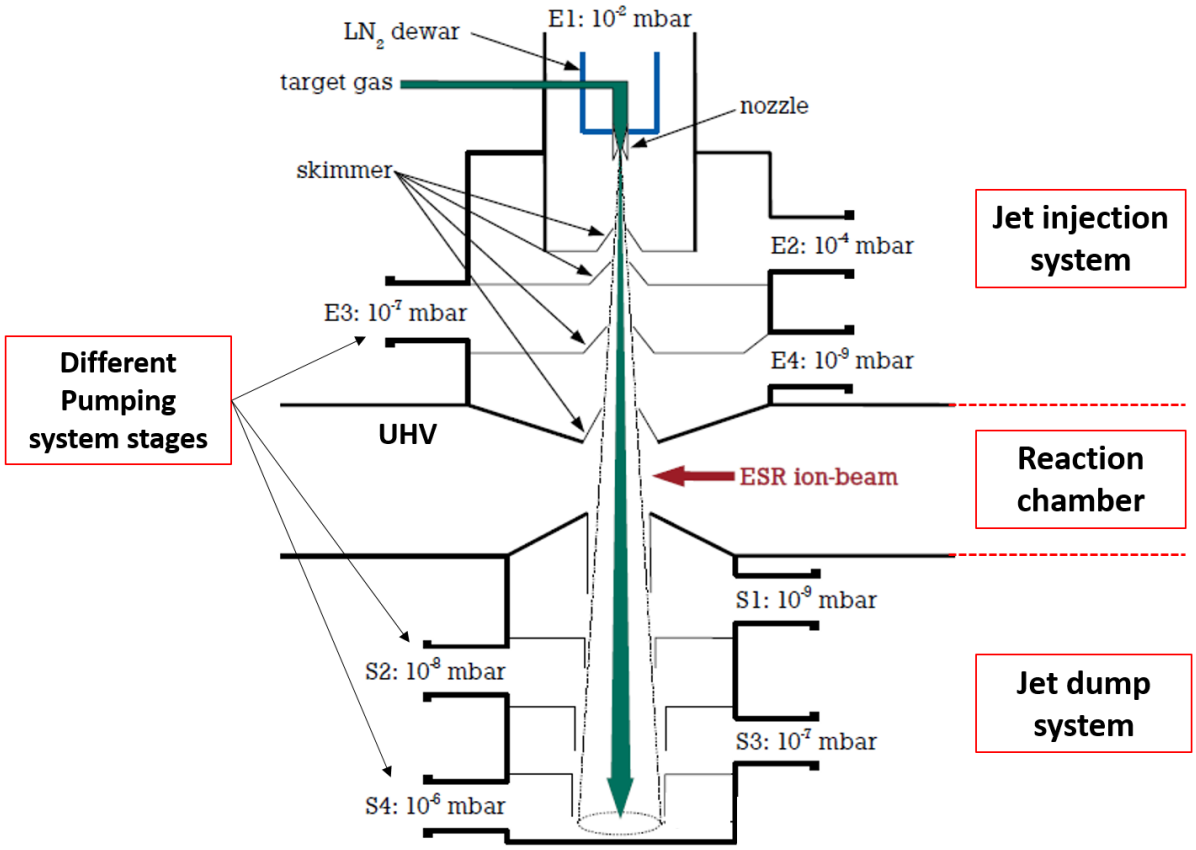

Figure 3.9: Schematic view of the internal target of the ESR. The target can be divided from the top to the bottom in three different parts: (a) the jet injection system which allows for the production of a molecular neutral beam by mean of a Laval nozzle followed by several collimating orifices at different pressure stages, (b) the reaction chamber where the interaction with the beam takes place and (c) the jet-dump section where a four-staged differential pumping system is used to dump the target beam.

Chapter 4

Proof of principle experiment

The discussed limitations on the surrogate reaction method, in direct and inverse kinematics, can be addressed by performing the surrogate experiment in inverse kinematics at storage rings. The objectives of NECTAR are to develop a set-up and a methodology for the simultaneous measurement of γ emission, neutron-emission and fission probabilities induced by transfer and inelastic scattering reactions in inverse kinematics at the storage rings of the GSI-FAIR facility (Darmstadt, Germany). The measured probabilities are then used to infer the neutron-induced reaction cross sections.

In the last weeks of June 2022 a first proof-of-principle experiment was successfully performed at the ESR storage ring of GSI/FAIR facility . In this experiment, we investigated the interaction of a fully stripped $^{208}Pb^{82+}$ beam with a hydrogen (H_2) gas-jet target. The aim was to simultaneously measure the gamma ($^{208}Pb^{\star} \rightarrow \gamma + {}^{208}Pb$) and neutron ($^{208}Pb^{\star} \rightarrow n + {}^{207}Pb$) emission probabilities of $^{208}Pb^{\star}$. The excited $^{208}Pb^{\star}$ was produced by means of the surrogate reaction $^{208}Pb(p,p')^{208}Pb^{\star}$ which is associated to the $n + {}^{207}Pb \rightarrow {}^{208}Pb^{\star}$ neutron-induced reaction. Both the inelastic $^{208}Pb(p,p')$ and elastic $^{208}Pb(p,p)$ scattering reactions were considered in the experiment.

Since this was the first time a surrogate reaction was studied at a storage ring, multiple aspects of the experimental methodology proposed by the NECTAR project had to be carefully investigated, namely, (a) the excitation energy resolution and systematic uncertainties, (b) the transmission efficiency along the storage ring of the heavy residues produced after the ^{208}Pb de-excitation, and (c) the separation of the beam-like residues. The preparation of the experimental set-up relied significantly on our own simulations, which were used to define the detector properties.

4.1 Reaction kinematics

The kinematics of two-body scattering reactions involving a heavy projectile (^{208}Pb) at 30 MeV/u and a light target (a proton) leads to target-like residues (protons) covering a broad

range of angles from 0 to 90°, whereas the associated projectile-like residues (^{208}Pb) are very much forward focused with maximum emission angles of less than 0.3°, for all possible excitation energies $E^{\star}$. This can be understood by looking at the vector diagram, figure 4.1, describing the elastic scattering reaction $X(y,w)B$, where $w = y$ and $B = X$ in inverse kinematics. In the drawing, θ and ϕ represent the angles in the laboratory frame of the target-like velocity ($\vec{v}_w^{lab}$) and beam-like velocity ($\vec{v}_B^{lab}$) with respect to the z-axis (beam axis), while θ^{cm} is the angle of the target-like velocity ($\vec{v}_w^{cm}$) in the center of mass with respect to the z-axis (beam axis).
The velocity of the centre of mass in the laboratory frame is given by a large fraction of the beam velocity because of the large difference between the beam (m_X) and the light target (m_y) masses. The center of mass velocity expression, for $m_X >> m_y$, can be written as:

$$\vec{v}_{cm} = \frac{m_X}{m_X + m_y} \cdot \vec{v}_X \approx \vec{v}_X \tag{4.1}$$

where the $\vec{v}_X$ is the beam velocity. Furthermore, the target particle is initially at rest and hence the length of the target-like velocity vector $\vec{v}_w^{cm}$ is equal to the length of the centre of mass velocity as measured in the laboratory frame, $\vec{v}_{cm}$. Therefore, the velocities of the target -like (w) and beam-like (B) residues are related to the initial beam velocity as follows:

$$\vec{v}_w^{cm} = \frac{m_X}{m_X + m_y} \cdot \vec{v}_X \tag{4.2}$$

$$\vec{v}_B^{cm} = \frac{m_y}{m_X + m_y} \cdot \vec{v}_X \tag{4.3}$$

For $m_X >> m_y$ (inverse kinematics case), we can finally see that in the center of mass $|\vec{v}_w^{cm}| \approx |\vec{v}_X|$, while $|\vec{v}_B^{cm}|$ is very small.
For a scattering angle of 180° (backscattering) in the centre of mass frame, the light particle is stationary in the laboratory frame $\vec{v}_w^{lab} \simeq 0$. For $\theta^{cm} < 180°$ the light particles emerge with $\theta < 90°$ in the laboratory frame and with a velocity that increases approximately linearly with decreasing centre of mass angle. In the case of forward-scattering in the centre of mass frame ($\theta^{cm} = 0$), the light particles travel in the direction of the incoming beam with the largest velocity, and the beam-like particle also continues in that direction, being just slightly slowed down. Since the velocity in the center of mass is very small, the velocity of the beam-like products in the laboratory is given $\vec{v}_B^{lab}$ by the sum of the velocities $\vec{v}_{cm} + \vec{v}_B^{cm}$ and will be very close to the beam velocity $\vec{v}_X$. The scattering angle of the heavy residues in the laboratory ϕ is also very small and it is related to the scattering angle in the center of mass ϕ^{cm} by the formula:

$$tg(\phi) = \frac{m_y \cdot sin(\phi^{cm})}{cos(\phi^{cm}) + m_X/m_y} \tag{4.4}$$

In figure 4.2, the proton energy as a function of the scattering angle in the laboratory system is shown for the elastic scattering channel. The energy of the emitted protons increases for small

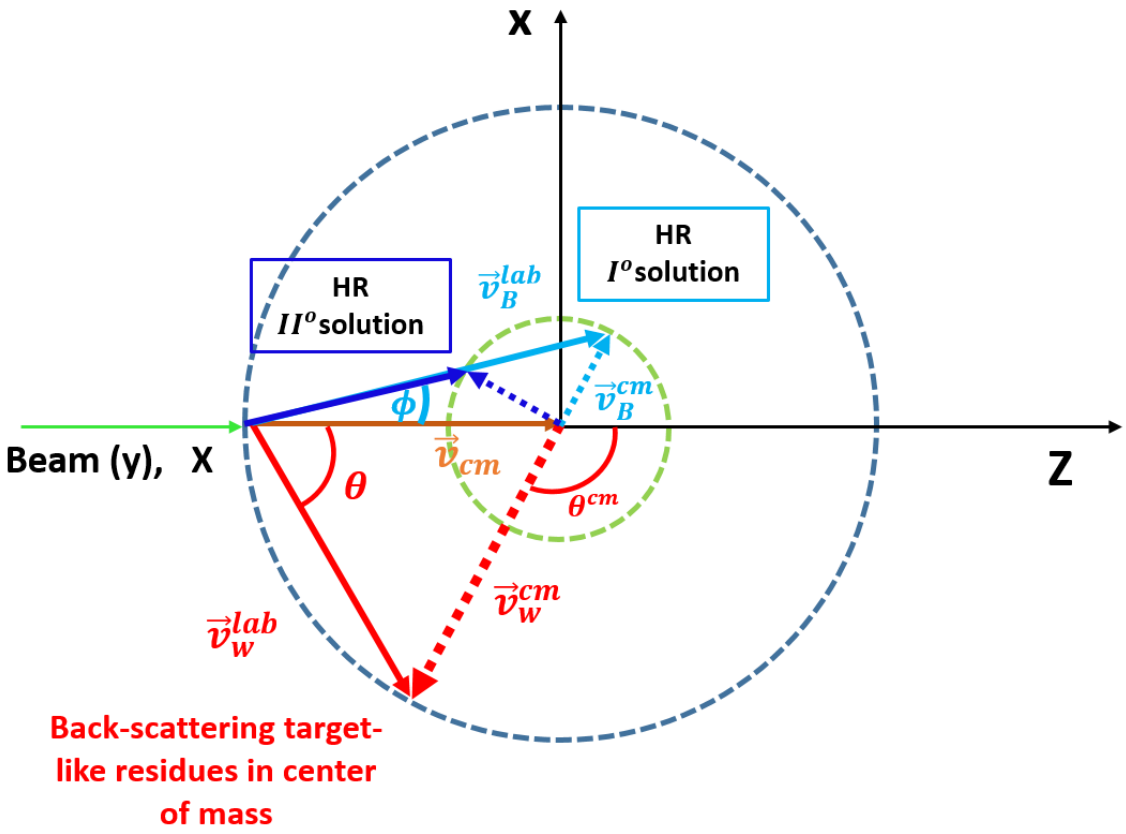

Figure 4.1: Classical velocity addition diagram for the reaction $X(y,w)B$ in inverse kinematics. In this case we consider elastic scattering where $y = w$ and $X = B$ (see the text for details). Since the target-like residue velocity is intercepting the (circumference) in one point (red arrow), only one kinematic solution is available. In the case of heavy residues (HR), on the contrary, the circumference is intercepted in two points (blue arrows) indicating that there are two different kinematic solutions.

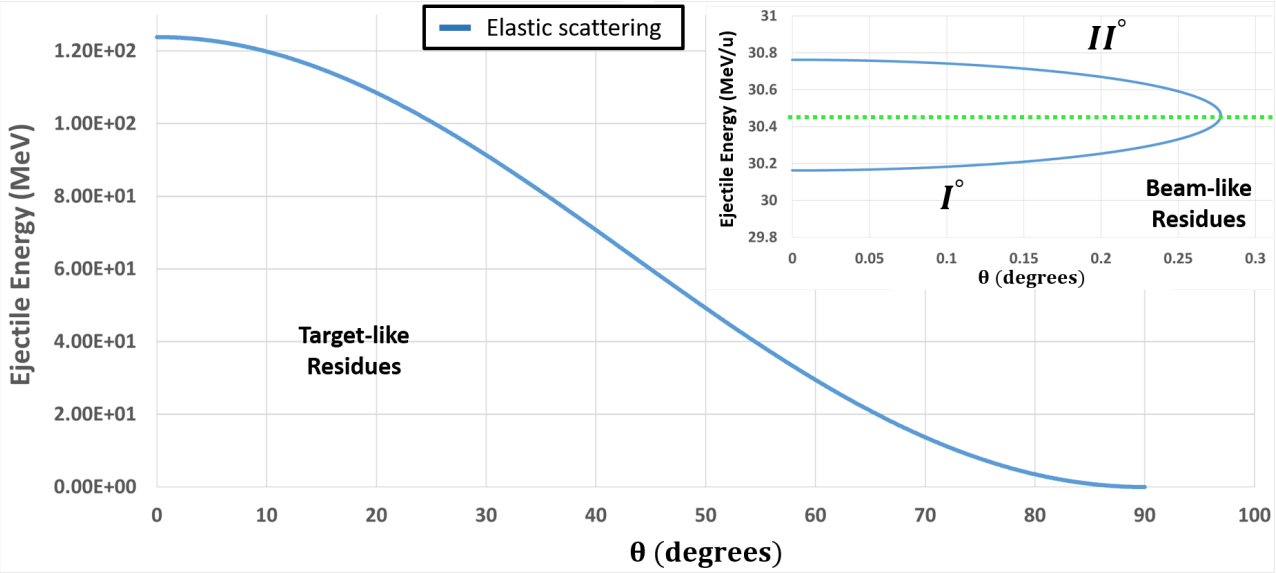

Figure 4.2: The energy of elastically scattered protons as function of the scattering angle in the laboratory for the $^{208}Pb(p,p)$ reaction at 30.77 MeV/u.

scattering angles, while the maximum emission angle of the ejectile in the laboratory system is at 90°. As can be deduced from the velocity diagram, only one solution is kinematically possible for the target residues since the velocity in the laboratory system is intercepting the circumference[1] in one point. On the contrary, the heavy residues velocity in the laboratory system is intercepting the circumference at two different points, highlighting the presence of two different kinematics solutions which are associated to the same angle in the laboratory system. The two solutions are displayed in the inset of figure 4.2.

When part of the available energy is converted into internal excitation of the heavy ions (in our case ^{208}Pb), an inelastic scattering reaction takes place. In this situation, a smaller amount of energy in the center of mass is available, with respect to the elastic case, for conversion into the momentum of the scattered particles. Due to the smaller energy of the ejectile in the center of mass system, the maximum scattering angle in the laboratory system decreases and a second kinematic solution appears. In figure 4.3, the velocity diagram for the inelastic scattering reaction is shown, where the possibility of the second solution can be seen very clearly. In this case the scattered heavy ions is excited, so in the two body kinematics it is labelled as $B^{\star}$. With the increase of the excitation energy of the heavy ion, the maximum emission angle of the ejectile decreases, while the kinetic energy of the second solution increases. This is shown in figure 4.4, where the energy of the target-like residues is plotted as a function of the scattering angle in the laboratory system. The corresponding energy of the beam-like residues associated to the ejectiles one is presented in the inset. As can be seen, high energy beam-like residues

[1]The circumference indicates all the possible target-like residue velocities in the center of mass.

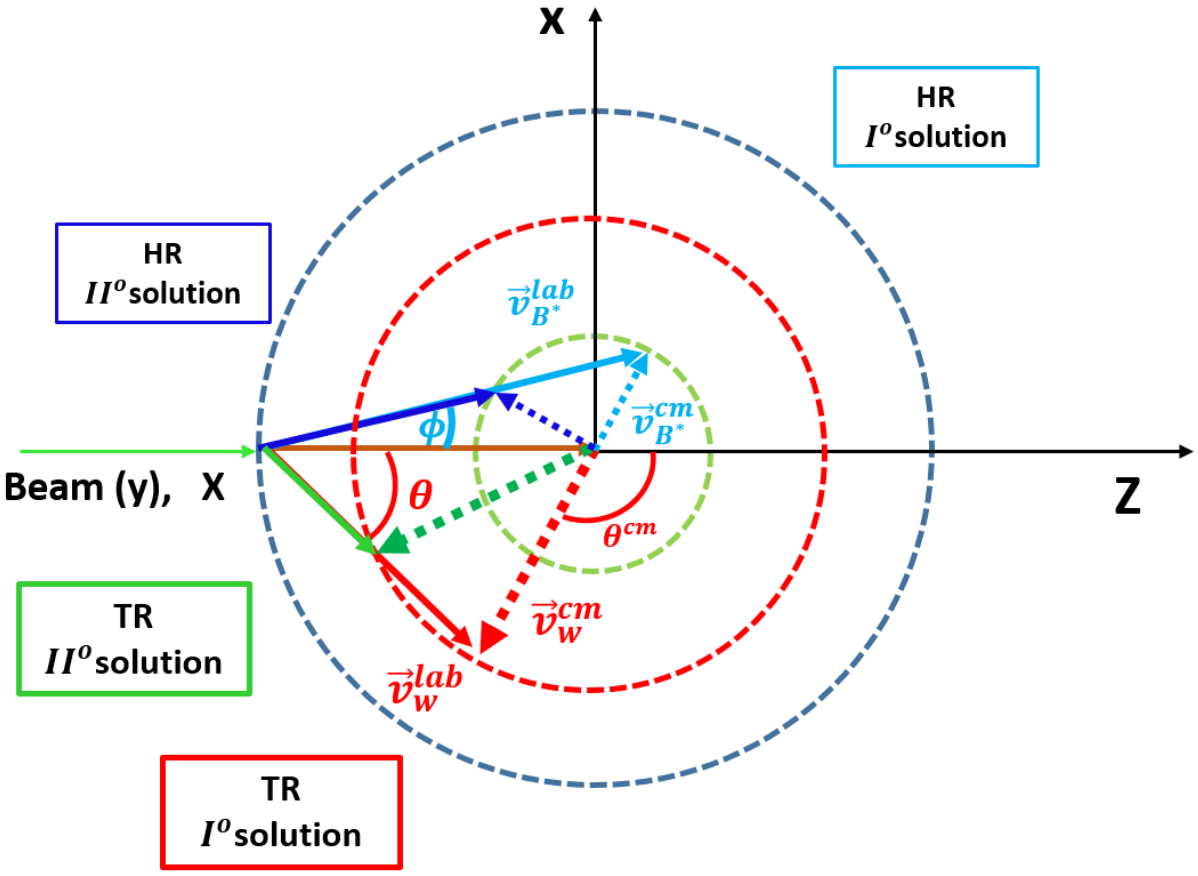

Figure 4.3: The classical velocity addition diagram for inelastic scattering in inverse kinematics, showing that due to the smaller energy available the light (target) particles emerge with a smaller velocity respect to the beam. For this reason the maximum emission angle will decrease and a second kinematic solution will appear for the target residues.

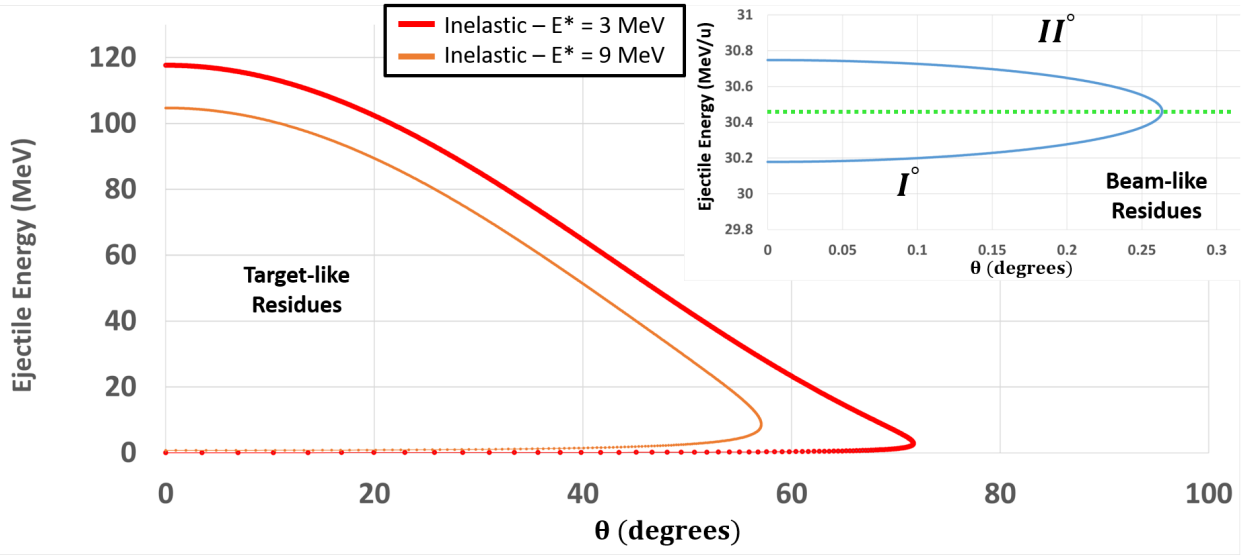

Figure 4.4: The energy of the inelastically scattered protons as a function of the scattering angle in the laboratory system for the $^{208}Pb(p,p')$ reaction at 30.77 MeV/u. The excitation energies considered for the beam like residues are $E^{\star} = 3$ and 9 MeV. As can be seen, with the increase of the excitation energy the maximum emission angle decreases. The inset shows the kinetic energy of the beam like residues as a function of the angle in the laboratory reference system.

correspond to lower energy target-like residues and vice versa.
From now on, we will refer to the two possible kinematics solutions obtained for the inelastic scattering reactions with the name of first ($I°$) and second solution ($II°$).

4.2 Set-up overview

In figure 4.5, a global overview of the set-up used for the proof of principle experiment at the ESR is shown. Two main detection systems were used: one was located at the target chamber consisting on a position-sensitive particle telescope ($\Delta E - E$) and the second one was located downstream from the first dipole, after the target section, equipped with a position sensitive detector. The two detection systems were placed inside stainless steel pockets with 25 μm thick stainless steel windows to isolate the detectors and preventing in this way the deterioration of the ring UHV. An x-ray setup with two germanium detectors was also placed around the target to record emitted photons from the K-REC[2] process. The cross section for this process is very well known and the intensity of the x-ray peaks can be used to determine the luminosity, see [Glo19]. However, this part of the experiment has not be considered in this Ph.D. work.

[2]K-REC, denotes the radiation emitted by REC (Radiative Electron Capture) into the projectile K shell.

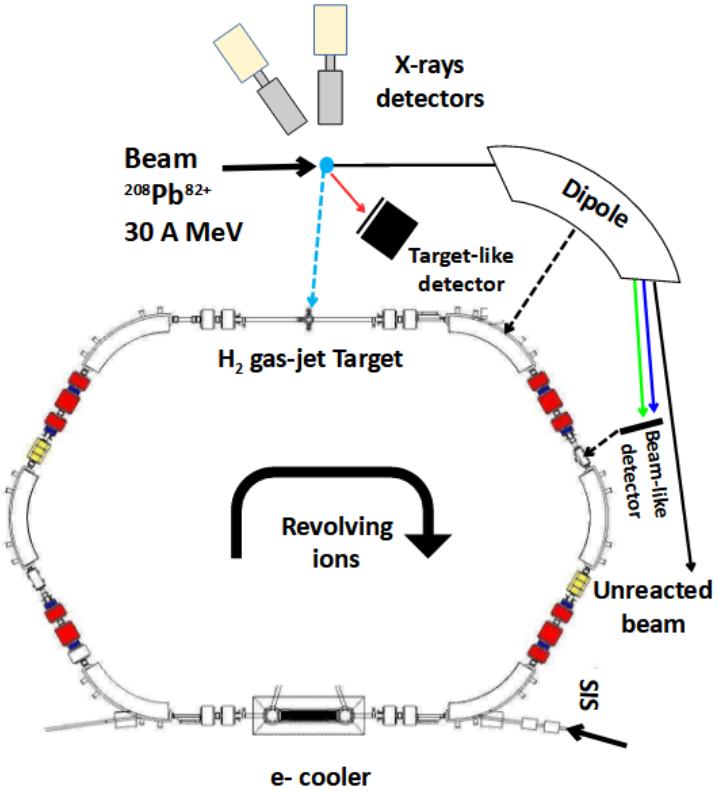

Figure 4.5: The lower part shows a schematic view of the ESR storage ring at GSI with its 6 dipole magnets and the clockwise revolving ions after injection from SIS. The zoomed-in section at the top illustrates the setup for the proof-of-principle experiment. The target residue detector is represented and the target residues are indicated by the red arrow. After the first dipole magnet downstream from the target, the heavy residue detector is shown. The black arrow represents unreacted beam particles which will pass it by. Heavy residues which have undergone γ and neutron emission are represented by the blue and green arrows, respectively.

The telescope made of Si-based charged particle detectors, manufactured by Micron Semiconductors [Micro21], was used to detect the target-like residues (protons) of the investigated scattering reactions and to measure their kinetic energy and polar angle. These quantities are used for the calculation of the excitation energy of the decaying nuclei $^{208}Pb^{\star}$ by applying the momentum and energy conservation, see section 4.4.2. Furthermore, the number of detected ejectiles corresponds to the total number of single events $N_s(E^{\star})$ used for determing the decay probabilities in equation (1.43).

The heavy residues (or beam-like residues) coming from the two body reaction were detected in coincidence with the scattered protons by the position sensitive detector located after the dipole. As we will see later, the ring dipole magnet acts as a recoil spectrometer separating the unreacted beam (black arrow), the $^{208}Pb^{82+}$ residues produced after γ-ray emission (blue arrow) and the $^{207}Pb^{82+}$ residues produced after neutron emission (green arrow) thanks to their different magnetic rigidity. The number of residues detected for decay channel χ in coincidence

Ions	Charge state	Ion mass	Beam energy	beam emittance & $\Delta p/p$	Target Radius
^{208}Pb	82+	208 amu	30 MeV/u	0.5 $mm \cdot mrad$, 10^{-4}	2.5 mm

Table 4.1: Values of physical quantities related to the beam and the target used as input parameters in the simulations.

with protons will provide the number of coincidences $N_\chi(E^\star)$ in equation (1.43).

4.3 Simulation

The preparation of the proof of principle experiment strongly relied on simulations. These simulations were very important in the definition of the detector set-up properties. Furthermore, they also allowed us for a deep understanding of the experimental problems. The simulations will be compared with the experimental results in chapter 5.

4.3.1 Simulation of the scattering reaction

4.3.1.1 Beam/target interaction

A Monte Carlo simulation was used to generate a number of beam ions (N_{ions}) randomly distributed in the target volume following a 3D gaussian distribution. The standard deviations of the gaussians were defined by the beam emittance and the momentum spread. The emission angle of the beam and target residues after the scattering reaction with the target were obtained applying two-body kinematics relations. Table 4.1 shows the values of the different physics quantities used in the simulation. Figure 4.6 shows the simulated position in the target where the reaction takes place for a small and a large beam emittance. As can be seen, a variation in the beam emittance translates in a lower or a larger spread in the position of the reaction vertex.

4.3.1.2 De-excitation process and propagation of beam-like ions through the ring

After the reaction, the beam-like residues are excited. The excitation energy is released by the emission of prompt neutrons and gamma rays. This emission induces a recoil of the beam-like residues, due to momentum conservation. Because of the absence of mass of gamma rays, the induced recoil can be neglected. However, this is not the case for neutron emission. We have modelled the effect of neutron emission in the most conservative way, i.e. by assuming that the neutron carries all the available excitation energy $E^\star - S_n$ in the form of kinetic

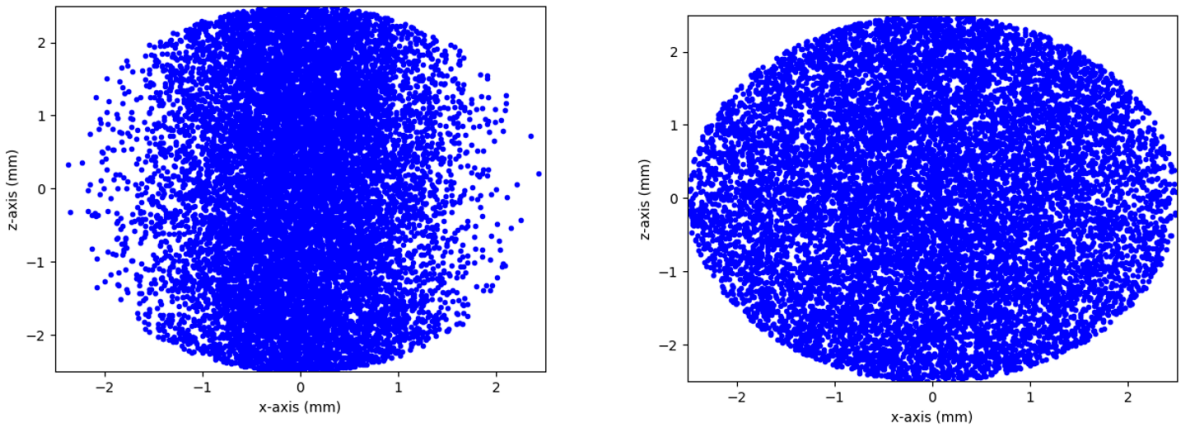

Figure 4.6: Distribution of the interaction points of the beam in the target. On the left panel a beam with an emittance of 0.05 $mm \cdot mrad$ was used while on the right side an emittance of 0.5 $mm \cdot mrad$ was considered. In figure the beam axis is the z-axis.

energy and leave the beam-like residue in the ground state. Neutron emission is assumed to be isotropic and will therefore cause a broadening of the momentum distribution of the beam-like residues.

After determining the kinematic properties of the scattered target and beam-like residues (including the effects of the subsequent de-excitation process of the beam-like residues), the transport of the charged particles through the ring optical elements was simulated with the G4beamline particle tracking program based on the Geant4 toolkit [G4bl]. In G4beamline, the user defines an input file where the beam line elements (magnets, beam pipes, windows, RF resonators, etc.) are defined together with their geometry, material composition, electric or magnetic fields etc. and their position in the space, usually along the beam direction. In order to simulate the propagation of beam-like residues from the target up to the heavy residue detection station, the lattice of the ESR ring provided by the GSI was reproduced using G4beamline. A particular effort was done to model the dipole magnet in a realistic way, by considering the real edge angles which are not included in the standard elements of G4beamline and can have a significant impact to the ion trajectories.

In figure 4.7, the different elements of the ring from the target up to the heavy-residue (HR) detector station, including the beam-pipes, the quadrupoles and the dipole magnet, are shown. If an ion trajectory intercepts one of these elements, e.g. the beam-pipe walls, the considered ion is automatically discarded. In this way, we can simulate the transmission efficiency of the beam-like residues through the ring and account for the possible beam losses.

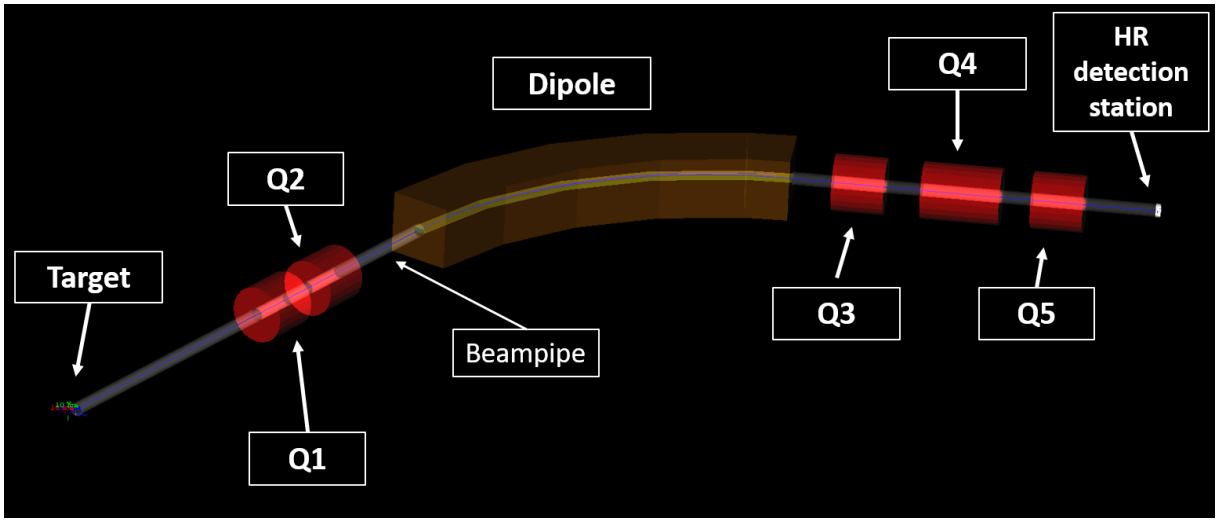

Figure 4.7: ESR ring lattice reproduced in G4beamline from the target up to the heavy residue (HR) detector station. The different optical elements, such as the beam-pipes, the quadrupoles (in red) and the dipole (in orange) are indicated.

4.4 Detector simulations

G4beamline offers also the possibility to insert active material layers, which can be used as real detectors. These detectors produce a TTree ROOT file consisting of a list of independent parameters carrying the values of the quantities describing the interaction between the layer and the impinging ions, such as the hit position, energy deposited, time-of-flight, etc.

In figure 4.8 the simulation plot for the target residue telescope is shown. The telescope is facing the target center with an angle of 60° from the beam axis at a distance of 101.3 mm. The ΔE and the E detector made of a stack of thick detectors are placed behind the stainless steel window. Further details on the detectors will be given in section (4.5.2).

In the definition of the telescope detector properties, both physical and mechanical constraints were considered in order to fit one of the available apertures of the existing target chamber at the ESR ring (as we will see in section 4.5.2). The selection of the optimal telescope position was the result of a rigorous study, which had to take into account multiple aspects and constrains of the present measurement.

Firstly, the detection of the protons from the elastic and inelastic scattering in inverse kinematics must be performed at forward angles with respect to the beam. Secondly, a very large cross section of the detected protons from the Rutherford scattering is expected for angles close to 90°. This can be seen in figure 4.9(a), where the differential cross section for the Rutherford scattering is shown as function of the emission angle of the target-like residue for the $^{208}Pb(p,p)$ reaction in inverse kinematics. Due to the large number of events, a saturation of the telescope detectors can occur close to 90°. Moreover, the detection of protons at small angles presents some additional difficulties in an inverse kinematics experiment. The energy of the ejectiles increases significantly at low scattering angles, see figures 4.2 and 4.4. Therefore, to stop com-

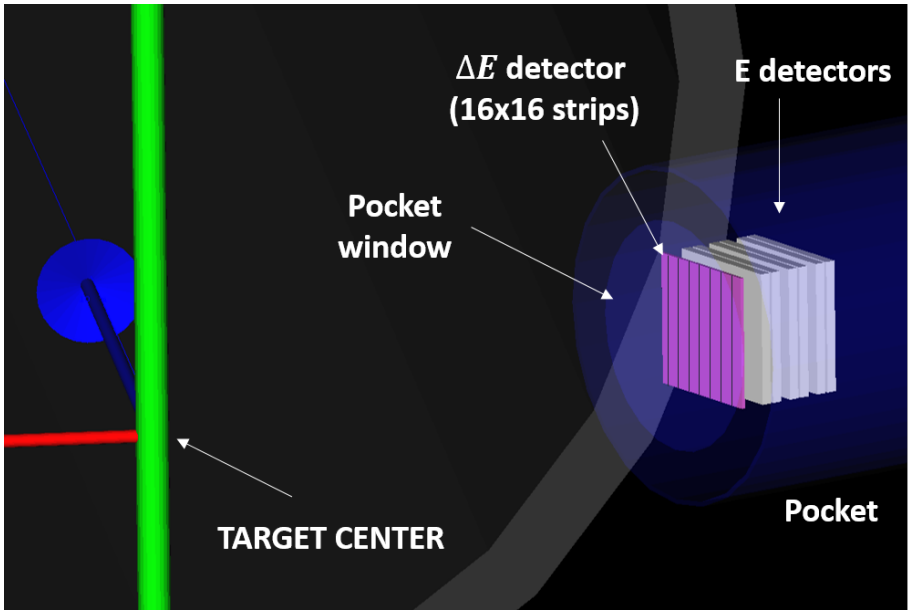

Figure 4.8: In the figure the target-like residue detector simulated in G4beamline is represented. Behind the staintess-steel window (blue color), the ΔE (pink color) and the E detector stack (white color) can be seen. The green, red and blue lines represent respectively the x, y and z-axis of the Cartesian coordinate system where the z-axis is the beam axis. The origin of the axis represent the center of the gas-jet target.

pletely these particles thick silicon detectors are needed. Unfortunately, this kind of detectors are very difficult to produce. Furthermore, an energetic heavy ion can transfer some energy to the bound orbital electrons of the target by electronic inelastic collisions. When the energy imparted to the electron is higher than the ionization energy, the electron is ejected from its orbit. The knock-out electrons or δ-rays have sufficient kinetic energy to travel a significant distance from the point of interaction.

In the case of energetic beams, the energy transfer can be very high, so δ-electrons can be enough energetic to penetrate the stainless steel window and deposited their energy in the detector saturating it. In figure 4.9(b), the energy of the δ-electrons as a function of the scattering angle, for a ^{208}Pb beam at 30.77 MeV/u, is shown. Since the energy required by the δ-electrons to penetrate the stainless steel window is about 60 keV, for small angles in the laboratory frame (below $\sim$35°) the produced knock-out electrons can be sufficiently energetic to pass the 25 μm stainless steel window and saturate the proton detector.

In conclusion, between all the available ports in the reaction chamber, the one at 60° was chosen for the experiment. The small size of this port imposed significant constrains on the design of the proton detectors, which had to fit inside the manufacted pocket. The final distance of the detector with respect to the target was about 101.3 mm and this allowed us to cover a θ angular range between 54° and 64°.

The total thickness of the telescope silicon layer was chosen to stop all the protons impinging on the detector. As can be seen from figure 4.2, the maximum energy of the protons reaching

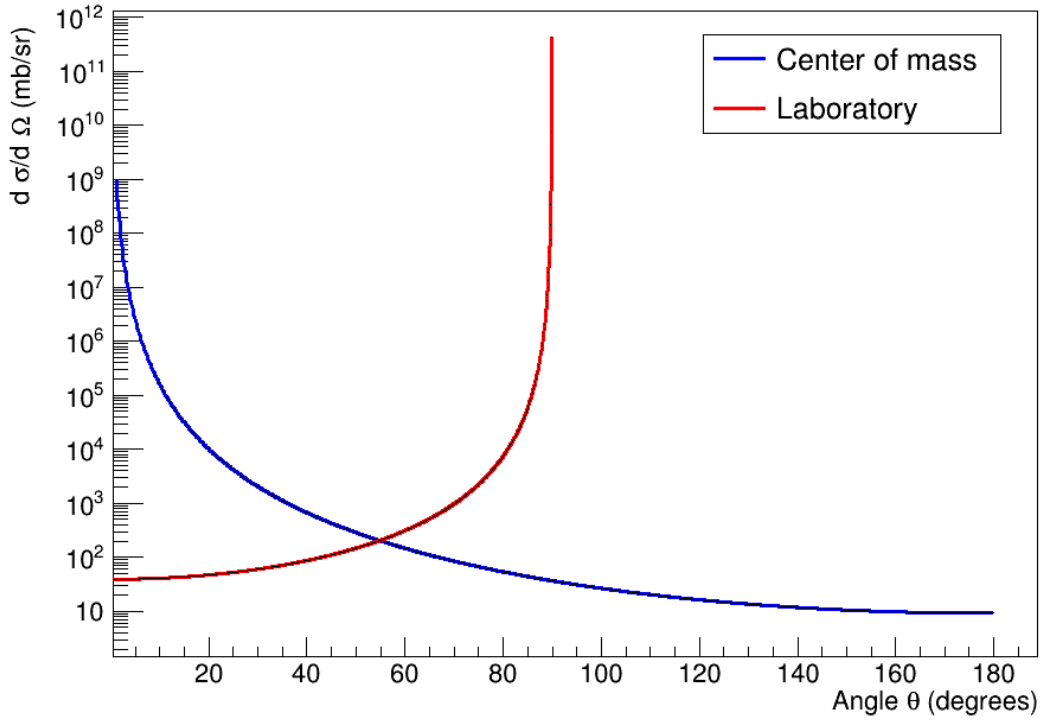

(a)

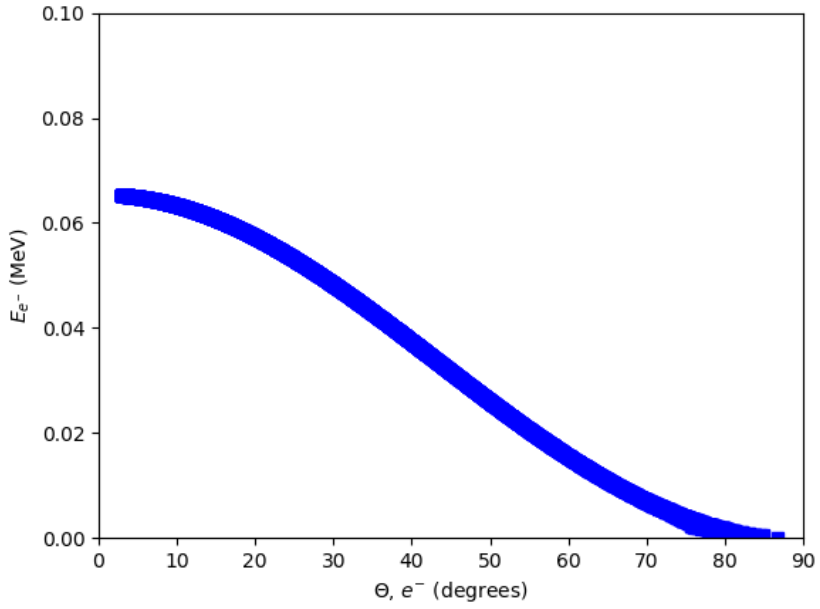

(b)

Figure 4.9: (a) Rutherford scattering differential cross section for the $^{208}Pb(p,p)$ reaction at 30.77 MeV/u as a function of the emission angle in the center of mass and laboratory systems of the target-like residue. (b) Energy of δ-electrons as a function of the emission angle.

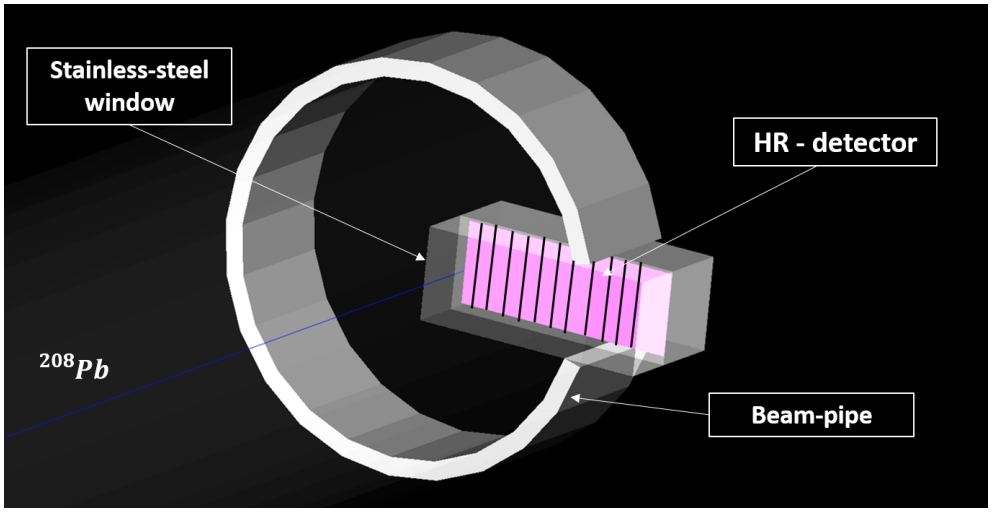

Figure 4.10: G4beamline simulation drawing for the position sensitive detector used to detect the heavy residues. Also in this case the detector was housed in a pocket with a stainless-steel window.

the telescope is about 40 MeV at an angle of 54°. To stop these particles a silicon layer of 9.5 mm is required.
In figure 4.10 the simulation of the heavy residue detector is shown. This detector is located after the dipole inside a movable pocket. Its position with respect to the beam axis was carefully defined with the help of technical drawings.
A root script was developed to implement in the generated data Tree two additional branches which allowed us to consider the detector segmentation, 16×16 strips for the ΔE of the telescope and 122×44 for the heavy residues (HR) detector.

4.4.1 Simulations for the target-like residues

In the simulation, protons produced by the elastic and inelastic scattering reactions were propagated up to the telescope detectors. The hit vertical and horizontal strips were used to calculate the scattering angle. The energy deposited in the different telescope layers together with the detector energy resolution were used to determine the measured proton energy. As we will see later, the energy resolutions were derived from measurements performed with an α-source. It was found to be 0.5% for the telescope ΔE and about 1.3% for the E detectors.
The reconstructed energy and scattering angle were used to verify the kinematics of the generated protons by comparing the reconstructed total energy as a function of the emission angle (E_p, θ) with the theoretical values obtained by applying energy and momentum conservation. In figure 4.11(a), the scatter-plot obtained from an ideal experiment ($\epsilon \to 0$, number of strip $N_{strip} \to \infty$, target radius $R \to 0$, $\Delta p/p \to 0$) is shown together with the theoretical curves. Under these conditions the protons coming from the elastic and the inelastic scattering reaction

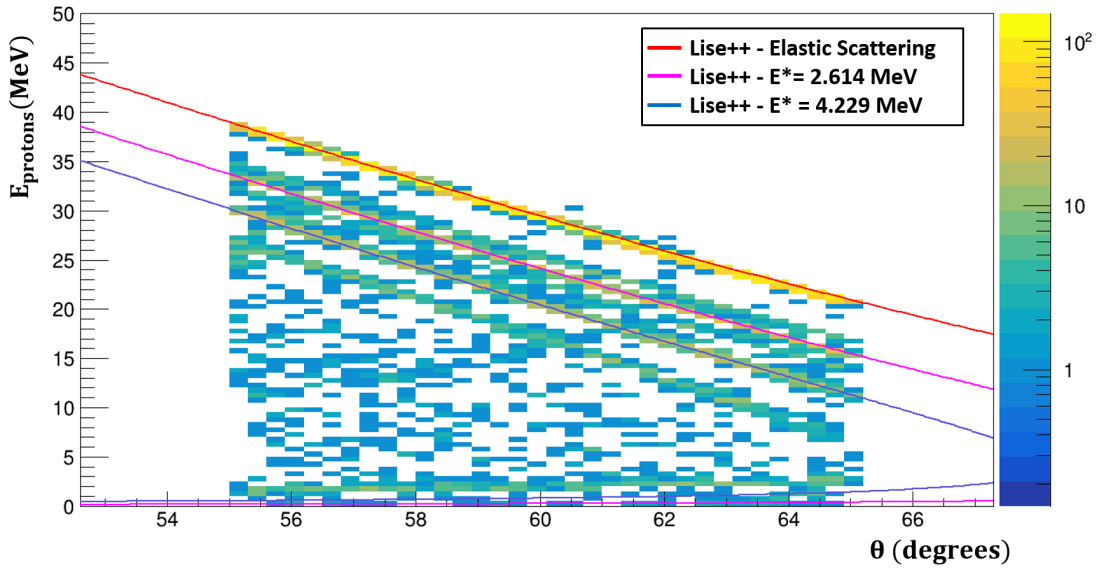

(a)

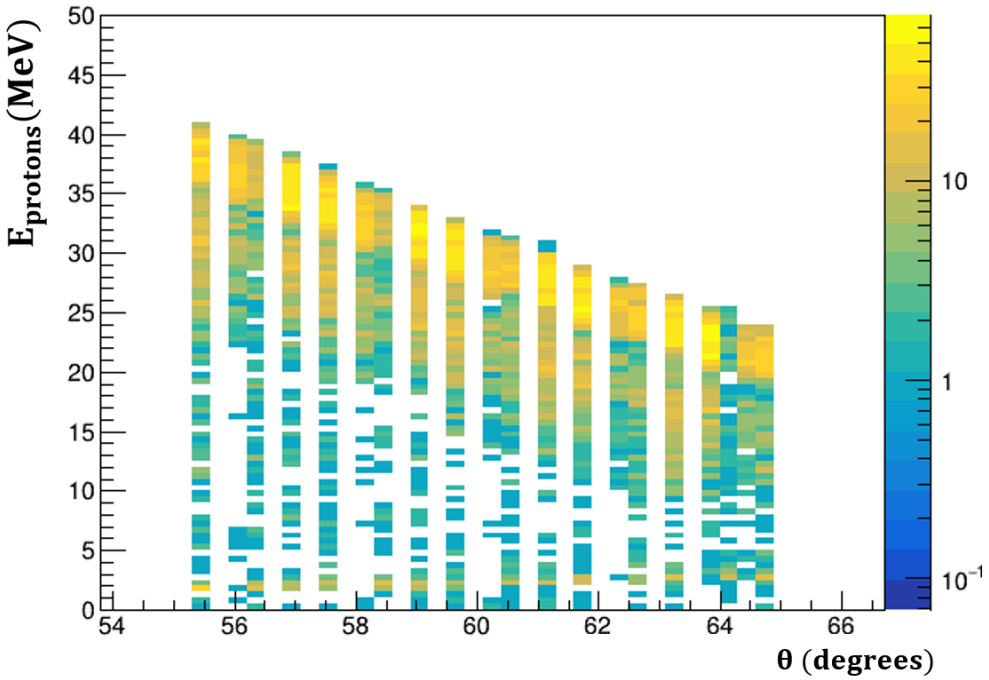

(b)

Figure 4.11: Simulated kinetic energy of the scattered protons as a function of the emission angle θ. In part (a) we assumed ideal conditions ($\epsilon \to 0$, $N_{strip} \to \infty$, $R \to 0\ mm$, $\Delta p/p \to 0$). In part (b) realistic conditions were assumed ($\epsilon \to 0.5\ mm \cdot mrad$, $N_{strip} \to 16$, $R \to 2.5\ mm$, $\Delta p/p \to 10^{-4}$). The simulated values are compared with theoretical calculations based on energy and momentum conservation for the ground and the two first excited states of ^{208}Pb.

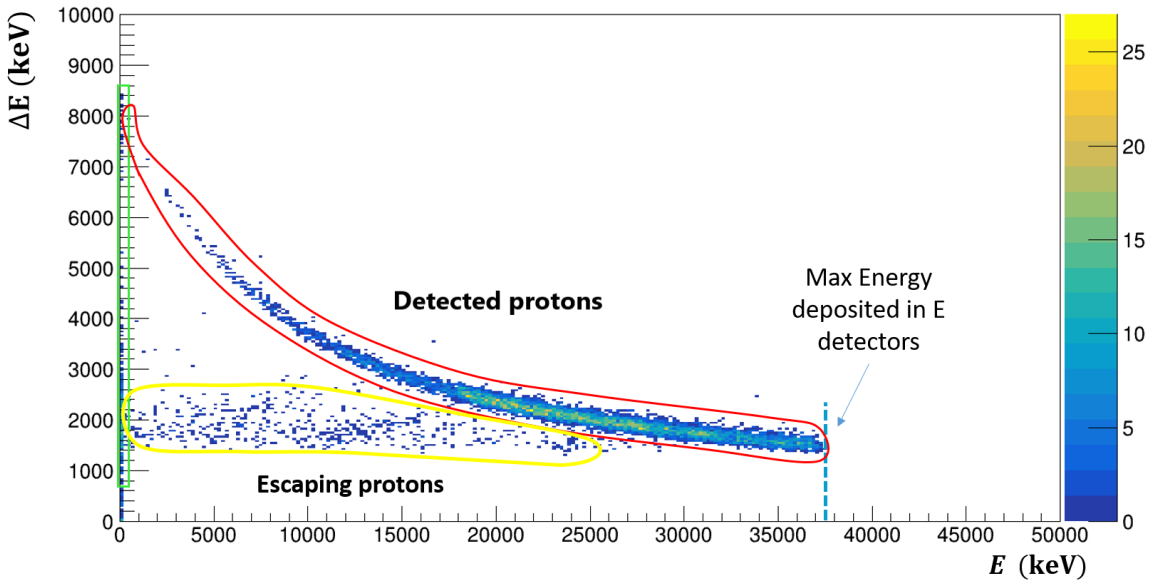

Figure 4.12: Simulated results for energy loss in the ΔE detector as a function of the total energy deposited in the E detectors for the $^{208}Pb(p,p)$ and $^{208}Pb(p,p')$ reactions in inverse kinematics at 30 MeV/u. The protons from the elastic and inelastic scattering reactions are within the red contour, while escaping protons and protons from the second kinematics solution are inside yellow and green contour, respectively.

can be easily identified. The good agreement with the theoretical curves allowed us to validate the kinematics implemented in our simulations.

Figure 4.11(b) shows the results obtained for realistic parameters. The limited number of strips is responsible for a discretization of the angles covered by the individual strips. Each strip defines a specific θ interval, whose width depends on the number of strips (N_{strip}) on the ΔE detector active area.

The ground and first excited states can not be distinguished due to the energy resolution of the telescope detectors and the uncertainty in the reconstruction of the reaction vertex. This last point will become more clear in the next sections where the uncertainty on the excitation energy resolution will be described in detail. In the simulation we considered the different cross sections for the elastic and inelastic scattering reactions by using $^{208}Pb(\alpha,\alpha')$ data of [Sán19a].

The identification of the protons is performed by representing the energy deposited in the ΔE detector versus the residual energy measured by the E detectors. According to the Bethe-Bloch formula [Bis12], the energy loss ΔE is related to the kinetic energy E_k, charge Z and mass A by the equation:

$$\Delta E \propto \frac{A \cdot Z^2}{E_k} \tag{4.5}$$

Figure 4.12 shows the simulation results for the energy loss versus residual energy spectrum. The protons, that go through the ΔE detector and are stopped in one of the E detectors, lie

on the hyperbolic curve within the red contour ($I°$ kinematic solution). The protons, from the second ($II°$) kinematics solution of the inelastic scattering reaction, are stopped in the ΔE detector and are located in the left lower part of the histogram, inside the green square. When a proton goes through the telescope, it can escape from the telescope itself before being stopped completely. This is due, for example, to the incident angle of the particle or a change in the particle direction after a scattering events in the detector. These events are inside the yellow contour line. Since the only possible ejectiles expected in this experiment are the protons from the elastic and inelastic scattering, it is reasonable to assume that a similar spectrum will be obtained experimentally.
Neglecting the energy loss of the scattered particles in the gas-jet target, the kinetic energy of the ejectiles $E_{k,w}$ is given by the total energy deposited in the telescope ($\Delta E + E$) corrected by the energy loss in the stainless steel window (E_{window}):

$$E_{k,w} = \Delta E + E + E_{window} \tag{4.6}$$

where E is the sum of the energy deposited in the different detectors of the stack $E = \sum_i E_i$. E_{window} was obtained by simulating the interaction of inelastic and elastic scattered protons with a 25 μm layer of stainless steel in front of the telescope by means of G4beamline [G4bl]. To determine the scattering angle θ, we need to know the interaction point in the target and the position of the detected proton in the ΔE. Determining the interaction point in the target is a difficult task due to the finite dimensions of the beam and the target. In the present work, the position of the reaction vertex was approximated to the target center for all the ejectiles, see the figure 4.13. As it will be discussed later, this assumption leads to a significant increase of the uncertainty on the scattering angle with the increase of the target size.

In the simulation of the scattering angle, the position of the activated ΔE detector pixel (x, y, z) in the coordinate system S, with the z-axis perpendicular to the ΔE detector, is transformed to the coordinates (x', y', z') of the system S'. The new system is rotated by φ=60° with respect to the y-axis and the z-axis is parallel to the beam axis, see figure 4.13. This is done by applying the following linear transformation of coordinates:

$$x' = z \cdot sin(\varphi) + x \cdot cos(\varphi) \tag{4.7}$$

$$y' = y \tag{4.8}$$

$$z' = z \cdot cos(\varphi) - x \cdot sin(\varphi) \tag{4.9}$$

where φ is the beam axis rotation. The scattering angle θ is then calculated using the Cartesian coordinates (x', y', z') of the system S' by the expression:

$$\theta = arctan(\frac{\sqrt{x'^2 + y'^2}}{z'^2}) \tag{4.10}$$

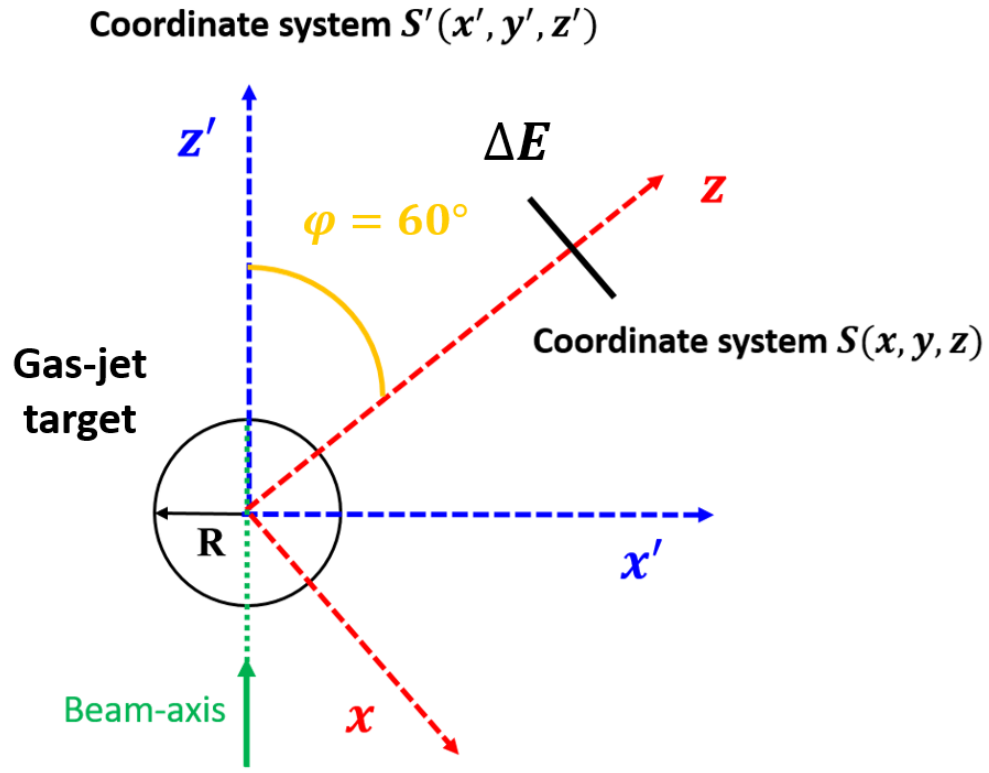

Figure 4.13: Schematic representation of the target and the ΔE detector of the telescope. The coordinate system S and S' used in the simulation for determing the proton scattering angle θ are shown.

4.4.2 Excitation energy of the compound nucleus

Applying two-body kinematics, the excitation energy of the ^{208}Pb compound-nucleus can be deduced from the kinetic energy and emission angle of the scattered protons. In the general case of a reaction $X(y, w)B^{\star}$, the kinematical properties of each particle are listed in figure 4.14, where m corresponds to the atomic mass, E_k is the kinetic energy and $\vec{p}$ is the momentum vector of the particle. Note that the recoiling nucleus B is here the ^{208}Pb compound-nucleus formed after the inelastic scattering reaction. Performing the calculations in relativistic kinematics, the conservation of the total energy (shared between kinetic and excitation energy) gives:

$$E_X + m_y c^2 + Q = E_B + E_w + Ex = E_{tot.} + Ex \tag{4.11}$$

where $E = E_k + m \cdot c^2$ is the particle total energy (kinetic + rest-mass energy), $Q = [m_y + m_X - (m_B + m_w)] \cdot c^2$ is the Q-value of the reaction and $Ex = E_w^{\star} + E^{\star}$ is the sum of the excitation energies of nuclei w and B. For the present reaction, $^{208}Pb + p$, the ejectile has no excitation

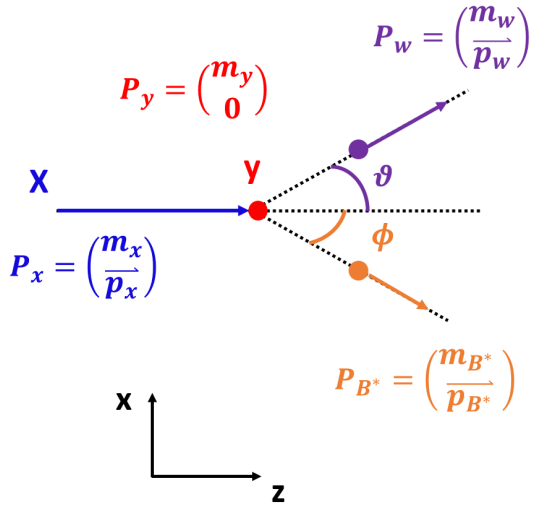

PARTICLES	NOTATION	PARAMETERS
^{208}Pb	Projectile (X)	$m_X, \overrightarrow{p_X}, E_{k,X}, E_X$
p	Target (y)	m_y
p'	Ejectile (w)	$m_w, \overrightarrow{p_w}, \vartheta, E_{k,w}, E_w$
$^{208}Pb^*$	Recoiling nucleus (B^*)	$m_{B^*}, \overrightarrow{p_{B^*}}, \phi, E_{k,B^*}, E_{B^*}$

Figure 4.14: The two-body $^{208}Pb(p,p')^{208}Pb^\star$ nuclear reaction scheme and the associated kinematical quantities (or parameters).

energy[3]. The excitation energy is fully transferred to the recoiling nucleus.

The equations for momentum conservation along the z and x can be written as,

$$z: \qquad p_X = p_w \cdot cos(\theta) + p_{B^\star} \cdot cos(\phi) \tag{4.12}$$

$$x: \qquad 0 = p_w \cdot sin(\theta) - p_{B^\star} \cdot sin(\phi) \tag{4.13}$$

Squaring the equations (4.12) and (4.13), and combining them we obtain the relation:

$$p_{B^\star} = p_X^2 + p_w^2 - p_X \cdot p_w \cdot cos(\theta) \tag{4.14}$$

The total energy of the nucleus $B^\star$ can be defined as the sum of the excitation energy $E^\star$ and the ground state rest mass energy $m_B \cdot c^2$:

$$m_B^\star \cdot c^2 = E^\star + m_B \cdot c^2 \quad \rightarrow \quad E^\star = m_B^\star \cdot c^2 - m_B \cdot c^2 \tag{4.15}$$

For the particle $B^\star$ having a total energy $E_{B^\star}$ and a momentum $\vec{p_{B^\star}}$, we can define a 4-momentum vector $P_{B^\star} = (E_{B^\star}, \vec{p}_{B^\star})$ where the square $P_{B^\star}^2 = E_{B^\star}^2 - |\vec{p}_{B^\star}|^2 = m_{B^\star}^2$ is the invariant mass. Applying to equation (4.15) to the invariant mass expression, and using the equation (4.14) we obtain the final expression:

$$E^\star = \sqrt{[E_{k,X} + m_X - E_{k,w} + Q]^2 - p_X^2 - p_w^2 + 2 \cdot p_X \cdot p_w \cdot cos(\theta)} - m_B \tag{4.16}$$

[3]A huge excitation energy of about 300 MeV would be required to excite a proton.

where $E_{k,X}$ and $E_{k,w}$ are respectively the projectile and ejectile kinetic energies. With the relation (4.16) it is possible to calculate the excitation-energy range accessible with our experimental set-up by considering the total angular range covered by the telescope, between 54° and 64°, and the energy of the scattered protons. From kinematic considerations (and not taking into account the cross section) a maximum excitation energy of ∼10.3 MeV is reachable by detecting protons down to 54°. Since the neutron separation energy of ^{208}Pb is 7.36 MeV, this will ensure a range of about 2.6 MeV where the competition between gamma and neutron emission can be studied.

4.4.3 Excitation energy resolution

One of the most important quantities that we aim to investigate is the excitation energy resolution. The latter is determined by the uncertainty of the proton kinetic energy (σ_{E_k}) and the uncertainty in the proton scattering angle θ (σ_θ). The total uncertainty on the ejectile energy ($\sigma_{E_{k,w}}$) is given by the quadratic sum of the energy resolution of the ΔE and E detectors:

$$\sigma_{E_{k,w}} = \sqrt{(\sigma_{\Delta E})^2 + \sum_i (\sigma_{E_i})^2} \tag{4.17}$$

where the summation runs over the total number of E detectors used.
The resolution of the detectors was measured by a standard 3α source (see section 4.5) and it was observed to be about 0.5% for the ΔE and about ≃1.3% for the E detectors. The equation (4.11) does not take into account the impact of the energy loss and straggling caused by the stainless steel window. However, this effect is expected to be smaller than the uncertainty on the energy for protons with energies above 20 MeV.
The total uncertainty on the excitation energy ($\sigma_{E^\star}$) can be written as:

$$\sigma^2_{E^\star} = \left(\frac{\partial f_{E^\star}}{\partial E_{k,w}}\right)^2 \cdot \sigma^2_{E_{k,w}} + \left(\frac{\partial f_{E^\star}}{\partial \theta}\right)^2 \cdot \sigma^2_\theta \tag{4.18}$$

By using the two body kinematics equation (4.16) for the calculation of the excitation energy in equation (4.18), keeping the same notation, we obtain:

$$\frac{\partial f_{E^\star}}{\partial E_{k,w}} = \frac{1}{2 \cdot \sqrt{[E_{k,X} + m_{k,X} - E_{k,w}]^2 - (C) - (D) + 2 \cdot \sqrt{C} \cdot \sqrt{D} \cdot cos(\theta)}} \cdot \\ [-2 \cdot (E_{k,X} + m_{k,X} - E_{k,w}) + \frac{2 \cdot \sqrt{C} \cdot E_y \cdot cos(\theta)}{\sqrt{D}}] \tag{4.19}$$

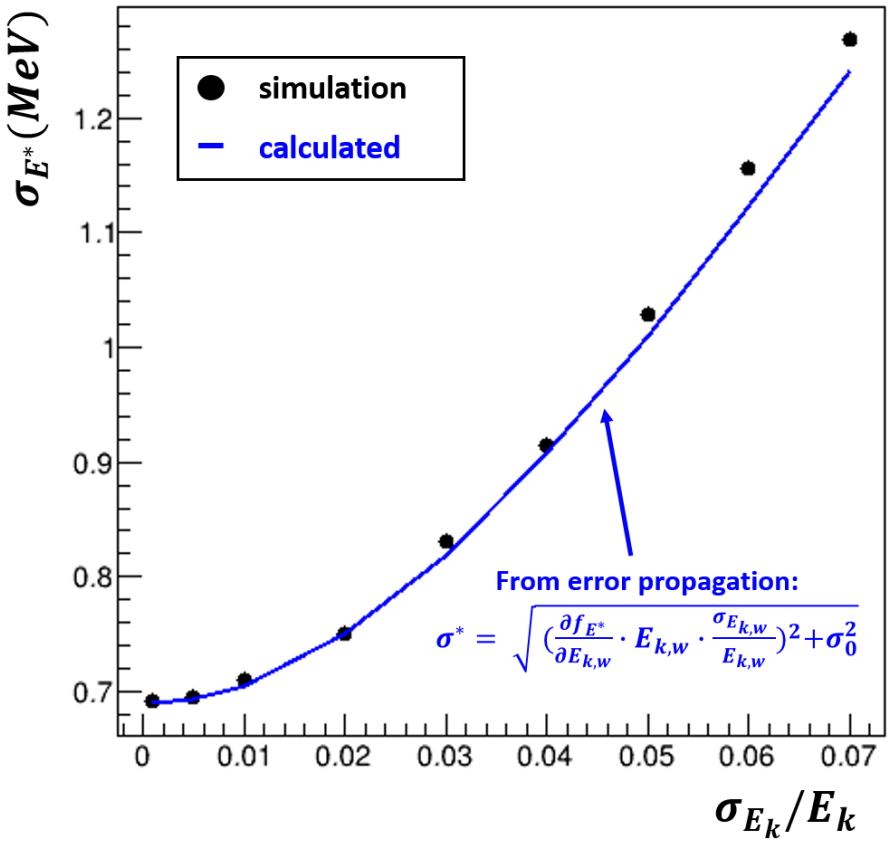

Figure 4.15: Uncertainty in the excitation energy $\sigma_{E^\star}$ as a function of the proton kinetic energy resolution $\sigma_{E_{k,w}}/E_{k,w}$ for elastic scattered protons emitted at 60°. The black points indicate the result obtained from the simulation. The blues line represents the calculated excitation energy resolution obtained from equation (4.12), considering a contribution from σ_θ equal to σ_0, which is obtained from the simulation.

$$\frac{\partial f_{E^\star}}{\partial \theta} = -\frac{2 \cdot \sqrt{C} \cdot \sqrt{D} \cdot sin(\theta)}{\sqrt{[E_{k,X} + m_{k,X} - E_{k,w}]^2 - (C) - (E_w^2 - m_w^2) + 2 \cdot \sqrt{C} \cdot \sqrt{D} \cdot cos(\theta)}} \tag{4.20}$$

where for convenience we represent $E_X^2 - m_X^2$ and $E_w^2 - m_w^2$ as C and D. Figure 4.15 shows the $\sigma_{E^\star}$ as a function of the energy resolution $\sigma_{E_{k,w}}/E_{k,w}$ obtained from the simulation and equation (4.18). As can be seen, the simulation and the analytical expression show that the uncertainty increases significantly for $\sigma_{E_{k,w}}/E_{k,w} > 3\%$. For $\sigma_{E_{k,w}}/E_{k,w} \to 0$, $\sigma_{E^\star}$ does not go to zero but it approaches a lower limit $\sigma_0 = 0.690\ \ MeV$. This value represents the contribution coming from the σ_θ term of the equation (4.18).

Let us now assume $\sigma_{E_{k,w}}/E_{k,w} \to 0$ and vary some properties such as the number of strips N_{strips} of the ΔE detector and the emittance of the beam. In figure 4.16 the excitation energy resolution dependence with respect to the inverse strip number $(1/N_{strip})$ and the beam emittance are displayed. We can see that a decrease of the number of strips below 16 can significantly degrade $\sigma_{E^\star}$, while a larger number of strips does not provide a significant improvement. From

the emittance variation no degradation or improvement of $\sigma_{E^\star}$ can be seen. Let us know estimate the uncertainty in $E^\star$ due to the target radius. As mentioned in section 4.4.1, the proton scattering angle θ is calculated from equation (4.10) by assuming that the interaction between the beam and the target nuclei takes place in the target center. This approximation introduces an uncertainty with respect to the real position of the reaction vertex. The impact of the target radius is illustrated in figure 4.17 for protons impinging on the center of the ΔE. Along the z-axis, the beam direction, we assume that the the scattering reaction can take place at any position between $-R$ and R (see figure 4.17), following a uniform probability distribution. The quantity $\Delta\theta$ can be derived from the following equation, which is obtained from figure 4.17:

$$tg(\theta + \Delta\theta) = \frac{x}{(z - R)} = \frac{L \cdot sin(\theta)}{L \cdot cos(\theta) - R} \tag{4.21}$$

where L is the distance between the target and the ΔE detector and R is the target radius. Solving the equation (4.21) and using using L=101.3 mm and R=2.5 mm we obtain $\Delta\theta$=1.23°. The standard deviation σ_θ for a uniform distribution in a range $2 \cdot \Delta\theta$ is given by:

$$\sigma_\theta = \sqrt{\frac{1}{12} \cdot (2 \cdot \Delta\theta)^2} \tag{4.22}$$

which gives σ_θ=0.71° corresponding to 0.012 rad. For $\sigma_{E_{k,w}}/E_{k,w}$ equal to zero, the $\sigma_{E^\star}$ can be expressed from the equation (4.18) as:

$$\sigma_{E^\star} = \frac{\partial f_{E^\star}}{\partial\theta} \cdot \sigma_\theta \tag{4.23}$$

where $\frac{\partial f_{E^\star}}{\partial\theta} = 50.34\ MeV/rad$ for proton of 29.1 MeV emitted at 60°. Using equation (4.23) and σ_θ= 0.012 rad we can provide an estimation of $\sigma_{E^\star}$:

$$\sigma_{E^\star} = 50.34\ \frac{MeV}{rad} \cdot 0.012\ rad = 0.623\ MeV \tag{4.24}$$

This value does not take into account the contribution from N_{strip}, ϵ, $\Delta p/p$ and the energy resolution. In any case, the result of equation (4.18) gives a good idea of the huge impact of the target radius on $\sigma_{E^\star}$.

In figure 4.18, $\sigma_{E^\star}$ is represented as a function of the target radius obtained from the simulations (black circles) using the experimental conditions of the proof of principle ($N_{strips} = 16$, $\epsilon = 0.5\ mm \cdot mrad$, $\Delta p/p = 10^{-4}$, $\sigma_{E_{k,w}}/E_{k,w} \approx 2\%$). They show that a reduction of the target radius by a factor 5 ($R = 0.5\ mm$) can significantly improve $\sigma_{E^\star}$, achieving a value of 250 keV. However, a further reduction of the target size will not provide any further improvement since the other contributions will dominate $\sigma_{E^\star}$. The blue circles were obtained considering also an improvement of the detector properties (larger number of strips and better detector energy resolution). In this case, $\sigma_{E^\star}$ can reach values lower than 200 keV.

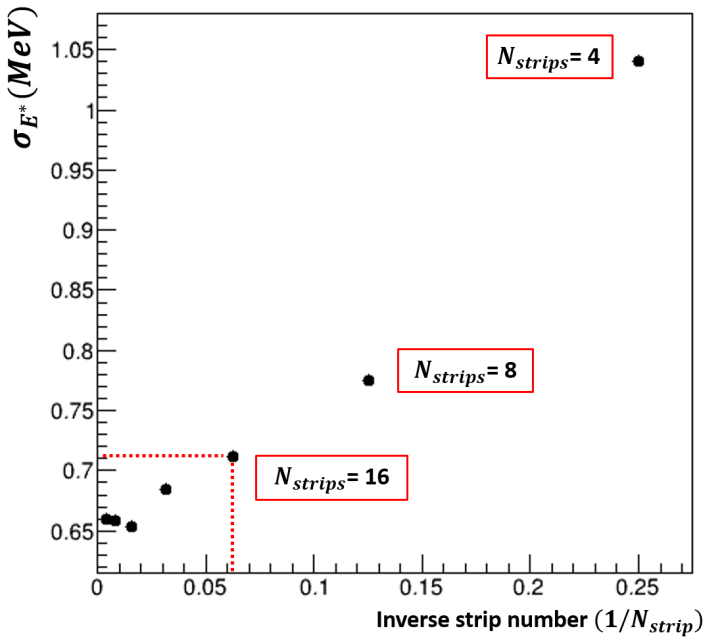

(a)

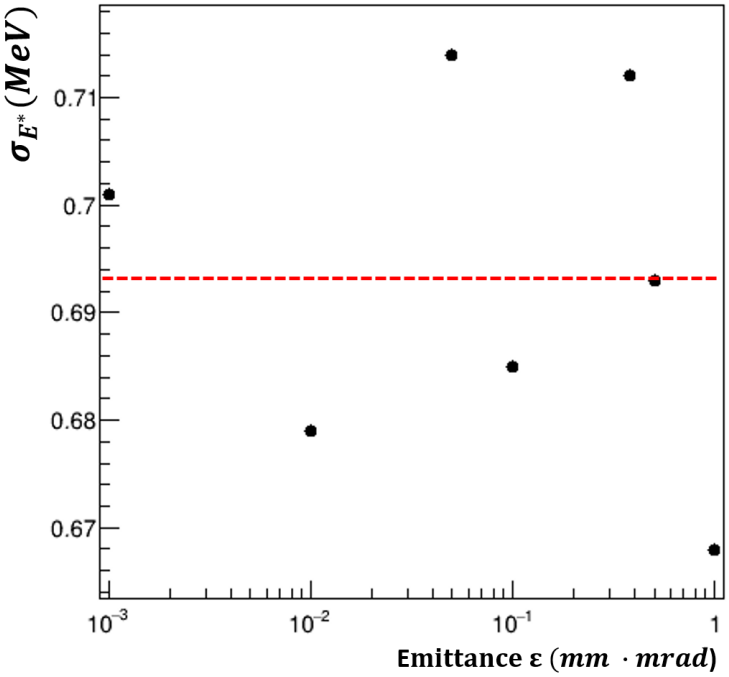

(b)

Figure 4.16: The variation of $\sigma_{E^\star}$ with respect to the inverse strip number $(1/N_{strip})$ and emittance is shown in figures (a) and (b) respectively. The dotted line indicate in panel (a) the strip number used during the experiment and the correspondent excitation energy resolution expected from the simulation. In panel (b) the dotted line is inserted to better see the fluctuation of the excitation energy resolution due to the emittance variation.

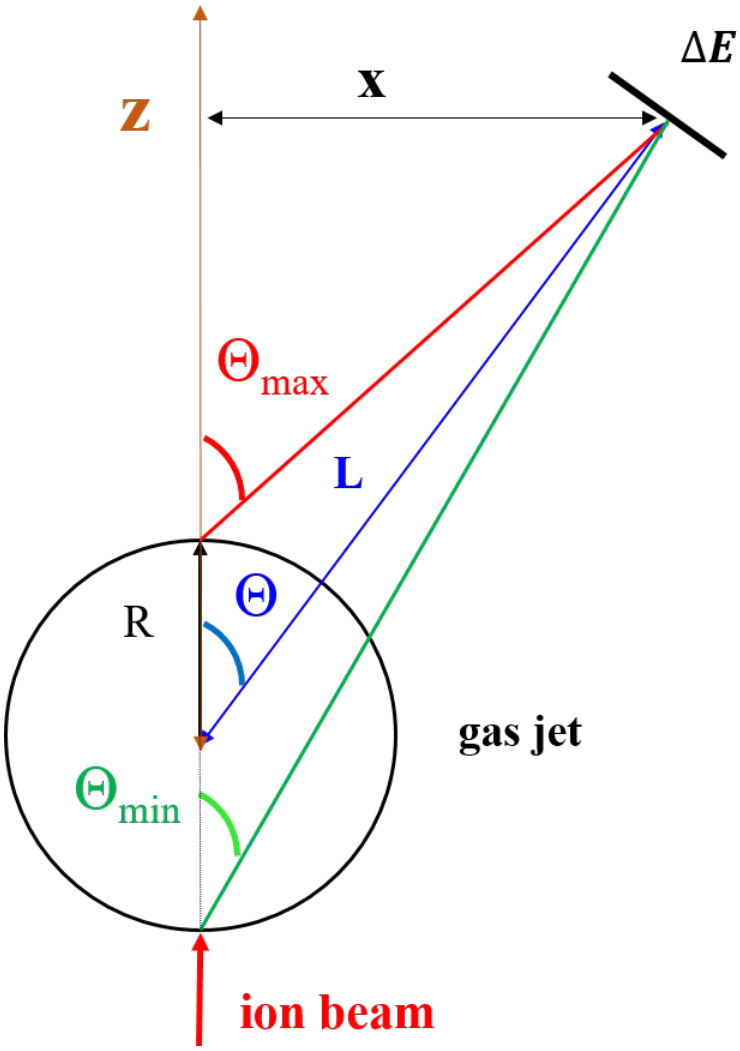

Figure 4.17: Schematic representation of the impact of the target radius on the determination of the scattering angle θ. L is the distance from the target center to the ΔE detector center and R is the target radius.

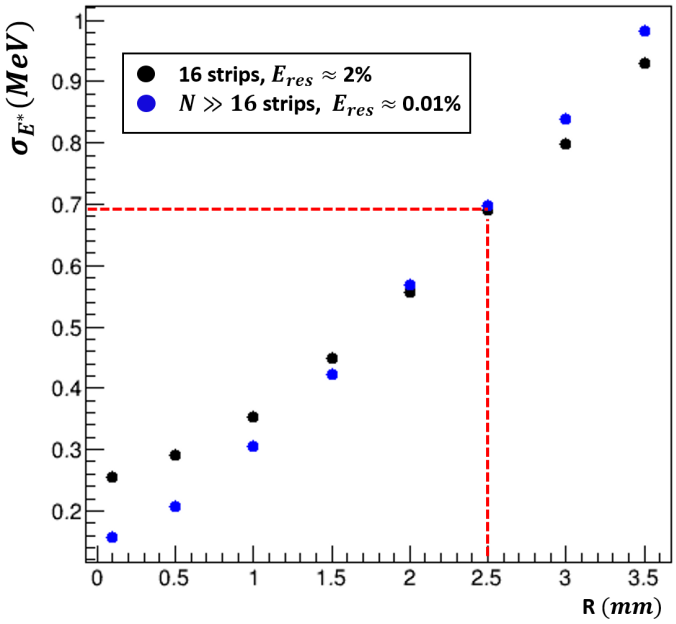

Figure 4.18: The impact of the target radius on $\sigma_{E^\star}$ is shown for an ideal set-up (blue circles) and for the set-up used during the proof of principle experiment (black circles).

If we take the value of $\sigma_{E^\star}$ at R=2.5 mm we obtain $\sigma_{E^\star}$=700 keV which is rather close to the value of equation (4.24) and demonstrates the significant effect of the target radius on $\sigma_{E^\star}$.

4.4.4 Simulations for beam-like residues

4.4.4.1 Heavy residue trajectories

The beam-like residues originating from the elastic scattering and the de-excitation of the $^{208}Pb^\star$ were propagated through the simulated ring lattice up to heavy residue detector, together with the unreacted beam. The dipole magnet downstream from the target section of the ESR ensures a separation between the ions having different magnetic rigidities $\beta\rho$, where β is the magnetic field of the dipole and ρ the bending radius of ions inside the dipole. Using the Lorentz and the centripetal forces we obtain the well known formula:

$$B\rho = p/q \tag{4.25}$$

where p denotes the momentum of the ions with charge state q. The momentum of the beam-like ions depends on the energy and angles of the ejectile. In the case of elastic scattering and γ-emission the decrease of the ^{208}Pb ions velocity due to the scattering process is the reason for the momentum decrease, while if neutron-emission takes place (at excitation energies $E^\star > S_n$) also the change in the ions mass from ^{208}Pb to ^{207}Pb must be considered. As mentioned above the momentum change due to γ-ray emission in the $^{208}Pb^\star$ de-excitation process can be neglected.

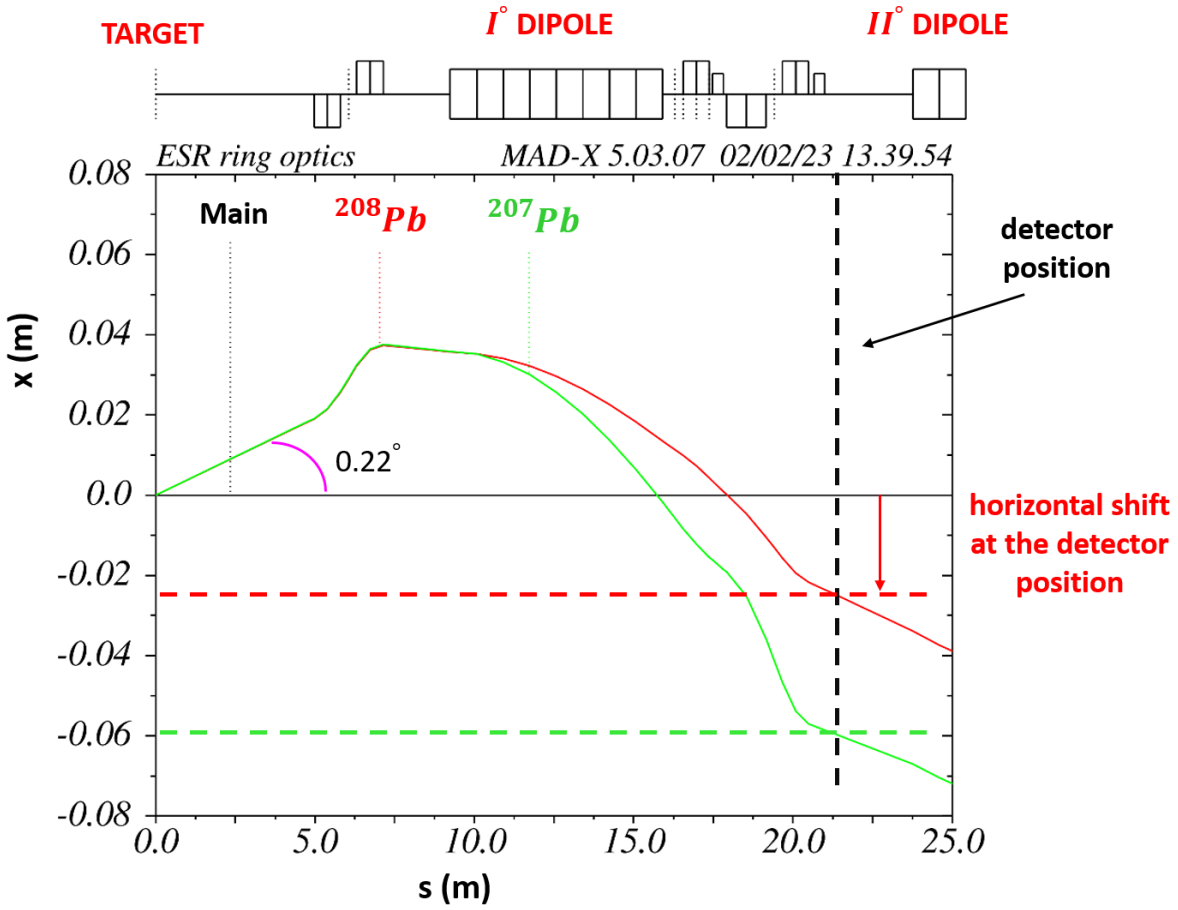

Figure 4.19: MAD-X trajectories for the x coordinate along the ring lattice of the ^{208}Pb (in red) and ^{207}Pb (in green) heavy residues from the $^{208}Pb^{\star}$ de-excitation. The horizontal shift indicates the expected distance from the main beam position in black.

The trajectories of a ^{208}Pb (in red) and a ^{207}Pb ion (in green) produced after the compound nucleus de-excitation along the beam path are shown in figure 4.19. The two ion species are associated with scattered protons detected by the telescope. In the same figure the centre of the main ion beam is marked in black. The trajectories are calculated with the ion optics analytical code MAD-X [MAD02], where the ESR lattice was included. This code is very useful to get a fast calculation of the evolution of the ions trajectories as a function of their longitudinal position in the ring. As can be seen, the momentum reduction of the two residues results in a smaller bending radius and thus larger deflection in the dipole magnetic field with respect to the main ion beam trajectory. Because the rigidity of the ^{207}Pb ion is lower than that of the ^{208}Pb ion, ^{207}Pb is more deflected in the dipole field than the ^{208}Pb residue.
We would like to stress the importance of having a fully stripped beam. The loss of electrons in the target would lead to an increase of the charge, and thus a reduction of the magnetic rigidity. This leads to a huge background that could seriously damage our detector. Indeed, electron-loss is an atomic process with typically orders of magnitude higher cross section than the nuclear process. In the case of fully stripped ion beams, electron capture processes are possible and take place from the interaction with the gas-jet target. Also in this case, the atomic reaction cross section is higher than the nuclear process, but luckily heavy ions capturing an electron have a larger $B\rho$ than the beam and thus are moved to trajectories outside the main beam trajectory. Therefore, they will not hit our heavy-residue detector.

4.4.4.2 Heavy residue position

Depending on their momentum, the ion trajectories are deflected by the dipole magnets toward the inner or the outer side of the ring. Our detector, inserted from the inner side of the ring, allowed us to detect the heavy residues emitted at the target location outwards with respect to the ring, see figure 4.18.

When we consider a fixed proton emission polar angle (θ) and excitation energy $E^\star$ of the scattered beam-like residues, the heavy residues 2-d position distribution at the detection plane (x,y) is a ring. This can be seen in figure 4.20(a) where, the position of heavy residues produced after the gamma and neutron emission for $\theta = 55°$ and $E^\star = 8\ MeV$ is shown. The ring shape indicates that the azimuthal angle of the target and beam-like residues is randomly distributed from 0 to 2π. The thickness of the ring is related to the momentum spread of the scattered heavy ions.
Figure 4.20(b) shows the position of the heavy residues at the focal point. This point is characterized by a strong focussing of the ion trajectories on the horizontal direction, which translates into a much better separation of the heavy residues. However, the focal point is not accessible

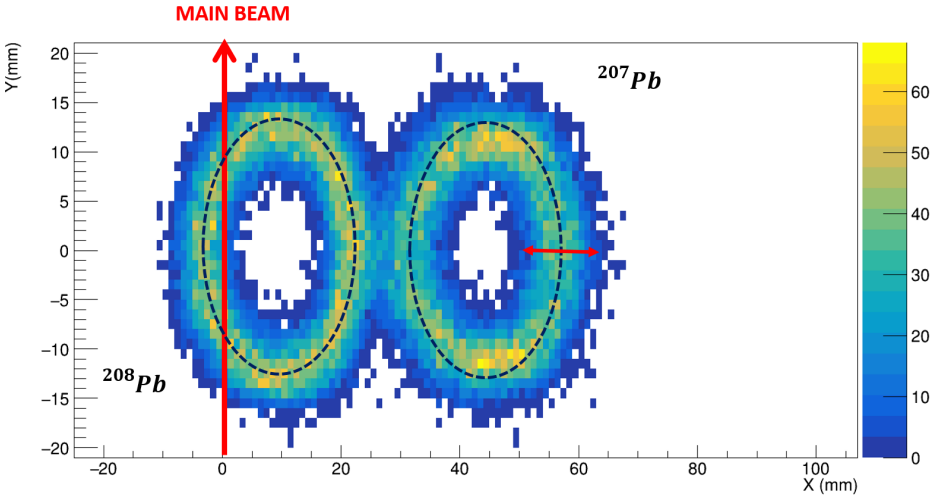

(a)

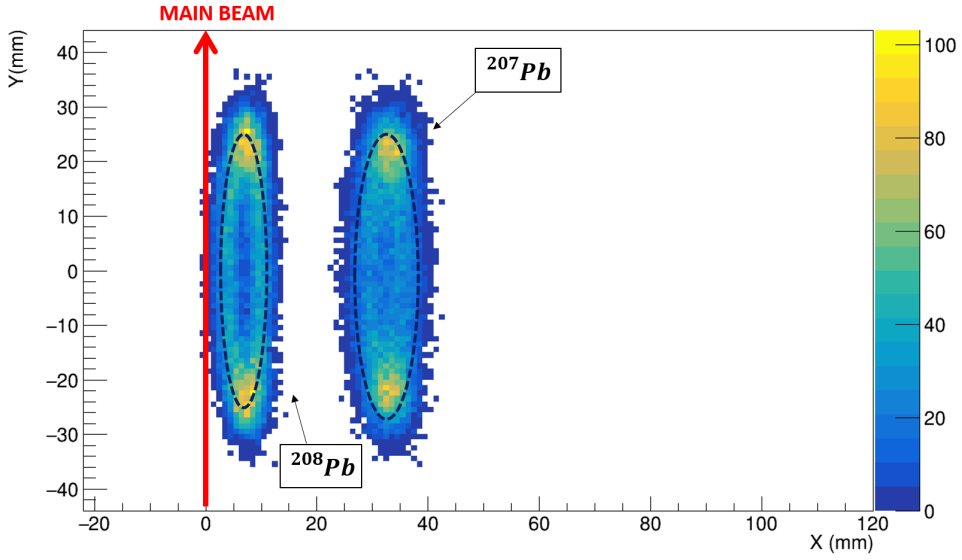

(b)

Figure 4.20: Simulated position of the heavy residues in the detection place (x,z) at different positions of the detector along the ring. The heavy ions are coming from a inelastic scattering reaction having target-like residues emitted at $\theta = 55°$ and an excitation energy of $E^{\star} = \ 8\ MeV$. In figure (a) the HR are detected at the detection station of the proof of principle experiment. In figure (b) the heavy ions are detected at the focal point. The arrows indicate the position of the beam.

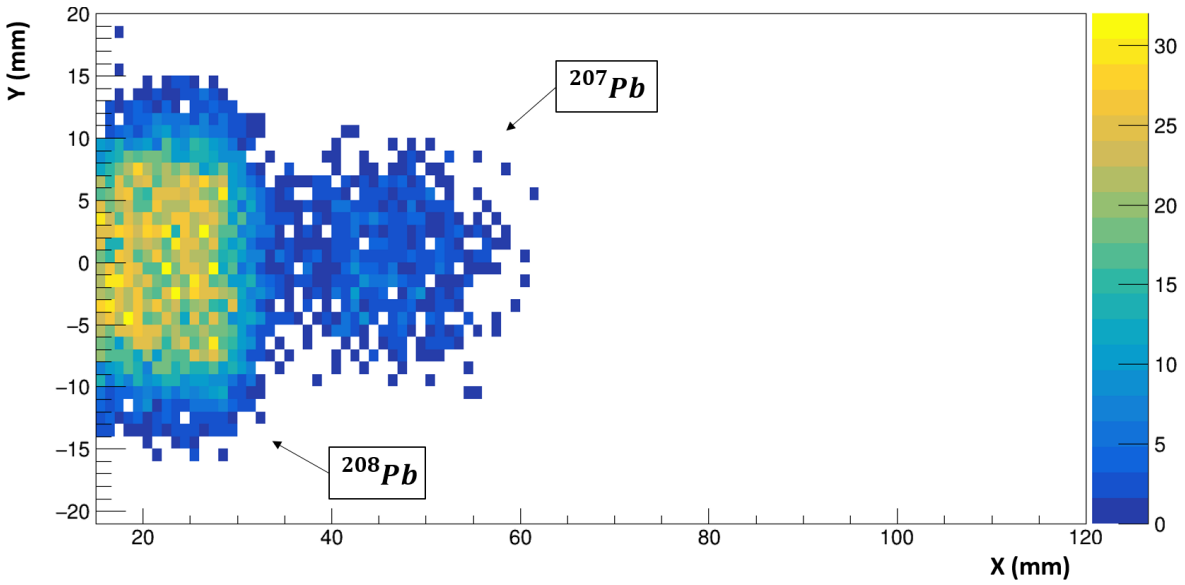

Figure 4.21: Simulated heavy residue position (x,y) in the DSSSD active area. Two different peaks or bumps can be seen, one related to ^{208}Pb and the other to $^{207}Pb^{82+}$ residues.

because it is located inside a quadrupole magnet (Q4 in figure 4.7). For a given target residue angle θ of the first kinematics solution, the position of the HR detected in coincidence will move towards the beam axis when the excitation energy increases, because its kinetic energy increases and it is less bent. The same effect will be observed when the scattering angle θ is increased.

When the coincidence between the telescope and the heavy residue is considered, only part of the ring defined by the heavy residues in the detection plane is observed, because only a small range of azimuthal angles for protons are selected. Note that a selection of the azimuthal angle of the scattered protons implies also a selection of the azimuthal angle of the heavy residues. A simulation of the position of the ions detected in coincidence with the telescope is shown in figure 4.21. As can be seen, there are two bumps one centred respect to the main beam around 20 mm corresponding to $^{208}Pb^{82+}$ ions and the other centred around 45 mm corresponding to $^{207}Pb^{82+}$ ions. The bump of the unreacted beam is not shown in this figure and would be centred at 0 mm. It is clear that a low segmentation of the HR detector translates in a worse separation of the residues which will make difficult the identification of the compound nucleus decay channel.

As we will see in the next section, the distance of the heavy residue detector to the beam axis is chosen such that the rate of elastic scattered ions is kept at a reasonable level of few hundred $counts/(cm^2 \cdot s)$ to limit the detector radiation damage. This implies that some of the residues produced after the gamma emission cannot be detected. The detector efficiency of the heavy residues, needed to determine the decay probabilities, will be determined with the help

of the simulations we have just described.

4.4.5 Elastic scattering

To evaluate the rate of elastic scattered beam residues impinging in the HR detector we used the Rutherford cross section, see equation (4.21):

$$\sigma_{Rutherford} \sim \frac{1}{E_k^2 \cdot sin^4(\theta_{CM}^{HR}/2)} \tag{4.26}$$

where the θ_{CM}^{HR} is the emission angle of the HR in the centre of mass. Since the cross section tends to infinity as $\theta_{CM}^{HR} \to 0$, in the simulation we considered an angular range $36° \leq \theta_{CM}^{HR} \leq 180°$. By multiplying the integral of the Rutherford cross section from 36° to 180° with an average luminosity of $10^{26}\ cm^{-2} \cdot s^{-1}$, the Rutherford events were propagated to the HR detector with the G4beamline simulation. Figure 4.22(a) shows the position of the elastic scattered events at the detector plane. The red square indicates the detector active area. The detector edge is placed at 1.5 cm from the beam axis. As can be seen in figure 4.22(b), the rate of elastic scattered events increases as we move towards the beam axis reaching a maximum rate of about 110 $events/(cm^2 \cdot s)$. This rate agrees with the limit given before for avoiding the radiation damage of the HR detector.

4.5 Experimental Set-up

4.5.1 Beam preparation and Ring pattern

The ratio of inelastic over elastic cross section increases with the beam energy. However, increasing the beam energy implies increasing the energy of the elastic scattered protons, and thus the thickness of the detectors needed to stop them. The beam energy of 30 MeV/u was the result of a compromise between the inelastic scattering cross section and the proton detector thickness.
The $^{208}Pb^{76+}$ ion bunches from the UNILAC were accelerated in the SIS18 synchrotron. In the SIS, the beam was accumulated with multiturn injection, where the horizontal phase space is filled with 4 fast ramped bump magnets until the horizontal acceptance of the SIS18 is reached. With electron cooling stacking several multiturn injections were performed, allowing for the accumulation of about 10^9 ions. After acceleration to about 275 MeV/u, the beam was extracted from the SIS18 and transmitted to the ESR. In the transmission line towards the ESR, a copper foil of 40 mg/cm^2 was used to further ionize the beam and produce $^{208}Pb^{82+}$ ions. The production yield of fully stripped ions ranges between 20% and 40%. At the injection in the ESR the number of ions was about 10^8 ions (one order of magnitude smaller). Considering the energy loss in the copper stripper foil, the beam was injected at the ESR with an energy

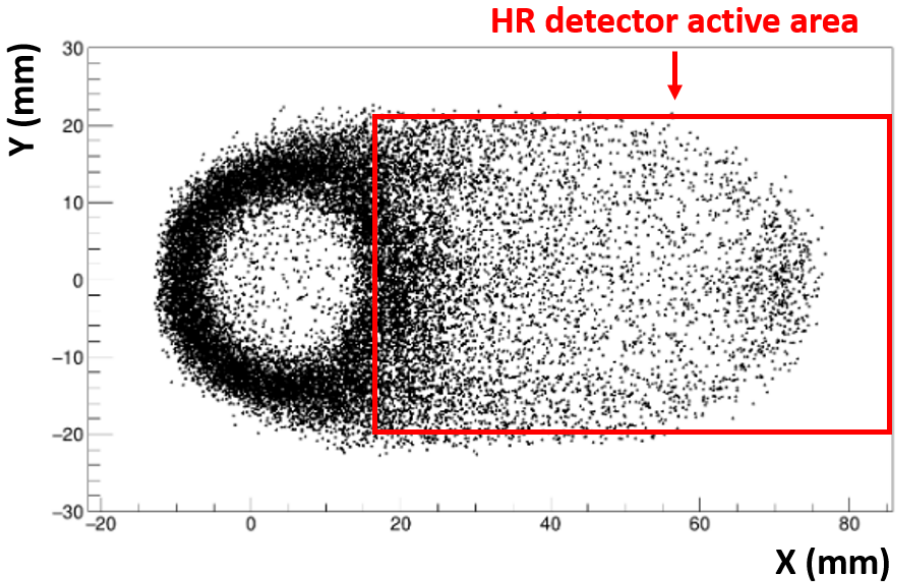

(a)

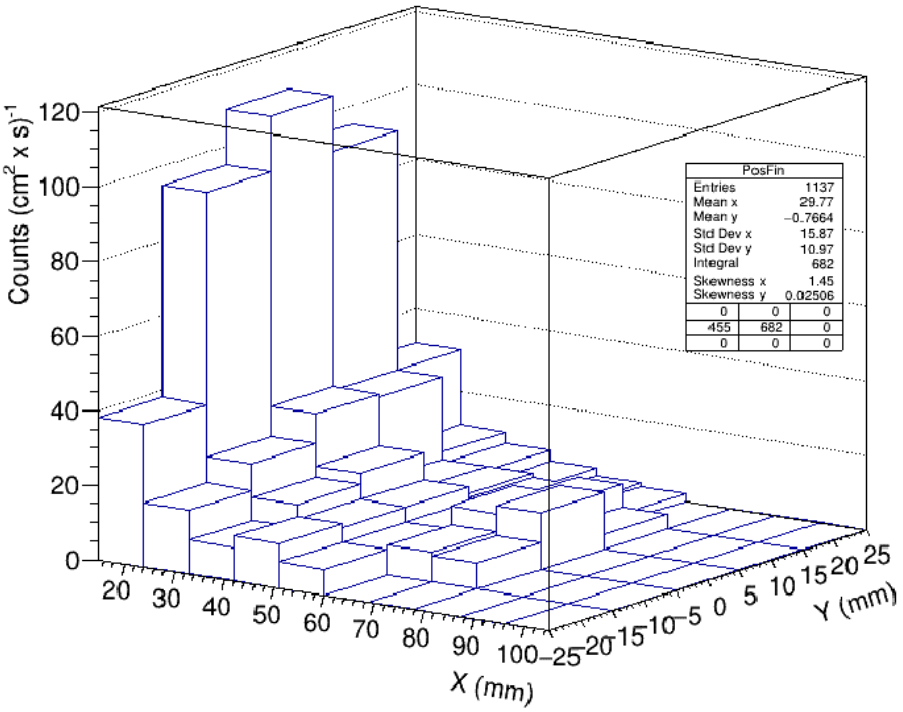

(b)

Figure 4.22: In figure (a) the position of the heavy residues at the detection plane associated to the Rutherford scattering is shown. The hole in the Rutherford events distribution is coming from the previously mentioned cut below 36°. The rectangle represents the HR detector active area. Figure (b) shows the rate of the Rutherford scattered ions in units of $cm^{-2} \cdot s^{-1}$ as a function of the position in the HR detector plane.

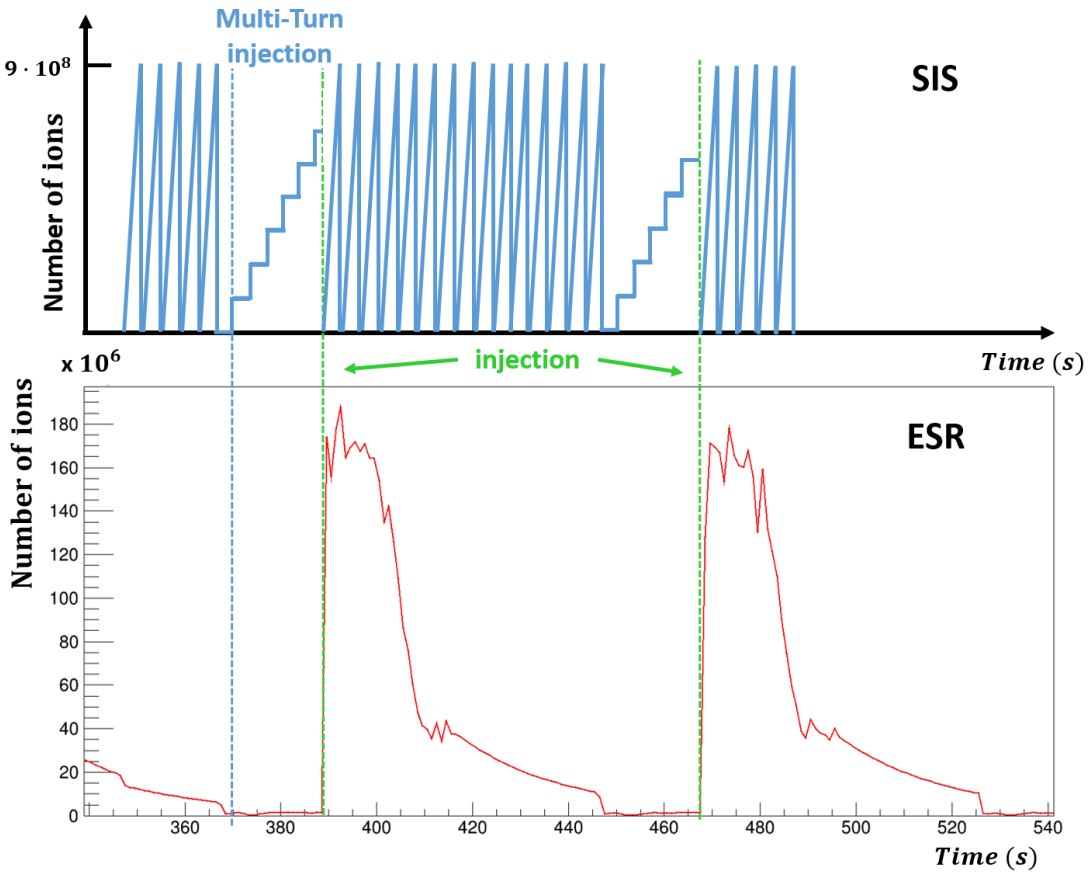

Figure 4.23: Representation of the number of ions as a function of time in the SIS (top figure) and at the ESR (bottom figure). The multiturn injection process at the SIS is indicated as well as the instant when the accumulated beam pulse from SIS is injected to the ESR.

of 271.4 MeV/u.
In figure 4.23, the number of ions as a function of time at the SIS18 (top) and at the ESR (bottom) is shown. The number of ions in the ESR decreased with time until when the beam was dumped away. A request signal was then sent to the SIS, which prepared the next ion pulse and sent it to the ESR while the ESR magnets were ramped up to the injection value.
The beam was injected in the ESR with single turn injection in an external orbit[4]. The strong increase of the number of ions to about 10^8 at the injection can be clearly seen in figure 4.24. After the injection the beam emittance was several $mm \cdot mrad$. Electron cooling was applied for about 13 s (dotted squared contour in figure 4.24) to reduce the ion beam temperature. Afterwards the beam was decelerated to 30 MeV/u. As shown in 4.24 the deceleration process took about 10 s. During the deceleration process ion losses occurred, reducing the stored ion number to about $5 \cdot 10^7$. The beam was then again electron cooled (second dotted contour) to reduce the beam emittance. At the final energy, a local closed orbit shift of the stored ion beam took place at the target location in order to set up the optimum overlap of the ions with the gas target. At this point we had about $5 \cdot 10^7$ ions with a final emittance of 0.37 $mm \cdot mrad$ (measured during the experiment, see chapter 5) and the beam was ready for the measurement. The total amount of time required for the beam preparation was around $T_s \approx 50\ s$. In figure 4.24 we can see that the measurement time was about $T_m \approx 30\ s$.
During the measurement time, the gas-jet target was switched on, while the heavy ions were revolving at a frequency of 0.695 MHz. The electron cooler was left operative to compensate the energy loss and the emittance increase of the stored ions, induced by the reactions in the hydrogen target. During the measurement time the number of ions decreased due to e^- capture reactions in the target, the electron cooler and the residual gas. The total cycle time, considering both the preparation and measurement time was finally about 80 s.

The procedure described above is called ring pattern and is repeated during the whole experiment every time a new ion pulse is injected in the ESR. In the following, a schematic list summarizing the main steps of the beam preparation and measurement phases is given:

- Beam preparation
  - injection
  - e-cooling
  - ramp down $\rightarrow$ 30 MeV/u (deceleration)
  - e-cooling and local closed orbit shift at the target location
- Measurement
  - detector in

[4]This is done to optimise the beam injection process. The magnetic field used in the injection (kicker) must rise/fall in a very short time. Injection at external orbits requires a smaller field making more simple the injection process [Bar11].

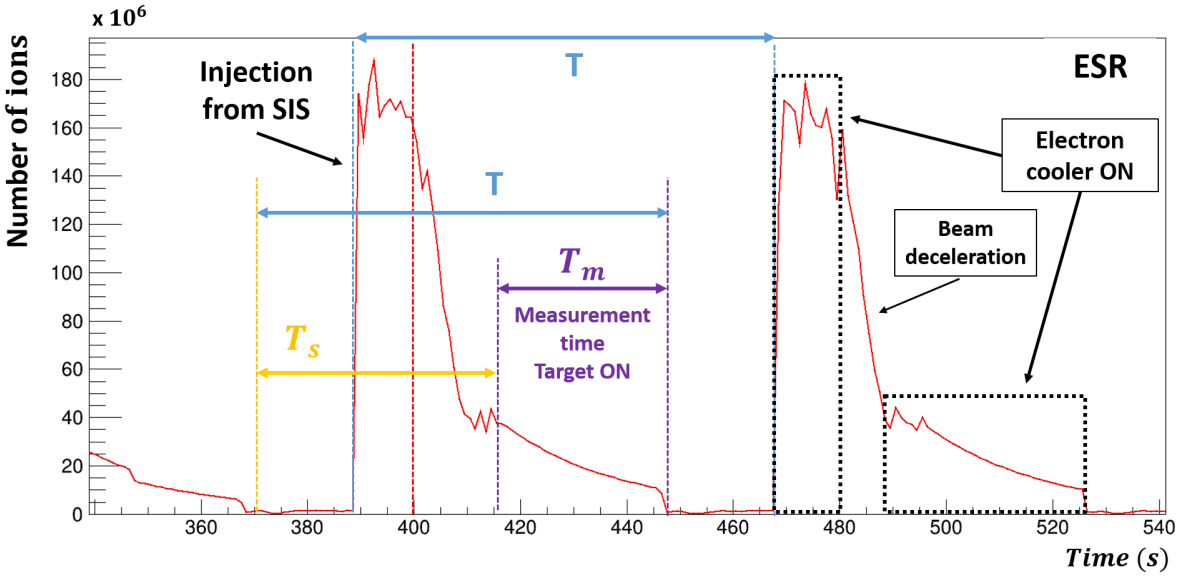

Figure 4.24: Measured number of ions in the ESR as a function of time. The different steps of the ring pattern are indicated as well as the preparation time T_s, the measurement time T_m and the total cycle time T.

  - target ON
  - target OFF
  - detector out

- beam dumped away during ramp up

The measurement time T_m was chosen in order to maximize the average luminosity, which is defined as:

$$< L >= N_0 \cdot f_0 \cdot n_{t,eff} \cdot \frac{\int_{T_s}^{T} e^{-(t-T_s)/\tau} dt}{T} \tag{4.27}$$

here the luminosity at beginning of the measurement at $t = t_s$ is given by $L_0 = N_0 \cdot f_0 \cdot n_{t,eff}$, where N_0 is the number of decelerated and cooled ions at $t = t_s$ (about $5 \cdot 10^7$), f_0 is the revolution frequency (0.69 MHz for ^{208}Pb at 30 MeV/u in the ESR) and $n_{t,eff}$ is the effective target areal density, which depends on the overlap between the ion beam and the target. The lifetime τ of the stored ions was determined by fitting the variation of the ion number as a function of the time when the target was on, obtaining a value of 21.2 s (see section 5.1.2). The effective target thickness $n_{t,eff}$ was measured to be around $3.14 \cdot 10^{13}$ $atoms/cm^2$. By calculating the luminosity $< L >$ at different cycle times T, we can see in figure 4.25 that the maximum $< L >$ of $2.1 \cdot 10^{26}$ $(cm^{-2} \cdot s^{-1})$ was obtained for $T \simeq 80$ s. Since the preparation time was about 50 s, this leads to a measurement time of 30 s.

During the preparation phase, large fluctuations of the horizontal beam position can occur. Therefore, during this phase the detectors should be at a sufficient distance from the beam

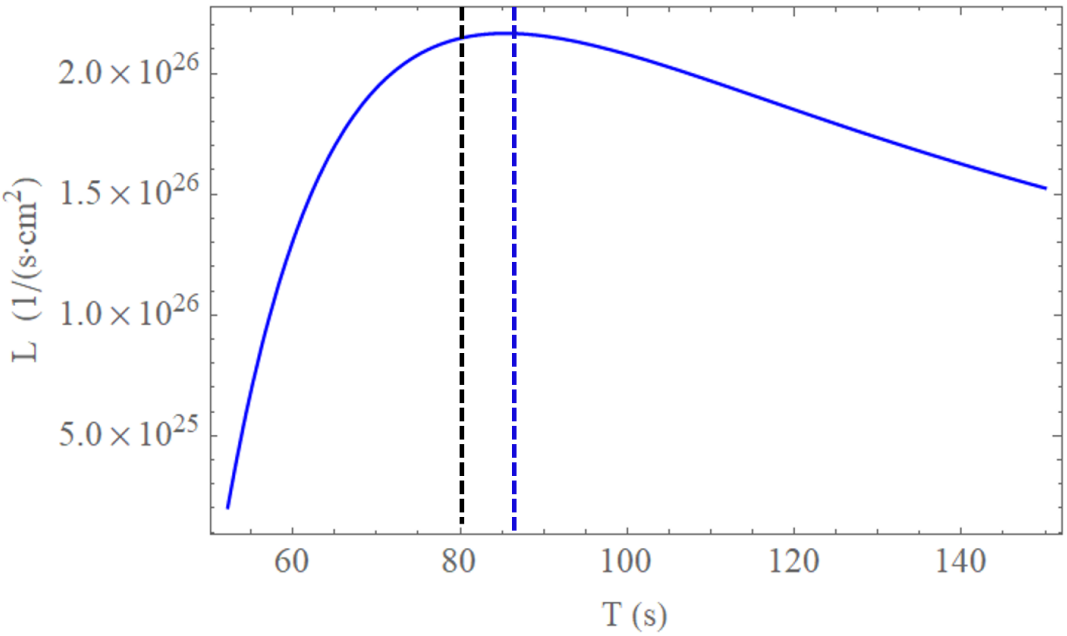

Figure 4.25: Calculated average luminosity as function of the total cycle time.

Table 4.2: Beam parameters during the experiment.

Beam	Energy	Number of ions	Emittance	Storage lifetime	Average luminosity
$^{208}Pb^{82+}$	30.77 MeV/u	$5 \cdot 10^7$	0.37 $mm \cdot mrad$	21.2 s	$2 \cdot 10^{26}$ $(s^{-1} \cdot cm^{-2})$

axis. For this reason the heavy residue detector was mounted on a movable pocket and was moved in and out of the ring when the gas-jet target was switched on and off.

4.5.2 The target residue (TR) detectors

4.5.2.1 Target chamber and pocket

The particle telescope was installed at the existing target reaction chamber, see figure 4.26(a), where an average vacuum of 10^{-10}-10^{-11} $mbar$ was established. The gas-jet was injected perpendicular to the ion beam coming from the left. Several fittings surrounding the target, at different angles with respect to the beam axis (from 35° up to backward angles), were available to insert the required set-up for the target-like residue detection. As already said, to prevent the detector components from degrading the UHV of the ring, the employed detectors were housed in pockets. As described in section 4.4, the telescope position and angle were defined considering both mechanical and physical constrains.

In the present experiment, the Si telescope for target residue detection was mounted in a circular stainless-steel pocket inserted into the target reaction chamber at 60° with respect to the beam axis, see figure 4.26(b). The pocket was operated in air. The inner diameter of the pocket was 50 mm, while the tube thickness was of 1.5 mm. As can be seen in figure 4.26(c), the bottom side edge of the pocket closest to the beam axis had a 25 μm stainless steel window with a diameter of 35 mm. This window provided a barrier between the ultra-high vacuum (UHV) of the target chamber and the air inside the pocket, while its small thickness allowed the passage of the scattered protons, from the elastic and inelastic reactions, down to an energy of 2.4 MeV. The total length of the pocket was 296 mm, ensuring a distance from the beam axis of 70 mm. This value was chosen to prevent the detector from being hit by the beam during the preparation phase, after the injection at the ESR. The target residue pocket was manufactured at the Max Planck Institute for Nuclear Physics in Heidelberg.

4.5.2.2 The detectors

The proton detector was a telescope composed by a thin position sensitive ΔE detector and an E detector for residual energy measurement made of a stack of thick silicon E detectors. The ΔE detector was a double-sided Si strip detector (DSSSD) manufactured by Micron Semiconductor Ltd [Micro21], model BB8. The ΔE detector had a thickness of 529 μm, 16 front strips (fig. 4.27(a)) and 16 back strips (fig. 4.27(b)) at a pitch of 1250 μm, over an active area of 20x20 mm^2. The DSSSD detector was followed by six single-sided, single area detectors (model MSX04 from Micron Ltd) having the same active surface without segmentation and a thickness of 1509 μm each. In figure 4.28(a) the technical drawing of a MSX04 detector package is presented. To reduce the size of the package, the MSX04 detectors were assembled in pairs with the package shown in figure 4.28(b). The signals extracted from the detectors

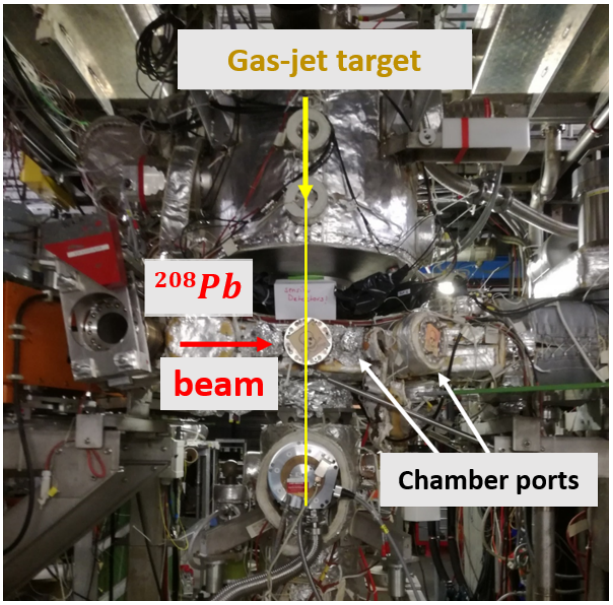

(a) Picture of the target interaction chamber at the ESR

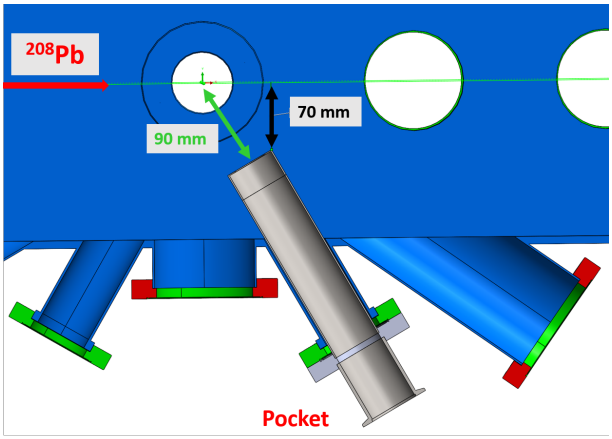

(b) Top-view schematic diagram of the ESR target reaction chamber showing the telescope pocket

(c) Detail of the telescope pocket

Figure 4.26: Picture of the target interaction chamber (a) and drawing showing a top-view of the target chamber with the pocket housing the experimental particle telescope (b). In figure (c), the pocket housing the telescope and the pocket window are shown.

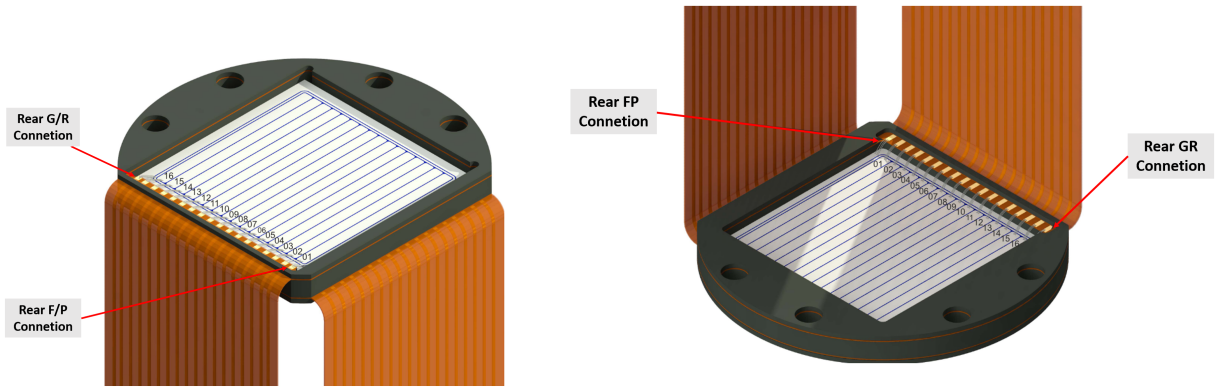

(a) BB8 - Front-side strip

(b) BB8 - Back-side strips

Figure 4.27: Technical drawing of BB8-DSSSD detector used during the experiment. The detectors with a thickness of 529 μm, consisted of 16 front and 16 back strips. The strip signal transmission outside the pocket was ensured by flexi rigid PCBs.

were transported by single flexi rigid PCBs of 220 mm long.

The detectors were mounted inside the detector pocket by means of the mechanical support illustrated in figure 4.29(a). The BB8 and the stack of MSX04 detectors were housed in a dedicated holder fixed by rods to the support for electronic connections at the back of the pocket. The single flexi rigid PCBs carrying the signals from the detectors were connected to a rigid PCB allowing to interface the front end electronics at the pocket flange (green in the picture). Following the provider specifications, the detectors were biased from the N-side with a positive high voltage of around 54 V for the BB8, while 165 V were applied to the 1.5-mm-thick MSX04 detectors. In figure 4.29(b), a side view of the detectors mounted on the mechanical support with the electrical polarities is represented. As can be seen, the voltage was applied from the N-side while the P-side was kept at ground. In this way we ensured that the surfaces of the MSX04 detectors with the same polarities would be facing each other. In table 4.3, the general information about the detector dimensions and the bias-voltage specified by the manufacturer are reported. After the insertion in the pocket, the BB8 was situated at $\sim$3.8 mm from the pocket stainless-steel window, while the first MSX04 detector was positioned about 2.5 mm behind the BB8. Each one of the three custom-made assemblies was characterized by two MSX04 detectors separated by 0.4 mm. The MSX04 detectors belonging to different assemblies were spaced by 1.6 mm.

Both the BB8 and the MSX04 detectors were tested by means of a standard 3α source. This allowed us to determine the detector resolution and, in the case of DSSSD, the absence of damaged strips. The detectors were tested under primary vacuum conditions (about 10^{-3} $mbar$) by mounting the source with and without a collimator in front of the active detector area. A first test was performed on the BB8 without collimator in order to irradiate the full detector surface and check the normal functioning of the strips. In figure 4.30, the position of the α-particles

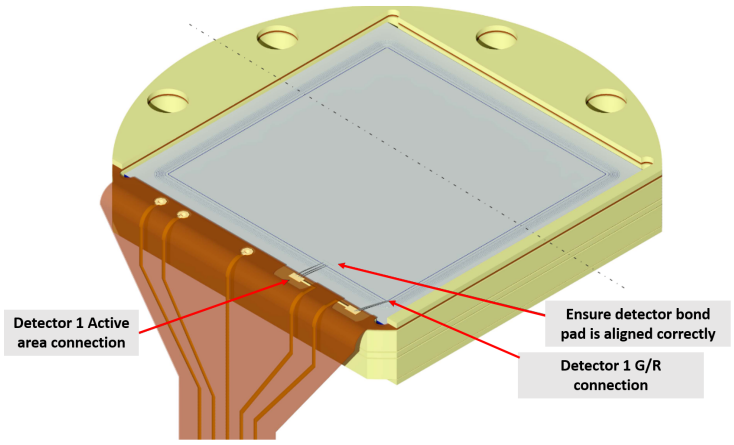

(a) MSX04 - Front view

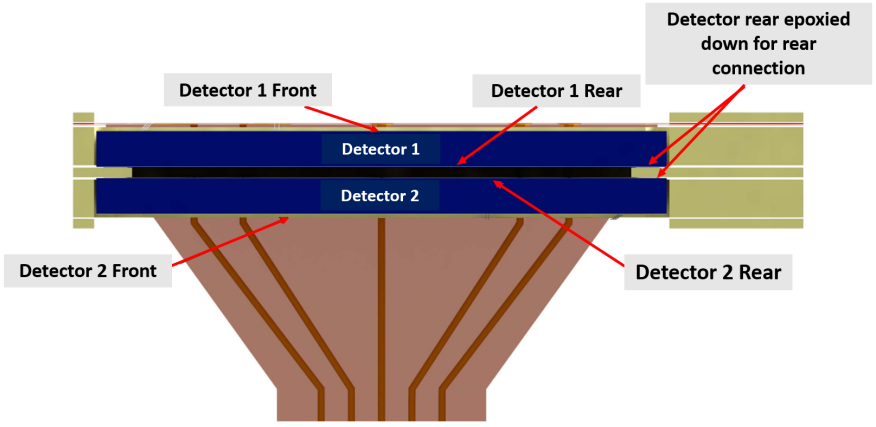

(b) MSX04 packaging profile

Figure 4.28: (a) Technical drawing of a MSX04 detector used during the experiment. (b) Two MSX04 detectors were assembled together and a flexi rigid PCB ensured the signal transmission.

Table 4.3: Summary of the main characteristics of the target-residue telescope detectors.

Type	Name	N°	Thickness	Size	Channels	Voltage (V)
ΔE	BB8	1	529 μm	20×20 mm^2	16×16	+54
E	MSX04	6	1509 μm	20×20 mm^2	1	+165

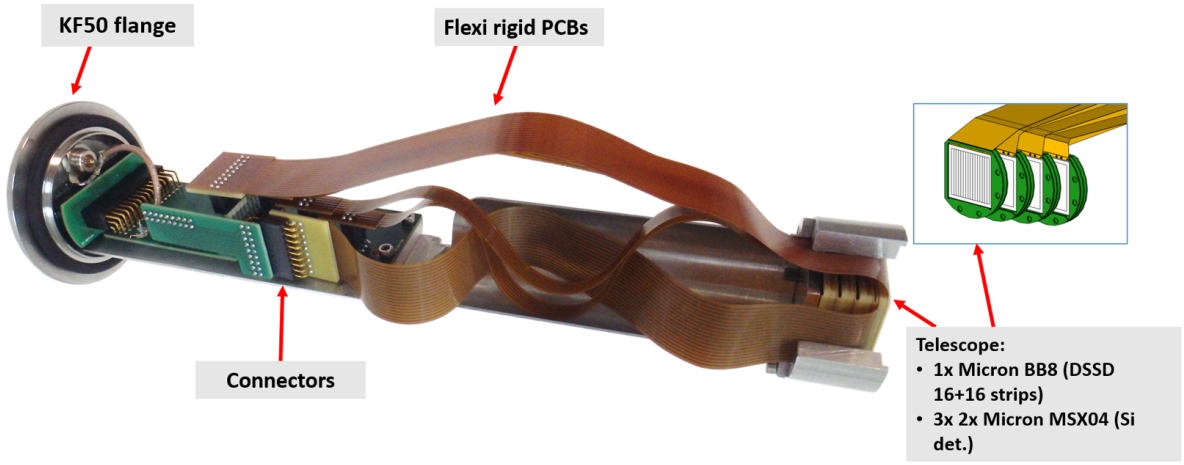

(a)

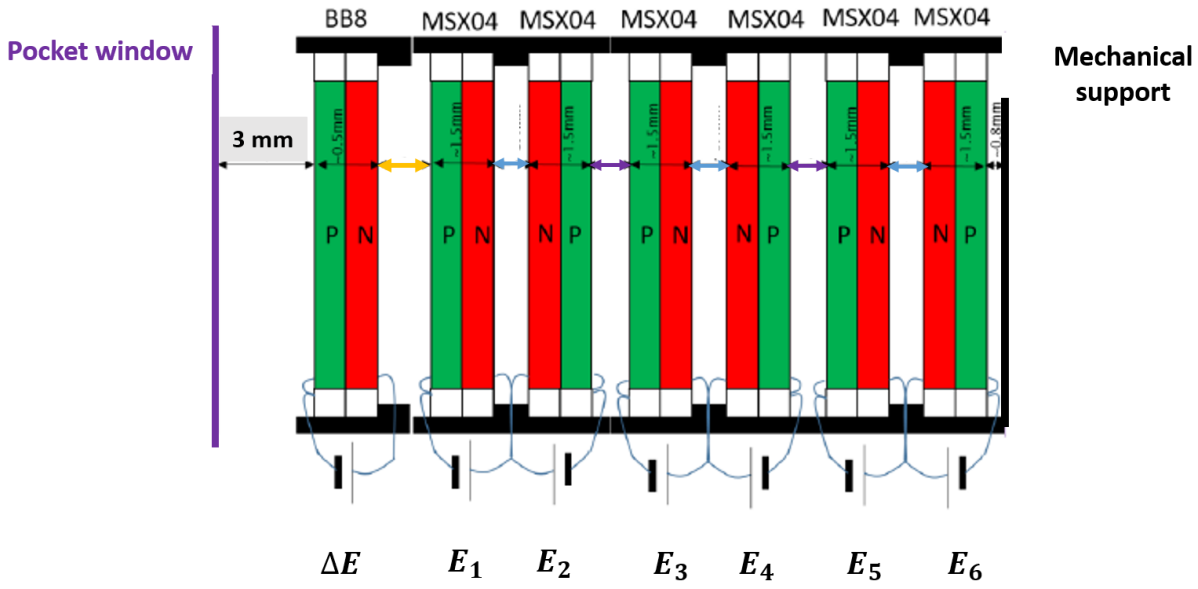

(b)

Figure 4.29: (a) A picture of the telescope detector with its mechanical support inside the pocket is shown. (b) Side-view diagram of the telescope detectors, indicating the electrical polarities and contacts for the BB8 and MSX04 detectors.

impinging on the BB8 is plotted as a function of the hit vertical and horizontal strip number. As can be seen, the shape of the source is well visible in this 2d scatter-plot, which allowed us to verify the normal response of the different strips. An example of the signal amplitude obtained

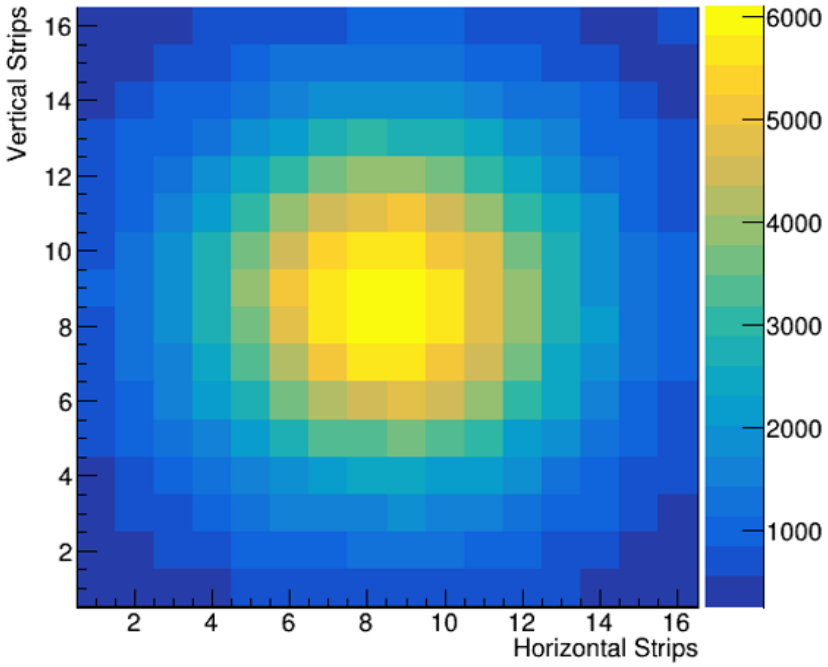

Figure 4.30: Number of detected alpha particles as a function of the strip number.

with the 3α source is shown in figure 4.31, for a vertical strip of the DSSSD (left panel) and for a MSX04 (right panel). The information about the α particle energies and FWHMs measured with each detector is reported in figure 4.32. The MSX04 energy resolution was measured by applying a collimator in front of the α-source. The RMS resolution for an α particle of 5.48 MeV of the ΔE detector was $\sigma_{\Delta E} \simeq 24\ keV$ and for the E detector $\sigma_E \simeq 68\ keV$. The use of a packaging containing two MSX04 detectors was very useful to produce a compact telescope. However, as discussed in appendix C, this prevented us from the possibility to inspect the detector response when irradiating the MSX04 in the back side.

4.5.3 The heavy residue (HR) detector

The beam-like residue or heavy residue (HR) detector station was located downstream from the first dipole placed downstream from the target reaction chamber. This station, shown in figure 4.33(a), includes a movable drive system, which allowed us to move in and out of the ring the pocket housing the HR detector. This pocket, shown in figure 4.33(b), belongs to GSI and is made of stainless steel 316L with a rectangular inner tube section of $57\times37\ mm^2$, length of 528.5 mm, and a thickness of 1.5 mm.
The fast movement at a speed of few tens of centimeters per second was ensured by a pneumatic system, while a bellow mounted between the pocket and the ring allowed for the preservation

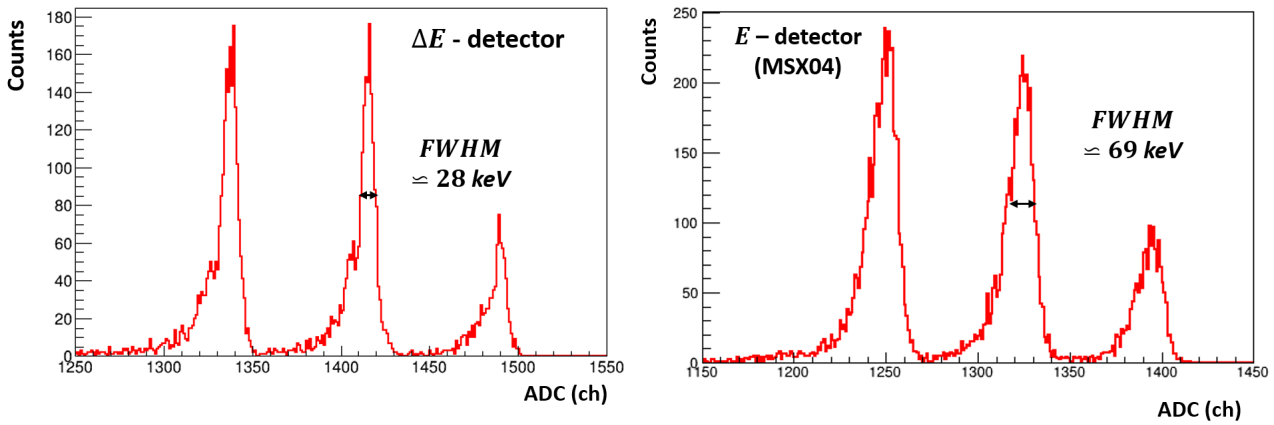

Figure 4.31: Pulse height distribution obtained for the ΔE DSSSD (on the left) and one MSX04 (on the right) detector when irradiated with a standard 3α source.

	Energy of α particle	Measured energy resolution						
Source isotopes	Average $E_\alpha(MeV)$	$FWHM_{\Delta E}$ (keV)	$FWHM_{E_1}$ (keV)	$FWHM_{E_2}$ (keV)	$FWHM_{E_3}$ (keV)	$FWHM_{E_4}$ (keV)	$FWHM_5$ (keV)	$FWHM_{E_6}$ (keV)
^{239}Pu	5.149	37 (0.7%)	76 (1.5%)	80 (1.6%)	69 (1.3%)	76 (1.5%)	69 (1.3%)	74 (1.4%)
^{241}Am	5.480	28 (0.5%)	85 (1.6%)	67 (1.2%)	69 (1.3%)	67 (1.2%)	69 (1.3%)	70 (1.3%)
^{244}Cm	5.795	25 (0.4%)	55 (1.0%)	67 (1.2%)	69 (1.2%)	76 (1.3%)	74 (1.3%)	83 (1.4%)

Figure 4.32: Energy resolution of the ΔE and E detectors obtained with a standard 3α source, see text for details.

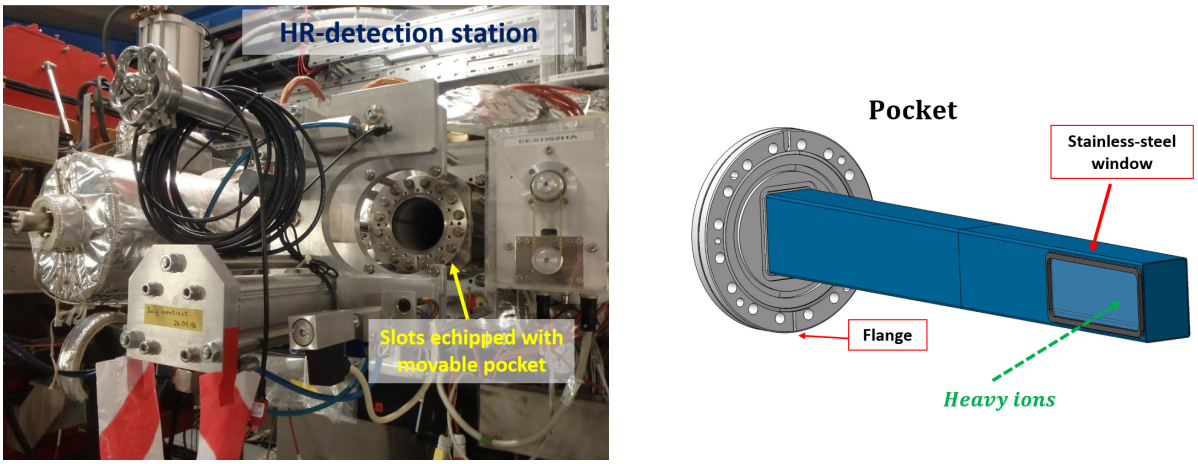

(a) (b)

Figure 4.33: In figure (a), the station downstream from the dipole for the detection of heavy residues is shown. It consisted of a pneumatic system, which allowed to insert and remove with high speed the pocket housing the position sensitive detector. Figure (b) shows a drawing of the front-end part of the heavy-residue detector pocket, including the window.

of the UHV conditions outside the pocket during the displacement. The detector drive made possible to position the pocket within 1 s with an accuracy of about 0.1 mm [Ste03].

The passage of the incident heavy residues through the pocket wall was ensured by a stainless steel window of 25 μm thickness and an area of 122×44 mm^2, see figure 4.33(b). The ions impinging on it had enough energy to penetrate the window and reach the position sensitive detector.

The detector, implemented for the heavy residues, was a double sided silicon strip detector (DSSSD) from Micron Semiconductor Ltd Model BB29 (see left side of figure 4.34). Its characteristics are summarized in Table 4.4. The detector, size and active area were specifically designed for the integration into the pocket. The detector had an active surface of 122×40 mm^2 divided in 122 vertical and 40 horizontal strips. The range of the heavy residues in silicon was about 358 μm, for this reason a detector thickness of 500 μm was sufficient to completely stop the lead ions. The bias voltage applied to the BB29 detector was about 100 V. As for the telescope detectors, the signal were extracted from the detector and brought outside the pocket by flexi rigid single PCBs connected to a feedthrough interface. On the right side of figure 4.34, a picture of the assembly used during the test with α-source of the heavy residue detection system including the pocket and the front-end electronic is shown. The final assembly included additional flexi PCBs extensions.

A discussed in section (4.4.3), a large number of strips was required to accurately separate the ^{208}Pb and ^{207}Pb ions impinging on the detector and correctly identify the decay channel of the coincidence events.

During the preparation of the experiment, the BB29 detector strips were tested using a single

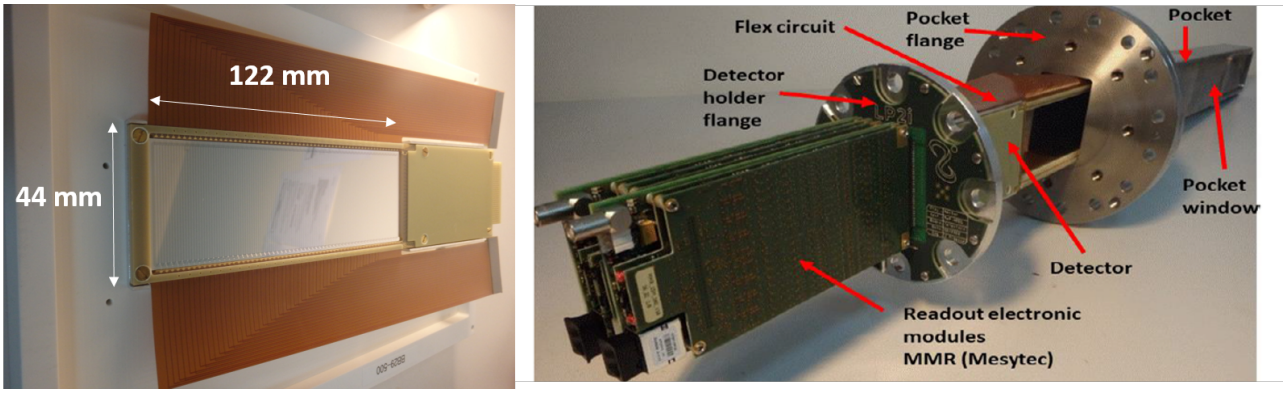

Figure 4.34: On the left side a picture of the DSSSD BB29 used for the HR detection and inserted in the GSI movable pocket is shown. On the right a picture of the final HR detection assembly with the specification of the different elements is presented.

Table 4.4: Summary of the main characteristics of the heavy residue detectors.

Particles	Detector type	Thickness	Active Area	N° of strips
Beam-like residues	DSSSD (BB29)	500±50 μm	122×40 mm^2	vertical: 122 horizontal: 40

α-source (^{241}Am). The source was mounted on a movable support and fixed by rods to the pocket flange, see figure 4.35(a). This allowed us to irradiate different regions of the detector active surface. The response of the different strips was checked by plotting the position, in terms of vertical and horizontal strips, of the observed events, see the scatter plot in figure 4.35(b).

4.6 Electronics and data acquisition system

4.6.1 Readout electronics architecture

The readout electronics was based on MMR (Mesytec Multiplexed Readout) modules commercially available from Mesytec, see figure 4.36(a). The MMR modules consist of a stack of several front-end boards, which performs time multiplexing, analogue to digital conversion, data storage and triggered data transmission via optical link to a central data collector module, the VMMR-8, also produced by Mesytec. The VMMR provides a local clock, which is synchronised by the VME master to a central time with a precision of about 30 ps rms [Mesy21]. As can be seen in figure 4.36(b), the VMMR-8 was equipped with 8 optical buses. It synchronized the front-end clocks and the triggers request, and accepted external gates from the back-end.

In figure 4.37, the readout system used for the target-like, the heavy residue and the Ge detectors is schematically shown. The 122 vertical and the 40 horizontal strips of the BB29 HR detector were read respectively by a MMR128 and a MMR64. These stacked boards were

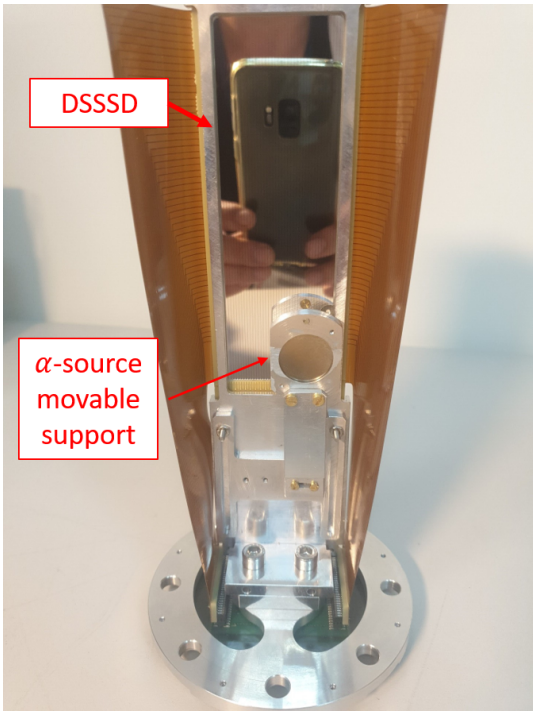

(a)

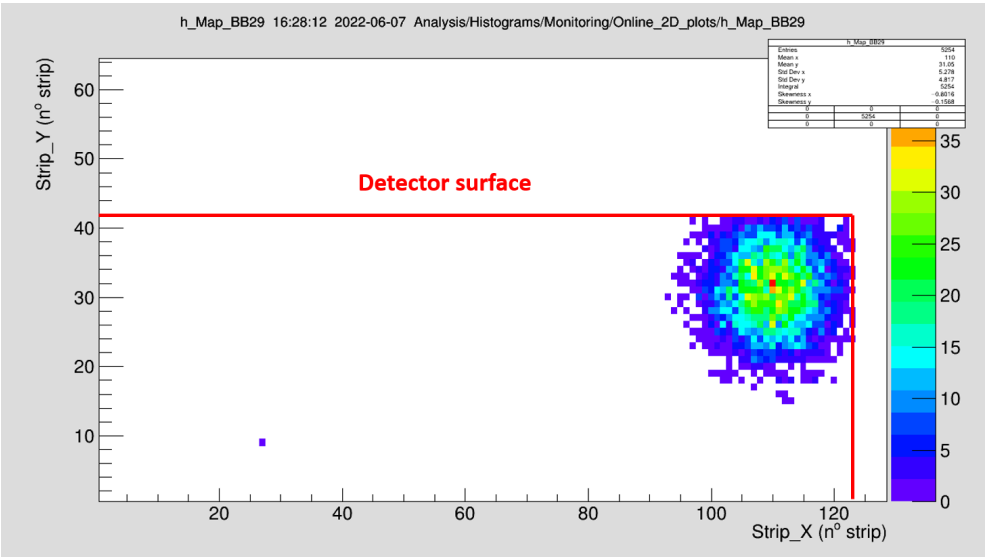

(b)

Figure 4.35: (a) Set-up used to test the BB29 detector. (b) Number of detected particles as a function of the vertical and horizontal strip number.

plugged on connectors fixed on the pocket flange. Each board was able to read respectively up to 128 and 64 channels. The signals from each MMR were sent by optical fibers to two different optical buses of a VMMR-8. For the target residue (TR) telescope, the readout was performed by a single MMR64 of mixed polarities. In this case, half of the channels, designed for input signals of mixed polarities, were used to read the vertical and horizontal strips of the

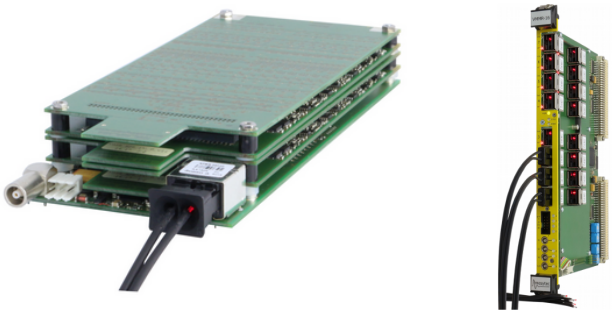

(a) MMR (b) VMMR

Figure 4.36: Figure (a), a MMR (Mesytec Multiplexed Readout) board is shown. Figure (b), picture of a VMMR, the VME-receiver module. The VMMR-8 has 8 or 16 optical buses available for MMR connection.

ΔE detector (BB8). The six thick detectors were read out by six of the remaining channels of the same MMR64. The latter MMR64 was coupled to another VMMR-8. The required bias voltage for the detectors and the MMR modules low voltage supply was ensured by two CAEN DT1419ET and two GSI F178 modules, respectively. The MMRs provided multiplexed signals with the maximum amplitude measured by each strip. They were sent to the VMMRs via optical fibers of 10 and 35 m, see figure 4.37.
Each VMMR could provide an output logic signal t_0, the trigger request. For the HR VMMR the thresholds were set in a way that only the 122 vertical strips would participate to the OR that generates t_0. For the TR VMMR, the t_0 was generated by an OR of the 16 vertical strips. The trigger request were sent to the VULOM (VME Universal logic Module) produced by GSI. The signals from the two Germanium detectors were sent to a spectroscopy amplifier (ORTEC 671) and to a timing filter amplifier (ORTEC 474). The outputs of the spectroscopy amplifier were sent to a peak sensing ADC (Analog to Digital Converter), model V785 by CAEN. The outputs of the timing filter amplifier were sent to a constant fraction discriminator (ORTEC CF8000) whose outputs generated the start signals of the time to digital converter (TDC V775 by Caen), the inputs of a scaler and were also sent to the VULOM.

4.6.2 Trigger logic

The VULOM generated coincidences and anti-coincidences with a gate that was open while the target was on. In this way we could have six triggers:

1. At least one vertical strip of BB8 hit & target on
2. At least one vertical strip of BB8 hit & target off
3. At least one vertical strip of the BB29 hit & target on
4. At least one vertical strip of the BB29 hit & target off

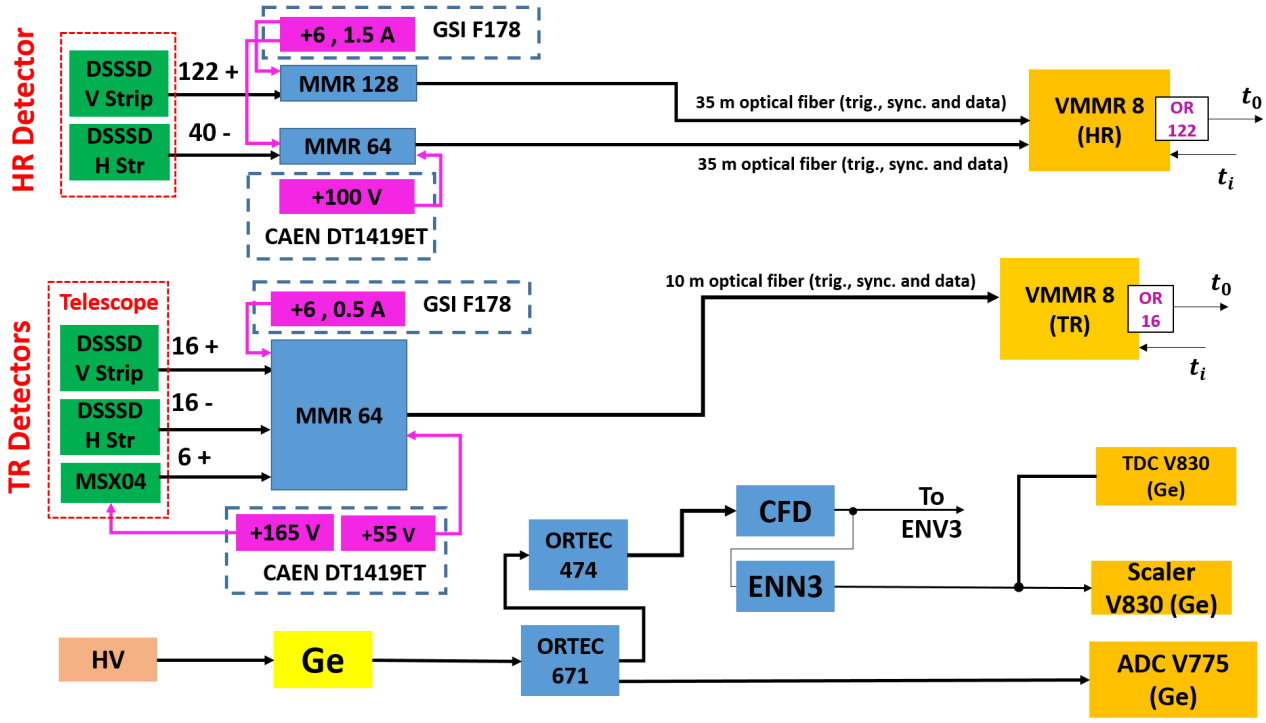

Figure 4.37: Illustration of the electronics readout system used for the target-like, heavy residue and Ge detectors. See text for details.

5. At least one Germanium (Ge) detector hit & target on

6. At least one Germanium (Ge) detector hit & target off

An OR of these triggers was sent to the GSI TRIVA module unless if arrived while the DAQ system was busy, the TRIVA module sent a signal that blocked the VULOM. Otherwise, the VULOM generated an accepted trigger that was sent to the t_i input of the VMMRs, to the gate of the *Ge* ADC and scaler and to the stop of the *Ge* TDC. Figure 4.38 shows a time diagram for the functioning of the MMRs and VMMRs. A signal in the MMR above the threshold generates the trigger request t_0 after 750 ns. If this trigger request is accepted by the VULOM and TRIVA modules, it generates an accepted trigger t_i. The accepted trigger generates an adjustable, configurable window of interest in both VMMRs. The VMMR measures the time difference between the start of the window of interest and t_0, this is the ΔT. In figure 4.38 we see the ΔT for the telescope and the HR detector. The ΔT will allow us to identify the coincidences telescope-HR.

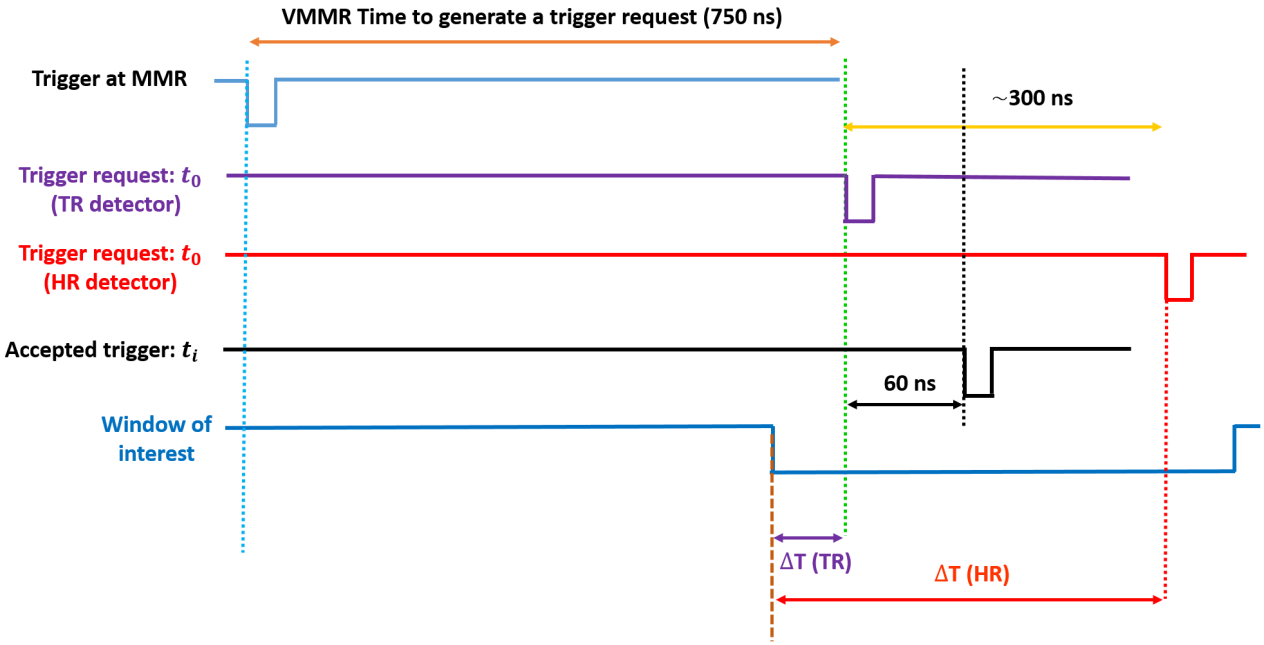

Figure 4.38: An example of time diagram showing for the telescope VMMR, the VMMR encoding time of 750 ns for t_0 and 750 ns + 60 ns for t_i, the t_o and t_i signals and the window of interest position. For the event shown in this figure, the TR detector generates a trigger request that is accepted and opens the window of interest. Two time differences ΔT can be measured, between the window start and the t_o of the TR detector and between the window start and the t_o of the HR detector. For a coincidence event between the telescope and the HR, the time difference between t_o (TR) and t_o (HR) is 300 ns, which corresponds to the time of flight of the HR from the target to the HR detector.

Chapter 5

Data Analysis

In this chapter we will show how the data obtained during the proof of principle experiment have been analysed to fulfil the three main objectives: (a) validation of the developed simulations and measurement of the heavy ion transmission efficiency between the target and the heavy residue detector, (b) extraction of the gamma and neutron decay probabilities as a function of the excitation energy, (c) evaluation of the excitation energy resolution achievable in inverse kinematics experiments at storage rings.

5.1 Beam and target properties

In this section we will describe how we determined some important beam properties. These quantities are the beam energy, the storage lifetime, and beam emittance.

5.1.1 Beam energy

The energy of the decelerated $^{208}Pb^{82+}$ ions was determined by measuring the cathode potential ϕ_{cath} of the electron cooler. The latter potential is linked to the kinetic energy of the electrons E_{e^-} by the expression:

$$E_{e^-} = \phi_{cath} \cdot e = (\gamma_e - 1) \cdot m_e \cdot c^2 \tag{5.1}$$

where e is the electron charge, γ_e is the electron Lorentz factor and m_e the electron mass. After the electron cooling process, the beam ions have exactly the electron velocity and thus the same Lorentz factor $\gamma_{ions} = \gamma_e$. Considering this and using the equation (5.1) for the electrons and the ions, we obtain the expression:

$$\frac{E_{ion}}{m_{ion} \cdot c^2} = \frac{e \cdot \phi_{cath}}{m_e c^2} \quad \rightarrow \quad E_{ion} = \frac{m_{ion}}{m_e} \cdot e \cdot \phi_{cath} \tag{5.2}$$

During the experiment the cathode potential was 16887 V. Since we were using a beam of $^{208}Pb^{82+}$ ions having a mass of 207.932 u, we obtained that the beam kinetic energy was 30.77 MeV/u, which implies $\beta = \frac{v}{c} \approx 0.25$.

5.1.2 Beam lifetime

As we can see in section 4.5.1, the lifetime of the stored $^{208}Pb^{82+}$ beam at 30.77 MeV/u is an important quantity because it is directly related to the average luminosity.
The main processes which limit the beam lifetime are the interaction with the residual gas, with the internal gas-jet target and with the electrons inside the electron cooler. For unstable short-lived nuclei the lifetime related to the radioactive decay must also be considered.
The interaction proceeds through atomic e^- capture reactions, whose cross sections depend on the charge state and the energy of the stored ions [She18]. The capture cross section is $\sigma \propto Q^{3.9}/(E/A)^{4.8}$ [Sch83], so highly charged ions at low energies have a high probability to capture an electron in the interaction with matter. After changing the charge, the ion will be lost due to its change in magnetic rigidity.
The total beam lifetime is obtained by considering the contribution coming from all these processes:

$$\frac{1}{\tau} = \frac{1}{\tau_t} + \frac{1}{\tau_v} + \frac{1}{\tau_{ECOOL}} \tag{5.3}$$

where τ_t is the lifetime due to the gas-jet target, τ_v the lifetime due to the residual gas in the ring and τ_{ECOOL} the lifetime due to radiative electron capture of free electrons during the passage through the e^--cooler [Bey89, Eis07]. The recombination with the electrons of the electron beam is proportional to the electron density, thus a stronger cooling results in faster particle losses.
To quantify the impact of the target, the beam lifetime was measured at two different positions of the beam with respect to the target. In position $I°$ the beam was crossing the target center (target on), while in position $II°$ (target off) the beam was shifted outside the target, see figure 5.1. This beam shift was done by modifying the magnetic field of the local bump place before the reaction chamber. The lifetimes at the two positions were obtained by measuring the number of ions as a function of time. The results where then fitted with the functions $\propto e^{-t/\tau}$, with τ being the lifetime, see figure 5.2. A lifetime of τ_{off}=122.8 s was obtained for position $II°$ (target off) and a lifetime of τ_{on}=21.2 s for position $I°$ (target on). The target lifetime τ_t can be calculated from τ_{on} and τ_{off} using the expression (5.4):

$$\frac{1}{\tau_t} = \frac{1}{\tau_{on}} - \frac{1}{\tau_{off}} \tag{5.4}$$

The final target lifetime extracted using equation (5.4) was about $\tau_t \approx 25.6$ s.

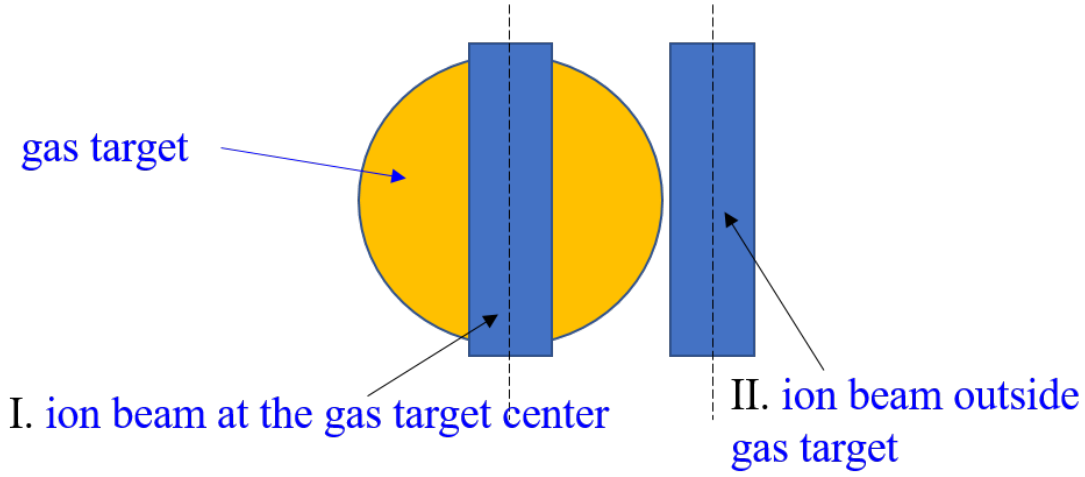

Figure 5.1: Beam position with respect to the target used for the storage lifetime measurement. In position $I°$, the beam was crossing the target center (target on condition) while for $II°$ the beam was not intercepting the target (target off condition).

5.1.3 Target and beam profiles

To get informations on the target and beam profile we scanned the gas jet target along the x-axis with the ion beam, which was deviated locally using the closed orbit bump. The shift of the beam position with respect to the center has the effect to reduce the effective target thickness and thus a reduction of the luminosity.
For the measurement of the luminosity we measured the X-rays (up to 100 keV) produced by electron capture reactions of the beam with the target. The photons were measured with the two Ge detectors located outside the target reaction chamber. The ratio of figure 5.3 shows the number of X-rays N_x divided by the number of stored ions N_i as a function of the beam position in the target. The ratio N_x/N_i is maximum when there is a maximum overlap between the beam and the target. The normalized ratio $N_x/N_0(x_i)(x_i)$ as a function of the beam position x_i, can be determined as the convolution between the ion beam profile and the target profile. Assuming a gaussian profile for the beam and a gas jet target, the ratio N_x/N_i is given by the equation (5.5):

$$\frac{N_x}{N_i}(x_i) = A \cdot \int_{-R+x_t}^{R+x_t} \underbrace{\frac{e^{-\frac{(x-x_i)^2}{2\sigma}}}{\sqrt{2\pi}\sigma}}_{ion\ \ beam\ \ profile} \cdot \underbrace{\sqrt{R^2-(x-x_i)^2}}_{Target\ \ profile} dx \tag{5.5}$$

where respectively x_t is the position of the target center, R the target radius and σ_x the standard deviation of the horizontal beam profile. By setting x_t =-7.5 mm, R =2.5 mm and fitting the function (5.5) to the experimental values of $N_x/N_i(x_i)$ (see figure 5.3) we deduced σ_x =2.1 mm. Using equation (3.2) we can obtain the horizontal emittance ϵ_x:

$$\epsilon_x = \frac{\sigma_x^2}{\beta_x} \tag{5.6}$$

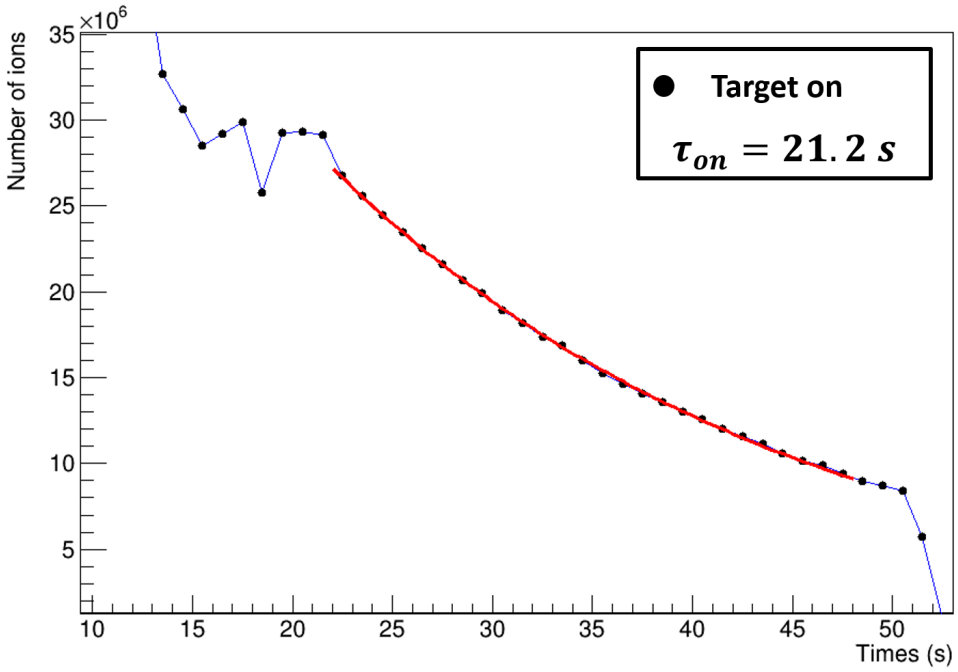

(a)

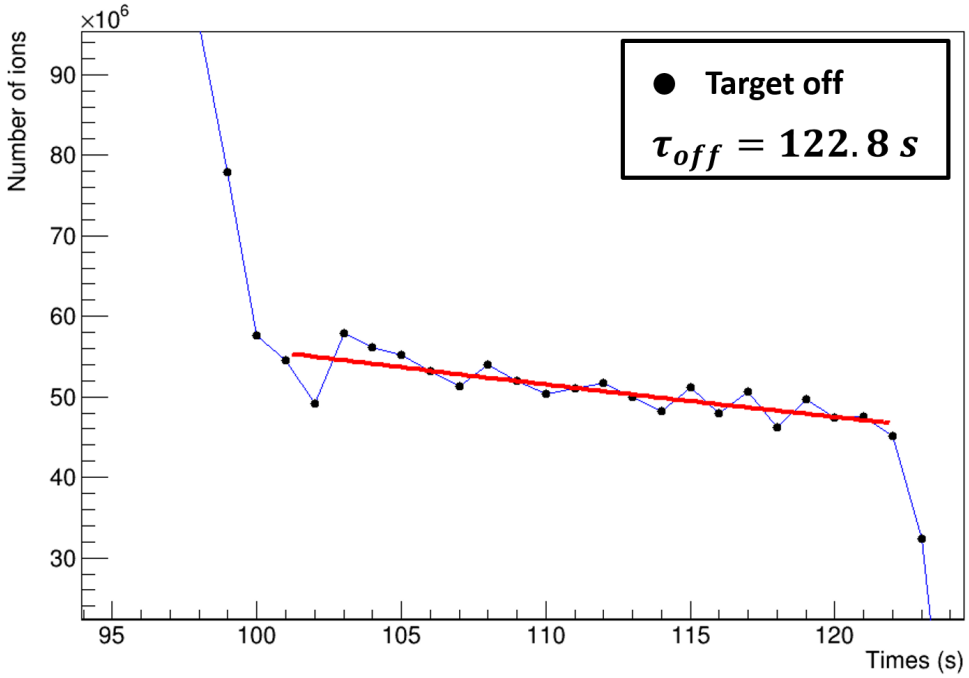

(b)

Figure 5.2: Number of stored ions as function of time for the target positions $I°$ and $II°$. The ion number was measured with the DC transformer of the ESR and the beam lifetimes shown in figure 5.1 were extracted with an exponential fit function $c \cdot e^{-t/\tau}$.

where the β_x is the horizontal component of the lattice beta function at the target location (β_x =11.48 m). Setting β_x =11.48 m in equation (5.6) an emittance of 0.38 $mm \cdot mrad$ was

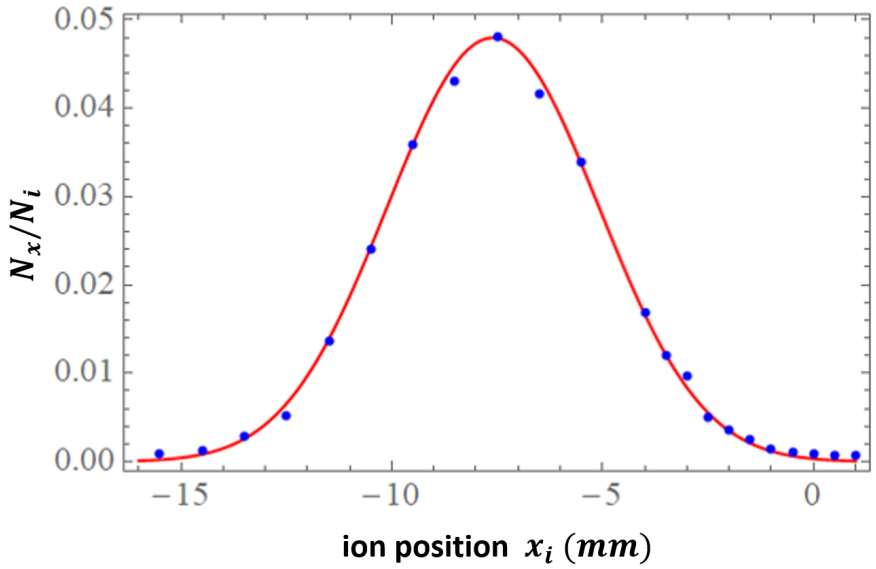

Figure 5.3: Evolution of the ratio between the x-rays N_x and the stored ions N_i (N_x/N_i) as a function of the beam position. The experimental points are represented by the blue circles and the fit obtained using equation (5.5) is indicated in red.

obtained, slightly smaller than the expected value of 0.5 $mm \cdot mrad$.

5.2 Determination of the decay probabilities

To explain the different steps necessary to determine the decay probabilities, we recall equation (1.43):

$$P_{\chi}^{surr.}(E^{\star}) = \frac{N_{\chi}(E^{\star})}{N_s(E^{\star}) \cdot \epsilon_{\chi}(E^{\star})} \tag{5.7}$$

where:

- $N_s(E^{\star})$ indicates the number of single events, i.e. number of protons detected with the telescope as a function of the excitation energy. These events are selected by means of contours in the $\Delta E - E$ spectra obtained with the telescope. The energy of the selected protons is then reconstructed, using equation (4.6) and from this energy the $^{208}Pb^{\star}$ excitation energy is calculated with the equation (4.16).

- $N_{\chi}(E^{\star})$ is the number of coincidences for the specific decay channel χ as a function of the excitation energy. As mentioned in the previous chapters, this number is obtained by selecting the beam residues located at different positions in the heavy residue detector measured in coincidence with the detected protons. As shown in section (4.4.4), we expect to see two well separated distributions associated to $^{208}Pb(\gamma\text{-decay})$ and ^{207}Pb(n-decay).

- The detection efficiencies ϵ_{γ} and ϵ_n represent the probability to detect a HR produced

Table 5.1: Energy of the alpha particles provided by the 3α source used for the calibrations. In the second column the calculated energy of the alpha particles after passing through the detector dead layers is shown. The dead layers of the telescope detectors consisted of 0.3 μm Al and 0.5 μm Si layers.

Isotopes	$E_\alpha(MeV)$	$E_\alpha(MeV)$ - $\Delta E_{dead\ layer}$
^{239}Pu	5.149	4.994
^{241}Am	5.480	5.332
^{244}Cm	5.795	5.653

after γ or neutron emission for reactions where the scattered protons have been detected in the telescope. These quantities serve to account for losses in N_χ due to the presence of heavy residues that do not hit the HR detector. The simulations used to determine the efficiencies are validated by comparing them to data where the γ-emission probability is 1.

5.2.1 Telescope energy calibration

5.2.1.1 Calibration with alpha particles

As described in equation (4.6), the reconstruction of the scattered proton energies requires to measure the energy deposited in the different detectors of the telescope. For this reason, it is necessary to accurately calibrate these detectors in energy.
Some observations have shown that there is a small difference in the pulse height of Si detector signals measured for protons and alpha particles of the same energy. However, such differences are usually of the order of 1% or less [Kno17] and can be neglected in our case since the uncertainty in the excitation energy is dominated by the uncertainty in the position of the reaction vertex (see section 4.4.2). For this reason we performed a first calculation of the DSSSD and the E detectors with a 3α source (see table 5.1).
The calibration of the E detectors was performed by inserting the alpha source in the target residue pocket. A primary vacuum pump was used to establish primary vacuum ($\approx 10^{-3}\ mbar$) inside the pocket. The detector signals were sent to the MMR module described in the previous chapter. The source was placed behind a collimator with a hole of 4 mm diameter. An accurate energy calibration requires to account for the energy loss of the alpha particles in the detector dead layers. The second column of table 5.1, shows the energy of the α-particles after passing through the dead layers at the surface of the detectors, consisting of a layer of Al of 0.3 μm and a layer of Si of 0.5 μm. The pedestal level of each detector was measured by taking the mean value of the recorded noise without source and it was used as offset of the

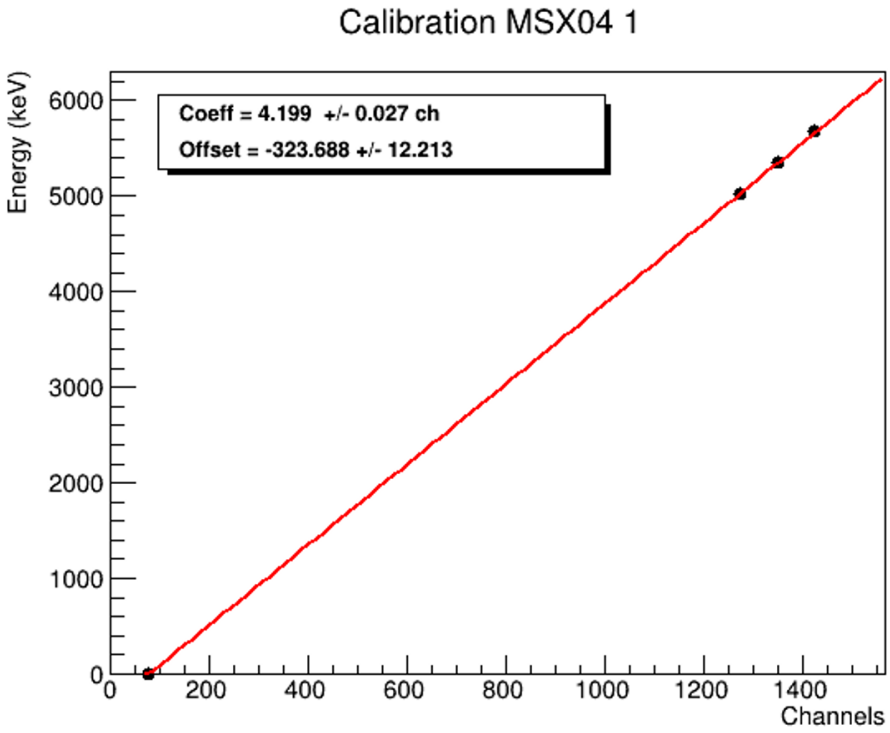

Figure 5.4: α calibration of the E_1 detector. The symbols are the measured data and the full line is the calibration curve fitted to the data. The calibration coefficients are indicated.

detector response. The final channel to energy conversion was achieved with a linear fit over the offset and the three α signals. In figure 5.4, the calibration curve obtained for the E_1 detector is presented. In Appendix (D) the energy calibrations for the detectors E_2 and E_3 are shown.

In the case of the DSSSD detector, the same procedure as for the E detector was followed to individually calibrate the 32 strips (16 vertical and 16 horizontal). The 3α-source was inserted in the target residue pocket facing the vertical strips, i.e. the front side of the detector. After establishing primary vacuum the detector signals from each strip were sent to the MMR board. Also in this case the pedestal of each strip was measured by taking the mean value of the recorded signal amplitude distribution without the source. For the ΔE detector the calibration is complicated by the presence of interstrip events, where the charge produced by the impinging particle is shared between two strips.
Since our DSSSD was irradiated with α particles from the front side, we can distinguish two different cases. If the incoming α particle intercepts only one vertical strip, the charge produced in the bulk is completely collected in the front side by the fired strip. However, in the back side, depending on the particle trajectory, one or more strips can be activated. The situation is represented in figure 5.5(a) where the amplitude of the signal provided by the horizontal strip 9 (E_9^H) is compared to the signal amplitude of the adjacent strips 8 (E_8^H) and 10 (E_{10}^H). Here the peaks around E=1530 ch on the x and y axes correspond to single-strip events in the back-side.

When an interstrip event between the horizontal strips E_9^H-E_8^H and E_9^H-E_{10}^H occurs, the energy is shared and this leads to the formation of the three diagonals connecting the single-strip event peaks. In this case, the total energy of the particle can be reconstructed by adding the signal amplitude provided by the two strips.
When the incident particle crosses the interstrip gap between two strips the generated charge can not be completely collected [Yor87, Blu99, Tak07, Ere03]. This charge deficiency will prevent us from correctly reconstructing the full particle energy. In the alpha calibration, this situation takes place when the α particle hits the interstrip gap between two vertical strips, which will share the produced charge, while in the back side again, one or more strips can be activated. This situation is well represented in figure 5.5(b) where the events with two vertical strips activated are selected. We can clearly see the effect of incomplete charge collection, which leads to smaller amplitudes for the single-strip and interstrip events.
For this reason, when analyzing data collected with DSSSDs, it is very important to select events that produce signals with the correct full energy amplitude and to reject interstrip events producing signals of smaller amplitude. Only events having a multiplicity (number of activated strips) equal to 1, both in the front and back side, were used for the DSSSD energy calibration. In figure 5.6 an example of calibration curve for the horizontal strip 3 is presented.
If the particle punches through the detector and crosses the interstrip gap region between two horizontal strips, an incomplete charge collection will also take place, as described previously for the vertical strips. In our experiment the energy of the detected protons ranged between few MeV up to 40 MeV. Therefore, since most of them traverse the DSSSD detector, to avoid problems in the energy reconstruction, only events with a "regular" detector response were considered. By "regular" detector response we mean events where only one vertical and one horizontal strip were hit, producing signals of the same amplitude.

5.2.1.2 Calibration with protons

We have also performed the energy calibration of the telescope by using the elastic scattered protons detected during the experiment. Figure 5.7 shows the energy loss in strip 3 of the ΔE detector as a function of the energy deposited in the E_1 detector measured during the experiment, together with the simulated spectrum on the bottom. As can be seen, the protons stropped in the E_1 detector produce the expected hyperbolic curve. The protons whose energy is sufficiently high to punch through the E_1 detector lose less and less energy in both the ΔE and E_1 detectors. This produces a kind of kink in the spectrum with events moving downwards in the histogram. The peak corresponding to elastic scattered protons is clearly visible. The mean value and the standard deviation of this peak, in channels, can be associated to the simulated values, in keV, providing a useful point for the calibration of the ΔE and E detectors. Furthermore, by selecting different strips of the DSSSD it was possible to consider different energies of the scattered protons providing additional points for the calibration of the E detectors.

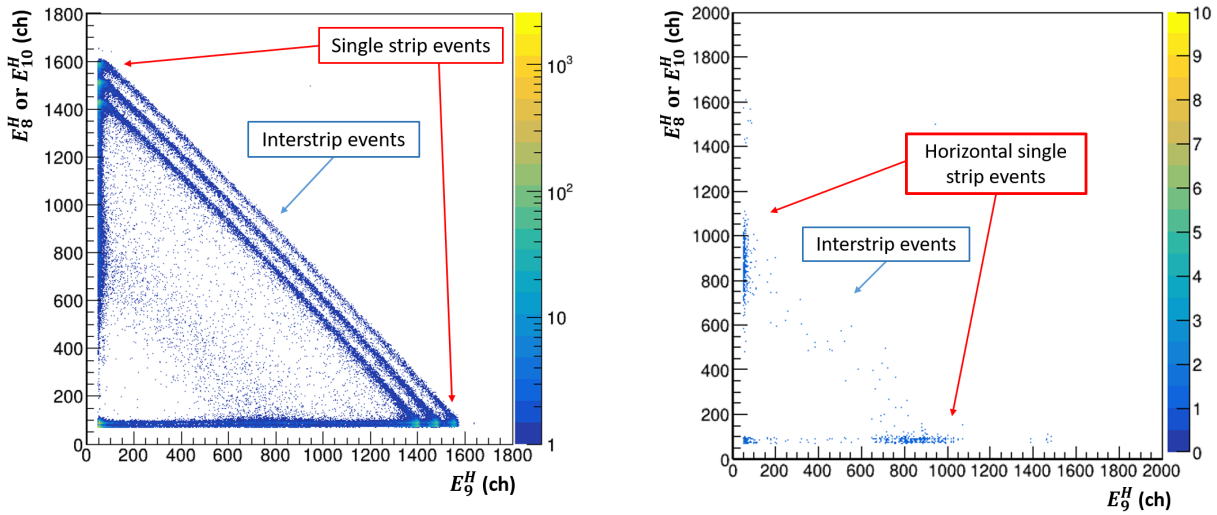

(a) (b)

Figure 5.5: Correlation spectra between one horizontal strip 9 and the two adjacent strips 8 and 10 measured with the 3α source. In figure (a) the horizontal strip signals are shown without any condition on the vertical strips. Part (b) is the same as part (a) but for events with more than one vertical strip hit.

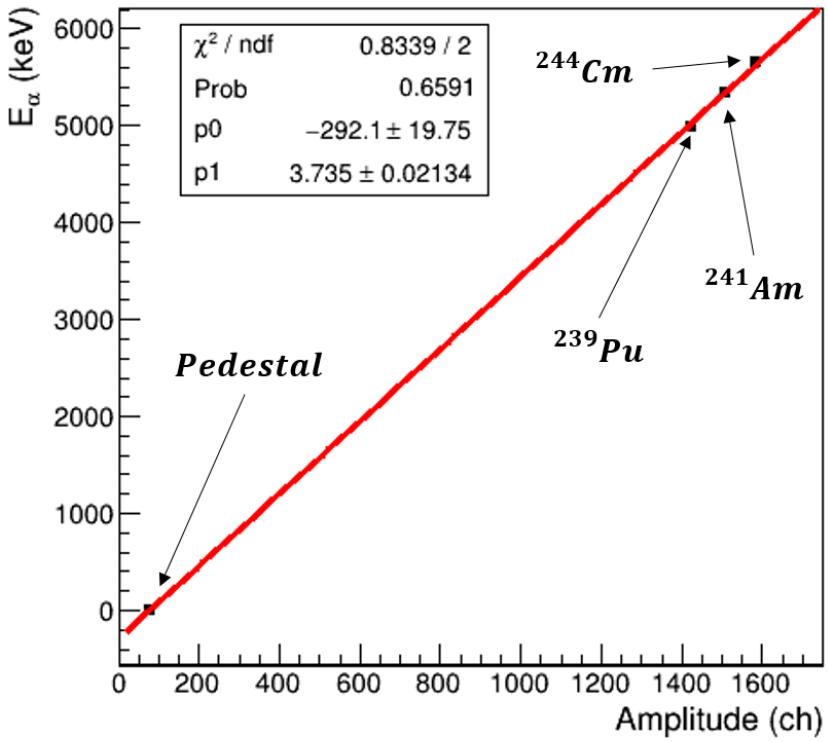

Figure 5.6: α calibration curve of the horizontal strip 3 of the ΔE detector.

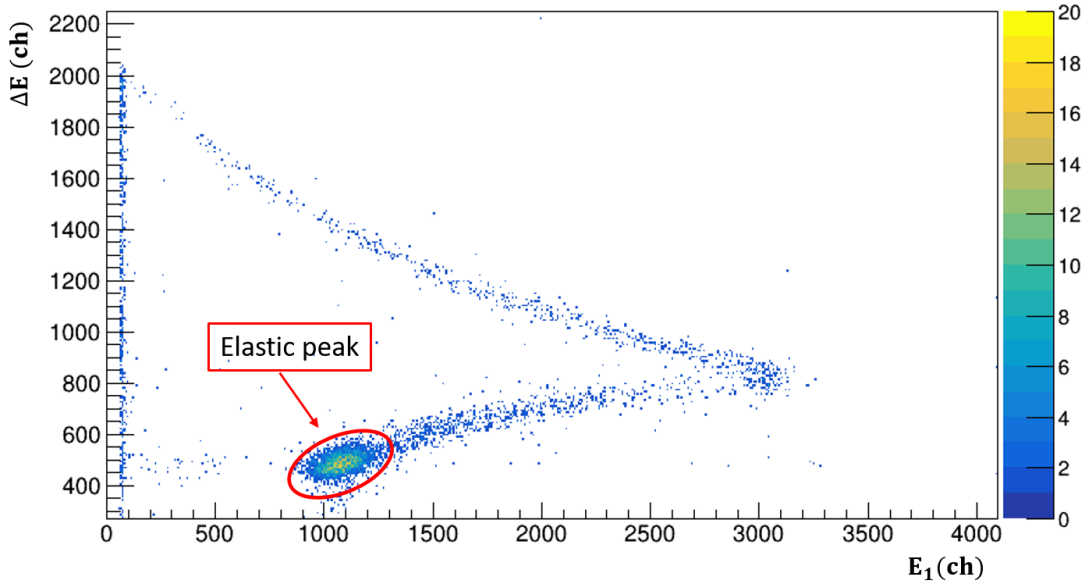

(a)

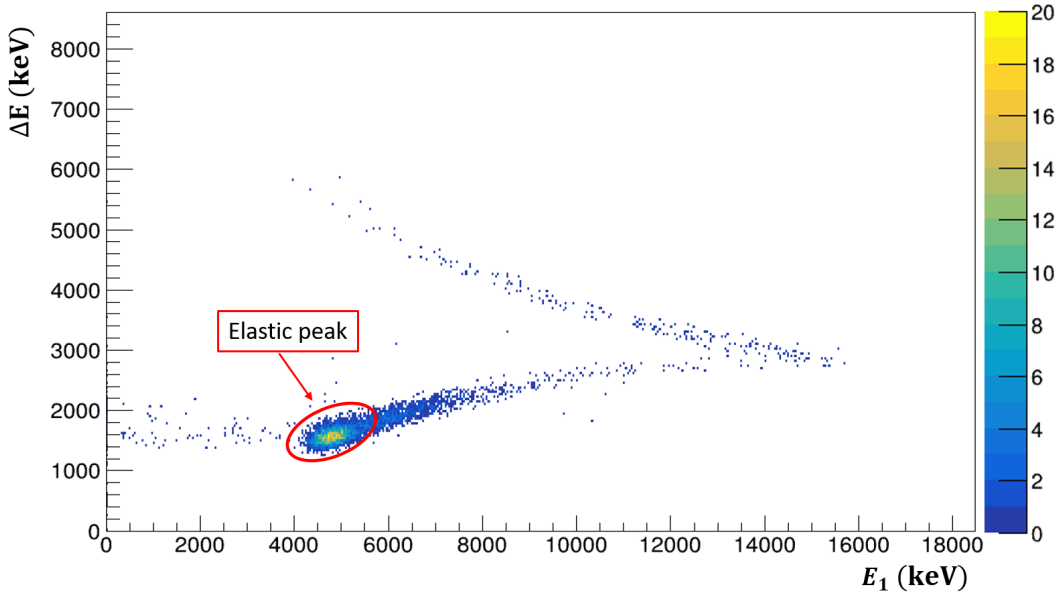

(b)

Figure 5.7: Energy loss in strip 3 of the ΔE detector versus energy deposited in E_1 from the experimental data (a) and from the simulations (b).

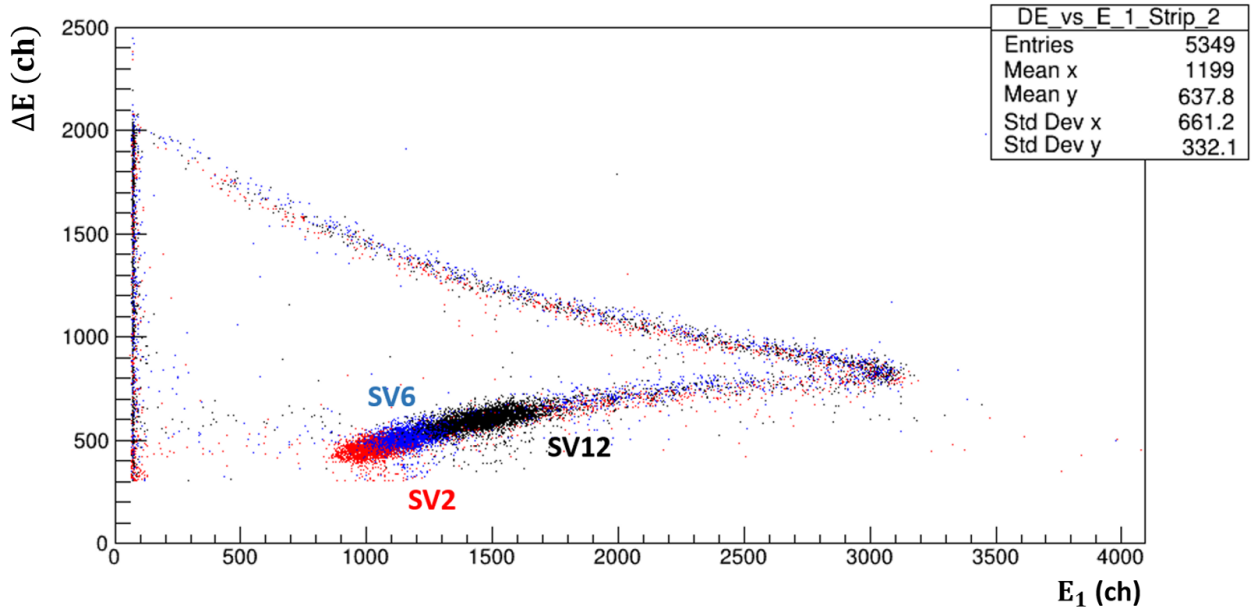

Figure 5.8: Measured ΔE versus E spectrum obtained for the vertical strips 2 (red) at 55.5°, 6 (blue) at 58.3° and 12 (black) at 62.5° of the DSSSD.

In figure 5.8, an example of $\Delta E - E_1$ spectrum using three vertical strips is shown. With the increase of the strip number, larger scattering angles are selected and the energy of the proton decreases. The effect in the $\Delta E - E_1$ spectrum is a visible upwards movement of the elastic proton peak. During the experiment, the energy of the stored beam was increased to 37 and 42 MeV/u in order to increase the proton energy and obtain additional points for the calibration. Thanks to this, dedicated calibrations with protons were done for the ΔE detector strips and three E detectors. As for the α-calibration, the noise level was used in the calibration as a pedestal of the detector response.

Figure 5.9 shows that the proton and alpha calibration for a ΔE detector strip are in good agreement. A small difference is found at high energies but it is smaller than 1%. This result confirms the reliability of the simulations for determing the energy deposited in the ΔE and E detectors by the elastic scattered protons and justifies the use of the α calibration for this detector.

An interesting result is obtained when the α and proton calibrations curves for the E detectors are compared, as shown in figure 5.10 and in Appendix (D) figure D.2. For the E_1, E_2 and E_3 detectors a significant difference was found with increasing energy. Considering the good agreement observed for the calibrations of the ΔE detector strips, this discrepancy cannot be due to a wrong simulated energy. As described in Appendix (C) more in detail, this problem comes from an incomplete charge collection, due to the fact that the E detectors were not fully depleted. Fortunately, the proton calibration, which was performed using protons that traversed the detectors, accounts to some extent for the charge loss due to the under-depletion.

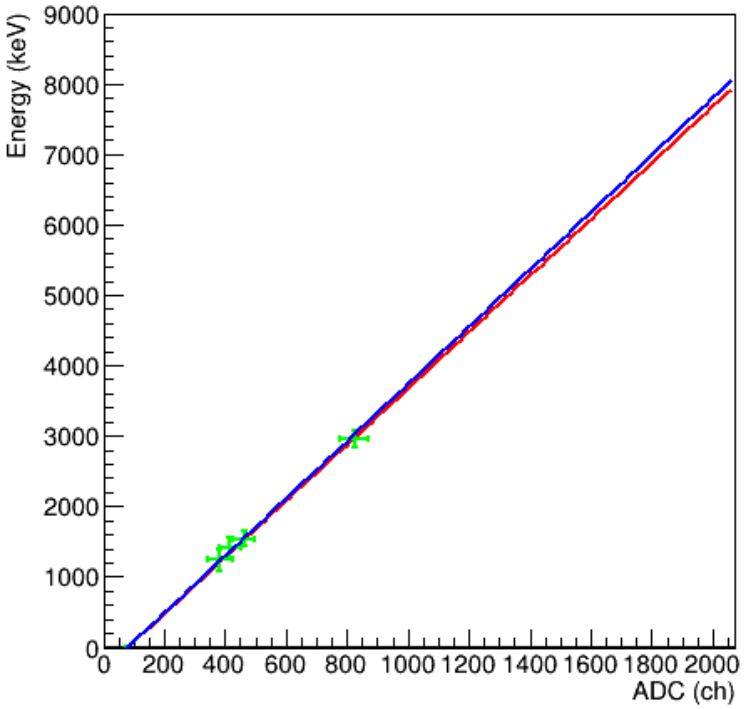

Figure 5.9: Comparison between the proton (red) and alpha (blue) calibration curves for the strip 3 of the telescope DSSSD. The green crosses represent the calibration points obtained with the elastic scattered protons.

For this reason the proton calibrations were used for the E detectors.

5.2.2 Singles spectra

Figure 5.11 represents the energy loss in all the strips of the ΔE detector as a function of the total deposited energy in the E detectors. By comparing the experimental spectrum in figure 5.11(a) with the simulated one in figure 5.11(b), we observe a difference in the maximum energy of the protons of about 3 MeV and some structures appearing at the interface between the E detectors belonging to the same packaging ($E_1 - E_2$, $E_3 - E_4$, $E_5 - E_6$).
As it is described in detail in Appendix (C), this mismatch between the simulations and the experimental data arises from the under-depletion problem of the E detectors mentioned above, which causes a deficiency in the energy reconstruction of the protons crossing the interfaces $E_1 - E_2$, $E_3 - E_4$ and $E_5 - E_6$. For this reason, only protons stopped in the DSSSD, belonging to the II° kinematics solution, and the ones from the I° kinematics solution stopped in the E_1 detector have been used for the determination of the decay probabilities.

The single events were therefore selected using identification spectra, $\Delta E - E_1$, were only the energy deposited in the first E_1 detector was considered. An example is shown in figure 5.12, where we can identify the protons from the second solution (red contour), the ejectiles stopped in the E_1 detector (pink contour), and the ones punching through it (orange contour).

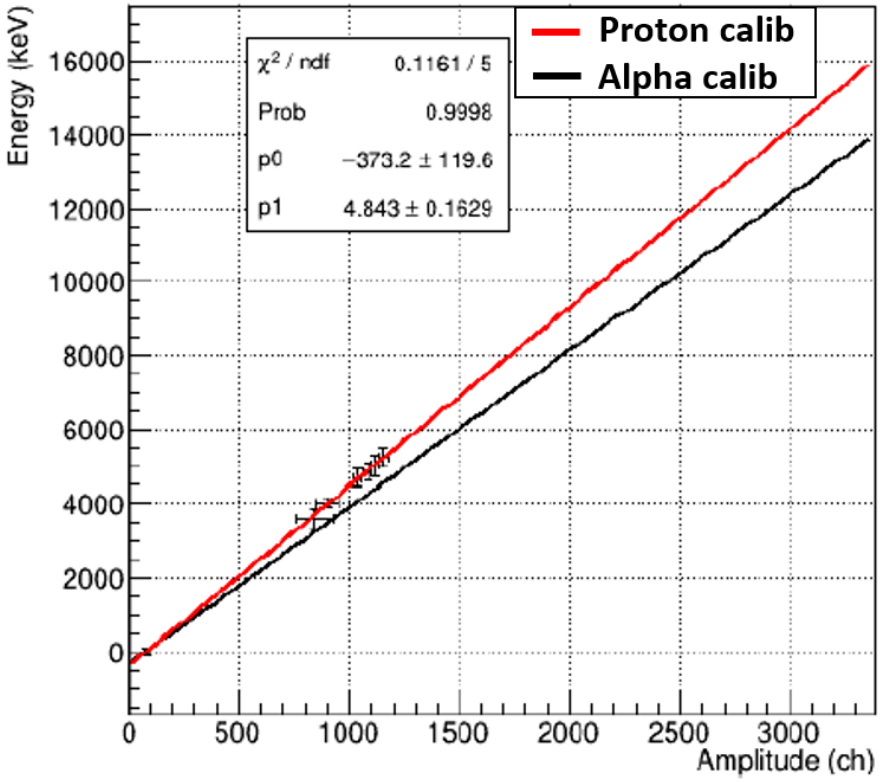

Figure 5.10: Comparison between proton (red line) and alpha (black line) calibration curves for E_1. The black crosses correspond to the calibration points obtained with the protons.

As already stressed, single events from the first and second kinematics solution were treated separately.

5.2.3 Singles spectra for the I° kinematics solution

Protons from the first solution which pass through the DSSSD detector can be selected by means of a graphical contour in the $\Delta E - E_1$. Figure 5.13 shows that the maximum energy deposited by the protons in E_1 detector is lower than the simulated value. This difference also arises from the under-depletion problem affecting the E_1 detector. The events not affected by the under-depletion problem are those that agree with the simulation and which are included in the orange contour of figure 5.13. Single event spectra as a function of the excitation energy were produced for vertical strips from 2 up to 9, allowing us to cover an excitation energy range from 5.6 MeV up to 9.5 MeV.

This range allows us to obtain some data point below the S_n where γ-emission is the only possible decay channel for ^{208}Pb and to explore the region where γ and neutron emission compete at $E^\star > S_n$. In figure 5.14 the spectrum $E^\star vs E_k$ is shown where we can clearly see for each strip the excitation energy covered and the relation with the kinetic energy of the proton E_k. Due to the single event selection, each vertical strip covers only a small excitation energy range. In figure 5.15 the 1-dimension singles spectra for strips 2,3,4 and 5 are shown.

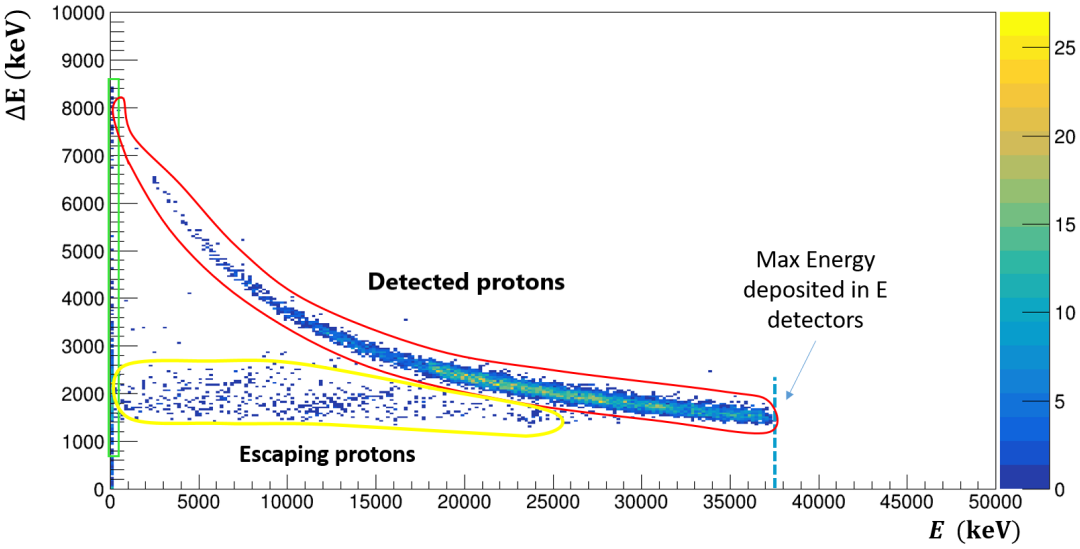

(a)

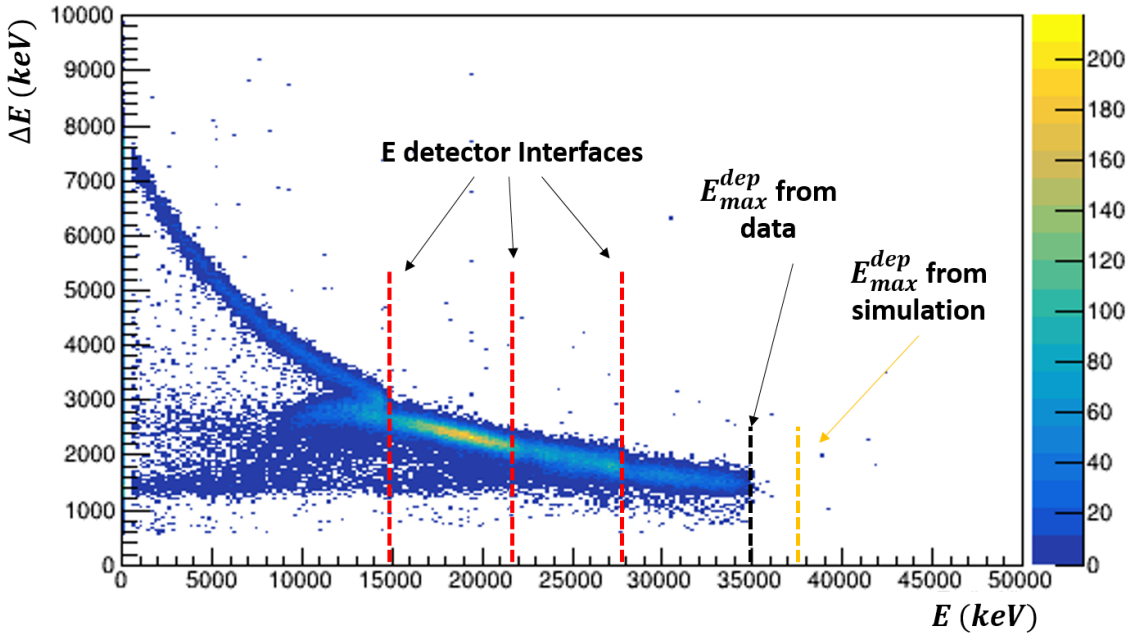

(b)

Figure 5.11: Spectra representing the energy loss in all the strips of the ΔE detector as a function of the total energy deposited in the E detectors respectively from the simulations (a) and the experimental data (b). The regions where protons traverse the interface between neighbouring E detectors are indicated, as well as the maximum energy deposited in the telescope obtained with the simulations and with the experimental data.

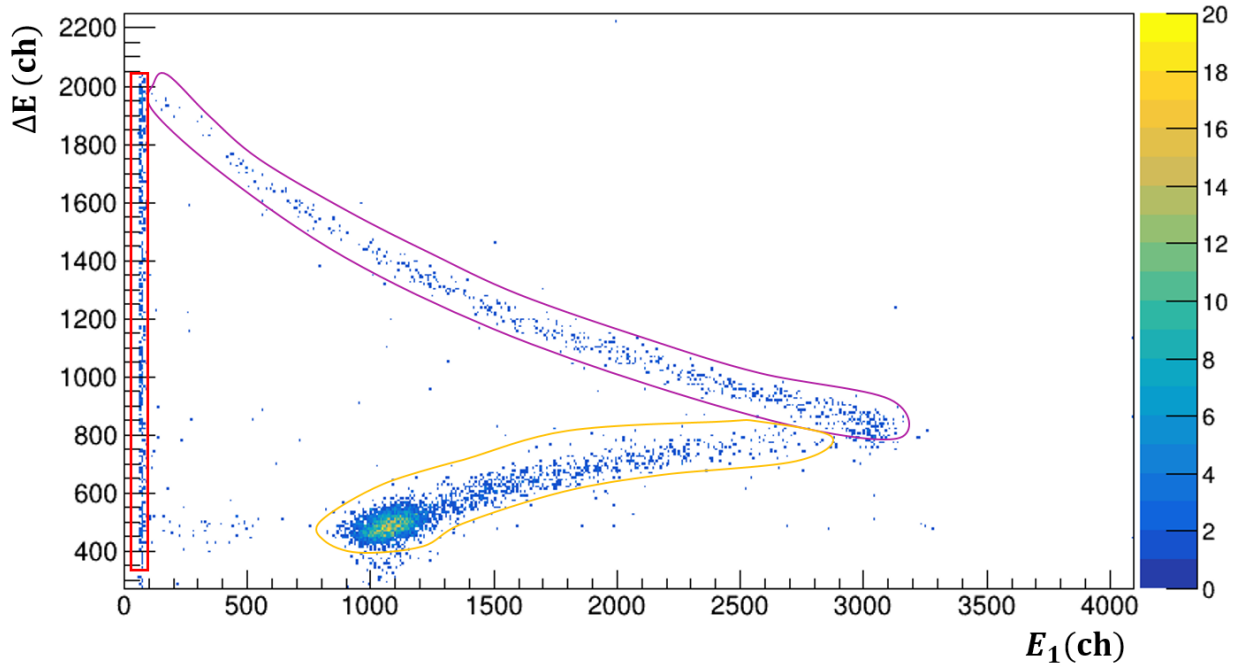

Figure 5.12: Example of identification spectrum measured for vertical strip number 3. The different contours indicate, respectively, the protons stopped in the E_1 detector (in pink), the protons punching through the E_1 detector (in orange) and the low energy protons stopped in the ΔE DSSSD (in red).

5.2.4 Singles spectra for the II° kinematics solution

The energy of the protons from the second kinematics solution deposited in the E_1 detector is below the electronic threshold which corresponds to three times the pedestal. Therefore, these events can be easily identified with respect to the other events in the $\Delta E - E_1$ plot of figure 5.13. An identification plot $\Delta E vs E_1$ was done for each vertical strip and, as for the E_1 detector, the signal provided by the DSSSD was accepted if it was three times larger than the pedestal (threshold condition).

A disagreement between the maximum proton energy from the simulation and the data can be observed in figure 5.13 where the comparison between the simulated $\Delta E - E_1$ plot from the first solution and the data is shown. Protons stopped in the DSSSD are supposed to deposit up to 8.54 MeV in the ΔE detector while the data show a maximum deposited energy of 8 MeV. This is an indication that the DSSSD was probably also affected by an under-depletion problem due to the application of insufficient bias voltage. As shown by the $\Delta E - E_1$ spectrum in figure 5.13, the simulated and experimental energies agree when the proton energy increases since less energy is deposited by the proton in the under-depletion region. Unfortunately the protons from the second kinematic solution are stopped in the DSSSD and so any comparison

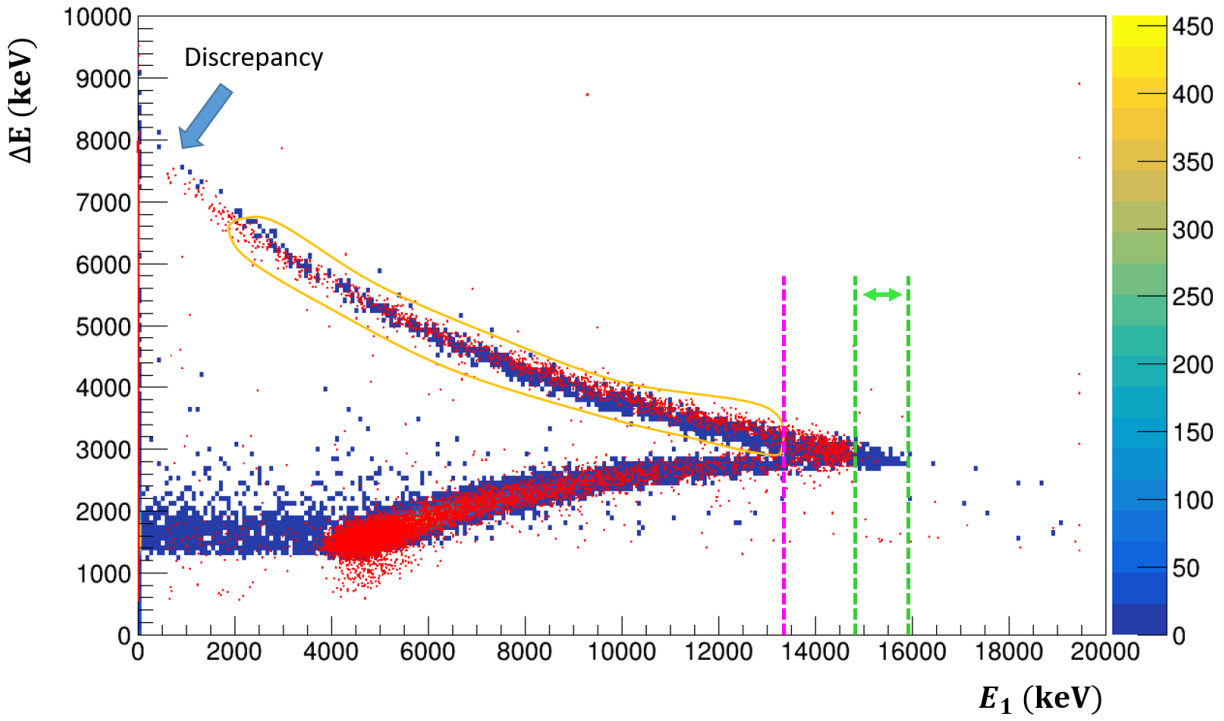

Figure 5.13: ΔE-E_1 identification spectrum showing the comparison between the experimental (in red) and simulated data (in blue) at $\theta \approx 55.5°$. The regions where we observe differences between the data and the simulations are indicated. The contour selects the events that are not affected by the under-depletion problems.

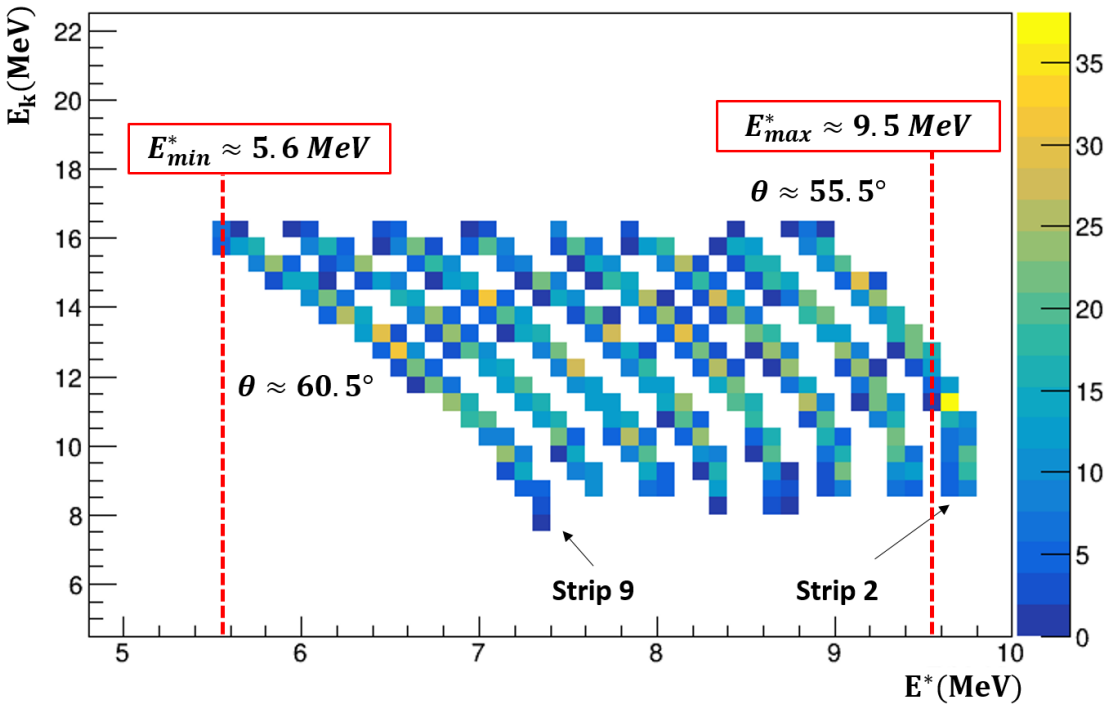

Figure 5.14: Kinetic energy of the protons as a function of the $E^{\star}$ of ^{208}Pb for different strips. The minimum and maximum value of excitation energy and the scattering angles associated to strips 2 and 9 are indicated.

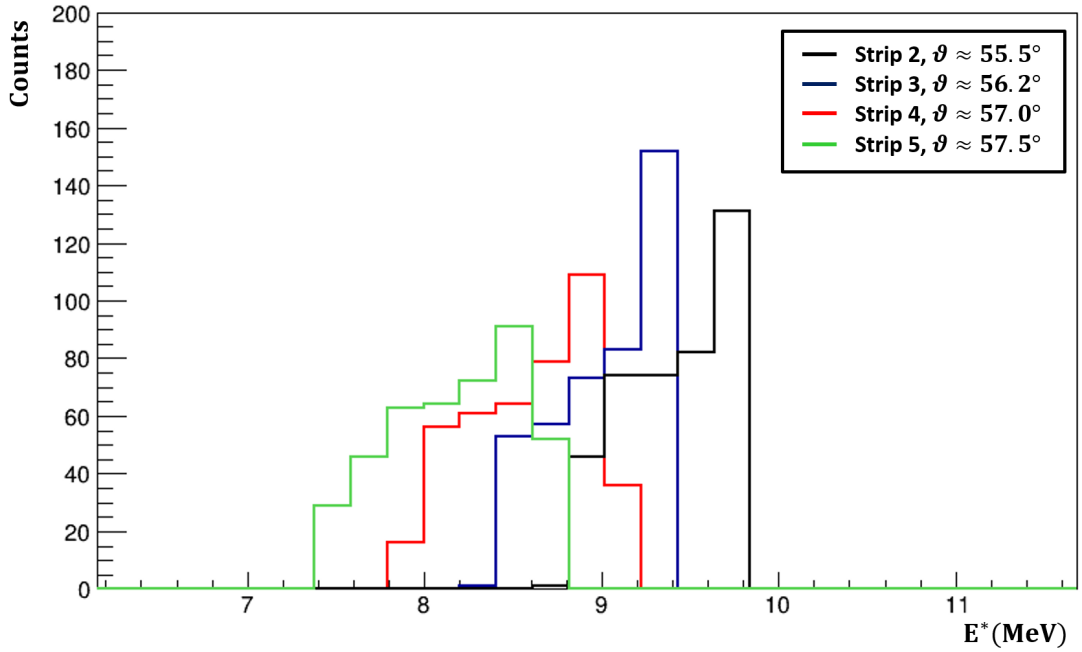

Figure 5.15: Singles spectra measured for the I° kinematics solution for the vertical strips 2 (in black) at 55.5°, 3 (in blue) at 56.2°, and 4 (in red) at 57.0°, and 5 (in green) at 57.5°.

with the simulation can not be performed.
The under-depletion region is located in the back part of the detector but we do not know its thickness. Therefore, it is not possible to calculate precisely above which proton energy under-depletion effects start. For this reason, during the analysis we considered different maximum proton energies between 7.5 MeV and 9 MeV, to see if this had an impact on the deduced decay probabilities. No significant change in the results was observed and for this reason the under-depletion effects in the ΔE detector were considered to be included in the data uncertainty.
In the construction of the singles spectra for the second solution we considered the vertical strips of the DSSSD from 3 up to 9, corresponding to an angular range between 56.2° and 60.5°. In figure 5.16(a) the kinematic plots (E_k, θ) obtained experimentally are compared with kinematic calculations for excitation energies of 7 (brown line), 8 (pink line) and 9 (red line) MeV. The black circles in the lines indicates the points where the transition from the second solution to the first solution occurs. From this plot we can see that few low energy protons from the first solution were stopped in the ΔE detector, in particular for excitation energies between 7 and 8 MeV. Simulations were implemented to define a graphical cut which allowed us to remove these events. If we compare the latter figure 5.16(a) with the kinematic plot from the simulation, figure 5.16(b), where only the second solution is included, we can see that these events are located in the region delimited by the red line. From the simulation the selection in red was defined and applied to the experimental data.
After implementing the graphical cut, an excitation energy range from 6.5 MeV up to 9.3 MeV could be investigated for the second kinematics solution. The protons kinetic energy as a function of the $E^\star$ is shown in figure 5.17. Also in this case the excitation energy range covered by each strip can be seen. In figure 5.18 the singles spectra obtained from the strip 3,4 and 5 are represented.

5.2.5 Determination of the excitation energy resolution

We have chosen to investigate the $^{208}Pb(p, p')$ reaction because the ground state of ^{208}Pb is separated by 2.16 MeV from the first excited state. Therefore, the width of the elastic scattering peak in the singles spectra of ^{208}Pb can provide a direct measurement of the excitation energy resolution.
Unfortunately, the under-depletion problem significantly complicated the determination of the excitation energy for the ground and the first excited states, since the related protons were energetic enough to punch through the first E_1 detector. As can be observed in figure 5.12, the elastic scattered protons passing through the E_1 detector form a well defined peak in the $\Delta E - E_1$ spectrum of a specific strip. By selecting this peak and projecting it on the x and y-axis we obtain the distribution of the measured deposited energy of the elastic scattered protons in the E_1 and ΔE detectors. The shape of these peaks includes all the effects, that define the excitation energy resolution, such as the target radius, beam emittance, detector segmentation,

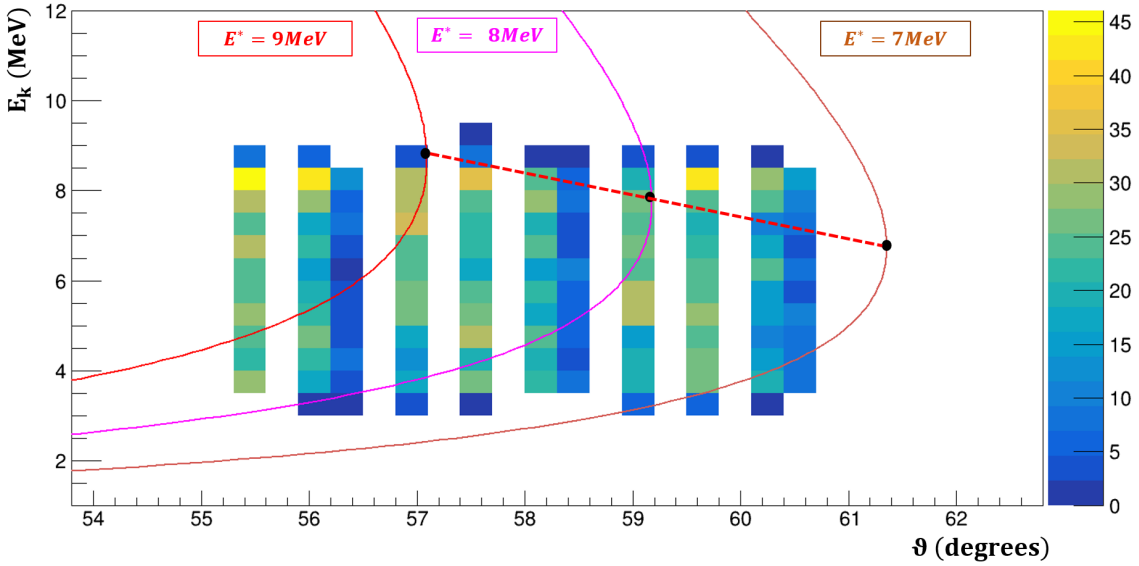

(a)

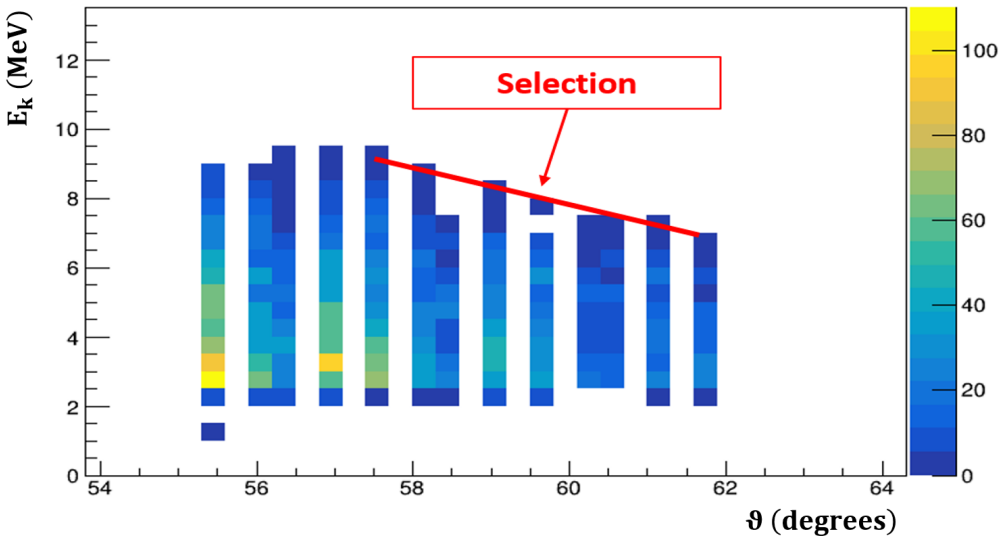

(b)

Figure 5.16: (a) Measured proton kinetic energy as a function of the scattering angle θ. The kinematic curves for different excitation energies, 7 MeV (brown line), 8 MeV (pink line) and 9 MeV (red line) are superimposed to the data. (b) Simulated results for the proton kinetic energy versus the scattering angle. The selection in red allows to remove the protons from the first solution stopped in the ΔE DSSSD.

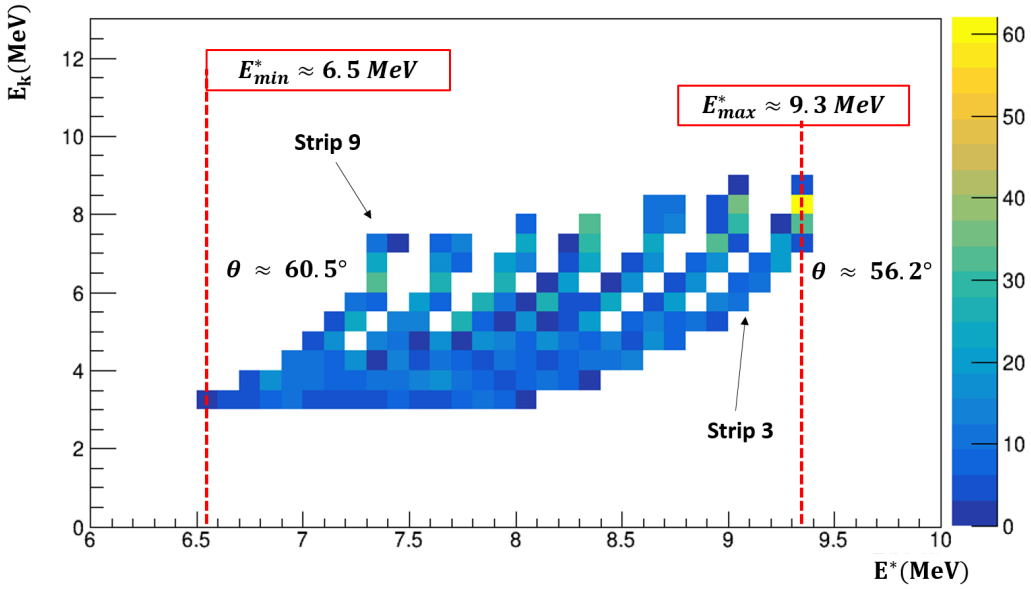

Figure 5.17: Kinetic energy of the protons as a function of the $E^\star$ of ^{208}Pb for different strips. The minimum and maximum value of excitation energy and the scattering angles associated to strips 3 and 9 are indicated.

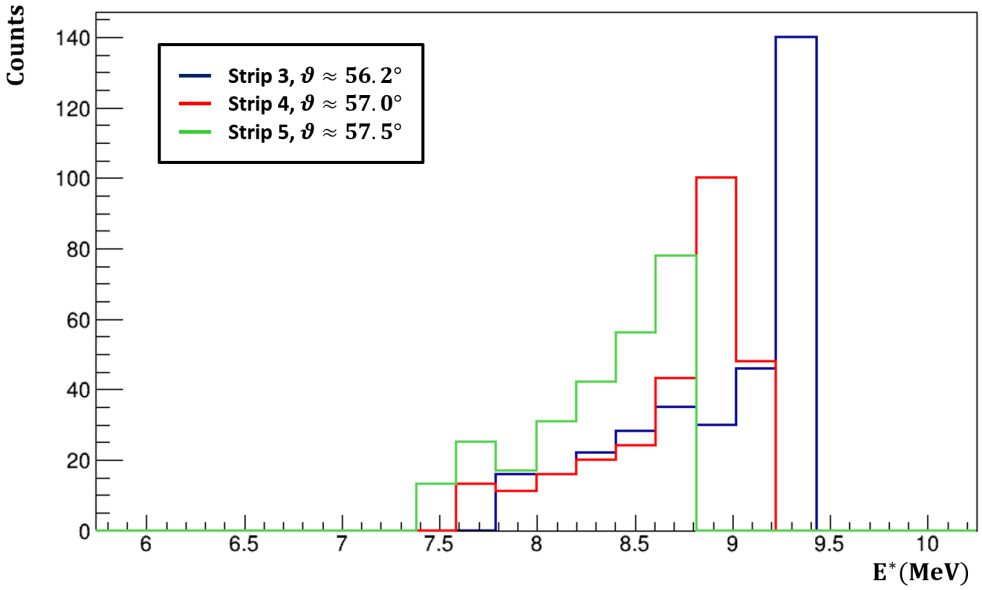

Figure 5.18: Singles spectra measured for the $II°$ kinematics solution for the vertical strips 3 (in blue) at 56.2°, and 4 (in red) at 57.0°, and 5 (in green) at 57.5°.

energy resolution, etc. Therefore, if we can reproduce these peaks with our simulation, we can use the simulation to infer the $E^\star$ resolution.

The projections of the elastic scattered peak as the ΔE and E_1 axes are shown in figure 5.19. We observe a good agreement for both the ΔE and E_1 detectors one. These results give confidence on the simulation capability to infer the excitation energy resolution of our experiment, which for the elastic scattered protons at $\theta \approx 55^\circ$ was found to be 750 keV (standard deviation). The smaller values, respect to the one evaluated in chapter 4, is due to the different scattering angle and energy of the detected protons.

5.2.6 Coincidence spectra

In this section we will describe the identification of the coincidence events between the heavy residue detector and the telescope for both the I° and II° kinematics solutions.

5.2.6.1 Rutherford scattering events

Before we proceed with the description of the coincidence spectra, it is interesting to analyse the HR detector position spectrum without asking for a coincidence condition with the telescope. This spectrum is shown in figure 5.20(a). The vertical strips closer to the beam axis are the ones on the left. As expected, there is a very large number of scattered beam ions hitting these strips. By normalizing the simulated spectra to the maximum number of events detected in the first bin of figure 5.20(a), we can compare the experimental distribution of Rutherford events in the heavy residue detector to the simulated one. This is shown in figure 5.20(b) where we can see that the simulation reproduces very well the increase of the number of events when approaching the edge of the detector. A maximum rate of few hundreds events/$(s \cdot cm^2)$ was observed experimentally. In section (4.4.5) a maximum of 110 events/$(s \cdot cm^2)$ was deduced from the simulations which is slightly different but has the same order of magnitude. This difference can be easily explained considering possible fluctuations in the luminosity events number or in the beam position.

The large rate of events due to the Rutherford scattering affected the response of the detector strips, particularly those closer to the beam. In figure 5.21 the signal amplitude of the vertical strips is shown at the beginning and at the end of the experiment. The peaks associated to the energy deposited by the lead residues, appears very clearly at an amplitude between 1400 and 1500 ch. Still, the radiation damage effect did not affect the efficiency of the detector because the signal amplitude induced by the heavy residues remained much larger than the threshold during the whole measurement. The decrease of the signal amplitude and the broadening observed for the lead residue peaks reflects the effects of the radiation damage.

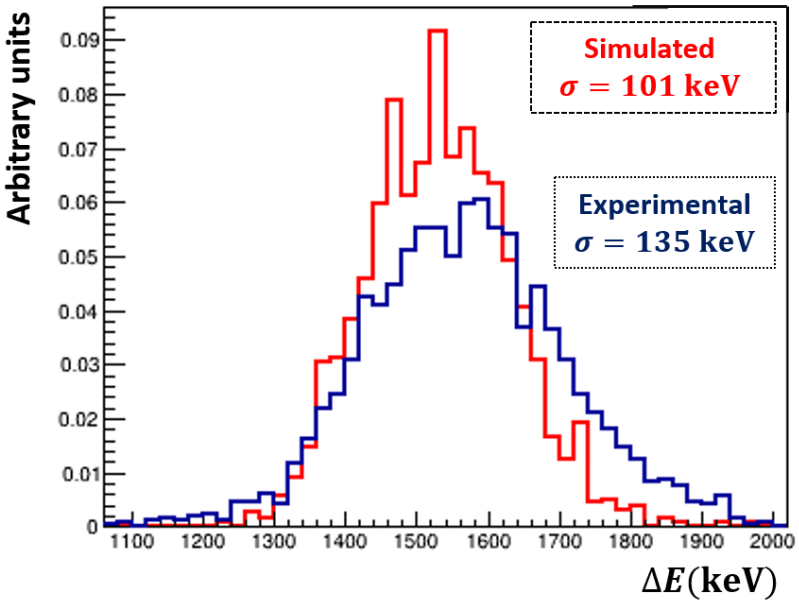

(a)

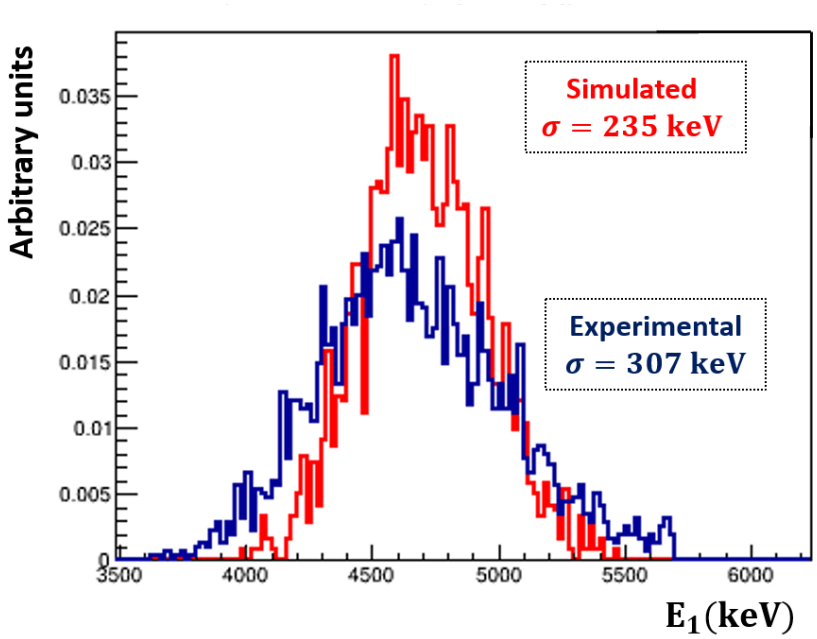

(b)

Figure 5.19: Comparison between the simulated (in red) and experimental (in blue) distribution for the energy deposited by the elastic scattered protons at 55° in the ΔE detector (a) and in E_1 (b). The standard deviation of the peaks are indicated.

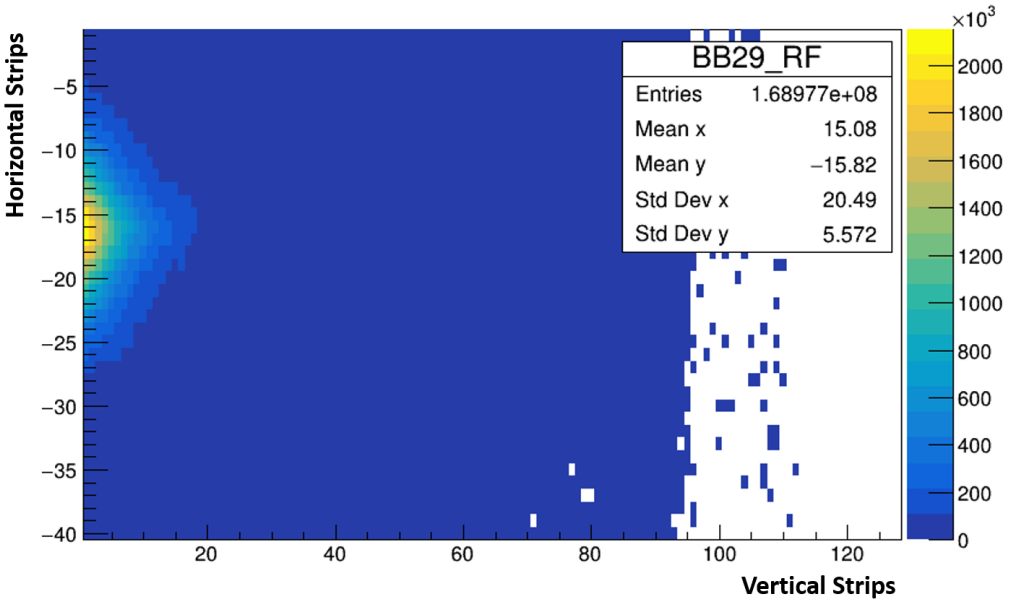

(a) Rutherford background

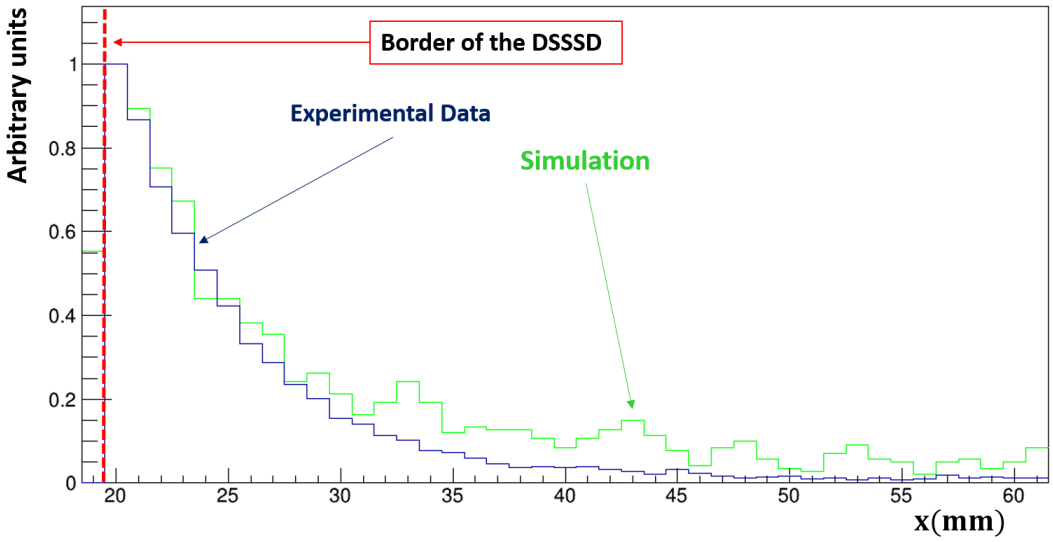

(b) Comparison Rutherford experiment and simulations

Figure 5.20: (a) Number of events as a function of the vertical and horizontal strip number measured for the HR detector. The spectrum is dominated by the Rutherford scattering background. (b) HR horizontal position profile where X represents the distance of the detected residues to the beam axis. The red curve corresponds to the experimental data and the green to the simulated one. The spectra have been normalized to the number of counts in the first strip.

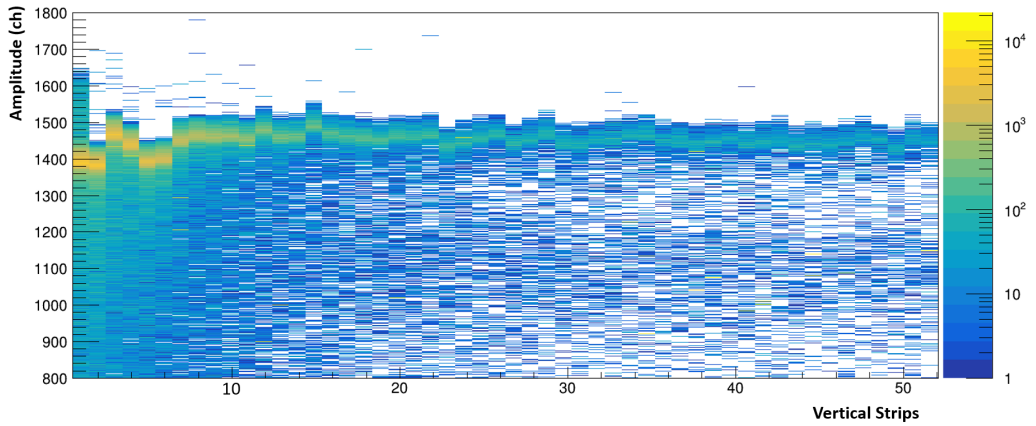

(a)

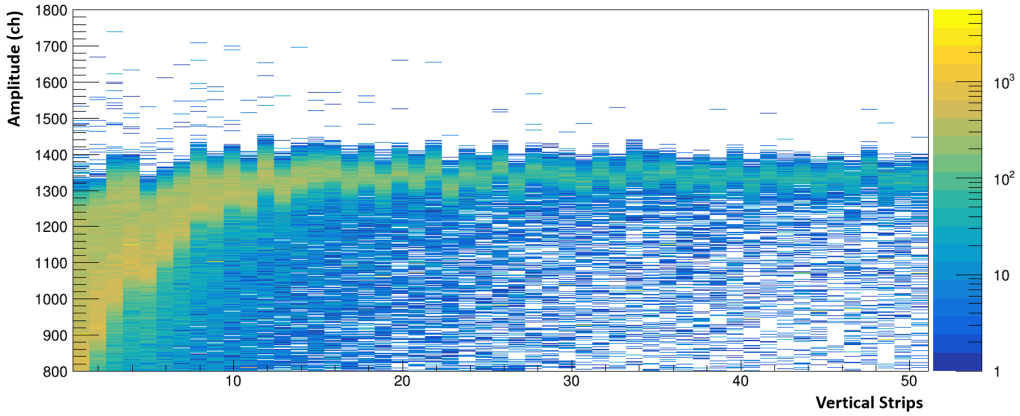

(b)

Figure 5.21: Signal amplitude as a function of the vertical strip number in the HR detector at the beginning (a) and at the end (b) of the experiment. The radiation damage is responsible for the signal amplitude decrease in the strips closer to the beam.

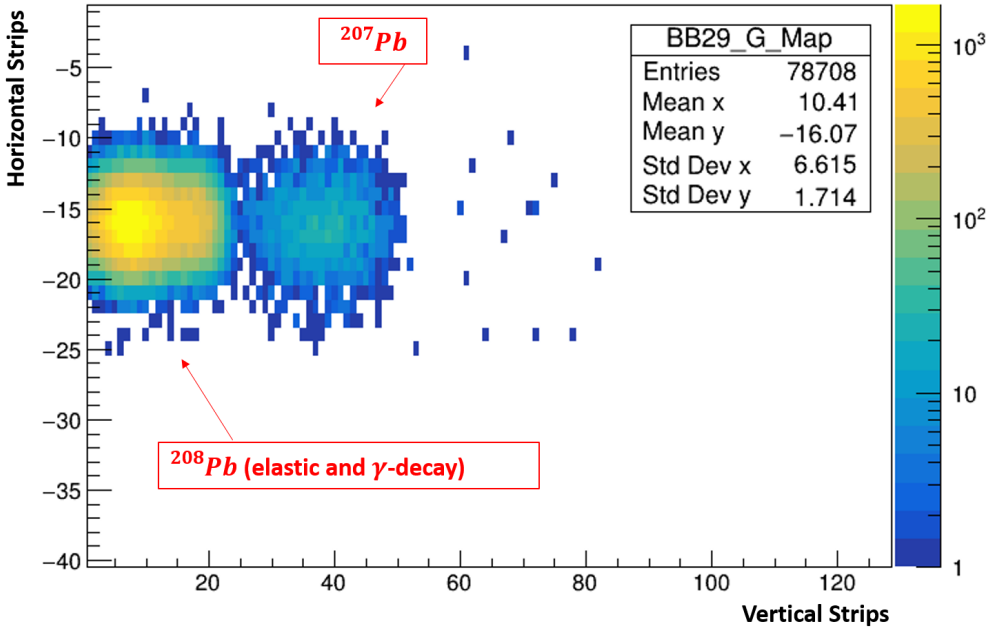

Figure 5.22: The same as in figure 5.20 but measured in coincidence with protons in the telescope without time condition. In this case all the protons belonging to the banana in figure 5.11(b) are considered.

5.2.6.2 Coincidence spectra for the I° kinematics solution

The first step to produce the coincidence spectra is to ask for a coincidence between the events in the singles spectra and the HR detector. Because the rate of Rutherford scattering events ($\sim$ few hundred Hz) is much larger than the rate of events detected in the telescope ($\sim$ few Hz) only with this condition we can remove the background coming from the Rutherford scattering events. In figure 5.22 we can see the spectrum representing the heavy residue positions after imposing the coincidence with the protons inside the $\Delta E - E$ hyperbolic shape of figure 5.11. Two bumps can be clearly observed. In the left bump are $^{208}Pb^{82+}$ ions from elastic scattering reactions and from the inelastic scattering reactions where the HR de-excites by emitting γ-rays. In the right bump are $^{207}Pb^{82+}$ ions produced by inelastic scattering reactions where the HR de-excites by neutron emission.
In figure 5.23 the HR position distribution in coincidence with the singles events, selected in figure (5.13), is shown. The coincidence events $N_\gamma(E^\star)$ are inside the green contour and the coincidence $N_n(E^\star)$ events inside the red contour.
The time coincidence peak was also considered in the selection of the heavy residues. The time difference ΔT histogram of the HR detector is represented in figure 5.24. In this histogram we give an example of events where the window of interest (see section 4.6) is generated by the HR detector itself, they correspond to self trigger events and are located in the sharp peak at $\sim$600 ch. Furthermore the events associated to the single events selection of figure (5.13), where the

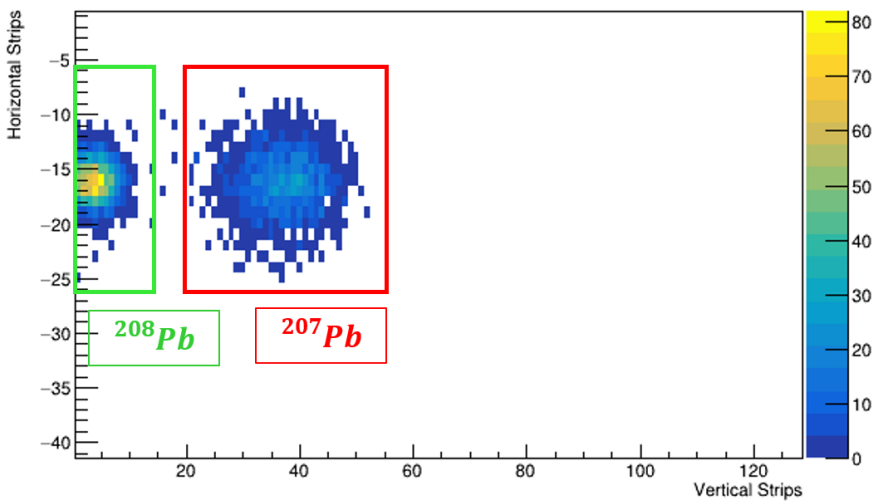

Figure 5.23: The same as figure 5.20 but measured in coincidence with protons from the first kinematics solution detected in the telescope and associated to excitation energies between 5.6 MeV and 9.5 MeV. The green and red contours indicate the selections used to identify coincidence events from, respectively gamma and neutron emission, respectively.

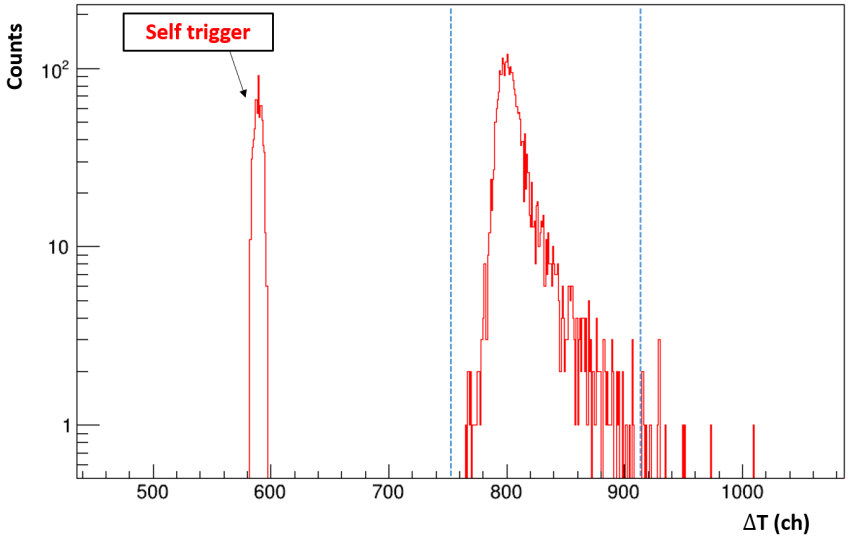

Figure 5.24: Time difference histogram measured for the heavy residue detector. The vertical dashed lines indicate the selection used to define the coincidence events between the protons from the I° solution and the HR detector.

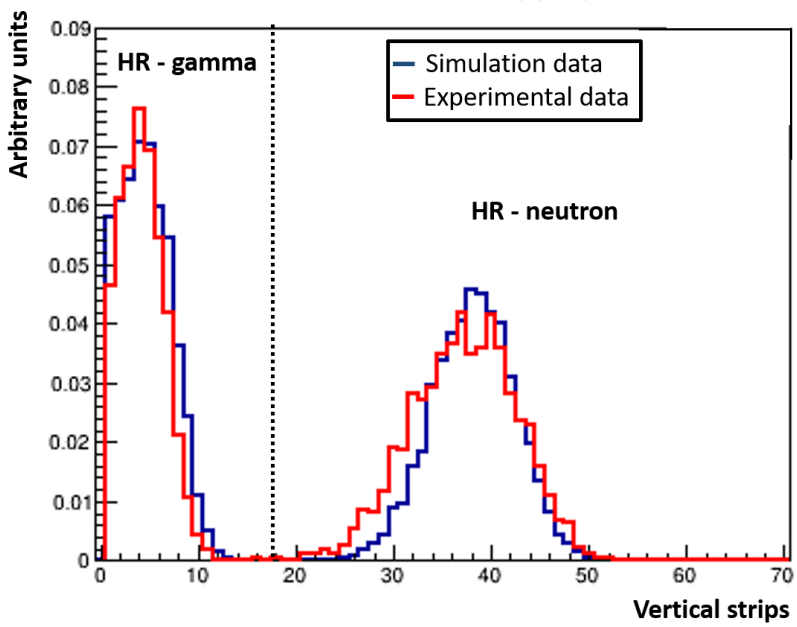

Figure 5.25: Comparison of the simulated and experimental horizontal position distributions of the heavy residues. Excitation energies between 5.6 and 9.5 MeV were considered. The edge of the heavy residue detector is at $x = 0$.

window of interest is generated by the telescope, are located in the coincidence peak.
Heavy residues produced by gamma and neutron emission from $^{208}Pb^{\star}$ with excitation energies between 5.6 MeV and 9.5 MeV were simulated and propagated up to the HR detector. The results of the simulation are compared to the experimental data in figure 5.25. As can be seen, the simulation reproduces very well the position and the shape of the distribution for both the gamma and the neutron emission residues. These results show clearly the quality of the simulation, which will be used in the next section to infer the detection efficiency ϵ_{χ}.

5.2.6.3 Coincidence spectra for the II° kinematics solution

We followed the same procedure to extract the coincidence events for the second kinematics solution. In this case, the heavy residues have a larger kinetic energy. This can be seen in figure 4.4, where the kinematic plot showing the energy per nucleon of the target and beam-like residues as function of the emission angle is represented. The heavy residues are therefore less bent by the dipole magnet and follow trajectories that are closer to the beam axis. As indicated by the simulations, see figure 5.26(a), most of the heavy residues produced after γ-emission can not be detected, whereas the neutron emission residues are located well inside the detector active area. In figure 5.26(b) we can see the experimental results where the neutron emission coincidence events $N_n(E^{\star})$ are located inside the contour. The time coincidence window used for the coincidence selection is shown in figure 5.27. Also in this case, the experimental horizontal profile of the HR is in good agreement with the simulations, see figure 5.28.

5.3 Detection efficiencies

The detection efficiency of the heavy residues depends on the transmission efficiency between the gas target and the heavy residue detector as well as the geometrical and intrinsic efficiency of the HR detector.

The good quality of our simulations was demonstrated in sections (5.2.6.2) and (5.2.6.3), where the measured distributions of the heavy residue position in the detection plane have been compared with the simulations. For the determination of the transmission efficiency, ^{208}Pb and ^{207}Pb residues produced after elastic and inelastic scattering and associated to protons detected in the telescope were propagated up to the HR detection station. We found that all the ^{207}Pb and ^{208}Pb residues reach the heavy residue detector station, indicating that the transmission efficiency is 100%.

The intrinsic efficiency of the heavy residue detector for the ^{207}Pb and ^{208}Pb residues is also 100%. This was verified in different ways. Firstly, we checked that the amplitude of the HR signal is much larger than the threshold (around 500 ch) also for interstrip events. In figure 5.29, the signal amplitude, measured by the vertical strip 2 is represented as a function of the amplitude in strip 1. Only HR measured in coincidence with protons of the I° kinematics solution are considered. The threshold condition is represented in the spectrum by the dashed black lines at channel 500. If an event falls inside the region delimited by the dashed lines, the amplitude is below the threshold and it will be automatically lost. From figure 5.29 we can see that, a part from the events in the pedestal corresponding to events were other strips were hit, all the single and interstrip events have an amplitude larger than 500 ch. In the y-axis, representing the amplitude of the strip 2, the events within the red contour are interstrip events between the vertical strips 2 and 3. Strips 2 and 3 received the largest rates of Rutherford scattered events. However, figure 5.29 shows that the amplitudes remained well above the threshold during the experiment for single strip and interstrip events, demonstrating that the intrinsic detection efficiency is 100%.

Secondly, we checked that the number of detected protons was equal to the number of HR for protons emitted at low scattering angle and low excitation energy of the compound nucleus, where we know that, the HR detector geometrical efficiency is 100%. This also demonstrates that the intrinsic efficiency is 100 %.

On the contrary, the geometrical efficiency for γ emission can be significantly reduced due to the position of the HR. As described in section 4.4.5 and 5.2.6.1, due to the high rate of Rutherford scattering events, we had to place the HR detector at 15 mm from the beam axis preventing us to detect the γ-emission residues following trajectories close to the beam.

For the neutron emission the ^{207}Pb ions are significantly deflected by the dipole, due to their lower mass, and their position in the HR detector is located far from the edge. This implies that

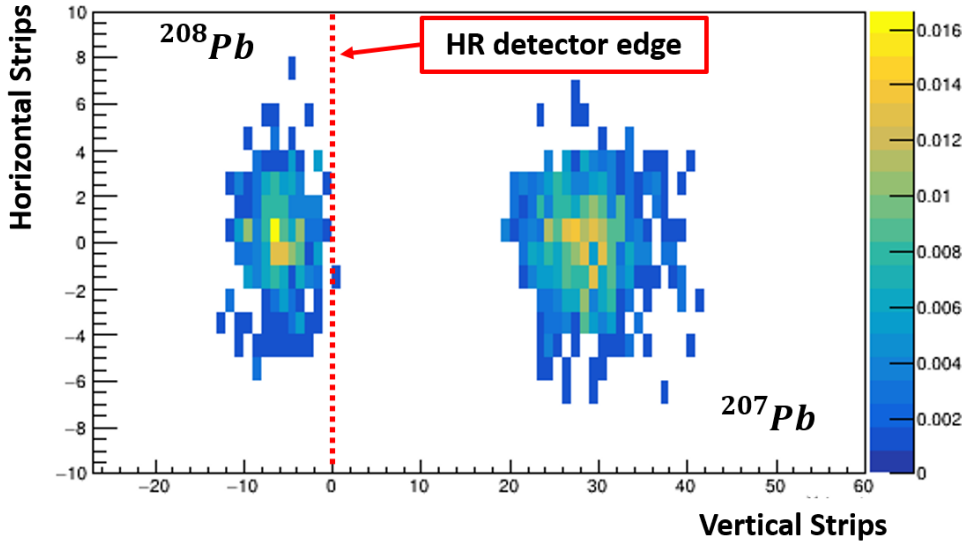

(a)

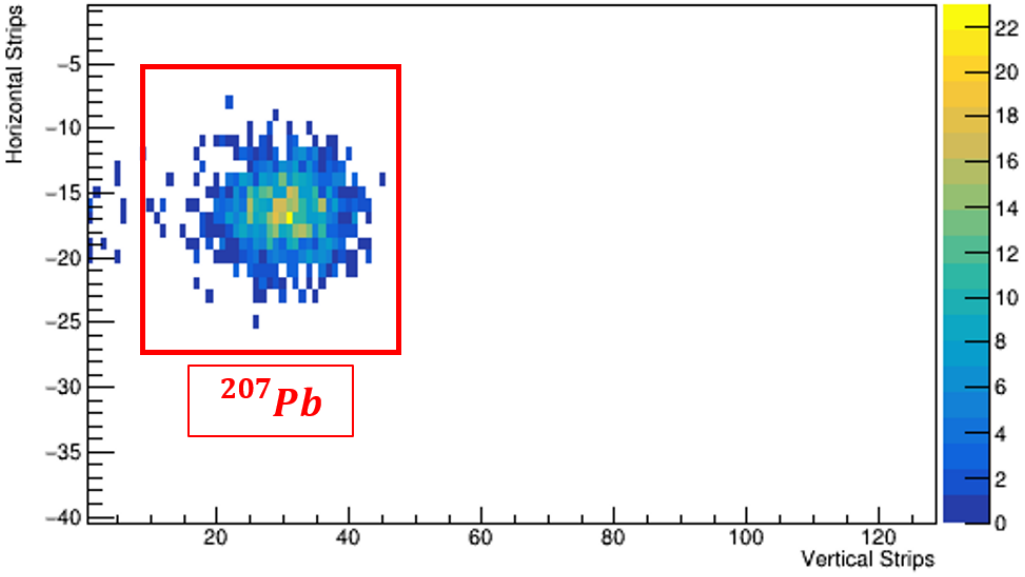

(b)

Figure 5.26: Figure (a) shows the position distributions of the heavy residues obtained from the simulations. The edge of the detector is indicated by the dotted line. Figure (a) shows the experimental results and the contour selects the neutron-emission coincidence events. The heavy residues are detected in coincidence with protons from the second kinematics solution.

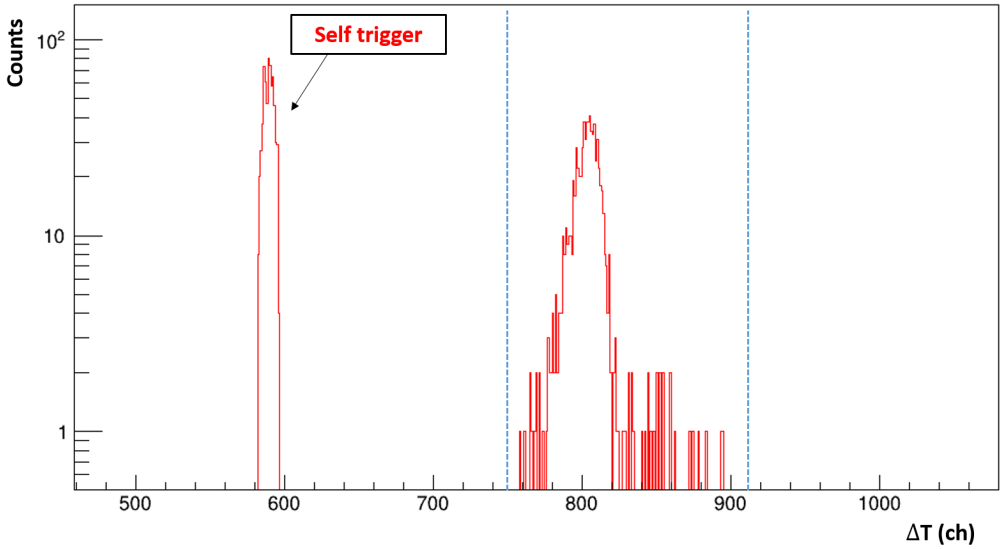

Figure 5.27: Time difference histogram measured for the telescope and the heavy residue detector. The vertical dashed lines indicate the selection used to define the coincidence events for the second kinematics solution.

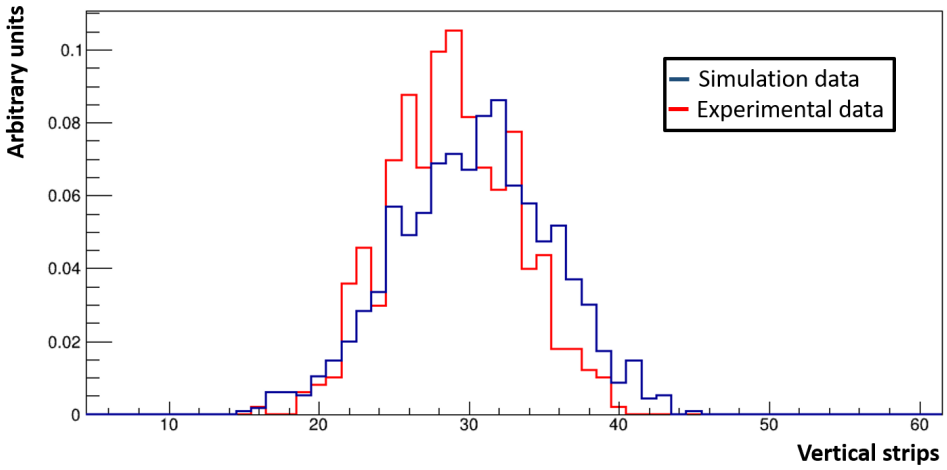

Figure 5.28: Comparison of the simulated and experimental horizontal position of the heavy residues for the second solution. Only the neutron emission residues could be detected in this case.

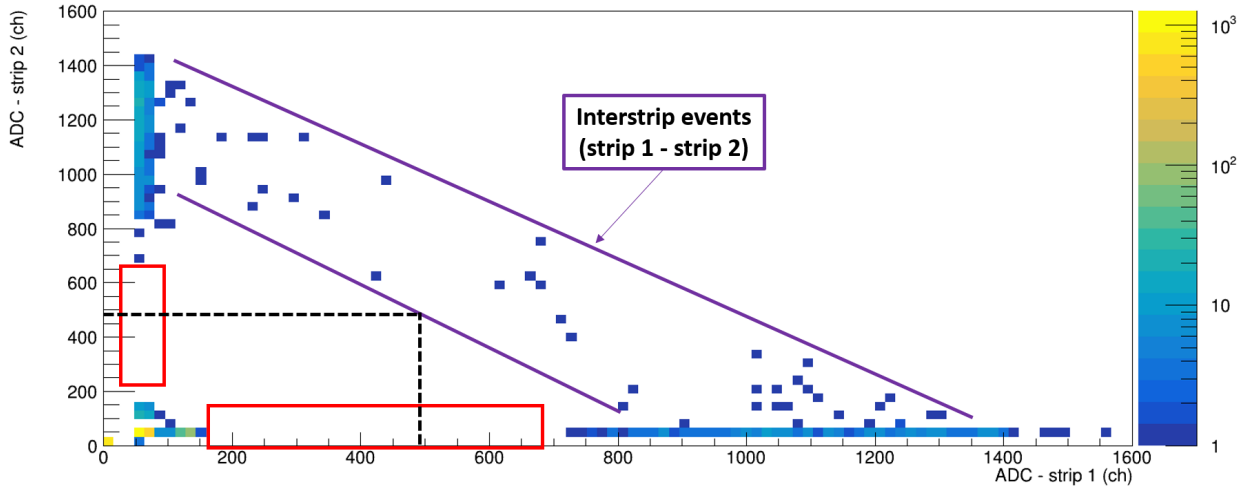

Figure 5.29: Amplitude measured in strip 2 versus amplitude in strip 1 for HR detector in coincidence with protons of the I° kinematic solution. The interstrip events are between the purple lines and the red contour continuous interstrip events with other vertical strips. The black dashed lines mark the threshold used for the selection of the HR.

the detection efficiency for neutron emission, independently from the scattering angle θ and the excitation energy, is 100%. To benchmark the simulations, we compared the simulated detection efficiency ϵ_γ with the one obtained experimentally at $E^\star < S_n$. Indeed, for $E^\star < S_n = 7.37\,MeV$ γ emission is the only possible decay channel. Therefore, the ratio of the number of coincidences over the number of singles events, $N_\gamma(E^\star)/N_s(E^\star)$, is equal to the detection efficiency ϵ_γ. The simulated and experimental efficiencies obtained for strips 8 and 9 are compared in figure 5.30. The results agree within the error bars giving us confidence on the simulation. In the experiment the ϵ_γ varied between 55% to 100% depending on $E^\star$ and θ. The efficiencies ϵ_γ are much larger than the efficiencies achievable in direct kinematics of typically 5% [San20]. The uncertainty in the detection efficiency is given by fluctuations in the position of the detector and in the position of the HR. The first type of fluctuation is defined by the accuracy in the positioning of the pneumatic system of the HR detector drive, which has been been estimated to be 0.1 mm [Ste03]. The second type of fluctuations was estimated by monitoring the position of the HR during the experiment. We observed position fluctuations of about 0.7 mm. To define the uncertainty in ϵ_γ we varied the position of the HR detector in the simulation by ± 0.7 mm. This resulted in an absolute variation of ϵ_γ of 5-8 %.

Note that the beam position fluctuations do not affect the neutron detection efficiency ϵ_n, which has no uncertainty. This aspect and the 100% value of ϵ_n demonstrate the enormous advantages of our new methodology.

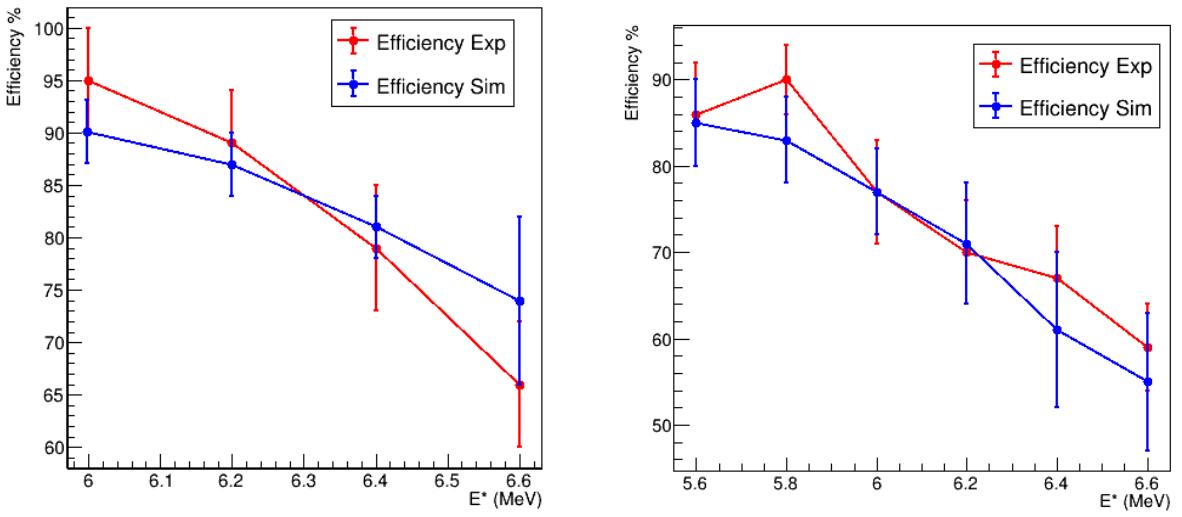

(a) (b)

Figure 5.30: Comparison between the simulated (blue circles) and experimental (red circles) γ-emission detection efficiency ϵ_γ as a function of the excitation energy. The experimental efficiency is given by the ratio $N_\gamma(E^\star)/N_s(E^\star)$. The results obtained for strip 8 are shown in panel (a) and for the strip 9 in panel (b).

5.4 Uncertainty analysis

The uncertainties of the probabilities were derived using the error propagation formula (5.8), which relies on the assumption that the uncertainties are small enough so that the function of the measured quantities x_i, $f(x_1, x_2, .., x_n)$, can be approximated by a first order Taylor expansion $f \approx f(x_0) + f'_{x_0} \cdot (x - x_0)$:

$$(\Delta f(x_1, ..., x_n))^2 = \sum_{i=1}^{n} \sum_{j=1}^{n} \frac{\partial f}{\partial x_i} \frac{\partial f}{\partial x_j} \sigma_{x_j} \sigma_{x_i} \rho_{ij} \tag{5.8}$$

where ρ_{ij} are the correlation coefficients $\rho_{ij} = cov(x_i, x_j)/\sqrt{\sigma_{x_i}^2 \cdot \sigma_{x_j}^2}$ and $cov(x_i, x_j)$ is the covariance between x_i and x_j. Let us recall equation (1.43):

$$P_\chi(E^\star) = \frac{N_\chi(E^\star)}{N_s(E^\star) \cdot \epsilon_\chi(E^\star)} \tag{5.9}$$

Inserting equation (5.9) into equation (5.8) we obtain:

$$\frac{\sigma^2(P_\chi(E^\star))}{(P_\chi(E^\star))^2} = \frac{\sigma^2(N_\chi(E^\star))}{(N_\chi(E^\star))^2} + \frac{\sigma^2(N_s(E^\star))}{(N_s(E^\star))^2} + \frac{\sigma^2(\epsilon_\chi(E^\star))}{(\epsilon_\chi(E^\star))^2} - 2\cdot\frac{Cov(N_\chi(E^\star),N_s(E^\star))}{N_\chi(E^\star)\cdot N_s(E^\star)} - 2\cdot\frac{Cov(N_\chi(E^\star),\epsilon_\chi(E^\star))}{N_\chi(E^\star)\cdot\epsilon_\chi(E^\star)} + 2\cdot\frac{Cov(N_s(E^\star),\epsilon_\chi(E^\star))}{N_s(E^\star)\cdot\epsilon_\chi(E^\star)} \tag{5.10}$$

Previous work of our collaboration [Kes15, Duc15] has already demonstrated the importance of considering the covariance terms, indicated in equation (5.10), which can significantly impact the uncertainty on the probabilities. In our experiment the detection efficiencies ϵ_χ are determined with the simulations and are therefore completely independent from the measured quantities, allowing us to neglect the two last terms in equation 5.10.
This implies that the covariance term between N_χ and N_s can significantly reduce the uncertainty of P_χ. The covariance term $Cov(N_\chi, N_s)$ measures how fluctuations in N_s affects the value of N_χ. G. Kessedjian et al. [Kes15] showed that:

$$Cov(N_\chi, N_s) = \sigma^2(N_\chi) \tag{5.11}$$

Assuming that N_χ and N_s follow Poissons statistics it results that $\sigma^2(N_\chi) = N_\chi$ and $\sigma^2(N_s) = N_s$. In [Duc15] it was shown that it is possible to infer the $Cov(N_\chi, N_s)$ directly from the experimental data by dividing the single events in groups with a number of events N that fluctuated following a gaussian distribution with mean value w and standard deviation $\sqrt{w}$. The number of coincidence events associated to each group of single events was then represented as a function of the number of singles events in each group. This representation clearly illustrates the degree of correlation between the two quantities and enable the determination of $Cov(N_\chi, N_s)$. In this work, we have applied this procedure by considering a fluctuating number of singles events in the excitation energy range from 7.7 MeV to 7.9 MeV. The resulting number of coincidence events for γ and neutron emission are represented as a function of the number of events in figure 5.31. The same group of single events was used with the number of single events fluctuating around a value of 50 events. The correlation between N_χ and N_s can be clearly seen in figure 5.31(a). Using the equation:

$$Cov(N_\chi, N_s) = \frac{1}{n}\sum_{i=1}^{n}(N_\chi - < N_\chi >)\cdot(N_s - < N_s >) \tag{5.12}$$

where $< N_\chi >$ and $< N_s >$ are the mean values and n is the number of groups of data sampled. With the data in figure 5.31, we obtain the covariances $Cov(N_\gamma, N_s) = 82$ and $Cov(N_n, N_s) = 93$, which are in agreement with $\sigma^2(N_\gamma) = 81$ and $\sigma^2(N_n) = 91$, respectively, thus validating

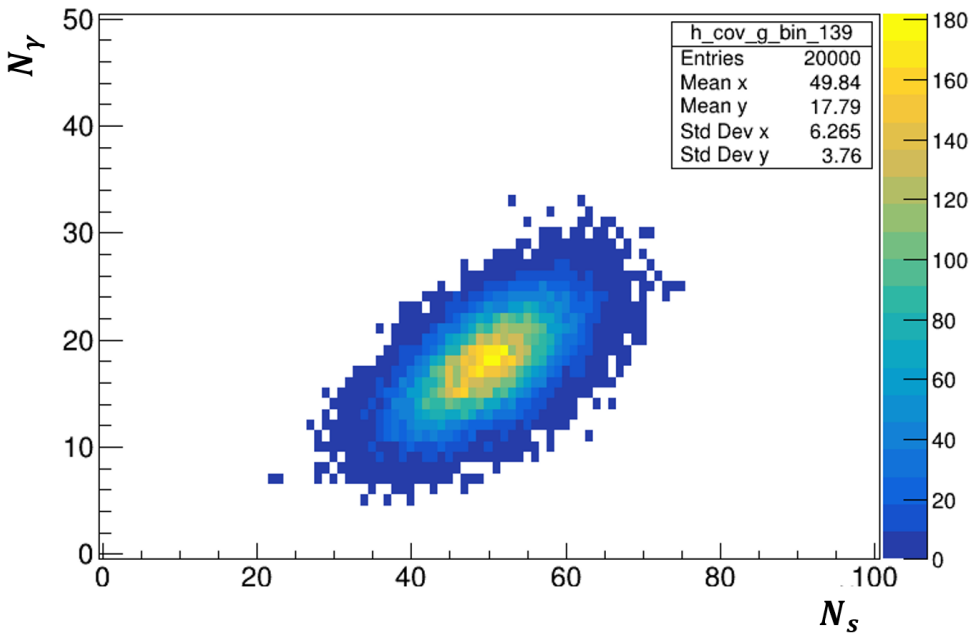

(a)

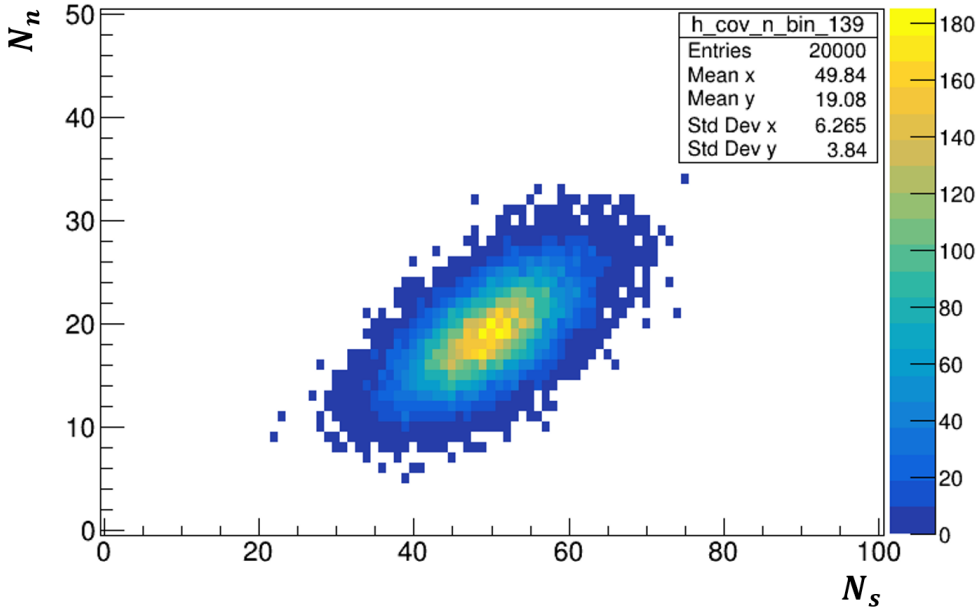

(b)

Figure 5.31: Bi-dimensional spectrum showing the correlation between the number of coincidence N_χ and the number of singles N_s events in the excitation energy range from 7.7 MeV to 7.9 MeV. Figure (a) shows the correlation N_γ versus N_s while figure (b) shows correlation N_n versus N_s.

equation (5.12). If we use equations (5.10), (5.12), $\sigma(N_\chi) = \sqrt{N_\chi}$ and $\sigma(N_s) = \sqrt{N_s}$ we get:

$$\sigma(P_\chi(E^\star)) = \sqrt{P_\chi^2(E^\star)(\frac{1}{N_\chi(E^\star)} + \frac{1}{N_s(E^\star)} + \frac{\sigma_{\epsilon_\chi}^2(E^\star)}{\epsilon_\chi^2(E^\star)} - \frac{2}{N_s(E^\star)})} \tag{5.13}$$

When the decay probability is close to 1 and the detection efficiency is close to 100 %, $N_\chi \approx N_s$ and from equation (5.13) we see that the uncertainty in the decay probability is determined by the uncertainty in the detection efficiency. Our experiment is characterized by very large and precise efficiencies. This will lead to rather low uncertainties, even with limited statistics, in particular when the probabilities are close to 1. Equation 5.13 was used to evaluate the uncertainty of the decay probabilities for the individual strips and for the first and second kinematics solutions. Note that for the neutron emission probability there is no uncertainty in ϵ_n and so the third term of the equation 5.13 is equal to zero. For every strip the singles spectrum was divided in $E^\star$ bins with a width of 200 keV. This bin size was chosen to ensure sufficient statistics to achieve a maximum error on the probabilities of about 20%.

5.5 Results

For each excitation energy bin the probabilities provided by different strips $P_i(E^\star)$ were determined together with the corresponding uncertainties σ_{P_i}. The different $P_i(E^\star)$ are in agreement within the error bars. Therefore, the final probabilities for each $E^\star$ bin was then obtained by calculating the weighted mean of the probabilities $P_\chi(E^\star)$:

$$< P > (E^\star) = \frac{\sum_i P_i(E^\star)/\sigma_{P_i}^2(E^\star)}{\sum_i 1/\sigma_{P_i}^2(E^\star)} \tag{5.14}$$

The corresponding standard deviation is given by the expression:

$$\sigma_{<P>}(E^\star) = (\sum_i 1/\sigma_{P_i}^2(E^\star))^{-1/2} \tag{5.15}$$

Figure 5.32 shows the gamma (red circles) and neutron (blue circles) decay probabilities as a function of the excitation energy obtained with equation (5.14) and (5.15). The sum of the two probabilities is represented by the black circles. The horizontal error bars correspond to the chosen bin size in excitation energy.
We can see that the gamma emission probability is 1 at lowest $E^\star$ and starts to decrease near S_n, due to the competition with the neutron emission. Since gamma and neutron emission are the only open de-excitation channels within the covered excitation energy range, the sum of the two probabilities has to be equal to 1. This is well satisfied by our data as reflected by the black dots. This result is very important as it validates our new methodology and in particular the determination of the γ detection efficiency ϵ_γ.

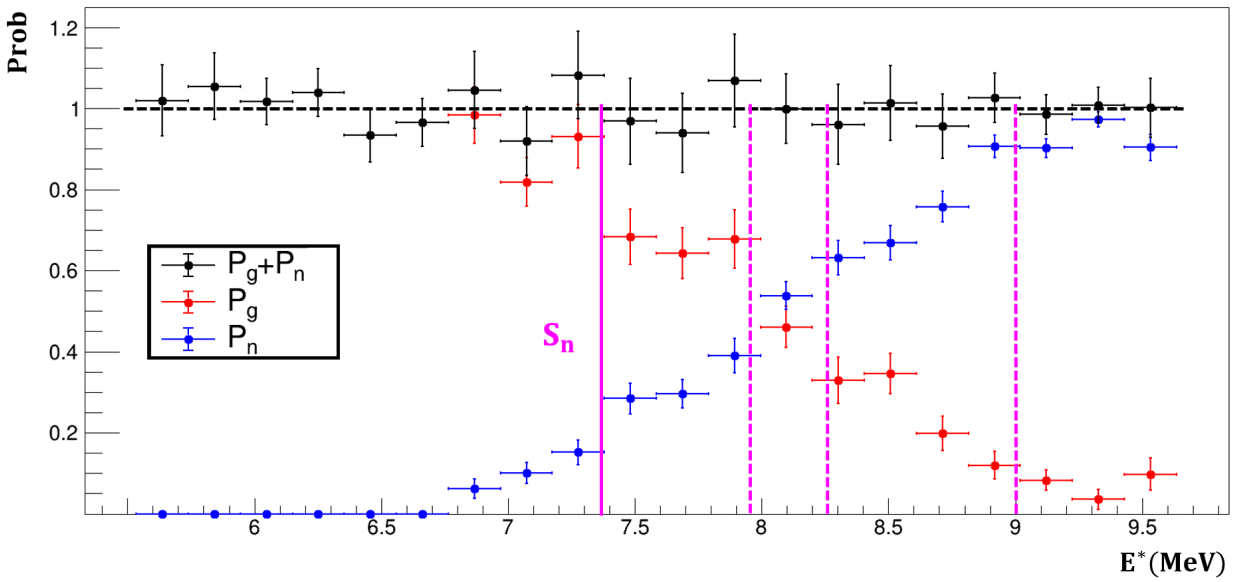

Figure 5.32: The probabilities for gamma (red circles) and neutron (blue circles) emission obtained with first kinematic solution are shown as a function of the excitation energy $E^{\star}$ of ^{208}Pb. The black points represent the sum of the γ and neutron-emission probabilities. The pink vertical line indicates the neutron separation energy S_n of $^{208}Pb^{\star}$ and the constant horizontal line at P=1 is to guide the eye.

We stress that it is the first time that the neutron emission probability is measured and this probability sets in at an $E^{\star}$ somewhat below S_n. As we will see in chapter 6, this can be explained by the excitation energy resolution. A strong variation of the probabilities is observed at several places, like near S_n and at $E^{\star} \simeq 9\ MeV$, with a strong increase (decrease) of the neutron emission (gamma emission) probability. In next chapter we will compare the probabilities with theoretical calculations and give an interpretation for the different structures.
For the second kinematics solution, as discussed in sections 5.2.6.3, the residues from gamma emission could not be detected by the HR detector. Therefore, only the neutron decay probability as function of the excitation energy was determined, see figure 5.33. Also in this case the probability sets in below the neutron separation energy and some structure can be observed.

Figure 5.34 shows the comparison between the neutron emission probabilities obtained for the I° and II° kinematics solution and overall a good agreement can be found. The second solution shows structures at S_n and around 9 MeV, but there are differences with respect to the I° solution around 9 MeV were the II° shows less pronounced effects. We will further discuss the results in the next chapter.

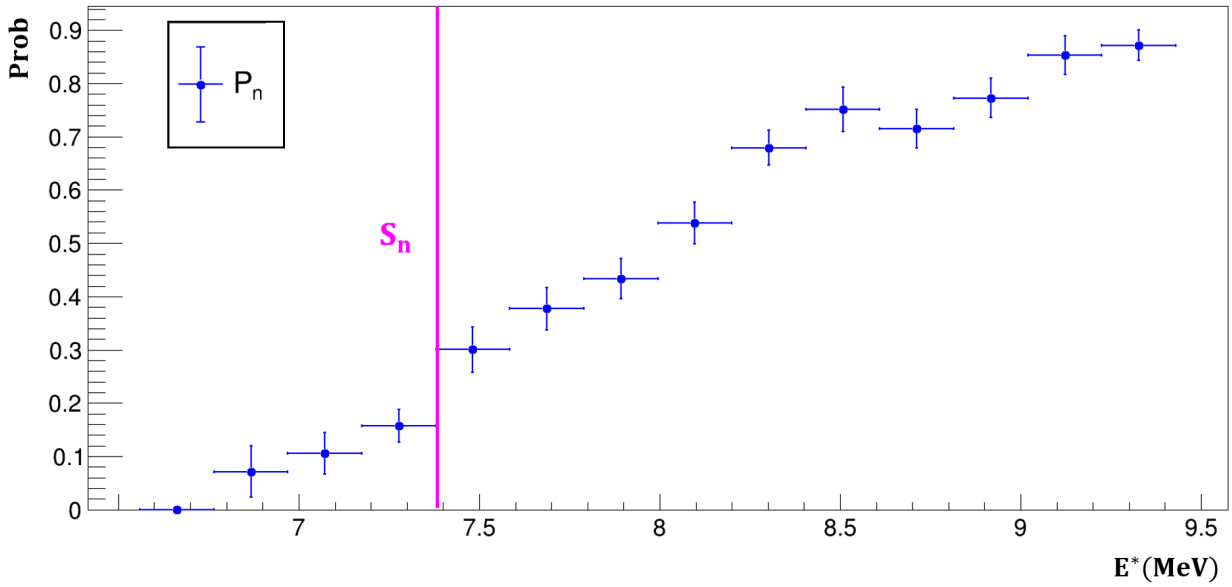

Figure 5.33: Neutron emission probability of ^{208}Pb as a function of the excitation energy obtained with the II kinematics solution. The pink vertical line indicates the neutron separation energy S_n of $^{208}Pb^{\star}$.

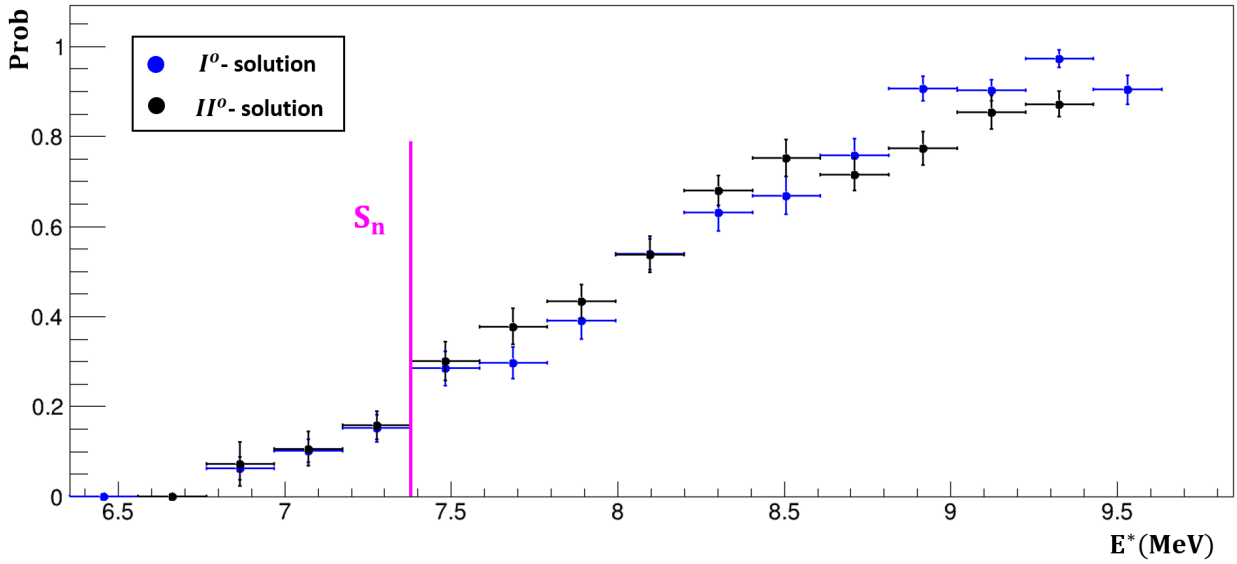

Figure 5.34: Comparison between the neutron emission probabilities of ^{208}Pb obtained with the $I°$ (blue circles) and the $II°$ (black circles) kinematic solution. The pink vertical line indicates the neutron separation energy S_n of $^{208}Pb^{\star}$.

Chapter 6

Comparison with model calculations

In this chapter we will compare our experimental results with statistical model calculations. As described in chapter 1, the condition for the applicability of the surrogate method is the formation of a compound nucleus whose decay can be described by the Hauser-Feshbach formalism [Hau52]. In section 1.4 we saw that the probability for the de-excitation of a compound nucleus through the decay channel χ obtained with a surrogate reaction is given by:

$$P_{\chi}^{surr.}(E^{\star}) = \sum_{J^{\pi}} F_{surr.}^{CN}(E^{\star}, J^{\pi}) \cdot G_{\chi}(E^{\star}, J^{\pi}) \tag{6.1}$$

where $F_{surr.}^{CN}(E^{\star}, J^{\pi})$ is the spin-parity distribution of the formed compound nucleus at $E^{\star}$, populated by the surrogate reaction, and $G_{\chi}(E^{\star}, J^{\pi})$ is the branching ratio for the de-excitation of the compound state via decay channel χ. In this work the spin-parity distribution term $F_{surr.}^{CN}$ was calculated by M. Dupuis (CEA/DAM/DIF) and the branching ratios G_{χ} with Talys code version 1.96.

6.1 Calculation of the spin-parity distribution

The model used to infer the J^{π} distribution populated in the $^{208}Pb(p,p')$ reaction was validated by comparison with the experimental angular distribution of several excited states of ^{208}Pb populated by the $^{208}Pb(p,p')$ reaction at different energies. As can be seen in figure 6.1, the calculations agree well with experimental data, giving confidence on the model. The capability of this model to describe also the (n,n), (n,n'), (p,p), (p,p') angular distributions of ^{208}Pb neighbouring nuclei is shown in [Dup19].

Since the spin-parity distribution depends on the scattering angle, the calculations were done for two different angular domains in the center of mass corresponding to the first ($\theta^{CM} = 125-145°$) and the second ($\theta^{CM} = 150-165°$) kinematics solution. In figure 6.2 the average spin as a function of the excitation energy is shown for different angular ranges. In the calculation spins up to 16 $\hbar$ are considered. Within the $E^{\star}$ range of interest, for this work the average spin

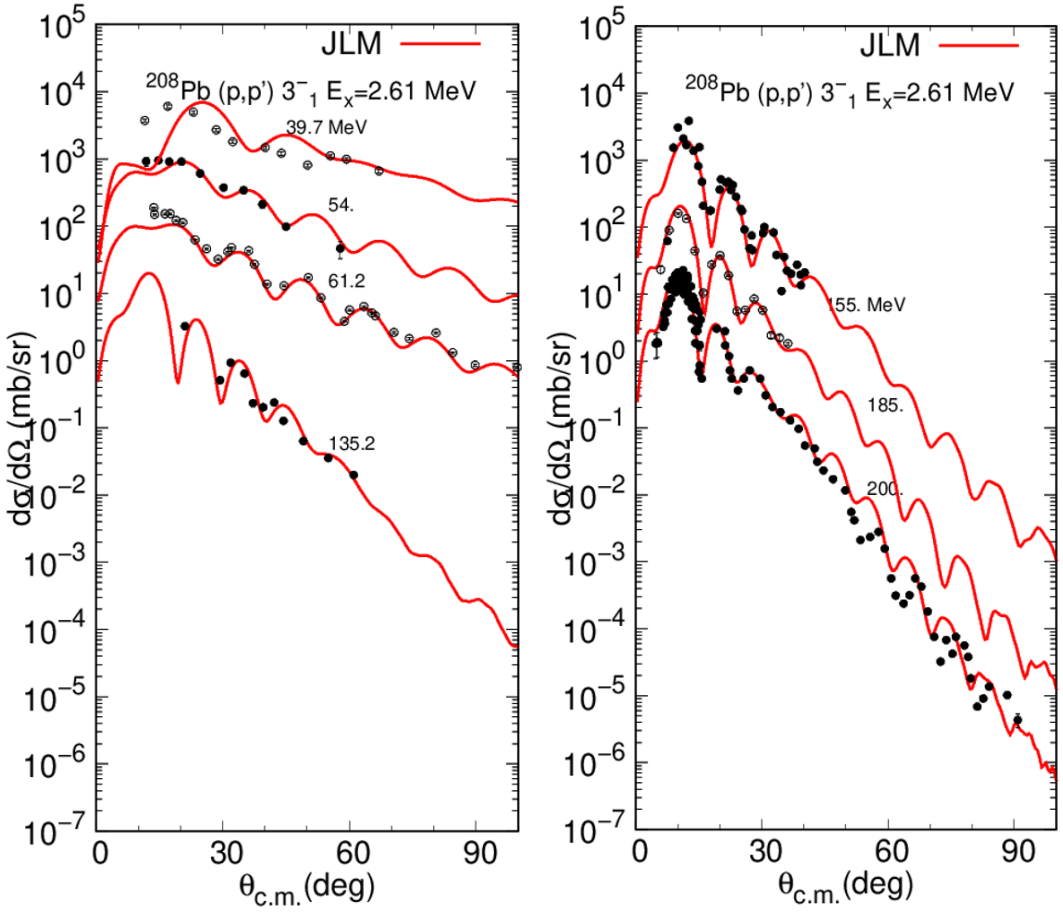

(a) (b)

Figure 6.1: Comparison between experimental data (symbols) and calculations for the inelastic scattering reaction $^{208}Pb(p,p')$ to the first excited state (3^- state) of ^{208}Pb. Incident energies are indicated above each curve. Cross sections are offset by a factor of 10. The calculations were provided by M. Dupuis.

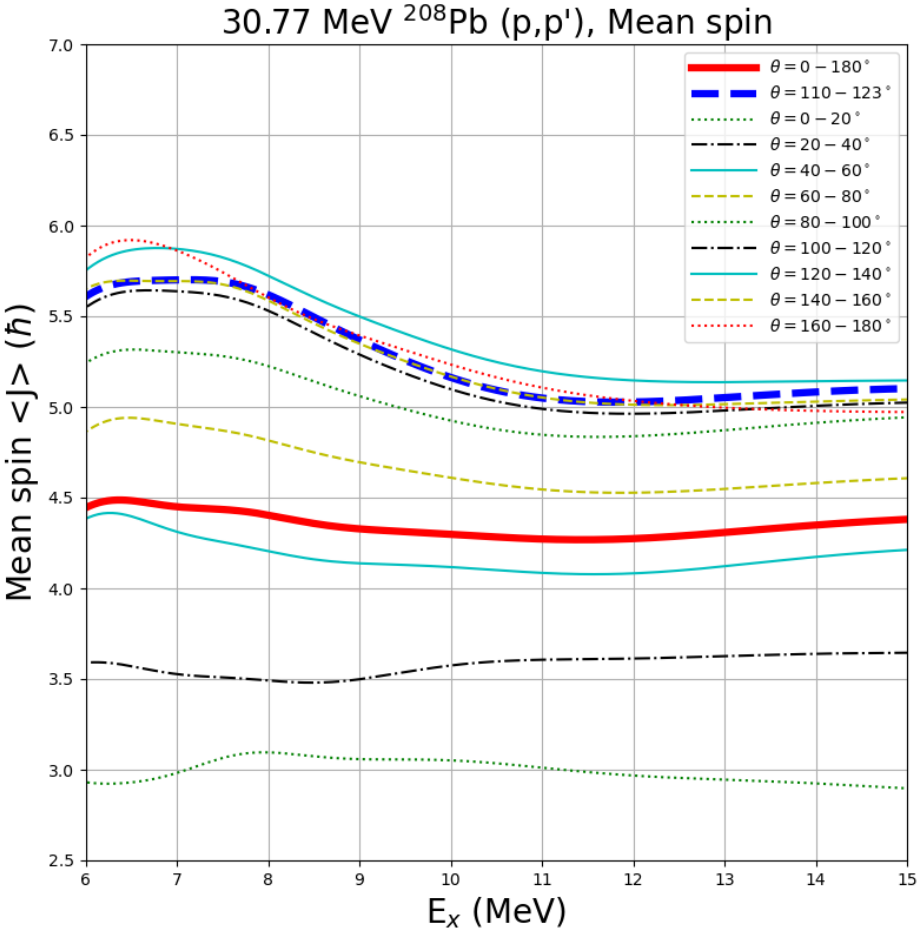

Figure 6.2: Calculated average angular momentum populated in the $^{208}Pb(p,p')$ reaction. Different angular ranges in the center of mass are considered. The calculations were done by M. Dupuis following the approach of [Dup19, Dup06].

varies from ~ 5.3 to 5.8 $\hbar$. A slight decrease of the spin is observed with increasing excitation energy.

In figure 6.3 we compare the spin parity distributions at $E^{\star}$ of 7, 8 and 9 MeV for positive (a) and negative (b) parities in the angular range $125° - 145°$. Natural parity states $\pi = (-)^{J}$ are more populated than the non-natural states $\pi = (-)^{J+1}$. For negative parities, we can see an increase of the spin distribution at 7 $\hbar$. In figure 6.4, we observe a similar feature for the second angular range $145° - 165°$, corresponding to the second kinematic solution. As it will be shown later, the peak at 7 $\hbar$ has a significant impact on the decay probabilities.

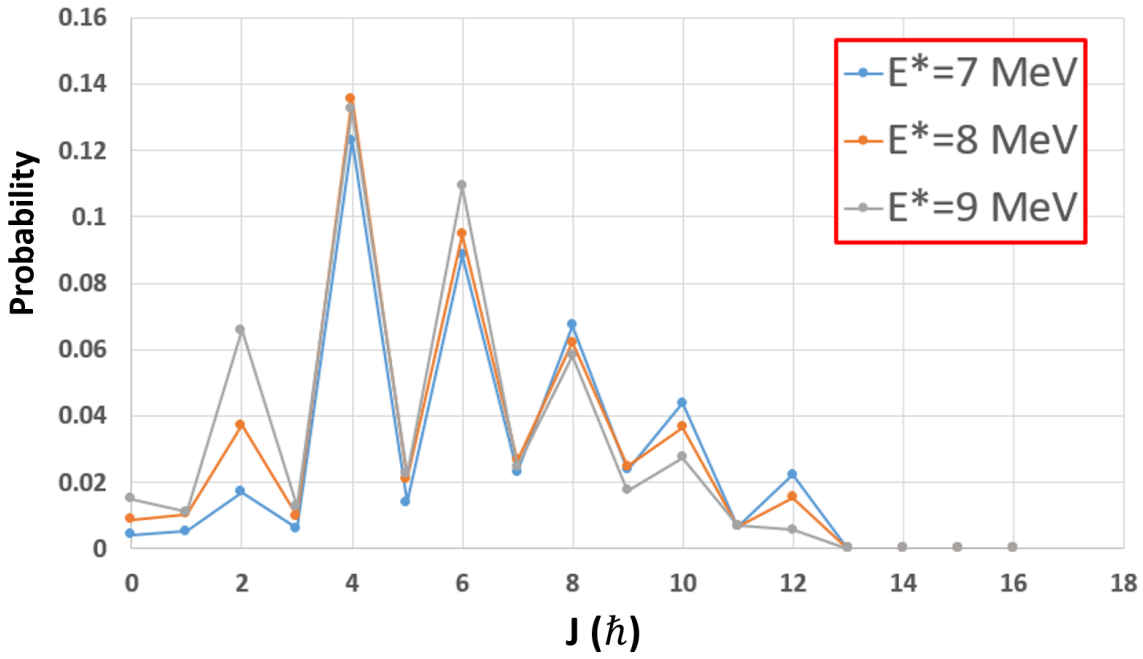

(a)

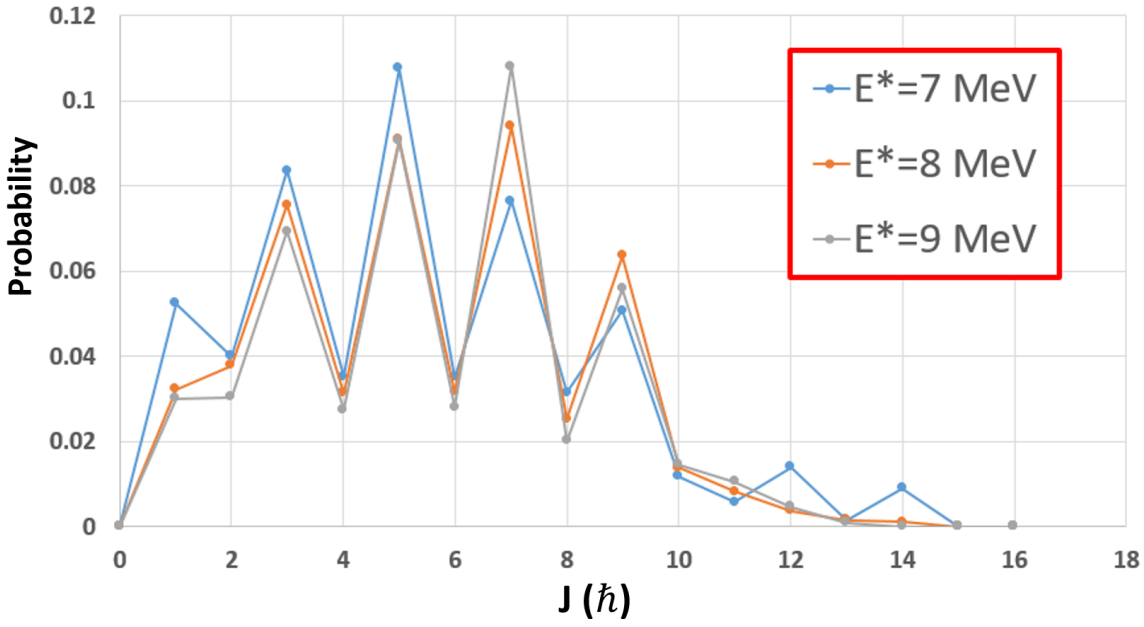

(b)

Figure 6.3: Calculated angular momentum distributions at different $E^{\star}$ and $\theta_{CM} = 125 - 145°$. Positive parities are shown in (a) and negative parities in (b). The calculations were performed by M. Dupuis with the formalism of [Dup06, Dup19] for the $^{208}Pb(p,p')$ reaction at an incident energy of 30.77 MeV.

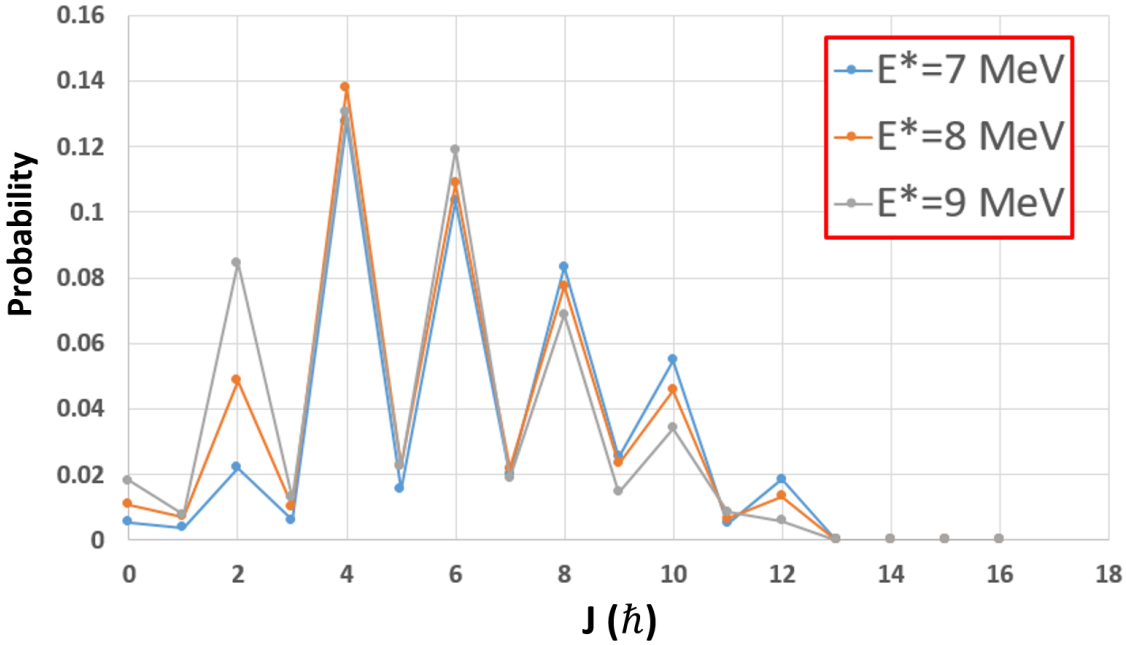

(a)

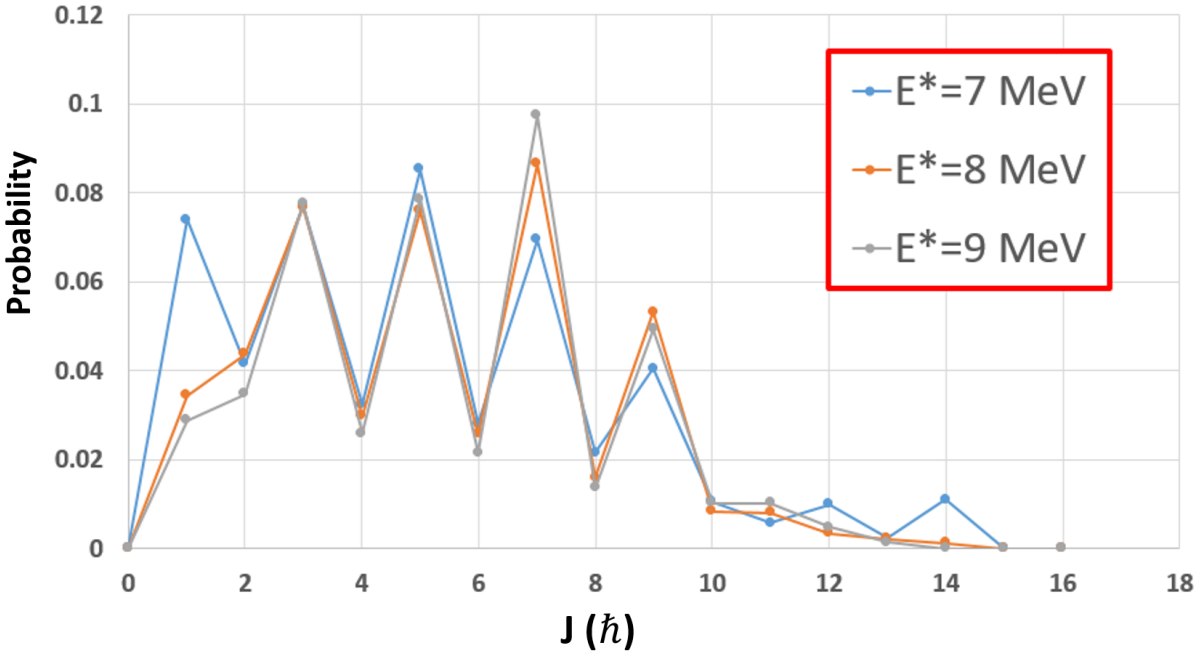

(b)

Figure 6.4: The same as figure 6.3 but for the angular range $\theta_{CM} = 150 - 165°$.

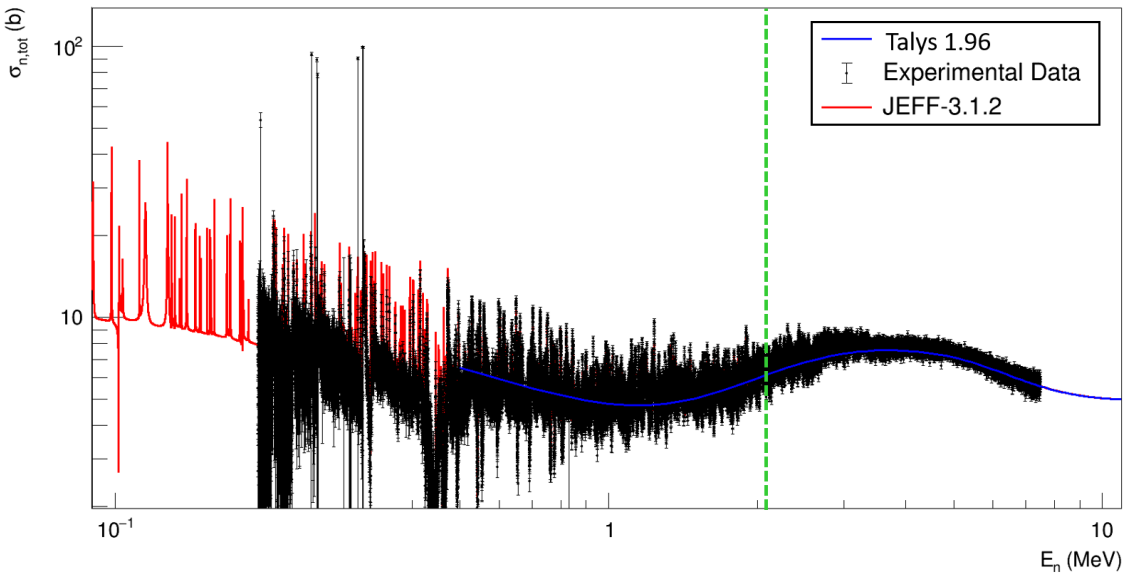

Figure 6.5: Total cross section as a function of incident neutron energy for the $n + {}^{207}Pb$ reaction. The blue solid line is the Talys, the red line is from JEFF-3.1.2 and the symbols are the experimental data from Koehler et al. [Koe87]. The green vertical line represents the maximum equivalent incident neutron energy achievable in this experiment.

6.2 Validation of Talys calculations

As shown in chapter 1, the results provided by Talys depend on a number of parameter values. In this work we did not use the default option of Talys but the so-called "best" option, where the parameters are adjusted in order to best reproduce the data of the reaction under consideration, in our case $n + {}^{207}Pb$. To check the quality of the Talys results, we compared them with experimental data and the JEFF 3.3 evaluation, which represents rather well all the other evaluations. A good agreement will give us confidence in the use of Talys for calculating the branching ratios G_χ of the ${}^{208}Pb$ compound nucleus.

6.2.1 $n + {}^{207}Pb$ Total and elastic reaction cross sections

Abundant high-quality measurements are available for the total cross section. In figure 6.5, the results of Talys for the total cross section as a function of the neutron kinetic energy are compared with the results of the international evaluation JEFF-3.3 and the data of Koehler et al. [Koe87]. Our data allow to explore excitation energies of ${}^{208}Pb$ up to 9.5 MeV, which is equivalent to 2.15 MeV incident neutron energy. At low neutron energies the experimental data show a clear resonance structure. By definition, the statistical model framework cannot describe these structures because this model can only provide energy averaged cross sections. We can see, however, that Talys reproduces very well the smoothed trend of the cross sections. In figure 6.6, the differential cross sections for elastic scattering as function of angle are shown,

for three different energies E_n of the incident neutron. The Talys results (blue line) are compare with the experimental data (black points) and the results of the international evaluation JEFF-3.1.2 (red line). A general good agreement is found between the Talys calculation and the data, although some differences with respect to the data can be observed for low scattering angles (at E_n =1.0 MeV) and large scattering angles (at E_n =0.6 MeV).

6.2.2 Radiative capture and inelastic scattering cross section

In figure 6.7 the radiative capture (n, γ) cross section obtained with Talys is compared to the experimental data by Macklin et al. [Mac64] and the JEFF-3.3 evaluation. The calculated cross section obtained from Talys is in good agreement with the evaluation up to 5 MeV. The inelastic scattering cross section is compared with the experimental data and the JEFF evaluation in figure 6.8. Also in this case, Talys result is found in good agreement with the experimental data up to the maximum equivalent neutron energy reachable in our experiment.

6.3 Validity of the compound nucleus hypothesis

As already said, the applicability of the surrogate reaction method relies in the validity of the CN hypothesis for the neutron and the surrogate reactions. In figure 6.9, the compound nucleus cross section σ_{CN} is compared with the direct σ_{Direct} and pre-equilibrium σ_{PE} cross sections for the $n + {}^{207}Pb$ reaction. The sum of these components is equal to the reaction cross section σ_R, which is represented by the blue line. Below the maximum neutron equivalent energy accessible with our experiment ≈2.15 MeV, we can see that the contribution from the pre-equilibrium and direct reactions can be neglected, supporting the validity of the compound nucleus hypothesis for the $n + {}^{207}Pb$ reaction.
In the case of the ${}^{208}Pb(p, p')$ reaction, the calculations performed with the model [Dup19, Dup06] show also that for $E^\star < 10$ MeV direct and pre-equilibrium components of the γ-emission and neutron emission channels are negligible. This implies that, for this reaction, γ and neutron emission by ${}^{208}Pb$ occur only after the formation of a compound nucleus.

6.4 Calculation of decay probabilities

We used the theoretical spin-parity distributions $F(J^\pi, E^\star)$ obtained for the angular domains 125°-145° and 145°-165° to define the initial state of the nucleus ${}^{208}Pb$ and we employed the statistical model implemented in Talys to describe its decay. This allowed us to calculate the decay probabilities of the compound nucleus as a function of the excitation energy for the first and second kinematics solutions. More precisely, the branching ratios $G_\chi(E^\star, J^\pi)$ from Talys were weighted with the value of $F^{CN}_{surr.}$ corresponding to the same values of J^π and $E^\star$. The

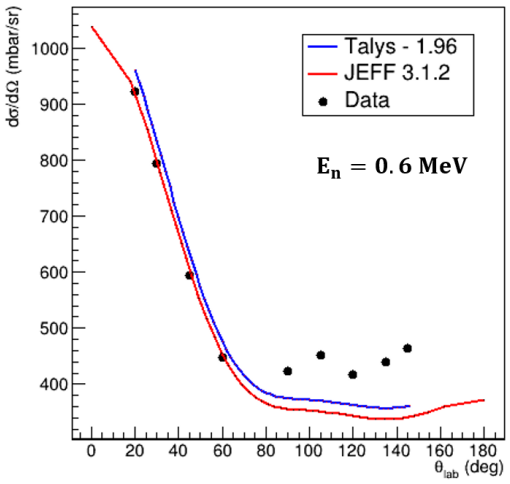

(a)

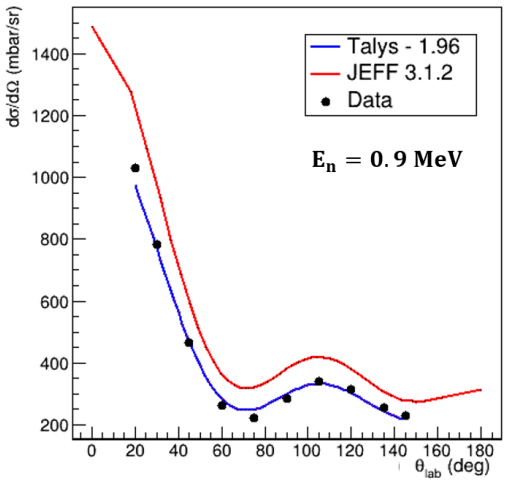

(b)

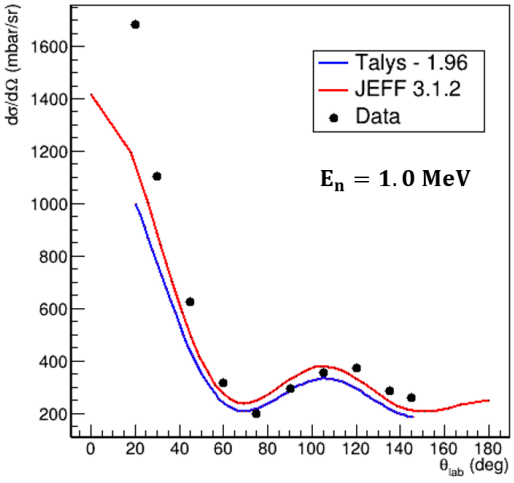

(c)

Figure 6.6: Differential cross sections for neutron elastic scattering $^{207}Pb(n,n)$ as a function of the scattering angle for different neutron incident energies. Talys results are compared with the results from JEFF-3.1.2 and experimental data from Guenther et al. [Gue78].

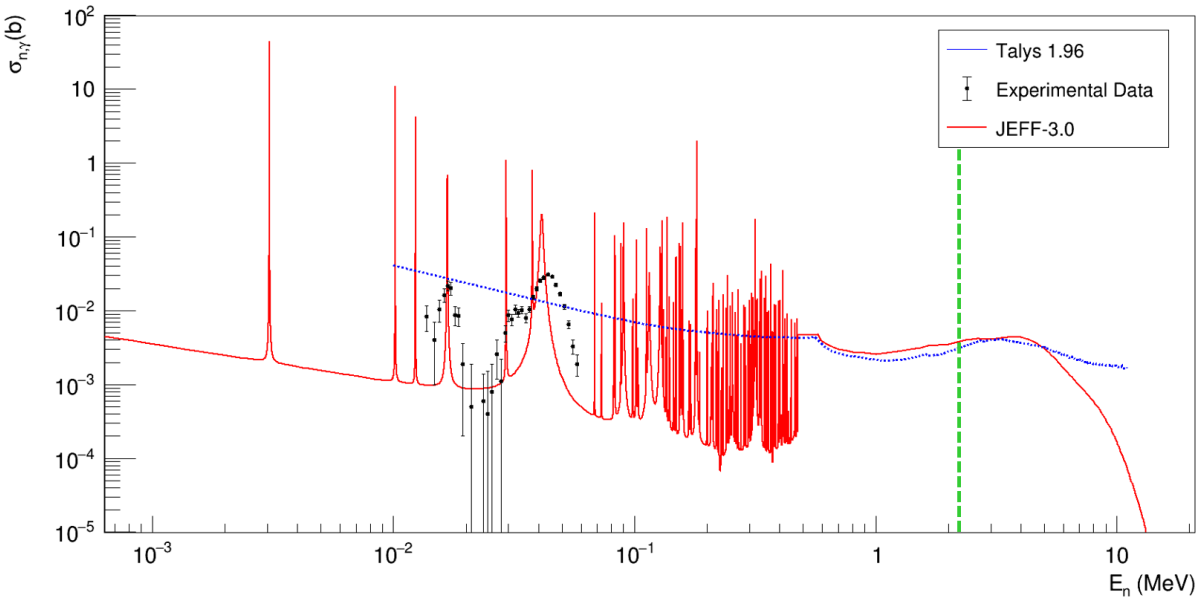

Figure 6.7: The radiative capture cross section $^{207}Pb(n,\gamma)$ of Talys (blue dotted line) is compared to the JEFF evaluation and the experimental data [Mac64]. The maximum incident neutron energy reachable in our experiment of about 2.15 MeV is indicated by the dashed green line.

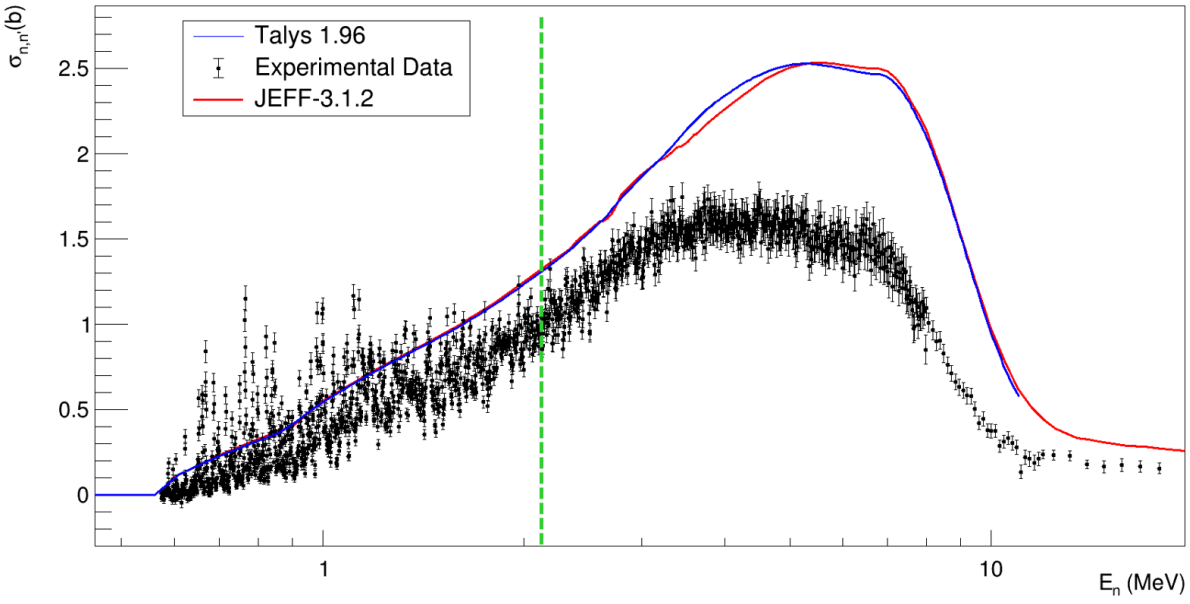

Figure 6.8: The inelastic scattering cross section ^{207}Pb(n,n') calculated by Talys 1.96 (blue line) is compared with the evaluation JEFF-3.1.2 (red line) and the experimental data from [Mih06] (black circles). The vertical line represents the maximum neutron equivalent energy covered by our data.

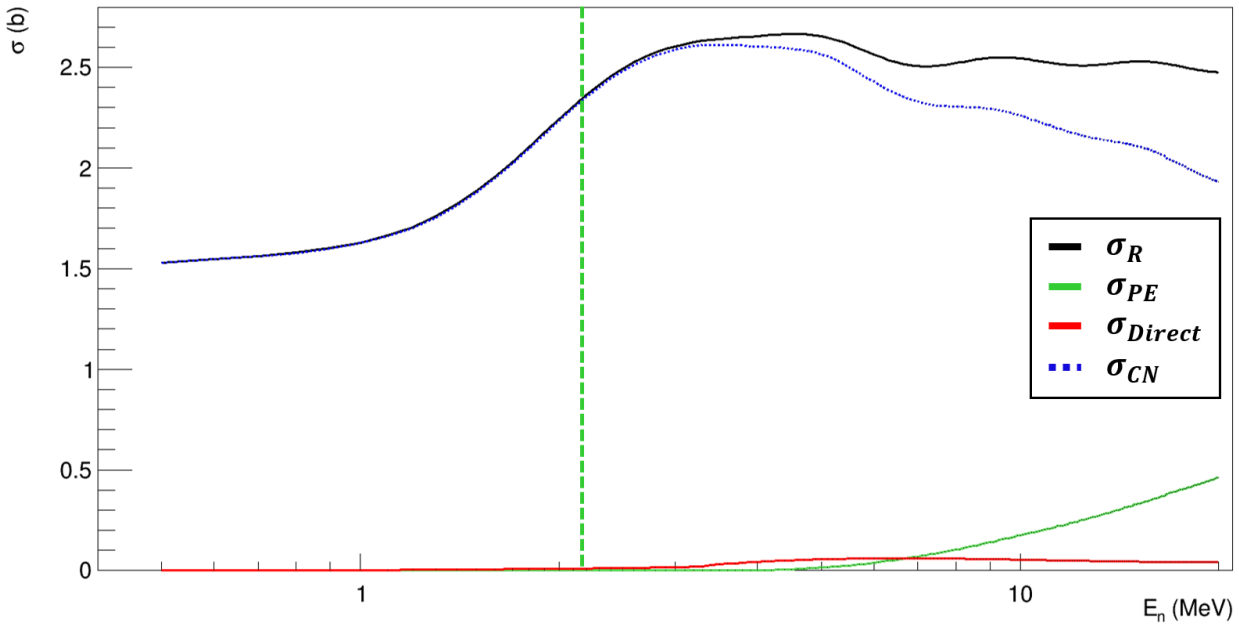

Figure 6.9: Talys results for the reaction (R), compound nucleus (CN), direct (D) and pre-equilibrium (P) cross section as a function of the incident neutron energy on a ^{207}Pb target. The reaction cross section (blue line) is the sum of the other three cross sections. The vertical line represents the maximum neutron equivalent energy covered by our data.

$E^\star$ bin size of Talys calculation was 132 keV. In figure 6.10 the calculated decay probabilities are compared with the experimental ones. A good agreement for both the first and second solution is observed. The experimental results and Talys calculations show clear structures or changes of slope near S_n at around 9 MeV. The structure can be understood by considering the difference between the spin of the decaying nucleus ^{208}Pb and the spin of the ground and first excited states of the residual nucleus produced after neutron emission, ^{207}Pb. This was already discussed in section 1 and is illustrated in figure 6.11 which shows the spins, parities and energies of the ground and first excited states of ^{207}Pb. Figure 6.2 and 6.3 show that for $E^\star > S_n$ the average spin of ^{208}Pb is about 5-6 $\hbar$ for positive parities, with a high probability for J=7 $\hbar$ for negative parities. The spin difference for the third excited state is smaller than for the other excited states, which explains why the probability to decay into the 3rd excited state is enhanced. As remarked in chapter 4, the neutron emission probabilities calculated for the first and second solution were observed to set in before the neutron separation energy S_n at 7.37 MeV. This effect can be understood by considering the impact of the excitation energy resolution. Note for example that Talys neutron emission probability starts slightly below S_n. This is due to the $E^\star$ bin size of the calculations of 132 keV.

To see the impact of the excitation energy resolution we convoluted the decay probabilities calculated from Talys (for the first and second solution) with the excitation energy resolution. This was done with the help of our simulation, by sampling the γ-emission and n-emission

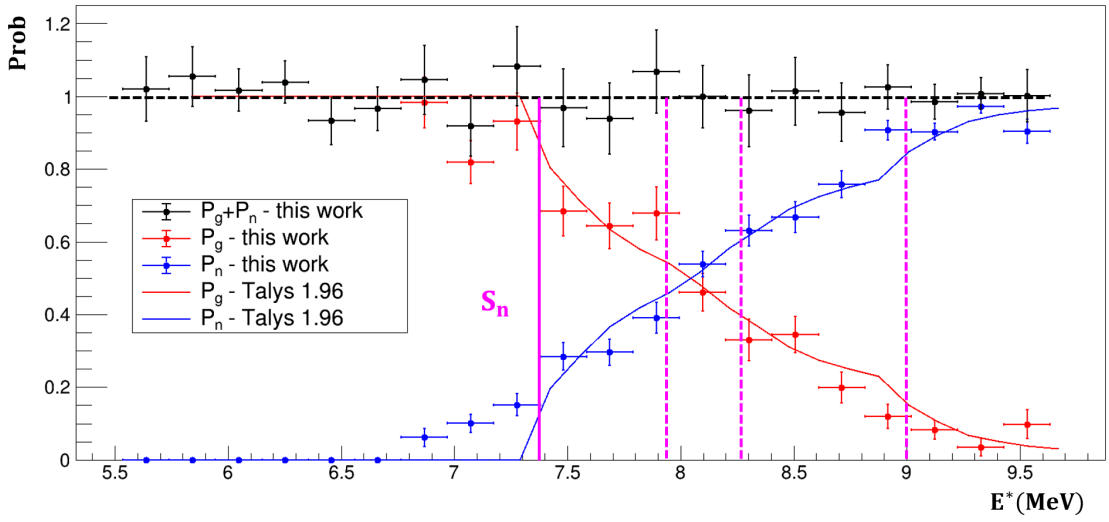

(a)

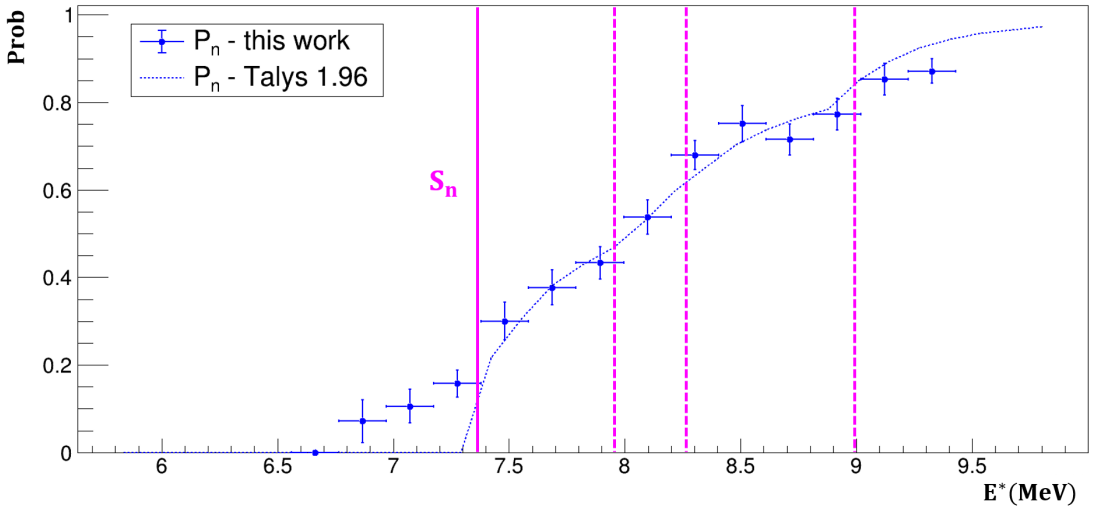

(b)

Figure 6.10: Comparison of the experimental probabilities as a function of the excitation energy of ^{208}Pb, from the first (a) and the second (b) kinematics solution, with the ones calculated with Talys. The γ-decay probability is shown in red and the neutron emission probability in blue. The symbols represent the experimental data and the full lines Talys calculations. In figure (a) the experimental sum of the two probabilities is shown in black. The vertical full lines represents the neutron separation energy and the vertical line dashed lines the position of the first excited states of ^{207}Pb. The horizontal line at $P = 1$ serves to guide the eye.

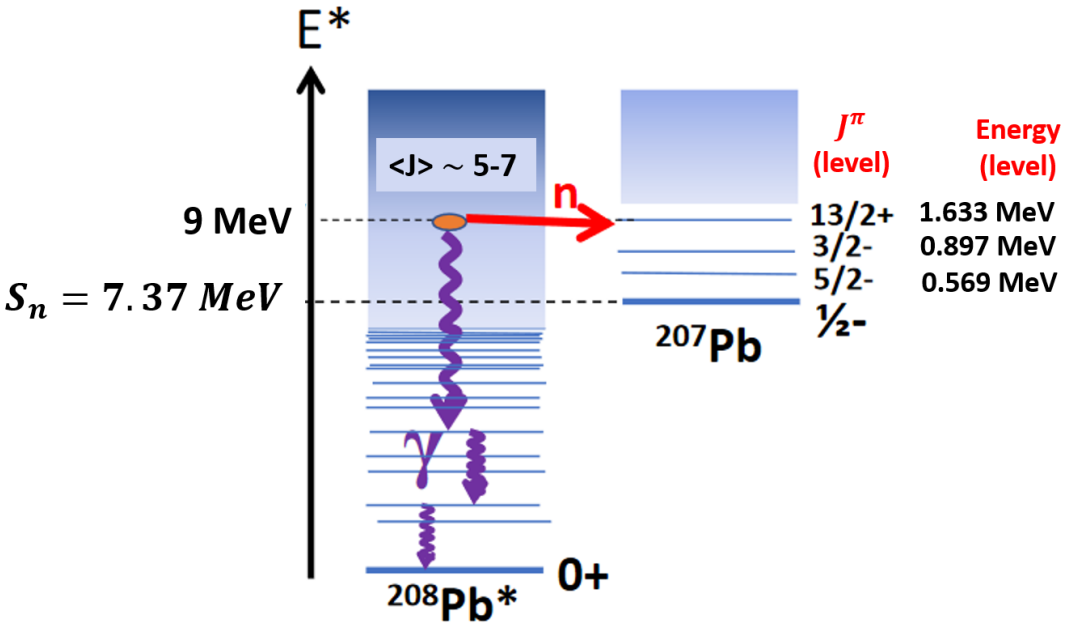

Figure 6.11: Levels scheme of ^{208}Pb and ^{207}Pb. The energy and spin of the first excited states of ^{207}Pb is specified together with the average spin $< J >$ on the formed compound nucleus.

events at different excitation energies with a proportion as given by the decay probabilities of Talys. By tracking the evolution of the target and heavy residues through our set-up (including beam effects, target size, detector resolution, etc), we could then evaluate the probabilities as a function of the measured excitation energy. In figure 6.12 a comparison between the convoluted probabilities and the experimental ones is presented for the first and second solution. The results obtained are in remarkable good agreement, explaining the onset of neutron emission probabilities before S_n by the present excitation energy resolution.

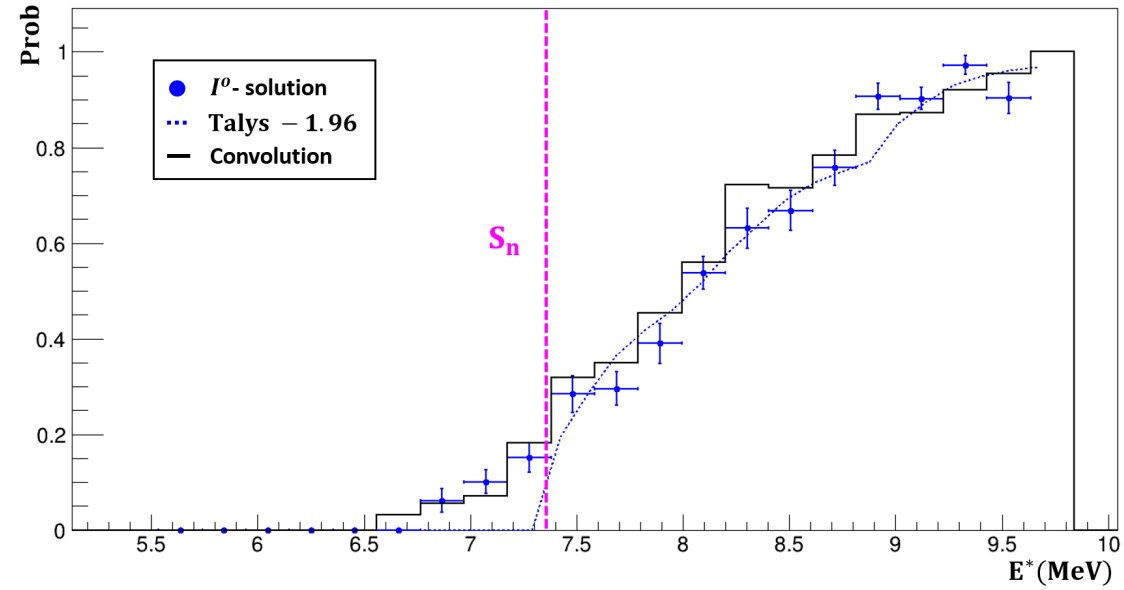

(a)

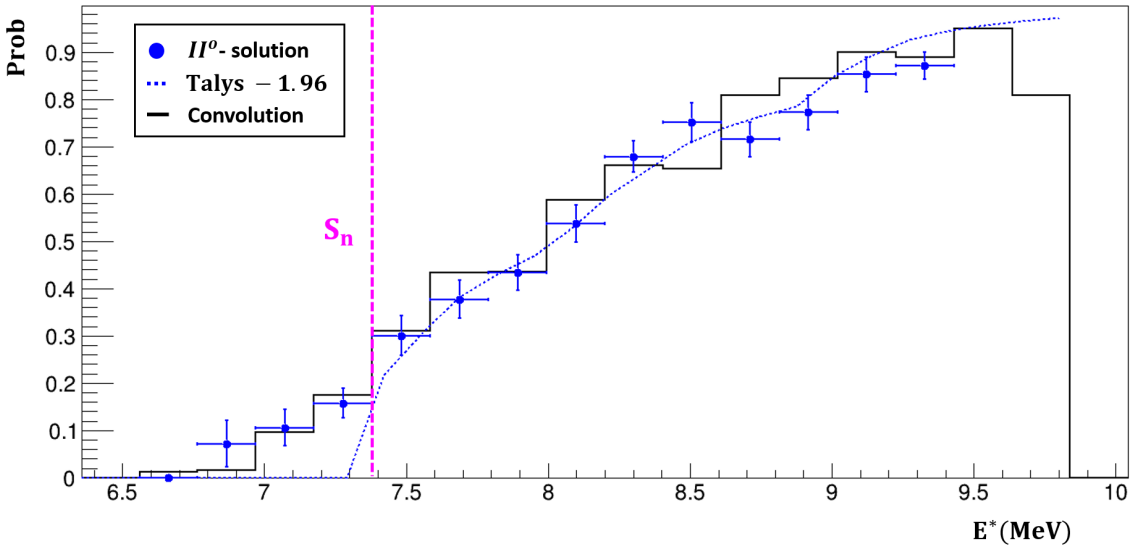

(b)

Figure 6.12: Comparison of the experimental neutron emission probabilities as a function of the excitation energy of ^{208}Pb with the Talys results convoluted with the excitation energy resolution. The results for the first kinematics solution and for the second solution are shown in figures (a) and (b), respectively.

Chapter 7

Conclusion and perspectives

7.1 Conclusion

The surrogate-reaction method is a powerful tool to indirectly infer neutron-induced cross sections of short-lived nuclei. Heavy-ion storage rings offer ideal conditions to use the surrogate reaction method in inverse kinematics. The beam cooling capabilities of the ring combined with the use of ultra-thin, windowless targets will allow for the determination of the excitation energy with unprecedented resolution. In addition, the magnetic dipoles of the ring enable for the separation of the beam-like reaction residues produced after γ-ray and neutron emission, and their detection with very high efficiencies. In this way, it will be possible to determine simultaneously the decay probabilities of many short-lived nuclei with unrivalled precision.
We successfully conducted a first proof-of-principle experiment at the ESR storage ring of the GSI/FAIR facility. In this experiment a ^{208}Pb beam at 30.77 MeV/u interacted elastically and inelastically with a hydrogen gas-jet target. To conduct this measurement we developed two detection systems, one for the scattered protons and the other for the heavy residues produced after the de-excitation of the ^{208}Pb nucleus. The proton detector was a Si-telescope made of a double sided Si strip ΔE detector and a stack of thick E detectors. The heavy residue detector was a double sided silicon strip detector. To preserve the very demanding UHV conditions of the ESR, the detectors were housed in pockets with very thin stainless steel windows of 25 μm.
We have developed a very complete simulation of our experiment, which includes all the detectors as well as a very detailed description of the ESR lattice. This simulation was used to define our detection systems and was validated with our experimental data. This shows that we have a good control of our experiment and allowed us to validate our experimental set-up and methodology to simultaneously infer the γ and neutron emission probabilities.
Indeed, we have been able to confirm the full separation and highly efficient detection of the beam-like residues produced after the γ and neutron emission. We have obtained a γ-detection efficiency ranging from 55 to 100% with an absolute uncertainty of 5-8% and a neutron detection efficiency of 100%. This represents a huge improvement with respect to standard direct

kinematic experiments where the γ detector efficiency is only few percent. Thanks to these high efficiencies it was possible to infer the γ and neutron emission probabilities with high precision, inspite of the limited statistics. Note that this was the first time that the neutron emission probability was measured. Our decay probabilities cover an excitation energy range from about 5.5 MeV to 9.5 MeV and an angular range in the center of mass from 125° to 145° and from 150° to 165°.
With the help of the data on the energy deposited in the ΔE and the first E detector of the telescope, and the simulations, we were able to evaluate the excitation energy resolution, which was about 600 keV. The excitation energy resolution is dominated by the uncertainty in the target residue emission angle caused by the large radius of the hydrogen target at 2.5 mm.
The measured decay probabilities as a function of the excitation energy were compared with calculations based on the statistical model of Talys where the spin/parity distributions populated in the $^{208}Pb(p,p')$ reaction were calculated with a model based on the quasi-particle random phase approximation QRPA and the distorted wave Born approximation (DWBA). The agreement between the data and the calculations is very good, except at the neutron separation energy. In fact, our neutron emission probabilities set in below the neutron emission threshold, which can be explained by the excitation energy resolution. A clear structure is observed at an excitation energy of 9 MeV in the data and the calculations. This structure can be explained by the presence of an excited state with a spin 13/2, which is very close to the predicted spin of the ^{208}Pb compound nucleus.

7.2 Perspectives

In the next months, we will perform a sensitivity study to identify the most relevant parameters of the statistical model calculations and use our decay probabilities to fix them. The tuned parameters will be then implemented in Talys to infer the neutron induced radiative capture and inelastic cross sections of ^{207}Pb.
In 2024, we plan to perform a second proof of principle experiment with a $^{238}U^{92+}$ beam and a deuterium target. We will investigate the $^{238}U(d,d')^{238}U^{\star}$ and the $^{238}U(d,p)^{239}U^{\star}$ surrogate reactions by measuring, in addition to the γ-ray and neutron emission probabilities, the fission probabilities of ^{238}U and ^{239}U. For this purpose, we will complete the setup used in the first proof-of-principle experiment with three fission detectors, one of which will be made of solar cells. Note that it will be the first time that a fission reaction is studied in a storage ring.
In the longer term, our experiments at the ESR will benefit from the availability of a gas-jet target with a radius of 0.5 mm. Our simulations predict that with such a target we can reach an excitation energy resolution of 250 keV or even better. Moreover, within the frame of NECTAR, we will develop a dedicated reaction chamber for the ESR, which will allow us to significantly increase the solid angle of the target-residue and fission detectors. With this chamber we will be able to significantly increase the $E^{\star}$ and angular range covered, allowing

us to measure not only the γ, neutron and fission probabilities but also two-neutron emission probabilities.

In the future we may also build a dedicated set-up for the CRYRING storage ring. One of the greatest advantages of this ring is that the focal point is accessible. Building a detector station at this point, would allow us to fully separate and detect with near 100% efficiency the heavy residues independently of their azimuthal angular distribution. This can lead to a significant increase of the studied angular and excitation energy ranges.

Once the methodology and the experimental set-up are validated and optimized, we will be able to fulfil the ultimate goal of NECTAR, which is to indirectly infer the neutron induced reaction cross sections of many short lived nuclei in different regions of the chart of nuclei using radioactive beams. First, we will use primary beams of e.g. ^{238}U and ^{208}Pb and nearby secondary beams produced by fragmentation. In the longer term, we aim to explore the region of neutron-deficient actinides and pre-actinides towards the N=126 shell closure. It will be the first time that fission probabilities are measured near a shell closure. This is particularly interesting since the low density of states typical of near-closed-shell nuclei can significantly impact their decay probabilities. These systematic studies will help to provide much better theoretical predictions for the fission barriers and cross sections of neutron-rich nuclei towards the shell closure at N=184, which are essential for the r-process [Gor15, Vas19] and not yet accessible to experiments.

Appendices

Appendix A

Beam Properties

A.1 Beam Energy

The typical definition of the energy of the beam from an ion source is made purely in terms of the kinetic energy, i.e. the rest mass energy is ignored. The energy is then well defined by the voltage used to accelerate the ions, i.e.

$$E_k = q \cdot e \cdot U \tag{A.1}$$

where q is the charge state of the ion, e is the electron charge and U is the applied voltage (or equivalent) used for acceleration. In the case that different ion species are to be delivered by an ion source, and accelerated, it is very common to use the kinetic energy per nucleon (E_k/u) as a definition:

$$E_{k,u} = \frac{E_k}{A} = \frac{q \cdot e \cdot U}{A} = \frac{1}{2} \cdot m_u \cdot v^2 = (\gamma - 1) \cdot m_u c^2 \tag{A.2}$$

where A is the mass number of the ion, m_u is the rest nuclear mass unit ($1.67{\cdot}10^{-27} kg$), c is the speed of light, v the velocity of the particle and γ ($\gamma = 1/\sqrt{1 - v^2/c^2}$) is the relativistic gamma factor. The final two terms demonstrate that the kinetic energy per nucleon is only dependent on the velocity of the particle (either v or γ).

A.2 Beam structure and Intensity

A first collective beam parameter is the time structure. We make the distinction between a continuous beam being a continuous flow of particles and a bunched beam. A continuous beam can be sustained, in general, only by Direct Current (DC) accelerating fields or when no acceleration is required. A pulsed beam, on the contrary, consists of a finite number of bunches or a continuous stream of particles accelerated for a finite length of time by means of Radio frequency (RF) fields.

In this frame, the beam intensity is usually expressed in terms of electrical current. In an accelerator the current is formed by N particles of charge state q per unit of time t or unit of length l and velocity v. The electrical current is:

$$I_{beam} = \frac{q \cdot e \cdot N}{t} = \frac{q \cdot e \cdot N}{l} \cdot v \tag{A.3}$$

with e being the elementary charge. In a beam transport line, this is the total charge passing per unit time, where the unit time is as long as the distance between beam pulses while in a circular accelerator it is, for example, the total circulating charge divided by the revolution time.
At storage rings facilities for example, the measurement of the circulating beam current is provided in a non-destructive way by current transformers. Knowing the beam current, it is possible to derive the total number of ions stored dividing it by the stored ions revolution frequency and the total ion charge. For example, in the case of a 1.5 mA current of $^{40}Ar^{18+}$ at an energy 65.3 MeV/u turning with a frequency f of 1 MHz, the total number of ions is given by:

$$N_{Ar,stored} = \frac{I_{beam}}{f \cdot q_{ion}} \tag{A.4}$$

where the current is divided by the frequency and the total charge q_{ion} for ion in Coulomb ($q_{ion} = e \cdot n_q$) with n_q the space charge state of the ion. In this specific case the number of stored ions is $N \sim 3.2 \cdot 10^8$ $ions$.

A.3 Beam space charge and Intra-beam scattering (IBS)

As already mentioned the beam is a collection of particles, having the same charge polarity, whose longitudinal and transverse momentum are close enough and remain more or less close to each other. The particles of the beam can interact each other by Coulomb interaction and the net effect of the Coulomb interaction in a multiparticle system can be classified into two regimes [Rei94]:

- the collisional regime, dominated by binary collisions caused by close particle encounters, i.e. single-particle scattering;
- the collective regime or space charge regime, dominated by the self-field produced by the particle distribution, which varies appreciably only over large distances compared to the average separation of the particles;

The collisional part of the total interaction force arises when a particle is scattered by its immediate neighbours. This force will cause small random displacements of the particle's trajectory and statistical fluctuations in the particle distribution as a whole, leading for example to Intra-Beam scattering (IBS) effects in high-energy storage rings [Piw74] (see also the Touschek

effect [Ber63]). The diffusion effects caused by multiple Coulomb scattering on charged particle beams in a storage ring, in both the transverse and the longitudinal beam dimensions induces the growth in beam emittances and, in some situations, leads to the redistribution of partial beam emittances and energy spread. Thereby, it can cause undesirable beam dilution in phase space or could heat the beam as a whole, i.e. increase the partial beam emittances and energy spread simultaneously. As indicated in [Wie19] an increase of the ions in the stored beam as far as a small momentum spread increase the rate of increase of the beam emittances and so the beam heating. However the effect of Intra-Beam scattering is decrease by the increase of the beam velocity.

On the other hand, space charge forces lead to collective behaviour of the beam, driving for example envelope oscillations, emittance, and energy spread growth [Ser97]. In this respect, the electric charges of a particle beam can become a major contribution to the forces encountered by individual particles while travelling along a beam transport line or orbiting in a circular accelerator. These forces may act directly from beam to particle or may originate from electromagnetic fields being excited by the beam interaction with its surrounding vacuum chamber. Furthermore, individual particles in an intense beam are under the influence of strong repelling electrostatic forces creating the possibility of severe stability problems. Particle beam transport over long distances could be greatly restricted unless these space-charge forces can be kept under control.

An interesting effect of space charge forces is taking place in circular accelerators (as storage rings). Here the betatron tune is defined as the number of transverse oscillations (in directions perpendicular to the beam) of the particles in one turn of a ring accelerator. This quantity is one of the most important parameters since an undesired betatron tune increases the amplitude of the transverse oscillation so that many particles are lost from the ring sooner than designed. Without going into too much details, we can say that since a betatron tune is controlled by the magnetic fields in the ring, the ripple of the magnet current directly displaces the betatron tune from its designated value. Imperfections of the magnetic fields are unavoidable and can originate from manufacturing uncertainties, misalignments of magnets or field gradients at the beginning and end of each magnet. Such field errors perturb the particle trajectories and if the betatron oscillations are resonant with these perturbations, the errors add up coherently leading to an unrestricted increase of the oscillation amplitude. To avoid significant losses of the beam particles, it is important to provide a betatrone tune far from this resonances. However, the space charge force can make difficult to satisfy the condition since they can induce a tune spread larger than $|\Delta Q| < 0.5$, as described in [Ros92, Del80], typically required to avoid major resonances.

Appendix B

Beam processes

B.1 Charge stripping

Whereas intense beams of highly charged light ions can directly be produced in modern ion sources or electron-beam ion traps/sources (EBIT/S), the efficient production of beams of highly charged heavy ions is presently done by stripping bound electrons of the swift projectiles when passing through a thin stripper target [Sig04].
For this purpose, low charged ions from an ion source are accelerated to high energies by employing linear accelerators, cyclotrons and/or synchrotrons. The accelerated high energy beam of primary particles is then focused onto a dedicated stripper target. In first order, the so-called Bohr criterion [Sig04] can be used to estimate the velocity needed to achieve a required charge state. The criterion predicts that bound electrons are stripped off the projectile most efficiently during the penetration through matter if their "classical" orbital velocities $\beta = v_0/c = Z \cdot \alpha/n$, are in the order of the velocity of the projectile, where Z is the proton number, α the fine structure constant $\alpha = 1/137$, and n is the principal quantum number.
For example, to produce the heaviest available stable beam, uranium, as a bare (fully-ionized) ion the velocity $\beta = v_0/c \sim 0.67$ is needed, which corresponds to primary uranium beam energy of at least 325 MeV/u. If the stripper target is thick enough, the charge state distribution at the exit of the target becomes independent of the initial charge state of the projectile, that is the probabilities for stripping and pick-up of electrons are equal leading to the equilibrium charge state distribution. The equilibrium charge state distribution depends on the proton number of the projectile and of the stripper material and on the exit energy from the target [She20].
For many experiments, the production of ions with one- (hydrogen-like, H-like), two- (helium-like, He-like), three- (lithium-like, Li-like) and so on bound electrons is required. In such cases it may be efficient to select stripper foils to be much thinner than the equilibrium thickness. In first order, the thickness of the foil has to be equal to $n \cdot < x >$, where n is the number of electrons to be removed from the projectile and $< x >$ the mean free path between atomic

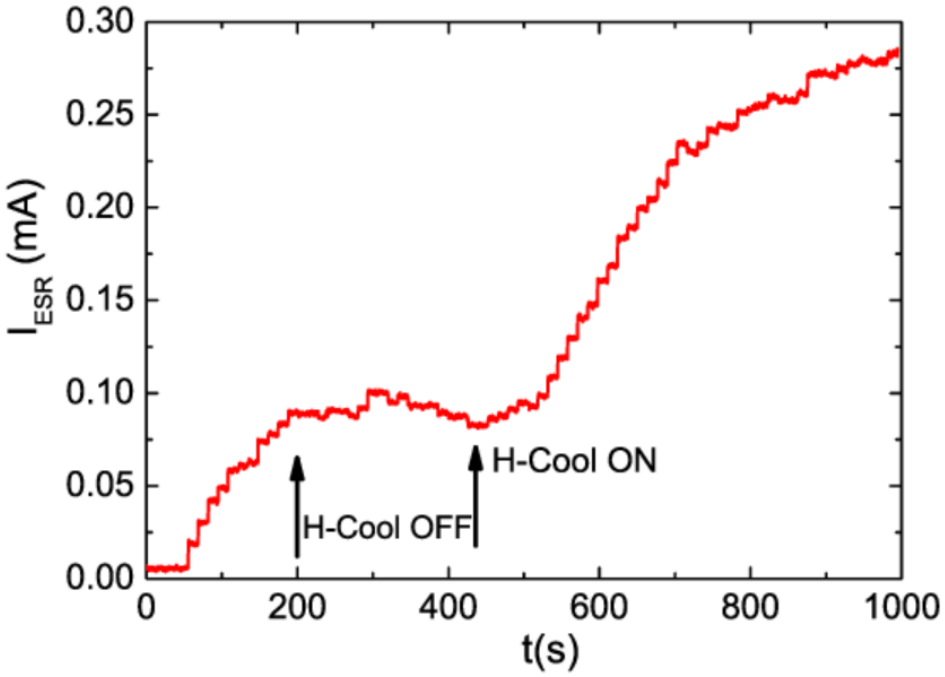

Figure B.1: Beam Accumulation as function of the time. It can be seen the impact of the horizontal cooling to compress the beam phase space allowing in this way the staking process.

collisions in the target.

B.2 Beam accumulation

The intensity required by experiments performed in storage rings is not always available from the injector feeding the ring and the lack of intensity is usually more pronounced for experiments using radioactive ion beams.
In storage rings, accumulation methods are employed to increase the stored beam intensity. The accumulation methods are based on beam cooling which allows one to overcome the limit of the intensity due to the value defined by the acceptance of the storage ring and the emittance of the injected beam.
The general scheme is based on the ability provided by cooling to force particles within the acceptance to a certain phase space volume and thus emptying a major part of the acceptance for repeated injection, see figure B.1. This makes beam accumulation an indispensable method to provide useful beam intensities, particularly for radioactive ion beams.

In low-energy storage rings a routine method to inject the beam into the ring is transverse multiturn injection. This method allows filling of the transverse ring acceptance during a time corresponding to several turns, typically some ten turns, with a beam of smaller emittance. Consequently, the compression to the smaller phase space volume is repeated for even more injections. The repeated multiturn injection has been used with beams from electrostatic accel-

erators, linear accelerators and cyclotrons. The particles accumulated with this method range from protons, unpolarized and polarized, to highly charged heavy ions. The efficiency of the accumulation depends on the emittance of the incoming beam and the acceptance of the storage ring, but also the lifetime of the beam which needs to be significantly longer than the cooling time affects the performance of the accumulation procedure. The gain factor depends on the beam lifetime. Long-lived secondary particles at high energy are more suitable for accumulation than short-lived isotopes. Low energy beams should have a long lifetime with respect to the vacuum to allow a large gain factor.

Appendix C

Investigation of the detectors response

As described in chapter 5, we found some differences between the experimental results and the simulations in the reconstruction of the energy deposited by the protons in the telescope. Simulations and detector tests carried out after the experiment allowed us to better understand the origin of these discrepancies. They are presented in the following sections.

C.1 Comparison with the simulations

In figure C.1 the structure of the telescope used during the experiment is presented. As can be seen, three blocks with two thick E detectors each were place after the stainless steel window and the ΔE detector. Thanks to the simulations carried out and described in chapter 4, we were able to produce the $\Delta E - E$ identification spectrum, see figure C.2(a), and compare it with the experimental one in figure C.2(b). We can see some differences between the two spectra: a mismatch in the maximum energy detected by the telescope of a few MeV and the appearance of structures at the interface regions (red dashed lines) between the E detectors of the same stack ($E_1 - E_2$, $E_3 - E_4$, $E_5 - E_6$). Furthermore as shown in figure 5.13, a difference of about 500-600 keV was found in the maximum energy deposited by the protons in the ΔE detector.

To investigate possible problems in the charge collection, we compared the energy deposited by the protons in two adjacent E detectors. An example of this correlation plot is shown in figure C.3 where, using the simulations, the energy deposited in the first E_1 detector is compared to the energy deposited in E_2. When the proton energy is not large enough to punch through the first E detector, the signal delivered by the second detector is in the pedestal or noise. These events are then located along the horizontal axis until the maximum energy that can be deposited in E_1 is reached, around $\approx$15.4 MeV. For larger energies, the energy deposited in E_2 increases, while the energy deposited in the first detector decreases. In this way a correlation curve is obtained, as the one shown in figure C.3, between the energy in E_1 and E_2. The events

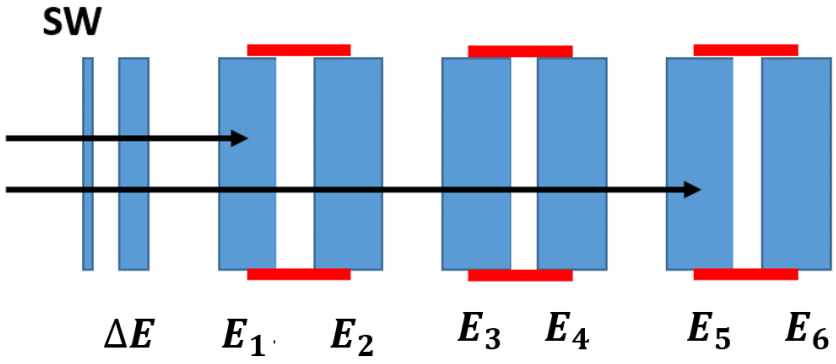

Figure C.1: Telescope structure. As can be seen, the stainless-steel window (SW) and the ΔE are followed by three stacks containing each of them two E detectors. The black arrows represent two incident protons with different energies, which are stopped in different E detectors.

located below the correlation curve are associated to protons that escape from E_2 and deposit only part of their energy in the detector.

Figure C.4 shows the measured correlation spectra for $E_1 - E_2$, $E_2 - E_3$, and $E_3 - E_4$ in channels[1]. A nice agreement with the simulations can be found for the correlation plot $E_2 - E_3$ in figure C.4(b). On the contrary, for figures C.4(a) and C.4(c), showing the energy correlation between detectors of the same stack, a clear difference can be seen with respect to the simulations. In particular, we can observe a change of the shape of the correlation curve as well as a difference in the maximum energy deposited in E_1 at which a signal larger than the noise can be seen in E_2. In the simulation, this energy is equal to the energy at which the protons start to punch through the E_1 detector and deposit energy in E_2. This difference reflects a problem in the measurement of the energy deposited at the detector back side. Because of the absence of thick dead layers between the detectors, this problem can arise from the application of an insufficient bias voltage, which does not allow to efficiently collect the charge produced on the back side of the detectors. In the simulations, we approximated these inefficient charge collection region by a dead layer at the back side of the detectors. It is interesting to note that a good agreement with the experimental results was obtained in this way. The thickness of these regions in gray in figure C.5(a), about few hundreds μm on the E detectors and few tens of μm in the ΔE detector, was estimated considering the different values provided by the simulation and the experimental results of the maximum energy deposited by the protons. In figure C.5(b) the $\Delta E - E$ spectrum obtained with the simulation is shown. As we can see, the structures observed experimentally at the detector interfaces are well reproduced.

[1]These plots are shown in channels to remove from the present investigation possible problems related to the energy calibration of the detectors.

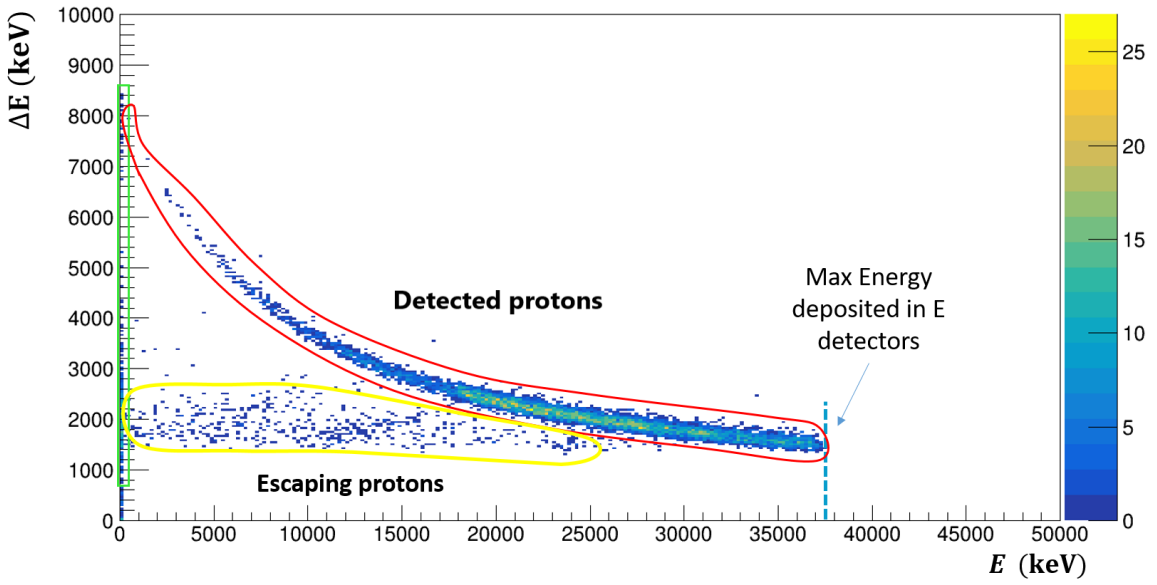

(a)

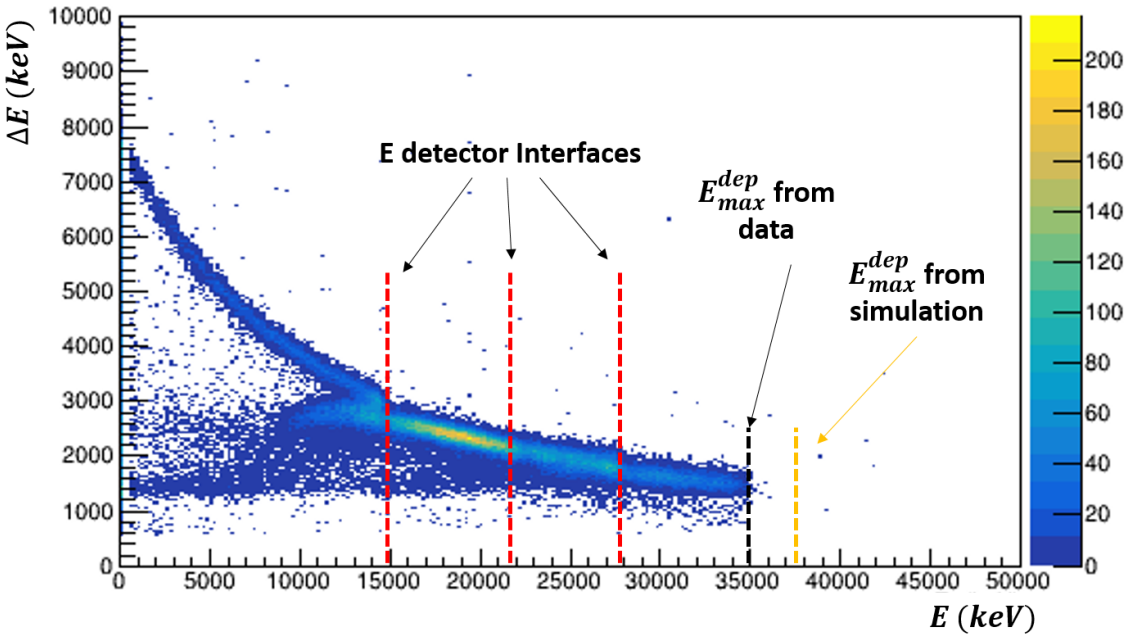

(b)

Figure C.2: $\Delta E - E$ identification spectra obtained with the simulation, figure (a), and with the experimental data, figure (b). The vertical dashed red lines indicate the energies of the protons, which are stopped at the interface between two E detectors of the same stack. The difference between the maximum proton energy from the simulation and the experiment is indicated by the vertical black and yellow dashed lines.

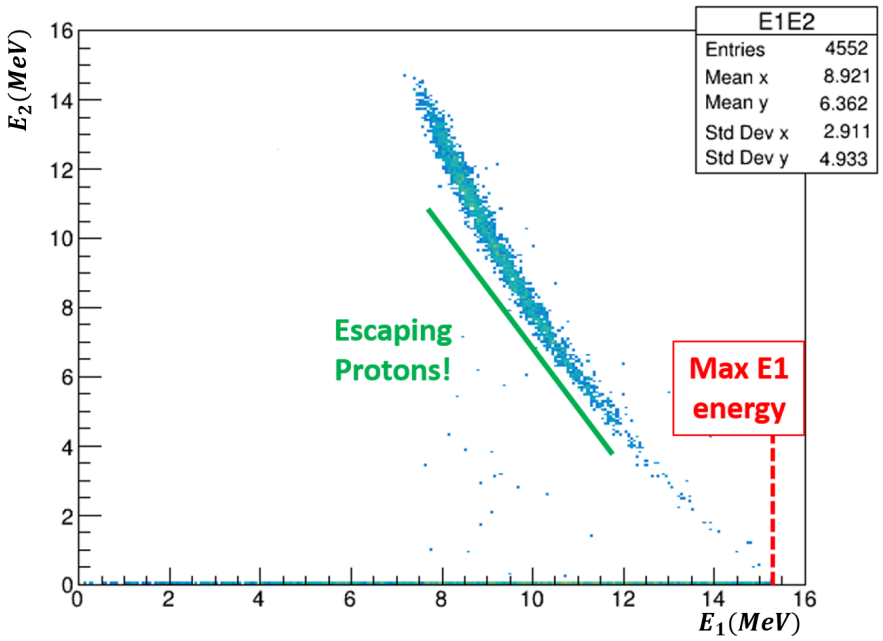

Figure C.3: Simulated E_2vsE_1 correlation plots. The green line indicates the energies below which protons that escape from the detector are located. The red line indicates the max-energy of protons stopped in detector E_1.

C.1.1 Experimental tests with α-source

To verify the correctness of the insufficient bias hypothesis of the detectors during the experiment, we performed some detector tests with the triple-alpha source. Since α-particles have a short range in silicon, about 29 μm, the charge induced by their interaction is localized close to the detector surface. Therefore, by placing the source on the front and back sides of the detector we could investigate the charge collection efficiency in these two regions of the detector as function of the applied bias voltage.

C.1.1.1 MSX04 detector

Figure C.6 shows a schematic representation of the detector assembly used during the experiment and during the tests. During the tests with α-particles we used a new assembly provided by Micron Semiconductors containing only one E detector. This allowed us to irradiate both the front and back sides of the detector.

We performed tests in primary vacuum ($1{\cdot}10^{-3}$ $mbar$ - $2{\cdot}10^{-2}$ $mbar$). When the source was facing the front, which is depleted first, we could see the three peaks from the alpha source even at voltages as low as 5 V. Figure C.7(a) shows some examples of pulse height spectra of α-particles at different bias voltages, 160 V (blue line), 180 V (green line) and 200 V (red line). The three alpha peaks are well separated and no significant change can be seen in the resolution and the mean peak position.

When the source irradiates the back side of the detector, the situation is completely different.

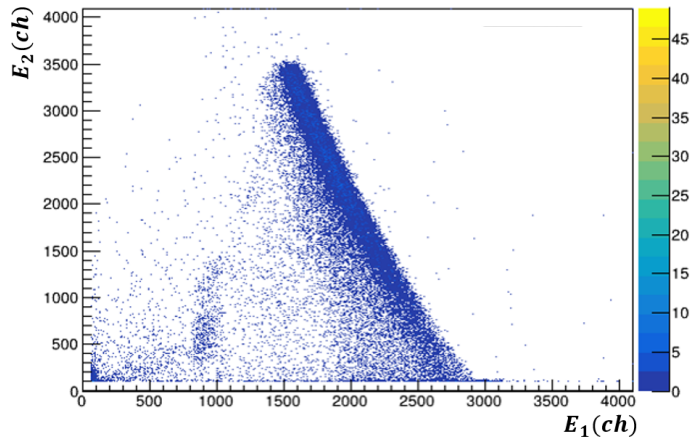

(a)

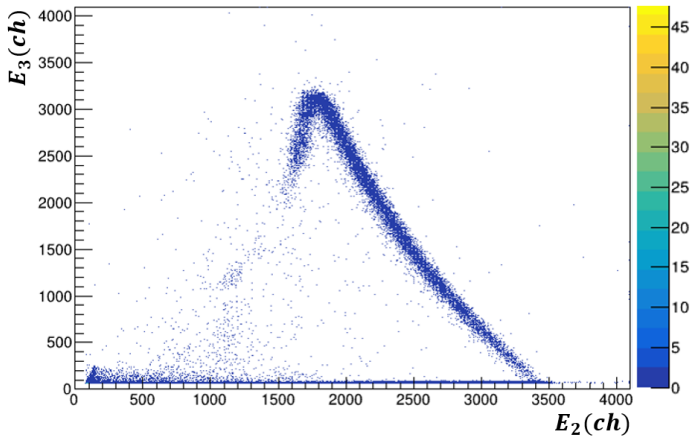

(b)

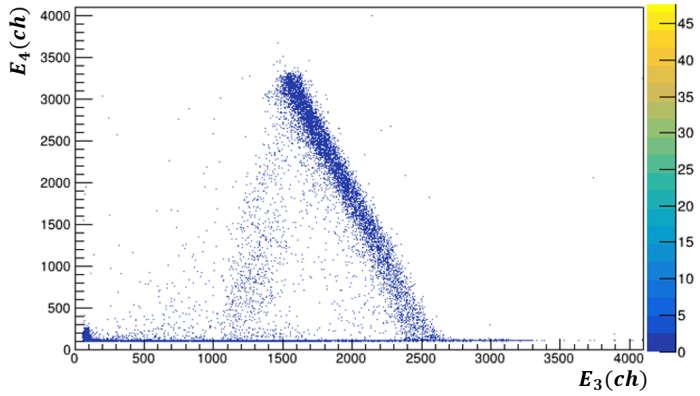

(c)

Figure C.4: Correlation plots obtained by comparing the amplitude of the signals produced in two adjacent E detectors of the telescope.

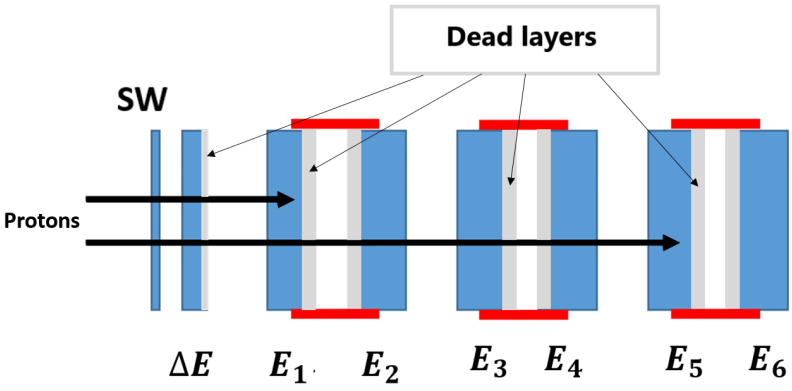

(a)

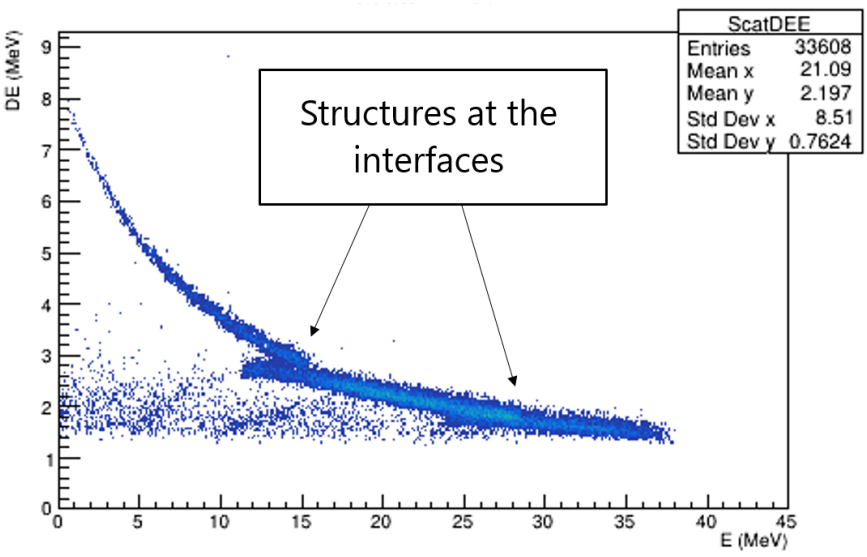

(b)

Figure C.5: (a) Schematic representation of the telescope structure. The region characterized by the inefficient charge collection estimated from the simulation is marked in gray. (b) The simulated $\Delta E - E$ spectrum including the dead layers is shown. The structure at the detector interfaces are indicated.

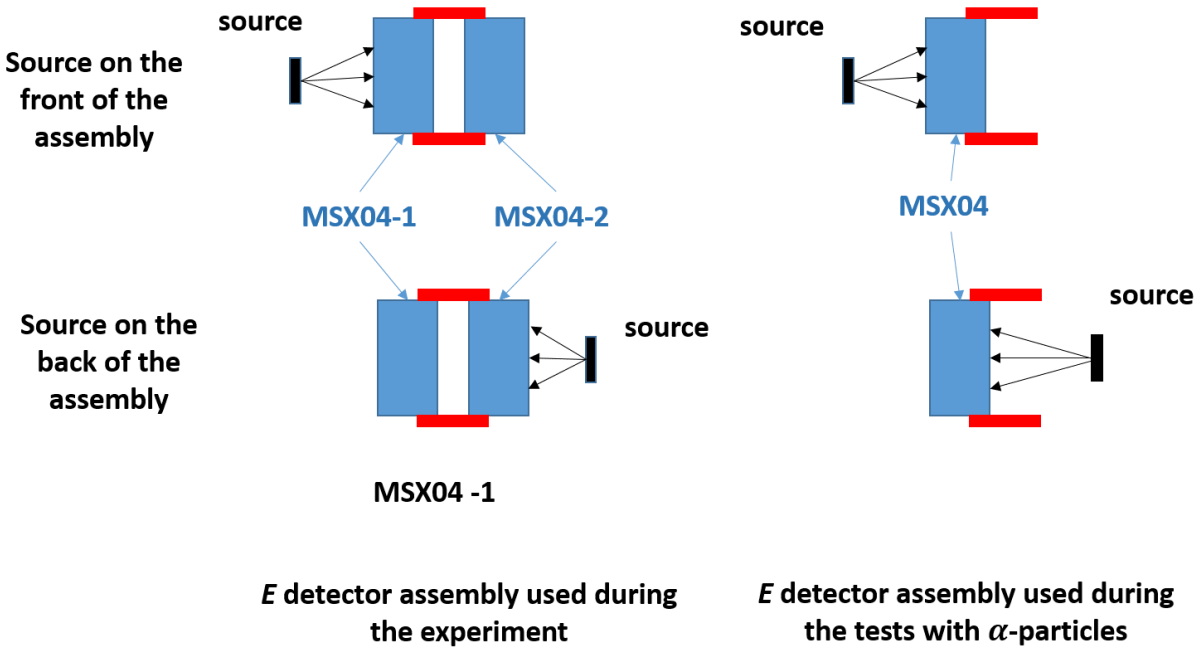

Figure C.6: Source position with respect to the E detector assembly used during the experiment and during the alpha tests. The detector back side can only be reached with α-particles when a single E detector is used as shown on the right figures.

In figure C.7(b) the measured pulse height spectra of α-particles are shown at a bias voltage of 160 V (blue line), 180 V (green line) and 200 V (red line). In this case, where the charge is produced close to the detector back side, significant differences can be seen with the increase of the voltage, i.e. a great improvement of the resolution and an increase in the mean peak position.
In figure C.8(a) the mean amplitude of the central peak is shown as a function of the voltage when the source is facing the front (blue circles) and the back (orange circles) detector side. The plot clearly shows that, when the source is located in the front, as the bias voltage is raised the amplitude increases before gradually levelling off as one approaches 150 V. Since the signal amplitude is proportional to the charge collected and no significant variation can be seen above 150 V, we can conclude that almost all the charge is collected at this voltage. When the source faces the back detector side, we can see that a high voltage is require to measure a values of the mean amplitude of the central peak comparable to the front case. Considering an experimental error associated to the detector resolution of 10-15 ch, the variation in the peak amplitude from a bias of 260 V fall inside the experimental error. From this result, we can conclude that the complete charge collection, if the charge production takes place close to the back side, is reached only applying a voltage of at least 260 V. It is important to stress that for high voltages a significant increase of the current consumed by the circuit was observed about, 2.9 μA at 260 V. Due to the presence of a 12 $M\Omega$ resistor in the preamplifier the high circuit current implies on the resistor a drop of the voltage of 35 V at 260 V. This translates in an effective bias applied on the detector of 225 V.
During the experiment, considering the voltage drop in the preamplifier resistor, an effective bias voltage of about 154.6 V was applied to the E detectors. Consequently, the tests demonstrate that for this voltage a problem in the charge collection takes place when the charge generation occurs close to the detector back side.
In figure C.8(b), we can see the improvement of the α particles energy measurement as function of the bias voltage when the charge production occurs at the back side of the detector. Considering the energy loss in the thin detector dead layer, the α-particles are expected to deposit an effective energy of 5.332 MeV which is represented by the horizontal dashed line in figure C.8(b). The ratio between the measured energy at a bias voltage of 154.6 V and the expected one underlines that only the 75% of the energy is measured when the charge is deposited completely at the detector back side.

C.1.1.2 BB8 detector

The same investigations were performed with the BB8 (ΔE) detector. Also in this case, to verify the presence of an incomplete charge collection close to the detector back side, tests were done using the 3-α source in primary vacuum conditions and the detector response was analysed as a function of the bias voltage.

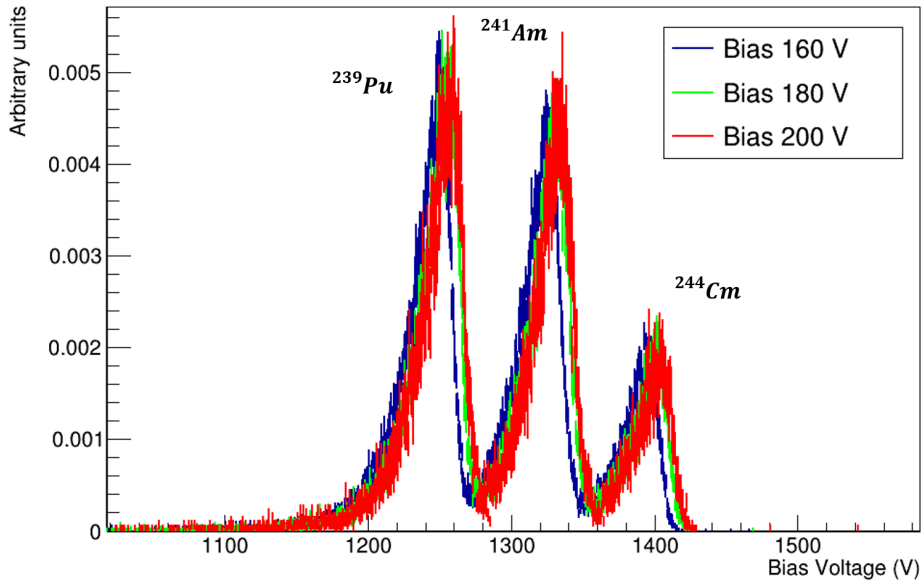

(a)

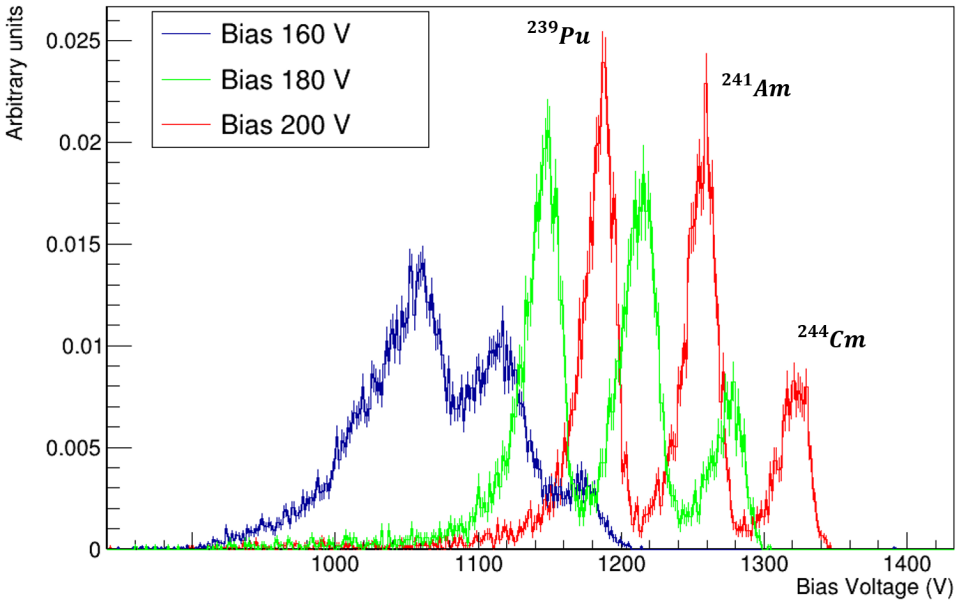

(b)

Figure C.7: (a) Pulse height distribution measured for an MSX04 detector during the irradiation with alpha sources on the front side (a) and on the back side (b) at different bias voltages: 160 V (blue line), 180 V (green line) and 200 V (red line).

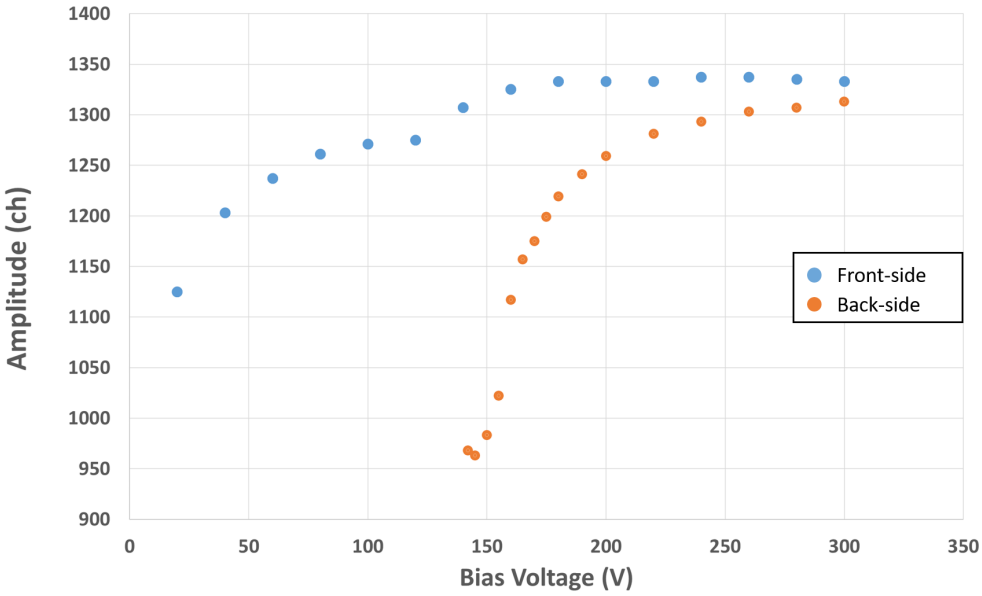

(a)

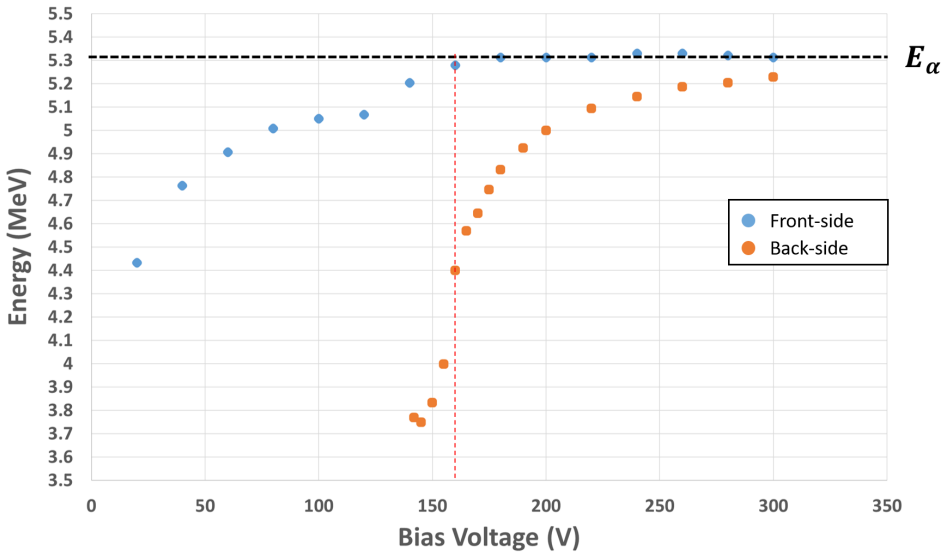

(b)

Figure C.8: Mean values of the central peak mean amplitude vs applied voltage (V) for the source facing the front side of the MSX04 detector (blue data points) and the back side of the detector (orange data points). Results in channels are shown in (a) and in MeV in (b). The red dashed line indicates the bias voltage applied during the experiment.

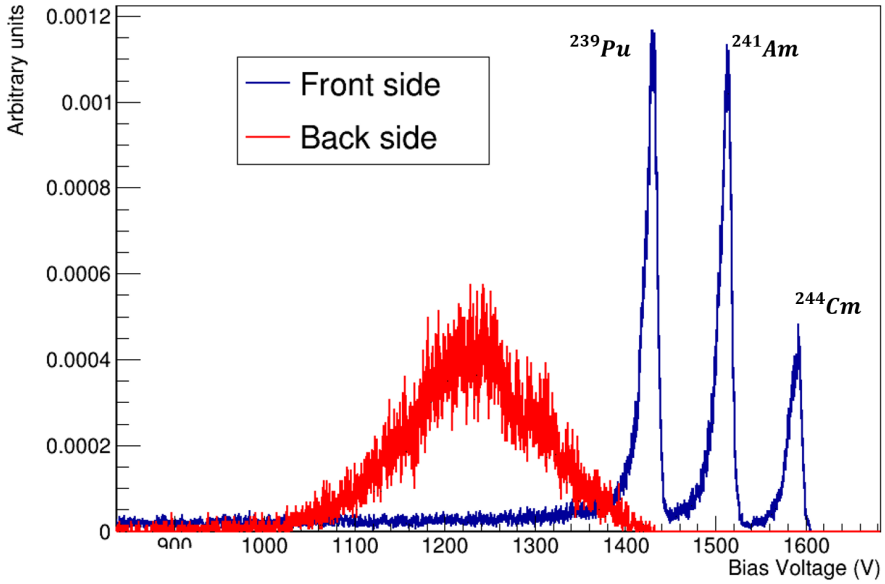

Figure C.9: Pulse height distribution produced during the irradiation with alpha source on the front side (blue line) and on the back side (red line) at a bias voltage of 54 V.

In figure C.9 we compare the pulse height spectra of α-particles obtained for the horizontal strip 7 with the source facing the front (blue line) and back (red line) detector sides. The bias voltage was the same as the one applied during the experiment 54 V. As for the MSX04, a voltage drop occurs on the preamplifier resistor and it must be taken into account to determine the effective bias applied on the detector. For the $BB8$ detector, at 54 V, this drop is about 1.6 V leading to an effective bias voltage on the detector of 52.4 V. When the charge is produced in the detector front-side, this voltage is sufficient to ensure a good separation of the three alpha peaks. However, when the charge is produced in the detector back side we cannot separate the three alpha peaks, whose amplitude lies at smaller values, indicating a charge collection problem.

The mean central peak position in channels as a function of the bias voltage is shown in figure C.10(a) when the source is on the front (blue circles) and on the back (orange circles) side of the detector. In the first case the maximum amplitude is reached at 54 V and it remains constant. As for the E detector tests we can conclude that almost all the charge is collected with a voltage of 54 V. The situation is changing again when the source is placed in the back side of the detector. In this case, a larger bias voltage must be applied and, considering an uncertainty in the determination of the peak position between 10-15 ch, the tests highlighted that at least 80 V are needed. At this voltage the potential drop of the preamplifier resistor is about 2 V leading to an effective bias on the detector of 78 V. With larger bias voltages, the related variation in the amplitude was observed to fall inside the experimental error.

These results confirm the presence of an incomplete charge collection problem for the ΔE detector. The mean central peak measured energy is displayed as a function of the bias voltage in figure C.10(b). We assume for the ΔE detector the same dead layer as for the MSX04 and

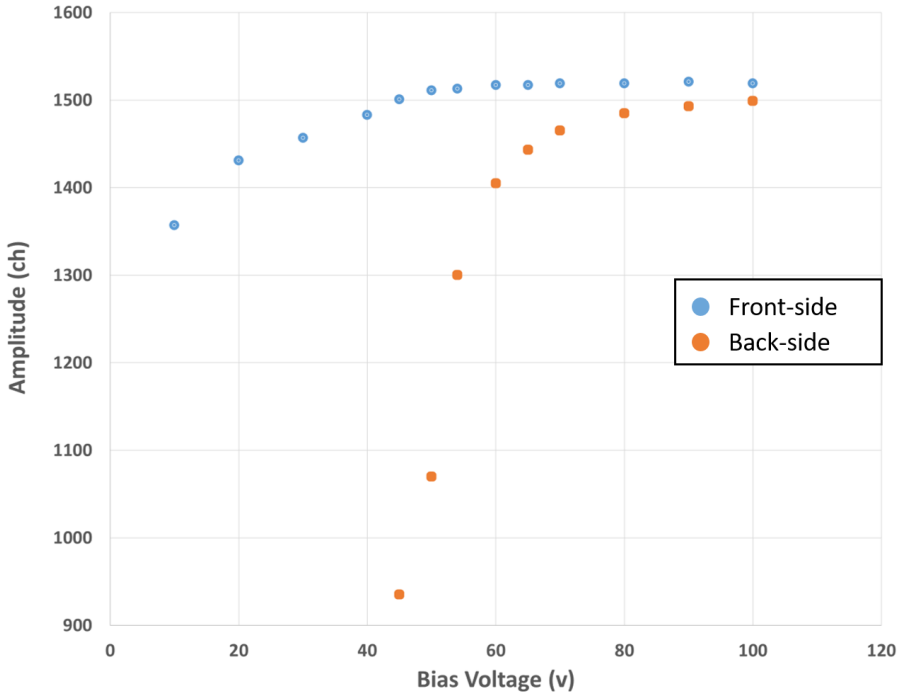

(a)

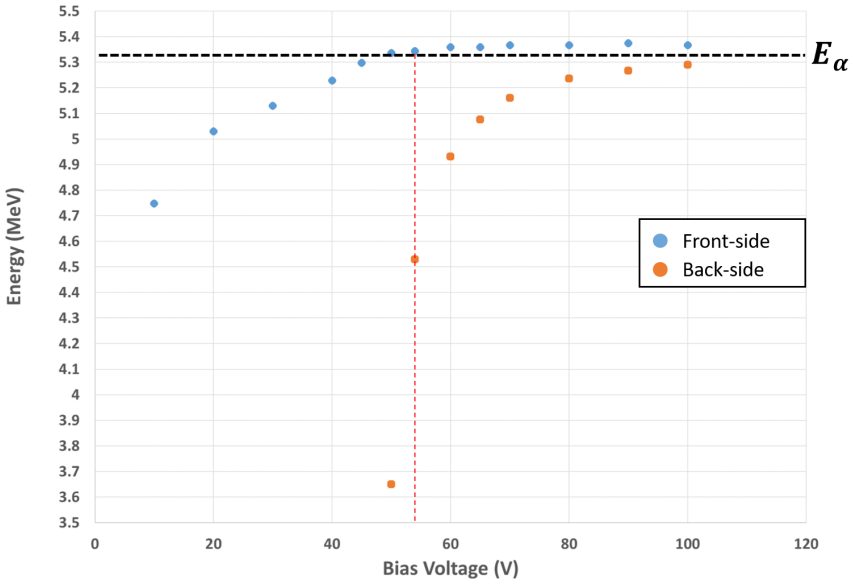

(b)

Figure C.10: Mean values of the central peak mean amplitude vs applied voltage (V) for the source facing the front side of the BB8 detector (blue data points) and the back side of the detector (orange data points). Results in channels are shown in (a) and in MeV in (b). The red dashed line indicates the bias voltage applied during the experiment.

an energy deposited by the α-particles of 5.332 MeV, which is represented in figure C.10(b) by the horizontal dashed line. Since during the experiment a bias voltage of 52.4 V was used, considering the ratio between the measured and the expected energy of α-particles, the tests underline that if the charge is produced at detector back side only the 85 % of the energy is measured.

C.2 Evolution of electric field with detector depth

The electric field extends from the n-p junction in the front side to the back side of the detector. Following the properties of a n-p junction described in section 2.1 of the second part of the thesis, we can see that the electric field responsible for the charge drift decreases linearly as function of the depth in the detector (see equation 2.8). The tests described above demonstrated that the charge collection improves with the increase of the bias voltage, which is responsible for an increase of the junction electric field intensity. For this reason, we can conclude that during the experiment the electric field close to the detector back side was too low to allow for a complete charge collection.

In this frame, Micron semiconductor provides in the website a range of possible values of the ΔE and E detectors resistivity. We used the results of the investigations done on the detectors response, described in section C.1.1, to refine this range and get an accurate value of the detectors resistivity. By knowing accurately these detectors property it was possible to determine, for the bias voltage applied during the experiment, the electric field intensity as a function of the detector depth for the ΔE and the E detector, as shown with blue circles in figure C.11(a) and C.11(b). We can see that the electric field intensity decreases significantly and it is close to zero at the detector back side. From the α tests it is possible to deduce the minimum electric field $|\vec{E_{min}}|$ at the detector back required to achieve the full charge collection and we estimate the maximum range of protons in the detectors for which the charge produced is completely collected.

During the test with α-particles, we observed that the full charge collection and maximum signal amplitude in the full detector volume is reached with an effective bias voltage of 78 V for the ΔE detector and 225 V for the E detector. In figure C.11(a) and C.11(b) we displayed respectively for the ΔE (orange circles) and the E (orange circles) detectors the electric field intensity variation as a function of the depth. We can see that with the bias applied during the experiment (blue circles) $|\vec{E_{min}}|$ is reached in the ΔE detector around 350 μm and in the E detector around 1000 μm. These values provide an estimation of the maximum range of protons whose energy reconstruction is not affected by the charge collection inefficiency.

These ranges are associated to protons that deposit an energy of 6.5 MeV in the ΔE detector and 12.3 MeV in the E detector, respectively. Note however that, contrary to the ΔE, the E detector tested with α particles was not the one used in the experiment which can lead to slight differences on the maximum protons energy not affected by charge collection issues. For

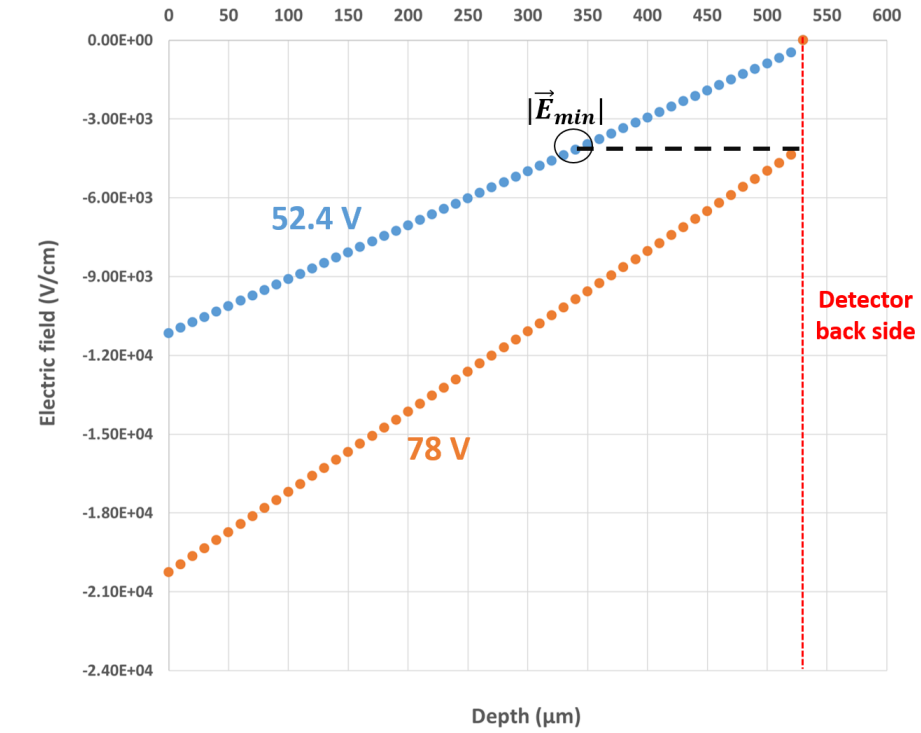

(a)

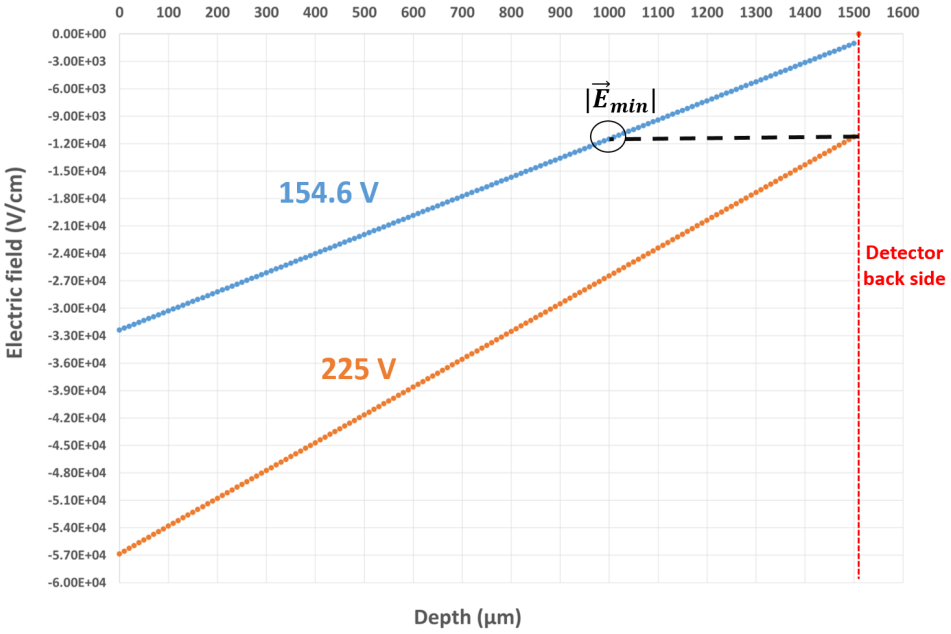

(b)

Figure C.11: Electric field intensity as a function of the detector depth for the (a) ΔE and (b) E detectors. The blue circles corresponds to the bias voltage used during the experiment and the orange circles to the bias voltage necessary to have a complete charge collection over the full detector depth. The vertical dashed lines indicate the detector back side and the horizontal black dashed lines the minimum electric field $|\vec{E_{min}}|$ necessary for the complete charge collection.

protons that deposit up to 2.5 MeV in the E_1 detector, a significant part of their Bragg peak falls in the region with inefficient charge collection of the ΔE detector.
The region of energy deposited in the E detector between 2.5 MeV and 12.3 MeV is therefore free from under-depletion problems. This region corresponds rather well to the region included in the yellow contour of figure 5.13, which was used to obtain the decay probabilities with the first kinematics solution. Regarding the second solution, in section 5.2.4 we investigated the effect on the probabilities of remaining protons whose energy is above 7.5 MeV. These protons deposit about 6.5 MeV in the ΔE detector which is in good agreement with the value given above.

Appendix D

MSX04 detector calibrations

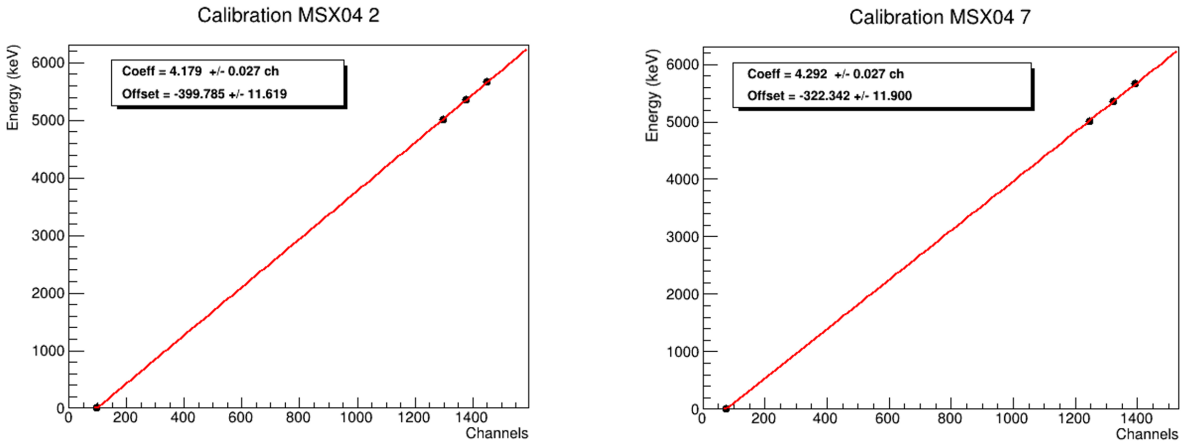

(a) E_2 detector (b) E_7 detector

Figure D.1: α calibration curves of the E_2 (a) and E_3 (b) detectors.

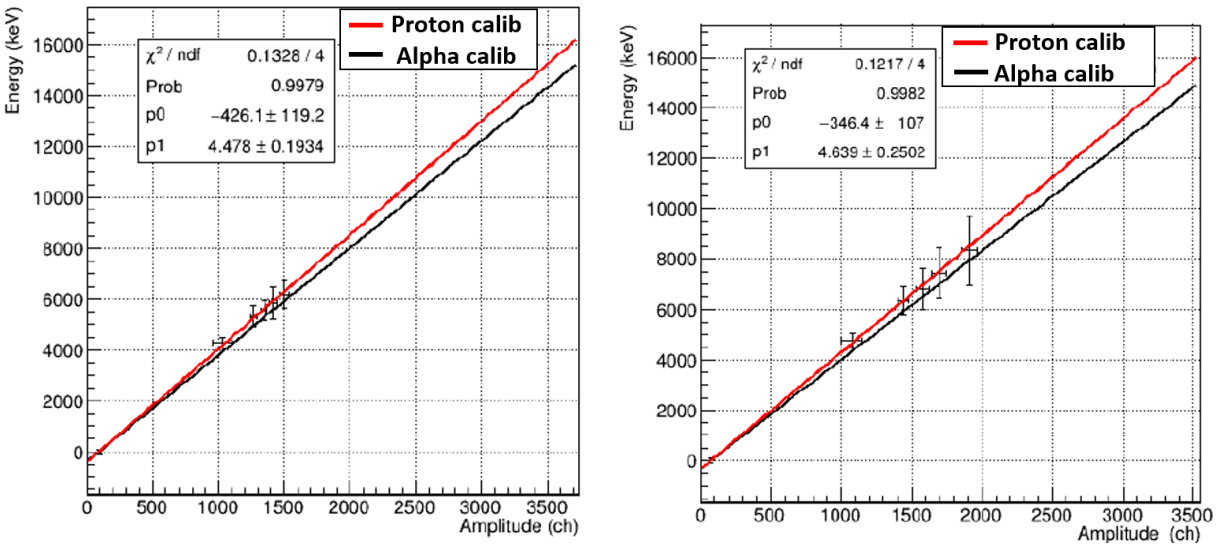

(a) (b)

Figure D.2: Comparison between proton (red lines) and alpha (black lines) calibration for E_2 and E_3. The black crosses correspond to the calibration points obtained with the procedure previously described. As already observed for E_1 a significant discrepancy can be observed with the increase of the energy.

Bibliography

[Abb17] B.P. Abbott et al., Phys Rev Lett. 119, 161101, 2017

[Ach15] O. Achakovskiy, A. Avdeenkov, S. Goriely, S. Kamerdzhiev, and S. Krewald, Phys. Rev. C 91, 034620, 2015

[Aer04] G. Aerts et al., AIP Conference Proceedings 769, September 2004

[Aji91] N. Ajitanand, et al., Nucl. Instrum. Methods Phys. Res. A 300 (2), 354-356, 1991

[Arn03] M. Arnould and S. Goriely, Phys. Reports 384, 1, 2003

[Arn07] M. Arnould et al., Phys. Reports 450, 97, 2007

[Aus70] N. Austern, ISBN 0471037702, no. XXV, 1970

[Bac74a] B. B. Back et al., Phys. Rev. C, vol. 9, 1924–1947, May 1974

[Bac74b] B. B. Back, et al., Phys. Rev. C, vol.10, 1948-1965, Nov 1974

[Bar73] G. A. Bartholomew et al., Adv. Nucl. Phys. 7, 229-324, 1973

[Bar11] M.J. Barnes et al., CERN, Geneva, Switzerland, 2011

[Ben22] S. A. Bennett, private communication, 2022

[Ber63] C. Bernardini et al., Phys. Rev. Lett. 10, 407–409, 1963

[Ber05] L.A. Bernstein and J.T. Burke, AIP Conference Proceedings, vol. 769, no. 1, pages 890–893, 2005

[Ber06] L. Bernstein, UCRL-PROC-220800, Proceeding NEDPC 2005, 2006

[Ber07] O. Bersillon et al., eds., TALYS-1.6: Proceedings of the International Conference on Nuclear Data for Science and Technology 2007, EDP Sciences, Nice, France, 2007

[Bey89] H. F. Beyer at al., Particle Accelerators 24, 163, 1989

[Bis12] H. Bichsel et al., Particle Data Group, Revised January 2012

[Bla85] K. Blasche et al. The SIS heavy ion synchrotron project. IEEE Trans.Nucl.Sci., vol.32, 2657, 1985

[Blu99] Y. Blumenfeld et al., Nuclear Instruments and Methods in Physics Research Section A: Accelerators, Spectrometers, Detectors and Associated Equipment 421 (3), 471, 1999

[BNL15] The Brussels Nuclear Library for Astrophysics Applications, maintained by Institut d'Astronomie et d'Astrophysique, Université Libre de Bruxelles, 2015

[Boh39] Niels Bohr and John Archibald Wheeler, Phys. Rev., vol. 56, 426–450, Sep 1939

[Bou11] G. Boutoux, Ph.D. thesis, U. Bordeaux, 2011

[Boy06] S. Boyer et al., Nucler Physics A, 775(3):175-187, 2006

[Bri79] H.C. Britt & J.B. Wilhelmy, Nucl. Sci. and Eng., vol. 347, no. 2, p.222, 1979

[Bro07] D. Browne et al., Rapport technique, 2007

[Bro18] D. A. Brown, M. B. Chadwick, R. Capote, A. C. Kahler, A. Trkov, M. W. Herman, A. A. Sonzogni, Y. Danon, A. D. Carlson, M. Dunn et al., Nuclear Data Sheets 148, 1, 2018

[Boul13] O. Bouland et al., Phys. Rev. C 88, 054612, Nov 2013

[Bout12] G. Boutoux et al., Physics Letters B, 712(4):319-325, 2012

[Caa13] M. Caamano, O. Delaune, F. Farget, X. Derkx, K.-H. Schmidt, L. Audouin, C.-O. Bacri, G. Barreau, J. Benlliure, E. Casarejos et al., Phys. Rev. C 88, 024605, 2013

[Can21] D. Cano Ott, nTOF collaboration , NSTAPP 2021

[Cap09] R. Capote et al., Nuclear Data Sheets, 110(12):3107-3214, 2009. Special Issue on Nuclear Reaction Data

[Cat14] W. N. Catford, Scheidenberger C., Pfutzner M. (eds) The Euroschool on Exotic Beams, Vol. IV. Lecture Notes in Physics, vol 879. Springer, Berlin, Heidelberg, 2014

[Cha02] M. Chanel, Proceedings, 8th European Particle Accelerator Conference, 2002, p. 563

[Cha02] Alexander Wu Chao and Maury Tigner, World Scientific Publishing, Handbook of Accelerator Physics and Engineering, ISBN 9810235005, 2002

[Chi15] C. J. Chiara et al., Phys. Rev. C 91, 044309, 2015

[Cra70a] J.D. Cramer and H.C. Britt, Nucl. Sci. Eng., 41, p. 177, 1970

[Cra70b] J.D. Cramer and H.C. Britt, Phys. Rev. C, 2(6), 1970

[Cyb10] R. H. Cyburt et al., Astrophys. J. Suppl. Ser. 189, 240, 2010

[Del80] P. Delahaye et al., Proc. 11th Int. Conf. on High Energy Accelerators, Geneva, p. 299, 1980

[Del16] O. Delaune, Ph.D. thesis, Universite de Caen, 201215, 2016

[Der10] X. Derkx et al., EPJ Web of Conferences, vol. 2, p. 07001, 2010

[Dol07] A. Dolinskii, F. Nolden, M. Steck, Proceedings, Workshop on Beam Cooling and Related Topics, pp. 106-109, 2007

[Duc15] Q. Ducasse, Ph.D. thesis, U. Bordeaux, 2015

[Duc16] Q. Ducasse et al., Phys. Rev. C, 94:024614, Aug 2016

[Due14] J.A. Duenas et al., Nuclear Instruments and Methods in Physics Research Section A: Accelerators, Spectrometers, Detectors and Associated Equipment, 743:4450, 2014

[Dup06] M. Dupuis et al., Phys. Rev. C 73, 014605, 2006

[Dup19] M. Dupuis et al., Phys. Rev. C 100, 044607, 2019

[Ege03] P. Egelhof et al., Phys. Scripta T 104, 151, 2003

[Egi09] T. von Egidy and D. Bucurescu, Phys. Rev. C 80, 054310, 2009

[Eic15] M. Eichler et al., The Astrophysical Journal 808, 30, 2015

[Eis07] J. Eichler et al., Physics Reports 439, 2007

[Eks97] C. Ekstrom, Nucl. Phys. A 626, 405c, 1997

[Ere03] V. Eremin et al., Nuclear Instruments and Methods in Physics Research Section A: Accelerators, Spectrometers, Detectors and Associated Equipment 500 (1–3), 121, 2003

[Esc06] J. E. Escher and F. S. Dietrich, Phys. Rev. C 74, 054601, 2006

[Esc12] J. E. Escher et al., Rev. Mod. Phys. 84, 353, 2012

[Esc18] J. E. Escher et al., Phys. Rev. Lett., 121:052501, Jul 2018

[Fes54] H. Feshbach, C. E. Porter and V. F. Weisskopf, Phys. Rev. 96, 448, 1954

[Fes80] H. Feshbach et al., Annals of Physics, vol. 125, no. 2, pages 429 – 476, 1980

[For19] Peter Forck, Proceedings of the General Introductory CAS course on Accelerator Physics & Technologies, 2019 and beyond GSI Helmholtz-Zentrum fur Schwerionenforschung, Darmstadt, Germany

[Fra87] B. Franzke, Nucl. Instr. Meth. Phys. Research Section B: Beam Interactions with Materials and Atoms 24-25, 1987

[Fra93] B. Franzke et al., Particle Accelerator Conference, 1993, Proceedings of the 1993, page 1645 vol.3, 1993

[Gan19] R. Gandhi et al., Phys. Rev. C 100, 18 Nov 2019

[GEF16] K.-H. Schmidt, B. Jurado, C. Amouroux, and Ch. Schmitt, Nuclear Data Sheets 131, 107, 2016

[Gei92] H. Geissel et al., Nucl. Instrum. Methods Phys. Res., Sect. B, 70(1):286 – 297, 1992

[Gho50] S. N. Ghoshal, Phys. Rev., 80:939-942, Dec 1950

[Gil65] A. Gilbert and A.G.W. Cameron, Can. J. Phys., no. 43, pages 1446–1496, 1965

[Gla86] J. Glatz., Proceedings of LINAC86, Stanford, page 321, 1986.

[Glo19] Jan Glorius et al., Phys. Rev., Lett. 122, 092701, 2019

[Gol08] B. L. Goldblum et al., Phys. Rev. C 78, 064606, Dec 2008

[Gol09] B. L. Goldblum et al., Phys. Rev. C 80, 044610, Oct 2009

[Gor08] S. Goriely et al., Phys. Rev. C 78, 064307, 2008

[Gor15] S. Goriely, Eur. Phys. J. A 51, 22, 2015

[Gra14] L. Grassi et al., Nuclear Instruments and Methods in Physics Research Section A: Accelerators, Spectrometers, Detectors and Associated Equipment, 767:99111, 2014

[Gra22] A. Grana-González et al., FAIR next generation scientists - 7th Edition Workshop, (FAIRness2022), 23-27 May 2022

[Gri15] K. Grigoryev, Physica Scripta T166, 2015

[Gru89] A. Gruber et al., Nuclear Instruments and Methods in Physics Research A282, 87-93 87, North-Holland, Amsterdam, 1989

[Gue78] P.T. Guenther et al., Nuclear Science and Engineering, Vol.65, p.174, 1978

[Gum05] A. Gumberidze, T. Stohlker, D. Banas, et al., Phys. Rev. Lett. 94, 223001, 2005

[Gut87] M. Guttormsen et al., Nuclear Instruments and Methods in Physics Research Section A: Acceleratios, Spectrometers, Detectors and Associated Equipment, 255(3):518 - 523, 1987

[Gut96] M. Guttormsen et al., Nuclear Instruments and Methods in Physics Research Section A: Acceleratios, Spectrometers, Detectors and Associated Equipment, 374(3):371 - 376, 1996

[Gut13] M. Guttormsen et al., Phys. Rev. C. 88, 024307, Aug 2013

[Hag07] S. Hagmann, T. Stohlker, C. Kozhuharov et al., Nuclear Instruments and Methods in Physics Research Section B: Beam Interactions with Materials and Atoms 261 (2007) 218 – 221.

[Hau52] W. Hauser and H. Feshbach, Phys. Rev., vol. 87, pages 366–373, Jul 1952

[Hil76] Hilton, "A possible vibrational mode in heavy nuclei", unpublished 1976, Int. Conf. on Nuclear Structure (Dubna)

[Hoc75] R. W. Hockenbury et al., Conference on Nuclear Cross Sections and Technology, volume 2 of Conference on Nuclear Cross Sections and technology, pages 584-586, 1975

[Hop62] J. C. Hopkins and B. C. Diven, Nuclear Science and Engineering 12, 169, 1962

[Igna75] Av Ignatyuk, GN Smirenkin and As Tishin, Sov. J. of Nucl. Phys., 21(3), p.255-257, 1975

[Jur17] B. Jurado et al., EPJ Web Conf., 146:11006, 2017

[Kaj19] T. Kajino et al., Progress in Particle and Nuclear Physics 107, 109, 2019

[Kes08] G. Kessedjian et al., Ph.D. thesis, U. Bordeaux, 2008

[Kes10] G. Kessedjian et al., Phys. Lett. B, 692(5):297-301, 2010

[Kle03] O. Klepper, C. Kozhuharov, Nuclear Instruments and Methods in Physics Research Section B: Beam Interactions with Materials and Atoms 204, 553 – 556, 2003

[Kno10] G. F. Knoll, "Radiation Detection and Measurement", John Wiley & sons, Inc., 2010

[Kno17] G. F. Knoll, "Radiation Detection and Measurement", 4th Edition, John Wiley & sons, Inc., 2017

[Koe87] Koehler et at., Phys. Rev. C. 35, p.1646, 1987

[Kon03] A.J. Koning and J.P. Delaroche, Nuclear Physics A 713.3-4 (2003), pp. 231–310

[Kun74] C. Kunz, Deutsches Elektronen-Synchrotron, Hamburg, Germany, 1974

[Lap16] T.A. Laplace et al., Phys. Rev. C. 93, 014323, Jan 2016

[Lar11] A.C. Larsen et al., Phys. Rev. C. 83, 034315, Mar 2011

[Les12] M. Lestinsky et al., "CRYRING@ESR: A study group report, GSI and FAIR Report", 2012

[Les16] M. Lestinsky, V. Andrianov, B. Aurand, et al., Physics book: CRYRING@ESR, The European Physical Journal Special Topics 225, 797–882, 2016

[Les17] M. Lestinsky et al., Phys. Rev. C 96, 034617, 2017

[Lid16] S. N. Liddick et al., Phys. Rev. Lett. 116, 242502, 2016

[Lit11] Yu.A. Litvinov and F. Bosch, Rep. Prog. Phys. 74, 016301, 2011

[Lit13] Yu.A. Litvinov, NIM B 317 603–616, 2013

[Lon86] M. A. Lone, Neutron induced reactions, Proc. 4th. Int. Symp., Smolenice, Czechoslovakia, 1985, J. Kristiak, E. Betak (Eds.), D. Reidel, Dordrecht, Holland, 238, 1986

[Lyl07] B. F. Lyles et al., Phys. Rev. C, vol. 76, 014606, Jul 2007

[Mac64] R. L. Macklin et al., Phys. Rev., vol. 136, p. B695, 1964

[MAD02] MAD - Methodical Accelerator Design, CERN - BE/ABP Accelerator Beam Physics Group, released June 2002

[Mai11] R. Maier, Proceedings, 2011 Particle Accelerator Conference, p. 2014, 2011

[Pet18] P. Mann, "Liouville's Theorem and Classical Statistical Mechanics", June 2018

[Mar14] J.-F. Martin, SOFIA collaboration, CEA, DAM, DIF, Perspective on Nuclear Data for the Next Decade, Oct. 2014

[Mas94] I. N. Meshkov, Physics of Elementary Particles and Atomic Nuclei 25, 631, 1994

[Mih06] L.C. Mihailescu et al., Euratom Reports N0.22343, 2006

[Mol92] S.P. Moller, 3rd European Particle Accelerator Conference, Berlin, Germany, 24-28 Mar 1992, pp.158

[Mor14] L. G. Moretto et al., http://arxiv.org/abs/1406.2642, 2014

[Mul08] A. Muller, Advances In Atomic, Molecular, and Optical Physics, Vol. 55, Academic Press, 2008

[Mum19] M. R. Mumpower et al., Progress in Particle and Nuclear Physics, 86, 2019

[Nol04] F. Nolden et al., Nucl. Instr. Meth. Phys. Research A 532, 329, 2004

[Nol04] F. Nolden, K. Beckert, P. Beller et al., Physics Research Section A: Accelerators, Spectrometers, Detectors and Associated Equipment 532, 329 – 334, 2004

[Nol09] F. Nolden, Int. J. Mod. Phys., E 18, 474, 2009

[Nol11] F. Nolden, P. H¨ulsmann, Y. Litvinov, et al., Nuclear Instruments and Methods in Physics Research Section A: Accelerators, Spectrometers, Detectors and Associated Equipment 659, 69 – 77, 2011

[Nor15] W. Nortershauser, R. Sánchez, Physica Scripta T166, 014020, 2015

[Nor59] J. A. Northrop, R. H. Stokes, and K. Boyer, Phys. Rev., 115, 1959

[Nov19] O. Novoty, P. Wilhelm, D. Paul et al., Science 365, 676, 2019

[Obl87] P. Obloinsky, Phys. Rev. C, vol. 35, no. 2, 407-414, Feb 1987

[Pal78] F. Palumbo, N. Lo Iudice, 1978 Phys. Rev. Lett. 41 1532

[Pan19] J. Pandey et al., Phys. Rev. C 99, 014611, 2019

[Pet04] M. Petit et al., Nucl. Phys. A, vol. 735, no. 3-4, pages 345 – 371, 2004

[Pet11] N. Petridis, A. Kalinin, U. Popp et al., Nucl. Inst. and Meth. in Physics Research Section A: Accelerators, Spectrometers, Detectors and Associated Equipment, 656, 2011, 1 – 4

[Pet11] N. Petridis, A. Kalinin, U. Popp, et al., Nucl. Inst. and Meth. in Physics Research Section A: Accelerators, Spectrometers, Detectors and Associated Equipment, 656, 2011, 1

[Piw74] A. Piwinski, Proc. 9th Int. Conf. on High Energy Accelerators, Stanford, CA, 1974

[Ple05] C. Plettner et al., Phys. Rev. C 71, 051605, 2005

[Plo20] A. J. M. Plompen, O. Cabellos, C. De Saint Jean, M. Fleming, A. Algora, M. Angelone, P. Archier, E. Bauge, O. Bersillon, A. Blokhin, A. et al., JEFF-3.3, Eur. Phys. J A 56, 1, 2020

[Pot90] H. Poth, Physics Reports 196, 1990, 135

[Rat19] A. Ratkiewicz et al., Phys. Rev. Lett., 122:052502, Feb 2019

[Rei97] H. Reich et al., Nucl. Phys. A, 626(1–2):417, 1997

[Rei14] R. Reifarth, C. Lederer and K.Kappeler, J. Phys. G: Nucl. Part. Phys. 41, 053101, 2014

[Rei17] R. Reifarth et al., Phys. Rev. Accel. Beams 20, 044701, 2017

[Rei94] M. Reiser, Theory and Design of Charged Particle Beams, Wiley, New York, 1994

[Ren14] T. Renstrøm et al., EPJ Web of Conferences Volume 93, 2015

[Res11] J. J. Ressler et al., Phys. Rev. C, vol. 83, page 054610, May 2011

[Rod14] C. Rodriguez-Tajes et al., Phys. Rev. C 89, 024614, 2014

[Ros92] J. Rossbach and P. Schmüser, Basic course on accelerator optics, CAS Jyvaskyla 1992, CERN 94–01, p. 76

[Ros13] D. M. Rossi et al., Phys. Rev. Lett. 111, 242503, 2013

[RIPL-3] R. Capote et al. "RIPL - Reference Input Parameter Library for calculation of nuclear reactions and nuclear data evaluation". In: Nucl. Data Sheets 110 (2009), p. 3107

[Sán19a] R. Pérez Sánchez, Ph.D. thesis, U. Bordeaux, 2019

[Sán19b] R. Pérez Sánchez et al., Nucl. Instrum. and Methods in Physics Research Section A Accelerators Spectrometers Detectors and Associated Equipment 933(6), April 2019

[Sán20] R. Pérez Sánchez et al., Phys. Rev. Lett. 125, 122502, 2020

[San20] M. S. Sanjari, D. Dmytriiev, Y. A. Litvinov, et al., Review of Scientific Instruments 91 (8), 083303, 2020

[Sch83] A. S. Schlachter et al., Physical Review A 27, 3372, 1983

[Sch00] A. Schiller et al., Nuclear Instruments and Methods in Physics Research Section A: Acceleratios, Spectrometers, Detectors and Associated Equipment, 447(3):498 - 511, 2000

[Sci10] N. D. Scielzo et al., Phys. Rev. C, vol. 81, page 034608, Mar 2010

[Ser97] L. Serafini and J.B. Rosenzweig, Phys. Rev. E 55, 7565, 1997

[She18] V. Shevelko, Y.A. Litvinov, T. Stöhlker, I.Y. Tolstikhina, Nucl. Instrum. Methods Phys. Res. B 421, 2018, 45–49

[She20] V. P. Shevelko, N. Winckler, I. Y. Tolstikhina, Phys. Rev. A 101, 012704, 2020

[Shi11] K. Shibata, O. Iwamoto, T. Nakagawa, N. Iwamoto, A. Ichihara, S. Kunieda, S. Chiba, K. Furutaka, N. Otuka, T. Ohsawa et al., Journal of Nuclear Science and Technology 48, 1, 2011

[Sie79] G. Siegert, et al., Nucl. Instrum. Methods Phys. Res. 164 (3), 437-438, 1979

[Sie19] D. M. Siegel, Eur Phys J A. 55, 203, 2019

[Sig04] P. Sigmund, Stopping of heavy ions: a theoretical approach, Springer tracts in modern physics, Springer, Berlin, 2004

[Spi06] P. Spiller,"FAIR at GSI", Proceedings of HB2006, Tsukuba, Japan, 2006

[Spy14] A. Spyrou et al., Phys. Rev. Lett. 113, 232502, 2014

[Ste00] M. Steck, K. Beckert, P. Beller, et al., Proceedings, 7th European Particle Accelerator Conference, pp. 587–589, 2000

[Ste03] M. Steck et al., Phys. Scr., 64, 2003

[Ste04] M. Steck, P. Beller, K. Beckert, B. Franzke, F. Nolden, Nuclear Instruments and Methods in Physics Research Section A: Accelerators, Spectrometers, Detectors and Associated Equipment, 532, 357 – 365, 2004

[Steck04] M. Steck et al., Instrum. Methods Phys. Res., Sect. A, 532(1–2):357, 2004

[Ste04] M. Steck et al., Nucl. Instr. Meth. Phys. Res., A 532, 357, 2004

[Ste15] M. Steck, "Beam Cooling", CAS, Warsaw, 27 September – 9 October, 2015

[Str11] B. Streicher et al., 8th International Conference on Nuclear Physics at Storage Rings-Stori, 11 January 2011

[Suz77] Suzuki T, Rowe D J 1977 Nucl. Phys. A 289 461

[Tak07] S. Takeda et al., Nuclear Instruments and Methods in Physics Research Section A: Accelerators Spectrometers Detectors and Associated Equipment 579 (2), 859, 2007

[Tal15] P. Talou et al., J. Phys. G: Nucl. Part. Phys. 42, 034025, 2015

[Tor13] D. Torresi et al., Nuclear Instruments and Methods in Physics Research Section A: Accelerators, Spectrometers, Detectors and Associated Equipment, 713:1118, 2013

[Tor15] D. Torresi et al., Journal of Physics: Conference Series, 590:012029, apr 2015

[Tov10] F. Tovesson and T. S. Hill, Nuclear Science and Engineering 165, 224, 2010

[Vas19] N. Vassh et al., J. Phys. G: Nucl. Part. Phys. 46, 065202, 2019

[Wan14] S. Wanajo et al., Astrophys. J. 789, L39, 2014

[Wan14] S. Wanajo et al., Astrophys. J. 789, L39, 2014

[Wan20] X. Wang et al., Astrophys. J. Letter 903, L3, 2020

[Wat19] D. Watson et al., Nature 574, 497, 2019

[Wei57] V. Weisskopf. Nuclear Physics, Rev. Mod. Phys., 29:174-181, 1957

[Wei57] V. F. Weisskopf, Nuclear Physics. Rev. Mod. Phys., vol. 29, pages 174–181, Apr 1957

[Wen19] W. Wen, H. Wang, Z. Huang, et al., Laser cooling and precision laser spectroscopy of highly charged ions at the storage ring CSRe and the future HIAF, Hyperfine Interactions 240, 2019, 45.

[Wie19] Helmut Wiedemann, Particle Accelerator Physics pp 701–735, 2019

[Wil20] E. Wilson and B. J. Holzer, "Beam Dynamics", Open Access First Online, 28 May 2020

[Wil12] J. N. Wilson et al., Phys. Rev. C 85, 034607, Mar 2012

[Wu19] M.-R.Wu et al., Phys. Rev. Lett. 122, 062701, 2019

[Wuo07] A.H. Wuosmaa et al., Nuclear Instruments and Methods in Physics Research, A 580, 1290–1300, 2007

[Xia02] J. Xia, W. Zhan, B. Wei, et al., Nuclear Instruments and Methods in Physics Research Section A: Accelerators, Spectrometers, Detectors and Associated Equipment 488, 2002, 11 – 25.

[Yam13] Y. Yamaguchi, M. Wakasugi, T. Uesaka, et al., Nuclear Instruments and Methods in Physics Research Section B: Beam Interactions with Materials and Atoms 317, 2013, 629

[Yan13] J. Yang, J. Xia, G. Xiao, et al., Nuclear Instruments and Methods in Physics Research Section B: Beam Interactions with Materials and Atoms 317, 2013, 263 – 265.

[Yan13] J. Yang, J. Xia, G. Xiao, et al., Nuclear Instruments and Methods in Physics Research Section B: Beam Interactions with Materials and Atoms 317, 2013, 263 – 265.

[Yan09] X. Yang, et al., Commissioning of electron cooling in CSRe, in: Proceedings, COOL09: Lanzhou, China, 2009

[Yor87] J. Yorkston et al., Nuclear Instruments and Methods in Physics Research Section A: Accelerators, Spectrometers, Detectors and Associated Equipment, 262(2):353358, 1987 Gesellschaft für Schwerionenforschung, D-6100 Darmstadt, FRG

[Yor87] J. Yorkston et al., Nuclear Instruments and Methods in Physics Research Section A: Accelerators, Spectrometers, Detectors and Associated Equipment, 262 (2–3), 353, 1987

[You03a] W. Younes and H. C. Britt., Phys. Rev. C, vol. 67, 024610, Feb 2003

[You03b] W. Younes and H. C. Britt., Phys. Rev. C, vol. 68, 034610, Sep 2003

[Zam17] J. C. Zamora et al., Phys. Rev. C 96, 034617, 2017

[Zei19] F. Zeiser et al., Phys. Rev. C 100, 024305 – Published 5 August 2019

[Zen17] Q. Zeng, M. Wang, X. H. Zhou et al., Phys. Rev. C 96, 031303, 2017 doi:10.1103/PhysRevC.96.031303.

[Zer18] V. V. Zerkin, B. Pritychenko, Nucl. Instrum. Methods A 888, 31, 2018

[Zer18] V.V. Zerkin, B. Pritychenko, Nuclear Instruments Methods A, 888, 31, 2018

[Zha19] J. Zhang, K. Yue, H. Li et al., Nuclear Instruments and Methods in Physics Research Section A: Accelerators, Spectrometers, Detectors and Associated Equipment 948, 162848, 2019

[Zhu19] G. Zhu, J. Wu, F. Caspers et al., Nuclear Instruments and Methods in Physics Research Section A: Accelerators, Spectrometers, Detectors and Associated Equipment 932, 83–89, 2019

[Zhu21] Y. L. Zhu et al., Astrophysics, ApJ 906 94, 2021

[FAIR] FAIR Baseline Technical Report (2006)

[G4bl] Tom Roberts, G4beamline User's Guide v3.06, February 2017, http://g4beamline.muonsinc.com

[GSI] GSI website: ion sources specifications

[Mesy21] Mesytec website, https://www.mesytec.com/products/nuclear-physics/MMR.html, accessed June 2021

[Micro21] Micron Semiconductor Ltd., http://www.micronsemiconductor.co.uk/, accessed June 2021

[Tal19] Talys 1.9 users' manual, 2019. www.talys.eu/documentation.

[Tar] Lise++ software, O.B.Tarasov and D.Bazin ,https://lise.nscl.msu.edu/lise.html

Part II

Chapter 1

Motivation

In part I of the manuscript we have seen that our detectors were located in pockets behind very thin stainless steel windows. However, this solution will not be possible for our future fission studies, because the fission fragments can have energies as low as few MeV/u and can be stopped in the stainless steel window. For this reason, the fission detectors have to be placed directly in the ring. Solar cells appears as an interesting alternative with respect to Si detectors because of their radiation hardness. In this part of the manuscript we will describe our studies on the response of solar cells and their UHV compatibility.

Solar cells are semiconductor devices especially designed to perform an efficient conversion of solar light into an electrical current. They have a wide range of applications from satellites up to household panels for energy production but they appear also as a very interesting and cost-effective option for the detection of heavy ions.

This possible use of solar cells was discovered by Siegert in 1979, when these devices were used for the first time as fission fragment detectors [Sie79]. The fission fragments produced and detected by the solar cells covered a broad range of nuclei ranging from mass number $A = 60$ to 160 with a typical kinetic energy of 1 MeV/u. From Siegert's experiment, the real potential and the multiple advantages of solar cells for the detection of heavy ions were clearly identified. The main advantages are the low cost, the flexible geometry, the radiation resistance and the quality of the response to fission fragments.

Additional experiments were performed some years later. Ajitanand et al. [Aji91] highlighted radiation hardness of solar cells, as well as their capability to detect fission fragments in an intense background of light charged nuclei. An important step in the investigation of the response of solar cells to ions was done by Liatard et al. [Lia88] in 1987. In this experiment they exposed solar cells to scattered ions of ^{12}C up to energies of 240 MeV, revealing a linear energy response up to 80 MeV [Lia88]. In this study the time resolution between two cells of 10×10 mm^2 was also measured obtaining a value of 12 ns FWHM. A dependence of the time resolution on cell size was also observed. Since then, solar cells have been used in several experimental campaigns as fission fragment detectors, see e.g. [Kes10, Kes15, Kog17, San19],

demonstrating the great possibilities of solar cells in nuclear physics experiments as heavy ion counters for coincidence measurements.

An important contribution to the study of solar cells properties as heavy ion detectors and their compatibility with UHV was done by Henriques et al. [Ana20]. In this work of our collaboration, a first exploratory study was performed on the solar cell response to heavy ions with energies up to 13 MeV/u and on their compatibility with UHV. The solar cell energy and time response was studied at the GANIL facility, where cells of different sizes and substrate materials were exposed to ^{84}Kr and ^{129}Xe beams from 7 to 13 MeV/u. At the same time the radiation hardness was investigated by monitoring energy and time signal of solar cells where increasing the beam intensity. The best results obtained, in terms of energy and time resolution, were obtained with silicon substrate cells of 10x10 mm^2. They showed an energy resolution between 1% and 4% (RMS) and a time resolution ranging between 3.6 and 7 ns (FWHM). Regarding the radiation hardness, a stable behaviour was observed for rates ranging between 100 and 1000 *pps*. Irradiation tests at larger beam intensities, around 50 thousand *pps*, were also performed to study the cell response in extreme conditions. At this rate, the cells showed a decrease of the energy resolution, while the time resolution remained stable. All these results confirmed that solar cells can be used to count heavy ions and measure time coincidences over a broad range of incident energies well above 1 MeV/u and for high rates.

Regarding the UHV compatibility, the first tests performed in our laboratory showed a very low outgassing, below $10^{-11} mbar \cdot l/(s \cdot cm^2)$ after bake-out for 48 h at 200 $^{\circ}C$. Furthermore, additional tests demonstrated that solar cells were not damaged by the bake-out operation.

However, several properties of solar cells still need to be carefully investigated for their use as heavy ion detectors in storage rings. First of all, the behaviour of the solar cell response as a function of the energy of the impinging heavy ions it is still unclear. The response in time and energy changes significantly with the intrinsic properties of the cells and their dimensions. For example, the previous tests pointed out that the cell response deteriorates when the size is increased, i.e. larger than 10x10 mm^2. In storage rings, where the available space is limited, the use of small solar cells in the design of large area detector arrays can be a problem since this will require to handle a large number of channels. In this respect, a key objective of current studies on solar cells is binding cells capable to ensure, also for large dimensions, performances comparable to the ones of the small 10x10 mm^2 roof cells usually implemented. This kind of study requires to better understand the operation of these devices and the process responsible for the signal formation, the so-called "field funneling effect".

The radiation resistance is another key property of solar cells. The behaviour of solar cells at constant irradiation rates of few thousand of *pps*, over a long period (situation quite close to the experimental conditions expected at storage rings) still needs to be investigated. A direct comparison with the degradation of the response of a standard silicon detector, exposed to the same ion rates, can be very useful in the evaluation of the radiation resistance.

In addition, for their use in storage rings, new and more accurate compatibility studies of solar

cells with UHV need to be performed.

Chapter 2

Properties of solar cells

In this chapter the basic properties of a n-p junction will be described together with the main characteristics of solar cells. This will allow for a better understanding of the main differences with respect to standard silicon detectors. In the end, the behaviour of solar cells as particle detectors will be discussed, focussing on the charge collection process called "field funneling effect".

2.1 Basic np-junction properties

In a completely pure semiconductor, all the electrons in the conduction band and all the holes in the valence band are generated by thermal excitation. Neglecting the possible residual impurities which can slightly modify the electric properties in pure semiconductor materials, the equilibrium established by the thermal excitation of electrons from the valence to the conduction band and their subsequent recombination, leads to equal numbers of electrons (n_i for cm^{-3}) and holes (p_i for cm^{-3}),

$$n_i = p_i \tag{2.1}$$

where the quantities n_i and p_i are known as the intrinsic carrier densities. As described in chapter 11 of [Kno17], these densities can vary depending on the semiconductor bandgap energy and temperature. Intrinsic hole or electron densities at room temperature are 1.5×10^{10} cm^{-3} in silicon, and 2.4×10^{13} cm^{-3} in germanium.
Due to the small number of available carriers, intrinsic semiconductors as silicon are characterized by a bad electrical conductivity and a high resistivity (about $2.3 \cdot 10^5$ $\Omega \cdot cm$). In order to improve the semiconductor electrical conductivity, a doping process is performed where the balance of electrons and holes in a silicon crystal lattice is shifted by "doping" it with other atoms. Different types of atoms allow one to obtain different types of doped semiconductors. In figure 2.1, the main elements used are represented. Atoms with one more valence electrons than silicon are used to produce "n-type" semiconductor material. These n-type materials are group V elements in the periodic table, and thus their atoms have 5 valence electrons that can form

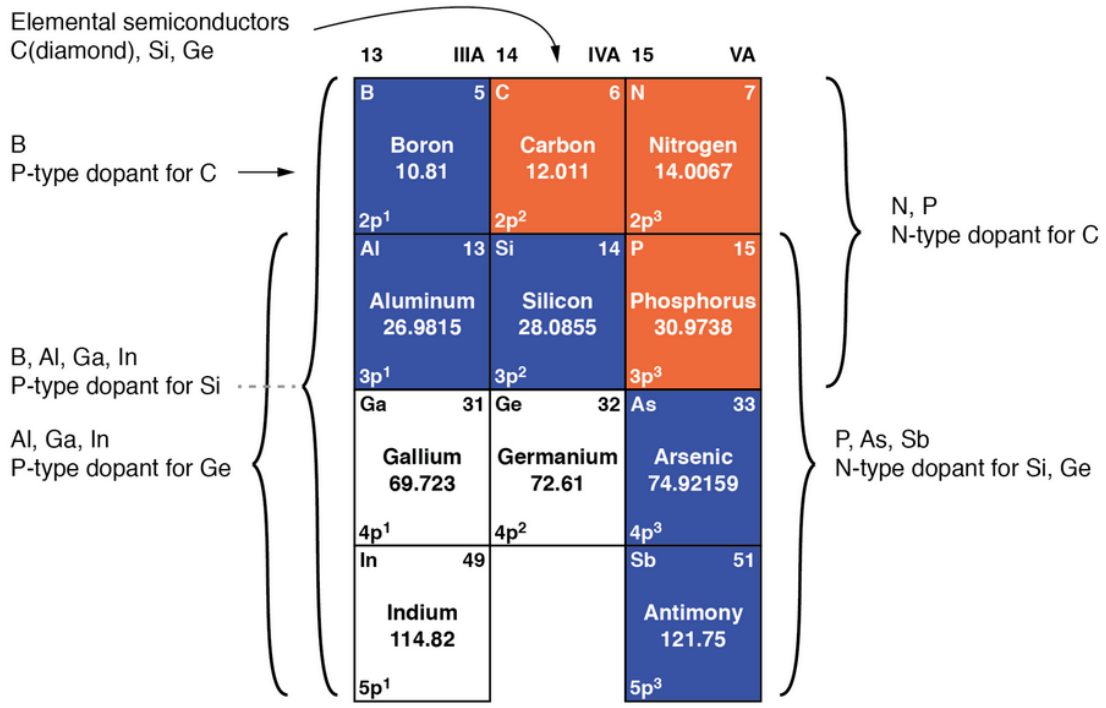

Figure 2.1: Group III and V elements used as dopants for silicon and germanium semiconductors. Typical examples of dopants are Boron (B) and Phosphorus (P) to produce p and n-type material, respectively.

covalent bonds with the 4 valence electrons of silicon atoms. Because only 4 valence electrons are needed from each atom (silicon and n-type) to form the covalent bonds around the silicon atoms, the extra valence electron present, when the two atoms are bond, is free to participate to the conduction (left side of figure 2.2). By increasing the concentration of dopants, more electrons are added to the conduction band, hence increasing the number of electrons present.

On the contrary, atoms of the group III elements in the periodic table with one less valence electron result in "p-type" material. The p-type material has only 3 valence electrons with which to interact with silicon atoms. The net result is a hole, as not enough electrons are present to form the 4 covalent bonds surrounding the atoms (right side of figure 2.2). In p-type material, the number of electrons trapped in bonds is higher, thus effectively increasing the number of holes.

In a doped material, there is always one type of carrier which is more present than the other and the type of carrier with the higher concentration is called a "majority carrier", while the lower concentration carrier is called a "minority carrier". The number of conduction electrons is then completely dominated by the contribution from the donor impurities, and we can write $n_i \approx N_D$ (for n-type) and $p_i \approx N_A$ (for p-type), where N_D and N_A are the dopants densities. Semiconductor detectors are based on the favourable properties that are created near the junction between n- and p-type semiconductor materials. In the junction, which is produced by

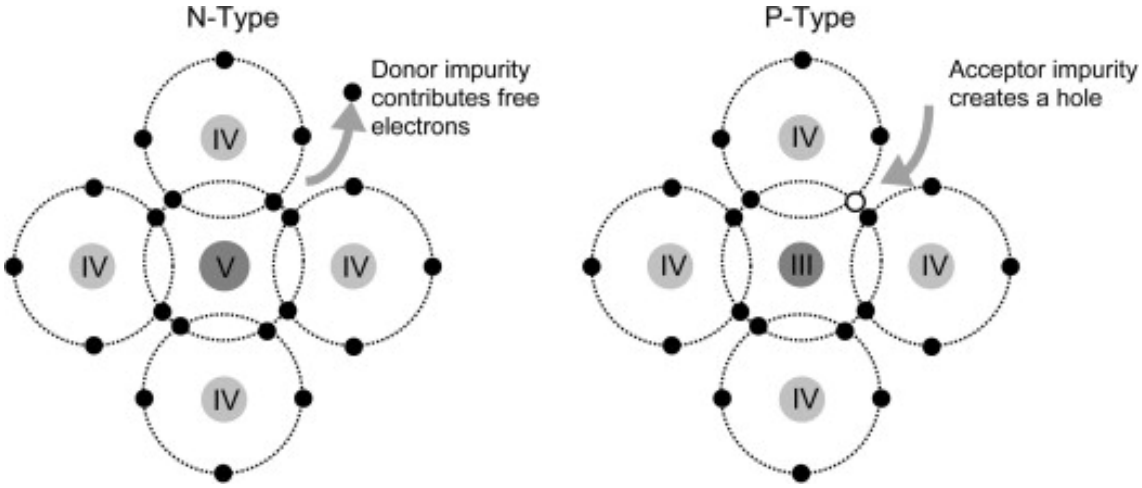

Figure 2.2: Example of doping performed on a semiconductor of the group IV elements. On the left figure a n-doping is realized by implanting an atom of the group V while in the right side a p-doping obtained with an element of the group III is shown.

changing the doping conditions in the crystal, the charge carriers are able to migrate across the junction.

As illustrated in figure 2.3(a), we can consider the case of a crystal having a high concentration of N_D decreasing with the distance from the semiconductor surface and a uniform concentration of acceptors N_A after a distance x from surface. Due to the charge migration, shown in figure 2.3(b), there is a net diffusion of conduction electrons into the p-type material and a similar symmetric movement of the holes into the n-type material. The combined effect is the build up of a net negative space charge on the p-side and a positive space charge on the n-side of the junction, as shown in figure 2.3(c). The accumulated space charge creates an electric field that diminishes the tendency for further diffusion. At equilibrium, the field is just adequate to prevent additional net diffusion across the junction, and a steady-state charge distribution is therefore established. The region over which the charge imbalance exists is called the "depletion region" and extends into both the p and n sides of the junction. The concentration of donors and acceptors in the n-type and p-type has a significant impact on the definition of junction properties. For example, if $N_A \approx N_D$, the diffusion conditions are approximately the same for both holes and electrons, and in this case the depletion junction has the same thickness in both the n and p sides.

In figure 2.4, the n-p junction is shown with a representation of the potential as a function of the position in the bottom of the figure. The fixed charges establish an electric field, and create a potential difference between p- and n-sides. This potential is called "built-in potential" and it is given by the expression:

$$V_0 = V_T \cdot ln\left(\frac{N_A \cdot N_D}{n_i^2}\right) \tag{2.2}$$

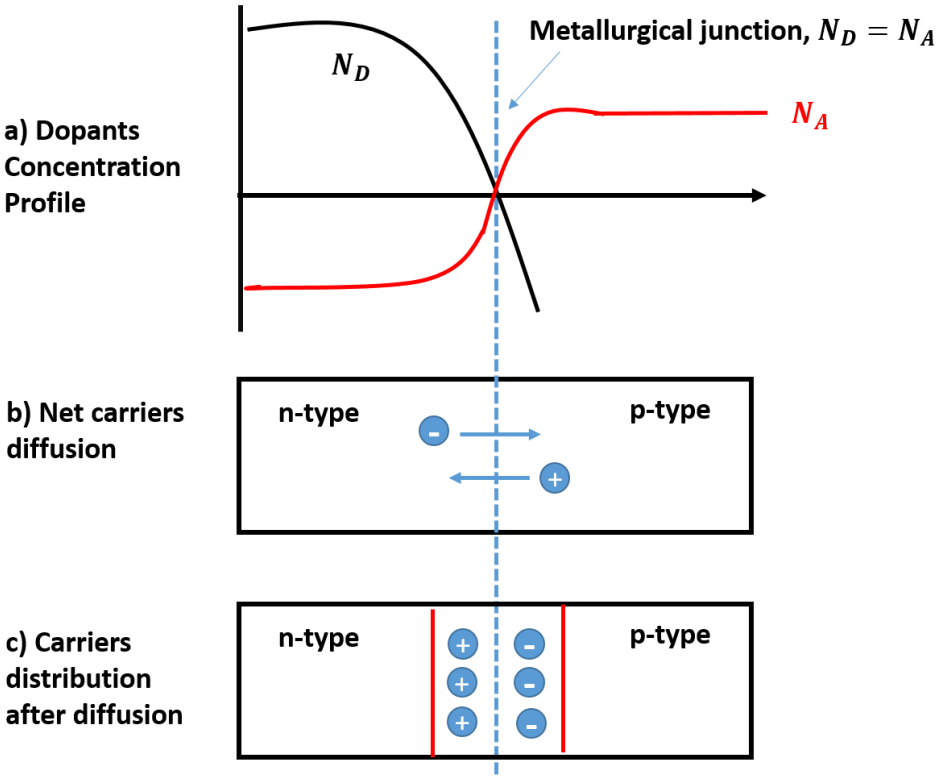

Figure 2.3: In the top figure are shown the dopant concentration profiles of the n-p junction presented in the bottom image. The N_D donor impurity concentration is large close to the junction surface and decreases sharply as one moves deeper inside. The N_A acceptor impurity concentration first increases before becoming constant. The center of the junction is located where N_A is equal to N_D. In figures (b) and (c) the diffusion of the charge carriers and the final distribution after the junction formation are shown.

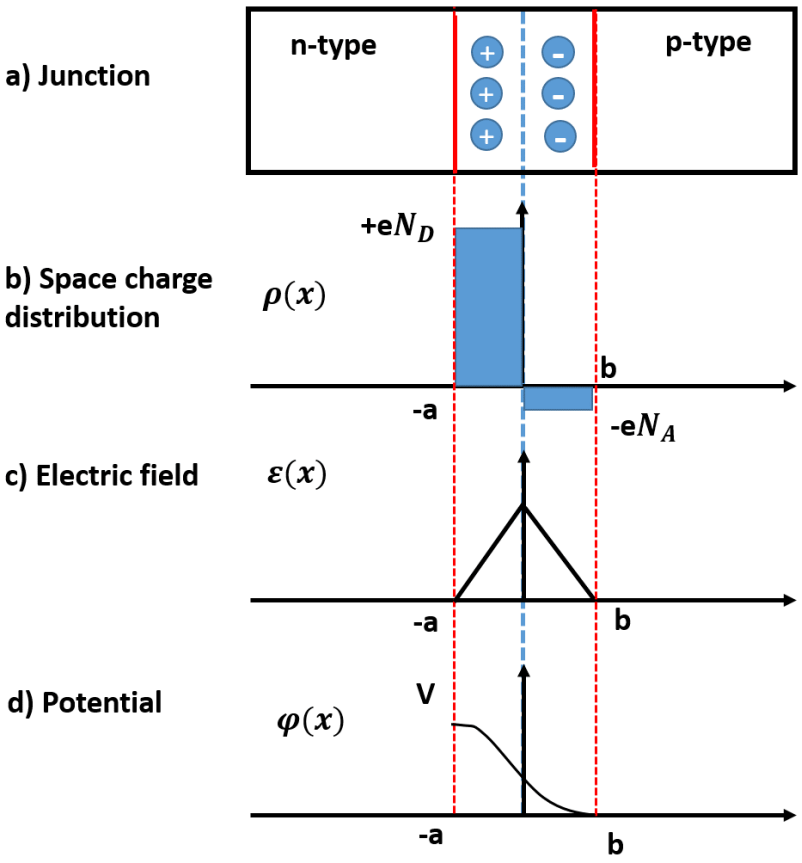

Figure 2.4: The profiles as a function of the position along x for the space charge $\rho(x)$, electric field $\epsilon(x)$ and electric potential $\phi(x)$ are shown for the n-p junction in the top.

where V_T is the thermal voltage[1] ($\approx 26\ mV$ at room temp), and n_i is the intrinsic carrier density. In one-dimension, the value of the potential ϕ at any point can be found by solving Poisson's equation

$$\frac{d^2\phi}{d^2x} = -\frac{\rho(x)}{\epsilon} \tag{2.3}$$

where ϵ is the dielectric constant of the medium and ρ the space charge distribution profile in figure 2.4(b). When a difference in electrical potential exists, there must also be an electric field E, whose magnitude is:

$$E(x) = -\frac{d\phi}{dx} \tag{2.4}$$

The electric field will extend over the width of the depletion region, in which charge imbalance is significant leading to a potential gradient.
Considering the formulation provided by [Kno17], some interesting properties of the junction can be derived from the one-dimensional case by considering the idealized charge distribution sketched in figure 2.4(b):

$$\rho(x) = \begin{cases} +e \cdot N_D, & (-a < x <= 0) \\ -e \cdot N_A, & (0 < x <= b) \end{cases} \tag{2.5}$$

Here the electron diffusion is assumed to result in a uniform positive space charge (the ionized donor sites) over the region $-a < x < 0$ on the n side of the junction. A corresponding negative space charge (the filled acceptor sites) resulting from hole diffusion is assumed to extend over the region $0 < x < b$ on the p-side.
The equation (2.3) can be applied obtaining the equation:

$$\frac{d^2\phi(x)}{d^2x}(x) = \begin{cases} \frac{-e \cdot N_D}{\epsilon}, & (-a < x <= 0) \\ \frac{e \cdot N_A}{\epsilon}, & (0 < x <= b) \end{cases} \tag{2.6}$$

We now carry out an integration and apply the boundary conditions that the electric field $E = \frac{-d\phi}{dx}$ must vanish at both edges of the charge distribution:

$$\frac{d\phi}{dx}(x = -a) = 0 \qquad \textit{and} \qquad \frac{d\phi}{dx}(x = b) = 0 \tag{2.7}$$

The result is then:

$$\frac{d\phi(x)}{dx} = \begin{cases} \frac{-e \cdot N_D}{\epsilon}(x + a), & (-a < x <= 0) \\ \frac{e \cdot N_A}{\epsilon}(x - b), & (0 < x <= b) \end{cases} \tag{2.8}$$

[1]The thermal voltage is calculated as $V_T = k_B \cdot T/q$ with k_B Boltzmann constant and q the elementary charge. As can be seen it is directly related to the temperature.

The potential as function of the position x can be calculated by integrating the electric field, which leads to:

$$\phi(x) = \begin{cases} \frac{-e \cdot N_D}{2\epsilon}(x+a)^2, & (-a < x <= 0) \\ \frac{e \cdot N_A}{2\epsilon}(x-b)^2, & (0 < x <= b) \end{cases} \tag{2.9}$$

The potential at $x = -a$ must be equal to the built-in potential V_0:

$$\phi(-a) = \frac{e}{2\epsilon} \cdot (N_A \cdot b^2 + N_D \cdot a^2) = V_0 \tag{2.10}$$

Let us assume that larger $N_D >> N_A$ and because $N_D \cdot a = N_A \cdot b$, it follows that $b >> a$. Therefore the space charge extends much further into the p side than into the n side, following the relations:

$$a = \frac{N_A}{N_A + N_D} \cdot W \qquad\qquad b = \frac{N_D}{N_A + N_D} \cdot W \tag{2.11}$$

where W is the depletion region width. By combining the equations in (2.10) with the equations in (2.11), we can then determine the depletion width and see that:

$$W = \sqrt{\frac{2\epsilon}{e} \cdot \left(\frac{1}{N_A} + \frac{1}{N_D}\right) \cdot V_0} \tag{2.12}$$

We can see that W depends on the dopant concentrations and on the voltage V_0. A reverse bias voltage V can be applied to increase the depletion width. We can then rewrite the equation (2.12) by replacing V_0 by the external potential V.
Because of the fixed charges that are built up on either side of the junction, the depletion region exhibits some properties of a charged capacitor. If the reverse bias is increased, the depletion region grows thicker and the capacitance represented by the separated charges therefore decreases. The value of the capacitance per unit area is:

$$C = \frac{\epsilon \cdot A}{W} = A \cdot \sqrt{\frac{e\epsilon}{2V} \cdot \frac{N_A N_D}{N_A + N_D}} \tag{2.13}$$

where A is the surface area of the junction. From equation 2.13 we can see the dependence of the capacitance, dopant concentration and on the n-p junction surface.

2.2 Material properties of solar cells

Solar cells can be produced with a number of semiconductor materials, most commonly silicon (Si) in mono-crystalline, polycrystalline, or amorphous form, but also with other semiconductor materials such as $GaAs$, $GaInP$, $Cu(InGa)Se2$, $CdTe$, and Ge [Par16]. Aluminium contacts present as thin strips in the front and as a uniform layer in the back face of the cell allow for the charge collection.

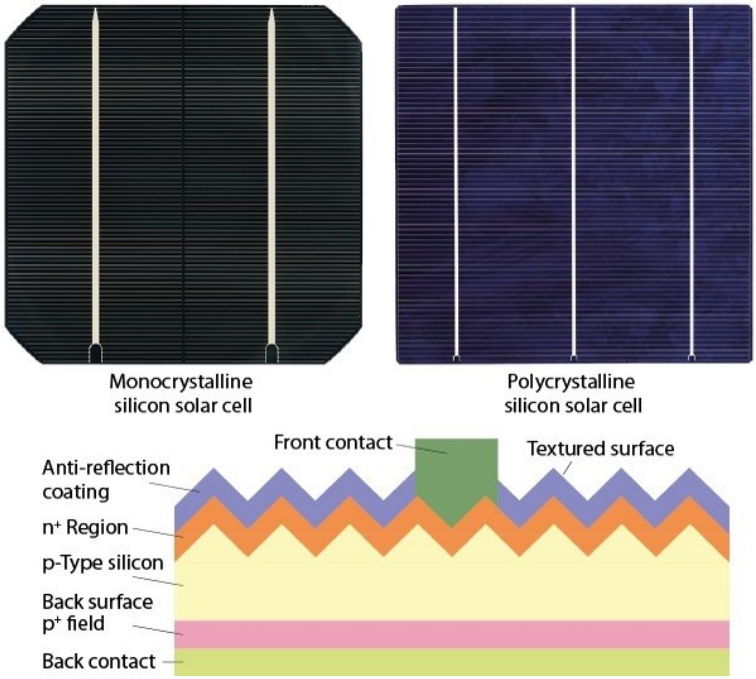

Figure 2.5: In the top some examples of solar cells. The finger contacts and the large busbars are clearly visible. The bottom part shows a section view of a single-junction solar cell with the different layers.

Currently, as shown in figure 2.5, the prevailing Si solar cell design is based on a front-lit or front-junction where the pn junction is formed very close to the front surface that faces the sun. It is made of a substrate also called "base" usually of p-type semiconductor with a variable thickness (up to few hundred μm) with on the top a thin layer of n-type semiconductor called "emitter". As electrodes, thin grid lines of cathode, usually of Al or Ag, are deposited on the n-type window layer, and a full anode layer, usually of Al, is deposited on the back side. As shown in figure 2.5, a busbar is also present to collect the signal from the different grid lines contacts.

We have to consider that the largest light absorption in solar cells occurs in the top layer (few μm) facing the sun. In this respect they are designed to efficiently separate and collect the charge produced, before it recombines, without the use of an external voltage. This requires to have a high built-in potential V_0 obtained by increasing, see equation 2.2, the density of dopants. As it will be explained in the following the larger dopants concentration in cells as important implication on other properties, making them different from the standard silicon detectors.

The doping concentration is commonly expressed in terms of resistivity since this is a readily measurable quantity. The resistivity measures how strongly the considered material resists to the electric current and it provides a simple way to compare solar cells and silicon detectors. The dependence of the resistivity with the dopants concentration is given by:

$$\rho = \frac{1}{q_o(\mu_n \cdot n + \mu_p \cdot p)} \tag{2.14}$$

where q_0 is the elementary charge, and μ_p, μ_n are the carriers mobility and n and p represent the carriers concentration in the semiconductor. Depending on the type of doping used, as described in section 2.1, we can have respectively $n \approx N_D$ or $n \approx N_A$. Usually, solar cells are characterized by a very low resistivity from 0.1 up to few tens of $\Omega \cdot cm$, which significantly affects other properties such as the capacitance (very high, about few tens of nF/cm^2) or the depletion region which is very small. However, some studies were performed to explore the possibilities of solar cells with high resistivity bulk material ($\rho > 86\ \Omega \cdot cm$) to improve the radiation resistance [Gor85, Aug19].

Silicon detectors have usually a resistivity of $\approx\ k\Omega \cdot cm$ and this is possible thanks to a very small concentration of dopants (around $10^{13} cm^{-3}$ in the base). For solar cells having a p-type base, the dopants concentration ranges between $10^{15} - 10^{16} cm^{-3}$ for high resistivity cells (few tens of $\Omega \cdot cm$) and $10^{20} cm^{-3}$ for low resistivity cells (0.001 $\Omega \cdot cm$). In a standard silicon detector, the application of the external reverse voltage produces an increase of the n-p junction depletion region and of the applied electric field. This makes possible to efficiently separate and collect the charge produced by the interaction with the incident particle before it recombines. The thickness of the depletion region is a fundamental parameter to obtain a detector proportional to the particle energy. In fact, the depletion thickness should be larger than the particle range in the detector in order to separate and collect all the charge produced.

The resistivity, which is related to the dopant concentration, plays a key role in the definition of the maximum thickness of the depletion region D, of the voltage required to reach a full depletion V_{FD} and capacitance:

$$V_{FD} = \frac{D^2}{2\epsilon\mu\rho} \tag{2.15}$$

$$C = A \cdot \sqrt{\frac{\epsilon_0 \epsilon_r}{2\mu\rho|V|}} \tag{2.16}$$

where ϵ_0 is the vacuum dielectric permittivity, ϵ_r is the silicon dielectric constant, and ϵ the absolute permittivity, μ the carrier mobility, A the total area of the detector and V the applied external voltage. The full depletion voltage is inversely proportional to the resistivity of the detector, while the capacitance is inversely proportional to the squared root of the resistivity and the voltage V_{FD}. To get a full depletion of a 200 μm thick solar cell, a resistivity $\rho \sim 5 \cdot \Omega \cdot cm$, a voltage of at least $\sim 3 \cdot 10^4\ V$ is required. At the same time the capacitance, which depends also on the total detection surface, will increase for low resistivities affecting in this way the signal amplitude.

The depletion thickness (W) is related to the voltage and the resistivity by the following relation:

$$W = \sqrt{2 \cdot \epsilon \cdot \mu \cdot \rho \cdot |V|} \tag{2.17}$$

In figure 2.6 some examples of the variation of depletion width with the applied voltage are shown for different resistivity values. A high resistivity is required to reach a large depletion width, while for low ρ values we can see that essentially no change takes place. The previous equations describe clearly the impact of the resistivity on the main properties a particle detector and they reflect the main problems related to the use of solar cells for particle detection.

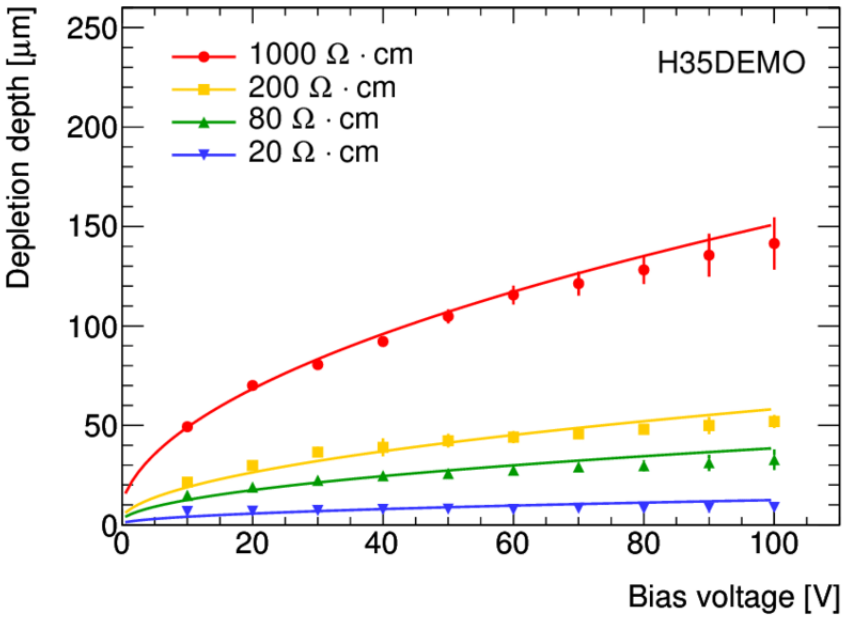

Figure 2.6: Increase of the depletion depth as a function of the applied bias voltage for different values of the resistivity [And18].

2.3 Solar cell circuit

A simple equivalent circuit model for a photovoltaic cell consists of a real diode in parallel with an ideal current source. However, a more complex solar cell equivalent circuit is needed where some resistive elements are included to account for power losses, such as a parallel

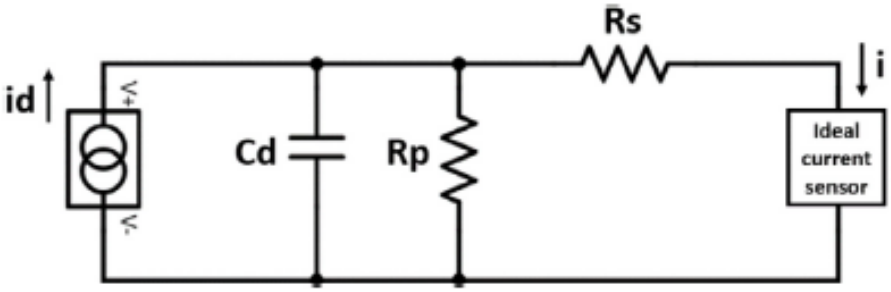

Figure 2.7: Solar cell electronic model [Ana20].

leakage (or shunt) resistance R_p, a series resistance R_s and a capacitance C_d in parallel. The series resistance, which must be very small (in the order of few Ω), is the contact resistance associated with the bond between the cell and its wire, plus the resistance of the semiconductor itself. The shunt resistance, on the contrary, shows the effect of manufacturing defects in the cells, which can create an alternative path of the current. Low values of R_p can cause power losses in the solar cells so we expect this resistance to be very high. An example of solar cell electronic model is presented in figure 2.7. This model was verified by performing impedance measurements using the Potencio-Electrochemical Impedance Spectroscopy technique at the IMS laboratory of the University of Bordeaux, considering silicon cells of different sizes. In this way the different values of the parameters as the C_d, R_p and the R_s were measured, see section (3.1). The transfer function of the electronic circuit shown in figure 2.7 is:

$$i = i_d \cdot \frac{1}{1 + j \cdot \frac{R_p \cdot R_s}{R_p + R_s} \cdot C_d \cdot w} \tag{2.18}$$

where i_d is the current generated by an impinging particle and i is the real output current of the cell. When considering that $R_s << R_p$, the transfer function can be simplified to:

$$i = i_d \cdot \frac{1}{1 + j \cdot R_s \cdot C_d \cdot w} \tag{2.19}$$

The latter expression reveals a low pass filter behaviour with a cutoff frequency ($f_c = \frac{1}{2\phi \cdot R_s \cdot C_d}$ dependent on C_d and R_s values. In the frequency domain, a large capacitance translates in a lower cutoff frequency. While in the time domain, the integration or time constant ($\tau = RC$) is larger, therefore for the same pulse duration one obtains smaller amplitudes for larger capacitances and thus larger solar cells.

2.4 Charge collection and field funneling effect

We have seen that solar cells have a semiconductor structure, similar to silicon detectors, with a larger concentration of dopants that reduces the detector materials resistivity (ρ). As a consequence, solar cells are characterized by a smaller depletion zone and a huge capacitance (typically a thousand times larger than the capacitance of standard silicon detectors). For this reason, due to the large capacitance, a specifically designed pre-amplifier device needs to be used. Due to the low resistivity, no net increase of the depletion width is obtained by applying a bias voltage while only an increase of the noise level can be observed.
In the usual mode of operation of a solar cell, when a photon strikes a cell, an electron–hole (e-h) pair is produced deeply in the bulk and the charge is collected by thermal diffusion up to the electrode.
In conventional silicon detectors, where the depletion region can range from few tens to hundred

of μm (depending on the bias voltage), the charged particle losses all or part of the energy, producing an high density of electron-hole pairs along the track. These e-h pairs are rapidly separated and collected thanks to the high electric field of the junction achieved by the application of the external bias. In this case, if the resultant ionization track does not traverse the depletion region, all the charge produced is collected and any modification of the depletion zone can be observed.

As explained in 1981 by Hsieh et al. [Hsi81], if a particle with a high ionizing power (such as an α particle) has an ionization track traversing the depletion region of a silicon device, a severe transient distortion called "field-funneling effect" takes place, which has significant implications in the charge collection. The field funneling effect depends strongly on the specific ionisation (dE/dx) profile of the particle and it requires a high plasma density to take place. For this reason, the relevance of the transient is larger for ions than for light particles (electrons, protons, etc).

In figure 2.8(a), a field funneling transient is produced after the passage of an energetic ionizing particle in a silicon sensor. At the onset of an ionizing radiation event, a cylindrical track of electron-hole pairs (quasi-neutral) with a radius of up to few μm and very high carrier concentration is formed in the wake of the energetic ion passage. When the resultant ionization track traverses the junction or its depletion region, if the high density of carriers generated n_i and p_i (around $10^{18} - 10^{19} cm^{-3}$ for an α-particle) is larger than the dopant background density, the initial junction depletion layer in the vicinity of the plasma column is neutralized and a transient transformation of the local equipotential lines around the track into a funnel shape (the so-called field-funneling effect) takes place (see figure 2.8(b)).

In detail, the initial electric field is screened by the electrons being draw of at the positive electrode and, as a consequence, the electric field initially confined to the junction is pushed down into the substrate. As long as the plasma density remains much greater than the substrate doping density (for a time of approximately $10^{-10} s$ for a Si bulk doping density of $10^{16}\ cm^{-3}$), the initial junction depletion layer will be neutralised. The funnel greatly enhances the efficiency of the drift collection by extending the high field depletion region deeper into the substrate and thus increases the amount of charge collected by the drift process.

The drift collection during the funneling process is possible thanks to a radial and a longitudinal charge separation of the electrons and the holes in the plasma column. The radial separation tends to occur near the outer edge of the column and the holes are drawn away, while the electrons are constrained to remain near the plasma column. At this point, the electrons are drifted up by the longitudinal field to be collected at the electrode. The size of the funnel increases with decreasing substrate doping (higher substrate resistivity) [Hu82].

With the expansion of the plasma column and the decrease of the plasma density, the junction depletion layer begins to reform. As the field is restored in the depletion region, the screening field along the column rapidly decreases until the junction depletion layer is completely reformed and the drift collection stops. At this point the remaining charge, produced by the

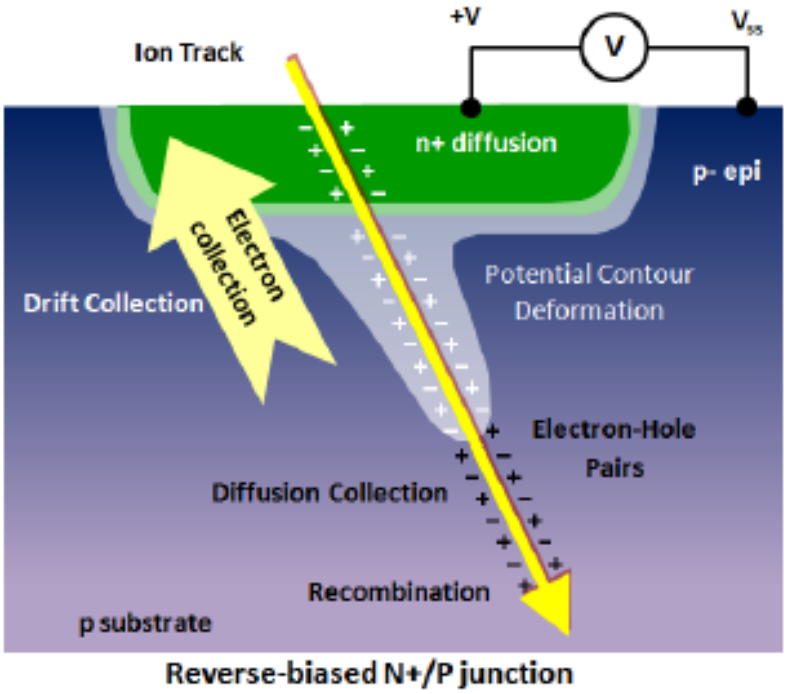

(a)

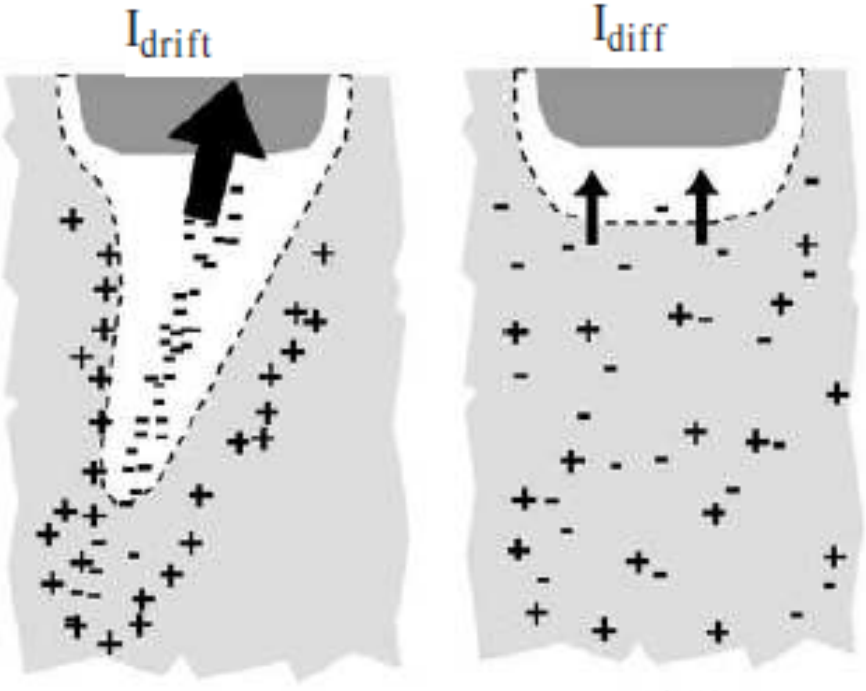

(b) (c)

Figure 2.8: Schematic representation of charge collection in a silicon junction immediately after (a) an ion strike, (b) prompt (drift) collection, (c) diffusion collection.

ionizing particle and still available in the bulk after the column collapse, is collected by diffusion, which becomes the dominant collection process (see figure 2.8(c)).
In figure 2.9, an example of current induced by a funneling effect transient is reported schematically. As can be seen, after the particle interaction (onset of event) a fast increase of the current due to the drift collection of the charge is observed. This "prompt" collection phase is typically completed within a few hundreds of ps (for biased detectors) and it is followed by a phase where diffusion dominates the collection process.

The electrons diffuse into the depletion region on a longer time scale. They can be collected

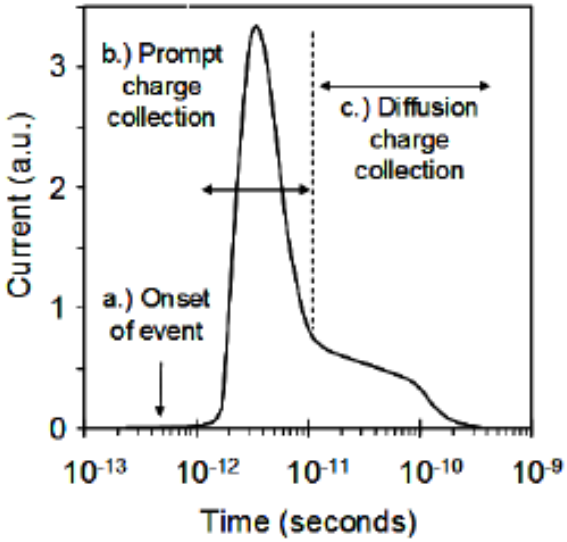

Figure 2.9: Current induced by the funneling transient effect in a biased silicon detector. As can be seen, the onset of the event is followed by the prompt charge collection (drift component of the signal). As soon as the plasma column collapses, the last part of the collection is performed by diffusion.

by diffusion until when all excess carriers have been collected, recombined, or diffused away from the junction area.
Even though the diffusion process is slow, a large amount of charge is collected during this phase. Ions typically produce larger signal in lightly-doped substrates, since funneling and, hence, the charge collection efficiency increases by decreasing doping.
Due to the properties of solar cells, particle detection can only take place if the incoming particle ionization profile is high enough to induce the complex funneling effect. For example, light charged particles (electrons, protons etc) lose only a small energy in the depletion zone and, the plasma density produced, is not high enough to produce the desired funneling effect. Therefore, solar cells are substantially insensitive to electrons, protons, neutrons, etc. For this reason, they can be used to detect heavy ions even if an intense flux of light particles is present.

Chapter 3

Investigation of solar cells response

In this work, we aimed to complete and improve the results obtained by our collaboration in Ana Henriques et al. [Ana20] on the investigation of the solar cells response to heavy ions at energies above 1 MeV/u. The studies described in this section were performed at the GANIL facility, where the cells were irradiated with a Krypton beam (^{84}Kr) at energies between 5 and 15 MeV/u. The objectives of this measurement:

- investigate the response of the solar cells in energy and time as a function of the beam energy, measure the energy and time resolution and compare the results with those of a standard Silicon detector. Solar cells of different sizes and types were used to study also the dependence of the response on the capacitance.
- irradiate cells at a rate of about $5 \cdot 10^3$ *pps* for about 4 hours providing the equivalent total irradiation dose expected during a measurement of one week in storage rings at rates of 10^2 *pps*.
- investigate the behaviour of the cells at high rates above 10^5 *pps*. Cells irradiated at these rates can be achieved when the stored beam accidentally hits a cell.

Before the measurements in GANIL, preliminary tests were performed with a californium source (^{252}Cf) at the LP2I of Bordeaux, to verify the quality of the cells to be tested.

3.1 Characteristics of the tested solar cells

In table 3.1, a list of the cells studied during the experiments is shown with their features. The cell types investigated devices were solar cells are either used for energy production on earth (roofs cells) [Sol19] or in space (space cells) [Sol19]. They were extracted from larger panels by means of a laser cut process. They had sizes of 10x10 mm^2 and 20x20 mm^2 and their thickness varied between 220 and 250 μm.
The composition and structure of the cells have a significant impact in the formation of the

List of tested solar cells					
Name	**Supplier**	**Application**	**Type**	**Size** (mm^2)	**N° of cells**
10x10 Si	Solar made	Household	Si, Single junction	10x10	3
20x20 Si	Solar made	Household	Si, Single junction	20x20	2
20x20 Si-s	Solar made	Space	Si, Single junction	20x20	2

Table 3.1: List of solar cells used during the experiments.

Supplier	**Application**	**Semiconductor**	$R_p(k\Omega)$	$R_s(\Omega)$	$C_d(nF/cm^2)$
Solar made	Household	Si, Single junction	1-12	0.1-6.9	39
Solar made	Space	Si, Single junction	5-10	10	12

Table 3.2: Results of the R_p, R_s, C_d measurement performed on solar cells.

electrical signal and therefore in the response of the solar cell when exposed to heavy ions. Hence, to better understand the behaviour of the tested cells, different measurements were performed.

The composition of the solar cells was verified via the Rutherford backscattering (RBS) method, using alpha particles of 2 MeV at the AIFIRA facility [Bar20] in Bordeaux, France. This analysis allowed us to identify the main components of the top layers of the cells and of the substrate semiconductor material.

As said in the previous section, we measured the resistances R_s, R_p and the C_d junction capacitance of the solar cells equivalent electrical circuit described in section (2.4). The results are summarized in table 3.2. As indicated in [Cur75, Yam01], space solar cells are characterized by a large resistivity respect to the roof ones since they needs to provide a better radiation resistance. In this respect, we observed that the capacitance of the space cells is about 3 times smaller than the roof cells. Considering equation 2.18, since the same size, this can be explained by a larger resistivity. As it will be shown later, these properties of space silicon cells will improve the quality of their response.

3.2 Preliminary tests

Before mounting the solar cells and measuring their properties, they were cleaned two times through an ultra-sound bath using demineralized water and ethanol (96%) to remove impurities and the dust accumulated in the surface.

The cells were irradiated with a spontaneous fission source of ^{252}Cf. The fission fragments produced have masses from 60 to 160 and energy of 1 MeV/u. Measuring the signal amplitude produced by the solar cells, a spectrum of the fission fragments can be produced for each cell. The quality of the cells response was evaluated by using the criteria defined in [Sch66]. They are presented in figure 3.1(a) while figure 3.1(b) shows one of the spectra we measured. The reference values for the parameters, defined by [Sch66] are listed in Table 3.3 together with the results obtained during the preliminary test.

The tests were performed at the LP2i of Bordeaux in an experimental chamber at primary vacuum conditions (around 10^{-2} $mbar$). The cells were mounted on dedicated PEEK (PolyEtherEther Ketone) supports in which integrated copper frames connected to kapton cables allowed the extraction of the signals through a single ended BNC connectors on the flange. The detectors were operated without bias and the signal collected from the front contact was sent to a special pre-amplifier developed for cells. This preamplifier was used also in [Ana20] and it consists of a transimpedance pre-amplifier (i.e. a current to voltage converter) and a fast shaper.

In figure 3.2(a), 3.2(b), 3.2(c) and 3.2(d) we present the mean amplitude of the signal induced by light and heavy fragments on different solar cells and on a silicon detector. The data (red symbols and blue symbols) were measured in two different experimental campaigns. In figure 3.2(a), for example, we can see the response of three different solar cells 10x10 Si. Due to defects and impurities[1], which are characteristic of each cell, differences in the response of cells of the same type and size can be observed. These differences are also reflected by the values of R_s, R_p and C_d which vary for one cell to the other (see table 3.2). Particularly relevant is the case of the 10x10 mm^2 cell (n° 4) providing a response about 15% lower than the others 10x10 mm^2 Si tested. Together with the solar cells, the response of a ORTEC silicon detector having a diameter of 10 mm and a thickness of 300 μm is shown in figure 3.2(d).

The previous plots provide a global view of the signal amplitude and they clearly show the strong impact of the capacitance on the cell signal amplitude. This is evident if we compare the 20x20 mm^2 and the 10x10 mm^2 silicon solar cells, while space cells show a response similar to the 10x10 Si.

Both the silicon solar cells for household panels of 10x10 mm^2 and space silicon cells of 20x20 mm^2 presented a good agreement, within the experimental error bars, with the reference parameters. On the contrary, the household panel cells with a size of 20x20 mm^2 were not able to produce spectra meeting the previously described criteria. This decrease in the quality of the detector response comes from the large surface, which leads to an increase of the capacitance and a significant decrease of the amplitude. Note that the space cells were able to provide a better response, even though they had a surface of 20x20 mm^2.

[1] In solar cell materials, defects and impurities can have a huge impact on the final product, acting as recombination centres for charge carriers. The main defects in multicrystalline Si (mc-Si) affecting performance are point defects (e.g. particulate impurities), linear defects (dislocations) and planar defects (e.g. grain boundaries).

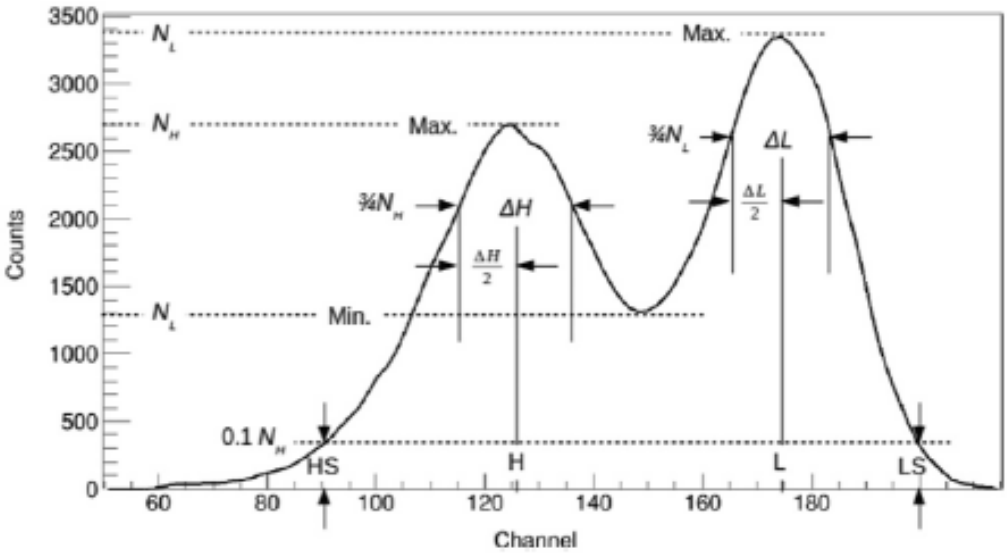

(a)

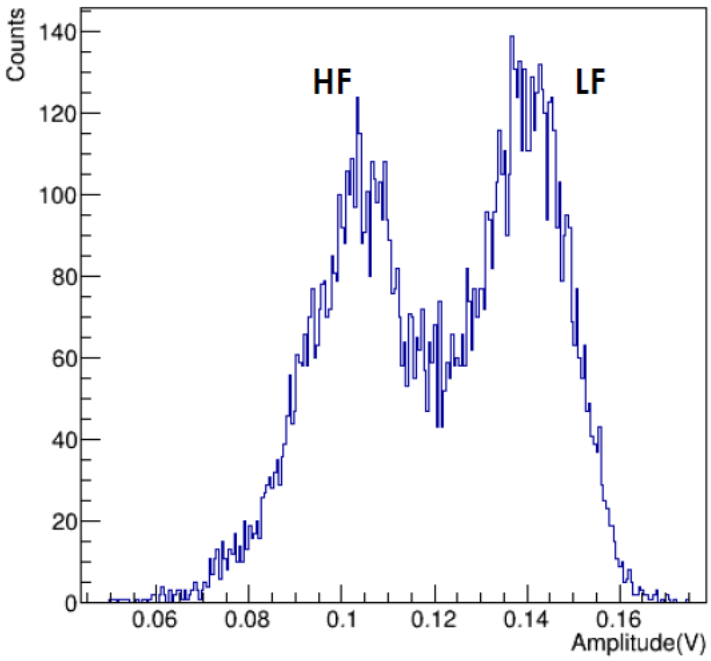

(b)

Figure 3.1: Figure (a) shows a smoothed ^{252}Cf fission fragment spectrum illustrating the spectrum parameters for detector performance evaluation defined by [Sch66]. Figure (b) shows an example of spectra measured from a solar cell 20×20 for space.

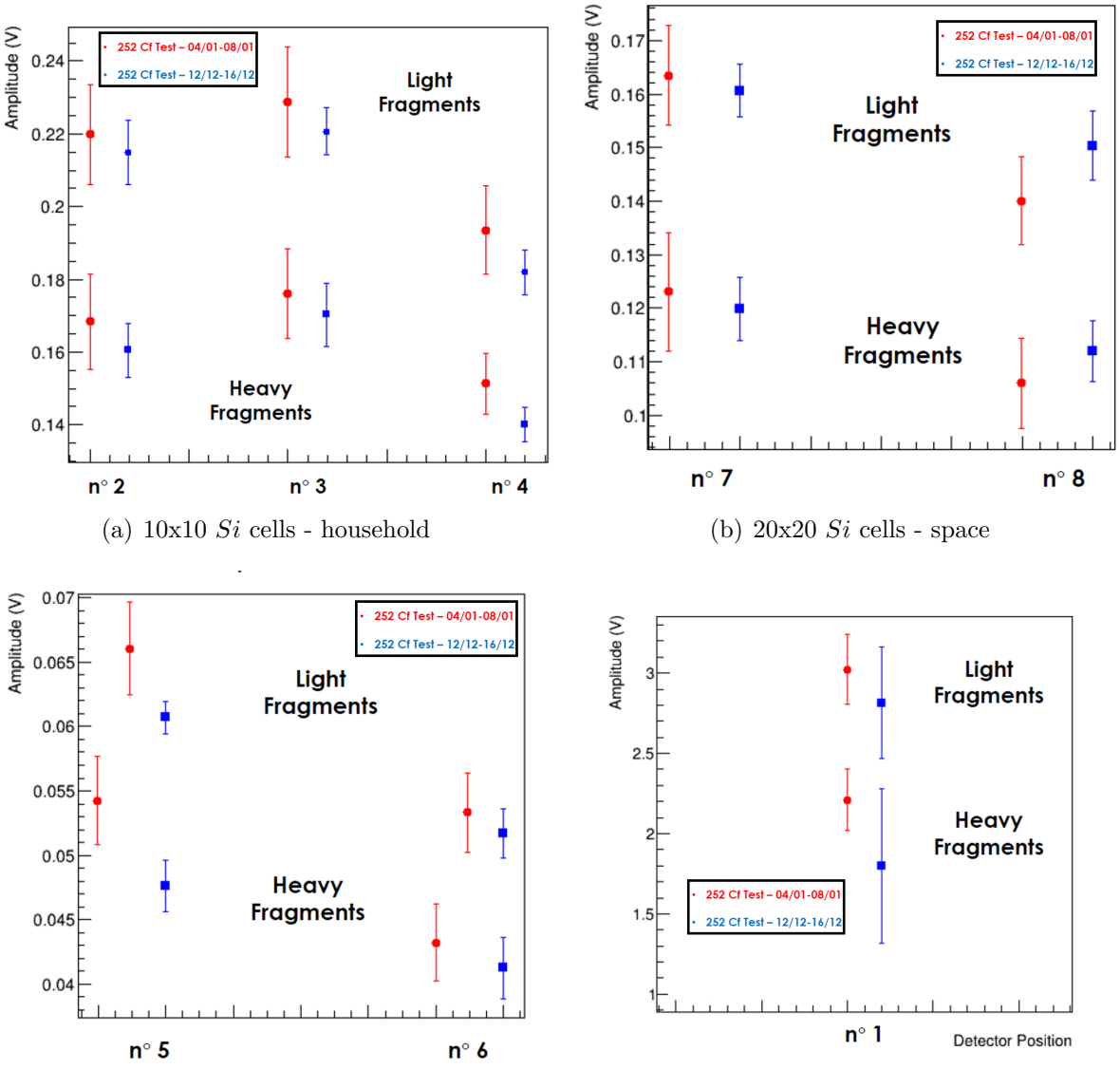

(a) 10x10 *Si* cells - household

(b) 20x20 *Si* cells - space

(c) 20x20 *Si* cells - household

(d) ORTEC silicon detector

Figure 3.2: Mean values of the amplitudes of the light and heavy fragments peaks in the measured fission fragment spectra. The position is defined by the H and L parameters, while the uncertainty are the width $\Delta H/2$ and $\Delta L/2$ of the heavy and light group as defined in figure 3.2(a). The red and blue colors indicate the results obtained in two different measurement campaigns with the same set-up. The dates of the two campaigns are indicated.

Performance of solar cells			
Cell Type	C_L/C_V **(∼ 2.85)**	C_H/C_V **(∼2.2)**	C_H/C_V (∼ 1.3)
Silicon detector	2.80 ± 0.34	2.43 ± 0.31	1.15 ± 0.14
10x10 Si household	2.75 ± 0.34	1.98 ± 0.25	1.39 ± 0.17
20x20 Si household	1.59 ± 0.14	1.34 ± 0.12	1.19 ± 0.11
20x20 Ge space	2.8 ± 0.34	2.52 ± 0.31	1.13 ± 0.14

Table 3.3: Results of the spectra analysis performed using Schmitt's parameters. The reference values of Schmitt [Sch66] are shown in bold format on the top of the columns 2,3 and 4.

3.3 Experiment at the GANIL facility

3.3.1 Experimental set-up

In March 2021, we performed new tests aimed to study the response of solar cells when irradiated with heavy ions at energies above 1 MeV/u at the GANIL (Grand Accélérateur National d'Ions Lourds) facility [Bea92] in France. The GANIL facility is dedicated to the acceleration of heavy ion beams for nuclear physics, atomic physics, radiobiology and material irradiation. The lightest heavy ion that can be accelerated is ^{12}C in the energy range from 20 MeV/u to 100 MeV/u. The heaviest available ion is ^{238}U up to 25 MeV/u. The intensity can be varied between 10 to 10^{14} pps.

The CIME heavy ion cyclotron [Lau97] which is part of the SPIRAL[2] installation was used to accelerate a beam of ^{84}Kr up to energies of 5, 10 and 15 MeV/u. After being accelerated, the heavy ions were sent to the test solar cells placed at the diagnostic chamber L5 downstream the CIME cyclotron where the solar cells were located. In figure 3.3(a), the layout of the SPIRAL facility around the CIME cyclotron is shown including the L5 diagnostic chamber, where a propulsor with the cells was located. To reduce the beam intensity to rates of few 100 pps, a carbon stripper foil (1 μm thick) was inserted at the exit of the cyclotron.

The goal was to reduce the beam intensity by splitting it over different charge states, see figure 3.3(b), and to use the dipole D11 to select the charge state that correspond to the specific rate of particles per second to be sent on the solar cells.

The solar cells were mounted on a stainless-steel rotating structure able to host up to 9 cells, see figure 3.4, this structure was installed on a propulsor. Thanks to the propulsor it was possible to insert the cells support perpendicular to the beam line and to irradiate a particular cell. Different cells could be tested with the aid of a goniometer integrated in the propulsor

[2]Separateur et Postaccelerateur d'Ions Radioactifs Accelerés en Ligne

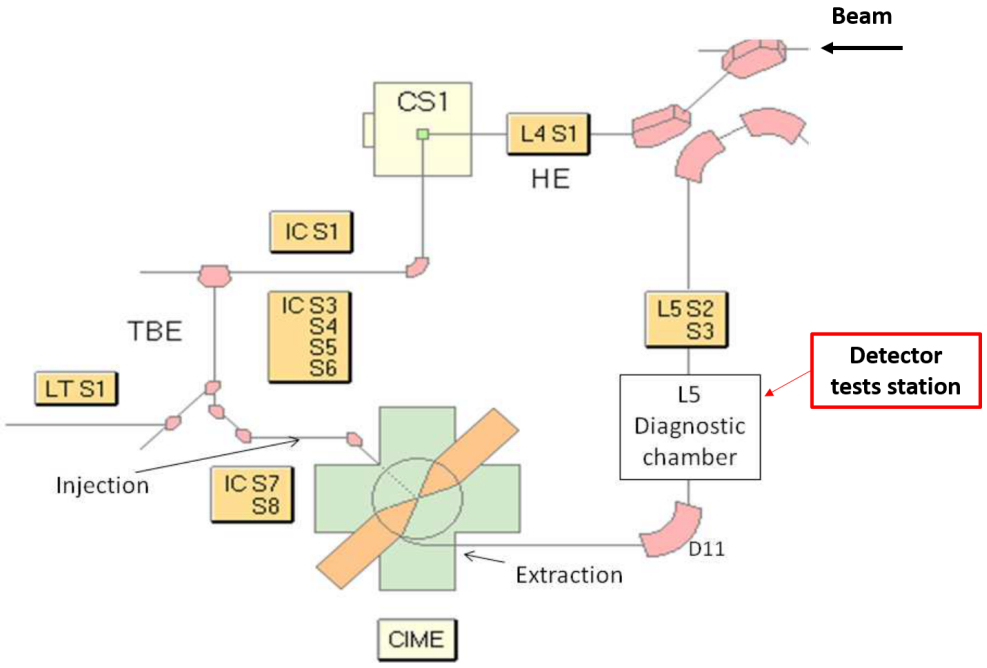

(a)

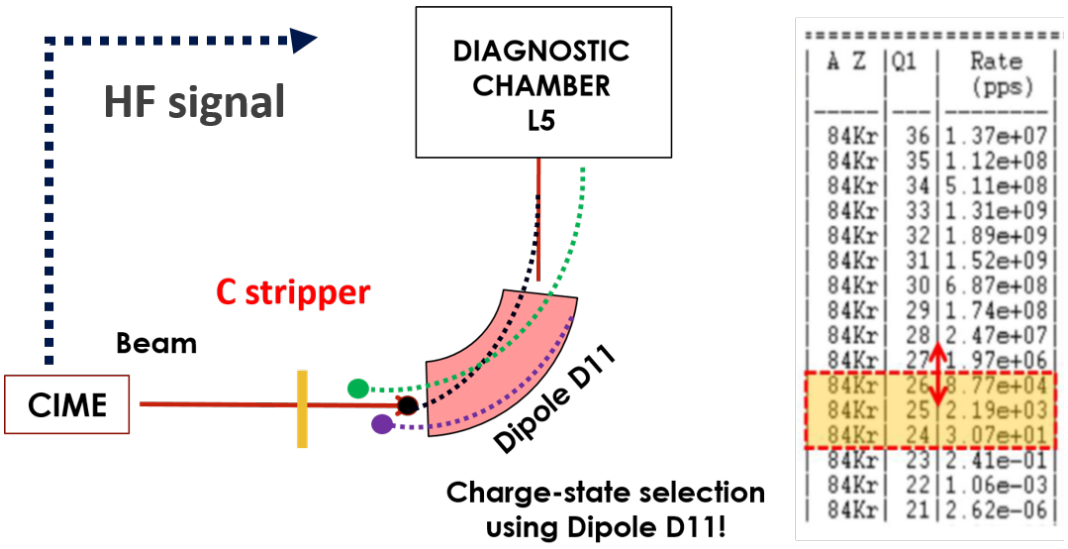

(b)

Figure 3.3: Figure (a)shows a schematic drawing of part of the SPIRAL facility and the CIME cyclotron. The ^{84}Kr beam was coming from the top and injected into the CIME cyclotron for acceleration up to 5, 10 and 15 MeV/u. Once the desired energy was reached the ion bunches were sent to the diagnostic chamber L5 where the cells were located. In figure (b), the schematic representation of the charge state selection operated by the dipole D11 is shown. In the table some values of the expected rate for different charge states are reported.

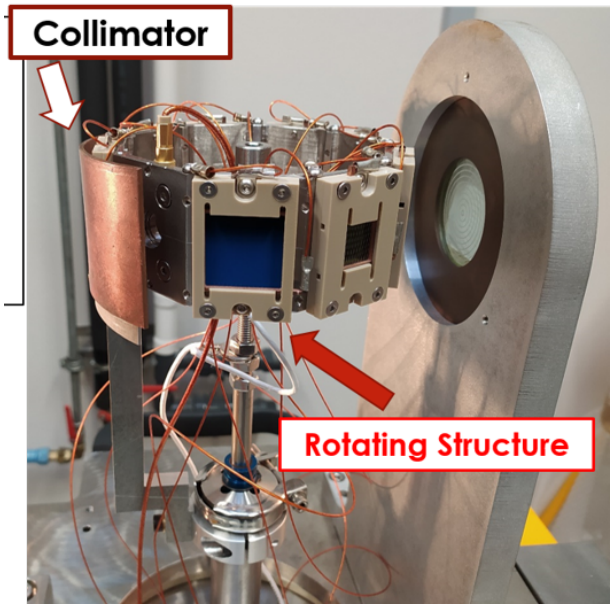

Figure 3.4: The rotating holder mounted on the propulsor is shown with the mounted solar cells during the alignment procedure. This propulsor was used to move the cell rotating structure in and out of the beam line.

allowing to turn manually the cells holder. The cells were removed from the beam axis during the tuning of the intensity.

The properties of the solar cells mounted on the rotating support and tested during the experiment are specified in table 3.1. A Si detector from ORTEC, mentioned in section 3.2, was also mounted and used as a reference. As was done during the preliminary tests, the solar cells were sandwiched with PEEK supports made of two rectangular pieces. Copper frames, integrated on each PEEK support allowed us to collect the signals from the front part of the cell and to connect the backside to the ground. Aluminium foils were used to improve the contact of the solar cell backside with the copper frames. Only UHV compatible mechanical contacts were used to connect the solar cells to the ground and the signal transmission. In detail, kapton insulated cables were employed in vacuum and the connection of the signal cables with the single ended BNC feedthroughs on the flange was done with $BeCu$ connectors. Furthermore, a collimator with a hole of 8 mm diameter was placed in front of the rotating cell holder to stop the undesired charge states outside of the central trajectory.

The signal provided by the solar cells was sent firstly to the dedicated preamplifier mentioned in the previous section. The signal delivered by the preamplifier device was sent to a Tektronix oscilloscope used to measure the rise time and amplitude. An example of the signal collected by mean of a Tektronix oscilloscope at the output of the preamplifier, for a 10x10 Si cell irradiated with a ^{84}Kr beam at 15 MeV/u, is shown in figure 3.5. After the characterization of the signal output from the pre-amplifier, the signal was sent to a linear amplifier and a fast amplifier. The linear amplifier was operating with a shaping time of 0.5 μs and a variable gain (specific for each type of cell tested). The amplified signal was delivered to an ADC module.

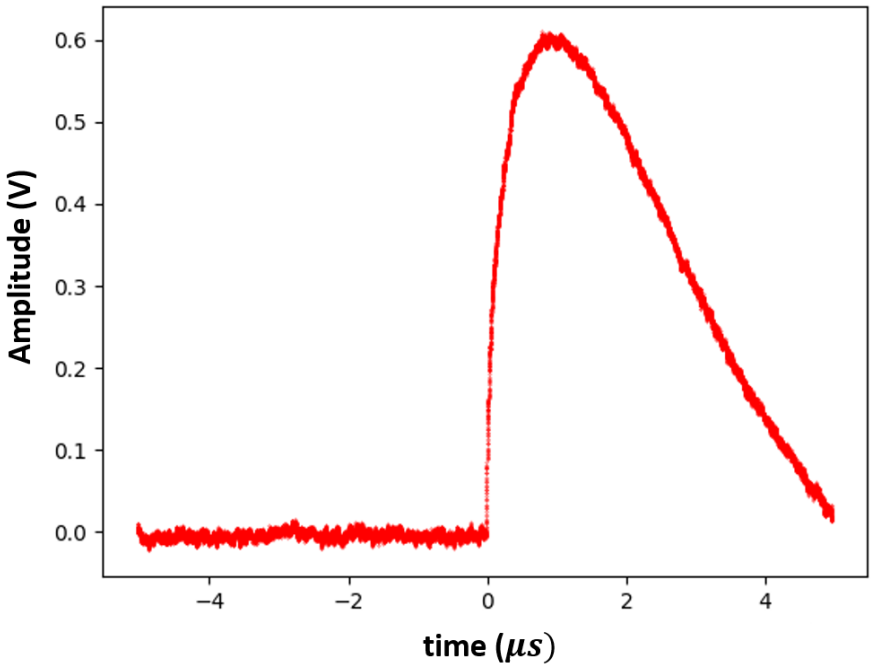

Figure 3.5: Signal at the output of the preamplifier of a solar cell of 10x10 mm^2 exposed to a 15 MeV/u ^{84}Kr beam.

After passing through a constant fraction discriminator (CFD), the output signal from the fast amplifier was delivered to a trigger module to generate the trigger signal, opening a gate. The gate defined the time during which the peak-sensing Analog to Digital Converter (ADC) would track the maximum of the output signal of the amplifier. The time measurements were performed using TAC (time to analog converter) module were the output of the CFD was used as a START signal, while the STOP signal was provided by the operating frequency (HF) of the CIME cyclotron (typically in the 10 MHz range). The output of the TAC module was finally sent to the ADC module.

3.4 Results

3.4.1 Signal rise-time and amplitude

An important step towards a better understanding of the solar cells response is the characterization of the output signals coming from the preamplifier. These kind of analysis can provide relevant information about the signal behaviour as a function of the energy for the different types of cells tested, and it is fundamental for the final optimization of the pre-amplifier system. In fact, as already described in chapter 2, the solar cell size and composition have significant implication on the cell capacitance influencing the final output signal amplitude and

rise time. The measurement were realized using a Tektronix oscilloscope [Tek], which allowed us to extract for each cell and beam energy the mean values of the recorded signal amplitudes and rise times. The rise time was defined as the time difference between the times at 5% and 95%.

In figure 3.6, the mean values of the rise times measured as a function of the ions beam energy are shown. In panel (a) the response of the silicon detector is compared to a 10x10 mm^2 household cell and a 20x20 mm^2 space cell, while in panel (b) the response of the tested 10x10 mm^2 cells is compared to the largest 20x20 mm^2 of the same type (household). The measured rise time ranged from 100 ns to 1 μs (for the largest 20x20 mm^2 household cells) and as already pointed out in [Ana20] a dependence on the beam energy was observed. In this experiment we were able to measure more precisely the increase of the rise time. This increase was found to be linear for the reference silicon detector. In the case of the solar cells, a non-linear increase was observed, with slightly variations from one cell to the other.

The space solar cells showed a lower rise time than the other 20x20 cells for all the beam energies. They ranged between 100-450 ns and were comparable to those of the smallest 10x10 mm^2 household cells. This difference in the rise time and, as it will be seen later, in amplitude can be explained by the lower cell capacitance, which probably comes from the larger resistivity of semiconductors materials used in space cell to improve the cells radiation resistance [Cur75].

As indicated by equation (2.18), the capacitance increases with the cell surface. This produces in large surface cells a decrease of the cutoff frequency of the cell lower pass filter (see section 2.3) and a significant increase of the rise time with the increase of the beam energy, as can be seen in figure 3.6(b). Regarding the reproducibility of the cells response, we can conclude that even if small differences can occur, in general cells of the same type and dimensions have a similar response and behaviour as a function of the beam energy of the ^{84}Kr beam.

In figure 3.7, the measured amplitudes as a function of the beam energy are shown. In figure 3.7(a) we can see the impact of the large capacitance of household 20x20 cells, which is reducing significantly the signal amplitude. However, despite the large dimensions, solar cells for space applications were able to provide a signal amplitude close to the 10x10 mm^2 household cells. In figure 3.7(b) we can see a comparison between the amplitude, of the silicon detector (black symbols), a 10x10 household cell (pink symbols) and one space 20x20 cell (red symbols). In this respect the linearity of the increase can not be verified with the measurement performed with the oscilloscope.For all the cells tested we observed that the signal amplitude increases when the beam energy increases from 5 to 10 MeV/u and then it decreases for 15 MeV/u. This unexpected non-linear response of the cells as function of the beam energy is investigated in detail in the next section (3.4.2).

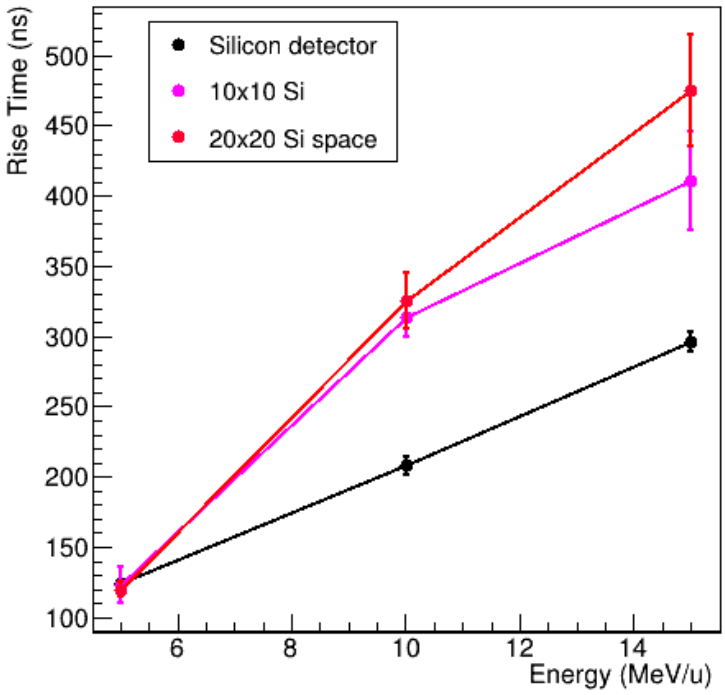

(a)

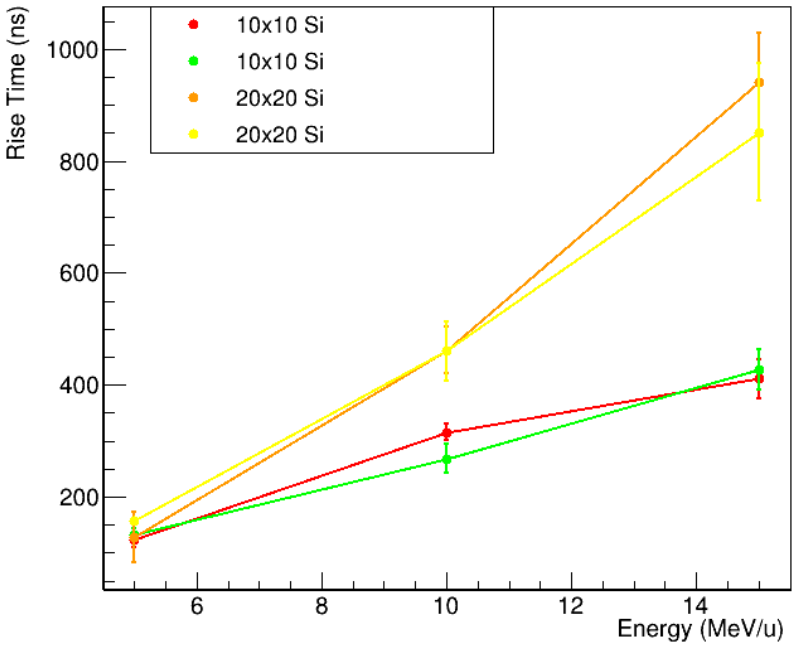

(b)

Figure 3.6: Average rise time observed for the reference Silicon Detector and different solar cells as function of the beam energy. The rise times were measured with the oscilloscope.

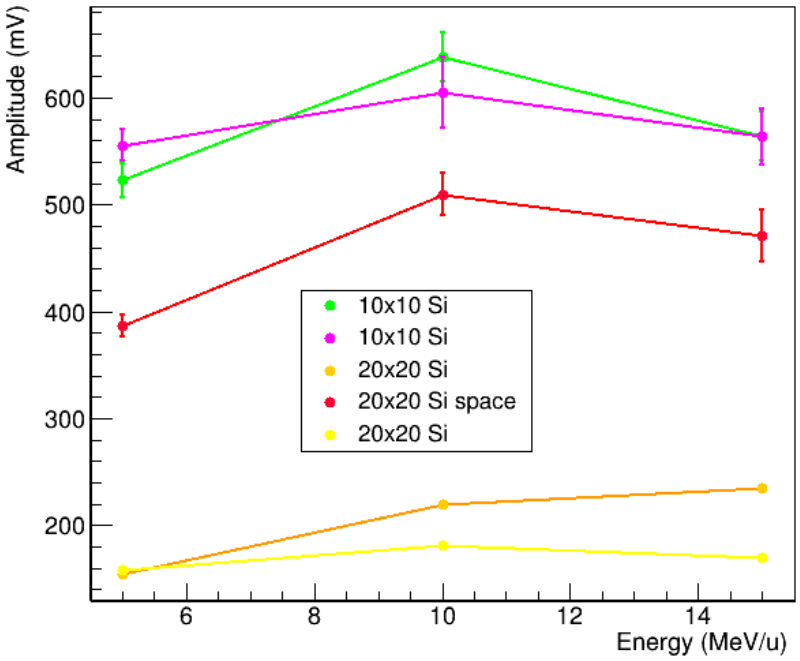

(a)

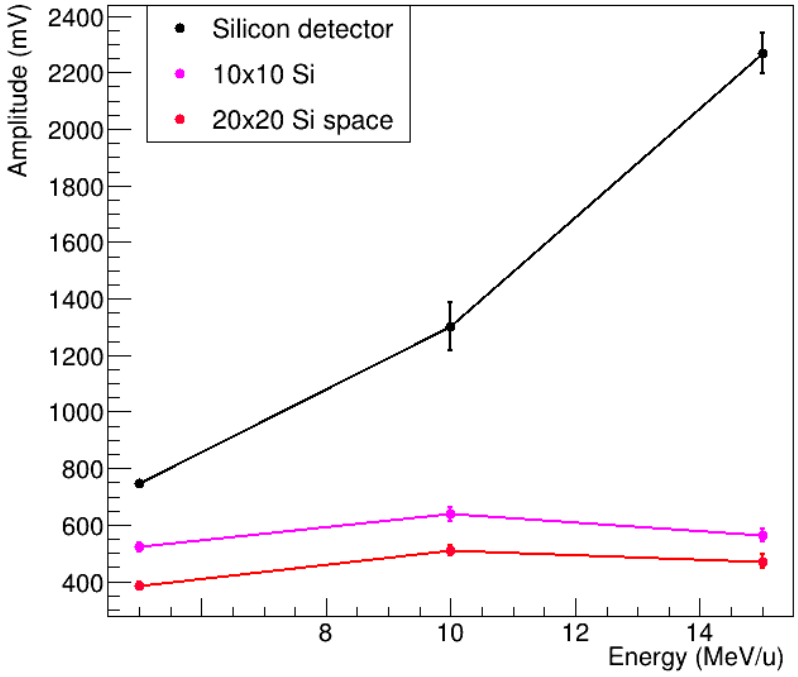

(b)

Figure 3.7: Average amplitude of the solar cell signals as a function of the beam energy, figure (a). The amplitudes of one 10x10 and a space 20x20 are compared to the reference silicon detector in figure (b). The amplitudes were measured with the oscilloscope.

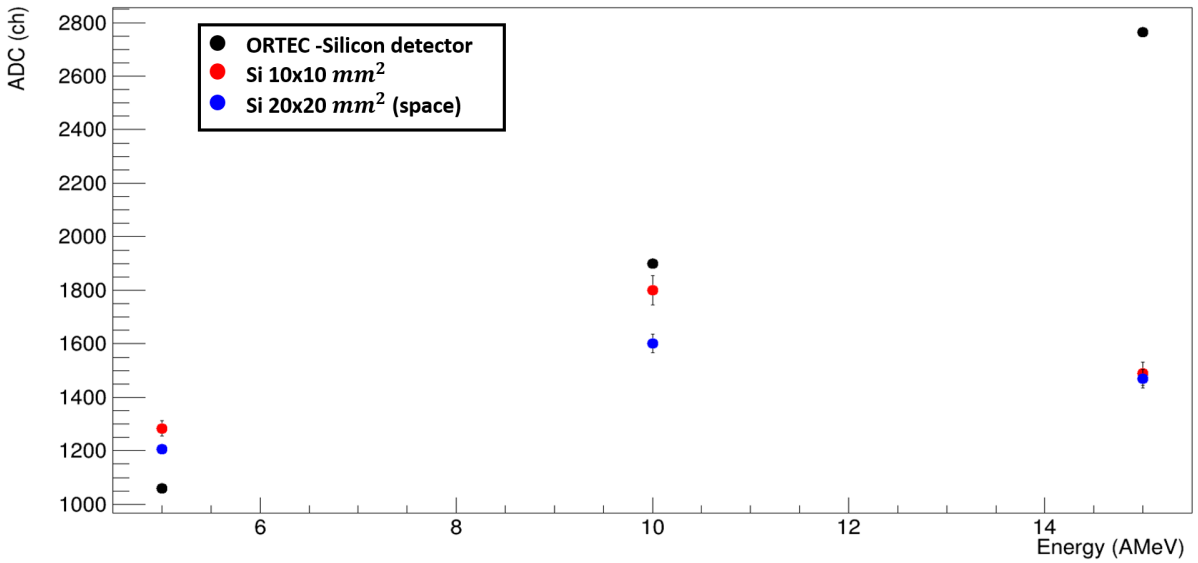

Figure 3.8: Average amplitude measured with the ADC energy spectra as a function of the beam energy for the silicon detector, a space cell of 20x20 mm^2 and a household cell of 10x10 mm^2.

3.4.2 Solar cells non-linear response

The response of the tested cells was carefully analyzed by measuring the amplitude of the amplified signal with an ADC. In figure 3.8, the signal amplitude (in channels) provided by a 10x10 and a space 20x20 cells are compared to the reference ORTEC silicon detector for the different beam energies.

The maximum range of ^{84}Kr ions at 15 MeV/u in silicon is about 150 μm, and since the tested Si detector and solar cells had a thickness D >150 μm, the impinging ions were stopped inside the detectors. Assuming that the energy of the ions is deposited via ionizing processes and that the detector is able to collect the full charge produced, the final signal amplitude is expected to increase linearly with the ion energy due to the increased amount of the electron-hole pairs produced. For the reference silicon detector (black markers in figure 3.8) we observe an attenuation of the amplitude for the largest energies (10 MeV/u and 15 MeV/u), which can be explained by the pulse height defect (PHD). Several processes can lead to this effect as the: (i) loss of free electrons in recombination processes, (ii) loss of energy in low-energy non-ionizing collisions with the target atoms, (iii) loss of energy in surface dead layers, (iv) loss of free electrons trapped by lattice defects or impurities and others. For heavy ions, due to the large density of minor carriers produced, the Auger recombination is the dominant as explained in [Edm91] where charge losses up to 20% are predicted from simulations.

All the solar cells tested confirmed the behaviour found with the oscilloscope. Namely that the signal amplitude was found to increase up to 10 MeV/u and then decrease for 15 MeV/u, as shown in figure 3.8.

With the increase of the energy, the heavy ions are able to penetrate deeper inside the bulk.

In this way, the distance that the produced charges need to cover during the diffusion phase is significantly increased and, since no external bias is applied, also the collection time increase considerably. Depending on the silicon bulk resistivity, the time required by the charges to reach the electrode can be larger than their recombination time τ in the doped silicon. In conclusion, we can say that in the case of ^{84}Kr ions around an energy of 10 MeV/u, the particle path ends deep inside the solar cell bulk and the collection by funneling (drift) and diffusion is not enough fast and efficient to collect all the charge produced deep inside the bulk. Therefore, the increase of the heavy ion energy, will not produce a proportional increase of the cell signal amplitude. The non-linear behaviour of the cells amplitude will be investigated with the help of simulations in chapter 4.

3.4.3 Energy and time resolution

In figure 3.9 is shown an example of the spectra used for the characterization of solar cells in terms of energy (a) and time resolution (b). These spectra were obtained for the ^{84}Kr beam at 5 MeV/u.
The energy resolution was calculated as the ratio of the root mean square (RMS) and the mean value of the distribution in the amplitude spectrum, while the time resolution was obtained via the FWHM of the distribution. We used the calibration coefficient of the time spectrum to convert the value in ns. For the resolution measurements, the beam intensity was kept between few tens and hundreds particles per second (pps).
In figure 3.10, an example of spectra obtained from the silicon detector is shown for both the energy and time response. The smaller widths of the two distributions is representative of the better performance of the silicon detector.

The energy and time resolution obtained for the different beam energies are plotted in figure 3.11. The best results for the energy and time resolution belong to the smallest 10x10 and the space 20x20 cells. The energy resolution was observed to range between 1% and 3 %. The possibility to better investigate the cells behaviour as a function of the beam energy revealed a deterioration of the resolution with the increase of the beam energy. Due to the deeper penetration of the ions into the cell substrate when increasing the energy, the diffusion of the charges to the electrode will be longer and recombination effects are more probable, leading to an increase of the uncertainty on the collected charge. Therefore we expect a deterioration of the E resolution as observed for most of the cells, with slightly variation for each cell. However, this interpretation seems to be in contradiction with the behaviour of the 10x10 mm^2 cells represented by the yellow dots and for this specific case we do not have any explanation.

Regarding the time resolution, the response of the three 10x10 cells was found to be similar. For all the 10x10 cells tested, it ranges between 3.2 and 4.2 ns. For each beam energy, the difference in resolution between the 10x10 cells is equal or smaller than 0.5 ns. In general, the results show a small degradation of the resolution with the increase of the beam energy.

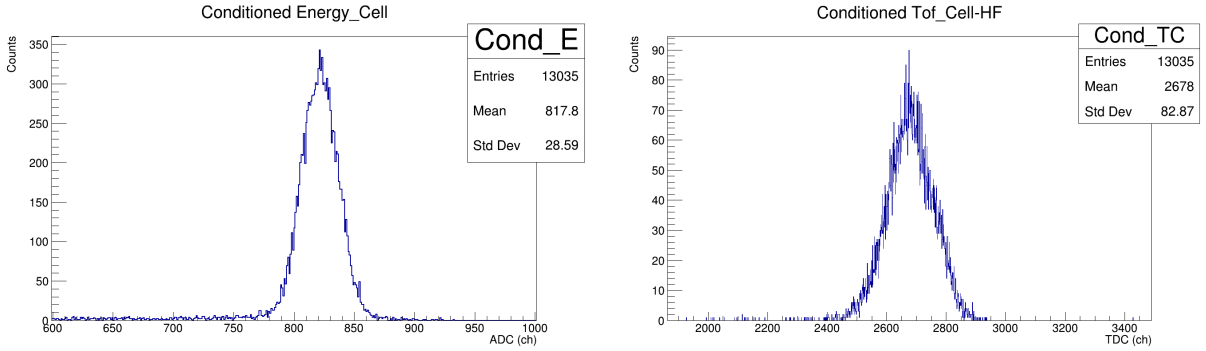

(a) 10x10-Si energy spectrum

(b) 10x10-Si time spectrum

Figure 3.9: Energy (left) and time (right) spectra of a 10×10 mm^2 cell irradiated with a ^{84}Kr beam at 10 MeV/u. The time spectrum was obtained from the time difference between the cell signals (START) and the cyclotron frequency signal (STOP). The calibration value to convert channels into ns is given.

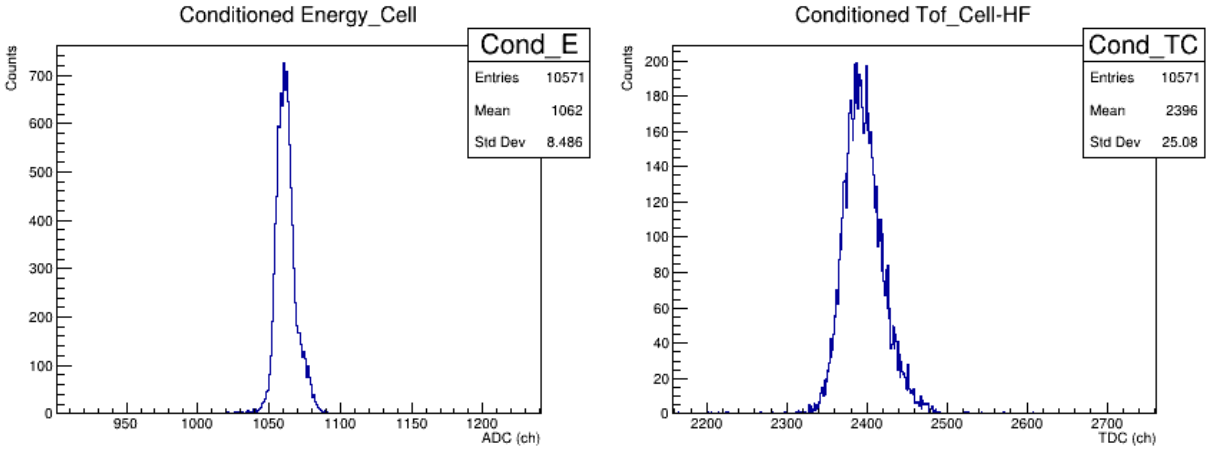

(a) Silicon detector energy spectrum

(b) Silicon detector time spectrum

Figure 3.10: Energy (left) and time (right) spectra of the silicon detector used as reference irradiated with a ^{84}Kr beam at 5 MeV/u. As for the case with the solar cells, the time spectrum was obtained from the time difference between the cell signals (START) and the cyclotron frequency signal (STOP).

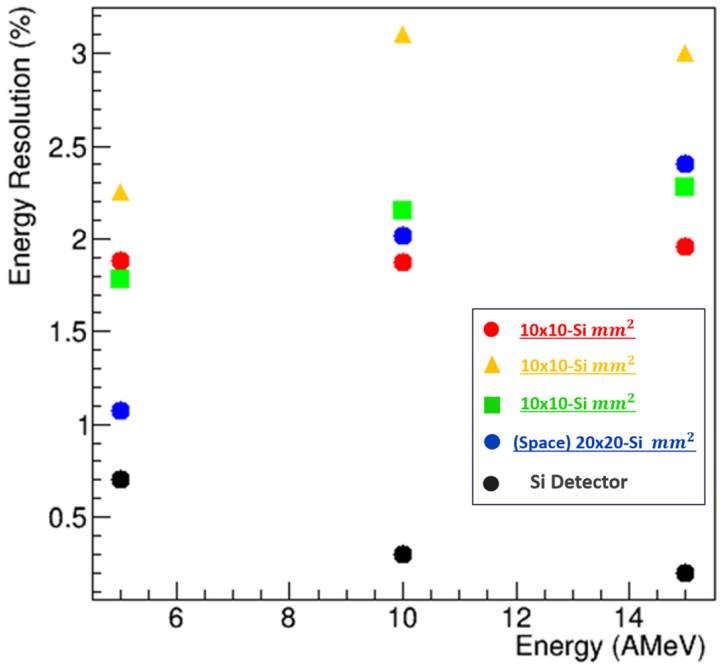

(a)

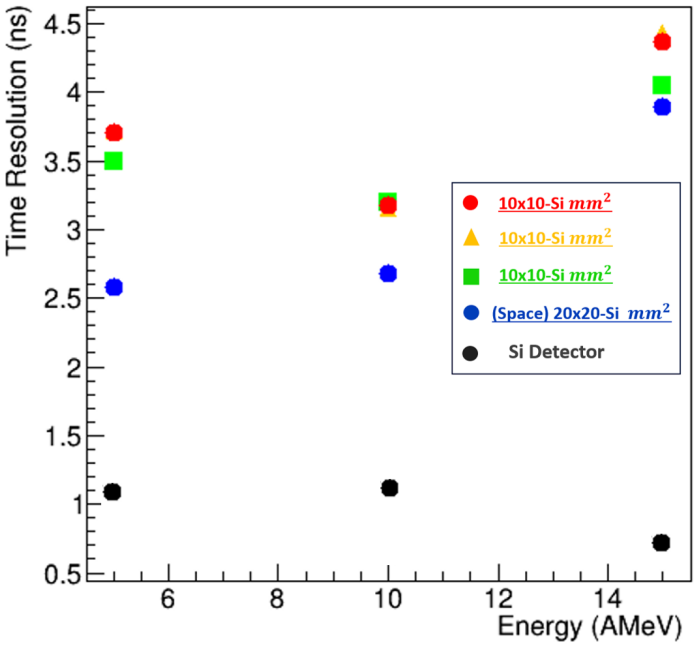

(b)

Figure 3.11: (a) Energy (RMS/$< E >$) and (b) Time resolution (FWHM) measured as a function of the beam energy. The response of three household cells of 10x10-Si and one 20x20-Si for space applications and the silicon detector are shown.

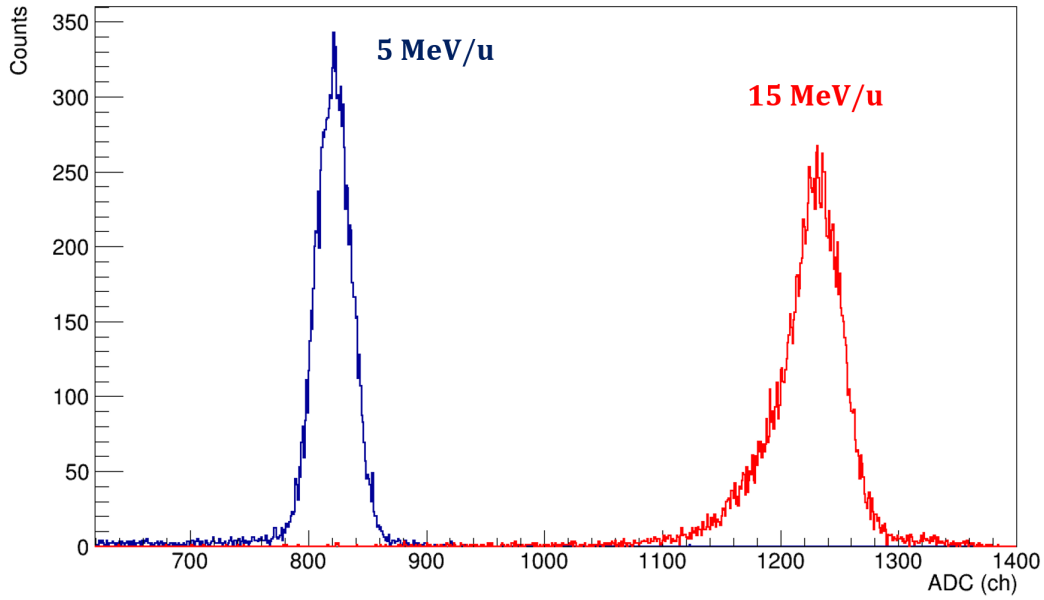

Figure 3.12: Pulse height measured with the ADC for the space 20x20 mm^2 cell at 5 and 15 MeV/u.

Probably, the reason is the time measurement of the signal which is performed using the fast component of the signal produced during the funneling by drift. This part of the signal is much less affected by the charge trapping processes and structure defects of the cell bulk.
The 20x20 mm^2 space cells provided the best energy resolution, around 1%, for a ^{84}Kr beam at 5 MeV/u, which is quite remarkable for a cell of these dimensions. The energy resolution gets worse with the increase of the beam energy. Figure 3.12 shows indeed that with the beam energy increases from 5 to 15 MeV/u, the amplitude distribution gets large and a tail appears at the lower amplitudes.
The 20x20 mm^2 space cell shows a better time resolution, ranging between 2.2 and 3.6 ns, than the 10x10 mm^2. However, an important degradation of the time resolution was observed for ^{84}Kr ions at 15 MeV/u.
The silicon detector provides an energy resolution of 1%. The energy resolution of the beam delivered by the CIME cyclotron is typically 0.5%. Therefore, the measured energy resolutions are dominated by the detectors response. The time response of a silicon detector, as expected, was found better than the response of the solar cells, being between about 0.8 and 1.2 ns. The main contributions to the time resolution were the detector response and the time spread of the pulses delivered by the CIME cyclotron of about 0.6 ns.

3.4.4 Study of the radiation hardness

The evaluation of the radiation resistance represents one of the most important purpose in order to validate the use of solar cells as in-ring fission fragment detectors. The radiation damage of Si detectors have been thoroughly investigated ([Kra84, Lin87, Hal95, Lin02]) also in

the case of heavy ions ([Shi69, Kur95]). According to Shiraishi et al. fission fragments produce more defects than lighter particles [Shi69]; Kurokawa et al. go further and evaluate the damages in silicon detectors as being 10^3 to 10^5 times larger for heavy ions than for protons [Kur95]. When a heavy ion impinges on a silicon detector, it can create a defect that can change the energy gap level of the material. Locally this translates in the creation of emission and capture centers which will be the source of a leakage current or decrease the output pulse height due to recombination of charge carriers degrading furthermore the energy resolution.

During our investigation a 10x10 cell and the space 20x20 cell were exposed to a ^{84}Kr beam at 15 MeV/u with a rate of few thousand *pps* for few hours. In figures 3.13 and 3.14 we can see the energy and time response as a function of the exposition time. Under a constant irradiation at few kHz, the amplitude mean value and the energy resolution decrease. This is clearly visible for both the household silicon cells, figure 3.13(a) and the space solar cells, figure 3.13(b).
After 2h17min of irradiation of the 10x10 mm^2 cell the signal amplitude deterioration stabilizes around the channel 1076 with a decrease in amplitude of 26%. The space 20x20 cell provided a better radiation resistance since, with the same irradiation rate the amplitude decreases to 1079 *ch* (from an initial amplitude of 1500 *ch*) after a longer period of exposition. In both the case we also observed an increase of the width of the distribution. As already said, together with the amplitude, also a degradation of the energy resolution was observed. In figure 3.15(a) the pulse height spectra before (in blue) and after (in red) the irradiation of a space 20x20 cell are shown. The radiation damage occurring in the cells was responsible for an important decrease of the signal pulse height and of the energy resolution which is moving from the 2.1% (value before the irradiation) to about ∼7%.

On the other side, the time response and resolution was found stable during the full irradiation period, indicating that the time response of solar cells is not affected by the irradiation, see figure 3.14. In figure 3.15(b) the time distributions in channel of the cells are shown before (in blue) and after the irradiation (in pink). It can be seen that the time distribution of the signal measured after the irradiation had almost the same width as the one measured before. As described in the previous section, the signal of the solar cells is produced thanks to two different mechanism: a fast drift collection and a slow diffusion collection of the charge produced in the bulk. During the fast drift collection, the charge close to the junction is collected producing a fast increase of the current. The main effect of the heavy ion irradiation is the creation of recombination centers produced by the interaction of the incident ions with host atoms in the silicon. The incident heavy ion will act to displace them from their lattice sites, generating defects in the silicon bandgap in the form of deep energy levels [Kim03]. Furthermore these recoiling atoms may themselves also create further displacements in the lattice, and by doing so, introduce additional defect states. As can be seen from the SRIM simulation presented in figure 3.16, where the number of displaced atoms is shown as a function of the penetration (in μm), the effect of the displacement is becoming significant deep inside the bulk in proximity of the heavy ion path end.

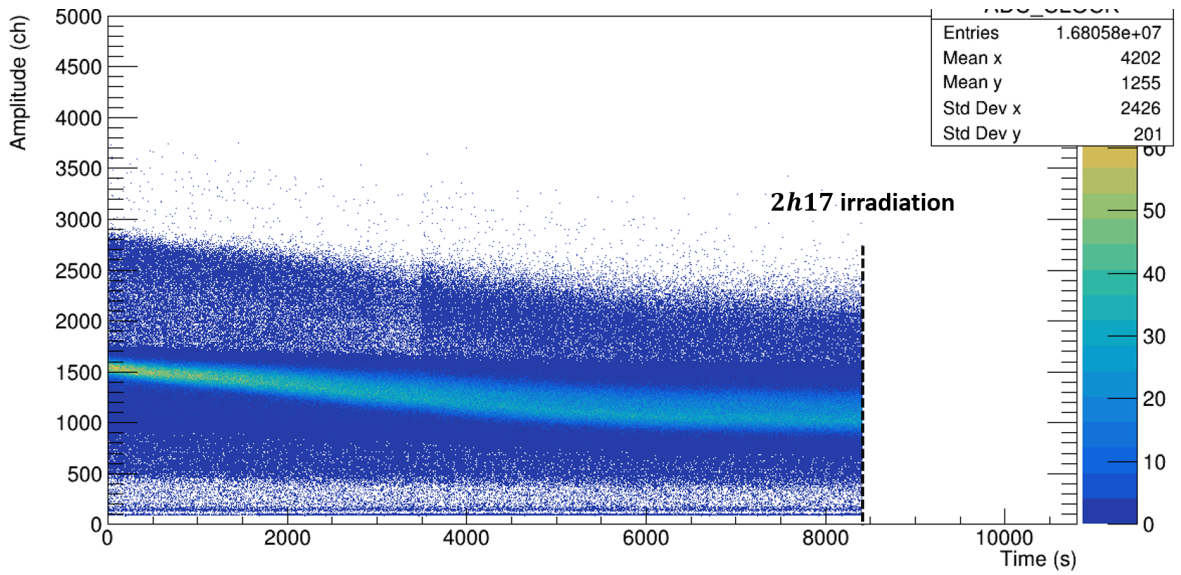

(a) Energy response - Si 10x10 mm^2.

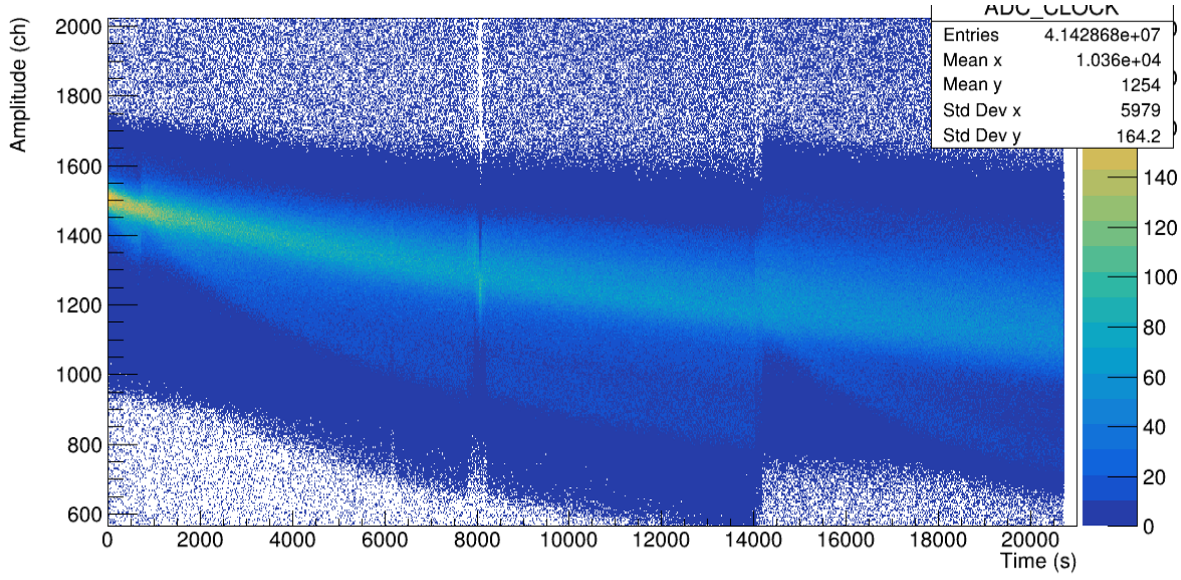

(b) Energy response - space Si 20x20 mm^2.

Figure 3.13: Energy response in channels as a function of the time, for a 10x10 mm^2 cell and a 20x20 mm^2 space cell irradiated during 2 and 5 hours a rate of few thousands *pps* with a 15 MeV/u ^{84}Kr beam.

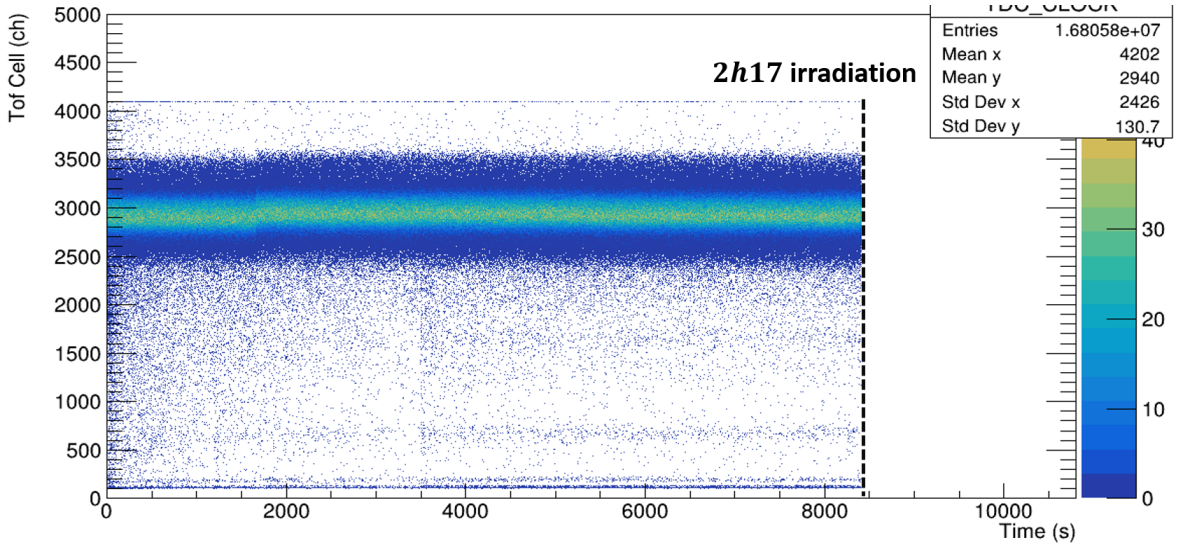

(a) Time response - Si 10x10 mm^2.

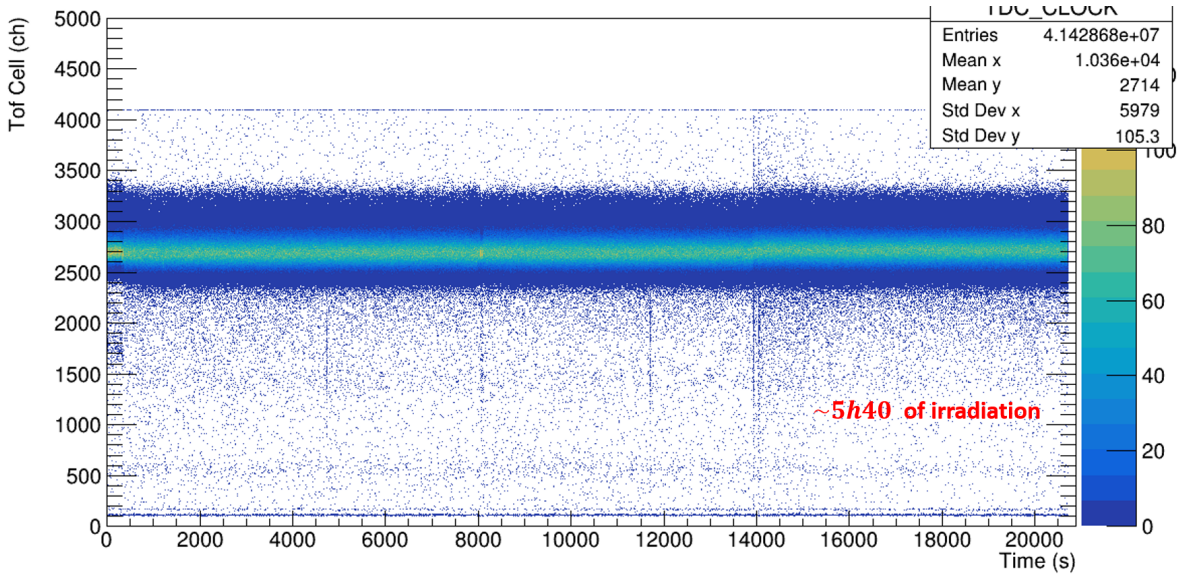

(b) Energy response - space Si 20x20 mm^2.

Figure 3.14: The same as figure 3.13 but for the time response.

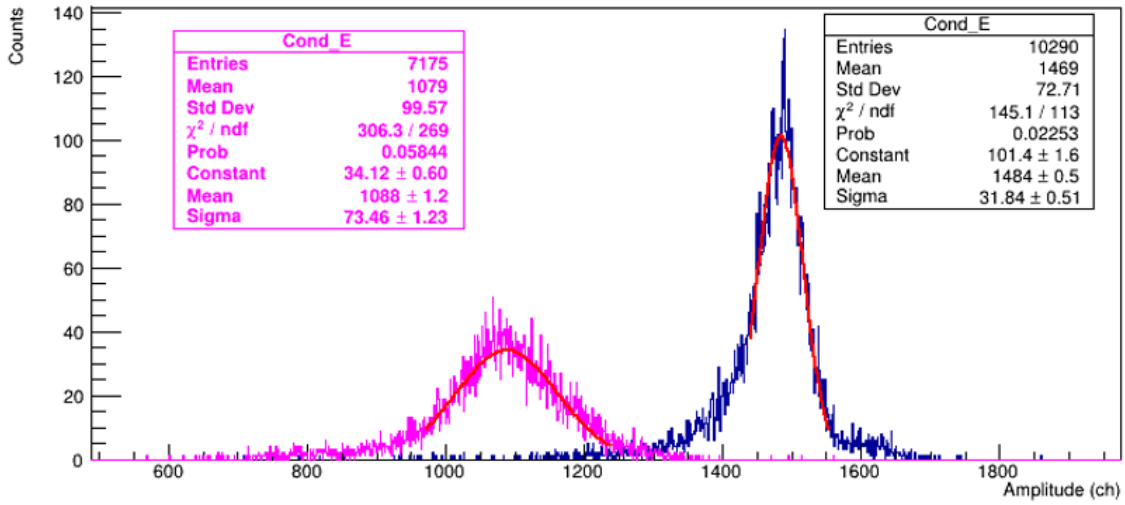

(a) Energy spectra - before and after the irradiation.

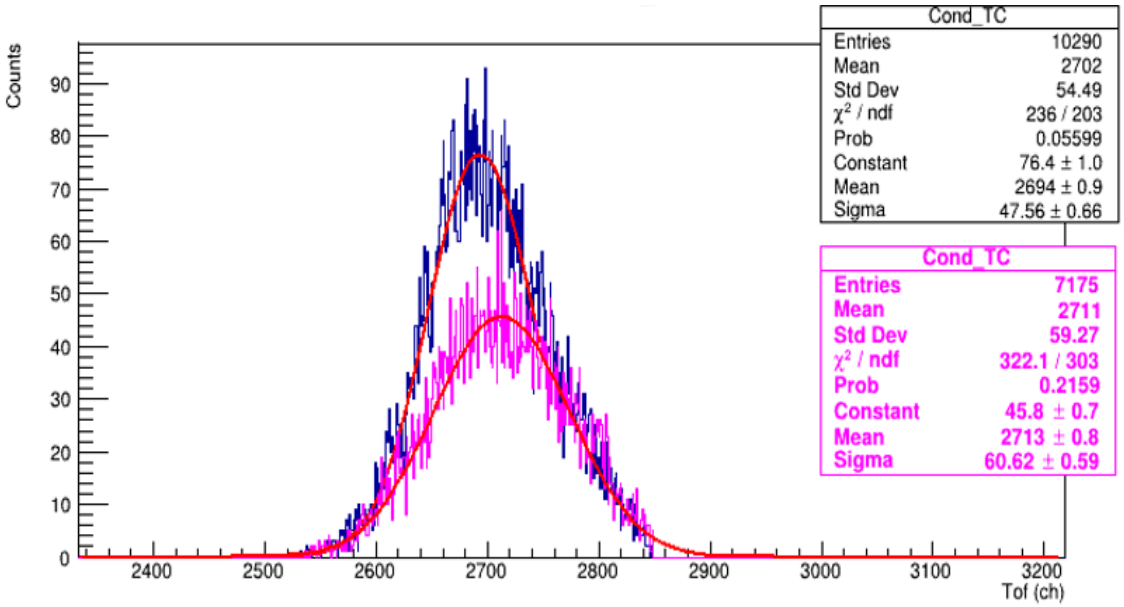

(b) Time spectra - before and after the irrradiation.

Figure 3.15: Comparison between the energy and time spectra obtained for a space 20x20 cell before (blue line) and after (purple line) an irradiation performed at a rate of few thousands *pps* with a 15 MeV/u ^{84}Kr beam during 5h40min.

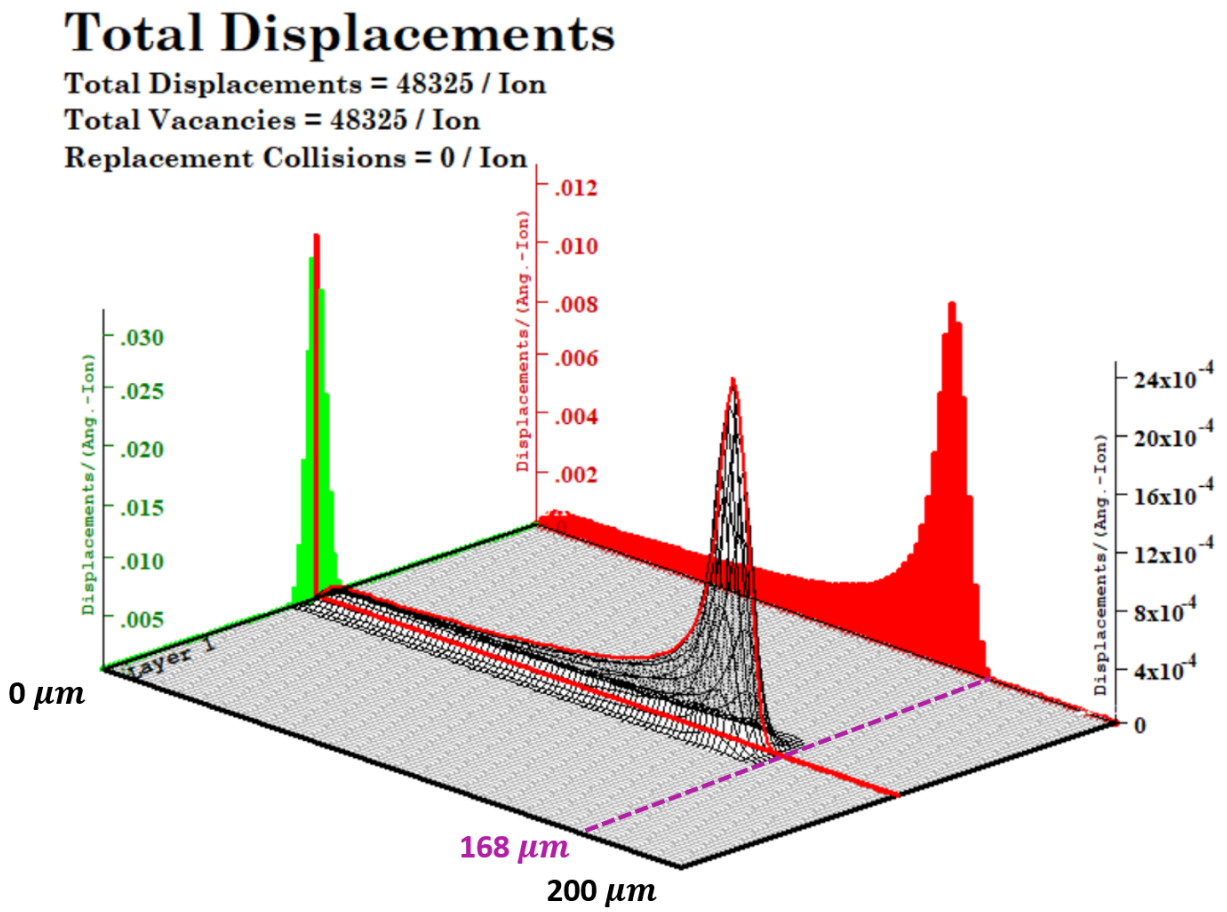

Figure 3.16: SRIM simulation of the number displacements induced by a ^{84}Kr ion at 15 MeV/u impinging on silicon.

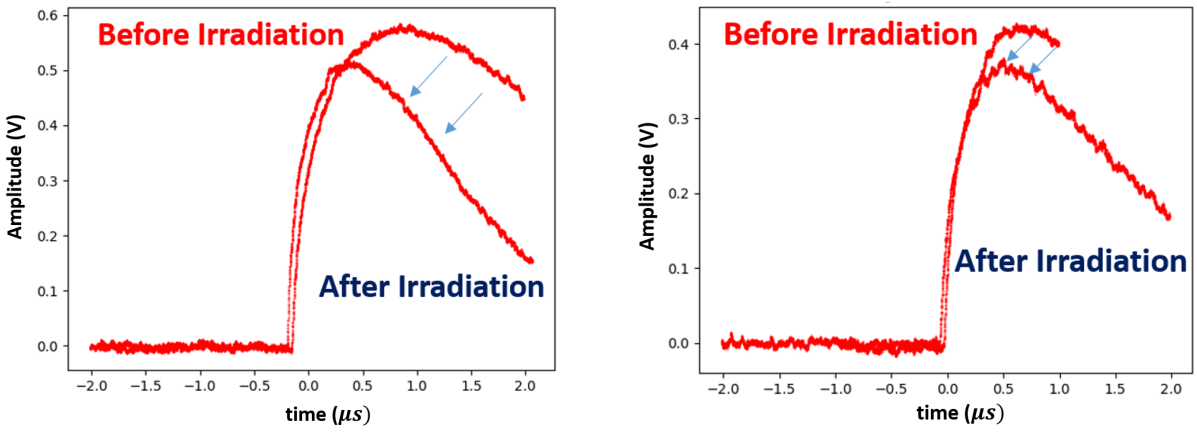

(a) Silicon solar cells - 10x10 mm^2

(b) Space silicon solar cells - 20x20 mm^2

Figure 3.17: Comparison of the solar cells signal, at the output of the preamplifier, before and after the irradiation performed with a 15 MeV/u ^{84}Kr beam.

In this way, only the charge generated far from the junction is affected by the irradiation. This results in a decrease of the charge collected by diffusion, while the drift component, which is the component related to the time response, is not affected. This can be clearly seen in figure 3.17 where a comparison between the solar cell preamplifier signals, before and after the irradiation process is reported. No modification in the drift component (first part of the signal) can be observed. The irradiation as however a significant impact on the fall time and the amplitude of the signal, due to its impact on the diffusion component.
The irradiation studies showed that rates higher than $50k$ *pps* performed for more than an hour, after the initial degradation of the energy response and the stabilization of the signal around plateaux values, produce only a small decrease of the energy response and a degradation of the resolution. The time response and resolution were not affected.
After the irradiation, the cells would continue to provide a signal amplitude 4 times lower (800 *ch*) in the energy spectrum. Interestingly, we found that the solar cells are able to recover partially from the radiation damage after few hours of inactivity or after a baking cycle.

Chapter 4

Solar cells simulation

The development of a simulation able to reproduce the solar cell response when irradiated with heavy ions is important for several reasons: (a) to explore the funneling effect in solar cells, (b) to investigate the signal formation from the interaction with an heavy ion, (c) to be able to reproduce, complete and extend the evolution of the solar cells response as a function of the heavy ion energy.
For the simulation we used the ATLAS[1] Silvaco software [ATLAS] in combination with the TINA simulation code, which reproduces the cell and preamplifier electrical circuit. The goal was to simulate the physical current $I(t)$ produced in the interaction with a heavy ion as a function of time with Silvaco. The resulting $I(t)$ represents the i_d current of the circuit and then was used as input of the TINA code to reproduce the solar cell signal at the preamplifier output. The properties of the calculated signal, such as the rise time and amplitude, can be directly compared with the measured ones.

4.1 3D device geometry

The development of the solar cell geometry was performed with the Devedit TCAD structure editor. In figure 4.1, an example of the solar cell 3-D geometry developed is presented. To reduce the simulation time, only a small part of the solar cell geometry was reproduced, about 80x80 μm^2 located below an aluminium grid. The top aluminium contact (in gold) represents the anode electrode while the back side, not visible in the figure, is characterized by a large aluminium grid corresponding to the cathode electrode. The solar cell n-p junction was produced by a n-layer of 1.00 μm uniformly doped with Phosphorus atoms (blue region in figure 4.1) interfaced to a p-layer of 230 μm (green region in figure 4.1) uniformly doped with Boron atoms.

[1]ATLAS is a Semiconductor Process and Device Simulation software providing general capabilities for physically-based two (2D) and three-dimensional (3D) simulation of semiconductor devices.

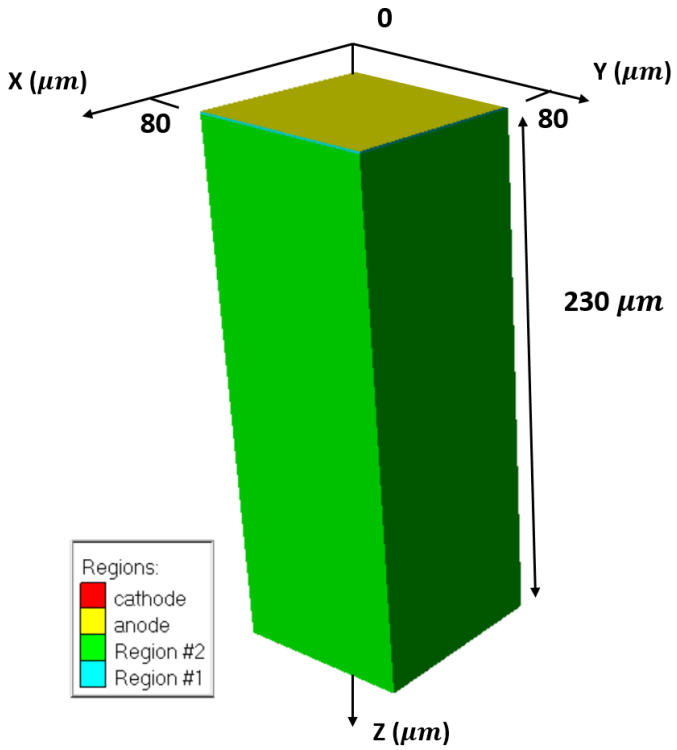

Figure 4.1: Solar cells 3D structure used in the simulation. The details of the full structure, including the front contact (anode) and the thick p-layer are shown.

From the literature, it is known that solar cells used in household panels are characterized by a resistivity of the bulk of about 1 $\Omega \cdot cm$ (see chapter 2). This value of the resistivity corresponds to a dopant concentration of the thicker p-layer of about 10^{16} cm^{-3} atoms, so a final concentration of $9.0 \cdot 10^{15}$ cm^{-3} was finally defined for the solar cells bulk. This implies, for an equivalent or larger concentration of the n-layer dopants, a junction width of 0.3 μm (expected for a capacitance of 36 nF/cm^2) and a built in voltage of about 0.7 V. The final dopant concentration was fixed around $1.80 \cdot 10^{16}$ cm^{-3} for the n-layer.

Figure 4.2 shows a 2d plot of the electric potential distribution close to the formed n-p junction. We can see the horizontal equipotential lines and the depletion region.

4.2 Heavy ion interaction and charge generation

As already described, when a heavy ion strikes a detector electron–hole pairs are generated in the form of a funnel along the ion track (see chapter 2).

In ATLAS Silvaco simulations, it is possible to specify the spacial and time properties of the generated charge along the ionizing particle's track. In this way, just defining some key parameters, we can simulate the interaction with the incoming ion by reproducing the charge

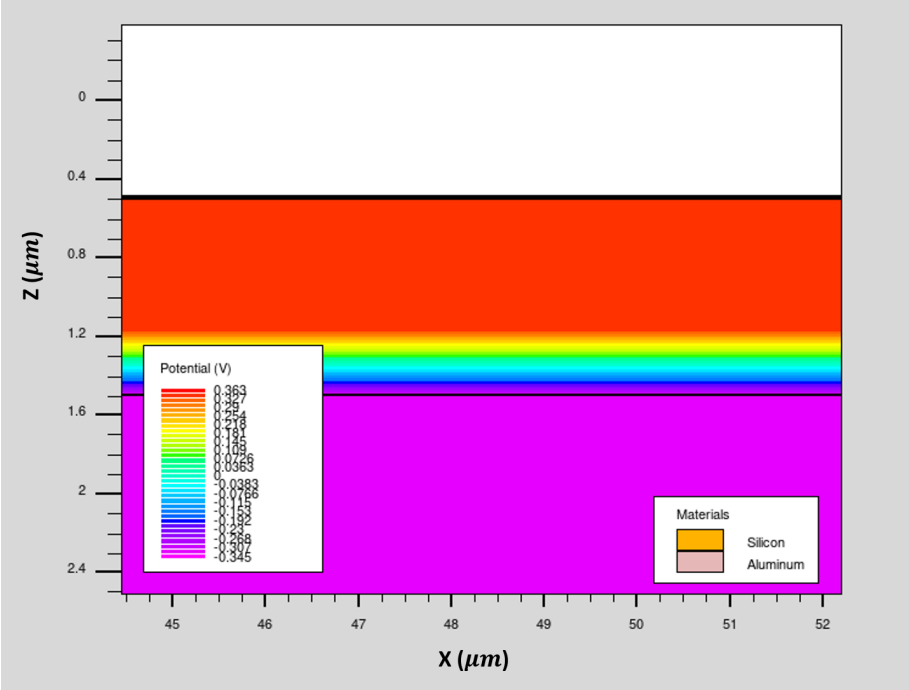

Figure 4.2: 2-D plot showing the potential lines close to the cell junction. The black lines represent the top and bottom surface of the n-type layer.

generation along the particle path. The properties of the particle strike include the definition of the entry location point (x_0, y_0, z_0) and the exit location point (x_1, y_1, z_1). The generation rate $G(r, l, t)$ in form of e-h pairs per cm^3 along the track, as a function of the longitudinal distance (l), the radial distance (r) and time (t), is defined by equation (4.1):

$$G(r, l, t) = \rho_0 \cdot L_1(l) \cdot R(r) \cdot T(t) \tag{4.1}$$

where $L_1(l)$ describes the variation of the charge/generation as a function of the range in the semiconductor, $R(r)$ and $T(t)$ represent, respectively, the radial and time dependency of the charge generation and ρ_0 is the initial carrier density in cm^{-3} produced at the beginning of the ion track. The SRIM software was used to determine the average energy deposited per unit length along the track and the radius of the carrier distribution for ^{84}Kr ions interacting with a silicon material. These quantities were then used to parametrize the different terms of the equation (4.1).

4.3 Signal formation via field funneling and diffusion

The electron-hole plasma produced by the interaction of a ^{84}Kr ion at energies of about few MeV/u has the form of a funnel along the particle path having a high density of carriers in the center (up to 10^{21} cm^{-3}), which decreases when moving outwards. Since the high density of

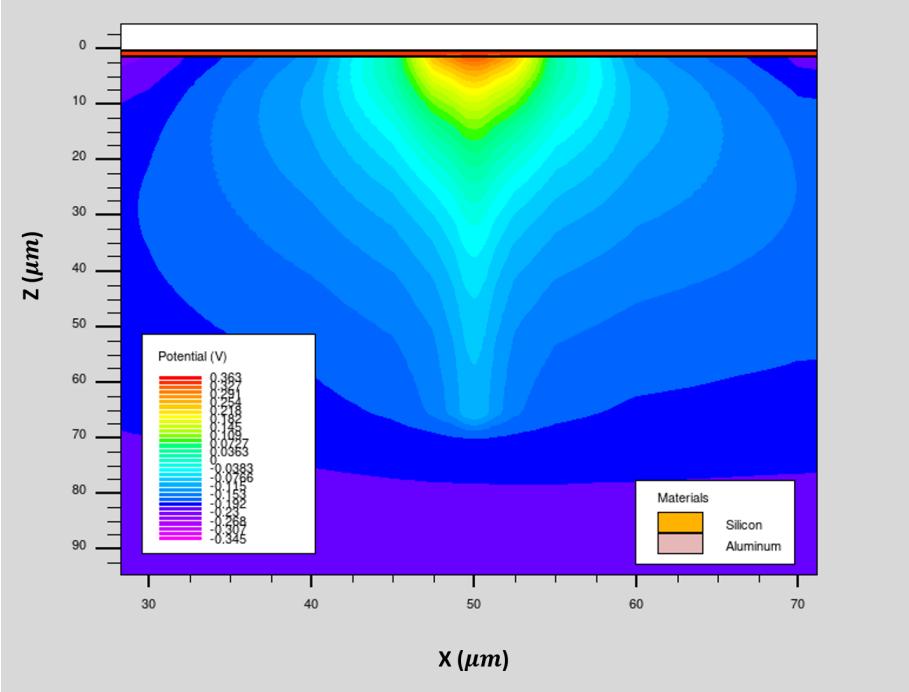

(a)

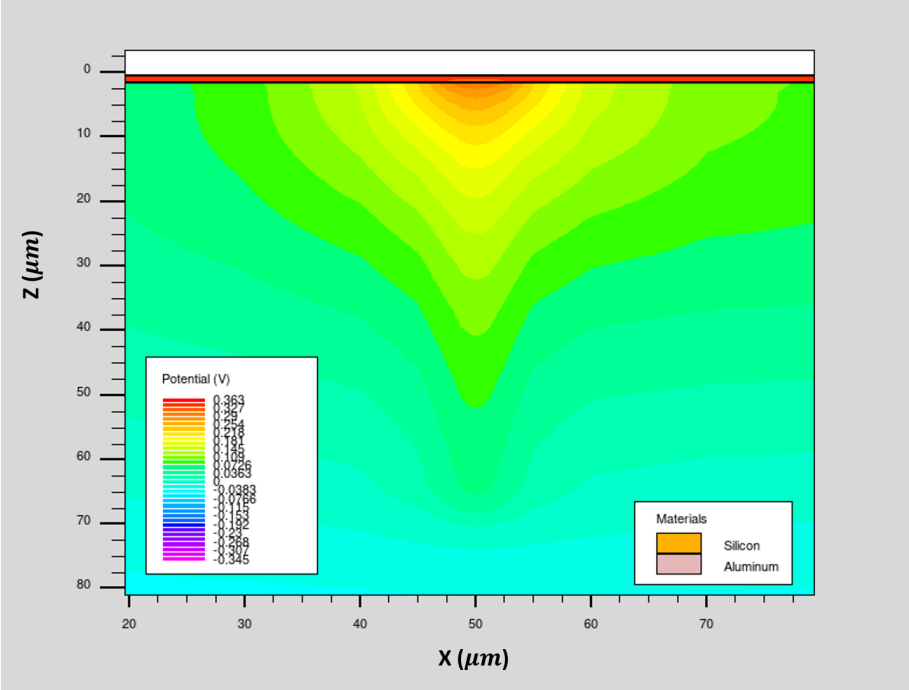

(b)

Figure 4.3: 2d plots showing the equipotential lines 0.1 ns (s) and 1 ns (b) after the passage of the ^{84}Kr ion at 7 MeV/u.

carriers produce a gradient of potential along the ion track, the electric field of the junction is extended beyond the depletion zone. Figure 4.3(a) shows the deformation of the equipotential lines associated to the ion track 10^{-10} s after the interaction.
The drift phase of the charge collection occurs thanks to the charge separation of the electrons and holes in the plasma column. In this respect, as described by [McL82], we can identify a radial separation occurring at the outer edge of the column (where the plasma density is of the order of the dopants density N_A) and a longitudinal separation. In the radial separation the holes are drawn away from the plasma column while the electrons are constrained by the radial field and drift up in response to the longitudinal field. During this phase a fast increase of the collected current at the anode takes place until few ns, see figure 4.4.
The electron-hole plasma funnel continues to expand radially due to the ambipolar diffusion[2] as can be seen in figure 4.3(b) showing the equi-potential lines deformation after 1 ns. After the interaction as the plasma density at the surface region is reduced throughout matching the bulk dopants concentration ($N_A = 9 \times 10^{15}\, cm^{-3}$), the original junction potential starts to reform at the plasma surface. After few nanoseconds, the intensity of the current decreases significantly, see figure 4.4, and since the original junction field is gradually re-established the plasma column rapidly disappears and the collection by drift stops.

At this point the collection process is not yet concluded since some residual charge, produced during the interaction with the heavy ions, is available in the solar cell bulk. For this reason the charge collection is completed by a diffusion stage which takes place in a longer amount of time (about hundreds of ns). The effect of the collection process by diffusion can be clearly seen in figure 4.4. After about 10 ns the fast drop of the current is slowed down by the diffusion collection. From the performed simulation, we can conclude that the collection by funneling ceases completely within approximatively 10 ns from the interaction with the impinging ^{84}Kr ion. Some models were developed in the past to provide an interpretation of the funneling effect estimating some key parameters. We recall the work of McLean and Oldman [McL82], where a simple phenomenological model of the charge funneling effect was developed and compared with the experimental results. It was based on the definition of an effective funnel length, which represents an average depth over which the fields exists, the charge separation occurs and drift currents are collected. As specified in their article, the estimations of the total charge collection obtained with the model are in good agreement with the experimental data, so it can be used to compare the expected funneling collection time with our simulations. In the article, τ_c is

[2]By ambipolar diffusion we refer to the diffusion of positive and negative species with opposite electrical charge due to their interaction via an electric field. When a plasma expands into an empty space, the species that moves faster diffuses first. However, as it moves outward, an electric field is created (due to the absence of the other charge species) that "pulls along" the heavier species. This electric-field pulling couples the diffusion rates of the two species. In this way if the pull is strong enough, then the diffusion rates become essentially equal despite the large difference in average speeds.

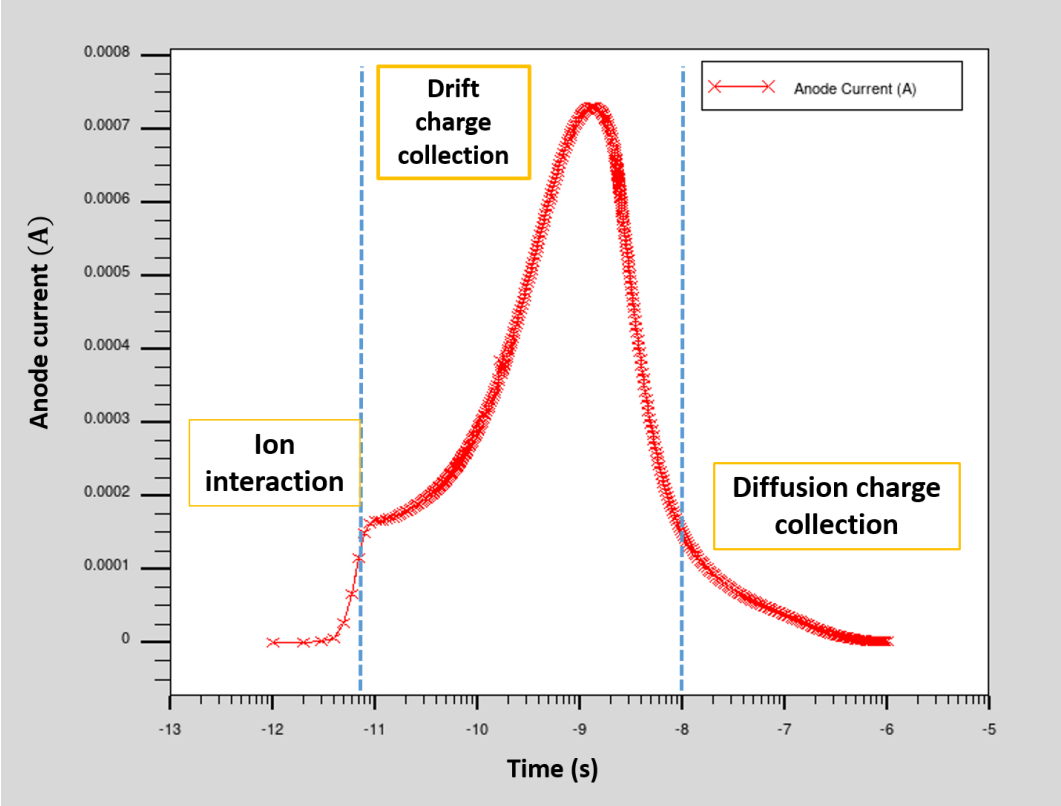

Figure 4.4: Simulated evolution of the collected current at the anode as a function of time. After the interaction taking place at 10^{-12} s, the different phases of the charge collection, through drift and diffusion can be seen. The vertical lines give an indication of the time during which charge collection via drift occurs.

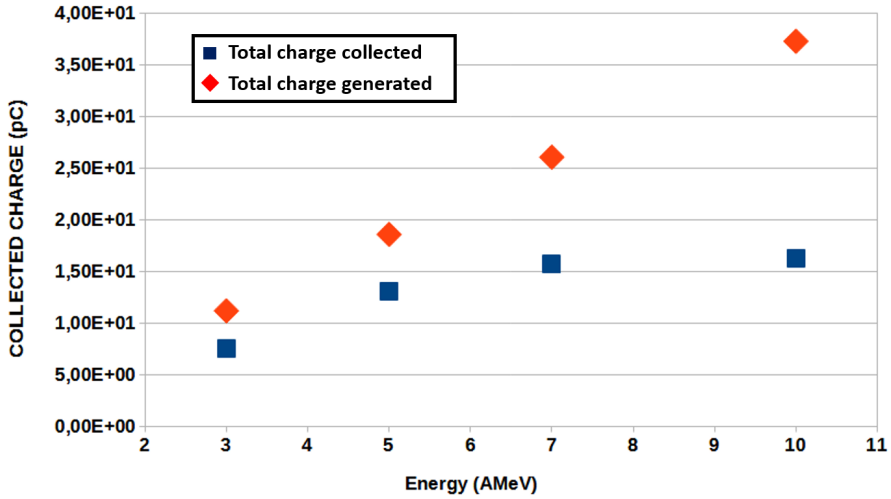

Figure 4.5: Total Collected charge as a function of the ^{84}Kr ions energy. The red symbols represent the total charge produced by the heavy ion in the solar cells while the blue symbols indicate the total charge collected (funneling+diffusion).

defined as the time during which the funnel effect is active and it is calculated as:

$$\tau_C = \left(\frac{3 \cdot N_0}{8 \cdot \pi \cdot N_A \cdot v_p \cdot D_a^{1/2}}\right)^{2/3} \tag{4.2}$$

where the N_0 is the initial linear plasma density at the surface, v_p the holes escape velocity, D_a the ambipolar diffusion constant ($\sim 25\ cm^2/s$ in Si). From this equation we can clearly see that larger plasma densities at the surface increase the funnel collection time (improving also the funnel efficiency), while large dopant concentrations reduce the funnel strength.
Considering the density of impurities N_A used in the 3D simulation, the N_0 linear density produced by a Krypton ion at 7 MeV/u and a small hole velocity of about 10^5 m/s we obtain $\tau_c \approx 10\ ns$. This value of the funnel collection time reproduces well the simulated behaviour of the solar cell signal, shown in figure 4.4, giving confidence on the results of the simulation.
In general, considering that the funneling effect is characterized by a specific duration and it is reasonable to expect that, with the increase of the ion range, a significant amount of charge produced in the bulk will not reach the junction before the funnel column collapsed. Furthermore, with the increase of the path length inside the bulk, occurring for larger energies of the same ion species, the drift component is supposed to decrease due to the non-uniform carrier density generation (Bragg peak). To evaluate the charge collection efficiency of the drift-diffusion mechanism, the total charge collected can be determined from the signal current $I(t)$, showed in figure 4.4 by integrating it over the collection time (about 1 μm). In figure 4.5, the total charge collected efficiency (funneling + diffusion mechanism, blue symbols) is shown as a function of the Krypton ion energy and compared with the total charge produced by the

impinging ion (red symbols). Until an energy of 7 MeV/u the solar cell response is found to be proportional to the total charge released in the semiconductor by the impinging ion, with a collection efficiency ranging between ≈80% at 3 MeV/u and ≈60% at 7 MeV/u. With the increase of the energy, the simulation demonstrates that a significant amount of the charge produced in the bulk is not collected and that a saturation in the total collected charge takes place. These results are in agreement with the experimental observations described in chapter 3 and highlight that the very low detection efficiency in the funneling process at larger energies is responsible for the non-linear behaviour of the solar cells response observed.
In addition, due to the longer time scale of the charge collection by diffusion, which can be of the order of μs, minority carriers produced in the bulk, in our case electrons, are more subject to recombination processes, which also contributed to the charge loss and the decrease of the collection efficiency at high energies.

4.4 Preamplifier output signal

To compare the simulation with the experimental results, the current I simulated in the previous section from the interaction with a ^{84}Kr ion was used as input of the TINA simulation reproducing the circuit model of the solar cell and the preamplifier. The signal provided by a 10x10 mm^2 silicon cell was simulated and the resulting rise times and amplitudes were compared to the experimental ones for different heavy ion incident energies.
Figure 4.6 shows the evolution of the simulated signals at the output of the preamplifier produced in the interaction with a Krypton ion at 5 MeV/u (purple line), 7 MeV/u (green line), 10 MeV/u (blue line) and 15 MeV/u (gray line). An increase of the amplitude occurs up to 7 MeV/u followed by a decrease for larger energies in agreement with the experimental observations. This can be seen in figure 4.7(a), where the simulated amplitude variation as a function of the ion energy is compared with the ones measured for two silicon household solar cells 10x10 mm^2. The amplitudes of the simulated signals reproduce well the evolution as a function of the ion energy but are about a factor two lower than the experimental ones. Regarding the rise time, the evolution as a function of the ion energy is shown in figure 4.7(b) and compared with the experimental results, showing a good agreement.
These results reflect the quality of the performed simulation and their capability to reproduce the solar cells response when irradiated with a heavy ion. This work has allowed us to better understand the collection process by funneling occurring in solar cells and to explain the non-linear response observed experimentally at energies larger than 7 MeV/u.

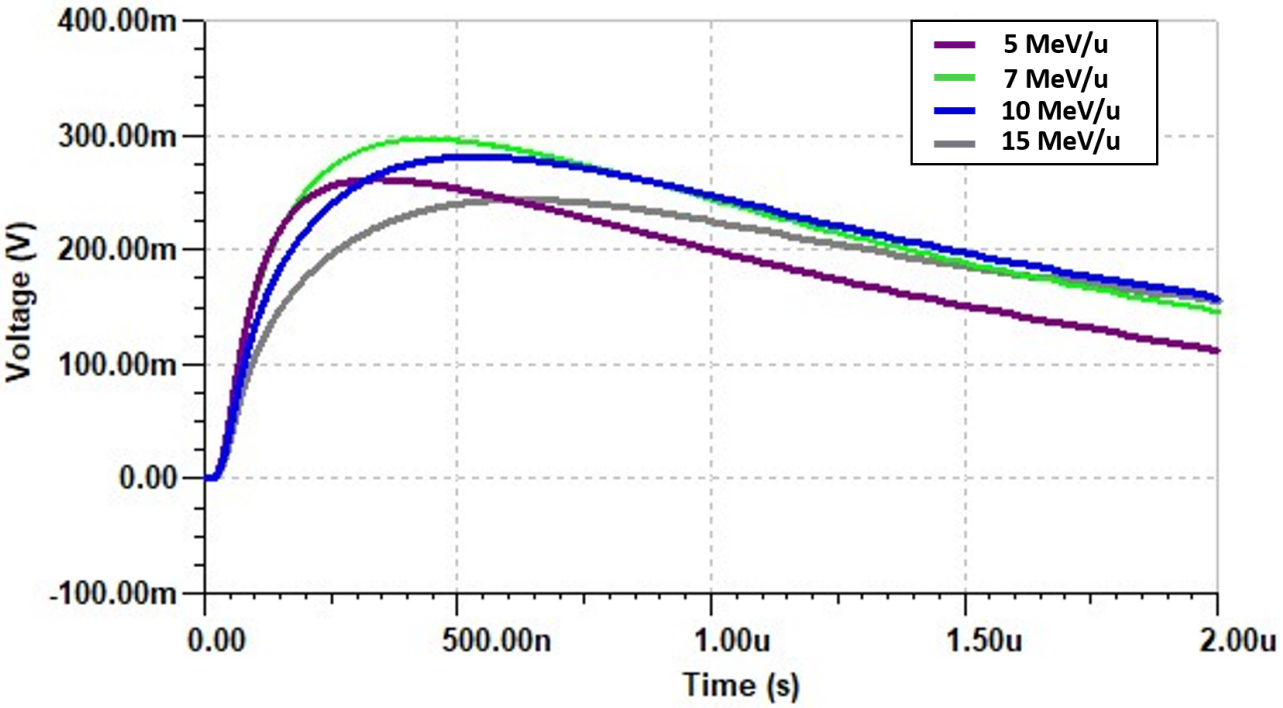

Figure 4.6: Simulated signal of a 10x10 mm^2 solar cell at different energies, respectively 5 MeV/u (purple line), 7 MeV/u (brown line), 10 MeV/u (blue line), 15 MeV/u (green line) at the output of the preamplifier.

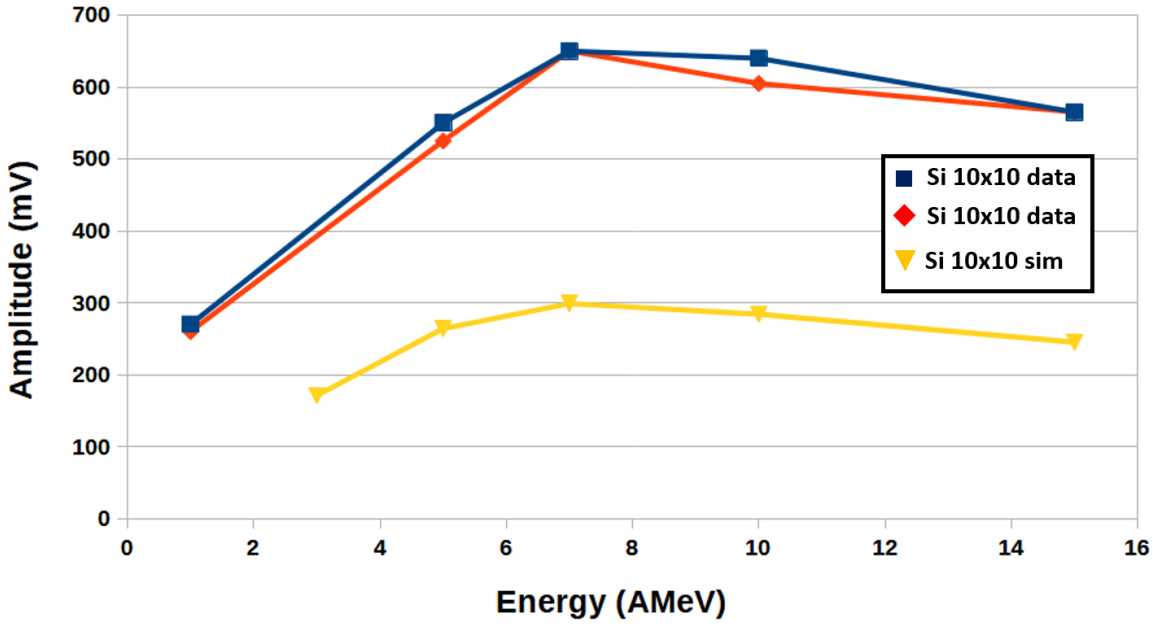

(a)

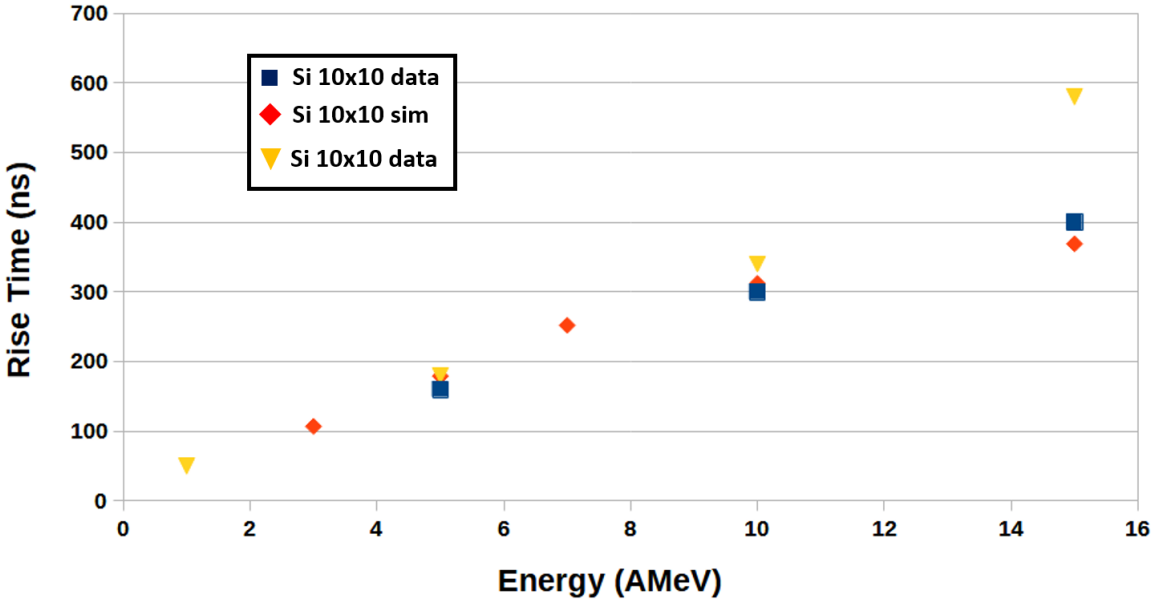

(b)

Figure 4.7: Comparison of the rise time (a) and amplitude (b) obtained from the simulation (red points) and from the experimental data (blue and gold points).

Chapter 5

UHV compatibility test

The use of solar cells for the in-ring detection of heavy ions requires to test the compatibility of these devices with UHV. This implies to verify their outgassing rate, which must respect specific constrains defined by the GSI vacuum service [Wil14], to avoid a degradation of the ring vacuum quality. Furthermore, since heating treatments at high temperature (up to 250 $°C$) are required for the storage ring and all the equipments installed on it to achieve UHV, the quality of the solar cells response after these processes must be accurately investigated.
In this chapter, after a brief introduction on the concept of material outgassing and bakeout, the results of the outgassing rate measurements realized at the LP2iB on two solar cell samples will be presented. In the last section, the possible degradation induced in the cells response by the bakeout processes will be presented.

5.1 Outgassing and bakeout process

Outgassing is the spontaneous release of gas from materials in vacuum and in particle accelerators, once leaks are excluded. Outgassing of "in-ring" materials is an important source of gas together with degassing[1] induced by the particle interaction of particles with walls.
We can identify four main mechanisms, illustrated in figure 5.1, responsible for the outgassing: a) the vaporisation (white circles) of the surface material itself, (b) the desorption (green circles) or reverse process of adsorption consisting on the release of molecules bound at the surfaces of the chamber and internal fixtures, (c) the diffusion (orange circles) - this is the movement of molecules from the inner structure of the material to the surface, and (d) the permeation (purple circles) consisting on the movement of molecules from the external atmosphere through the bulk to the vacuum surface.

The outgassing of a given material is defined by means of the outgassing rate (q), which is the flux of outgassing (quantity of gas leaving a material per unit time) divided by the sample

[1] deliberate removal of gas by heating or by interaction with particles.

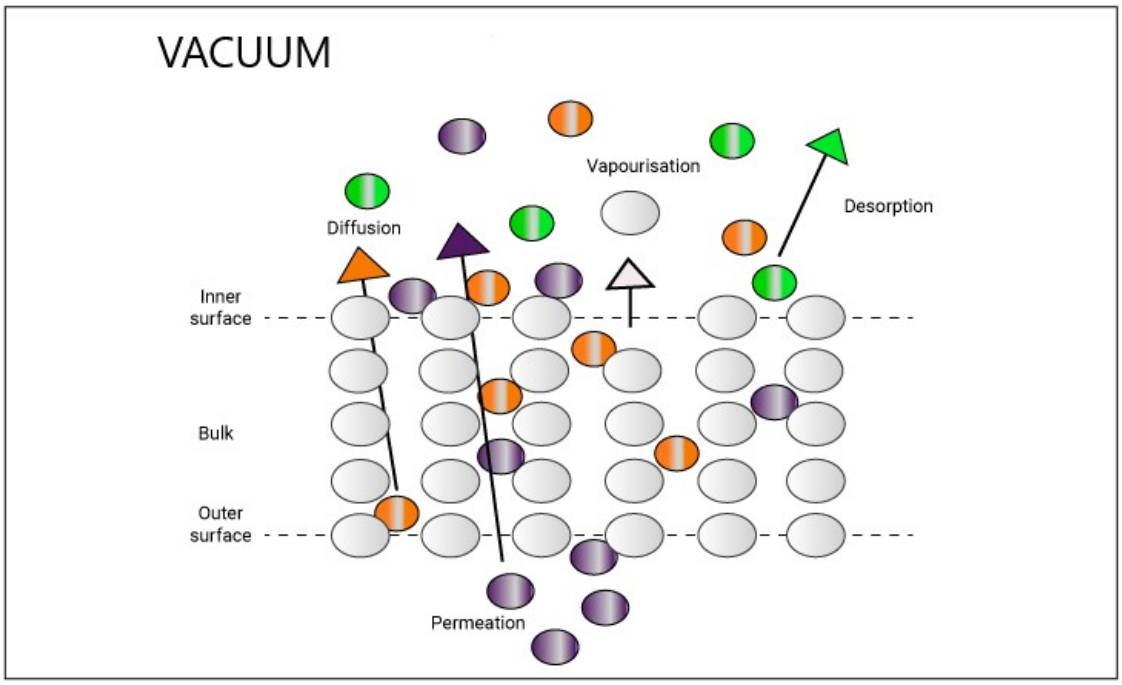

Figure 5.1: Surface and bulk phenomena leading to outgassing in vacuum.

surface S:

$$Q = \frac{d(pV)}{dt} \cdot \frac{1}{S} \tag{5.1}$$

where the pressure p is the pressure measured in a specific volume V containing the sample and S the sample surface. Several units can be used to represent the outgassing rate, however in this work we will define it in $(mbar \cdot l)/(s \cdot cm^2)$. The outgassing rate depends on the nature of the materials and gas species. Treatments such as the bakeout, the surface cleaning and pumping can be used to reduce the gas release. Some examples of material outgassing rates before and after bakeout treatments are listed in table 5.1.

A material is allowed to be present in a high vacuum environment only if its outgassing rate is not more than a permissible limit. Some material have a limited use in ultra high vacuum: liquids, plastics, elastomers, porous ceramics and organic materials. It is important to stress that the contamination onto surface is a source of gas release. In fact, also for vacuum materials, the outer surface layer of the materials is made of oil, grease and dirt coming from machining, manipulation, and storage in unclean rooms. Solvents and detergents [Edw77] have to be used to reduce the amount of these contaminants on the surface layer of the samples.

In the case of metals, e.g. stainless steel flanges, oxide-hydroxide and damaged layers are potential source of gas. In this case, the porosity of the layers lead to the trapping of gas molecules or liquids that are then released in vacuum. In addition gas molecules can also be released from surface oxides and hydroxides, due to chemical transformations. Dissolved atoms or molecules in the bulk can diffuse towards the surface and be released possibly after chemical reaction with other adjacent molecules. In metals only single atoms are dissolved (H, O, C, S, etc.), and

Detail	**Pumping time**	**Dominant Gas Species**	**q** ($\frac{mbar \cdot l}{s \cdot cm^2}$)
Unbaked austenitic stainless steel	10 h	H_2O	$3 \cdot 10^{-10}$
Unbaked austenitic stainless steel	100 h	H_2O	$3 \cdot 10^{-11}$
Baked stainless steel (150 $°C$)	24 h	H_2	$3 \cdot 10^{-11}$
Austenic stainlees steel (300 $°C$)	24 h	H_2	$5 \cdot 10^{-13}$
Kapton (Polymer 0.125 mm thick)	100 h	H_2O	$< 10^{-9}$
Vespel (Polymer 0.25 mm thick)	$\approx$100 h	H_2O	$< 10^{-8}$

Table 5.1: Typical values of specific outgassing rates for some selected cases, measured at room temperature for stainless steel and some polymers after a given pumping time. From these values we can clearly see the larger outgassing coming from polymers with respect to stainless steel. The illustrated data are taken from [Chi17, Ivo21]. The bakeout temperatures are indicated.

they can diffuse and recombine into molecules at surface. For example, between all the atoms only H has a relevant diffusivity and this explains the high outgassing rate of H_2 from surfaces. Other materials such as polymers can dissolve entire gas molecules (H_2O, O_2, CO_2, etc.) and liquids, e.g. the solubility in the bulk can be very high for H_2O. With respect to metals, an important characteristic of molecules in polymers is their high diffusivity, which increase the outgassing from the surface.
More than 99% of the outgassed species are the five low molecular weight gasses, H_2, H_2O, CH_4, CO, CO_2. Among all them, water vapor is the most problematic when the materials are exposed to air at ambient conditions. In fact, after less than one hour of exposure the surface layers can be saturated with water vapor being chemisorbed [2] or physisorbed[3] forming tens of monolayers on a metal surface. For example, 85% of the outgassing rate of unbaked stainless steel is coming from the desorption of H_2O molecules. Moreover, in the case of polymers the content of gas dissolved is recharged any time the polymeric components are exposed to the air.

Thermal treatments performed by the bakeout processes are used to reduce the material outgassing. This treatment consists in heating the whole vacuum system during part of the pump-down time. By heating, energy is provided to the molecules and atoms allowing them to

[2]Chemical adsorption occurs when the adsorbate molecule is held on the adsorbent surface by chemical forces, for example a covalent chemical bonding.
[3]Physical absorption occurs when the adsorbate gas molecules are held by physical forces like Van der Waals forces.

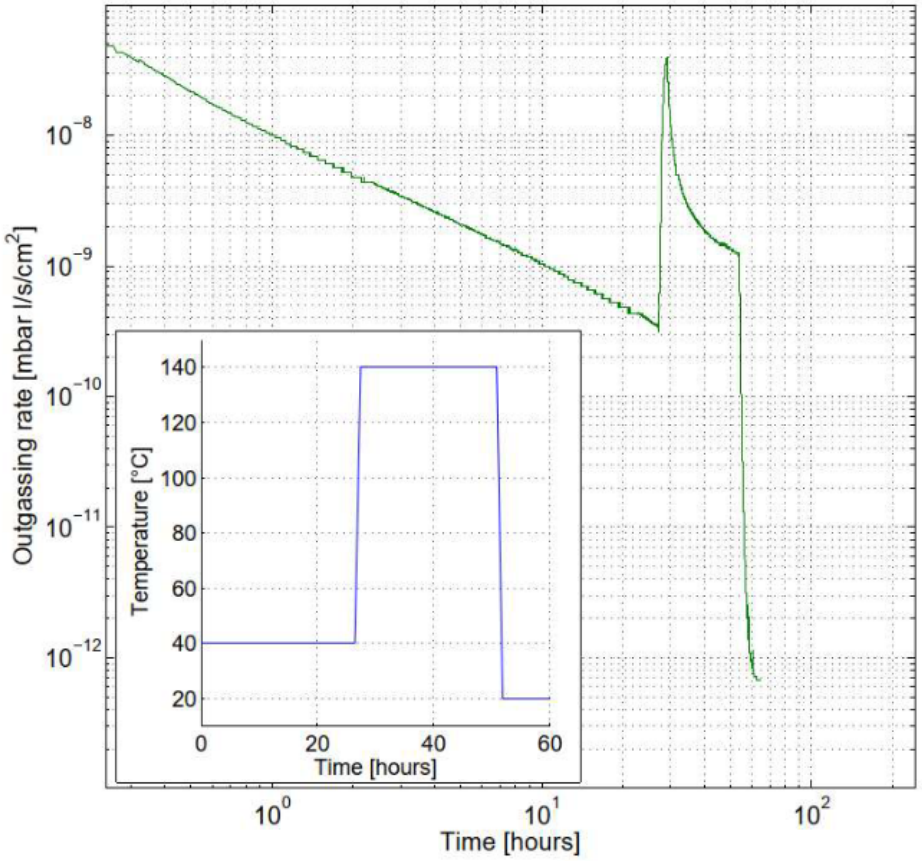

Figure 5.2: Pressure evolution in a metallic vacuum system. The pressure peak corresponds to the beginning of the bakeout ($140°C$). The sudden pressure drop is generated by the cooling of the vacuum vessel to room temperature. The bakeout cycle is shown in the box. The measurements were performed by Riccardo Renzi and José A. Ferreira Somoza at CERN [Ren14].

overcome easily potential wells of the lattice and the activation barrier of the bounding energy that keeps them in the surface. The final effect is to increase the diffusion and desorption rate. The release of molecules from the internal surfaces is accelerated and therefore, the pressure in the system is increased, as well as the quantity of gas evacuated. The decrease of the adsorbed gasses allows one to achieve a much lower pressure when the system is cooled down to room temperature, see the example in figure 5.2.

The bakeout is very important for metals, as stainless steel, and it is particular efficient to remove water layers from the surface. Baking cycles carried out for at least 12 h at temperatures higher than 120 $°C$ are required to remove the weakly bounded mono-layer of surface water. However to remove an innermost chemisorped layer of water from stainless steel, bakeout cycles at 300 $°C$ are required, allowing also for the reduction of other gases desorption such as CO, CO_2 and CH_4. The bakeout treatment is a key element to achieve a good vacuum level and in storage rings the whole ring is baked out at 300 $°C$ during weeks to establish UHV [Kra21].

5.2 Test line foR Extreme Vacuum Observations (TREVO)

TREVO is a test bench for extreme ultra high vacuum investigations developed by our collaboration to perform outgassing rate measurements on solar cells and additional equipments used in NECTAR. A drawing of the line is shown in figure 5.3(a). In figure 5.3(b) a picture showing the current status of the line can be seen.

Fitted with turbo-molecular and ionic pumps, this line is designed to maintain a lower pressure of at least P = 10^{-9} $mbar$. A Residual Gas Analyser [SRS09] allows for the identification of the gases released by measuring[4] an output current which is related to the abundance of the ions with a given m/z (mass to charge ratio). Bayard-Alpert (BA) Style Ionization Gauges [SRS04], located in different points of the lines, allow for a uniform pressure monitoring.

Four tanks can be used simultaneously to store the materials to be studied. The outgassing measurements are performed by closing the tanks over a period of time, which depends on the outgassed species and the precision required for the determination of the outgassing rates. The full line bakeout process is realized by means of heating bands covered by insulating bands, which allow us to reach a maximum temperature of 300 $°C$. The tanks bakeout is performed by means of dedicated heating jackets.

5.3 Outgassing measurements

Since the experiments realized at GANIL (see chapter 3) highlighted the great response of 20x20 mm^2 silicon cells for space applications, outgassing tests on this type of devices were performed to investigate their compatibility with UHV. In figure 5.4, the two cells used during the measurement are shown. The sample on the right side is a prototype obtained after the encapsulation of solar cell in multiple kapton layers developed for UHV applications.

The GSI guideline manual [Wil14] requires for equipments in contact with UHV an outgassing rate $< 5 \cdot 10^{-11} (mbar \cdot l)/(s \cdot cm^2)$ and that the ratio between all summed ion current peaks of mass numbers 41 ... 100 amu (excluding mass 44 amu) and all summed ion current peaks of mass numbers 1 ... 40 amu including 44 amu) must be < 0.01.

We performed the solar cell outgassing measurement by accumulation. In this method, the sample is isolated in a vessel, from the rest of the experimental line for a given amount of time. Because of the outgassing, the pressure in the tank will increase during this time. Subsequently, the valve is opened and the pressure variation due to the expansion of the gas contained in the tank is measured by a pressure gauge or a RGA. The process of accumulation is very sensitive and is the best solution for the measurement of small samples and low outgassing rates, which produce small pressure changes below the detection limit of commonly used vacuum pressure

[4]The RGA is characterised by a sensor exposed to the vacuum, which produces a beam of ions (via gas collisions with electrons emitted from a hot cathode) and filters them according to their mass-to-charge ratio, m/z.

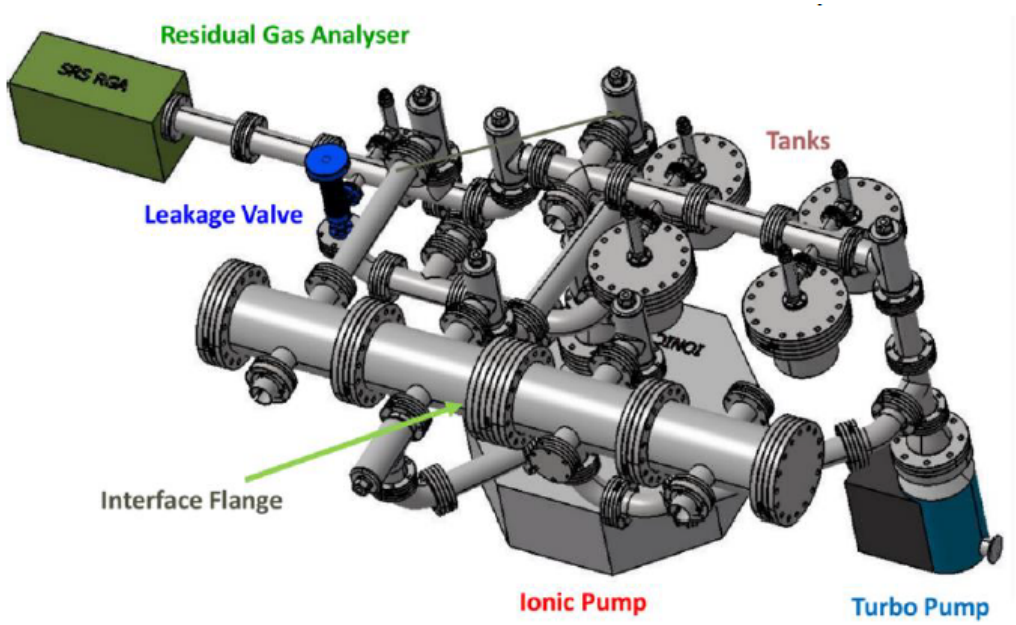

(a)

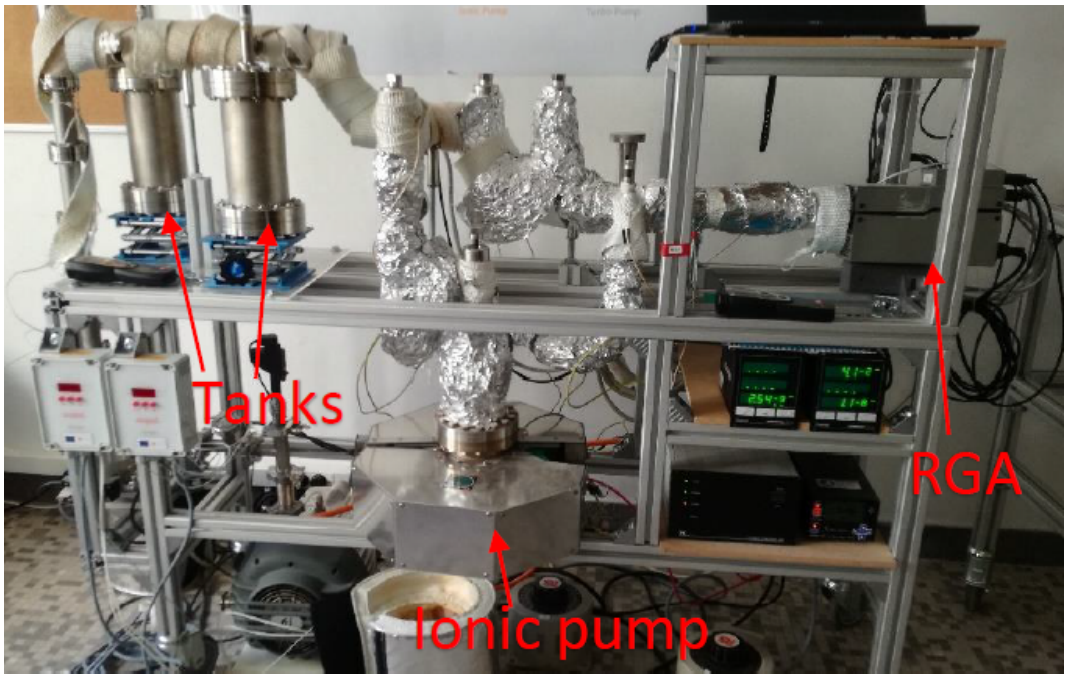

(b)

Figure 5.3: (a) Scheme of the test line TREVO and (b) picture of the TREVO test bench in its current status.

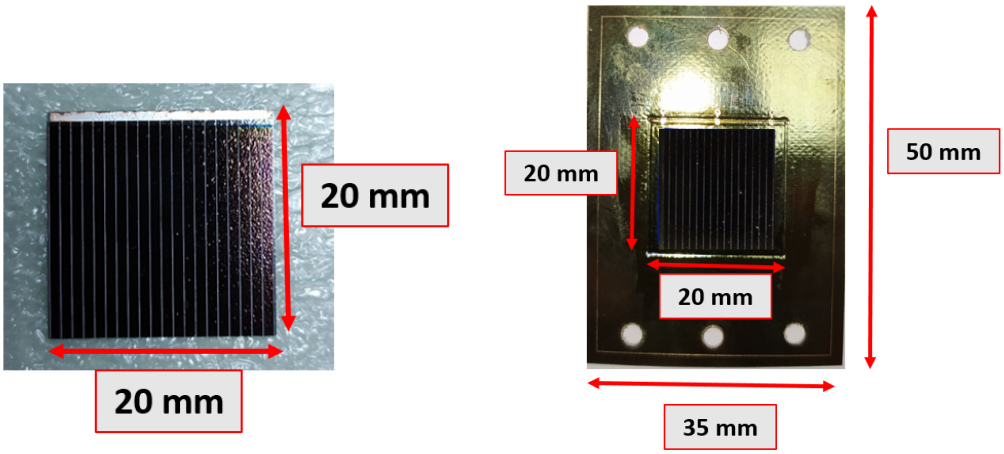

(a) (b)

Figure 5.4: 20×20 mm^2 silicon space cells for which the outgassing rate was measured. Part (a) shows the picture of a normal cell (not-encapsulated) while part (b) shows the encapsulated cell.

gauges.

During the tests, the selected sample was inserted in one of the tanks available in the test bench and a pumping down process with a Turbo Molecular (TM) pump followed by a bakeout cyles carried out for 24 h at 100 $°C$ was performed. An empty tank was subject to the same process (tank 1) in order to determine the gasses coming from the inner tank walls (background or blank). In figure 5.5, we present the evolution of the pressure measured during the pumping down (blue line for the tank containing the encapsulated cell and yellow line for the empty tank) and the bakeout process at 100 $°C$ (red line). We can see the contribution of the tested materials in the total outgassing by the larger initial pressure registered for the tank containing the cell. The significant impact of the bakeout process is reflected by the fast decrease of the pressure indicated by the red line.

This first baking procedure was required to reduce the tank outgassing caused by insertion of the sample, during which the inner tank walls were exposed to air. Even if N_2 treatment[5] was implemented during the opening to decrease the adsorption of gas, a baking cycle was required to remove the remaining contaminants (mainly water vapor).

The tank was then isolated by means of a valve and gasses were accumulated for a given amount of time. In parallel, one of the other tanks available in the line was subject to the same procedure (exposition to air, pumping, baking, etc.) and then closed for the same amount of time. The objective was to measure the pressure variation coming from the tank without the sample and use it as a background value in the outgassing calculation. After 24 h of accumulation the valve was progressively opened and the evolution of the partial pressure $P(t)$, as a function of the

[5]in this procedure nitrogen N_2 is introduced by means of a pipe on the tank, during the opening, to create a thin layer over the tanks internal surfaces reducing in this way the contamination by water vapor.

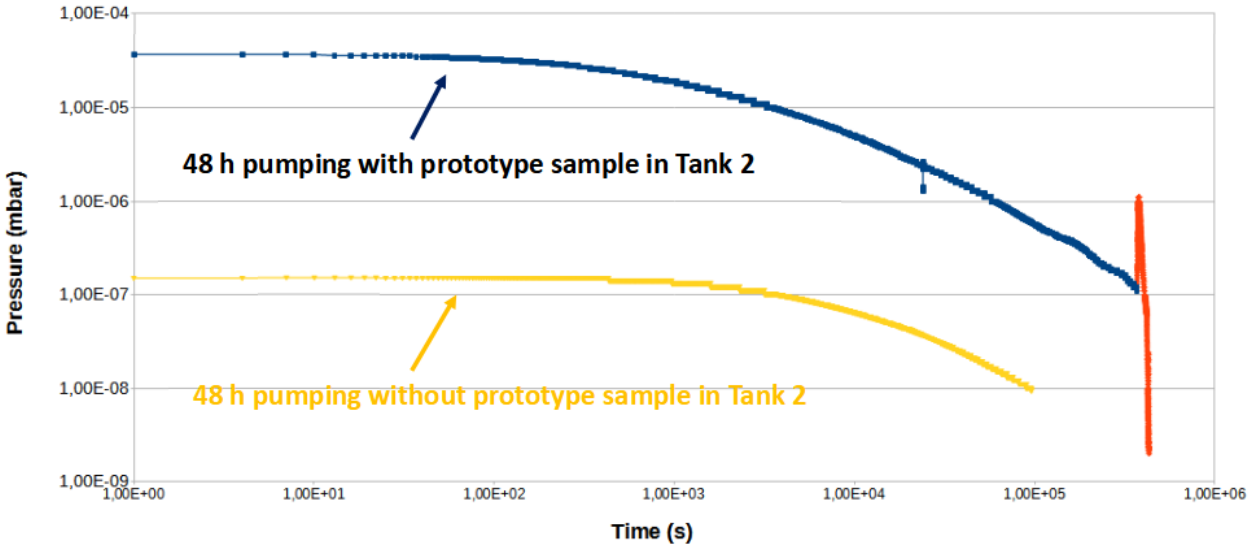

Figure 5.5: Pressure evolution as function of the time for a tank containing and not the sample. In the blue and yellow lines the effect of a pumping with TM pump is shown, while in red the increase and decrease obtained during and after the bakeout of 24 h at 100 $°C$.

time, was measured and recorded during the gas expansion by the RGA. The operation was repeated with the empty tank.

In figure 5.6 we show the evolution of the pressure after the opening of the tank containing the sample (red line) and the empty tank (blue line). In figure 5.6(a) the sample investigated was the not-encapsulated cell while in figure 5.6(b) the sample was the encapsulated cell. Respect to the not-encapsulated cell, for which the pressure evolution is close to the background value, the encapsulated one exhibits a large pressure increase even after the baking cycle at 100 $°C$. For this cell, an additional heating treatment at 200 $°C$ was required to reduce significantly the pressure increase from the sample tank. The effect of a second baking on both the tank and sample degassing can be seen in the mass spectrum of figure 5.7 obtained with the RGA at a specific instant of time after the stabilization of the pressure. In figure 5.7(a) the mass spectra obtained for the tank containing the encapsulated cell, after the first baking is compared to the empty tank (background). Water molecules can contribute to the peak at 18 but also to the peaks at 17 and 16, because O^+ and HO^+ is produced by the fragmentation of the H_2O molecules by the RGA. For the empty tank we can see a strong decrease of the water peaks and of hydrogen (H_2), not drawn in the spectrum. The main components, with a partial pressure larger than 10^{-9} $mbar$, are the CO and the CO_2 molecules characteristic of stainless steel after baking treatment. For the sample tank spectrum, with respect to the background, we observe an increase of the peaks associated to CO, CO_2, H_2O and of the peak at 40, corresponding to Argon. Together with the increase of the peak at 14 relative to N^+, we can observe that the relative intensity of the Ar^+ peak with respect to the peak at 28 (N_2^+) is close to about 1%, approaching the ratio that these two gases have in the atmosphere (1.2%). This fact, together

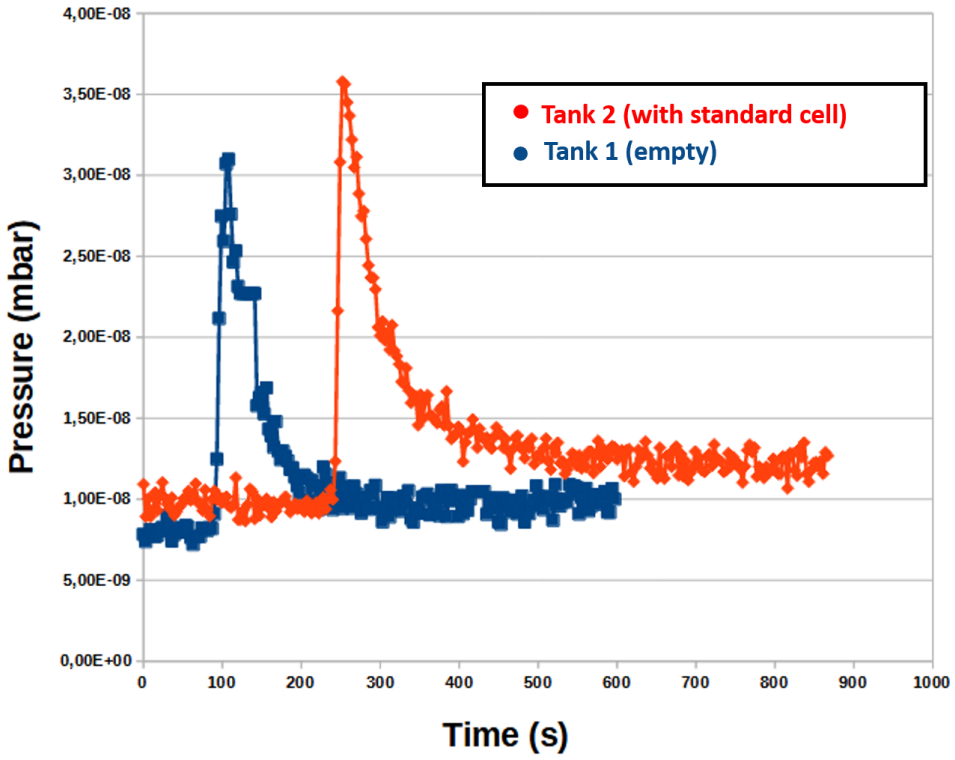

(a)

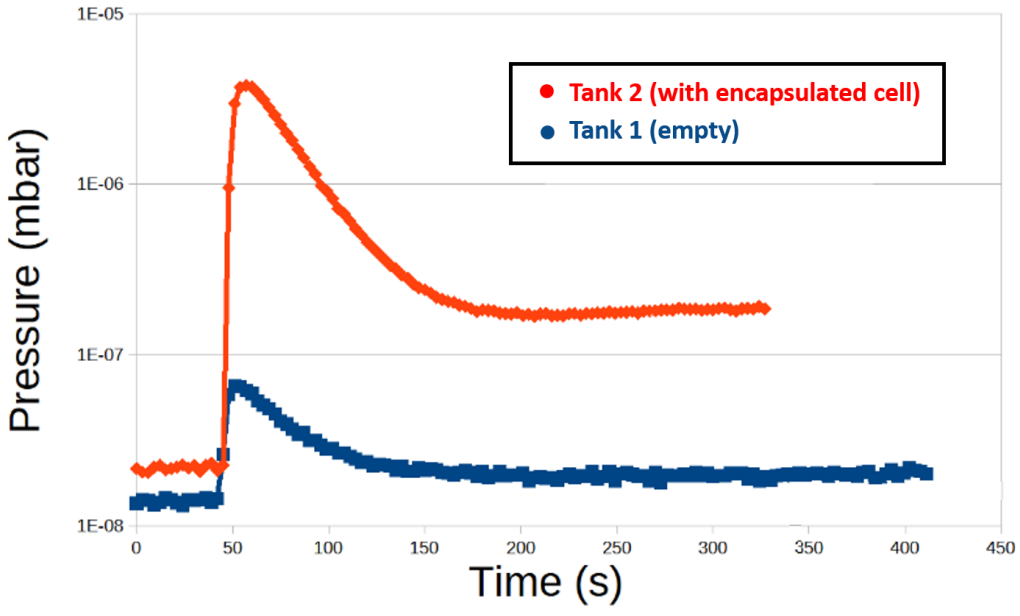

(b)

Figure 5.6: Evolution of the pressure after an accumulation of 24 h for a tank housing a sample (in red) and for an empty Tank (in blue) after a heating treatment at 100 $°C$. Part (a) shows the results for the standard cells and part (b) for the encapsulated cell.

with the slightly higher nitrogen and oxygen peaks, indicate the presence of trapped air in the kapton layer which encapsulate the cell. Masses larger than 50 amu are not displayed since no significant contribution from heavier components was observed. The absence of components larger than mass 50 (i.e. non-atmospheric components) indicated the high surface purity of the tested sample.
In figure 5.7(b) the mass spectrum after the second bakeout (in red) at 200 C° is compared to the one obtained from the first baking (in blue). Due to the high temperature bakeout, the trapped air is completely removed and the partial pressure of most of the components is below few 10^{-9} $mbar$. The peak of CO/N_2 is the unique one that shows a significant partial pressure, but this probably comes from the degassing of CO from the stainless steel walls of the tank or the gauge of the BA and RGA.

In the measurement of the outgassing the background B_i present in the experimental line was firstly measured for each mass (i). Subsequently the valves of the empty tank (T_1) and of the sample tank (T_2) were opened, following the procedure previously described, and the RGA was used to measure the partial pressure evolution as function of the time. Since the RGA provides in each scan (a) the measurement of the partial pressure P_i^a for a given mass (i), after subtracting the background B_i a sum over all the scans was realized to determine the total partial pressure P_i:

$$P_i = \sum_a (P_i^a - B_i) \tag{5.2}$$

The total partial pressure for each mass calculated in equation (5.2) was then normalized to accumulation time (t_{acc}). This procedure allows to calculate for each mass, the partial pressure rate respectively for the empty tank T_1 and for the tank T_2 housing the sample. In this way, the specific sample outgassing rate q could be calculated by the expression:

$$q = \sum_i (P_i^{T_2} - P_i^{T_1}) \cdot \frac{V_{tank}}{S_{sample}} \tag{5.3}$$

where the pressure rate for a specific component in tank T_1 (empty) is subtracted to the corresponding pressure rate in the tank T_2. Finally the different partial pressures are summed together and multiplied by the tank volume divided by the sample surface.
Outgassing rate measurements were performed before and after each heating treatment of the samples to monitor their effect. The results are summarized in table 5.2. Unfortunately, due to the large H_2 degassing coming from the tank walls, it was not possible to correctly measure the hydrogen partial pressure (mass 2) of our small surface samples. For this reason the hydrogen contribution was not taken into account in the outgassing measurement presented in this thesis work. However, as mentioned in [Bat18], hydrogen desorption is strongly reduced with baking cycles of 100 $^{\circ}C$ for 24 h in polymers like kapton. Furthermore, solar cell outgassing test results in [Ana20] highlighted a low outgassing rate $< 10^{-11}(mbar \cdot l)/(s \cdot cm^2)$ after baking cycles carrier for 48 h at 200 $^{\circ}C$ in this way the amount of hydrogen released can be neglected.

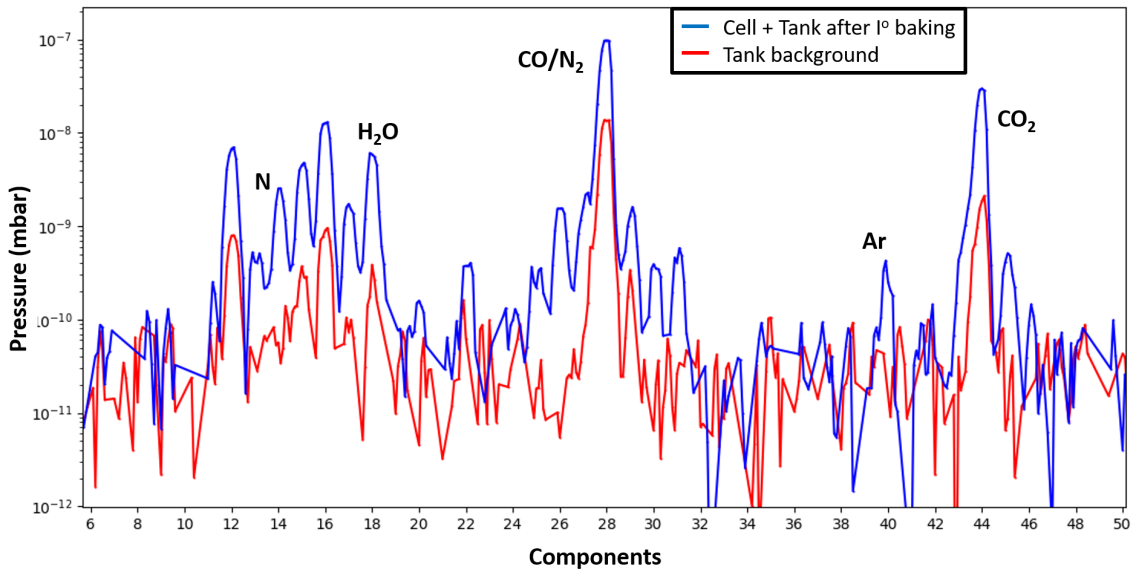

(a)

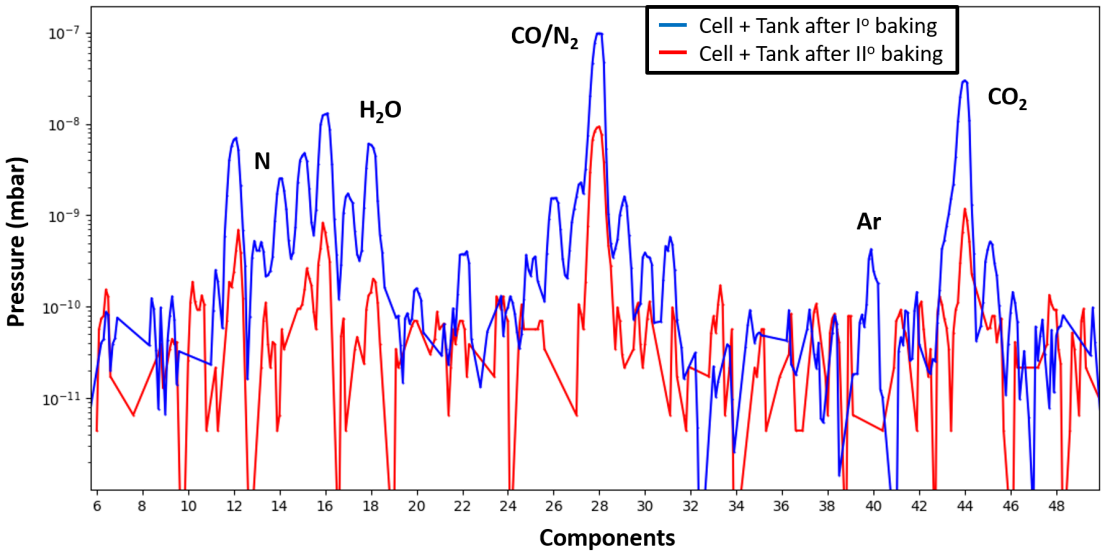

(b)

Figure 5.7: Comparison of the partial pressure mass spectra (from 5 up to 50 *amu*) measured for a tank containing the encapsulated cell. Figure (a) shows the mass spectra of the tank T_2 containing the sample (in blue) and the empty tank T_1 (in red) after the I° baking. In figure (b), the effect of the second baking cycle on the mass spectra (in red) is shown with respect to the first baking cycle (in blue) for the sample tank T_2. The main gas species contributing to the outgassing are specified.

Table 5.2: Results of the outgassing rate measurements carried out after different baking cycles.

	Bakeout 100 $°C$ for 24 h		**Bakeout 200 $°C$ for 24 h**	
	Outgassing $(\frac{mbar \cdot l}{s \cdot cm^2})$	**Ratio**	**Outgassing** $(\frac{mbar \cdot l}{s \cdot cm^2})$	**Ratio**
GSI requirement	$< 5 \cdot 10^{-11}$	< 0.01	$< 5 \cdot 10^{-11}$	< 0.01
Sample	**Tested solar cells**			
20×20 mm^2 space cell	$2.52 \cdot 10^{-13}$	0.0065	$< 10^{-13}$	<0.001
20×20 mm^2 space cell encapsulated	$1.045 \cdot 10^{-10}$	0.051	$5.15 \cdot 10^{-13}$	0.0055

Not encapsulated solar cells provided a very small outgassing already after the first baking process confirming the results observed in [Ana20]. Regarding the encapsulated cells, the kapton encapsulation is responsible for a significant outgassing still visible after the first baking cycle. A second heating treatment was required to reduce the final outgassing value below the reference provided by the GSI for UHV equipments.
Regarding the ratio between all summed ion current peaks of mass numbers 41...100 *amu* mainly hydrocarbons, (except 44 *amu*) and all summed ion current peaks of mass numbers 1...40 *amu* (including 44 *amu*) the results are almost the same. Standard cells meet the GSI requirement while, for the encapsulated ones, a secondary baking treatment was required to meet the GSI requirements, as shown in table 5.2.

5.4 Cell response after the bakeout processes

The quality of the solar cells response was tested after different bakeout processes at 100 $°C$ and 200 $°C$ carried out for 24 h by exposing them to a ^{252}Cf source before and after the bakeout process. The procedure described in section (3.2) to evaluate the quality of the solar cells with Schmitt parameters [Sch66] was used. In figure 5.8 the spectra before and after the heating treatment for standard (a) and encapsulated (b) cells are shown.

In general, no significant degradation of the cell performances can be observed from the spectra. In figure 5.8(a) we see that the amplitude of the cell decreases by about few hundred mV after the baking procedure. On the contrary, in figure 5.8(b) we see that the baking cycles lead to an increase of the cells amplitude. The negligible impact of the heating treatment on the cells response is confirmed also by the calculated Schmitt parameters presented in table 5.3, which are almost unchanged.

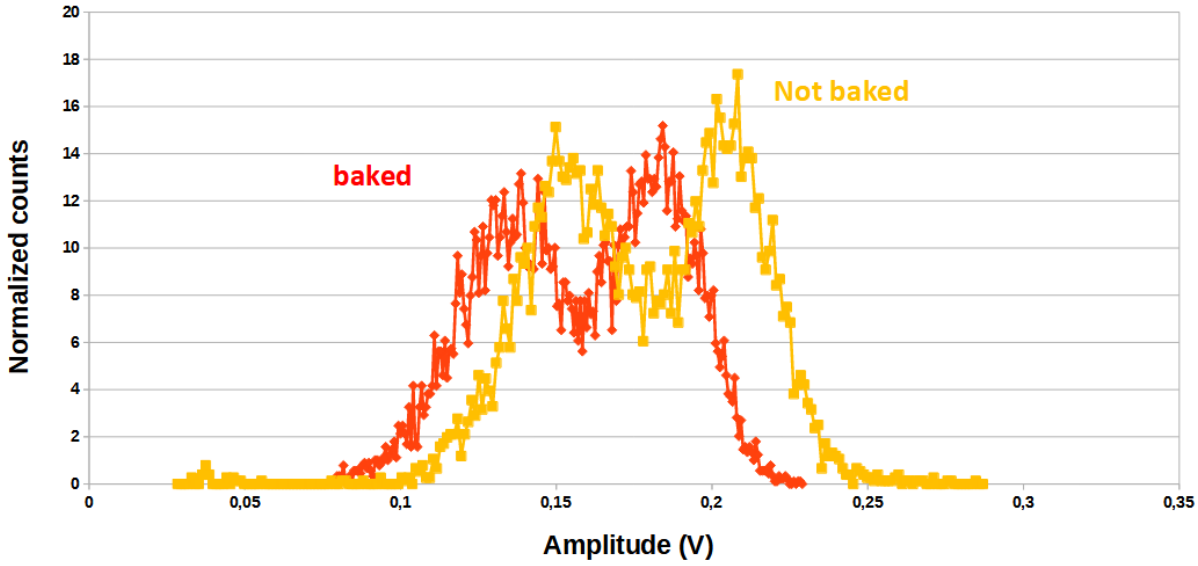

(a)

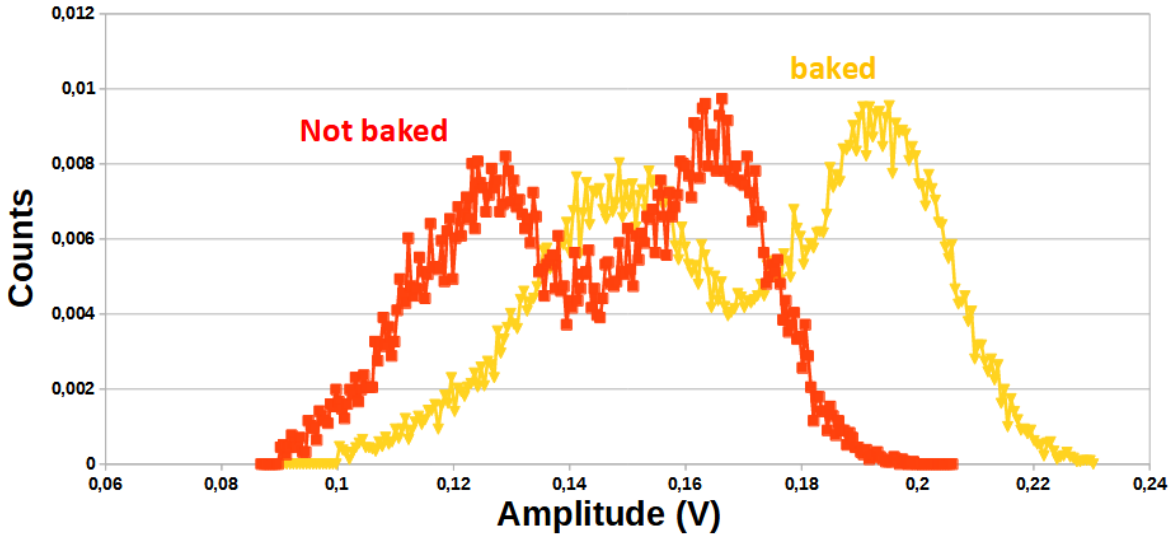

(b)

Figure 5.8: ^{252}Cf fission fragment spectra measured before and after the baking cycles for a standard cell (a) and the encapsulated (b) solar cell.

Cell Type	C_L/C_V **(∼ 2.85)**	C_H/C_V **(∼ 2.2)**	C_H/C_V **(∼ 1.3)**
Before Baking			
Encapsulated cell	2.69	2.5	1.19
Standard cell	2.49	2.09	1.19
After Baking (48 h 200 $°C$)			
Encapsulated cell	2.7	2.34	1.15
After Baking (24 h 100 $°C$, 24 h 200 $°C$)			
Standard cell	2.41	2.03	1.18

Table 5.3: Results of the spectra analysis perfomed using Schmitt's parameters [Sch66]. The reference values of the parameters are shown on the top of the 1st, 2nd adn 3rd column in bold.

Chapter 6

Conclusion and perspectives

Solar cells appears as a very promising alternative to standard silicon detectors for the detection of heavy ions. Indeed, the quality of the response of solar cells to heavy ions is comparable to the one of silicon detectors and solar cells have shown to be more resistant than Si detectors to radiation damage. In addition, they are very cost effective and have a very flexible geometry. The radiation resistance of solar cells is particularly interesting for experiments conducted inside storage rings, which are operated in UHV. For this reason the NECTAR project aims at developing an in-ring fission detector made of solar cells. This requires to evaluate first the response of solar cells to fission fragments with energies above 1 MeV and their UHV compatibility. These two aspects were the objectives of the second part of this thesis.

We performed an experiment at the GANIL facility with ^{84}Kr beam at 5, 10, 15 MeV/u where we characterized the response of household and space solar cells of 10x10 mm^2 and 20x20 mm^2 surface. We observed a saturation of solar cells amplitude signal with increasing beam energy and we measured an energy resolution ($\frac{RMS(E)}{<E>}$) ranging from 1% to 3% for household 10x10 mm^2 and 20x20 mm^2 space cells. The time resolution varied between 2.5 and 4.5 ns (FWHM). It was the first time that we observed such good performances for cells as large as 20x20 mm^2. The response of the cells was stable during irradiation for 1 one hour at a rate of few thousand pps. Above one hour of irradiation the amplitude started to gradually decrease and the energy resolution to deteriorate, until a stabilization was reached. A similar behaviour was found when the irradiating at larger rates of 50 thousands pps. Interestingly, the time response was stable for all the rates. Solar cells for space applications were found to be more radiation resistant.

We perform a significant effort to understand the observed response of the solar cells and the mechanism involved in the signal generation of the cell, the so-called field funneling effect. Within this frame, we used the ATLAS Silvaco software to simulate the current as a function of time generated by the interaction with a ^{84}Kr of different energies. With this simulation we could calculate the corresponding preamplifier output. This allowed us to reproduce the observed saturation, which takes place around 7 MeV/u and is due to a loss effective collection

of charges via drift funneling and to recombination effect that, take place when the energetic ions penetrate deeply into the substrate. To our knowledge, it is the first time that such an study has been performed.

We investigated the UHV compatibility of the 20x20 mm^2 space cells. The studies were done for a standard and an encapsulated cell. In both cases the measured outgassing was well below the limits given at GSI. In addition, the response was not affected by the bakeout processes at 200 $°C$.

All this work has demonstrated the good performances of 20x20 mm^2 space cells, which will be used to build a detector for counting fission fragments in coincidence for our next experiment in 2024. In this experiment we will use new pre-amplifiers which are being developed at the LP2iB and will provide and improve signal-to-noise ratio. It would be interesting to farther investigate the response of solar cells to different ion species and energies.

Another research axis to explore is to readout the finger contacts on the cell surface to extract information on the position. Future applications of solar cells will depend also on the possibility to produce customized detectors in terms of thickness while ensuring a low production cost.

Bibliography

[Aji91] N. Ajitanand, et al., Nucl. Instrum. Methods Phys. Res. A 300 (2), 1991 354–356.

[Ana20] Ana Henriques et al., Nuclear Inst. and Methods in Physics Research, A 969 163941, 2020

[And18] J. Anders et al., Journal of Instrumentation, Volume 13, October 2018

[ATLAS] ATLAS Silvaco International, https://silvaco.com/tcad/

[Aug19] André Augusto et al., IEEE 46th Photovoltaic Specialists Conference (PVSC), 2019

[Bea92] Jerome Beaucour, Conference Paper, February 1992, DOI: 10.1109/REDW.1992.247329

[Bar20] Philippe Barberet, "AIFIRA : Applications Interdisciplinaires des Faisceaux d'Ions en Région Aquitaine", Scientific committee IN2P3 - 25/02/2020, CENBG-Université de Bordeaux – CNRS/IN2P3

[Bat18] Katharina Battes, Article in Journal of Vacuum Science & Technology A Vacuum Surfaces and Films, March 2018

[Chi17] Paolo Chiggiato, CERN Accelerator School (CAS) on Vacuum for Particle Accelerators, June 18^{th} 2017

[Cur75] Denis J. Curtin et al., IEEE Transactions on Aerospace and Electronic Systems, Volume: AES-11, Issue: 4, July 1975

[Edm91] Larry D. Edmonds, IEEE Transactions on Nuclear Science 38(5):999 - 1004, November 1991

[Edw77] D. Edwards Jr., Journal Vacuum Science Technology, vol. 14, no. 1, pp. 606-610, 1977

[GEF19] Beatriz Jurado, Karl-Heinz Schmidt, "GEF: A General Description of Fission Observables", Version 2019/1.1

[Gor85] Chandra Goradia, Journal of Applied Physics 57, 4752, 1985

[Ker02] Mark J. Kerr and Andres Cuevas, Journal of Applied Physics 91, 2473, 2002

[Kes10] G. Kessedjian, et al., Phys. Lett. B 692 (5) 297–301, 2010

[Kes15] G. Kessedjian, et al., Phys. Rev. C 91 044607, 2015

[Kim03] Kimerling L C 2003 J. Appl. Phys. 45, 1839

[Kir79] S. Kirkpatrick, IEEE Trans. Electron Devices, ED-26, p. 1742-1753, Nov. 1979

[Kog17] J. Koglin, et al., Nucl. Instrum. Methods Phys. Res. A 854 64–69, 2017

[Kra84] H.W. Kraner, et al., Nucl. Instrum. Methods Phys. Res. B 225 615–618, 1984

[Kra21] A. Kramer, "Vacuum Requirements for GSI and FAIR", Accelerator Seminar (GSI Darmstadt), 2021

[Kur95] M. Kurokawa, et al., IEEE Trans. Nucl. Sci. 42 (3) 163–168, 1995

[Hah14] Giso Hahn and Sebastian Joos, "Chapter One - State-of-the-Art Industrial Crystalline Silicon Solar Cells", in Semiconductors and Semimetals, Volume 90, 2014, Pages 1-72, 2014

[Hal95] G. Hall, et al., Nucl. Instrum. Methods Phys. Res. A 368 199–214, 1995

[Hsi81] C. Hsieh, et al., Electron Device Lett. IEEE 2 103–105, 1981

[Hu82] C. Hu, IEEE Electron Device Letters, EDL-3, No. 2, pp. 31-34, Feb. 1982

[Ivo21] Ivo Wevers, "Outgassing of Technical Polymers PEEK, Kapton, Vespel & Mylar Vacuum, Surfaces & Coatings Group", Technology Department, ARIES 2021

[Lau97] B. Laune, AIP Conference Proceedings 392, 381, 1997

[Lia88] E. Liatard, et al., Nucl. Instrum. Methods Phys. Res. A 267 231–234, 1988

[Lin87] V.A.J. Van Lint, et al., Nucl. Instrum. Methods Phys. Res. A 253 453–459, 1987

[Lin02] G. Lindström, et al., Nucl. Instrum. Methods Phys. Res. A 512 30–43, 2002

[Lop16] Maria Cruz Lopez-Escalante et al., Solar Energy, Volume 131, Pages 61-70, June 2016

[McL82] F.B. McLean and T.R. Oldham, U.S. Army Electronics Research and Development Command, IEEE Transactions on Nuclear Science, Vol. NS-29, No. 6, December 1982

[Par16] M. Parans Parantham et al., "Semiconductor materials for solar photovoltaic cells", Springer series in Materials Science 218, 2016

[Pro14] Paul Procela et al., "Analysis of the impact of doping levels on performance of back contact - back junction solar cells", 4th International Conference on Silicon Photovoltaics, SiliconPV 2014

[Ren14] R. Renzi, Master Thesis, University of Padova (Italy), 2014

[San19] R. Pérez Sánchez, et al., Nucl. Instrum. Methods Phys. Res. A 933 63–70, 2019

[Sch52] W. Shockley and Read, W. T., Physical Review, vol. 87, p. 835, 1952

[Sch66] H. W. Schmitt and F. Pleasanton, Nucl. Instrum. Meth. 40, 204, 1966

[Sie79] G. Siegert et al., Nucl. Instrum. Methods Phys. Res. 164 (3) 437–438, 1979

[She06] Manav Sheoran et al., IEEE 4th World Conference on Photovoltaic Energy Conference, 2006

[Shi69] F. Shiraishi, et al., Nucl. Instrum. Methods Phys. Res. 69 316–322, 1969

[Sol19] Solar made, 2019, https://www.solarmade.com/

[SRS09] Stanford Research Systems, "Models RGA100, RGA200, and RGA300 Residual Gas Analyzer", Revision 1.8, May 2009

[SRS04] Stanford Research Systems ,"IGC 100 Ion Gauge Controller", 2004

[Tab99] G. Tabacaru et al., Nuclear Instruments and Methods in Physics Research A 428 (1999)

[Tek] https://www.tek.com/en/products/oscilloscopes/tbs2000

[Wil14] St. Wilfert, "Technical Guideline Number Vacuum Properties Acceptance Test with Bake-out", GSI, 2014

[Yam01] Masafumi Yamaguchi, Solar Energy Materials and Solar Cells, Volume 68, Issue 1, April 2001, Pages 31-53, 2011